

Plasma Chemistry Modelling for CO₂ and CH₄ Conversion in Various Plasma Types

Proefschrift voorgelegd tot het behalen van de graad van doctor in de wetenschappen aan de Universiteit Antwerpen te verdedigen door

Stijn Heijkers



PROMOTOR
prof. dr. Annemie Bogaerts

Faculteit Wetenschappen
Departement Chemie
Antwerpen 2020

 Universiteit
Antwerpen



Faculteit Wetenschappen
Departement Chemie

Plasma Chemistry Modelling for CO₂ and CH₄ Conversion in Various Plasma Types

Proefschrift voorgelegd tot het behalen van de graad
van Doctor in de Wetenschappen aan de
Universiteit Antwerpen te verdedigen door

Stijn Heijkers

Promotor: Prof. Dr. Annemie Bogaerts

Antwerpen, 2020

Dankwoord

Deze thesis zou niet tot stand gekomen zijn zonder de hulp en inzet van een heleboel mensen. Daarom bedank ik in eerste instantie mijn promotor Annemie Bogaerts, die mij de kans heeft gegeven zowel mijn masterthesis als deze thesis tot een goed einde te kunnen brengen. Ook bedank ik haar voor mijn shift naar een sportiever leven en specifiek om mij aan te sporen o.a. de ten miles mee te lopen. Daarnaast bedank ik ook mijn bureaumaatjes Kristof Bal, Jonas Van der Paal en Yannick Uytendhouwen die mijn aparte muzieksmaak en karakter uiteindelijk wisten te appreciëren en mij bij moeilijke momenten er terug bovenop hebben geholpen. Ik bedank Yannick specifiek ook voor het ontwerp van mijn cover. Ik bedank Ramses Snoeckx, Weizong Wang, Marleen Ramakers en Tomas Kozak voor de nodige initiële kennis, publicaties en extra begeleiding tijdens mijn masterthesis en doctoraat. Ik bedank Vincent Vermeiren, Inne Michielsen, Georgi Trenchev, Claudia Verheyen, Elise Vervloessem, Eline Biscop, Senne Van Alphen, Joachim Slaets, Fanny Girard, Yannick Engelmann, Qi Xin, Sanne Aerts, Jeroen Van Dijck, Charlotte Vets, Maryam Aghaei en Erik Neyts voor de interessante gesprekken tijdens een kopje koffie en tijdens de middagpauze. Daarnaast bedank ik de rest van PLASMANT en ook LADCA voor deze leerrijke ervaring.

Tijdens mijn doctoraat heb ik ook de kans gehad samen te werken met verschillende groepen en ik bedank in het bijzonder de samenwerking met Peter Koelman, Samaneh Tadayon Mousavi, Wouter Graef, Diana Mihailova, Jan van Dijk en Luca Matteo Martini van de TU Eindhoven en eveneens de samenwerking met Giorgio Dilecce en Paolo Tosi van Università di Trento.

Ik bedank uiteraard mijn naaste familie, nl. Annemie Goris (mama), Guido Heijkers (papa), Elke Heijkers (zus) en ook Robin Mampaey voor de mentale steun die ik af en toe nodig had. Daarbovenop bedank ik mijn vroegere overbuur Pia Struyf, de familie Truijen-Somers en vooral Stefaan Truijen, mijn vrienden uit het middelbaar en in het bijzonder Matthijs Van Boxel, Jean Beelaerts, Matthias Loeckx, Ruben Heremans en Sébastien Jacquet. Ik bedank ook mijn trainingmakers van I-fitness Lier en vooral Nils Reel, Erik Schulte, Kathleen Coenen, Frank Van Campenhout en Sandra Bracke om mij ook “in

shape” te houden. Ik bedank tenslotte ook Kenneth Bral, Mara Van Gisbergen, Danny Bierens, Britt Van Duyse, Lesley Heyndrickx, Liese Blevi, Joeri De Maeyer, Liesbeth Bens, Elien De Volder, Bram Van Moer en Sophie Iserbiet voor de leuke feestjes/festivals/skireizen die een welkome ontspanning waren.

Table of Contents

CHAPTER 1: INTRODUCTION.....	7
1.1 THE ENERGY CHALLENGE OF THE 21ST CENTURY AND THE STORAGE PROBLEM	8
1.2 CO ₂ AND ITS CONVERSION OPPORTUNITIES.....	9
1.3 VIBRATIONAL MODES OF CO ₂	12
1.4 MOTIVATION FOR PLASMA TECHNOLOGY	12
1.4.1 <i>What is plasma?</i>	12
1.4.2 <i>Plasma technology for gas conversion</i>	14
1.5 DIFFERENT PLASMA SOURCES USED FOR CO ₂ CONVERSION.....	15
1.5.1 <i>Dielectric barrier discharge (DBD)</i>	15
1.5.2 <i>Microwave (MW) discharge</i>	16
1.5.3 <i>Gliding arc (GA) discharge</i>	17
1.5.4 <i>Nanosecond Repetitively Pulsed (NRP) discharge</i>	19
1.6 AIM OF THIS PHD THESIS	20
CHAPTER 2: GENERAL MODEL DESCRIPTION	21
2.1 BASIC EQUATIONS	22
2.2 GENERAL APPROXIMATIONS IN THE 0D MODEL	27
CHAPTER 3: CO₂ CONVERSION IN A GLIDING ARC PLASMATRON (GAP).....	29
3.1 INTRODUCTION.....	30
3.2 CHEMISTRY SET.....	31
3.3 MODELING THE GAP REACTOR WITH A 0D APPROACH	32
3.4 PLASMA CHARACTERISTICS INSIDE THE ARC	38
3.5 OVERALL CO ₂ CONVERSION AND ENERGY EFFICIENCY	42
3.6 CHEMICAL PATHWAY ANALYSIS OF CO ₂ CONVERSION.....	44
3.7 ROLE OF THE VIBRATIONAL LEVELS IN THE CO ₂ DISSOCIATION	48
3.8 OPTIMIZING THE CO ₂ CONVERSION AND ENERGY EFFICIENCY.....	49
3.8.1 <i>Influence of the gas temperature</i>	51
3.8.2 <i>Removing the O₂ molecules</i>	54
3.9 CONCLUSION.....	55
3.10 APPENDIX	57
CHAPTER 4. DRY REFORMING OF METHANE IN A GAP.....	71
4.1 INTRODUCTION.....	72
4.2 CHEMISTRY SET.....	72
4.3 CALCULATED AND MEASURED CONVERSION AND ENERGY EFFICIENCY	76
4.4 CALCULATED PLASMA CHARACTERISTICS	79
4.5 CALCULATED SPECIES DENSITIES INSIDE THE PLASMA	84
4.6 CHEMICAL KINETICS ANALYSIS OF THE UNDERLYING PROCESSES	86
4.7 CONCLUSION.....	88
4.8 APPENDIX	90
CHAPTER 5: COMBINING CO₂ CONVERSION AND N₂ FIXATION IN A GAP	128
5.1 INTRODUCTION.....	129
5.2 CHEMISTRY SET	130
5.3 CALCULATED AND MEASURED CONVERSION AND ENERGY EFFICIENCY	131
5.4 UNDERLYING MECHANISMS AS REVEALED BY THE MODEL	134
5.5 CONCLUSION.....	149

5.6 APPENDIX	149
CHAPTER 6: CO₂ CONVERSION IN NANOSECOND REPETITIVELY PULSED (NRP) DISCHARGE.....	155
6.1 INTRODUCTION.....	156
6.2 CHEMISTRY SET.....	157
6.3 MODELLING THE NRP DISCHARGE WITH A 0D APPROACH	158
6.4 VALIDATION OF THE MODEL AND OVERALL PLASMA CHARACTERISTICS.....	167
6.5 CHEMICAL PATHWAY ANALYSIS OF CO ₂ CONVERSION.....	173
6.6 SIGNIFICANT ROLE OF THE CO ₂ VIBRATIONAL LEVELS.....	175
6.7 COOLING AS A SOLUTION TO IMPROVE THE CONVERSION AND ENERGY EFFICIENCY?	180
6.8 CONCLUSION.....	186
6.9 APPENDIX	188
CHAPTER 7: CH₄ CONVERSION IN THREE DIFFERENT PLASMA SOURCES.....	200
7.1 INTRODUCTION.....	201
7.2. CHEMISTRY SET.....	202
7.3. MODELLING THE DIFFERENT PLASMA REACTORS WITH A 0D APPROACH.....	204
7.3.1 Dielectric barrier discharge (DBD).....	204
7.3.2 Microwave (MW) plasma	207
7.3.3 Gliding arc (GA) plasma.....	210
7.4 DBD PLASMA.....	212
7.4.1 Comparison of calculated and measured conversion, energy cost and selectivities.....	212
7.4.2 Underlying reaction pathways	218
7.5 MW PLASMA.....	221
7.5.1 Comparison of calculated and measured conversion, energy cost and selectivities	221
7.5.2 Underlying reaction pathways	227
7.6 GAP	231
7.6.1 Comparison of calculated and measured conversion, energy cost and selectivities	231
7.6.2 Underlying reaction pathways	233
7.7 PLASMA VS. THERMAL CONVERSION	236
7.8 CONCLUSIONS	242
7.9 APPENDIX	243
SUMMARY AND FUTURE OUTLOOK.....	275
SAMENVATTING EN TOEKOMSTPERSPECTIEF	278
LIST OF ARTICLES PUBLISHED	281
LIST OF CONFERENCE CONTRIBUTIONS	282
BIBLIOGRAPHY.....	283

Chapter 1: Introduction

1.1 The Energy Challenge of the 21st Century and the Storage Problem

In our history, the Industrial Revolution was responsible for a huge leap in human development and welfare. This however required an enormous demand in energy and thus fossil fuels to achieve this. This demand in energy and fossil fuels kept rising with the further industrialisation of developing countries. The burning of fossil fuels has also led to an increasing emission of greenhouse gases, in particular CO₂. These anthropogenic emissions of greenhouse gases disturb the natural carbon cycle, resulting in an increase of atmospheric CO₂ concentrations from 280 ppm before the Industrial Revolution until 400 ppm in 2014¹⁻³. This increase in atmospheric CO₂ concentrations, mainly caused by mankind itself⁴, leads to accelerated global warming, which is illustrated in Figure 1. This in turn will lead to a higher frequency of extreme weather, which threatens our society more and more².

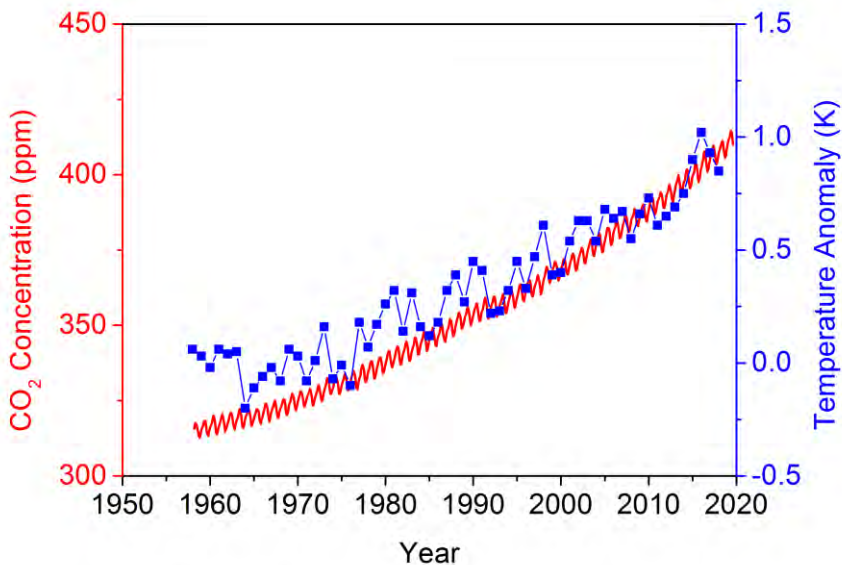


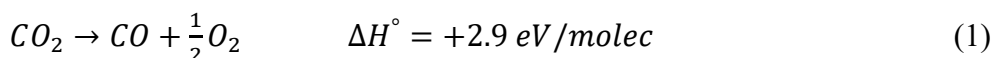
Figure 1: Annual trend of atmospheric CO₂ concentration (left y-axis) and globally-averaged temperature anomaly with respect to the average temperature in 1951-1980 (right y-axis). Data taken from NASA/NOAA⁵.

To reduce global warming, more investments in renewable energy sources are needed. In 2030, more than 30 % of our energy production should be based on renewable energy sources ⁶. These energy sources however have one big problem, their intermittency. The mismatch between supply and demand causes for a need to store the excess electrical energy generated at peak production. Peak shaving and novel technologies able to follow the irregular and, at times, intermittent supply of renewable electricity in a flexible way, will be needed to use renewable energy on a larger scale. One possible way is to use batteries for storage of the surplus electrical energy during peak productions or to use this energy to pump water from a lower reservoir towards a reservoir at higher altitude. However, chemical storage in fuels is more efficient ⁷. These fuels are usually called carbon-neutral fuels or solar fuels. They offer a higher gravimetric and volumetric energy storage capacity, have higher energy densities than electrical storage techniques and liquid solar fuels are easy to transport in the already existing liquid fuel infrastructure ^{7,8}.

The synthesis of fuels or value-added chemicals using renewable electricity, and based on greenhouse gases as a feedstock is therefore considered one of the main challenges of the 21st century ^{1,9,10}. Using these greenhouse gases, which are usually waste products, and converting them into new feedstock does not only fit within the framework of green and sustainable chemistry ^{11,12}, but also within the ‘cradle-to-cradle’ principle ¹³

1.2 CO₂ and its conversion opportunities

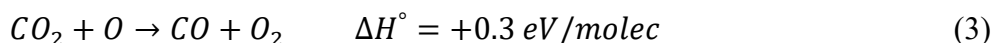
The overall dissociation of CO₂ can be represented by ^{14,15}:



This decomposition reaction starts with and is limited by:



The O radical preferably reacts further with CO₂ instead of recombining back to O₂ to achieve the highest energy efficiency:



From a thermodynamic point of view, CO₂ has a Gibbs free energy of formation (ΔG_f°) equal to 4.1 eV/molec, causing the chemical equilibrium, if no products are removed from the mixture, to be largely shifted towards the reactants, i.e.

CO₂¹⁵. Gas temperatures equal to 5000 K and larger are therefore needed to get 100 % conversion and an energy efficiency of 35 %, as seen in Figure 2. Since the entropy term at standard conditions is about 11 times lower than the enthalpy term for reaction (1)¹⁵, such high temperatures are needed to reduce the Gibbs free energy to a negative value and thus shift the equilibrium towards the dissociation products. The highest energy efficiency in thermal conversion is 47 %, at a conversion of about 70 %, reached at around 3300 K³. Hence, at this temperature almost half of the energy is effectively used to dissociate CO₂, while the other half is used for other energy channels, such as heating the gas mixture or excitation of the reaction products, which will increase with increasing temperature. Feeding extra thermal energy into the gas would therefore not give the same rise in CO₂ conversion, and therefore would reduce the energy efficiency, which explains the lower efficiency, i.e. 35 %, at 100 % conversion.

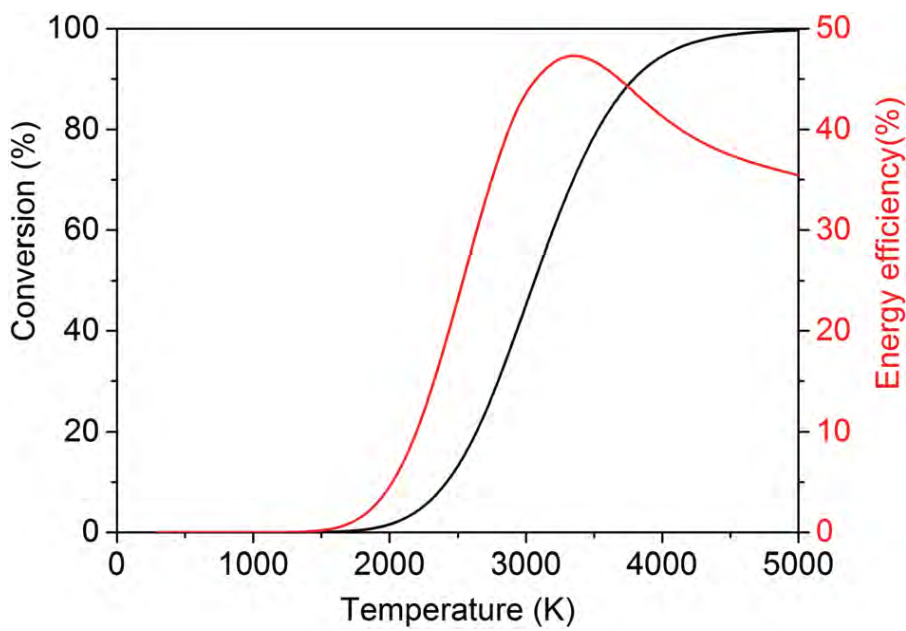


Figure 2: Calculated theoretical thermal conversion (left axis) and corresponding energy efficiency (right axis) as a function of temperature for splitting of CO₂ into CO and O₂³.

Besides thermal conversion, several other technologies are under development to convert CO₂, such as solar thermochemical, photochemical, biochemical,

electrochemical and plasma-chemical conversion with or without catalyst ¹⁶. Solar thermochemical, photochemical and, in an indirect way, biochemical conversion use solar power. Solar thermochemical conversion uses (concentrated) solar heat, whereas photochemical conversion uses the photoelectric effect to create electrons in situ needed for CO₂ reduction. Finally, electrochemical and plasma-chemical conversion rely on electricity, preferably created using wind turbines, hydroelectric power plants, solar panels etc., which are in first instance stored on the electrical grid. All these methods have their advantages and disadvantages. This PhD thesis is focused on plasma-chemical conversion. As explained later, it allows (in principle) to convert most of the energy in actual CO₂ splitting, avoiding unwanted energy channels, such as heating. It has been shown in earlier works ^{14,17,18} that plasma allows CO₂ to store electrical energy in an efficient way in its vibrational modes, which is directly used for dissociation, without (significant) heating (see Figure 3).

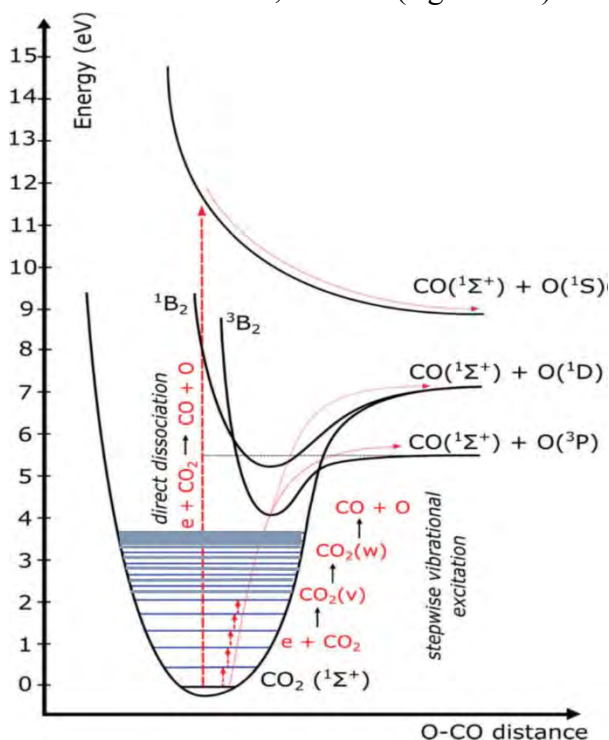


Figure 3: Schematic of several CO₂ electronic and vibrational levels, showing the importance of vibrational ladder-climbing in energy efficient CO₂ conversion.

1.3 Vibrational modes of CO₂

CO₂ is a linear triatomic molecule and therefore has four vibrational modes. More specifically, due to the symmetry, it has three vibrational modes, of which one is doubly degenerate. These modes are often designated by (a,b,c), where a, b and c are the quantum numbers of the corresponding three modes: the symmetric stretch mode (1,0,0), the doubly degenerate symmetric bending mode (0,1^l, 0) and the asymmetric stretch mode (0,0,1). The energies of the first vibrational level of each of these modes are 0.165 eV, 0.083 eV and 0.291 eV, respectively. The symmetric stretch and bending modes also show resonance, since the energy of the levels (0,2^l, 0) is almost equal to the energy of (1,0,0). When energy is fed into these vibrational levels, two main mechanisms take place, called vibrational-translational (VT) and vibrational-vibrational (VV) relaxation. In the first case, vibrational energy is transferred towards the translational degrees of freedom during collisions or, in other words, vibrational energy is transferred into heat. In the latter process, a vibrational quantum is transferred from one molecule to another. This quantum exchange can be between different vibrational modes, but also within one mode. In the latter case, one vibrationally excited molecule can gain even more vibrational energy, stored within that mode. The asymmetric stretch mode of CO₂ has the advantage of having a lower rate of VT relaxation and VV intermode relaxation than VV pumping of the levels purely in the asymmetric stretch mode¹⁴. As a result, the asymmetric stretch mode is able to efficiently store vibrational energy, creating highly vibrationally excited CO₂ levels, while keeping the gas temperature much lower. These highly vibrationally excited molecules are able to overcome the activation energy for endothermic reactions, such as CO₂ splitting. Therefore, selective excitation and vibrational pumping of this mode could be the solution to obtain higher energy efficiency, compared to pure thermal dissociation¹⁴. One possible way to achieve this, as mentioned above, is indeed by plasma technology³.

1.4 Motivation for plasma technology

1.4.1 What is plasma?

Plasma is an ionized gas, consisting of electrons, (positive and negative) ions and neutral species^{14,19}. The degree of ionization can vary between 100 % (fully

ionized) to very low values (e.g. 10^{-4} - 10^{-6} ; partially ionized gases). Plasmas occur in nature, such as stars and interstellar matter, which are omnipresent in the universe, but they can also be artificially made. These laboratory plasmas can be subdivided in high-temperature or fusion plasmas, and low-temperature plasmas or gas discharges, which are studied in this PhD thesis.

Gas discharge plasmas can be in thermal equilibrium or in non-equilibrium. Thermal equilibrium means that all species in the plasma (electrons, ions, various types of neutrals) can be characterized by one and the same temperature. This regime is also simply referred to as thermal plasma. High temperatures are needed to achieve this, ranging from 4000 K, for easy-to-ionize elements, such as cesium, till 20,000 K for hard-to-ionize elements, such as helium ²⁰. In addition, thermal plasmas usually occur at high pressures. This is caused by the fact that electrons initially gain energy from the applied electric field, which they lose partly during collisions with heavier particles, such as molecules, ions and radicals. This loss in energy due to subsequent collisions is called Joule heating, which eventually leads to heavy particles and electrons to be in thermal equilibrium. At higher pressures, such collisions, and thus Joule heating, is much more pronounced, leading faster towards a thermal plasma. Thermal plasmas are not only characterized by high temperature, but also by high intensity non-ionizing radiation and high energy density, which make them suitable for various applications, such as spray coating, welding, cutting and the treatment of hazardous materials ²¹. In addition, they can also be used for CO₂ conversion. However, the processes in thermal plasmas are determined by temperature and the maximum energy efficiency for CO₂ conversion is thus limited to the thermodynamic equilibrium efficiency, i.e. 47 %, and corresponding conversion, i.e. 80 %, at 3500 K ³, as mentioned earlier.

Higher energy efficiencies for CO₂ conversion can be obtained in non-thermal plasmas, with the highest claimed value up to 90 % ^{14,22}. In non-thermal plasmas different species have different temperatures. More precisely, the electrons have a much higher temperature than the other (heavier) species. This difference between electron temperature and temperature of the heavy species is of great use for CO₂ (and other gas) conversion, because the applied electric energy is used to heat the electrons, without the need to heat the gas as a whole. Subsequently, the hot electrons can activate the gas molecules, creating reactive

species that can easily form new molecules, thus leading to conversion of the gas into new compounds.

A non-thermal plasma is in its simplest form created by applying a potential difference between two electrodes with gas flowing between these electrodes. This potential difference creates an electric field, causing gas breakdown, thus producing ions and electrons. The electrons are accelerated by the electric field towards the positive electrode (anode). In the meantime, the electrons also collide with the gas molecules, causing ionization, dissociation and excitation. Ionization creates new electrons and positive ions. The latter are accelerated towards the negative electrode (cathode). These ions induce secondary electron emission, creating even more electrons. These newly formed free electrons are accelerated and cause therefore new ionization collisions. In this way the plasma is sustained. In this PhD thesis, the focus will be on non-thermal plasmas. Note however that the gas temperature in some non-thermal plasmas can also be quite high (e.g., 3000 K), but this is still lower than the electron temperature (typically above 10,000 K). This type of plasma is also called “warm plasma”.

1.4.2 Plasma technology for gas conversion

As mentioned above, plasma is a reactive cocktail of various species. Hence, next to the classical chemical reactions involving neutral species, also charged species play an important role in plasma. This is due to the fact that electrons in a plasma, accelerated by the electric field, induce a variety of chemical reactions. These electrons initially collide with the neutral gas molecules, either by elastic collisions or inelastic collisions. The latter type of collisions causes the rich plasma chemistry by creating ions and radicals upon electron impact ionization, attachment and dissociation, which are able to induce chemical reactions that are classically only possible at very high gas temperatures, such as greenhouse gas conversion¹⁹. Moreover, non-thermal plasmas are able to selectively excite the vibrational degrees of freedom of molecules. The electron temperature in many non-thermal plasmas used for CO₂ conversion is about 1-2 eV, causing most of the electron energy (up to >95 %) to be transferred into vibrational excitation of CO₂, which is initially (i.e., at short time-scales below 100 μs; see also Chapter 3), much faster than its relaxation into heat^{14,23}. This results in an overpopulation of these vibrational levels, which is beneficial in overcoming the energy barrier

of the highly endothermic CO₂ splitting reaction¹⁴. Moreover, these electron temperatures mainly selectively excite the asymmetric mode, from which relaxation into heat is the slowest. Provided the gas temperature can be kept low, so as to inhibit VT relaxation even further, vibrational pumping creates highly vibrationally excited CO₂ molecules, from which energy-efficient CO₂ dissociation occurs. The process of vibrational excitation and ladder climbing in CO₂ was illustrated in Figure 3. In practice, however, in warm plasmas VT relaxation is often not negligible, certainly at atmospheric pressure, so that the gas temperature rises up to ca. 3000 K (or more), and the vibrational distribution function is more or less in thermal equilibrium with the gas temperature, i.e., no overpopulation of the higher vibrational levels. This will be illustrated further in this PhD thesis.

From a practical point of view, plasmas can be turned on and off almost instantly and therefore can bridge the production-demand mismatch of green energy production by storing fluctuating renewable electricity. In addition, plasma reactors are made of abundant materials, giving rise to low investment costs.³ In the following Sections the most common type of plasma reactors used for CO₂ conversion will be discussed. As a feedstock, not only pure CO₂ can be used, but also mixtures with a co-reactant, more specifically CH₄, H₂ and H₂O, which are useful for creating valuable oxygenates and syngas (CO/H₂), next to CO and O₂. These co-reactants, all containing hydrogen, are the most desirable because they contain the building blocks for the synthesis of liquid fuels.

1.5 Different plasma sources used for CO₂ conversion

1.5.1 Dielectric barrier discharge (DBD)

A DBD (Figure 4) is created by applying an electric potential difference between two electrodes, of which at least one is covered by a dielectric barrier (e.g. glass, quartz, ceramics or also polymers) and is usually operated at atmospheric pressure^{19,24}. Usually, an AC voltage amplitude of 1-100 kV and a frequency of a few Hz to MHz is applied²⁴. In such discharges, breakdown is initiated in a large number of independent current microdischarges with nanosecond duration. A DBD usually exists in 2 different configurations, i.e. the volume discharge (VD) and the surface discharge (SD). VDs consist of two parallel plates forming a discharge gap in which microdischarges take place in thin channels, crossing

the discharge gap and randomly distributed over the electrode surface. This gap usually ranges from 0.1 mm to several cm^{19,24}. A variation of this planar type VD is when the electrodes are not planar but cylindrical, which is mostly the case for DBD plasmas used for CO₂ conversion, and studied in this thesis (see also Figure 4). In a SD several surface electrodes are placed on a dielectric layer, with a counter electrode on the reverse side. In this case the microdischarges are in fact individual discharge steps taking place in a thin layer on the dielectric surface. The latter configuration however is not used for CO₂ conversion, and will therefore not be further discussed here.

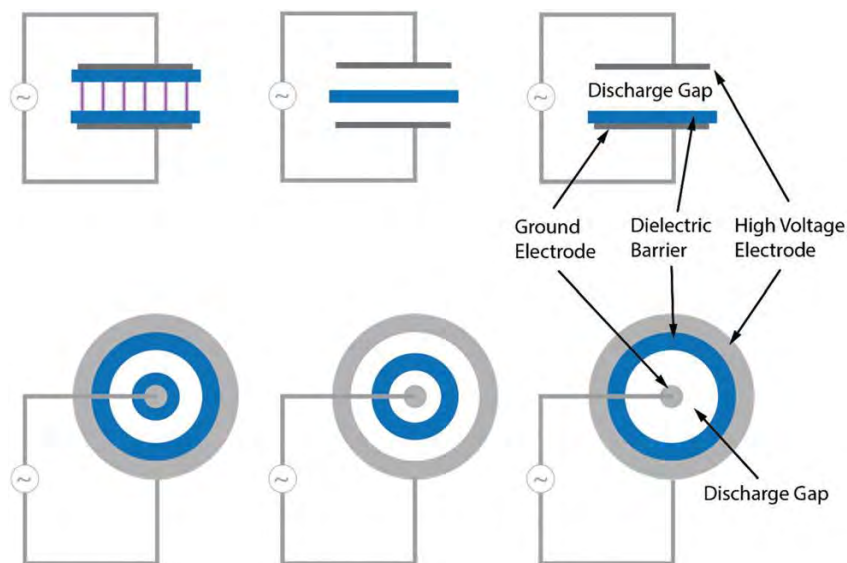


Figure 4: Schematic picture of a DBD discharge in planar (upper panels) and cylindrical (lower panels) configuration³.

1.5.2 Microwave (MW) discharge

In a MW discharge, electromagnetic radiation in the frequency range of 300 MHz - 10 GHz¹⁹ is used to ignite the plasma at pressures ranging between 0.1 Pa and atmospheric pressure¹⁴. MW discharges come in different configurations but one of the most used types, and also studied in this thesis, is the surface wave discharge (SWD) (see Figure 5). SWDs are generated by running or standing waves, which are conducted parallel to the surface of the dielectric walls enclosing the plasma^{19,20}. Due to the wide pressure range, both non-thermal plasmas and near thermal plasmas can be created. For CO₂ conversion, the best

results in terms of energy efficiency are obtained at moderate pressures between 100 and 200 mbar (or between 10^4 Pa and 2×10^4 Pa) where vibrational excitation of the asymmetric stretch mode and VV pumping are maximized. Higher pressures lead to lower reduced electric fields and to excitation of the lower symmetric mode levels, from which VT relaxation and thus gas heating occurs faster, which in turn further accelerates VT relaxation^{14,25}. However, these reduced pressures are not beneficial for industrial implementation, so high energy density atmospheric pressure plasmas would be desirable, if non-equilibrium could be maintained.

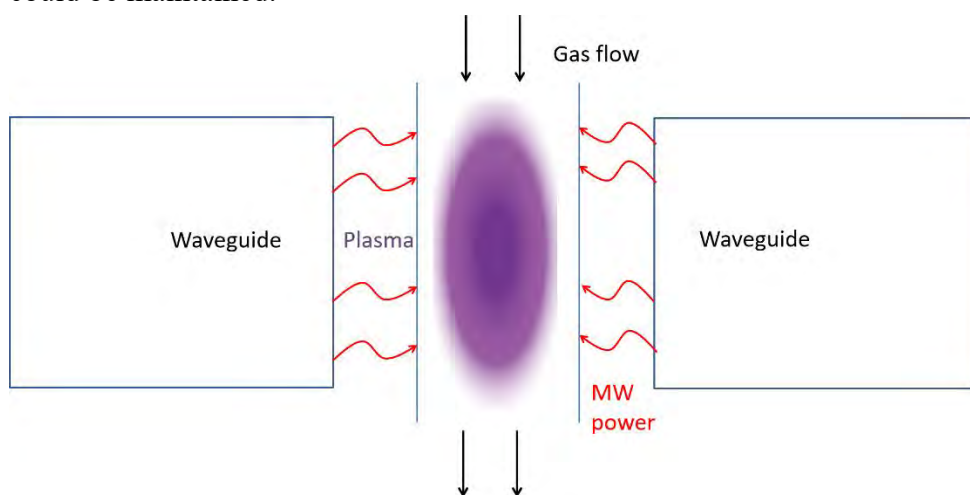


Figure 5: Schematic picture of a surface wave MW discharge.

1.5.3 Gliding arc (GA) discharge

A GA discharge can combine non-thermal plasma with high energy density²⁶. A classical GA is an auto-oscillating periodic discharge between two diverging flat electrodes where the gas flow pushes the arc onwards. The arc is ignited at the shortest interelectrode distance, forming an equilibrium arc plasma which, at a high enough gas flow rate, i.e. several L min^{-1} , cools down rapidly towards non-thermal conditions, while the arc elongates until it extinguishes (see Figure 6)^{26,27}. More specifically, the length of the arc increases with the voltage until it reaches a critical length, after which the heat losses from the arc begin to exceed the supplied energy, and the arc cannot sustain itself anymore in its thermal equilibrium state and evolves towards a non-thermal plasma. In this non-thermal state, the electron temperature is ~ 1 eV, which is suitable for efficient vibrational

excitation of CO₂. After this non-thermal stage the arc extinguishes and a new arc is formed at the shortest interelectrode distance, thus repeating the cycle. Up to 75-80 % of the energy can be dissipated in the non-thermal zone of the gliding arc, exploiting most of the non-equilibrium effect ²⁶.

However, because of the high current density of the discharge, conventional GA reactors suffer from electrode degradation. Moreover, a significant amount of gas does not pass through the active plasma (arc) region, so it will not be converted ^{28,29}. To tackle these issues, new types of GA discharge, based on cylindrical electrodes and tangential gas inlets, were developed. One of these configurations is also called “gliding arc plasmatron” (GAP), and is based on vortex flow stabilization, i.e. forward vortex flow (FVF) and/or reverse vortex flow (RVF) stabilization ³⁰⁻³². The highest energy efficiencies for CO₂ conversion were obtained using the RVF configuration, because it is characterized by a secondary, backwards oriented inner vortex gas stream within the outer tangential gas flow, confining the plasma, and resulting in nearly perfect heat insulation from the wall, better gas mixing with the arc, and therefore a higher conversion and energy efficiency ^{31,33}. The plasma chemistry for CO₂ conversion and dry reforming of methane (DRM) in the GAP has been studied in this thesis (Chapters 3, 4 and 5).

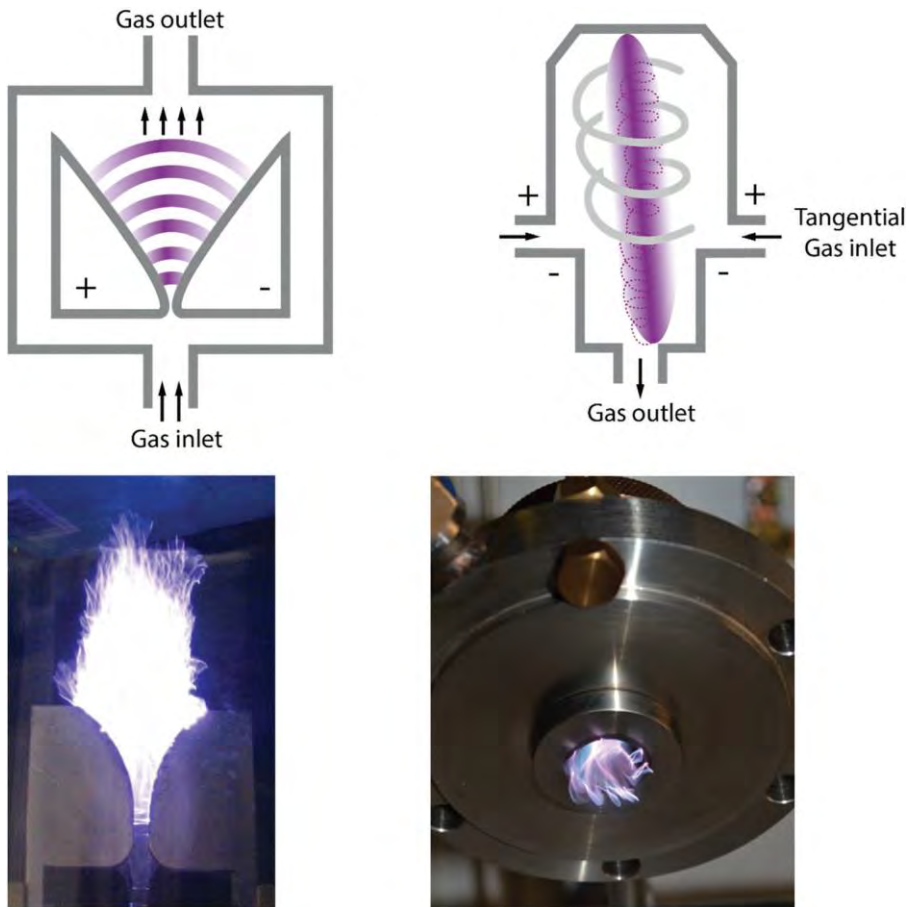


Figure 6: Schematic pictures (upper panels) and photos (lower panels) of the classical GA (left) and the GAP (right) ³.

1.5.4 Nanosecond Repetitively Pulsed (NRP) discharge

Another type of plasma that could combine a high degree of non-equilibrium and still being operational at atmospheric pressure is the NRP discharge ^{34,35}. Power is deposited in ns pulses, like in a DBD, but they are of high energy, resulting in powers of several MW, yielding high conversions just after these pulses, while keeping the overall power low (i.e. several tens of W), which makes them interesting for CO₂ conversion. NRP discharges can be generated in a pin-to-pin, pin-to-sphere and plane-to plane-configuration ³⁴⁻³⁸. A picture of a pin-to-sphere configuration, also studied in this thesis (Chapter 6), is shown in Figure 7.

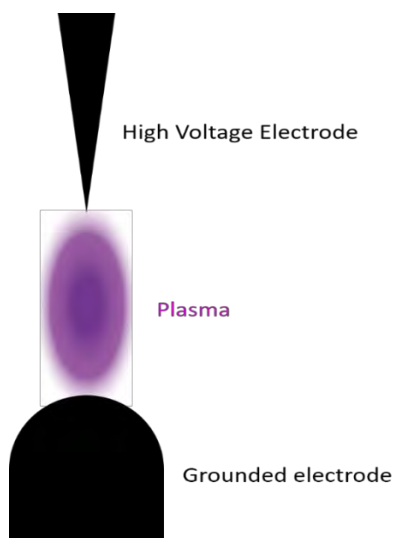


Figure 7: Schematic picture of the NRP discharge in the pin-to-sphere configuration.

1.6 Aim of this PhD thesis

Although plasma technology shows promising results for CO_2 and CH_4 conversion, it still needs improvement. For this purpose, better insight in the plasma chemistry occurring in the various plasma types is needed. Therefore, we developed in this PhD thesis a number of plasma chemistry models for various plasma sources, to study the underlying mechanisms for CO_2 and CH_4 conversion.

In Chapter 2, a general model description is given, including the approximations made in all the simulations. Also, the expressions for general calculation results of interest for this application, such as conversion, product selectivity, energy efficiency, energy cost and specific energy input, are given. In Chapters 3, 4 and 5 a chemical kinetics study is presented for the GAP, operating in pure CO_2 , CO_2/CH_4 and CO_2/N_2 , respectively. Next to the CO_2 , CH_4 and N_2 conversion, which are validated by experimental results, also the vibrational kinetics and the most important products formed are discussed. In Chapter 6, an NRP discharge is described by a 0D model and validated for pure CO_2 conversion. Finally, in Chapter 7, the underlying mechanisms of pure CH_4 , CH_4/H_2 and CH_4/N_2 mixtures in DBD, MW and GA plasmas are presented, again after validation with experimental conversions and product selectivities.

Chapter 2: General Model Description

2.1 Basic equations

This PhD thesis focuses on describing the plasma chemistry in various types of plasmas. This includes many different species and chemical reactions (see details in the following Chapters). For this purpose, 0D chemical kinetics modelling is most appropriate as it can handle a large chemistry without too much computational cost. In a 0D model, the most important approximation is that the plasma is treated as homogeneous, so no transport phenomena can take place^{20,39}. To explain the formalism of 0D modelling in more detail, we need to realize that all equations solved for modelling are approximations/derivations of solving the Boltzmann equation for every species s ⁴⁰:

$$\frac{\partial f_s}{\partial t} + \mathbf{v} \cdot \frac{\partial f_s}{\partial \mathbf{r}} + \boldsymbol{\gamma} \cdot \frac{\partial f_s}{\partial \mathbf{v}} = \left(\frac{\delta f_s}{\delta t} \right)_c \quad (4)$$

with $f_s(t, \mathbf{r}, \mathbf{v})$ the distribution function of species s , t the time, \mathbf{r} the position vector, \mathbf{v} the velocity vector, $\boldsymbol{\gamma}$ the acceleration vector of the species s and $\left(\frac{\delta f_s}{\delta t} \right)_c$ the rate of change of f_s due to collisions. It is computationally impossible to calculate the distribution function of every species inside a plasma. Therefore, in our 0D model, the Boltzmann equation is only solved for the electrons (in an approximative way), whereas for the heavy species, we describe macroscopic values, such as mass density, mean energy, momentum, as a function of time and space.

For the electrons, we rewrite equation 4 with the assumptions that $\boldsymbol{\gamma}$ and the collision term $\left(\frac{\delta f_e}{\delta t} \right)_c$ are spatially uniform and that the distribution function can be expanded in Legendre polynomials of $\cos \theta$ ⁴¹, with θ the spherical angle in velocity space²⁰. It is widely accepted that the two-term approximation of the Boltzmann equation is sufficient, in which the electric field and diffusion gradient are assumed to be sufficiently small^{41,42}:

$$f_e(t, \mathbf{r}, \mathbf{v}) \approx f_0(t, \mathbf{r}, \mathbf{v}) + \cos \theta f_1(t, \mathbf{r}, \mathbf{v}) \quad (5)$$

where f_0 and f_1 are the isotropic and anisotropic parts of f_e . The resulting time-independent two-term approximation of the electron Boltzmann equation is thus ⁴¹:

$$-\frac{d}{d\varepsilon} \left(\frac{4m_e}{M} Q(\varepsilon) \varepsilon^2 f_0(\varepsilon) - \left(\frac{2}{3} \frac{e^2}{Q(\varepsilon)} \left(\frac{E}{N} \right)^2 \varepsilon + \frac{4m_e}{M} Q(\varepsilon) \varepsilon^2 f_0(\varepsilon) \right) \frac{d}{d\varepsilon} f_0(\varepsilon) \right) = S_{coll} \quad (6)$$

with e the electron charge, m_e and M the electron and heavy species mass, $\frac{E}{N}$ the reduced electric field, and $Q(\varepsilon)$ the elastic momentum energy transfer cross section as a function of energy ε .

For the heavy species, the conservation equations of mass density, momentum and mean energy can be derived from the Boltzmann equation.

The density of a species s , n_s (usually in m^{-3}) as a function of position and time is defined as:

$$n_s(t, \mathbf{r}) = \int f_s(t, \mathbf{r}, \mathbf{v}) d\mathbf{v} \quad (7)$$

Based on the distribution function, average quantities $\langle b(t, \mathbf{r}) \rangle$ can be calculated:

$$\langle b(t, \mathbf{r}) \rangle = \frac{1}{n_s(t, \mathbf{r})} \int b(t, \mathbf{r}, \mathbf{v}) f_s(t, \mathbf{r}, \mathbf{v}) d\mathbf{v} \quad (8)$$

If these quantities are m_s , $m_s \mathbf{v}$ and $m_s \mathbf{v}^2$, the conservation equations for mass density, momentum and energy can be obtained, respectively. Since transport phenomena are not included in our model, the momentum conservation equation does not have to be solved.

The mass density conservation equation is:

$$\frac{\partial \rho_s}{\partial t} + \nabla(\rho_s \mathbf{u}_s) = S_s \quad (9)$$

with $\rho_s = n_s m_s$ (in kg m^{-3}) the mass density, \mathbf{u}_s the average velocity (in m s^{-1}) of species s and S_s the collision term which is:

$$S_s = m_s \sum_{i=1}^j [(a_{s,i}^R - a_{s,i}^L) R_i] \quad (10)$$

where j is the total number of reactions, $a_{s,i}^L$ and $a_{s,i}^R$ the stoichiometric coefficients at the left hand side and right hand side of the reaction and R_i the reaction rate (in $\text{m}^{-3} \text{s}^{-1}$), given by:

$$R_i = k_i \prod_s n_s^{a_{s,i}} \quad (11)$$

where k_i is the rate constant (in $\text{m}^3 \text{s}^{-1}$ or $\text{m}^6 \text{s}^{-1}$ for two-body or three-body reactions, respectively) and $a_{s,i}$ was defined above. Dividing equation (9) by m_s and due to the fact that in a 0D model no transport phenomena are included, we obtain the (number density) continuity equations in our 0D model:

$$\frac{\partial n_s}{\partial t} = \sum_{i=1}^j [(a_{s,i}^R - a_{s,i}^L) R_i] \quad (12)$$

In this work we use the ZDPlaskin code ⁴³ to solve the balance equations (12) of all species, which also has a built-in Boltzmann solver, called BOLSIG+ ⁴¹, to calculate the EEDF and the rate constants of the electron impact reactions, based on a set of cross sections, the plasma composition, the gas temperature and the reduced electric field (E/N).

The densities (calculated with equations (12)) are constantly updated by gas expansion, which can occur upon conversion of CO_2 , CH_4 and N_2 , e.g., when two new species are formed out of one ⁴⁴. Hence, we calculate the gas pressure and mass flow rate at every time step from the actual species densities, gas temperature and velocity. To conserve the gas pressure and mass flow rate, the species densities (as calculated with the above conservation equations; see equation (12)) and velocities are then corrected to account for this effect, as was done in Kozak and Bogaerts ⁴⁵. The velocity is thus recalculated after every timestep as:

$$v = \frac{Q_m p}{p_0 \rho} \quad (13)$$

with v the gas velocity (in m s^{-1}), Q_m the mass flow rate (in $\text{kg m}^{-2} \text{s}^{-1}$), the mass density $\rho = \sum_s n_s m_s$ (in kg m^{-3}), p the actual pressure calculated from the actual species densities and gas temperature using the ideal gas law, and p_0 the pressure which we want to keep constant. The new densities $n_{s,new}$ of every species before the next timestep are also recalculated as:

$$n_{s,new} = \frac{n_{s,old} p_0}{p} \quad (14)$$

The rate constants of the heavy particle reactions are either constant or dependent on the gas temperature, whereas the rate constants of the electron impact

reactions depend on the electron temperature T_e or the reduced electric field E/N (i.e., the electric field E divided by the number density of all neutral species N , usually expressed in Td = 10^{-21} V m²). The rate constants of the electron impact reactions are generally calculated according to the following equation ⁴⁶:

$$k_i = \int_{\varepsilon_{th}}^{\infty} \sigma_i(\varepsilon) v(\varepsilon) f(\varepsilon) d\varepsilon \quad (15)$$

with ε the electron energy (usually in eV), ε_{th} the minimum threshold energy needed to induce the reaction, $v(\varepsilon)$ the velocity of the electrons (in m s⁻¹), $\sigma_i(\varepsilon)$ the cross section of collision i (in m²), and $f(\varepsilon)$ the (normalized) electron energy distribution function (EEDF; in eV⁻¹) calculated using the Boltzmann equation.

The electric field (E ; in V m⁻¹) is calculated from a given power density, using the so-called local field approximation ²⁰:

$$E = \sqrt{\frac{P}{\sigma}} \quad (16)$$

with P the input power density (in W m⁻³) and σ the plasma conductivity (A V⁻¹ m⁻¹). The plasma conductivity is estimated at the beginning of the simulations as ²⁰:

$$\sigma = \frac{e^2 n_{e,init}}{m_e \nu_m} \quad (17)$$

with e the elementary charge (1.6022×10^{-19} C), $n_{e,init}$ the initial electron density (in m⁻³), m_e the electron mass (9.1094×10^{-31} kg) and ν_m the collision frequency (in s⁻¹) calculated using BOLSIG+. During the simulation the plasma conductivity is calculated as ²⁰:

$$\sigma = \frac{e v_d n_e}{\left(\frac{E}{N}\right)_{prev} n_0} \quad (18)$$

with v_d the electron drift velocity (in m s⁻¹), which is calculated using BOLSIG+ implemented in ZDPlaskin, and $\left(\frac{E}{N}\right)_{prev}$ the reduced electric field at the previous time step (in V m²).

In some cases, the energy balance equation is also solved, which is originally obtained by solving equation (8) with $m_s \mathbf{v}$ as observable b , and with the energy

or temperature of species s as a solution. Since the gas temperature T_g (in K) can be assumed to be the same for all neutral species, only one energy conservation equation needs to be solved. This simplified energy equation, built in ZDPlaskin, is the adiabatic isometric heat transport equation ⁴³:

$$N \frac{\gamma k}{\gamma-1} \frac{dT_g}{dt} = P_{e,el} + \sum_j R_j \Delta H_j - P_{ext} \quad (19)$$

where $N = \sum n_i$ is the total neutral species density, γ is the specific heat ratio of the total gas mixture, k is the Boltzmann constant (in J K⁻¹), $P_{e,el}$ is the gas heating power density due to elastic electron-neutral collisions (in W m⁻³), R_j is the rate of reaction j (in m⁻³ s⁻¹), ΔH_j is the heat released (or consumed when this value is negative) by reaction j (in J) and P_{ext} is the heat loss due to energy exchange with the surroundings (in W m⁻³). The exact expression for P_{ext} , as used in this thesis for the different plasma sources, will be given in each Chapter when applied. The specific heat ratio of the total (ideal) gas mixture is calculated from the specific heat ratios of the individual species in the model, γ_i , using the formula ⁴⁵:

$$N \frac{\gamma}{\gamma-1} = \sum_i n_i \frac{\gamma_i}{\gamma_i-1} \quad (20)$$

where n_i are the densities of the individual species i . The individual specific heat ratios, γ_i , can be calculated from the specific heat capacity at constant pressure $c_{p,i}$ (in J K⁻¹ kg⁻¹) using the relation:

$$c_{p,i} = \frac{\gamma_i}{\gamma_i-1} \frac{k}{M} \quad (21)$$

where k is the Boltzmann constant and M is the molar weight of CO₂ (in kg). Since the vibrational levels are treated as separate species, only the heat capacity due to translational and rotational degrees of freedom should be taken into account, and in the case of CO₂, also the heat capacity due to the symmetric vibrational modes, which are not treated as individual species ^{45,47}. A classical partitioning between the translational and rotational degrees of freedom is assumed, which gives a value for the specific heat ratio, at room temperature and above, of 1.67 for the atomic species and 1.40 for the diatomic molecules. Details about the calculation of the total heat capacity and the resulting specific heat ratio

for CO₂, calculated using equation (21), can be found in ⁴⁵. For O₃, which can be produced by CO₂ conversion, a value of 1.27 was taken ^{45,48}. When CH₄ and CH₄/H₂ mixtures are studied (Chapter 7), the specific heat ratio of CH₄ is taken to be 1.32, while values of 1.23 for C₂H₂, 1.24 for C₂H₄, 1.19 for C₂H₆, 1.13 for C₃H₈ and 1.15 for C₃H₆ are used ⁴⁹.

2.2 General approximations in the 0D model

Using a 0D model for describing various plasma types requires some approximations. Specific approximations will be discussed in the following Chapters, but the general approximations, independent of the plasma reactor studied, are listed here:

- A 0D model calculates the species densities as a function of time only, and neglects spatial variations. However, the time evolution can be translated into a spatial evolution (i.e. as a function of position in the plasma reactor) by means of the gas flow rate. In this way, local variations in the applied plasma power can be implemented in the model, as power pulses as a function of time (see details in the following Chapters).
- The conversion of a certain species *A*, i.e. in this thesis CO₂, CH₄ and N₂, is calculated as:

$$\chi_A(\%) = 100 \% \frac{n_{A,i} (m^{-3})v_i(m s^{-1}) - n_{A,f} (m^{-3})v_f(m s^{-1})}{n_{A,i} (m^{-3})v_i(m s^{-1})} \quad (22)$$

Where $n_{A,f}$ and $n_{A,i}$ are the densities of *A* at the end and the beginning of the simulation, respectively, mimicking the inlet and outlet of the reactor, and v_f and v_i are the corresponding velocities.

- The specific energy input *SEI* deposited on the initial feed flow is calculated as:

$$SEI (kJ L^{-1}) = \frac{P (W) 60 (s min^{-1})}{\Phi (sccm)} \quad (23)$$

P is the deposited power in the plasma and Φ the flow rate. This SEI value can be converted into eV molec⁻¹ as follows ³:

$$SEI (eV molec^{-1}) = \frac{SEI (kJ L^{-1}) 6.24 \times 10^{21} (eV kJ^{-1}) 24.5 (L mol^{-1}) p_0 (101325 Pa)}{6.022 \times 10^{23} (molec mol^{-1}) p (Pa)} \quad (24)$$

with p_0 and p the atmospheric pressure and pressure inside the reactor, respectively. This allows us to calculate the energy cost for the conversion of species A (either in kJ L^{-1} or eV molec^{-1} , depending on the unit of SEI):

$$EC = \frac{SEI \times 100 \%}{\chi_A(\%) \phi} \quad (25)$$

where ϕ is the fraction of species A present in the feed gas.

For pure CO_2 and CH_4/CO_2 plasmas (Chapters 3, 4 and 5), we also define the energy efficiency. For pure CO_2 plasmas the energy efficiency can be easily calculated as:

$$\eta(\%) = \frac{\chi_{\text{CO}_2}(\%) \Delta H_{\text{CO}_2}(\text{eV molec}^{-1})}{SEI(\text{eV molec}^{-1})} \quad (26)$$

where ΔH_{CO_2} is the energy cost to split one CO_2 molecule in CO and $\frac{1}{2}$ O_2 , i.e. $2.9 \text{ eV molec}^{-1}$. For dry reforming of methane (i.e. CH_4/CO_2 mixtures) the energy efficiency is calculated as:

$$\eta(\%) = \frac{\phi_{\text{CO},f} H_{f,\text{CO}} - (\chi_{\text{CH}_4} \phi_{\text{CH}_4,i} H_{f,\text{CH}_4} + \chi_{\text{CO}_2} \phi_{\text{CO}_2,i} H_{f,\text{CO}_2})}{SEI(\text{kJ L}^{-1}) V_{\text{mol}}(\text{L mol}^{-1})} \quad (27)$$

where H_f is the enthalpy of formation ($H_{f,\text{CO}} = -110.5 \text{ kJ mol}^{-1}$; $H_{f,\text{CH}_4} = -74.8 \text{ kJ mol}^{-1}$; $H_{f,\text{CO}_2} = -393.5 \text{ kJ mol}^{-1}$), $\phi_{\text{CO},f}$ the fraction of CO in the final plasma mixture, $\phi_{\text{CH}_4,i}$ and $\phi_{\text{CO}_2,i}$ the fraction of CH_4 and CO_2 in the initial feed gas, respectively and V_{mol} the molar volume at 0°C and atmospheric pressure, being 24.5 L mol^{-1} .

Chapter 3: CO₂ Conversion in a Gliding Arc Plasmatron (GAP)

The results presented in this Chapter were published in:

- Ramakers, M.; Trenchev, G.; Heijkers, S.; Wang, W.; Bogaerts, A. Gliding Arc Plasmatron: Providing a Novel Method for Carbon Dioxide Conversion. *ChemSusChem*. **2017**, *10*, 2642–2652
- Heijkers, S.; Bogaerts, A. CO₂ Conversion in a Gliding Arc Plasmatron: Elucidating the Chemistry through Kinetic Modeling. *J. Phys. Chem. C* **2017**, *121*, 22644–22655

3.1 Introduction

Gliding arc discharges are recently gaining considerable interest for CO₂ conversion, as they operate at atmospheric pressure and are clearly more energy efficient than a DBD, with values reported around 25-29 %^{28,50}. However, because of the high current density of the discharge, conventional GA reactors suffer from electrode degradation. Moreover, a significant amount of gas does not pass through the active plasma (arc) region, so it will not be converted^{28,29}. To tackle these issues, the so-called GAP, which is based on cylindrical electrodes and tangential gas inlets, was recently developed^{31,51}. Some experimental work and fluid dynamics modeling have been performed for the GAP, to study the CO₂ conversion under different operating conditions^{31,52,53} and to describe the typical gas flow and plasma characteristics in argon^{32,54} and in CO₂⁵⁴, respectively. Plasma chemistry modelling in pure CO₂ plasmas has already been performed in other discharges, such as a DBD^{55,56}, MW^{45,57} and conventional GA discharge²⁹. However, to our knowledge, no detailed kinetic study has been performed yet to elucidate the main dissociation mechanisms of CO₂ in a GAP. Nevertheless, this information is crucial to obtain insight in the underlying chemistry in order to improve the process.

In this Chapter we therefore present a detailed chemical study of the CO₂ conversion and energy efficiency in a GAP reactor, using 0D chemical kinetics modeling with a full description of the vibrational kinetics throughout the arc, and validated by experiments. This allows us to elucidate the most important CO₂ dissociation mechanisms, as well as to identify the limitations, which can be helpful to further improve the performance of the GAP for energy-efficient CO₂ conversion. In Section 3.2 we show the chemistry set used for this study, while Section 3.3 presents the specific approximations used in this Chapter. The calculated physical characteristics, such as electron density, electron temperature, vibrational temperature and conversion inside the arc, are discussed in Section 3.4. In Section 3.5 the calculated overall conversions and energy efficiencies for different conditions are compared with experimental results. Sections 3.6 and 3.7 discuss the underlying mechanisms for CO₂ conversion and the importance of vibrational kinetics for these underlying mechanisms, respectively. Finally, in Section 3.8 we give suggestions to make the conversion process more efficient.

3.2 Chemistry set

The chemistry set used in this Chapter is based on the original model of Kozák et al. ⁵⁷ which has been thoroughly reviewed by Koelman et al. ⁵⁸. The electron impact reaction rate constants are calculated using a pre-evaluated electron energy distribution function (EEDF; which is regularly updated during the simulations based on the new chemical composition in the plasma) and the cross section set of Phelps with the 7 eV threshold excitation reaction used for dissociation ⁵⁹⁻⁶¹, as suggested by Grovulovic' et al. ⁶², Bogaerts et al. ⁶³ and Pietanza et al. ⁶⁴⁻⁶⁶. The species described in the model are listed in Table 1.

The symbols 'V' and 'E' between brackets for CO₂, CO and O₂ represent the vibrationally and electronically excited levels of these species, respectively. All 21 levels (V1-V21) of the asymmetric mode till the dissociation limit (5.5 eV) are taken into account, since they are crucial for storing vibrational energy for efficient CO₂ dissociation ¹⁴. In addition, four effective low-lying symmetric stretching and bending mode levels are included in the model (Va-Vd). Only one electronically excited level (E1) is taken into account with an energy of 10.5 eV, as the excitation level with energy of 7 eV will immediately give rise to dissociation^{60,61}.

A large number of reactions are taken into account, such as electron impact reactions, electron-ion recombination reactions, ion-ion, ion-neutral and neutral-neutral reactions, as well as vibration-translation (VT) and vibration-vibration (VV) relaxation reactions. Furthermore, reactions considering carbon production are also included in the model. All the reactions and their corresponding rate coefficients, and the references where these data (or the cross sections) are adopted from, are listed in the Appendix (Tables A1 – A5). More information about the species and reactions included in the model can be found in the papers of Kozák et al. ⁵⁷, Koelman et al. ⁵⁸ and Bogaerts et al. ⁶³

Table 1: Species taken into account in the 0D model.

Molecules	Charged species	Radicals	Excited species
CO ₂ , CO	CO ₂ ⁺ , CO ₄ ⁺ , CO ⁺ , C ₂ O ₂ ⁺ , C ₂ O ₃ ⁺ , C ₂ O ₄ ⁺ , C ₂ ⁺ , C ⁺ , CO ₃ ⁻ , CO ₄ ⁻	C ₂ O, C, C ₂	CO ₂ (Va, Vb, Vc, Vd), CO ₂ (V1-V21), CO ₂ (E1), CO(V1-V10), CO(E1-E4)
O ₂ , O ₃	O ⁺ , O ₂ ⁺ , O ₄ ⁺ , O ⁻ , O ₂ ⁻ , O ₃ ⁻ , O ₄ ⁻	O	O ₂ (V1-V3), O ₂ (E1-E2)
	electrons		

3.3 Modeling the GAP reactor with a 0D approach

The GAP under study is based on the experimental design developed by Nunnally et al. ^{31,51}, illustrated in Figure 8. As explained in Chapter 1, it is a cylindrical GA reactor in which the gas flow enters through a tangential inlet, resulting in a vortex flow. A potential difference is applied between the reactor body and the outlet of the reactor, which act as cathode and anode, respectively. This potential difference creates an arc between the cathode and the anode. When the anode diameter is smaller than the cathode diameter, the incoming gas will not immediately escape the reactor through the outlet at the bottom of the reactor, as it follows a vortex flow with larger diameter, so it will be forced upwards in the cathodic part of the reactor, in a so-called forward vortex flow (FVF) pattern. Due to friction and inertia, the rotational speed will be reduced. Therefore, when the spiraling gas arrives at the top of the reactor, it will start to move downwards in a smaller vortex, towards the outlet at the bottom, i.e., in a reverse vortex flow (RVF). Due to this vortex flow, the arc plasma is stabilized in the center of the reactor and the reverse vortex gas flow is forced through the plasma. This is schematically illustrated in Figure 8, and described by fluid dynamics modeling by Trenchev et al. ^{32,33}.

The reactor body (or cathode) has a length of 20.3 mm and a diameter of 17.50 mm. Ramakers et al. ⁵² performed experiments with three different anode outlets, acting as grounded electrode (or anode), with a constant length of 16.30

mm, but different diameters, i.e., 7.08 mm, 14.30 mm and 17.50 mm. In our model, we use the anode with the smallest diameter, for which the RVF effect is most pronounced, and therefore it yields the highest conversion and energy efficiency, as explained in ⁵².

Combining a complete fluid dynamics and chemical kinetics description of CO₂ conversion in a GAP in a 2D or 3D model is computationally not yet affordable, but since the plasma confined in the inner vortex is more or less uniform ³², 0D modeling of this kind of plasma is justified. Indeed, a constant applied power density to the gas can be assumed, during its residence time in the plasma (i.e., when travelling in the inner (reverse) vortex). Although the power dissipation along the arc is not completely uniform due to the presence of cathode and anode spots, the size of these spots is small compared to the total arc, so we use a uniform power density as a first approximation. Hence, the species conservation equations (see equation (12) in Chapter 2) solve for the species densities as a function of time, but the time-dependence can be translated into a spatial dependence, i.e., as a function of position in the arc column, based on the gas velocity, due to the similarity between a batch reactor and a plug flow reactor. However, some assumptions need to be made:

- Trenchev et al. ³² and Ramakers et al. ⁶⁷ have revealed experimentally and theoretically that the arc width does not change significantly with electrical current and gas flow rate, and thus a constant arc radius for all calculations can be adopted. Based on 3D turbulent gas flow pattern calculations using the SST (Shear Stress Transport) RANS (Reynolds- Averaged Navier- Stokes) turbulent model ⁶⁸, in combination with a 3D fluid plasma model, explained in ³², and experimentally confirmed in ⁶⁷, the actual arc in the GAP seems to have a radius of about 1 mm for the current range between 50 mA and 350 mA. However, the temperature just outside the arc is still high enough (>2000 K) to induce CO₂ dissociation. Moreover, the 3D calculations were performed in argon, and CO₂ will be characterized by higher gas temperatures, due to the presence of VT-relaxation, so the arc region in a CO₂ plasma will be wider. Finally, due to the skewed spiral motion of the arc, the actual volume covered by the arc will be somewhat larger than predicted by the 3D-2D fluid simulations. Therefore, a constant arc radius of 2 mm is

assumed, which – in combination with a total arc length of 39.6 mm (see Figure 8), results in a total plasma volume of 497.6 mm³.

- The initial gas temperature, i.e. right before entering the arc region, is set to room temperature (293.15 K). Inside the arc, the gas will quickly heat up. The actual gas temperature inside the arc is adopted from 3D fluid model calculations³³, and not self-consistently calculated in the present model. Indeed, the latter might be too approximative, as it only accounts for gas heating due to collisions and chemical reactions, and heat loss to the environment, but not taking turbulent heat losses into account, which are stated to be important in the GAP³³. However, the position in the arc at which this gas temperature is reached, is determined by solving equation (19) in Chapter 2. As soon as this gas temperature is reached, the value is kept constant for the rest of the arc column (see below), based on³³. While solving equation (19), P_{ext} , i.e. the heat loss due to energy exchange with the surroundings (in W m⁻³) needs to be defined. P_{ext} is originally calculated as:

$$P_{ext} = \frac{8\lambda}{R^2} (T_g - 293.15 K) \quad (28)$$

where λ is the gas thermal conductivity (in W m⁻¹ K⁻¹), R the radius of the plasma zone (assumed as 2 mm; see above) and T_g the plasma gas temperature (in K). The gas thermal conductivity is calculated by the following formula, taken from Vesovic et al.⁶⁹:

$$\lambda(Wm^{-1}K^{-1}) = (0.071T_g - 2.33) \times 10^{-3} \quad (29)$$

However, according to 2D fluid dynamics simulations of Trenchev et al.³³, turbulent flow causes the cooling to be about 9 times higher than due to normal thermal conductivity. As this process cannot be explicitly accounted for in our 0D model, equation (28) is multiplied by a factor 9, to obtain a realistic cooling effect. This is a serious approximation of a 0D model, but it was the only feasible option, to describe both the detailed chemistry and account for cooling. Heat losses due to radiation are not specifically included in our model, because we believe turbulent cooling is the most important cooling mechanism in a GAP, providing almost perfect thermal insulation from the walls, so that the walls can even be touched by hand^{14,30}. Therefore,

we believe that accounting for turbulent cooling is sufficient for discharges where turbulence is important, such as the GAP, but also in NRP discharges (see Chapter 6).

- A constant mass flow rate through the reactor is assumed and the pressure is held constant at atmospheric pressure, in agreement with the 3D fluid dynamics calculations of Trenchev et al.³³. Since the gas temperature will rise as a function of residence time (or position in the arc), the particle densities will decrease, in order to maintain constant pressure. Furthermore, the gas velocity will increase to conserve the mass flow rate. As the conservation equations for the various species (equations (12) in Chapter 2) do not account for gas expansion at constant pressure, the gas pressure is calculated at every time step of the simulation from the actual species densities and gas temperature, and the species densities are then corrected to maintain a constant (atmospheric) pressure, following the approach of Kozak et al.⁴⁵, as also explained in Chapter 2.
- The initial gas velocities in the arc region, at each gas flow rate considered in this study, are adopted from the 3D gas flow patterns calculated by the fluid dynamics model of³³. The corresponding velocities are 1.96, 2.55, 3.14, 3.72 and 4.31 m/s, for gas flow rates of 10, 13, 16, 19, and 22 L/min, respectively. These velocities are updated during each time step of the simulation, as described above, to maintain constant mass flow rate and pressure.

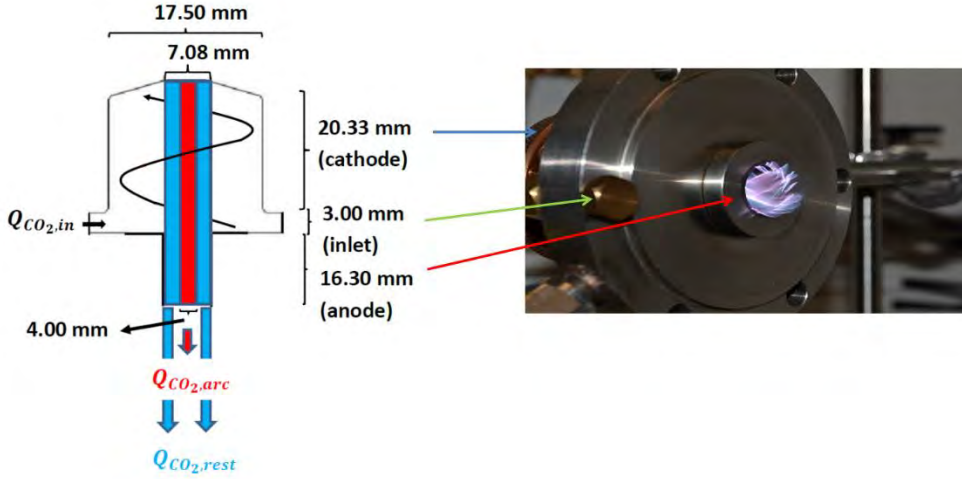


Figure 8: Schematic diagram of the GAP, with characteristic dimensions of cathode (reactor body), inlet region (insulator), anode (outlet) and arc region (red), and indication of the outer vortex (solid spiral). The inner (reverse) vortex is not depicted for the sake of clarity, but it is confined in the blue rectangle. The red rectangle shows the arc region, as considered in the model. $Q_{CO_2,in}$, $Q_{CO_2,arc}$ and $Q_{CO_2,rest}$ denote the flux of CO_2 entering the reactor, and leaving the arc and the rest of the reactor, respectively (see text for more explanation).

The CO_2 conversion after passing through the arc, $X_{CO_2,arc}$, is defined as:

$$X_{CO_2,arc}(\%) = 100 \% \left(1 - \frac{n_{CO_2,e} v_e}{n_{CO_2,i} v_i} \right) \quad (30)$$

where $n_{CO_2,e}$ and v_e are the CO_2 density (in m^{-3}) and gas velocity (in $m s^{-1}$) at the end of the arc region near the outlet, and $n_{CO_2,i}$ and v_i are the CO_2 density (in m^{-3}) and gas velocity (in $m s^{-1}$) at the beginning, right before entering the arc region, i.e., at room temperature. Note that the same formula can be used to calculate the CO_2 conversion as a function of position in the arc, simply by using the CO_2 density and gas velocity at that position in the arc.

Since not all gas in the reactor passes through the arc region, the total CO_2 conversion in the reactor, which is also measured experimentally, will be lower than the CO_2 conversion after passing through the arc region, as also the

unconverted CO₂ in the reactor needs to be taken into account. This total conversion, $X_{CO_2,tot}$, is defined as:

$$X_{CO_2,tot}(\%) = 100 \% \left(1 - \frac{Q_{CO_2,arc} + Q_{CO_2,rest}}{Q_{CO_2,in}}\right) \quad (31)$$

where $Q_{CO_2,in}$, $Q_{CO_2,arc}$ and $Q_{CO_2,rest}$ are the CO₂ fluxes (in s⁻¹) entering the reactor, exiting the arc region at the outlet and exiting the reactor without passing through the arc, hence without being converted. This means that the fraction of CO₂ that passes through the arc region needs to be defined, which is explained below.

The CO₂ flux entering the reactor $Q_{CO_2,in}$ is defined as:

$$Q_{CO_2,in} = n_{CO_2,i} \dot{V} \quad (32)$$

where $n_{CO_2,i}$ is the CO₂ density (in m⁻³) at the inlet of the reactor (at room temperature) and \dot{V} the volumetric flow rate (in m³ s⁻¹). The CO₂ flux exiting the arc region at the outlet $Q_{CO_2,arc}$ is defined as:

$$Q_{CO_2,arc} = n_{CO_2,e} v_e A_{arc} \quad (33)$$

with $n_{CO_2,e}$ and v_e the CO₂ density (in m⁻³) and gas velocity (in m s⁻¹) at the end of the arc region near the outlet, and A_{arc} the cross sectional area of the arc region, i.e. 12.57 mm². Finally, due to conservation of mass, the CO₂ flux $Q_{CO_2,rest}$ which is not treated by the plasma, is given by:

$$Q_{CO_2,rest} = Q_{CO_2,in} - n_{CO_2,i} v_i A_{arc} \quad (34)$$

Hence, the fraction of CO₂ that passes through the arc region is defined by the mass flow rate through the arc, and is 14.8 % of the total mass flow rate through the reactor. The remaining 85.2 % does not pass through the arc, and will not be converted.

The vibrational temperature T_v is calculated from the densities of the various asymmetric mode levels, assuming that they follow a Boltzmann distribution:

$$T_v(K) = \frac{1}{i} \sum_{i=1}^k \frac{(-E_{i-1} + E_i) * 11605}{\ln \left(\frac{n_i}{n_{i-1}}\right)} \quad (35)$$

with E_i and E_{i-1} the energies (in eV) of the i^{th} and $(i-1)^{\text{th}}$ asymmetric mode level and n_i and n_{i-1} the corresponding densities (in m^{-3}). 11605 is a conversion factor to change the units of eV into K, and k is the number of asymmetric mode levels taken into account, which follow a (quasi) Boltzmann distribution. In the beginning of the arc column (i.e., first 0.30 cm), only the first asymmetric mode level is taken into account ($k=1$) in calculating the vibrational temperature, since the vibrational distribution function (VDF) does not exhibit a Boltzmann distribution for higher levels for all flow rates studied (see Appendix: Figure A1). Between 0.30 and 0.60 cm, the first four asymmetric mode levels are taken into account ($k=4$), between 0.60 and 0.90 cm the first seven ($k=7$), and after 0.90 cm the first ten asymmetric mode levels ($k=10$) are taken into account, as they follow a Boltzmann distribution here (see Figure A1). The energies of the different vibrational levels included in the model are listed in Appendix: Table A6.

3.4 Plasma characteristics inside the arc

To understand the CO_2 conversion in the GAP, it is necessary to obtain a good insight in the main plasma characteristics defining the CO_2 conversion, i.e., the gas temperature, vibrational temperature, electron temperature and electron number density. They are plotted as a function of position in the arc column in Figure 9 for different flow rates, ranging from 10 till 22 L/min, i.e., the same values as used in the experiments of⁵². A plasma power of 650W is used, lying somewhat in the middle of the experimental range (529 – 712 W)⁵².

As is clear from Figure 9(a), the gas temperature rises quickly till its maximum defined value of 3340 K. Although this gas temperature seems quite high, 3D-2D fluid simulations show that the arc temperature in CO_2 is around 3100 K for a plasma power of 500 W³³. In this work, a power of 650 W is considered, so a slightly higher gas temperature in the arc is assumed. Furthermore, the rotational/gas temperature in a similar setup was measured in⁵¹, obtaining values of 2700 ± 50 K for a CO_2 plasma, doped with 1 % N_2 for a plasma power of 200 W. Since our plasma power is more than three times higher, the assumption of the arc temperature being 3340 K should be reasonable. Nevertheless, it has to be realized that it is only an estimation.

As the temperature inside the arc is very high, thermal decomposition of CO_2 is included in the model through the reactions $\text{CO}_2 + \text{M} \rightarrow \text{CO} + \text{O} + \text{M}$ and $\text{CO}_2 + \text{O} \rightarrow \text{CO} + \text{O}_2$, including their reverse processes. The calculations reveal that thermal conversion is responsible for about 90 % of the total CO_2 conversion at this high temperature.

The maximum temperature is reached faster at lower flow rates (i.e., even at 0.5 cm for 10 L/min), which is logical, as the gas has more time to heat up. The vibrational temperature (Figure 9(b)) and electron density (Figure 9(d)) follow the same trend, achieving their maximum values (~ 3340 K and $8.5 \times 10^{11} \text{ cm}^{-3}$, respectively) at the same positions. Comparing the electron density with experimental values was not possible, as such measurements in a CO_2 GAP were not found. In a conventional GA the electron density in air was measured to be 10^{12} - 10^{13} cm^{-3} ⁷⁰. However, CO_2 has more internal degrees of freedom than N_2 and O_2 , so less electron energy going to ionization and more towards vibrational excitation is to be expected, which can explain the lower electron density predicted by our model than in air. The fact that the calculated values are rather low may be attributed to the 0D approach, which does not capture non-uniformity in the arc discharge, e.g., higher power density in the center, which may lead to higher electron densities. However, according to⁵¹, the GAP operates in the transitional regime where the electron density lies typically in between 10^{11} and 10^{12} cm^{-3} , so the calculated values should be reasonable.

The initial electron temperature (Figure 9(c)) is equal to 2.3 eV but it lowers to 1.1 eV when the maximum gas temperature is reached. This higher electron temperature in the beginning of the arc can be attributed to the fact that the power is initially deposited over a small number of electrons. The values obtained for the gas and electron temperature are typical for the GAP and other types of so-called warm plasma^{32,33,51}.

The electron temperature is much higher than the gas temperature (1.1 eV or 12800 K versus 3340 K) and thus the plasma is in non-equilibrium, which is most suitable to activate the gas through electron impact dissociation, ionization and excitation, and thus for energy-efficient CO_2 conversion.

Initially, the vibrational temperature is about two times higher than the gas temperature, indicating that the vibrational levels are overpopulated, and show a non-thermal vibrational distribution function (VDF) (see Appendix:

Figure A1). The vibrational temperature also exhibits a sharp increase, showing the importance of vibrational excitation in a GAP, as also stated in ³¹. However, the sharp increase in vibrational temperature happens at the same positions as the gas temperature, and both temperatures become almost equal to each other, which means that the vibrational levels will become thermalized after a travelled distance of 0.60 cm, and they will exhibit a near Boltzmann distribution (see Figure A1). Thus, the non-thermal zone of the GAP is only found in the first 0.60 cm, hence only 15% of the total arc length. Afterwards, the vibrational temperature is equal to the gas temperature, and the plasma is quasi-thermal. It is still not entirely thermal, because the electron temperature is much higher than the gas temperature, as pointed out in previous section. . This distance of 0.60 cm is reached at residence times of about 600 μs or longer. Indeed, at temperatures above 1000 K, VT relaxation becomes important within this time, as also observed by Vermeiren and Bogaerts ²³. Also, in our simulations the vibrational temperature is less than two times higher than the gas temperature after 100 μs and the largest difference between the two temperatures is found between 20 μs and 60 μs , which corresponds well with the simulations of Vermeiren and Bogaerts ²³. Therefore, the highest vibrational levels will not be overpopulated, which would be needed for the most energy-efficient vibration-induced dissociation from the highest levels (see further).

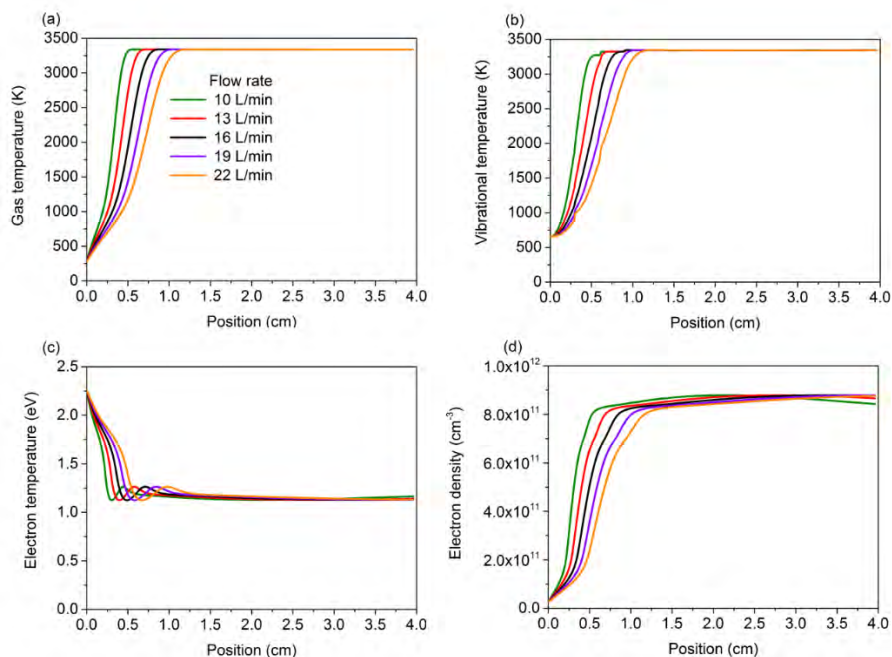


Figure 9: Gas temperature (a), vibrational temperature (b), electron temperature (c) and electron density (d) as a function of position in the arc column, calculated for different gas flow rates, at a plasma power of 650 W.

Figure 10 shows the evolution of the CO₂ conversion inside the arc, as a function of position in the arc column, for different flow rates and a plasma power of 650 W, calculated with the full chemistry set (solid lines), and accounting only for thermal reactions (dashed lines). The conversion starts to increase when the vibrational and gas temperature reach their maximum values. The conversion calculated with the full chemistry starts earlier in time/space, which indicates that vibration-induced dissociation, next to thermal dissociation, will play a significant role (see also Sections 3.5 and 3.6). Nevertheless, once the gas temperature has reached the same value as the vibrational temperature (see Figure 9), the conversions calculated with and without plasma processes rise to the same extent, which indicates that thermal conversion now dominates.

The conversion is higher at lower flow rates, which is again logical, because the gas has more time to be converted. At 22 L/min, the conversion rises more or less linearly, up to 35 % at the end of the arc column. At 10 L/min, the conversion reaches more than 50 % at the end of the arc column, but after a linear

increase up to 1.5 cm, the rise becomes less significant, indicating that the reverse reaction (i.e., recombination of CO into CO₂) will become important as soon as about 30 % of the CO₂ molecules are converted (see also Section 3.5 below).

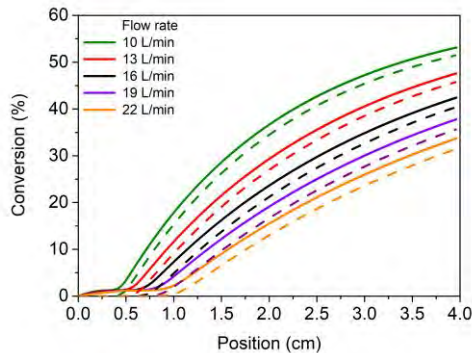


Figure 10: Calculated CO₂ conversion inside the arc, as a function of position in the arc column, for different gas flow rates, at a plasma power of 650 W. The corresponding values of specific energy input (SEI), calculated from the plasma power and gas flow rate (see equation (24) in Chapter 2), are also indicated. The solid lines are calculation results with the full chemistry set, while the dashed lines are calculation results without electron impact/plasma processes, hence accounting for pure thermal conversion.

3.5 Overall CO₂ conversion and energy efficiency

The overall CO₂ conversion will be lower than the values obtained inside the arc, as a significant fraction of the gas (i.e., about 85 %) does not pass through the arc column and will not be converted. Thus, the CO₂ conversion at the end of the arc column must be multiplied with 14.8 %, to obtain the overall CO₂ conversion, as explained in detail in Section 3.2 above. The overall CO₂ conversion is illustrated in Figure 11 as a function of SEI, together with the experimentally obtained conversions, as well as the energy efficiencies, for the conditions studied in ⁵², i.e., different combinations of gas flow rate and plasma power. It is clear that the overall conversion is more limited, i.e., maximum around 8 %. The calculated conversions and energy efficiencies show good agreement with the experimental results, with an average relative error of 6 % and a maximum relative error of 16 % at SEI = 0.48 eV/molec.

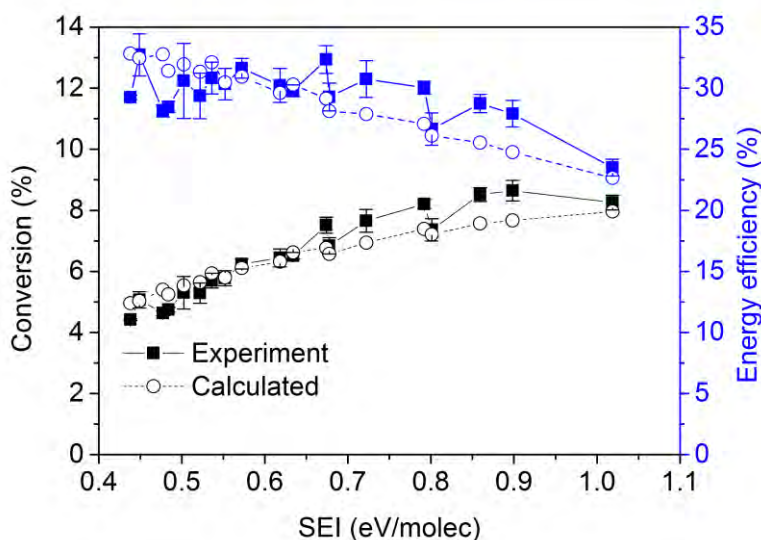


Figure 11: Calculated and measured CO₂ conversion (left y-axis) and corresponding energy efficiency (right y-axis) as a function of the specific energy input (SEI), which is a combination of different values of gas flow rate and plasma power. The experimental data are adopted from ⁵².

Both the model and the experiments indicate energy efficiencies up to 33 % for a CO₂ conversion of 7.5 %. Similar values of conversion between 2 % and 9 % and energy efficiencies between 22 % and 37 % were achieved in the GAP of³¹. Furthermore, in an AC-pulsed reverse vortex “tornado” flow GA plasma ⁵³, a CO₂ conversion of 6 % with a corresponding energy efficiency of 29 % was obtained, again very similar to the results reported here. These energy efficiencies are somewhat higher than earlier experiments with conventional GA plasmas, where maximum energy efficiencies of approximately 25 % were reported ⁵⁰, but at higher conversions of 18 %. In a more recent study of a conventional GA ²⁹, conversions in the range of 6-10 % were found with energy efficiencies between 20 % and 40 %, which is comparable and even slightly better than the results reported here. However, in this case, the GA was sealed in an insulated container, providing for recirculation of the gas through the arc, and hence a larger fraction of the gas can be treated.

Snoeckx and Bogaerts reported a very detailed comparison of the CO₂ conversion and energy efficiency in all types of plasmas that have been

investigated up to now³, which showed that the GAP is among the most energy-efficient plasma sources for CO₂ conversion. The highest energy efficiencies ever measured were in a microwave (MW) discharge with values up till 60 %^{71,72} and even 80-90 %^{14,22}. However, the latter results were obtained using supersonic flows combined with reduced pressure, and the latter is undesirable for industrial implementation. Furthermore, when MW plasmas operate at atmospheric pressure, the energy efficiency typically drops to 5-20 %⁷³, although results obtained at DIFFER show energy efficiencies of ~44 % for pressures approaching atmospheric pressure, i.e. larger than 600 mbar⁷². One of the most suitable plasma reactors for upscaling is the DBD reactor, due to its robust design and its operation at atmospheric pressure. However, the energy efficiency is generally (much) lower than in a GA, with values typically reported up to maximum 10-15 %, although recently energy efficiencies up till 23 % were achieved for a CO₂ conversion of 26 % in a DBD in burst mode⁷⁴.

Although the GAP thus shows promising results, also in comparison with other plasma types, the conversion and energy efficiency should still be improved for further exploitation. As there is very good agreement between the calculated and experimental conversions and energy efficiencies, we may conclude that the model provides a realistic picture of the CO₂ conversion, and that it can thus be used to elucidate the underlying reaction pathways, which is needed to further improve the performance. This will be discussed in the next Section.

3.6 Chemical pathway analysis of CO₂ conversion

In Figure 12 the rates, integrated over the entire residence time of the gas inside the plasma, of the most important loss and formation processes of CO₂ are plotted, as a function of SEI. The total time-integrated rate of the loss processes is only about a factor 2-3 higher than the total time-integrated rate of the formation processes, i.e. $1.0-2.5 \times 10^{18} \text{ cm}^{-3}$ versus $2.3 \times 10^{17}-1.3 \times 10^{18} \text{ cm}^{-3}$, for all conditions investigated. This indicates that a significant fraction of the dissociated CO₂ (in CO, O and O₂) will recombine again inside the plasma. Indeed, the reaction products of the dissociation processes are also the most important reactants for the formation of CO₂, as will be explained below.

It is clear from Figure 12(a) that vibration-induced dissociation plays a significant role in converting CO₂, but it mainly occurs from the lowest

vibrational levels, because the higher vibrational levels do not really show an overpopulation. The most important dissociation processes are the collisions of vibrationally excited CO₂ with an O atom, forming CO and O₂, followed by the collision with any neutral species (denoted as M), forming CO and O. Electron impact dissociation from the ground state and from the vibrationally excited states of CO₂ also play a role, but their rates are about three times lower. Hence, although the electron temperature, i.e. 1.1 eV, is perfect for vibrational excitation of the gas, the gas temperature becomes soon high enough so that thermal processes dominate above electron impact dissociation. This can also be seen in Figure 10 above, where both the plasma conversion and thermal conversion (i.e., without electron impact processes) rise to the same extent, and the plasma conversion is only a little higher than thermal conversion due to the initial importance of vibration-induced dissociation when the higher vibrational levels are still overpopulated.

The most important formation mechanism of CO₂ (see Figure 12b) is the reaction between CO and O₂, forming again CO₂ and an O atom, followed by the three-body recombination ($\text{CO} + \text{O} + \text{M} \rightarrow \text{CO}_2 + \text{M}$), although the rate of the latter process is almost one order of magnitude lower.

Since the most important formation processes are the reverse of the most important loss processes, the net rates of these processes (i.e., loss minus formation) are shown in Figure 12(c). It is clear that dissociation upon collision with an O atom or any neutral species M, primarily from vibrationally excited CO₂, contribute almost equally towards the CO₂ dissociation, with relative contributions of 38 % and 40 % at the lowest and highest SEI value, respectively. These processes are followed by electron impact dissociation from the ground state (14 % and 10 % at the lowest and highest SEI value) and from vibrationally excited CO₂ (~7 %, independent of the SEI).

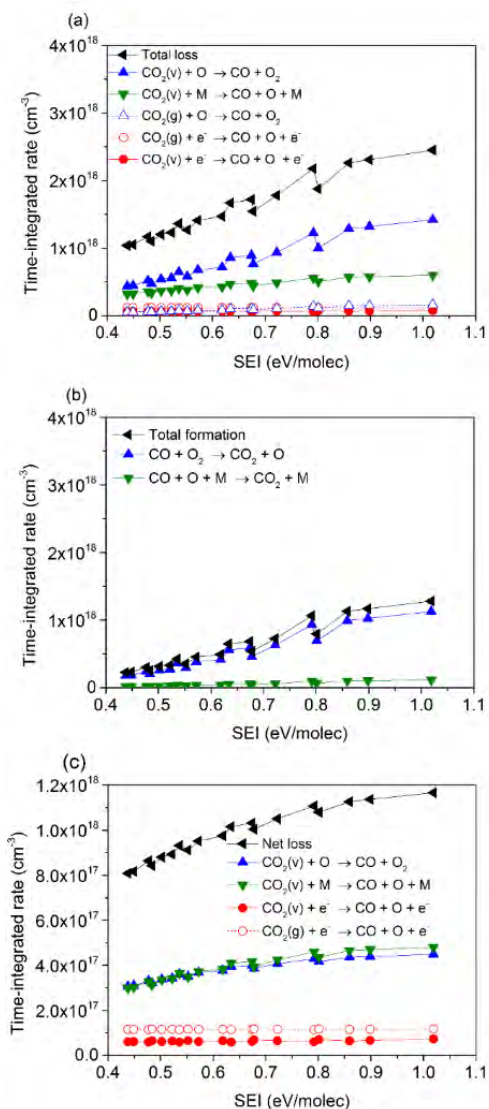


Figure 12: Time-integrated rates of the main loss (a) and formation (b) mechanisms of CO_2 , and of the main net loss mechanisms (c), as a function of the specific energy input (SEI). The same colors are used in (a,b,c) for the same processes; solid lines/closed symbols are used for the processes from the vibrational levels, while dashed lines/open symbols apply to the processes from the ground state.

A general reaction scheme illustrating the main pathways of CO_2 dissociation in the GAP is given in Figure 13. The process is initiated by electron impact

excitation from the CO_2 ground state, populating the vibrational levels (black arrows). Furthermore, the lowest vibrational levels ($\text{CO}_2(v_i)$) collide with each other, gradually populating the higher vibrational levels ($\text{CO}_2(v_{j>i})$) by so-called VV relaxation (yellow arrows). At the same time, the vibrational levels also collide with neutral species in so-called VT relaxation (red arrows), which leads to loss of the higher levels, and thermalization of the VDF. The VV relaxation is thus generally beneficial for energy-efficient CO_2 conversion, while the VT relaxation has a negative effect. The dissociation of CO_2 occurs upon collision with O atoms (blue arrows), any neutral species M (green arrows) and electrons (black arrows), mainly from the CO_2 vibrational levels, although electron impact dissociation mainly happens from the ground state (see Figure 12). At the same time, recombination of CO with O or O_2 also takes place, forming again CO_2 (purple arrows), which should be avoided. Note that CO_2 dissociation upon collision with O atoms and with any neutral species M occurs mainly from the lower CO_2 (symmetric mode) vibrational levels, because the higher vibrational levels are not overpopulated, i.e., the VDF is thermal. Hence, these processes (indicated with blue and green arrows) also denote the thermal conversion.

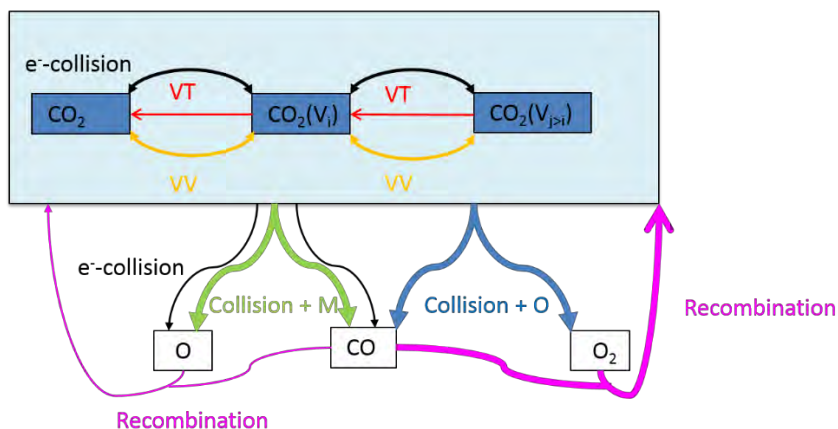


Figure 13: Reaction scheme illustrating the main pathways for CO_2 conversion in the GAP.

3.7 Role of the vibrational levels in the CO₂ dissociation

It is clear from Figure 12 that most of the CO₂ dissociation occurs from the vibrational levels. To understand which vibrational levels contribute most, the net contribution of the different vibrational levels towards the dissociation of CO₂ at 650 W, for different flow rates, as well as the main dissociation processes occurring at each vibrational level, at a flow rate of 16 L/min are plotted in Figure 14. As shown in Figure 14(a), for all flow rates studied, most dissociation occurs from the symmetric mode vibrational levels (i.e., combined levels Va-Vd; see Table 1 for the identification of these levels; overall contribution ~ 65 %), followed by the ground state (contribution ~16 %) and the first three asymmetric mode vibrational levels (overall contribution ~ 10 %). The remaining 9 % of the CO₂ dissociation arises from the higher asymmetric mode levels. This low contribution is due to the fact that the vibrational distribution function (VDF) quickly becomes quasi-Boltzmann distributed, at positions > 0.60 cm (see Figure A1 in the Appendix). This means that the highest levels will not be overpopulated, as is the case for instance in MW plasmas at reduced pressure^{25,57,75}. Therefore, dissociation will occur from the lowest levels instead of from the more desirable highest levels. Indeed, at atmospheric pressure and high gas temperatures (> 1000 K), VT relaxation will play an important role in thermalizing the VDF. The same was observed in^{14,25} for a MW discharge at atmospheric pressure.

Figure 14(b) demonstrates that vibration-induced dissociation of the symmetric mode levels, upon collision with an O atom or a neutral species M, contribute most to the dissociation of CO₂, while electron impact dissociation mainly occurs from the CO₂ ground state. This process, as well as collision with an O atom, becomes less important upon increasing asymmetric mode level. Indeed, for these higher levels, dissociation upon collision with any neutral species M is the most important. Since most dissociation occurs from the lowest levels, the dissociation kinetics from the higher asymmetric mode levels will not be discussed.

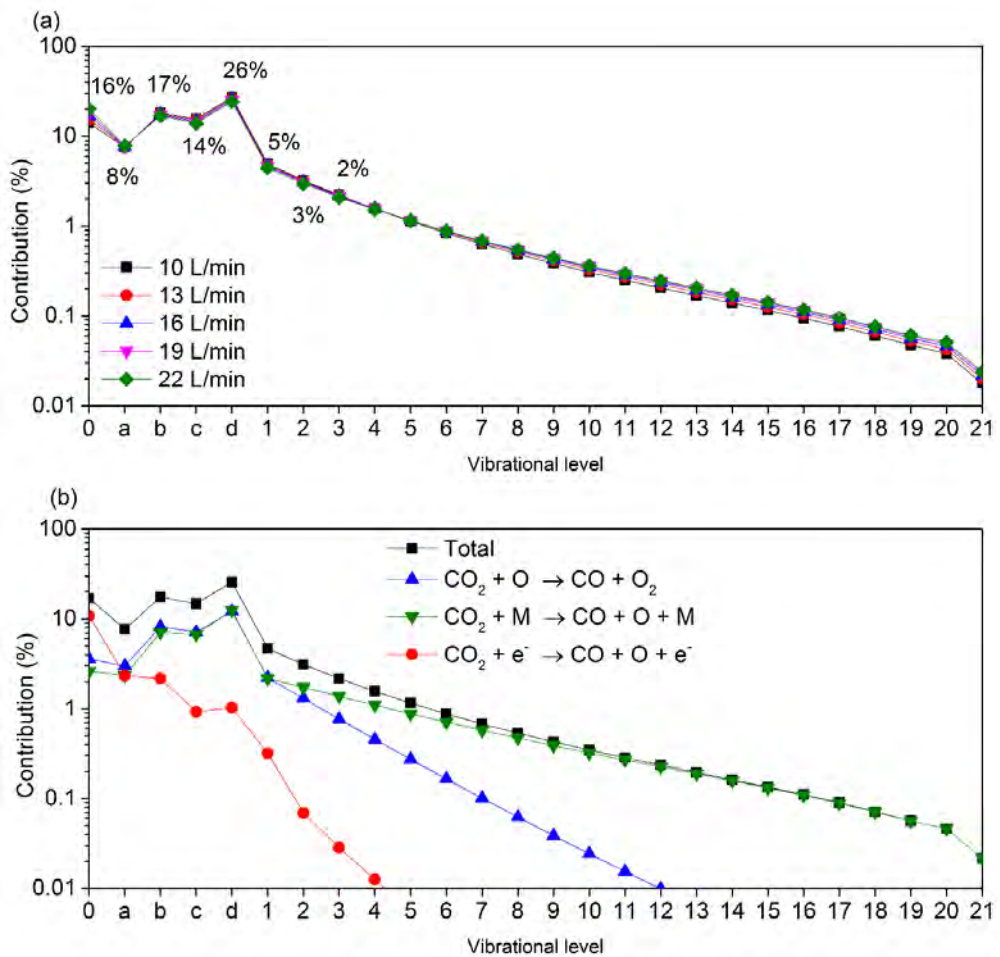


Figure 14: Relative contribution of the different CO₂ vibrational levels to the total dissociation of CO₂ for different flow rates at an input power of 650 W (a), and contributions of the individual processes for each vibrational level, at a flow rate of 16 L/min and an input power of 650 W.

3.8 Optimizing the CO₂ conversion and energy efficiency

Although the GAP already performs quite well compared to other plasma types³, it is clear that there is still room for improvement, if the role of the higher vibrational levels could be better exploited or if the rate of CO₂ formation could be reduced. 0D kinetic modelling allows us to study the effect of different plasma conditions, beyond what is experimentally feasible until now, on the CO₂

chemistry, and thus on the CO₂ conversion and energy efficiency, to give conceptual information about how to improve the GAP. In the following subsections, the effects will be studied of (i) lowering and increasing the gas temperature, as this will affect the VDF²⁵, and (ii) removing the O₂ molecules, in order to block the main formation process of CO₂. Also, the range of SEI values is extended from 0.1 eV/molec to 2.5 eV/molec, so a wide range of powers (between 147 W and 33.4 kW) and gas flow rates (between 22 L/min and 200 L/min) is investigated. It should be realized that some combinations, such as high SEI values and low gas temperatures (< 1000 K), cannot be experimentally achieved, but the results might give valuable insights for future reactor design. More specifically, we uncoupled the gas temperature from the SEI and thus from the power deposited inside the discharge, which gives us more information about how the performance could be improved if all energy goes into plasma processes (instead of heat), and thus if VT relaxation can be suppressed/controlled. In addition, we also assumed the arc dimensions to be the same. The flow rates used in the following subsections are 22 and 200 L/min. Indeed, the highest energy efficiency in the experiments was obtained for 22 L/min⁵², and on the other hand, flow rates around 200 L/min were applied in⁷⁶ where a high power GAP was designed for upscaling towards industrial applications. Although the assumptions used in the 0D model, originally based on 3D modelling, may not be valid anymore for very high flow rates, such as 200 L/min, the idea of increasing the flow rate, in the 0D model, is to see the effect of shorter residence times for the same discharge dimensions. In reality, however, arc dimensions and the flow pattern may change significantly, causing the residence time in the discharge to be different than by pure linear scaling of the initial velocities. However, in this way, it is easier to compare the chemistry at different conditions and to identify the effect of individual parameters.

The predicted conversions and energy efficiencies as a function of flow rate between 22 and 200 L/min, and for different values of the SEI, are plotted in Figures A2 and A3 of the Appendix, at a maximum gas temperature of 500 K and 3500 K, respectively. A gradual change is observed in both conversion and energy efficiency, between the values obtained at 22 L/min and 200 L/min. Therefore, in the following, we only show results for this minimum and maximum flow rate.

3.8.1 Influence of the gas temperature

As mentioned above, a high gas temperature (> 1000 K) enhances the VT relaxation, which has a negative effect on energy-efficient CO_2 conversion as it depopulates the higher vibrational levels. On the other hand, the rates of the dissociation reactions upon collision with O atoms or any neutral species M will also rise with temperature. Therefore, the effect of the maximum gas temperature in the arc column on the CO_2 conversion and energy efficiency needs to be investigated. The results are shown as a function of SEI in Figure 15 for a flow rate of 22 L/min and 200 L/min. In both cases, the SEI values are varied between 0.1 and 2.5 eV/molec. This corresponds to a plasma power between 147 W and 3.68 kW for a flow rate of 22 L/min, while at 200 L/min, this corresponds to values between 1.34 kW and 33.4 kW.

At 22 L/min (Figure 15(a,b)), the power seems too low for sufficient electron impact vibrational excitation followed by vibrational pumping towards the highest levels, and thus for dissociation from these highest levels, at all SEI values studied. At a low gas temperature of 500 K, where VT relaxation is suppressed, the calculations predict that dissociation upon collision with neutral species does not contribute at all towards CO_2 dissociation, and dissociation is almost entirely by electron impact dissociation from the ground state and the lowest vibrational levels. This is true for the entire range of SEI values (see Figures A4(a) and A5(a) for an SEI of 2.5 eV/molec and 0.2 eV/molec, respectively). Especially at low SEI values, electron impact dissociation mainly occurs from the ground state (see Figure A5(a)). This process is less energy-efficient than dissociation from the vibrational levels upon collision with neutral species. Thus, the CO_2 conversion and energy efficiency will rise with increasing gas temperature for 22 L/min, as is obvious from Figure 15(a,b), because dissociation upon collision with neutral species (either O atoms or any molecule M) from the (low) vibrational levels becomes more and more important at higher gas temperature (cf. Figure A4(b) and A5(b), where these processes are shown to be dominant for a gas temperature of 3500 K and an SEI of 2.5 eV/molec and 0.2 eV/molec, respectively).

As illustrated in Figure 15(a,b), at this flow rate of 22 L/min, a maximum conversion of 9 % is obtained at 3500 K and an SEI of 2.5 eV/molec, but it corresponds to a low energy efficiency of 10 %, while a maximum energy

efficiency above 80 % is predicted at the same temperature but at an SEI of 0.2 eV/molec, corresponding to a low conversion of 6 %. It should, however, be noted that in reality, temperatures of 3500 K are highly unlikely at an SEI below 0.34 eV/molec, and thus, an external heat source would be necessary to achieve this temperature. This would yield a higher overall SEI and thus lower energy efficiencies.

At a flow rate of 200 L/min (Figure 15(c,d)), the CO₂ conversion and energy efficiency follow the same trend as for 22 L/min, for SEI values below 0.7 eV/molec, with rising conversion and energy efficiency at higher temperatures. The maximum energy efficiency in this range was calculated to be 15 %, at an SEI of 0.34 eV/molec and 3500 K. In this case, dissociation upon collision with O atoms or molecules M also plays a significant role, although it is less significant than at 22 L/min, due to the higher plasma power for the same SEI and thus a larger contribution of electron impact dissociation (see Figure A6). As the latter process is less energy-efficient than dissociation upon collision with neutral species, this explains the lower energy efficiency.

For SEI values above 0.7 eV/molec, the behavior at 200 L/min is different from that at 22 L/min. Indeed, the conversion and energy efficiency rise upon lowering the gas temperatures to 1000 K and especially 500 K (see Figure 15(c,d)). The reason is that electron impact vibrational excitation followed by vibrational pumping, and hence vibration-induced dissociation from the highest levels, now becomes dominant, as can be deduced from Figure A7(a). Indeed, the contribution of vibration-induced dissociation from the highest vibrational levels is now 81 %, which is the most desired way of dissociating CO₂. However, this situation is only reached at very high plasma powers (> 10 kW), to obtain these high SEI values (above 0.7 – 1 eV/molec) at the flow rate of 200 L/min, and thus the energy efficiency (maximum 25 %) is still lower than the values obtained in experiments⁵², but the corresponding conversion is somewhat higher (ca. 12 %) than the best experimental values in⁵². At higher gas temperatures, the CO₂ conversion and energy efficiency drop due to thermalization of the VDF, until 3000 K where it rises again due to the increasing importance of dissociation upon collision with the neutral species (see also Figures A7(b) and A7(c)).

It can be concluded that for low flow rates (e.g., 22 L/min), a higher gas temperature leads to a higher conversion and energy efficiency, which is

attributed to thermal dissociation. This is true at all SEI values (and thus powers) investigated, but the energy efficiency is maximum at low SEI. On the other hand, at high flow rates and sufficiently high SEI values (and thus very high power values, i.e., several tens of kW), electron impact vibrational excitation followed by pumping, and thus vibration-induced dissociation from the highest levels, becomes much more significant at lower gas temperatures, due to less VT relaxation, and therefore, at these conditions, lower gas temperatures lead to higher conversion and energy efficiency.

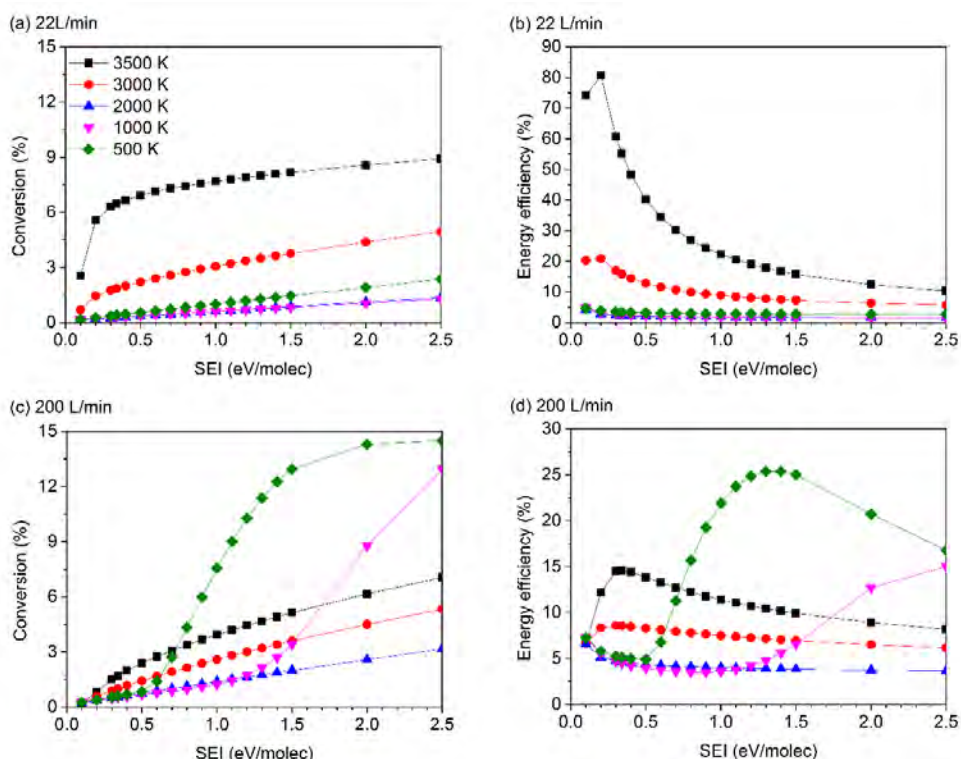


Figure 15: CO₂ conversion (a, c) and energy efficiency (b, d) as a function of SEI for different maximum gas temperatures in the arc column, at a flow rate of 22 L/min (a, b) and 200 L/min (c, d). The plasma power values needed to reach this SEI range vary between 147 W and 3.68 kW for 22 L/min, and between 1.34 kW and 33.4 kW for 200 L/min.

3.8.2 Removing the O₂ molecules

As shown in Figure 12, the total rate of CO₂ formation is only 2-3 times lower than the total rate of CO₂ loss, and this is mainly attributed to the recombination of CO with O₂ molecules. Hence, based on our model it is interesting to find out whether removing the O₂ molecules from the system can improve the overall CO₂ conversion. Separation methods, such as centrifugation, distillation and absorption, are difficult and not energy-efficient, due to the small difference in molar mass of CO and O₂,^{77,78} and probably not even applicable. Alternatively, inside the plasma itself, O₂ could be removed chemically by adding a hydrogen source, such as CH₄ and H₂, as was theoreticall and experimentally found by Aerts et al.⁷⁸ and Oren and Taylor⁷⁹. In addition, adding pure carbon as a reducing agent near the exhaust devours the free oxygen still present, as demonstrated by Peng et al.⁸⁰ Nevertheless, even if the separation is not yet feasible now, we investigate this effect here theoretically, because novel and more energy-efficient methods might be developed in future. The effect of removing the O₂ molecules from the system on the CO₂ conversion and energy efficiency is presented in Figure 16, for a flow rate of 22 L/min and 200 L/min, and typical maximum arc temperatures of 3000 and 3500 K.

At a flow rate of 22 L/min, O₂ removal has a slightly positive effect on the CO₂ conversion and energy efficiency at both temperatures investigated (see Figure 16(a,b)). The reason why the effect is so small is the following. When O₂ is removed, the CO₂ formation process due to recombination of CO with O₂ ($\text{CO} + \text{O}_2 \rightarrow \text{CO}_2 + \text{O}$) is indeed zero, but it also means that no O atoms can be formed by this process. Furthermore, no O atoms can be formed by dissociation of O₂ either. Hence, the O atom density drops significantly, and dissociation upon collision of vibrationally excited CO₂ with O atoms will also drop. Thus, not only the CO₂ formation decreases, but the CO₂ loss drops as well. Therefore, the net positive effect of O₂ removal on the CO₂ conversion and energy efficiency is very small. At 200 L/min, the effect of O₂ removal is even completely negligible (see Figure 16(c,d)).

In order to realize a higher CO₂ conversion, it would thus be necessary to remove the O₂ molecules, but at the same time the O atom production should not be disturbed or (more realistically) it should be replaced by another active agent that can contribute to CO₂ dissociation, such as H atoms. Adding a hydrogen

source like CH_4 or H_2 might thus provide a solution. Indeed, the combined CO_2/CH_4 conversion (i.e., dry reforming of methane)⁵³ and CO_2/H_2 conversion³¹ typically yield a higher CO_2 conversion and energy efficiency.

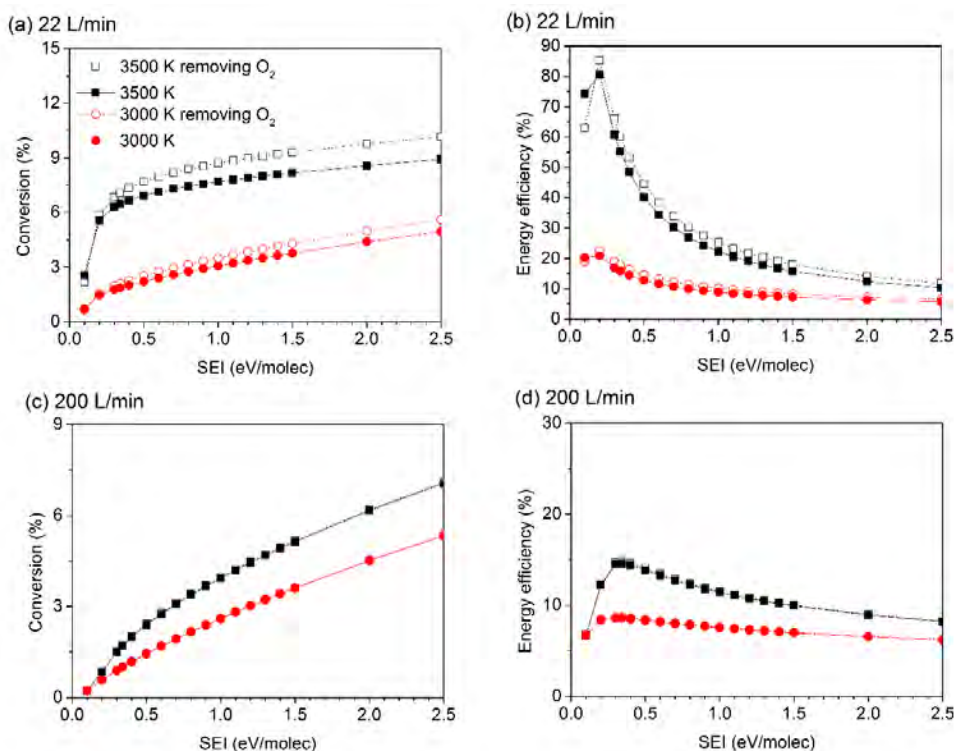


Figure 16: CO_2 conversion (a, c) and energy efficiency (b, d) as a function of SEI for 22 L/min (a, b) and 200 L/min (c, d), when the O_2 molecules are artificially removed from the system (dashed lines, open symbols) or not (solid lines, filled symbols).

3.9 Conclusion

We presented a chemical kinetics study to elucidate the main dissociation mechanisms of CO_2 in a GAP, with special emphasis on the role of the vibrational kinetics. The CO_2 conversion and energy efficiency calculated with the model in a wide range of SEI values (corresponding to different values of power and gas flow rate) are in good agreement with experimental values, obtained at the same conditions. This indicates that the model can provide a realistic picture of CO_2 conversion in the GAP, and can thus be used to identify the limitations, and propose solutions for further improvement.

The results obtained, both experimentally and in the model, demonstrate that the GAP is promising for CO₂ conversion, with energy efficiencies ranging between 23 and 33 %. This is explained by the large contribution of dissociation of the vibrationally excited levels upon collision with an O atom (CO₂ + O → CO + O₂) or any neutral species M (CO₂ + M → CO + O + M). However, because of the high gas temperature in the GAP (> 3000 K), the VDF exhibits a quasi-Boltzmann distribution with low population of the highest vibrational levels. Therefore, the dissociation mainly occurs from the lowest symmetric mode levels (contribution ~ 65 %), followed by the ground state (contribution ~ 16 %) and the first three asymmetric mode levels (contribution ~ 10 %), while the higher asymmetric mode levels have a negligible contribution.

A more pronounced overpopulation of the highest asymmetric mode levels, and thus dissociation from these levels, would further increase the energy efficiency. This overpopulation can in principle be achieved at lower gas temperature, because this reduces the VT relaxation. On the other hand, it also results in lower dissociation rates of the CO₂ vibrational levels upon collision with O atoms or neutral molecules M. Thus, the calculations reveal that lowering the gas temperature has in general no positive effect on the CO₂ conversion and energy efficiency. Only at 200 L/min and SEI values above 0.7 eV/molec, a gas temperature of 500 K yielded better results than higher temperatures, because the dissociation mainly occurs from the highest asymmetric mode vibrational levels. However, this energy-efficient dissociation mechanism cannot compensate for the large amount of power needed to induce it (>9.4 kW) and the maximum energy efficiency obtained is still limited to 25 %, although the conversion is slightly enhanced.

Furthermore, the calculations reveal that the recombination reaction (CO + O₂ → CO₂ + O) is the main factor limiting the overall CO₂ conversion, since a large fraction of the dissociated CO₂ (into CO, O and O₂) will recombine again into CO₂. Therefore, simulations were also performed by removing the O₂ molecules from the system. However, this has only a minor positive effect on the conversion and energy efficiency, since the O atom production through this process, and through the dissociation of O₂, is also inhibited, and these O atoms are needed to react with vibrationally excited CO₂ molecules, to provide more dissociation.

It is clear that the chemistry of CO₂ dissociation in a GAP is quite complicated, and simply reducing the gas temperature or removing the O₂ molecules from the system does not yield significantly better results than the ones obtained already experimentally. In order to further improve the performance of the GAP, a higher fraction of gas should pass the plasma column, because it is now limited to about 15 %. One possible way to achieve a higher gas treatment is to encapsulate the discharge with the same dimensions as the plasma arc itself, so that no gas can be passed untreated. This was successfully demonstrated in a confined design of an atmospheric pressure glow discharge, developed by Trenchev et al.⁸¹, where a ceramic tube was used to confine the discharge. On the other hand, this resulted in more heat losses towards the walls, so the energy efficiency was slightly lower than in the basic design, but the CO₂ conversion was significantly higher (12% in the confined design vs 3-4% in the basic design). This effect cannot be studied by 0D modeling, and 3D fluid dynamics simulations are needed for this purpose^{32,33,52}. Finally, also mixing the CO₂ gas with a hydrogen source, such as H₂ or CH₄, might improve the CO₂ conversion, as the H atoms can contribute to the CO₂ dissociation. This will be investigated in the next Chapter.

3.10 Appendix

Table A1: Electron impact reactions included in the model, calculated with cross sections data, using the calculated EEDF, as explained in Section 3.2, as well as the references where the data are adopted from.

No.	Reaction	Ref	Note
(X1) ^a	$e^- + CO_2 \rightarrow 2e^- + CO_2^+$	59-61	
(X2) ^a	$e^- + CO_2 \rightarrow 2e^- + O + CO^+$	59-61	
(X3) ^a	$e^- + CO_2 \rightarrow 2e^- + O^+ + CO$	82	
(X4) ^a	$e^- + CO_2 \rightarrow 2e^- + O_2 + C^+$	82	
(X5) ^a	$e^- + CO_2 \rightarrow 2e^- + O_2^+ + C$	83	
(X6) ^a	$e^- + CO_2 \rightarrow O^- + CO$	59-61	
(X7) ^b	$e^- + CO_2 \rightarrow e^- + O + CO$	59-61	
(X8) ^a	$e^- + CO_2 \rightarrow e^- + CO_2(E1)$	59-61	
(X9) ^b	$e^- + CO_2 \leftrightarrow e^- + CO_2(Vx)$	59-61	$x = a, b, c, d$
(X10) ^c	$e^- + CO_2 \leftrightarrow e^- + CO_2(Vi)$	59-61	$i = 1 - 21$
(X11) ^a	$e^- + CO \rightarrow 2e^- + CO^+$	84	
(X12) ^a	$e^- + CO \rightarrow 2e^- + C^+ + O$	85	
(X13) ^a	$e^- + CO \rightarrow 2e^- + C + O^+$	85	

(X14) ^a	$e^- + CO \rightarrow C + O^-$	86	
(X14bis) ^b	$e^- + CO \rightarrow e^- + C + O$	87	
(X15)	$e^- + CO \leftrightarrow e^- + CO(Vi)$	87	$i = 1 - 10$
(X16) ^b	$e^- + O_2 \rightarrow e^- + O + O$	88	
(X16M) ^a	$e^- + O_2 + M \rightarrow O_2^- + M$	88	
(X17) ^a	$e^- + O_2 \rightarrow O + O^-$	88	
(X18) ^a	$e^- + O_2 \rightarrow 2e^- + O_2^+$	89	
(X19) ^b	$e^- + O_2 \rightarrow 2e^- + O + O^+$	89	
(X20)	$e^- + O_2 \leftrightarrow e^- + O_2(Vi)$	88	$i = 1,2,3$
(X21)	$e^- + O_3 \rightarrow e^- + O_2 + O$	90	
(X22)	$e^- + O_3 \rightarrow 2e^- + O_2^+ + O$	90	
(X23)	$e^- + O_3 \rightarrow e^- + O^+ + O^- + O$	90	
(X24)	$e^- + O_3 \rightarrow O^- + O_2$	91	
(X25)	$e^- + O_3 \rightarrow O + O_2^-$	91	
(X26)	$e^- + O \rightarrow 2e^- + O^+$	92	
(X27)	$e^- + C \rightarrow 2e^- + C^+$	93	
(X28)	$e^- + CO \leftrightarrow e^- + CO(Ei)$	57,87	$i = 1 - 4$
(X29)	$e^- + C_2 \leftrightarrow e^- + C + C$	94	
(X30)	$e^- + C_2 \leftrightarrow 2e^- + C_2^+$	94	
(X31)	$e^- + C \leftrightarrow 2e^- + C^+$	95	
(X32)	$e^- + O_2 \leftrightarrow e^- + O_2(Ei)$	96	$i = 1,2$

a Same cross section also used for ground state.

b Cross section also used for the excited states, modified by lowering the energy threshold by the energy of the excited state.

c Cross section for the various levels (i,j) adopted from excitation from the ground state, $e^- + CO_2 \rightarrow e^- + CO_2(Vi)$, but scaled and shifted using Fridman's approximation^{14,57}

Table A2: Electron impact reactions using analytical expressions for the rate coefficients, given in $\text{cm}^3 \text{s}^{-1}$ and $\text{cm}^6 \text{s}^{-1}$, for two-body and three-body reactions, respectively, as well as the references where the data are adopted from. T_{gas} and T_e are given in K and eV, respectively.

No.	Reaction	Rate coefficient	Ref
(E1)	$e^- + CO_2^+ \rightarrow CO(V1) + O$	$2.0 \times 10^{-5} T_e^{-0.5} T_{gas}^{-1}$	97
(E2)	$e^- + CO_2^+ \rightarrow C + O_2$	$3.94 \times 10^{-7} T_e^{-0.4}$	83
(E3)	$e^- + CO^+ \rightarrow C + O$	$3.68 \times 10^{-8} T_e^{-0.55}$	98
(E4)	$e^- + C_2O_2^+ \rightarrow CO + CO$	$4.00 \times 10^{-7} T_e^{-0.34}$	99
(E5)	$e^- + C_2O_3^+ \rightarrow CO_2 + CO$	$5.40 \times 10^{-8} T_e^{-0.70}$	99
(E6)	$e^- + C_2O_4^+ \rightarrow CO_2 + CO_2$	$2.00 \times 10^{-5} T_e^{-0.50} T_{gas}^{-1.0}$	99
(E7)	$e^- + C_2^+ \rightarrow C + C$	$1.79 \times 10^{-8} T_e^{-0.50}$	99
(E8)	$e^- + O_3 + M \rightarrow O_3^- + M$	5.00×10^{-31}	99
(E9)	$e^- + O + M \rightarrow O^- + M$	5.00×10^{-31}	99
(E10)	$e^- + O_2^+ + M \rightarrow O_2 + M$	1.00×10^{-26}	100
(E11)	$e^- + O_2^+ \rightarrow O + O$	$6.00 \times 10^{-7} T_e^{-0.50} T_{gas}^{-0.50}$	97
(E12)	$e^- + O^+ + M \rightarrow O + M$	$2.49 \times 10^{-29} T_e^{-1.50}$	101
(E13)	$e^- + O_4^+ \rightarrow O_2 + O_2$	$2.25 \times 10^{-7} T_e^{-0.50}$	101

Table A3: Ion-ion and ion-neutral reactions, as well as the references where the data are adopted from. The rate coefficients are given in $\text{cm}^3 \text{s}^{-1}$ and $\text{cm}^6 \text{s}^{-1}$, for two-body and three-body reactions, respectively. T_{gas} is given in K.

No.	Reaction	Rate coefficient	Ref
(I1)	$CO_2 + CO^+ \rightarrow CO_2^+ + CO$	1.0×10^{-9}	102,103
(I2)	$CO_2 + O^- + M \rightarrow CO_3^- + M$	9.0×10^{-29}	99
(I3)	$CO_2 + O_2^- + M \rightarrow CO_4^- + M$	1.0×10^{-29}	99
(I4)	$CO + O^- \rightarrow CO_2 + e^-$	5.5×10^{-10}	102,104
(I5)	$CO + CO_3^- \rightarrow 2CO_2 + e^-$	5.0×10^{-13}	105
(I6) ^a	$CO_3^- + CO_2^+ \rightarrow 2CO_2(Vb) + O$	5.0×10^{-7}	106
(I7) ^a	$CO_4^- + CO_2^+ \rightarrow 2CO_2(Vb) + O_2$	5.0×10^{-7}	106
(I8) ^a	$O_2^- + CO_2^+ \rightarrow CO_2(V1) + O_2 + O$	6.0×10^{-7}	106
(I9)	$CO_3^- + O \rightarrow CO_2 + O_2^-$	8.0×10^{-11}	107
(I10a) ^a	$CO_4^- + O \rightarrow CO_3^- + O_2$	1.12×10^{-10}	102
(I10b) ^a	$CO_4^- + O \rightarrow CO_2 + O_2 + O^-$	1.4×10^{-11}	102

(I11)	$O + O^- \rightarrow O_2 + e^-$	2.3×10^{-10}	108
(I12)	$O + O_2^- \rightarrow O_2 + O^-$	3.31×10^{-10}	101,109
(I13)	$O_2^- + M \rightarrow O_2 + M + e^-$	$2.7 \times 10^{-10} \left(\frac{T_g}{300}\right)^{0.5} \exp(-5590/T_g)$	110,111
(I14)	$O^- + M \rightarrow O + M + e^-$	4.0×10^{-12}	99
(I15)	$O^+ + CO_2 \rightarrow O_2^+ + CO$	8.10×10^{-10}	83,102
(I16)	$O^+ + CO_2 \rightarrow O + CO_2^+$	9.00×10^{-11}	83,102
(I17)	$C^+ + CO_2 \rightarrow CO^+ + CO$	1.10×10^{-9}	83,102
(I18)	$O_3^- + CO_2 \rightarrow O_2 + CO_3^-$	5.50×10^{-10}	97,99
(I19)	$O_4^- + CO_2 \rightarrow O_2 + CO_4^-$	4.80×10^{-10}	99
(I20)	$CO_2^+ + CO_2 + M \rightarrow C_2O_4^+ + M$	3.00×10^{-28}	99
(I21)	$O^+ + CO \rightarrow O + CO^+$	$4.9 \times 10^{-12} \left(\frac{T_g}{300}\right)^{0.5} \exp(-4580/T_g)$	102
(I22)	$C_2O_3^+ + CO \rightarrow CO_2 + C_2O_2^+$	1.10×10^{-9}	99
(I23)	$C_2O_4^+ + CO \rightarrow CO_2 + C_2O_3^+$	9.00×10^{-10}	99
(I24)	$C_2O_3^+ + CO + M \rightarrow CO_2 + C_2O_2^+ + M$	2.60×10^{-26}	99
(I25)	$C_2O_4^+ + CO + M \rightarrow CO_2 + C_2O_3^+ + M$	4.20×10^{-26}	99
(I26)	$C^+ + CO \rightarrow C + CO^+$	5.0×10^{-13}	83
(I27)	$CO^+ + C \rightarrow CO + C^+$	1.1×10^{-10}	112
(I28)	$O_2^+ + C \rightarrow CO^+ + O$	5.2×10^{-11}	112
(I29)	$O_2^+ + C \rightarrow C^+ + O_2$	5.2×10^{-11}	112
(I30)	$C_2^+ + C \rightarrow C^+ + C_2$	1.1×10^{-10}	112
(I31)	$CO_2^+ + O \rightarrow CO + O_2^+$	1.64×10^{-10}	112
(I32)	$CO_2^+ + O \rightarrow CO_2 + O^+$	9.62×10^{-11}	112
(I33)	$CO_2^+ + O_2 \rightarrow CO_2 + O_2^+$	5.30×10^{-11}	112
(I34)	$CO^+ + O \rightarrow CO + O^+$	1.40×10^{-10}	112
(I35)	$CO^+ + O_2 \rightarrow CO + O_2^+$	1.20×10^{-10}	112
(I36)	$C_2O_2^+ + O_2 \rightarrow CO + CO + O_2^+$	5.0×10^{-12}	99
(I37)	$C_2O_2^+ + M \rightarrow CO^+ + CO + M$	1.0×10^{-12}	99
(I38)	$C_2O_2^+ + CO_3^- \rightarrow CO_2 + 2CO + O$	5.0×10^{-7}	99
(I39)	$C_2O_2^+ + CO_4^- \rightarrow CO_2 + 2CO + O_2$	5.0×10^{-7}	99
(I40)	$C_2O_2^+ + O_2^- \rightarrow CO + CO + O_2$	6.0×10^{-7}	99
(I41)	$C_2O_3^+ + CO_3^- \rightarrow 2CO_2 + CO + O$	5.0×10^{-7}	99

(I42)	$C_2O_3^+ + CO_4^- \rightarrow 2CO_2 + CO + O_2$	5.0×10^{-7}	99
(I43)	$C_2O_3^+ + O_2^- \rightarrow CO_2 + CO + O_2$	6.0×10^{-7}	99
(I44)	$C_2O_4^+ + M \rightarrow CO_2^+ + CO_2 + M$	1.0×10^{-14}	99
(I45)	$C_2O_4^+ + CO_3^- \rightarrow 3CO_2 + O$	5.0×10^{-7}	99
(I46)	$C_2O_4^+ + CO_4^- \rightarrow 3CO_2 + O_2$	5.0×10^{-7}	99
(I47)	$C_2O_4^+ + O_2^- \rightarrow 2CO_2 + O_2$	6.0×10^{-7}	99
(I48)	$O_2^+ + CO_3^- \rightarrow CO_2(Vb) + O_2 + O$	3.0×10^{-7}	97
(I49)	$O_2^+ + CO_4^- \rightarrow CO_2(Vb) + 2O_2$	3.0×10^{-7}	97
(I50)	$CO_4^- + O \rightarrow CO_2 + O_3^-$	1.4×10^{-11}	83
(I51)	$CO_4^- + O_3 \rightarrow CO_2 + O_3^- + O_2$	1.3×10^{-10}	83
(I52)	$C^+ + O_2 \rightarrow CO + O^+$	4.54×10^{-10}	113
(I53)	$C^+ + O_2 \rightarrow CO^+ + O$	3.8×10^{-10}	83
(I54)	$O^+ + O_2 \rightarrow O + O_2^+$	$1.9 \times 10^{-11} \left(\frac{T_{gas}}{300}\right)^{-0.5}$	83
(I55)	$O_2^+ + O_2 + M \rightarrow O_4^+ + M$	$2.4 \times 10^{-30} \left(\frac{T_{gas}}{300}\right)^{-3.2}$	101
(I56)	$O_2^- + O_2 + M \rightarrow O_4^- + M$	$3.5 \times 10^{-31} \left(\frac{T_{gas}}{300}\right)^{-1.0}$	101
(I57)	$O^- + O_2 \rightarrow O_3 + e^-$	1.0×10^{-12}	99
(I58)	$O^- + O_2 + M \rightarrow O_3^- + M$	$1.1 \times 10^{-30} \left(\frac{300}{T_{gas}}\right)$	99,101,109
(I59)	$O^- + O_3 \rightarrow O_3^- + O$	5.3×10^{-10}	99
(I60)	$O^- + O_3 \rightarrow 2O_2 + e^-$	3.0×10^{-10}	114
(I61)	$O_2^- + O_3 \rightarrow O_2 + O_3^-$	4.0×10^{-10}	114
(I62)	$O_3^- + O_3 \rightarrow 3O_2 + e^-$	3.0×10^{-10}	99
(I63)	$O^+ + O_3 \rightarrow O_2^+ + O_2$	1.0×10^{-10}	101
(I64)	$O^+ + O + M \rightarrow O_2^+ + M$	1.0×10^{-29}	101
(I65)	$O_2^- + O \rightarrow O_3 + e^-$	1.5×10^{-10}	109
(I66)	$O_3^- + O \rightarrow O_3 + O^-$	1.0×10^{-13}	109
(I67)	$O_3^- + O \rightarrow 2O_2 + e^-$	1.0×10^{-13}	99
(I68)	$O_3^- + O \rightarrow O_2^- + O_2$	2.5×10^{-10}	99,115
(I69)	$O_4^- + O \rightarrow O_3^- + O_2$	4.0×10^{-10}	101
(I70)	$O_4^- + O \rightarrow O^- + 2O_2$	3.0×10^{-10}	101
(I71)	$O_4^+ + O \rightarrow O_2^+ + O_3$	3.0×10^{-10}	101
(I72)	$O_2^- + O^+ + M \rightarrow O_3 + M$	$1.0 \times 10^{-25} \left(\frac{300}{T_{gas}}\right)^{2.5}$	83

(I73)	$O_2^- + O^+ \rightarrow O + O_2$	$2.7x10^{-7} \left(\frac{300}{T_{gas}}\right)^{0.5}$	109
(I74)	$O_2^- + O_2^+ \rightarrow O_2 + O_2$	$2.01x10^{-7} \left(\frac{300}{T_{gas}}\right)^{0.5}$	109
(I75)	$O_2^- + O_2^+ \rightarrow O_2 + 2O$	$4.2x10^{-7}$	97
(I76)	$O_2^- + O_2^+ + M \rightarrow O_2 + O_2 + M$	$1.0x10^{-25} \left(\frac{300}{T_{gas}}\right)^{2.5}$	83
(I77)	$O_3^- + O_2^+ \rightarrow O_2 + O_3$	$2.0x10^{-7} \left(\frac{300}{T_{gas}}\right)^{0.5}$	109
(I78)	$O_3^- + O_2^+ \rightarrow O_3 + O + O$	$1.0x10^{-7} \left(\frac{300}{T_{gas}}\right)^{0.5}$	109
(I79)	$O_3^- + O^+ \rightarrow O_3 + O$	$1.0x10^{-7} \left(\frac{300}{T_{gas}}\right)^{0.5}$	83
(I80)	$O_3^- + M \rightarrow O_3 + e^- + M$	$2.3x10^{-11}$	83
(I81)	$O^+ + O^- \rightarrow O + O$	$4.0x10^{-8} \left(\frac{300}{T_{gas}}\right)^{0.43}$	109
(I82)	$O^+ + O^- + M \rightarrow O_2 + M$	$1.0x10^{-25} \left(\frac{300}{T_{gas}}\right)^{2.5}$	83
(I83)	$O^- + O_2^+ \rightarrow O_2 + O$	$2.6x10^{-8} \left(\frac{300}{T_{gas}}\right)^{0.44}$	109
(I84)	$O^- + O_2^+ \rightarrow 3O$	$4.2x10^{-7} \left(\frac{300}{T_{gas}}\right)^{0.44}$	109
(I85)	$O^- + O_2^+ + M \rightarrow O_3 + M$	$1.0x10^{-25} \left(\frac{300}{T_{gas}}\right)^{2.5}$	109
(I86)	$O_4^- + M \rightarrow O_2^- + O_2 + M$	$1.0x10^{-10} \exp\left(-\frac{1044}{T_{gas}}\right)$	101
(I87)	$O_4^+ + M \rightarrow O_2^+ + O_2 + M$	$3.3x10^{-6} \left(\frac{300}{T_{gas}}\right)^{4.0} \exp\left(-\frac{5030}{T_{gas}}\right)$	101
(I88)	$O_2^+ + CO_2 + M \rightarrow CO_4^+ + M$	$2.3x10^{-29}$	83
a The primary source was not accessible			

Table A4: Neutral-neutral reactions, as well as the references where the data are adopted from. The rate coefficients are given in $\text{cm}^3 \text{s}^{-1}$ and $\text{cm}^6 \text{s}^{-1}$, for two-body and three-body reactions, respectively. T_{gas} is given in K. The α parameter determines the effectiveness of lowering the activation energy for reactions involving vibrationally excited levels of the molecules (see details in ^{14,57}).

No.	Reaction	Rate coefficient	α	Ref
(N1)	$CO_2 + M \rightarrow CO + O + M$	$1.81 \times 10^{-10} \exp\left(-\frac{49000}{T_{gas}}\right)$	0.80	¹¹⁶
(N2)	$CO_2 + O \rightarrow CO + O_2$	$2.8 \times 10^{-11} \exp\left(-\frac{26500}{T_{gas}}\right)$	0.50	^{117,118}
(N3)	$CO_2 + C \rightarrow 2CO$	$< 1.0 \times 10^{-15}$	n.a.	¹¹⁹
(N4)	$CO + O + M \rightarrow CO_2 + M$	$8.3 \times 10^{-34} \exp\left(-\frac{1510}{T_{gas}}\right)$	0.0	^{118,120}
(N5)	$O_2 + CO \rightarrow CO_2 + O$	$4.2 \times 10^{-12} \exp\left(-\frac{24000}{T_{gas}}\right)$	0.5	¹¹⁸
(N6)	$O_2 + C \rightarrow CO + O$	3.00×10^{-11}		⁹⁹
(N7)	$O + C + M \rightarrow CO + M$	$2.14 \times 10^{-29} \left(\frac{T_{gas}}{300}\right)^{-3.08} \exp\left(-\frac{2144}{T_{gas}}\right)$		^{117,118}
(N8)	$O + O + M \rightarrow O_2 + M$	$5.2 \times 10^{-35} \exp\left(\frac{900}{T_{gas}}\right)$	n.a.	^{117,118}
(N9)	$O_3 + CO \rightarrow CO_2 + O_2$	4.00×10^{-25}		⁸³
(N10)	$C + CO + M \rightarrow C_2O + M$	6.31×10^{-32}		¹²¹
(N11)	$O + C_2O \rightarrow CO + CO$	9.51×10^{-11}		¹²²
(N12)	$O_2 + C_2O \rightarrow CO_2 + CO$	3.30×10^{-11}		⁹⁹
(N13)	$O + O_3 \rightarrow O_2 + O_2$	$8.00 \times 10^{-12} \exp\left(-\frac{2056}{T_{gas}}\right)$		¹²³
(N14)	$O_3 + M \rightarrow O_2 + O + M$	$4.12 \times 10^{-10} \exp\left(-\frac{11430}{T_{gas}}\right)$		⁸³
(N15)	$O + O_2 + M \rightarrow O_3 + M$	$5.51 \times 10^{-34} \left(\frac{T_{gas}}{298}\right)^{-2.60}$		¹²⁴

Table A5: Neutral reactions between vibrationally excited molecules, as well as the references where the data are adopted from. The rate coefficients are given in $\text{cm}^3 \text{s}^{-1}$ and $\text{cm}^6 \text{s}^{-1}$, for two-body and three-body reactions, respectively. T_{gas} is given in K.

No.	Reaction	Rate coefficient	Ref
(V1)	$CO_2(Va) + M \rightarrow CO_2 + M$	$7.14 \times 10^{-15} \exp(-177T_g^{-1/3} + 451T_g^{-2/3})$	125-127
(V2a)	$CO_2(V1) + M \rightarrow CO_2(Va) + M$	$4.25 \times 10^{-7} \exp(-407T_g^{-1/3} + 824T_g^{-2/3})$	127-129
(V2b)	$CO_2(V1) + M \rightarrow CO_2(Vb) + M$	$8.57 \times 10^{-7} \exp(-404T_g^{-1/3} + 1096T_g^{-2/3})$	127-129
(V2c)	$CO_2(V1) + M \rightarrow CO_2(Vc) + M$	$1.43 \times 10^{-7} \exp(-252T_g^{-1/3} + 685T_g^{-2/3})$	127-129
(V3)	$CO(V1) + M \rightarrow CO + M$	$1.0 \times 10^{-18} T_g \exp(-150.7T_g^{-1/3})$	130
(V4)	$O_2(V1) + M \rightarrow O_2 + M$	$1.3 \times 10^{-14} \exp(-158.7T_g^{-1/3})$	126,127
(V5)	$CO_2(V1) + CO_2 \rightarrow CO_2(Va) + CO_2(Vb)$	$1.06 \times 10^{-11} \exp(-242T_g^{-1/3} + 633T_g^{-2/3})$	127-129
(V6)	$CO_2(V1) + CO_2 \rightarrow CO_2 + CO_2(V1)$	$1.32 \times 10^{-18} \left(\frac{T_g}{300}\right)^{0.5} \frac{250}{T_g}$	131,132
(V7)	$CO(V1) + CO \rightarrow CO + CO(V1)$	$3.4 \times 10^{-16} \left(\frac{T_g}{300}\right)^{0.5} \left(1.64 \times 10^{-6} T_g + \frac{1.61}{T_g}\right)$	133,134
(V8)	$CO_2(V1) + CO \rightarrow CO_2 + CO(V1)$	$4.8 \times 10^{-12} \exp(-153T_g^{-1/3})$	127,128

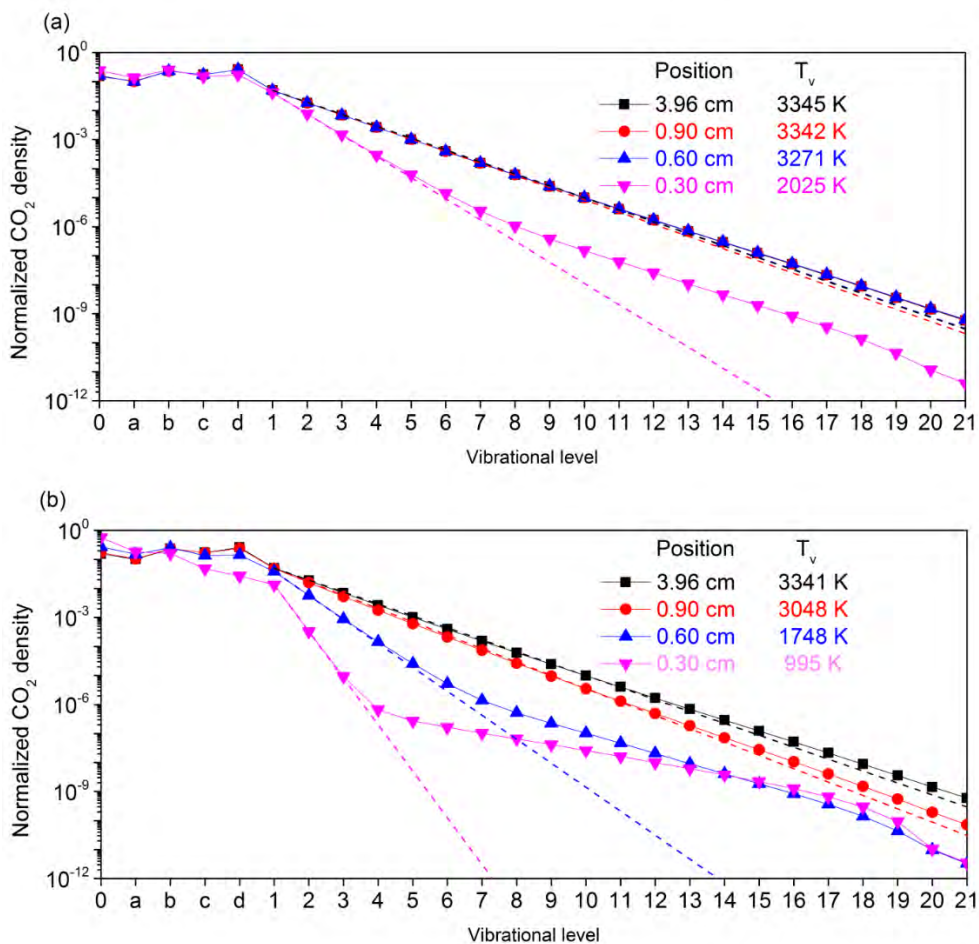


Figure A1: Vibrational distribution functions (VDFs) of CO₂ at a flow rate of 10 L/min (a) and 22 L/min (b) for a plasma power of 650 W, at different positions in the arc column. The vibrational temperature of the asymmetric mode is also indicated in the legend for each case. It is calculated from the slope, indicated with dashed lines.

Table A6: Notation of the different vibrational levels included in the model with their corresponding state and energy, following the model developed in ⁵⁷.

Notation	States	Energy (eV)
Ground state (g)	(000)	0.00
Va	(010)	0.08
Vb	(020)+(100)	0.17
Vc	(030)+(110)	0.25
Vd	(040)+(120)+(200)	0.33
V1	(001)	0.29
V2	(002)	0.58
V3	(003)	0.86
V4	(004)	1.14
V5	(005)	1.43
V6	(006)	1.70
V7	(007)	1.97
V8	(008)	2.24
V9	(009)	2.51
V10	(0010)	2.77
V11	(0011)	3.03
V12	(0012)	3.29
V13	(0013)	3.55
V14	(0014)	3.80
V15	(0015)	4.04
V16	(0016)	4.29
V17	(0017)	4.53
V18	(0018)	4.77
V19	(0019)	5.01
V20	(0020)	5.24
V21	(0021)	5.47

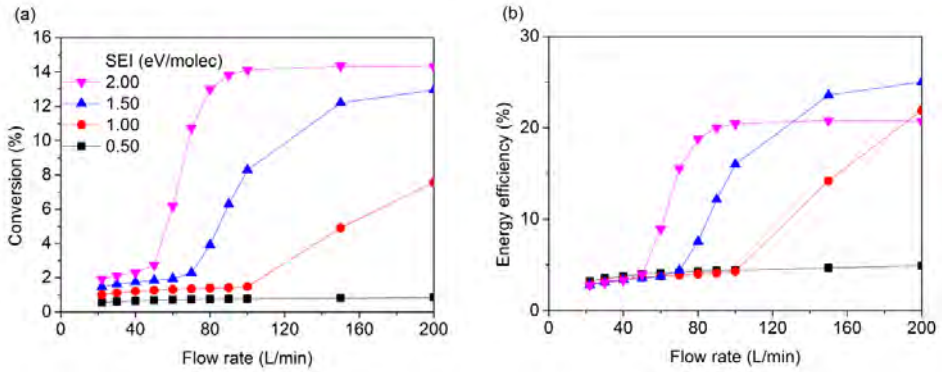


Figure A2: CO₂ conversion (a) and energy efficiency (b) as a function of flow rate for different SEI values and at a maximum gas temperature of 500 K. Note that for each curve the power will also increase with the flow rate, to keep the SEI constant.

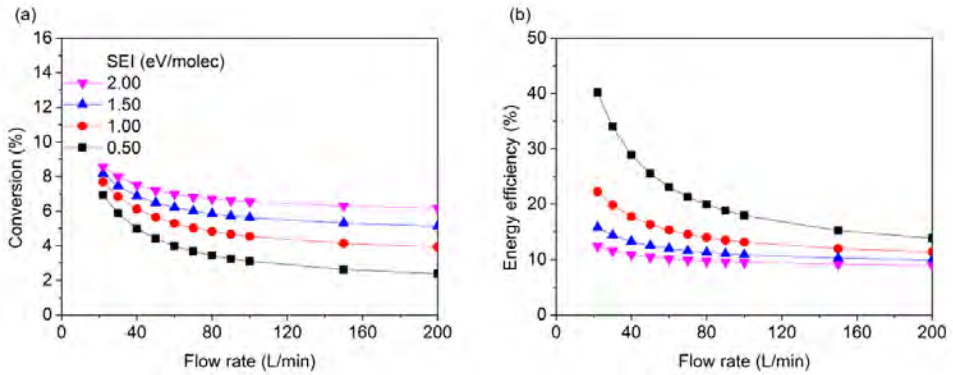


Figure A3: CO₂ conversion (a) and energy efficiency (b) as a function of flow rate for different SEI values and at a maximum gas temperature of 3500 K.

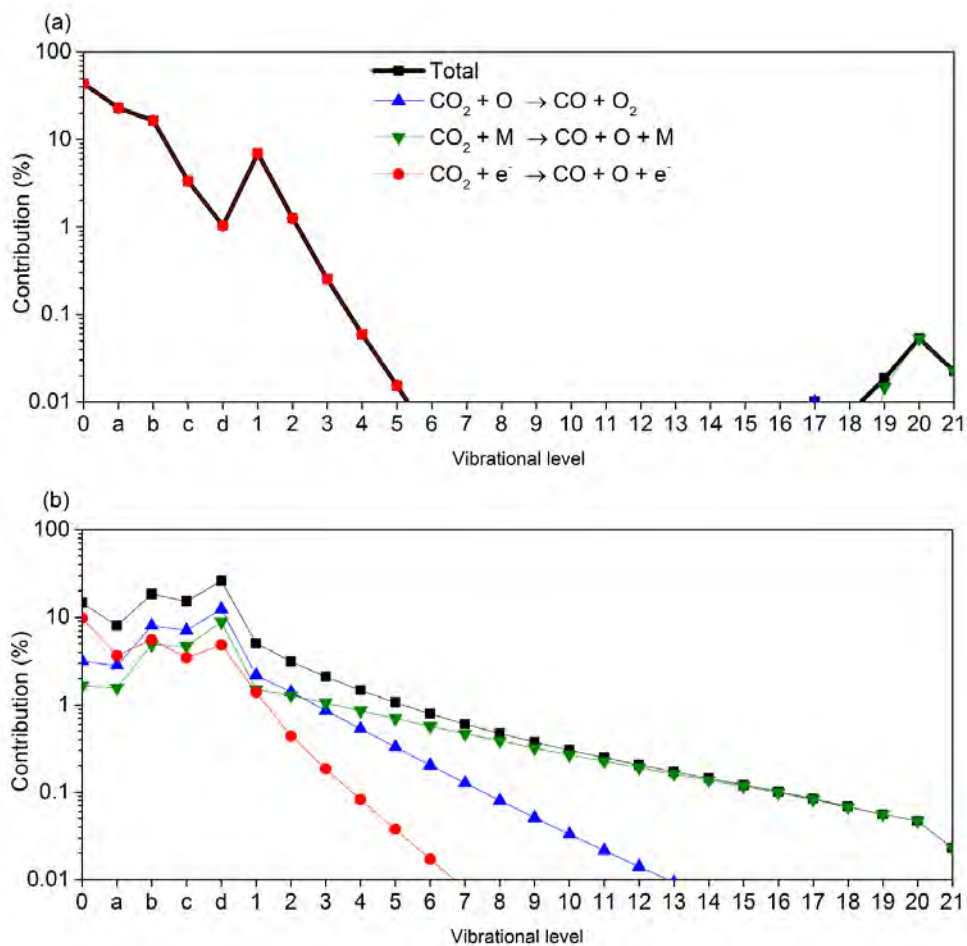


Figure A4: Contribution of the different CO₂ vibrational levels to the total dissociation of CO₂ at a flow rate of 22 L/min and a maximum gas temperature of 500 K (a) and 3500 K (b) at an SEI of 2.5 eV/molec.

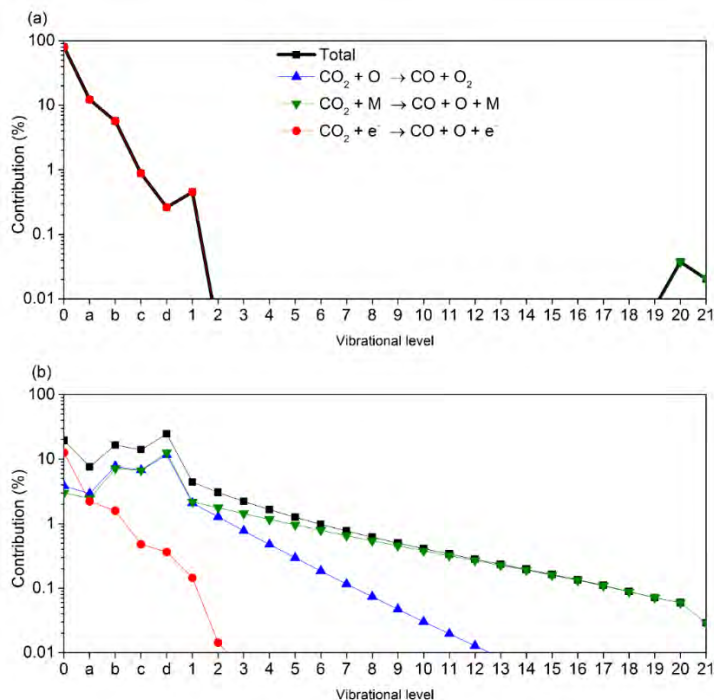


Figure A5: Contribution of the different CO₂ vibrational levels to the total dissociation of CO₂ at a flow rate of 22 L/min and a maximum gas temperature of 500 K (a) and 3500 K (b), at an SEI of 0.2 eV/molec, where the maximum energy efficiency is reached (see Figure 15(b) from the main text).

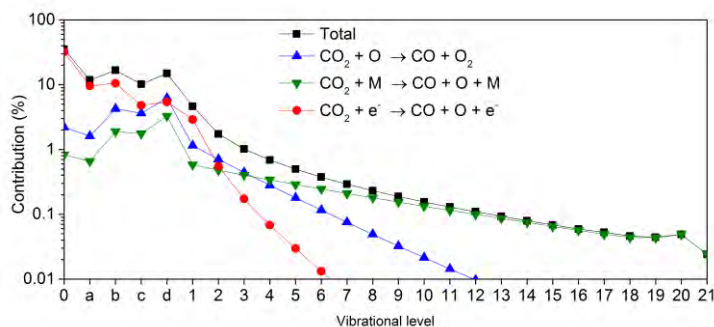


Figure A6: Contribution of the different CO₂ vibrational levels to the total dissociation of CO₂ at a flow rate of 200 L/min and a maximum gas temperature of 3500 K, at an SEI of 0.34 eV/molec, where the maximum energy efficiency is reached in case of 3500 K (see Figure 15(d) from the main text).

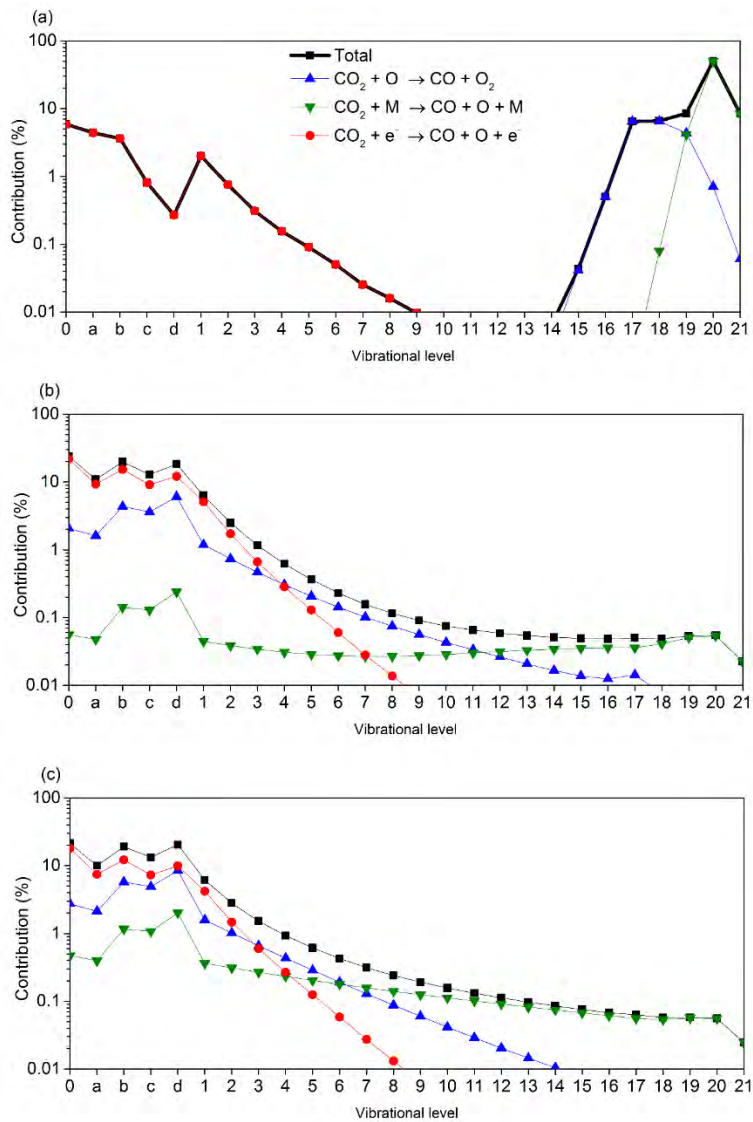


Figure A7: Contribution of the different CO₂ vibrational levels to the total dissociation of CO₂ at a flow rate of 200 L/min and a maximum gas temperature of 500 K (a), 3000 K (b) and 3500 K (c), at an SEI of 1.4 eV/molec, where the maximum energy efficiency is reached in case of 500 K (see Figure 15(d)).

Chapter 4. Dry Reforming of Methane in a GAP

The results presented in this Chapter were published in:

- Cleiren, E.; Heijkers, S.; Ramakers, M.; Bogaerts, A. Dry Reforming of Methane in a Gliding Arc Plasmatron: Towards a Better Understanding of the Plasma Chemistry. *ChemSusChem* 2017, *10*, 4025–4036

4.1 Introduction

Previous Chapter showed that the GAP is promising for CO₂ conversion, but only CO (and O₂) is formed by pure CO₂ splitting. A hydrogen source is needed to create value-added hydrocarbons or oxygenates. Since CH₄ is also a greenhouse gas, a mixture of CO₂ and CH₄ could be beneficial as feedstock in the GAP. Dry reforming of methane (DRM) has already been studied in different other plasma types, such as in a (pulsed) MW plasma¹³⁵, classical GA plasma⁵³, corona discharge¹³⁶, nanosecond pulsed discharge¹³⁷, and spark discharge¹³⁸ but mostly experimentally. In addition, models exist for DRM in a DBD^{139–143}, but no model has been developed yet for DRM in warm plasmas, such as MW or GA plasmas. There is extensive data for pure combustion chemistry modelling^{118,144–147}, but the combined description of typical plasma processes (such as electron impact and ionic reactions), together with an extensive set of combustion reactions, which is needed to model warm plasmas, has not been performed yet.

Therefore, in this Chapter, we present a chemical kinetics model to investigate the underlying mechanisms, and to support the recent experiments carried out for DRM in the GAP. We consider the same GAP as studied in Chapter 3, with the only difference that the cathode length is now 10.20 mm, because we found in previous Chapter (and in experiments) that a longer cathode does not yield better results, as the CO₂ conversion approaches steady state values for longer residence times, while the energy efficiency would drop because a higher power would be needed for the same power density. The anode length (16.30 mm) and the inlet of 3 mm are kept the same, so this yields a plasma volume of 371 mm³. In Section 4.2 the chemistry set is explained. Section 4.3 shows the calculated conversions and energy efficiencies and a comparison with experiments. Section 4.4 illustrates the calculated physical characteristics, such as the electron temperature, electron density and the vibrational distribution functions of CO₂, along with the corresponding vibrational temperature. Finally, Section 4.5 shows the most important products formed in our model, which is linked to the conversion mechanisms in Section 4.6.

4.2 Chemistry set

The chemistry set for the conversion of CO₂ and CH₄ (i.e., DRM) in the GAP used in this Chapter is based on the chemistry set for DRM in a DBD,¹⁴⁸ but

extended with the vibrational levels of CO₂. The latter were not included in the chemistry set of the DBD, where vibrationally excited species have a negligible effect, while they are crucial for the dissociation process of CO₂ in a GAP, due to the lower values of the reduced electric field.^{3,14} The vibrational levels of CH₄ are limited to the first two levels, because it is known from literature that they have a much smaller population than the vibrational levels of CO₂.¹⁴ The various plasma species considered in the model are listed in Table 2. The symbols ‘V’ and ‘E’ represent the vibrational and electronic excited levels of CO₂, CO, O₂, CH₄ and H₂. As in previous Chapter, all 21 levels (V₁-V₂₁) of the asymmetric stretch mode of CO₂ (*00n*), up to the dissociation limit of 5.5 eV, are included, because the asymmetric vibrational mode is the most important for energy-efficient dissociation of CO₂, as explained in previous Chapter.¹⁴ Besides the 21 levels of the asymmetric stretch mode of CO₂, again the same four lower lying symmetric stretch and bending modes are included in the model, as in previous Chapter, and only one electronically excited level of CO₂ (E₁), with a threshold energy of 10.5 eV, is considered, because the other low-lying energy levels immediately give rise to dissociation. The notation, energy and identification of all excited levels is given in Table 3. The extra reactions added are given in Tables A7-A10. The modeling approach is the same as in previous Chapter, so will not be repeated here. It should be noted that only C atom formation, but no solid carbon formation is included in our model, because we only describe the gas phase chemistry. We are aware that soot formation is important and will affect the chemistry near the walls of the reactor. This could affect the total concentrations of radical species, such as O and H. However, we estimate this effect to be minimal, due to the insulation of the walls by the reverse vortex flow (i.e., the plasma species do not come in contact with the reactor walls), and thus, the main pathways inside and right next to the arc will still be the same.

Since the arc width does not change much with changing the electrode dimensions, as shown by Ramakers et al.⁶⁷ for the anode, and the same arc radius was theoretically found by Trenchev et al.³³ at the same (shorter) cathode length as in this study, we can assume the same arc radius, and thus the same fraction of gas passing through the arc column, as in Chapter 3.

Table 2: Overview of the species included in the 0D model. An explanation of the notation of the excited species is given in Table 3.

<i>Neutral molecules</i>	<i>Charged species</i>	<i>Radicals</i>	<i>Excited species</i>
	electrons		
CO ₂ , CO	CO ₂ ⁺ , CO ₄ ⁺ , CO ⁺ , C ₂ O ₂ ⁺ , C ₂ O ₃ ⁺ , C ₂ O ₄ ⁺ , C ₂ ⁺ , C ⁺ , CO ₃ ⁻ , CO ₄ ⁻	C ₂ O, C, C ₂	CO ₂ (V _a , V _b , V _c , V _d), CO ₂ (V ₁ -V ₂₁), CO ₂ (E ₁ : 10,5 eV) CO (V ₁ -V ₁₀), CO (E ₁ -E ₄)
O ₂ , O ₃	O ⁺ , O ₂ ⁺ , O ₄ ⁺ , O ⁻ , O ₂ ⁻ , O ₃ ⁻ , O ₄ ⁻	O	O ₂ (V ₁ -V ₄), O ₂ (E ₁ -E ₂)
CH ₄	CH ₅ ⁺ , CH ₄ ⁺ , CH ₃ ⁺ , CH ₂ ⁺ , CH ⁺	CH ₃ , CH ₂ , CH	CH ₄ (V ₁ , V ₂)
C ₂ H ₆ , C ₂ H ₄ , C ₂ H ₂	C ₂ H ₆ ⁺ , C ₂ H ₅ ⁺ , C ₂ H ₄ ⁺ , C ₂ H ₃ ⁺ , C ₂ H ₂ ⁺ , C ₂ H ⁺	C ₂ H ₅ , C ₂ H ₃ , C ₂ H	
C ₃ H ₈ , C ₃ H ₆		C ₃ H ₇ , C ₃ H ₅	
H ₂	H ₃ ⁺ , H ₂ ⁺ , H ⁺ , H ⁻	H	H ₂ (V ₁ -V ₃), H ₂ (E ₁), H(² P)
H ₂ O, H ₂ O ₂	H ₃ O ⁺ , H ₂ O ⁺ , OH ⁺ , OH ⁻	OH, HO ₂	
CH ₂ O, CH ₃ OH, CH ₃ OOH		CHO, CH ₂ OH, CH ₃ O, CH ₃ O ₂	
C ₂ H ₅ OH, C ₂ H ₅ OOH		C ₂ HO, CH ₃ CO	
CH ₃ CHO, CH ₂ CO		CH ₂ CHO, C ₂ H ₅ O, C ₂ H ₅ O ₂	

Table 3: Notation, corresponding energy and identification of the excited levels considered in the model and listed in Table 2.

	<i>Notation</i>	<i>Energy (eV)</i>	<i>Identification</i>
Symmetric vibration modes of CO₂	CO ₂ (V _a)	0.083	(0 1 0)
	CO ₂ (V _b)	0.167	(0 2 0) + (1 0 0)
	CO ₂ (V _c)	0.252	(0 3 0) + (1 1 0)
	CO ₂ (V _d)	0.339	(0 4 0) + (1 2 0) + (2 0 0)
Asymmetric vibration modes of CO₂	CO ₂ (V ₁)	0.29	(0 0 1)
	CO ₂ (V ₂)	0.58	(0 0 2)
	CO ₂ (V ₃)	0.86	(0 0 3)
	CO ₂ (V ₄)	1.14	(0 0 4)
	CO ₂ (V ₅)	1.43	(0 0 5)
	CO ₂ (V ₆)	1.70	(0 0 6)
	CO ₂ (V ₇)	1.97	(0 0 7)
	CO ₂ (V ₈)	2.24	(0 0 8)
	CO ₂ (V ₉)	2.51	(0 0 9)
	CO ₂ (V ₁₀)	2.77	(0 0 10)
	CO ₂ (V ₁₁)	3.03	(0 0 11)
	CO ₂ (V ₁₂)	3.29	(0 0 12)
	CO ₂ (V ₁₃)	3.55	(0 0 13)
	CO ₂ (V ₁₄)	3.80	(0 0 14)
	CO ₂ (V ₁₅)	4.04	(0 0 15)
	CO ₂ (V ₁₆)	4.29	(0 0 16)
	CO ₂ (V ₁₇)	4.53	(0 0 17)
	CO ₂ (V ₁₈)	4.77	(0 0 18)
	CO ₂ (V ₁₉)	5.01	(0 0 19)
	CO ₂ (V ₂₀)	5.24	(0 0 20)
	CO ₂ (V ₂₁)	5.47	(0 0 21)
Electronically excited levels of CO₂	CO ₂ (E ₁)	10.5	¹ Δ _u
Vibrational levels of CO	CO(V ₁)	0.266	
	CO(V ₂)	0.528	
	CO(V ₃)	0.787	
	CO(V ₄)	1.040	
	CO(V ₅)	1.300	

	CO (V ₆)	1.540	
	CO (V ₇)	1.790	
	CO (V ₈)	2.030	
	CO (V ₉)	2.270	
	CO (V ₁₀)	2.510	
Electronically excited levels of CO	CO (E ₁)	6.22	A ³ Π
	CO (E ₂)	7.90	A ¹ Π
	CO (E ₃)	10.4	A ³ Σ, D ³ Δ, E ³ Σ, B ³ Σ
	CO (E ₄)	10.6	C ¹ Σ, E ¹ Π, B ¹ Σ, I ¹ Σ, D ¹ Δ
Vibrational level of O₂	O ₂ (V _n)	0.19 – 0.38 – 0.57 –	n = 1, ..., 4
		0.75	
Electronically excited levels of O₂	O ₂ (E ₁)	0.98	A ¹ Δ, B ¹ Σ
	O ₂ (E ₂)	8.40	B ³ Σ
Vibrational levels of CH₄	CH ₄ (V _n)	0.162 – 0.361	n = 1, 2
Excited levels of H₂ and H	H ₂ (V _n)	0.516 – 1.0 – 1.50	n = 1, 2, 3
	H ₂ (E ₁)	8.9	B ³ Σ
	H (² P)	10.2	

4.3 Calculated and measured conversion and energy efficiency

Before we will use this model for an analysis of the underlying chemistry of DRM in the gap, we first need to validate it against experimental data for conversion and energy efficiency. Figure 17 illustrates the CO₂ (a) and CH₄ (b) conversion as a function of the CH₄ fraction in the mixture, for an input power of 500 W and a gas flow rate of 10 L min⁻¹ (SEI = 0.75 eV/molec).

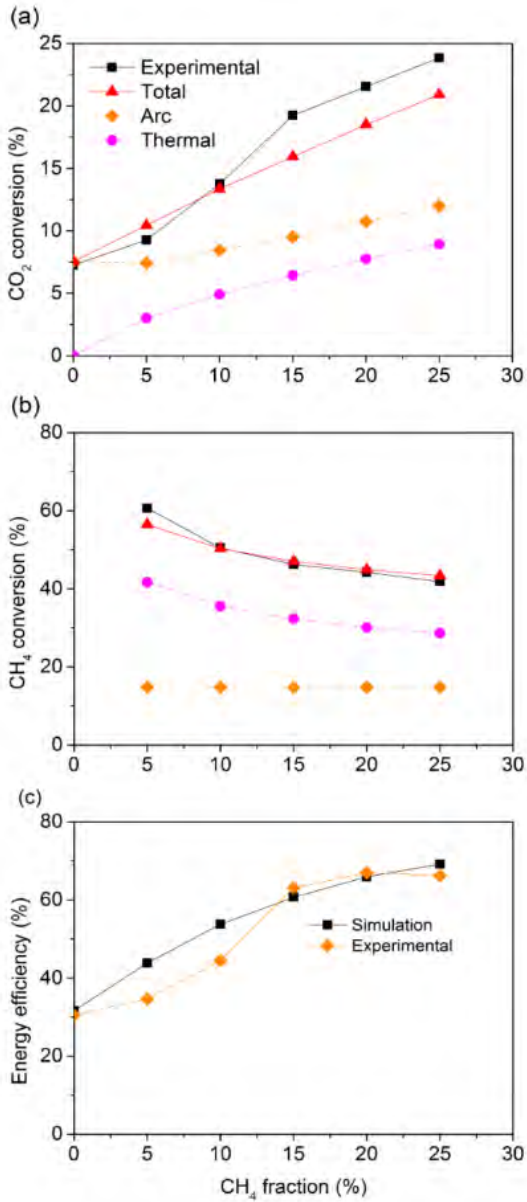


Figure 17: Measured and calculated CO₂ conversion (a) and CH₄ conversion (b), as well as energy efficiency (c) as a function of the CH₄ fraction in the mixture. The individual contributions of the conversion inside the arc and in the thermal area around the arc are indicated in dashed lines in (a) and (b).

As explained in previous Chapter, the arc is stabilized in the center of the GAP reactor, and only a fraction of the gas (i.e., 14.8 %) will pass through this arc column. However, as explained below, not only the conversion inside the arc column is considered, but also in a certain region around the actual arc column, which is still at rather high temperature (> 2000 K), thus allowing some thermal conversion to take place. Both contributions are indicated in Figure 17 (a,b) with dashed lines. Adding both contributions yields the total conversion, which we can compare with measured values. Both the rising trend in CO_2 conversion (Figure 17(a)) and the drop in CH_4 conversion (Figure 17(b)) are correctly predicted by the model, and also the absolute values are in very good agreement. It is clear from Figure 17(a,b) that only accounting for the conversion in the arc column would underestimate the total conversion, especially for CH_4 , where the thermal conversion outside the arc column appears to be even higher than the plasma conversion. This is attributed to the lower C-H bond dissociation energy, allowing thermal conversion to occur at lower temperatures. The relative contributions of the conversion inside the arc and the thermal conversion in the area around the arc are plotted for both CO_2 and CH_4 in the Appendix: Figure A8.

Furthermore, it can be deduced from Figure 17(b) that the CH_4 conversion inside the arc is constant at 14.8 %, independent from the CH_4 fraction in the mixture. The reason is that the CH_4 conversion inside the arc is in fact 100 %, but the overall contribution of the arc is limited by the fraction of gas that passes through the arc, which is predicted to be 14.8 %.

Figure 17(c) illustrates the measured and calculated values of the energy efficiency as a function of the CH_4 fraction. Again, the agreement is very good, with relative differences between 1.5 and 27 %, and on average 10 % difference between the values. The rising trend is not exactly the same at low CH_4 fraction, which may indicate that the thermal conversion is somewhat overestimated at 5 (and 10) % CH_4 in the mixture. Indeed, the model simply assumes the same area around the arc column where thermal conversion can take place, but this area will most probably be smaller at low CH_4 fractions, because CH_4 gives rise to a somewhat higher temperature. Obviously, the assumptions made here about the thermal conversion in a fixed area around the arc are a bit rough, due to the inherent nature of the 0D chemical kinetics model. A more accurate description

would require full 3D calculations,^{32,33} but the latter would result in excessively long calculation times when incorporating the complex CO₂/CH₄ chemistry. Nevertheless, in spite of the approximations that need to be made in the 0D model, the agreement is quite satisfactory. It should be noted that the CH₄ fraction is limited to 25 % in this study, because this was the maximum CH₄ fraction possible in the experiments, although biogas typically has a CH₄ fraction of approximately 60 %^{149,150}. Higher CH₄ fractions than 25 % unfortunately did not ignite the plasma without any other gas and therefore we did not model higher CH₄ fractions in binary CO₂/CH₄ mixtures. Nevertheless, a 25 % CH₄ fraction was also suggested for an industrial feasible super-dry reforming process, using a combination of different well-known industrial processes¹⁵⁰. Hence, the focus of this work is to explain why the performance of CO₂ conversion is enhanced by smaller amounts of CH₄ addition.

In general we can conclude that the model provides quite realistic predictions of the CO₂ and CH₄ conversion and of the energy efficiency, so that it can be used to investigate the underlying mechanisms. This will be carried out in the next Sections.

4.4 Calculated plasma characteristics

Before analyzing the underlying chemical reactions of the CO₂ and CH₄ conversion, the plasma characteristics in the arc column are further studied, which help to understand the mechanisms. The important characteristics inside the arc column, defining the plasma chemistry and thus the CO₂ and CH₄ conversion, are the gas temperature, electron temperature and density, and the vibrational temperature, which gives information on the degree of vibrational excitation (see below).

The gas temperature can in principle be calculated in the model, but in this study it is used as input value, based on 3D fluid dynamics simulation^{32,33} and measured data from literature⁵¹. Indeed, to obtain realistic calculations in this 0D model, more accurate data on the energy released by some chemical reactions and on the effect of vibration-translation relaxation of the CO₂ vibrational levels with CH₄ would be necessary, and these data are not available in literature. Furthermore, the effect of turbulent heat conductivity has also been demonstrated to be very critical in a GAP, yielding a significant drop in gas

temperature,³³ and this effect cannot be accounted for in a 0D model, as also explained in previous Chapter.

In Figure 18(a) we plot the assumed gas temperature profile inside the arc column (solid line) and in the thermal area around the arc (dashed line), as a function of position in the reactor. These values are assumed to be independent of the gas mixing ratio, which might be an approximation, but subtle differences for different gas mixtures would lie within the uncertainty of these values. The gas enters the arc column at room temperature, but is quickly heated to about 3500 K after 0.5 cm. The gas in the thermal area around the arc column rises more slowly, up to a value of 2700 K after about 1.2 cm. At this temperature, thermal conversion of CO₂ and CH₄ will indeed take place, as revealed by thermal conversion calculations.³

The calculated electron temperature and density are plotted in Figure 18(b,c) for different CH₄ fractions in the mixture. In the beginning of the arc column the electron density is still low, so that all the applied electrical energy is distributed over a limited number of electrons, explaining the high electron temperature in the beginning of the arc column. This electron temperature is a bit higher than expected for a GA,¹⁴ but it does not really affect the calculated plasma chemistry, because of the low electron density. After about 0.5 cm, the electron density rises, and as a consequence, the electron temperature drops to values of about 1.0 – 1.5 eV (for different CH₄ fractions), which are indeed typical values expected for a GA.¹⁴ The electron temperature slightly drops upon higher CH₄ fraction in the mixture, which is due to the slightly lower values of the reduced electric field (i.e., ratio of electric field over gas density, E/n , typically expressed in Td; 1 Td = 10⁻²¹ V m²). Indeed, the latter is calculated in the model to be 57 Td and 22 Td, for 0 % and 25 % CH₄ fraction, respectively. Furthermore, a higher CH₄ concentration yields a higher electron density, due to the lower ionisation potential of CH₄ (12.61 eV) vs CO₂ (13.78 eV).

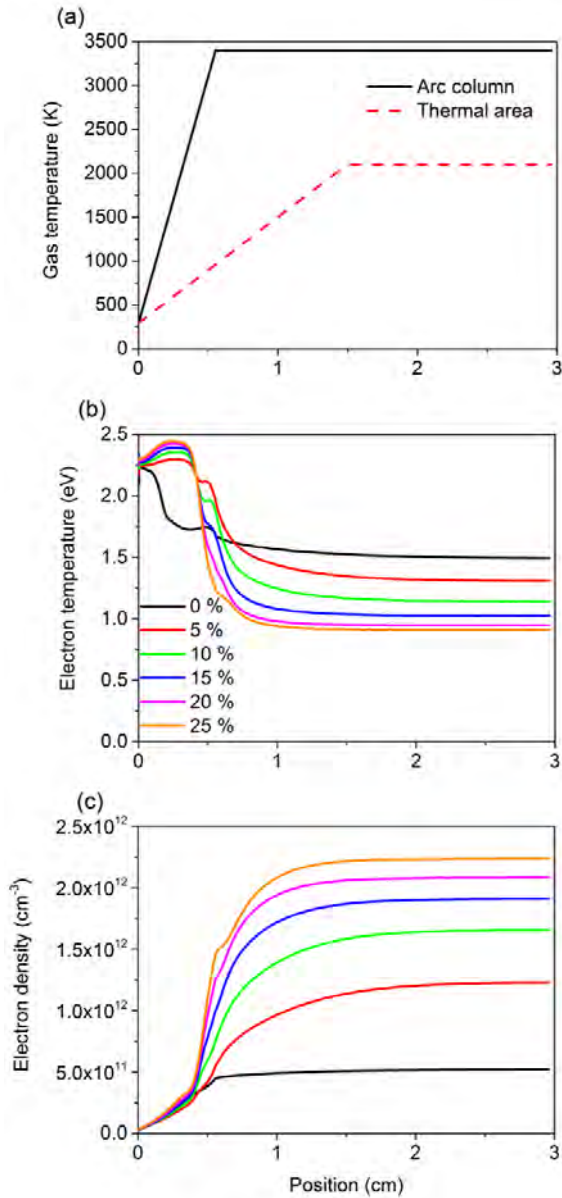


Figure 18: Assumed gas temperature inside the arc column (solid line) and in the thermal area around the arc (dashed line) (a), as well as calculated electron temperature (b) and electron density (c) for different CH₄ fractions in the mixture, as a function of position in the arc. The gas temperature is assumed to be independent from the gas composition.

Besides the gas temperature and electron temperature, also the vibrational temperature is an important characteristic of the GAP, because the vibrational levels play a key role in energy-efficient CO₂ dissociation. To calculate the vibrational temperature, the vibrational distribution function (VDF) of the 21 asymmetric mode levels of CO₂ ($v_1 - v_{21}$), as well as of the 4 effective symmetric mode levels ($v_a - v_d$), both inside the arc column and in the thermal area around the arc are plotted in Figure 19. According to the calculations, the VDF is independent from the CH₄ fraction in the mixture,. The faster drop of the VDF for the asymmetric mode levels in the thermal region will yield a somewhat lower vibrational temperature. The latter is a measure for the degree of vibrational excitation, and can be calculated from the VDF in case of a Boltzmann distribution for the asymmetric mode levels as follows:

$$T_v = \frac{1}{21} \sum_{n=1}^{21} \frac{-E_n}{\ln\left(\frac{n_n}{n_0}\right)} \quad (36)$$

where E_n is the energy of the n-th asymmetric mode vibrational level of CO₂, n_n is the density of this level, and n_0 is the density of CO₂ in the ground state.

The vibrational temperature of the asymmetric mode levels is calculated to be about 3400 K inside the arc, and about 2800 K in the thermal area around the arc, which (more or less) corresponds to the gas temperature adopted in both regions. This indicates that the VDF is quasi-thermal. Indeed, no overpopulation of the higher vibrational levels is observed in Figure 19. This also explains why the VDF is independent from the CH₄ fraction in the mixture. Indeed, for all fractions, the vibrational temperature is almost equal and a quasi-Boltzmann distribution is obtained (see Figure 19). The same behavior is also seen in the GAP and a classical GA operating in pure CO₂,^{29,47,151} (and see previous Chapter), as well as in a MW plasma in pure CO₂, when operating at atmospheric pressure.²⁵ Only in a MW plasma at reduced pressure, an overpopulation of the higher levels was observed,^{25,57,75,152} because of the less important role of thermalization due to VT relaxation.

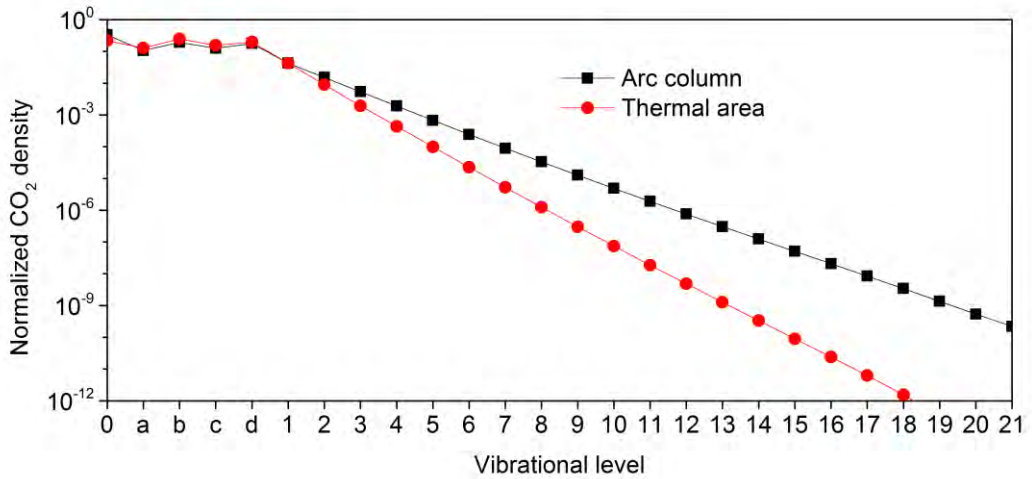


Figure 19: Vibrational distribution functions (VDFs) of all vibrational levels of CO₂ included in the model, both in the arc column and in the thermal area around the arc. These VDFs were found to be the same for all gas mixing ratios investigated. The notations of the vibrational levels are explained in Table 2 .

On the other hand, the electron temperature is much higher than the gas temperature and the vibrational temperature (i.e., 1 – 1.55 eV, or 11,000 – 18,000 K vs. 3400 – 3500 K in the arc). This indicates the non-equilibrium character of the GAP, and thus it explains why the CO₂ and CH₄ conversion in the GAP are quite energy efficient, because the electrons are energetic enough to activate the gas by ionization, excitation and dissociation. Nevertheless, if the vibrational temperature would be higher than the gas temperature, due to overpopulation of the higher vibrational levels of CO₂, the CO₂ conversion would still be more energy efficient. A possible way to realize such overpopulation of the higher vibrational levels could be operating at lower gas temperature (< 1000 K), in combination with a higher power (> 10 kW, see also Chapter 3),²⁵ or operating at reduced pressure (between 100 and 200 mbar), as demonstrated for MW plasmas^{25,57,75,152}. However, the latter is not beneficial for industrial applications, and the cost of the vacuum system would also have to be accounted for in the overall energy efficiency.

4.5 Calculated species densities inside the plasma

In Figure 20 we plot the densities of the most important plasma species at the end of the arc column, as a function of the CH₄ fraction in the mixture. No distinction is made between ground state and (vibrationally or electronically excited) levels of the various molecules, and the sum of both is just plotted. 84 % of the CO₂ molecules is found in the vibrationally excited levels. For CO, O₂, H₂ and CH₄, this fraction is much lower, i.e., 39 %, 24 %, 4 % and less than 1 %, respectively, and the fraction of electronically excited levels is also of minor importance. For other molecules in the mixture, no vibrational levels are accounted for (see details in Tables 2 and 3).

The CO density is higher than the CO₂ density (see Figure 20(a)), indicating that most of the CO₂ is converted inside the arc column. However, for the overall conversion, the fraction of CO₂ gas that cannot pass through the arc column must be taken into account, explaining why the overall conversion is much lower (cf. Figure 17 above). The same applies to the CH₄ density (see Figure 20(b)), which is extremely low, as it is entirely converted to H₂ and higher hydrocarbons inside the arc column. The densities of O₂ and O are only significant in pure CO₂ and they drop considerably upon higher CH₄ fraction in the mixture. This drop was also reflected in the measured O-based selectivity of O₂¹⁵³. Indeed, the O atoms, which recombine into O₂ (and CO) in the pure CO₂ plasma, will now recombine with H atoms, originating from CH₄, into OH, H₂O, CH₃OH and CH₂O, although the densities of the latter species are still quite low (cf. Figure 20(b)). The most important products are indeed CO and H₂, along with H₂O. The predominant formation of CO and H₂ is in good agreement with experimental selectivities¹⁵³. Although explosive compounds such as CO and H₂ are formed, the volume percentage of O₂ in the GAP is lower than 21 % so the flammability in air can be used¹⁵⁴. There is an explosion risk when O₂ levels are higher than 13%, but this is not the case in the GAP, i.e., these levels are below 8 %, and they drop upon increasing CH₄ fraction (see also Figure 20). On the other hand, there might be an explosion risk when the CO₂ conversion would be twice as high, for mixtures with 5% or 10 % CH₄.

Upon increasing CH₄ fraction in the mixture, more H atoms will be converted into H₂, as is clear from Figure 20(a). Furthermore, Figure 20(b)

reveals the following trend for the C₂-compounds: C₂H₆ < C₂H₅ < C₂H₄ < C₂H₃ < C₂H₂

This is in contrast to results obtained with a DBD, where C₂H₆ was obtained with the highest concentration of all hydrocarbons, due to recombination of CH₃ radicals.¹⁵⁵ This can be explained by the higher temperature in the GAP, leading to more dehydrogenation of C₂H₆, by electron impact reactions or collisions with O atoms.¹⁵⁶ This will be further discussed in detail in Chapter 7.

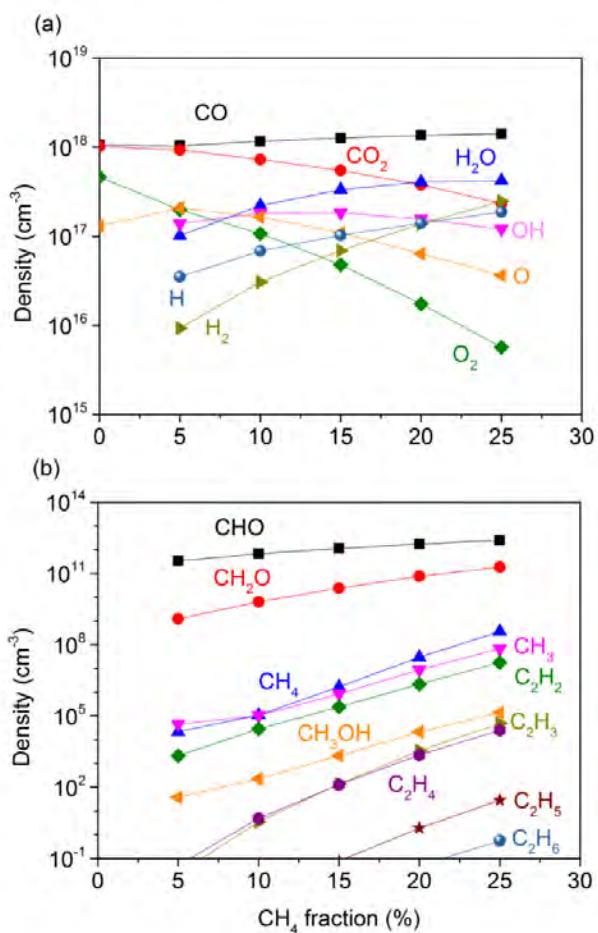


Figure 20: Densities of the most important plasma species at the end of the arc column, as a function of the CH₄ fraction in the mixture.

4.6 Chemical kinetics analysis of the underlying processes

The model allows us to obtain a better insight in the loss and formation processes of CO₂ and CH₄, from which the experimental trends of the CO₂ and CH₄ conversion upon rising CH₄ fraction in the mixture (cf. Figure 17 above) can be explained. A detailed analysis of these loss and formation processes is presented in the Appendix: Figures A9 – A12. Based on this analysis, the relative contributions of the main processes responsible for the (net) conversion of CO₂ and CH₄, as a function of the CH₄ fraction in the mixture are plotted in Figure 21(a,b).

Figure 21(a) illustrates that without CH₄ addition, the reaction of CO₂ (mainly in the vibrational levels) with either O atoms or any other molecules (indicated as M) are most important for the conversion of CO₂, like in previous Chapter. The reaction with O atoms becomes dominant at 5 % CH₄ in the mixture, but at larger CH₄ fractions, both processes become less important, while the reaction of CO₂ (again mainly in the vibrational levels) with H atoms becomes dominant, with contributions up to 80 % and more. Electron impact dissociation, both from the CO₂ ground state and vibrational levels, contributes for about 10 – 20 % to the total CO₂ conversion. It is also clear from Figure A10 that the net CO₂ loss rate rises upon increasing CH₄ fraction, and this is of course attributed to the increasing importance of the reaction with H atoms. Hence, the dissociation of CO₂ upon collision with H atoms explains why the CO₂ conversion rises upon increasing CH₄ fraction in the mixture.

As shown in Figure A9, the backward reaction of the most important loss process for CO₂ in the CO₂/CH₄ mixture ($\text{CO}_2 + \text{H} \rightarrow \text{CO} + \text{OH}$), i.e., the reaction of CO with OH radicals, forming again CO₂ and H atoms, is nearly equally important as the loss (i.e., forward) reaction, especially at low CH₄ fractions. Therefore, this reaction does not contribute to CO₂ conversion at 5 % CH₄ in the mixture, and only becomes important at larger CH₄ fractions, as is clear from Figure 21. Note that this backward reaction was also the limiting factor in CO₂ conversion in a DBD operating in a CO₂/H₂O mixture,¹⁵⁷ and it became even more important at higher H₂O fractions in the mixture, explaining why adding H₂O did not give rise to CO₂ conversion.³ The situation is a bit different in this

case, because at higher CH₄ fractions, the H atoms, formed upon dissociation of CH₄, play a more important role in the CO₂ conversion, i.e., the forward (loss) reaction upon collision with H atoms becomes more important than the backward reaction (production of CO₂).

In Figure 21(b) the relative contributions of the net processes contributing to CH₄ conversion are plotted, as a function of the CH₄ fraction in the mixture. The reaction of CH₄ with OH radicals is by far the most important, with a contribution of 75 % at low CH₄ fraction, decreasing to 45 % at the highest CH₄ fraction investigated, because of the somewhat lower OH concentration in the mixture (cf. Figure 20(a) above). At the same time, the reaction with C₂H₃ radicals becomes gradually more important, as the density of these radicals rises with increasing CH₄ fraction (cf. Figure 20(b)) above). Furthermore, the reaction of CH₄ with H or O atoms, or with C₃H₅ radicals also play a minor role, as appears from Figure 21(b).

Finally, it is clear from Figure A12 that the net CH₄ loss rate rises upon increasing CH₄ fraction. This is mainly due to the increasing CH₄ density in the mixture, and it explains why the effective CH₄ conversion rises. However, the absolute CH₄ conversion drops, and this is mainly attributed to the major loss process, i.e., the reaction of CH₄ with OH radicals, which becomes gradually less important at higher CH₄ fraction in the mixture.

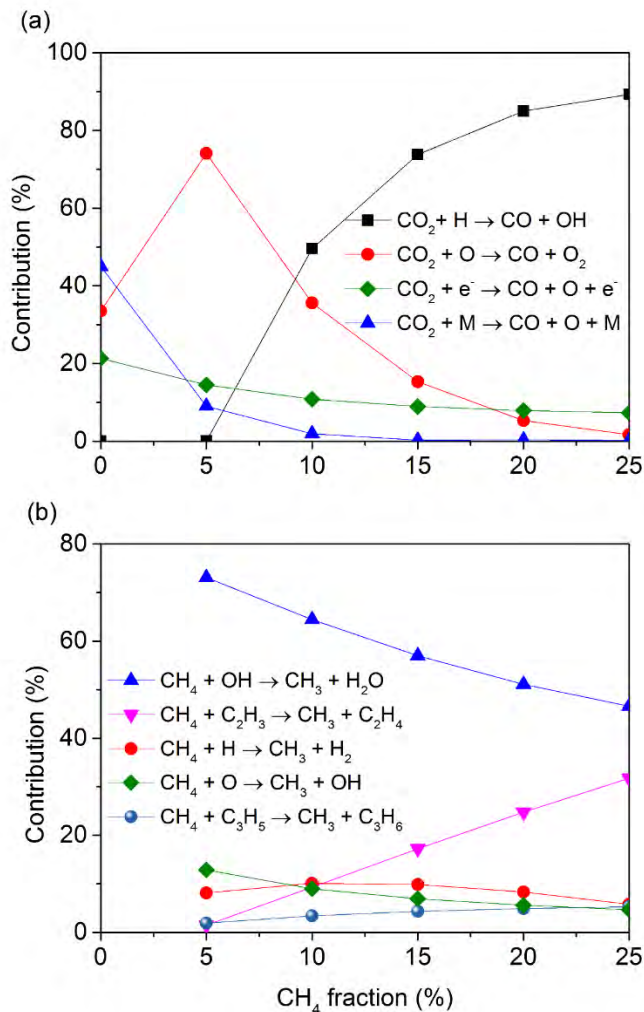


Figure 21: Relative contributions of the main processes responsible for the (net) conversion of CO₂ (a) and CH₄ (b), as a function of CH₄ fraction in the mixture.

4.7 Conclusion

We studied the underlying mechanisms of DRM in a GAP, for different CH₄ fractions in the mixture. A very good agreement is reached between the measured and calculated conversions and energy efficiency, so the model can indeed be used to elucidate the underlying chemical processes. The model reveals that, besides the conversion inside the arc plasma column, some (thermal) conversion

of CO₂ and CH₄ also takes place in the area around the arc column, which is still characterized by relatively high temperature (> 2000 K). Inside the arc column, the electron temperature is much higher than the gas temperature, indicating the non-equilibrium character of the plasma, which explains the good energy efficiency of this process. Indeed, the electrons activate the gas molecules by electron impact excitation, ionization and dissociation, creating reactive species which can more easily form new molecules. The model also demonstrates the important role of the CO₂ vibrational levels. Indeed, most of the CO₂ conversion takes place upon reaction of the CO₂ vibrational levels with radicals from the plasma. The vibrational distribution function (VDF) is, however, in thermal equilibrium with the gas temperature. A higher energy efficiency would still be possible if the higher vibrational levels of CO₂ could be overpopulated, e.g., by operating at low temperatures (< 1000 K) (in combination with high electric power, i.e. > 10 kW) or lower pressure (between 100 and 200 mbar).

The CO₂ conversion clearly rises upon increasing CH₄ fraction in the mixture, and this is explained by the model due to the reaction of CO₂ (mainly in vibrationally excited levels) with H atoms, formed upon dissociation of CH₄. The main process responsible for CH₄ conversion is the reaction with OH radicals. Furthermore, reactions with other radicals, such as C₂H₃, H, O and C₃H₅, also play a non-negligible role in the CH₄ conversion.

These results demonstrate that a GAP is very promising for DRM, also in comparison with other plasma types, certainly when considering the energy efficiency. The conversion should however be further improved. The latter is now limited by the fraction of gas that passes through the plasma column. Indeed, the conversion inside the arc plasma column itself ranges between 51 and 81 % for CO₂ and is already 100 % for CH₄, but a significant fraction of the gas (~ 85 %) does not pass through the plasma column, therefore lowering the overall conversion in the GAP. To improve the latter, more insight is needed in the gas flow dynamics, which is beyond the scope of the present 0D chemical kinetics model.

4.8 Appendix

Table A7: Electron impact reactions with the various molecules and radicals, included in the model. These reactions are treated by energy-dependent cross sections (or rate coefficients), and the references where these cross sections (or rate coefficients) were adopted from, are also included. For the vibrational and electronic excitations, several individual excitations are included, as indicated by the number between brackets.

CH₄	Reaction	Ref
	$e^- + \text{CH}_4 \rightarrow e^- + \text{CH}_4$	158
	$e^- + \text{CH}_4 \leftrightarrow e^- + \text{CH}_4(\text{v})$	158
	$e^- + \text{CH}_4(\text{g+v}) \rightarrow 2e^- + \text{CH}_4^+$	94
	$e^- + \text{CH}_4(\text{g+v}) \rightarrow 2e^- + \text{CH}_3^+ + \text{H}$	94
	$e^- + \text{CH}_4(\text{g+v}) \rightarrow 2e^- + \text{CH}_2^+ + \text{H}_2$	94
	$e^- + \text{CH}_4(\text{g+v}) \rightarrow e^- + \text{CH}_3 + \text{H}$	95,159
	$e^- + \text{CH}_4(\text{g+v}) \rightarrow e^- + \text{CH}_2 + \text{H}_2$	95,159
	$e^- + \text{CH}_4(\text{g+v}) \rightarrow e^- + \text{CH} + \text{H}_2 + \text{H}$	95,159
	$e^- + \text{CH}_4(\text{g+v}) \rightarrow e^- + \text{C} + 2\text{H}_2$	95,159
CH₃	Reaction	Ref
	$e^- + \text{CH}_3 \rightarrow 2e^- + \text{CH}_3^+$	94
	$e^- + \text{CH}_3 \rightarrow 2e^- + \text{CH}_2^+ + \text{H}$	94
	$e^- + \text{CH}_3 \rightarrow 2e^- + \text{CH}^+ + \text{H}_2$	94
	$e^- + \text{CH}_3 \rightarrow e^- + \text{CH}_2 + \text{H}$	95,159
	$e^- + \text{CH}_3 \rightarrow e^- + \text{CH} + \text{H}_2$	95,159
CH₂	Reaction	Ref
	$e^- + \text{CH}_2 \rightarrow 2e^- + \text{CH}_2^+$	94
	$e^- + \text{CH}_2 \rightarrow e^- + \text{CH} + \text{H}$	95,159
CH	Reaction	Ref
	$e^- + \text{CH} \rightarrow 2e^- + \text{CH}^+$	94
	$e^- + \text{CH} \rightarrow e^- + \text{C} + \text{H}$	95,159
C₂H₆	Reaction	Ref
	$e^- + \text{C}_2\text{H}_6 \rightarrow 2e^- + \text{C}_2\text{H}_6^+$	94
	$e^- + \text{C}_2\text{H}_6 \rightarrow 2e^- + \text{C}_2\text{H}_5^+ + \text{H}$	94
	$e^- + \text{C}_2\text{H}_6 \rightarrow 2e^- + \text{C}_2\text{H}_4^+ + \text{H}_2$	94
	$e^- + \text{C}_2\text{H}_6 \rightarrow 2e^- + \text{C}_2\text{H}_3^+ + \text{H}_2 + \text{H}$	94
	$e^- + \text{C}_2\text{H}_6 \rightarrow 2e^- + \text{C}_2\text{H}_2^+ + 2\text{H}_2$	94
	$e^- + \text{C}_2\text{H}_6 \rightarrow 2e^- + \text{CH}_3^+ + \text{CH}_3$	94
	$e^- + \text{C}_2\text{H}_6 \rightarrow e^- + \text{C}_2\text{H}_5 + \text{H}$	160,161
	$e^- + \text{C}_2\text{H}_6 \rightarrow e^- + \text{C}_2\text{H}_4 + \text{H}_2$	160,161
C₂H₅	Reaction	Ref

	$e^- + C_2H_5 \rightarrow 2e^- + C_2H_5^+$	94
	$e^- + C_2H_5 \rightarrow 2e^- + C_2H_4^+ + H$	94
	$e^- + C_2H_5 \rightarrow 2e^- + C_2H_3^+ + H_2$	94
	$e^- + C_2H_5 \rightarrow 2e^- + C_2H_2^+ + H_2 + H$	94
	$e^- + C_2H_5 \rightarrow e^- + C_2H_4 + H$	160,161
	$e^- + C_2H_5 \rightarrow e^- + C_2H_3 + H_2$	160,161
C₂H₄	Reaction	Ref
	$e^- + C_2H_4 \rightarrow 2e^- + C_2H_4^+$	94
	$e^- + C_2H_4 \rightarrow 2e^- + C_2H_3^+ + H$	94
	$e^- + C_2H_4 \rightarrow 2e^- + C_2H_2^+ + H_2$	94
	$e^- + C_2H_4 \rightarrow e^- + C_2H_3 + H$	160,161
	$e^- + C_2H_4 \rightarrow e^- + C_2H_2 + H_2$	160,161
C₂H₃	Reaction	Ref
	$e^- + C_2H_3 \rightarrow 2e^- + C_2H_3^+$	94
	$e^- + C_2H_3 \rightarrow 2e^- + C_2H_2^+ + H$	94
	$e^- + C_2H_3 \rightarrow e^- + C_2H_2 + H$	160,161
	$e^- + C_2H_3 \rightarrow e^- + C_2H + H_2$	160,161
C₂H₂	Reaction	Ref
	$e^- + C_2H_2 \rightarrow 2e^- + C_2H_2^+$	94
	$e^- + C_2H_2 \rightarrow e^- + C_2H + H$	160,161
C₂H	Reaction	Ref
	$e^- + C_2H \rightarrow e^- + C + CH$	160,161
C₃H₈	Reaction	Ref
	$e^- + C_3H_8 \rightarrow 2e^- + C_2H_5^+ + CH_3$	94
	$e^- + C_3H_8 \rightarrow 2e^- + C_2H_4^+ + CH_4$	94
	$e^- + C_3H_8 \rightarrow e^- + C_3H_7 + H$	160,161
	$e^- + C_3H_8 \rightarrow e^- + C_3H_6 + H_2$	160,161
	$e^- + C_3H_8 \rightarrow e^- + C_2H_4 + CH_4$	160,161
C₃H₇	Reaction	Ref
	$e^- + C_3H_7 \rightarrow 2e^- + C_2H_5^+ + CH_2$	160,161
	$e^- + C_3H_7 \rightarrow 2e^- + C_2H_4^+ + CH_3$	160,161
	$e^- + C_3H_7 \rightarrow 2e^- + C_2H_3^+ + CH_4$	160,161
	$e^- + C_3H_7 \rightarrow 2e^- + CH_3^+ + C_2H_4$	160,161
	$e^- + C_3H_7 \rightarrow e^- + C_3H_6 + H$	160,161
	$e^- + C_3H_7 \rightarrow e^- + C_2H_4 + CH_3$	160,161
	$e^- + C_3H_7 \rightarrow e^- + C_2H_3 + CH_4$	160,161
C₃H₆	Reaction	Ref
	$e^- + C_3H_6 \rightarrow 2e^- + C_2H_5^+ + CH$	160,161
	$e^- + C_3H_6 \rightarrow 2e^- + C_2H_4^+ + CH_2$	160,161

	$e^- + C_3H_6 \rightarrow 2e^- + C_2H_3^+ + CH_3$	160,161
	$e^- + C_3H_6 \rightarrow 2e^- + C_2H_2^+ + CH_4$	160,161
	$e^- + C_3H_6 \rightarrow 2e^- + CH_3^+ + C_2H_3$	160,161
	$e^- + C_3H_6 \rightarrow e^- + C_2H_2 + CH_4$	160,161
C₃H₅	Reaction	Ref
	$e^- + C_3H_5 \rightarrow 2e^- + C_2H_3^+ + CH_2$	160,161
	$e^- + C_3H_5 \rightarrow 2e^- + C_2H_2^+ + CH_3$	160,161
	$e^- + C_3H_5 \rightarrow 2e^- + CH_3^+ + C_2H_2$	160,161
	$e^- + C_3H_5 \rightarrow e^- + C_2H_2 + CH_3$	160,161
H₂	Reaction	Ref
	$e^- + H_2 \rightarrow e^- + H_2$	162
	$e^- + H_2 \leftrightarrow e^- + H_2(v)$	163
	$e^- + H_2 \leftrightarrow e^- + H_2(e)$	59
	$e^- + H_2(g+e) \rightarrow 2e^- + H_2^+$	164
	$e^- + H_2 \rightarrow e^- + 2H$	165
H	Reaction	Ref
	$e^- + H \leftrightarrow e^- + H(e)$	93
	$e^- + H(g+e) \rightarrow 2e^- + H^+$	164
H₂O	Reaction	Ref
	$e^- + H_2O \rightarrow O^- + H_2$	166
	$e^- + H_2O \rightarrow OH^- + H$	166
	$e^- + H_2O \rightarrow e^- + OH + H$	166
	$e^- + H_2O \rightarrow e^- + O + H_2$	166
	$e^- + H_2O \rightarrow e^- + O + 2H$	166
OH	Reaction	Ref
	$e^- + OH \rightarrow 2e^- + OH^+$	167
	$e^- + OH \rightarrow e^- + O + H$	167
OH⁻	Reaction	Ref
	$e^- + OH^- \rightarrow 2e^- + OH$	167
	$e^- + OH^- \rightarrow 2e^- + O + H$	168

Table A8: Electron-ion recombination reactions included in the model. These reactions are treated by energy-dependent rate coefficients, and the references where these rate coefficients were adopted from, are also included.

Reaction	Ref
$e^- + \text{CH}_5^+ \rightarrow \text{CH}_3 + 2\text{H}$	159,169
$e^- + \text{CH}_5^+ \rightarrow \text{CH}_2 + \text{H}_2 + \text{H}$	159,169
$e^- + \text{CH}_4^+ \rightarrow \text{CH}_3 + \text{H}$	159,169
$e^- + \text{CH}_4^+ \rightarrow \text{CH}_2 + 2\text{H}$	159,169
$e^- + \text{CH}_4^+ \rightarrow \text{CH} + \text{H}_2 + \text{H}$	159,169
$e^- + \text{CH}_3^+ \rightarrow \text{CH}_2 + \text{H}$	159,169
$e^- + \text{CH}_3^+ \rightarrow \text{CH} + \text{H}_2$	159,169
$e^- + \text{CH}_3^+ \rightarrow \text{CH} + 2\text{H}$	159,169
$e^- + \text{CH}_3^+ \rightarrow \text{C} + \text{H}_2 + \text{H}$	159,169
$e^- + \text{CH}_2^+ \rightarrow \text{CH} + \text{H}$	159,169
$e^- + \text{CH}_2^+ \rightarrow \text{C} + \text{H}_2$	159,169
$e^- + \text{CH}_2^+ \rightarrow \text{C} + 2\text{H}$	159,169
$e^- + \text{CH}^+ \rightarrow \text{C} + \text{H}$	159,169
$e^- + \text{C}_2\text{H}_6^+ \rightarrow \text{C}_2\text{H}_5 + \text{H}$	161
$e^- + \text{C}_2\text{H}_6^+ \rightarrow \text{C}_2\text{H}_4 + 2\text{H}$	161
$e^- + \text{C}_2\text{H}_5^+ \rightarrow \text{C}_2\text{H}_4 + \text{H}$	161
$e^- + \text{C}_2\text{H}_5^+ \rightarrow \text{C}_2\text{H}_3 + 2\text{H}$	161
$e^- + \text{C}_2\text{H}_5^+ \rightarrow \text{C}_2\text{H}_2 + \text{H}_2 + \text{H}$	161
$e^- + \text{C}_2\text{H}_5^+ \rightarrow \text{C}_2\text{H}_2 + 3\text{H}$	161
$e^- + \text{C}_2\text{H}_5^+ \rightarrow \text{CH}_3 + \text{CH}_2$	161
$e^- + \text{C}_2\text{H}_4^+ \rightarrow \text{C}_2\text{H}_3 + \text{H}$	161
$e^- + \text{C}_2\text{H}_4^+ \rightarrow \text{C}_2\text{H}_2 + 2\text{H}$	161
$e^- + \text{C}_2\text{H}_4^+ \rightarrow \text{C}_2\text{H} + \text{H}_2 + \text{H}$	161
$e^- + \text{C}_2\text{H}_3^+ \rightarrow \text{C}_2\text{H}_2 + \text{H}$	161
$e^- + \text{C}_2\text{H}_3^+ \rightarrow \text{C}_2\text{H} + 2\text{H}$	161
$e^- + \text{C}_2\text{H}_2^+ \rightarrow \text{C}_2\text{H} + \text{H}$	161
$e^- + \text{C}_2\text{H}_2^+ \rightarrow 2\text{CH}$	161
$e^- + \text{C}_2\text{H}^+ \rightarrow \text{C}_2 + \text{H}$	161
$e^- + \text{C}_2\text{H}^+ \rightarrow \text{CH} + \text{C}$	161
$e^- + \text{H}_3^+ \rightarrow 3\text{H}$	169
$e^- + \text{H}_3^+ \rightarrow e^- + \text{H}_2 + \text{H}^+$	169
$e^- + \text{H}_3^+ \rightarrow \text{H}_2 + \text{H}$	169
$e^- + \text{H}^- \rightarrow 2e^- + \text{H}$	168
$e^- + \text{H}^+ \rightarrow \text{H}$	168

$2e^- + H^+ \rightarrow e^- + H$	168
$2e^- + H_2^+ \rightarrow e^- + H_2$	168
$e^- + H_2^+ \rightarrow H^+ + H^-$	169
$e^- + H_2^+ \rightarrow e^- + H + H^+$	168
$e^- + H_2^+ \rightarrow 2H$	168
$e^- + OH^+ \rightarrow O + H$	169
$2e^- + OH^+ \rightarrow e^- + OH$	101
$e^- + H_2O^+ \rightarrow OH + H$	169
$e^- + H_2O^+ \rightarrow O + H_2$	169
$e^- + H_2O^+ \rightarrow O + 2H$	169
$2e^- + H_2O^+ \rightarrow e^- + H_2O$	101
$e^- + H_3O^+ \rightarrow H_2O + H$	169
$e^- + H_3O^+ \rightarrow OH + H_2$	169
$e^- + H_3O^+ \rightarrow OH + 2H$	169

Table A9 : Neutral-neutral reactions included in the model, as well as the corresponding rate coefficients and the references where these data were adopted from. The units of the rate constants are s^{-1} , cm^3s^{-1} and cm^6s^{-1} for one, two and three body reactions, respectively. The α parameter determines the effectiveness of lowering the activation energy for reactions involving vibrationally excited levels of the molecules.

Reaction	Rate Constant	Ref
$CH_4(V_1) + M \rightarrow CH_4 + M$	Due to similar energy difference the same rc for reaction V(2a) in Chapter 3 was adopted	
$CH_4(V_2) + M \rightarrow CH_4(V_1) + M$	Due to similar energy difference the same rc for reaction V(2a) in Chapter 3 was adopted	
$CH_4(V_2) + M \rightarrow CH_4 + M$	Due to similar energy difference the same rc for reaction V(2b) in Chapter 3 was adopted	
$H_2(V_x) + M \rightarrow H_2(V_{x-1}) + M$	$5.83 \times 10^{-7} \exp(-227 T_{gas}^{-\frac{1}{3}} + 529 T_{gas}^{-\frac{2}{3}})$	127
$CH_4 + CH_2 \rightarrow CH_3 + CH_3$	3.01×10^{-19}	118
$2xCH_3 \rightarrow CH_4 + CH_2$	$7.14 \times 10^{-12} \exp(-\frac{41.99}{RT_{gas}})$	170
$CH_4 + CH \rightarrow C_2H_4 + H$	9.97×10^{-11}	146
$CH_4 + C_2H_5 \rightarrow C_2H_6 + CH_3$ ($\alpha=0.8$)	$2.51 \times 10^{-15} \left(\frac{T_{gas}}{298}\right)^{4.14} \exp(-\frac{52.55}{RT_{gas}})$	118
$CH_4 + C_2H_3 \rightarrow C_2H_4 + CH_3$ ($\alpha=0.0$)	$2.13 \times 10^{-14} \left(\frac{T_{gas}}{298}\right)^{4.02} \exp(-\frac{22.86}{RT_{gas}})$	118
$C_2H_4 + CH_3 \rightarrow CH_4 + C_2H_3$ ($\alpha=0.0$)	$6.91 \times 10^{-12} \exp(-\frac{46.56}{RT_{gas}})$	146

$\text{CH}_4 + \text{C}_2\text{H} \rightarrow \text{C}_2\text{H}_2 + \text{CH}_3$ ($\alpha=0.0$)	$3.01 \times 10^{-12} \exp\left(-\frac{2.08}{RT_{gas}}\right)$	118
$\text{C}_2\text{H}_2 + \text{CH}_3 \rightarrow \text{CH}_4 + \text{C}_2\text{H}$	$3.01 \times 10^{-13} \exp\left(-\frac{72.34}{RT_{gas}}\right)$	118
$\text{CH}_4 + \text{C}_3\text{H}_7 \rightarrow \text{C}_3\text{H}_8 + \text{CH}_3$ ($\alpha=0.8$)	$3.54 \times 10^{-16} \left(\frac{T_{gas}}{298}\right)^{4.02} \exp\left(-\frac{45.48}{RT_{gas}}\right)$	171
$\text{C}_3\text{H}_8 + \text{CH}_3 \rightarrow \text{CH}_4 + \text{C}_3\text{H}_7$	$1.61 \times 10^{-15} \left(\frac{T_{gas}}{298}\right)^{3.65} \exp\left(-\frac{29.93}{RT_{gas}}\right)$	171
$\text{CH}_4 + \text{C}_3\text{H}_5 \rightarrow \text{C}_3\text{H}_6 + \text{CH}_3$ ($\alpha=0.8$)	$1.71 \times 10^{-14} \left(\frac{T_{gas}}{298}\right)^{3.40} \exp\left(-\frac{97.28}{RT_{gas}}\right)$	145
$\text{C}_3\text{H}_6 + \text{CH}_3 \rightarrow \text{CH}_4 + \text{C}_3\text{H}_5$	$1.68 \times 10^{-15} \left(\frac{T_{gas}}{298}\right)^{3.50} \exp\left(-\frac{23.78}{RT_{gas}}\right)$	145
$\text{CH}_4 + \text{H} \rightarrow \text{CH}_3 + \text{H}_2$ ($\alpha=0.5$)	$2.94 \times 10^{-10} \exp\left(-\frac{57.65}{RT_{gas}}\right)$	172
$\text{CH}_3 + \text{H}_2 \rightarrow \text{CH}_4 + \text{H}$ ($\alpha=0.4$)	$6.86 \times 10^{-14} \left(\frac{T_{gas}}{298}\right)^{2.74} \exp\left(-\frac{39.411}{RT_{gas}}\right)$	146
$2\text{xCH}_3 \rightarrow \text{C}_2\text{H}_5 + \text{H}$	$1.46 \times 10^{-11} \left(\frac{T_{gas}}{298}\right)^{0.10} \exp\left(-\frac{44.4}{RT_{gas}}\right)$	173
$\text{C}_2\text{H}_5 + \text{H} \rightarrow \text{CH}_3 + \text{CH}_3$	5.99×10^{-11}	146
$2\text{xCH}_3 + \text{M} \rightarrow \text{C}_2\text{H}_6 + \text{M}$	$1.68 \times 10^{-24} \left(\frac{T_{gas}}{298}\right)^{-7.00} \exp\left(-\frac{11.56}{RT_{gas}}\right)$	174
$\text{C}_2\text{H}_6 + \text{M} \rightarrow 2 \times \text{CH}_3 + \text{M}$	$4.52 \times 10^4 \left(\frac{T_{gas}}{298}\right)^{-8.24} \exp\left(-\frac{392.0}{RT_{gas}}\right)$	174
$\text{CH}_3 + \text{CH}_2 \rightarrow \text{C}_2\text{H}_4 + \text{H}$	7.01×10^{-11}	146
$\text{CH}_3 + \text{C}_2\text{H}_6 \rightarrow \text{C}_2\text{H}_5 + \text{CH}_4$	$1.74 \times 10^{-16} \left(\frac{T_{gas}}{298}\right)^{6.00} \exp\left(-\frac{25.28}{RT_{gas}}\right)$	146
$\text{CH}_3 + \text{C}_2\text{H}_5 \rightarrow \text{C}_2\text{H}_4 + \text{CH}_4$	$3.30 \times 10^{-11} (T_{gas})^{0.50}$	118
$\text{CH}_3 + \text{C}_2\text{H}_5 \rightarrow \text{C}_3\text{H}_8$	5.60×10^{-11}	174
$\text{C}_3\text{H}_8 + \text{M} \rightarrow \text{CH}_3 + \text{C}_2\text{H}_5$	$1.30 \times 10^{-5} \exp\left(-\frac{272.0}{RT_{gas}}\right)$	174
$\text{CH}_3 + \text{C}_2\text{H}_4 \rightarrow \text{C}_2\text{H}_3 + \text{CH}_4$	$6.91 \times 10^{-12} \exp\left(-\frac{46.56}{RT_{gas}}\right)$	146
$\text{CH}_3 + \text{C}_2\text{H}_3 \rightarrow \text{C}_2\text{H}_2 + \text{CH}_4$	3.00×10^{-11}	175
$\text{C}_2\text{H}_2 + \text{CH}_4 \rightarrow \text{CH}_3 + \text{C}_2\text{H}_3$	5.00×10^{-17}	176
$\text{CH}_3 + \text{C}_2\text{H}_3 + \text{M} \rightarrow \text{C}_3\text{H}_6 + \text{M}$	4.91×10^{-30}	177,178
$\text{C}_3\text{H}_6 \rightarrow \text{CH}_3 + \text{C}_2\text{H}_3$	$1.18 \times 10^{18} \left(\frac{T_{gas}}{298}\right)^{-1.20} \exp\left(-\frac{409.0}{RT_{gas}}\right)$	145
$\text{CH}_3 + \text{C}_3\text{H}_7 \rightarrow \text{C}_3\text{H}_6 + \text{CH}_4$	$3.07 \times 10^{-12} \left(\frac{T_{gas}}{298}\right)^{-0.32}$	171

$\text{CH}_3 + \text{H} \rightarrow \text{CH}_2 + \text{H}_2$	$1.00 \times 10^{-10} \exp\left(-\frac{63.19}{RT_{gas}}\right)$	146
$\text{CH}_2 + \text{H}_2 \rightarrow \text{CH}_3 + \text{H}$	5.00×10^{-15}	118
$\text{CH}_3 + \text{H} + \text{CH}_4 \rightarrow \text{CH}_4 + \text{CH}_4$	$3.0 \times 3.15 \times 10^{-30} (T_{gas})^{0.47} \exp\left(-\frac{269.74}{T_{gas}}\right)$	147,178
$\text{CH}_3 + \text{H} + \text{O}_2 \rightarrow \text{CH}_4 + \text{O}_2$	$1.0 \times 3.15 \times 10^{-30} (T_{gas})^{0.47} \exp\left(-\frac{269.74}{T_{gas}}\right)$	147,178
$\text{CH}_3 + \text{H} + \text{CO}_2 \rightarrow \text{CH}_4 + \text{CO}_2$	$2.0 \times 3.15 \times 10^{-30} (T_{gas})^{0.47} \exp\left(-\frac{269.74}{T_{gas}}\right)$	147,178
$\text{CH}_3 + \text{H} + \text{CO} \rightarrow \text{CH}_4 + \text{CO}$	$1.0 \times 3.15 \times 10^{-30} (T_{gas})^{0.47} \exp\left(-\frac{269.74}{T_{gas}}\right)$	147,178
$\text{CH}_3 + \text{H} + \text{H}_2\text{O} \rightarrow \text{CH}_4 + \text{H}_2\text{O}$	$6.0 \times 3.15 \times 10^{-30} (T_{gas})^{0.47} \exp\left(-\frac{269.74}{T_{gas}}\right)$	147,178
$\text{CH}_3 + \text{H} + \text{H}_2 \rightarrow \text{CH}_4 + \text{H}_2$	$2.0 \times 3.15 \times 10^{-30} (T_{gas})^{0.47} \exp\left(-\frac{269.74}{T_{gas}}\right)$	147,178
$\text{CH}_4 + \text{M} \rightarrow \text{CH}_3 + \text{H} + \text{M} (\alpha=0.8)$	$1.40 \times 10^{-06} \exp\left(-\frac{380.0}{RT_{gas}}\right)$	174
$2\text{xCH}_2 \rightarrow \text{C}_2\text{H}_2 + 2\text{xH}$	$3.32 \times 10^{-10} \exp\left(-\frac{45.98}{RT_{gas}}\right)$	179
$\text{CH}_2 + \text{C}_2\text{H}_5 \rightarrow \text{C}_2\text{H}_4 + \text{CH}_3$	3.01×10^{-11}	118
$\text{CH}_2 + \text{C}_2\text{H}_3 \rightarrow \text{C}_2\text{H}_2 + \text{CH}_3$	3.01×10^{-11}	118
$\text{CH}_2 + \text{C}_2\text{H} \rightarrow \text{C}_2\text{H}_2 + \text{CH}$	3.01×10^{-11}	118
$\text{CH}_2 + \text{C}_3\text{H}_8 \rightarrow \text{C}_3\text{H}_7 + \text{CH}_3$	$1.61 \times 10^{-15} \left(\frac{T_{gas}}{298}\right)^{3.65} \exp\left(-\frac{29.93}{RT_{gas}}\right)$	171
$\text{CH}_2 + \text{C}_3\text{H}_7 \rightarrow \text{C}_2\text{H}_4 + \text{C}_2\text{H}_5$	3.01×10^{-11}	171
$\text{CH}_2 + \text{C}_3\text{H}_7 \rightarrow \text{C}_3\text{H}_6 + \text{CH}_3$	3.01×10^{-12}	171
$\text{CH}_2 + \text{C}_3\text{H}_6 \rightarrow \text{C}_3\text{H}_5 + \text{CH}_3$	$1.20 \times 10^{-12} \exp\left(-\frac{25.94}{RT_{gas}}\right)$	145
$\text{CH}_2 + \text{H} \rightarrow \text{CH} + \text{H}_2$	$1.00 \times 10^{-11} \exp\left(\frac{7.48}{RT_{gas}}\right)$	146
$\text{CH} + \text{H}_2 \rightarrow \text{CH}_2 + \text{H} (\alpha=0.8)$	$1.48 \times 10^{-11} \left(\frac{T_{gas}}{298}\right)^{1.79} \exp\left(-\frac{6.98}{RT_{gas}}\right)$	180
$\text{CH} + \text{C}_2\text{H}_6 + \text{M} \rightarrow \text{C}_3\text{H}_7 + \text{M}$	1.14×10^{-29}	146,178
$\text{CH} + \text{H} \rightarrow \text{C} + \text{H}_2$	$1.31 \times 10^{-10} \exp\left(-\frac{6.70}{RT_{gas}}\right)$	181
$\text{C} + \text{H}_2 \rightarrow \text{CH} + \text{H} (\alpha=0.8)$	$6.64 \times 10^{-10} \exp\left(-\frac{97.28}{RT_{gas}}\right)$	182
$\text{C}_2\text{H}_6 + \text{C}_2\text{H}_3 \rightarrow \text{C}_2\text{H}_5 + \text{C}_2\text{H}_4$	$1.46 \times 10^{-13} \left(\frac{T_{gas}}{298}\right)^{3.30} \exp\left(-\frac{43.9}{RT_{gas}}\right)$	118
$\text{C}_2\text{H}_5 + \text{C}_2\text{H}_4 \rightarrow \text{C}_2\text{H}_6 + \text{C}_2\text{H}_3$	$5.83 \times 10^{-14} \left(\frac{T_{gas}}{298}\right)^{3.13} \exp\left(-\frac{75.33}{RT_{gas}}\right)$	118

$C_2H_6 + C_2H \rightarrow C_2H_2 + C_2H_5$	5.99×10^{-12}	118
$C_2H_2 + C_2H_5 \rightarrow C_2H_6 + C_2H$	$4.50 \times 10^{-13} \exp\left(-\frac{98.11}{RT_{gas}}\right)$	118
$C_2H_6 + C_3H_7 \rightarrow C_3H_8 + C_2H_5$	$1.19 \times 10^{-15} \left(\frac{T_{gas}}{298}\right)^{3.82} \exp\left(-\frac{37.83}{RT_{gas}}\right)$	171
$C_3H_8 + C_2H_5 \rightarrow C_2H_6 + C_3H_7$	$1.61 \times 10^{-15} \left(\frac{T_{gas}}{298}\right)^{3.65} \exp\left(-\frac{38.25}{RT_{gas}}\right)$	171
$C_2H_6 + C_3H_5 \rightarrow C_3H_6 + C_2H_5$	$5.71 \times 10^{-14} \left(\frac{T_{gas}}{298}\right)^{3.30} \exp\left(-\frac{83.06}{RT_{gas}}\right)$	145
$C_3H_6 + C_2H_5 \rightarrow C_2H_6 + C_3H_5$	$1.69 \times 10^{-15} \left(\frac{T_{gas}}{298}\right)^{3.50} \exp\left(-\frac{27.77}{RT_{gas}}\right)$	145
$C_2H_6 + H \rightarrow C_2H_5 + H_2$	$1.23 \times 10^{-11} \left(\frac{T_{gas}}{298}\right)^{1.50} \exp\left(-\frac{31.01}{RT_{gas}}\right)$	146
$C_2H_5 + H_2 \rightarrow C_2H_6 + H$ ($\alpha=0.8$)	$4.12 \times 10^{-15} \left(\frac{T_{gas}}{298}\right)^{3.60} \exp\left(-\frac{35.34}{RT_{gas}}\right)$	118
$2x C_2H_5 \rightarrow C_2H_6 + C_2H_4$	2.41×10^{-12}	146
$C_2H_5 + C_2H \rightarrow C_2H_4 + C_2H_2$	3.01×10^{-12}	118
$C_2H_5 + C_3H_7 \rightarrow C_3H_8 + C_2H_4$	1.91×10^{-12}	171
$C_2H_5 + C_3H_7 \rightarrow C_3H_6 + C_2H_6$	2.41×10^{-12}	171
$C_2H_5 + C_3H_5 \rightarrow C_3H_6 + C_2H_4$	$4.30 \times 10^{-12} \exp\left(\frac{0.55}{RT_{gas}}\right)$	145
$C_3H_6 + C_2H_4 \rightarrow C_2H_5 + C_3H_5$	$9.60 \times 10^{-11} \exp\left(\frac{-0.216}{RT_{gas}}\right)$	145
$C_2H_5 + H \rightarrow C_2H_4 + H_2$	3.01×10^{-12}	118
$C_2H_4 + H_2 \rightarrow C_2H_5 + H$ ($\alpha=0.8$)	$1.69 \times 10^{-11} \exp\left(-\frac{285.0}{RT_{gas}}\right)$	118
$C_2H_5 + H + M \rightarrow C_2H_6 + M$	9.20×10^{-30}	178,183
$C_2H_6 \rightarrow C_2H_5 + H$	$8.11 \times 10^{17} \left(\frac{T_{gas}}{298}\right)^{-1.23} \exp\left(-\frac{427.0}{RT_{gas}}\right)$	173
$C_2H_4 + C_2H \rightarrow C_2H_2 + C_2H_3$	1.40×10^{-10}	175
$C_2H_4 + H \rightarrow C_2H_3 + H_2$	$4.0 \times 10^{-12} \left(\frac{T_{gas}}{298}\right)^{2.53} \exp\left(-\frac{51.22}{RT_{gas}}\right)$	118
$C_2H_3 + H_2 \rightarrow C_2H_4 + H$ ($\alpha=0.0$)	$1.61 \times 10^{-13} \left(\frac{T_{gas}}{298}\right)^{2.63} \exp\left(-\frac{35.75}{RT_{gas}}\right)$	118
$C_2H_4 + H + M \rightarrow C_2H_5 + M$	$1.30 \times 10^{-29} \exp\left(-\frac{3.16}{RT_{gas}}\right)$	174
$C_2H_5 + M \rightarrow C_2H_4 + H + M$	$1.66 \times 10^{-07} \exp\left(-\frac{130.0}{RT_{gas}}\right)$	184
$2x C_2H_3 \rightarrow C_2H_4 + C_2H_2$	1.60×10^{-12}	118

$C_2H_4 + C_2H_2 \rightarrow C_2H_3 + C_2H_3$	$4.0 \times 10^{-11} \exp\left(-\frac{286.0}{RT_{gas}}\right)$	118
$C_2H_3 + C_2H \rightarrow C_2H_2 + C_2H_2$	1.60×10^{-12}	118
$2x C_2H_2 \rightarrow C_2H_3 + C_2H$	$1.6 \times 10^{-11} \exp\left(-\frac{353.0}{RT_{gas}}\right)$	118
$C_2H_3 + C_3H_8 \rightarrow C_2H_4 + C_3H_7$	$1.46 \times 10^{-13} \left(\frac{T_{gas}}{298}\right)^{3.30} \exp\left(-\frac{43.9}{RT_{gas}}\right)$	171
$C_2H_3 + C_3H_7 \rightarrow C_3H_8 + C_2H_2$	2.01×10^{-12}	171
$C_2H_3 + C_3H_7 \rightarrow C_3H_6 + C_2H_4$	2.01×10^{-12}	171
$C_3H_6 + C_2H_4 \rightarrow C_2H_3 + C_3H_7$	$1.00 \times 10^{-10} \exp\left(-\frac{316.0}{RT_{gas}}\right)$	145
$C_2H_3 + C_3H_6 \rightarrow C_3H_5 + C_2H_4$	$1.68 \times 10^{-15} \left(\frac{T_{gas}}{298}\right)^{3.50} \exp\left(-\frac{19.62}{RT_{gas}}\right)$	145
$C_2H_3 + C_3H_5 \rightarrow C_3H_6 + C_2H_2$	8.00×10^{-12}	145
$C_3H_6 + C_2H_2 \rightarrow C_2H_3 + C_3H_5$	$6.71 \times 10^{-11} \exp\left(-\frac{196.0}{RT_{gas}}\right)$	145
$C_2H_3 + H \rightarrow C_2H_2 + H_2$	2.01×10^{-11}	146
$C_2H_2 + H_2 \rightarrow C_2H_3 + H (\alpha=0.8)$	$4.00 \times 10^{-12} \exp\left(-\frac{272.0}{RT_{gas}}\right)$	118
$C_2H_3 + H + M \rightarrow C_2H_4 + M$	8.26×10^{-30}	178,183
$C_2H_4 + M \rightarrow C_2H_3 + H + M$	$4.30 \times 10^{-07} \exp\left(-\frac{404.0}{RT_{gas}}\right)$	174
$C_2H_2 + H \rightarrow C_2H + H_2$	$1.00 \times 10^{-10} \exp\left(-\frac{93.12}{RT_{gas}}\right)$	118
$C_2H + H_2 \rightarrow C_2H_2 + H (\alpha=0.8)$	$8.95 \times 10^{-13} \left(\frac{T_{gas}}{298}\right)^{2.57} \exp\left(-\frac{1.08}{RT_{gas}}\right)$	175
$C_2H_2 + H + M \rightarrow C_2H_3 + M$	$1.08 \times 10^{-25} \left(\frac{T_{gas}}{298}\right)^{-7.27} \exp\left(-\frac{30.18}{RT_{gas}}\right)$	118
$C_2H_3 + M \rightarrow C_2H_2 + H + M$	$1.91 \times 10^{-01} \left(\frac{T_{gas}}{298}\right)^{-7.50} \exp\left(-\frac{190.0}{RT_{gas}}\right)$	146
$2x C_2H \rightarrow C_2H_2 + C_2$	3.01×10^{-12}	118
$C_2H + C_3H_8 \rightarrow C_2H_2 + C_3H_7$	5.99×10^{-12}	171
$C_2H + C_3H_7 \rightarrow C_3H_6 + C_2H_2$	1.00×10^{-11}	171
$C_2H + C_3H_6 \rightarrow C_3H_5 + C_2H_2$	5.99×10^{-12}	145
$C_2H + H \rightarrow C_2 + H_2$	$5.99 \times 10^{-11} \exp\left(-\frac{118.0}{RT_{gas}}\right)$	118
$C_2 + H_2 \rightarrow C_2H + H (\alpha=0.8)$	$1.10 \times 10^{-10} \exp\left(-\frac{33.26}{RT_{gas}}\right)$	185
$C_2H + H + M \rightarrow C_2H_2 + M$	9.44×10^{-30}	178,183
$C_2H_2 + M \rightarrow C_2H + H + M$	$6.64 \times 10^{-08} \exp\left(-\frac{447.0}{RT_{gas}}\right)$	184

$C_3H_8 + C_3H_5 \rightarrow C_3H_6 + C_3H_7$	$5.71 \times 10^{-14} \left(\frac{T_{gas}}{298}\right)^{3.30} \exp\left(-\frac{83.06}{RT_{gas}}\right)$	145
$C_3H_6 + C_3H_7 \rightarrow C_3H_8 + C_3H_5$	$1.69 \times 10^{-15} \left(\frac{T_{gas}}{298}\right)^{3.50} \exp\left(-\frac{27.77}{RT_{gas}}\right)$	145
$C_3H_8 + H \rightarrow C_3H_7 + H_2$	$4.23 \times 10^{-12} \left(\frac{T_{gas}}{298}\right)^{2.54} \exp\left(-\frac{28.27}{RT_{gas}}\right)$	171
$C_3H_7 + H_2 \rightarrow C_3H_8 + H$ ($\alpha=0.8$)	$3.19 \times 10^{-14} \left(\frac{T_{gas}}{298}\right)^{2.84} \exp\left(-\frac{38.25}{RT_{gas}}\right)$	171
$2xC_3H_7 \rightarrow C_3H_6 + C_3H_8$	2.81×10^{-12}	171
$C_3H_7 + C_3H_5 \rightarrow 2xC_3H_6$	$2.41 \times 10^{-12} \exp\left(\frac{0.55}{RT_{gas}}\right)$	145
$2xC_3H_6 \rightarrow C_3H_7 + C_3H_5$	$4.20 \times 10^{-10} \exp\left(-\frac{231.0}{RT_{gas}}\right)$	145
$C_3H_7 + H \rightarrow C_3H_6 + H_2$	3.01×10^{-12}	171
$C_3H_7 + H + M \rightarrow C_3H_8 + M$	3.96×10^{-30}	178,183
$C_3H_8 \rightarrow C_3H_7 + H$	$1.58 \times 10^{16} \exp\left(-\frac{408.0}{RT_{gas}}\right)$	186
$C_3H_6 + H \rightarrow C_3H_5 + H_2$	$4.40 \times 10^{-13} \left(\frac{T_{gas}}{298}\right)^{2.50} \exp\left(-\frac{10.39}{RT_{gas}}\right)$	145
$C_3H_5 + H_2 \rightarrow C_3H_6 + H$	$1.39 \times 10^{-13} \left(\frac{T_{gas}}{298}\right)^{2.38} \exp\left(-\frac{79.49}{RT_{gas}}\right)$	145
$C_3H_6 + H + M \rightarrow C_3H_7 + M$	3.79×10^{-33}	145,178
$C_3H_7 \rightarrow C_3H_6 + H$	$1.25 \times 10^{17} \exp\left(-\frac{237.0}{RT_{gas}}\right)$	187
$C_3H_5 + H + M \rightarrow C_3H_6 + M$	1.33×10^{-29}	178,188
$C_3H_6 \rightarrow C_3H_5 + H$	$2.50 \times 10^{15} \exp\left(-\frac{363.0}{RT_{gas}}\right)$	145
$H + H_2 \rightarrow 3xH$ ($\alpha=0.8$)	$4.67 \times 10^{-07} \left(\frac{T_{gas}}{300}\right)^{-1.00} \exp\left(-\frac{55000.0}{T_{gas}}\right)$	189
$H_2 + M \rightarrow H + H + M$ ($\alpha=0.8$)	$1.88 \times 10^{-08} \left(\frac{T_{gas}}{298}\right)^{-1.10} \exp\left(-\frac{437.0}{RT_{gas}}\right)$	189
$H + H + M \rightarrow H_2 + M$	$6.04 \times 10^{-33} \left(\frac{T_{gas}}{298}\right)^{-1.00}$	146
$CH_4 + O \rightarrow CH_3 + OH$ ($\alpha=0.8$)	$8.32 \times 10^{-12} \left(\frac{T_{gas}}{298}\right)^{1.56} \exp\left(-\frac{35.503}{RT_{gas}}\right)$	146
$CH_3 + OH \rightarrow CH_4 + O$	$3.22 \times 10^{-14} \left(\frac{T_{gas}}{298}\right)^{2.20} \exp\left(-\frac{18.62}{RT_{gas}}\right)$	190
$CH_3 + O \rightarrow CH_2O + H$	1.12×10^{-10}	184
$CH_3 + O \rightarrow CO + H_2 + H$	2.80×10^{-11}	191

$\text{CH}_3 + \text{O}_2 + \text{M} \rightarrow \text{CH}_3\text{O}_2 + \text{M}$	$1.09 \times 10^{-30} \left(\frac{T_{gas}}{298}\right)^{-3.30}$	146
$\text{CH}_3\text{O}_2 + \text{M} \rightarrow \text{CH}_3 + \text{O}_2 + \text{M}$	$2.03 \left(\frac{T_{gas}}{298}\right)^{-10.0} \exp\left(-\frac{139.0}{RT_{gas}}\right)$	118
$\text{CH}_2 + \text{O} \rightarrow \text{CO} + \text{H}_2$	5.53×10^{-11}	192
$\text{CH}_2 + \text{O} \rightarrow \text{CO} + 2\text{H}$	8.29×10^{-11}	192
$\text{CH}_2 + \text{O}_2 \rightarrow \text{CO}_2 + \text{H}_2$ ($\alpha=0.0$)	$2.99 \times 10^{-11} \left(\frac{T_{gas}}{298}\right)^{-3.30} \exp\left(-\frac{11.97}{RT_{gas}}\right)$	193
$\text{CH}_2 + \text{O}_2 \rightarrow \text{CO} + \text{H}_2\text{O}$	1.42×10^{-12}	146,194
$\text{CH}_2 + \text{O}_2 \rightarrow \text{CH}_2\text{O} + \text{O}$	5.39×10^{-13}	146,194
$\text{CH} + \text{O} \rightarrow \text{CO} + \text{H}$	6.59×10^{-11}	146
$\text{CH} + \text{O}_2 \rightarrow \text{CO}_2 + \text{H}$	1.20×10^{-11}	192
$\text{CH} + \text{O}_2 \rightarrow \text{CO} + \text{OH}$	8.00×10^{-12}	192
$\text{CH} + \text{O}_2 \rightarrow \text{CHO} + \text{O}$	8.00×10^{-12}	192
$\text{CH} + \text{O}_2 \rightarrow \text{CO} + \text{H} + \text{O}$	1.20×10^{-11}	192
$\text{C} + \text{O}_2 \rightarrow \text{CO} + \text{O}$	2.45×10^{-13}	182
$\text{C}_2\text{H}_6 + \text{O} \rightarrow \text{C}_2\text{H}_5 + \text{OH}$	$8.54 \times 10^{-12} \left(\frac{T_{gas}}{298}\right)^{1.50} \exp\left(-\frac{24.28}{RT_{gas}}\right)$	146
$\text{C}_2\text{H}_5 + \text{OH} \rightarrow \text{C}_2\text{H}_6 + \text{O}$	$9.85 \times 10^{-19} \left(\frac{T_{gas}}{298}\right)^{8.80} \exp\left(-\frac{2.08}{RT_{gas}}\right)$	190
$\text{C}_2\text{H}_5 + \text{O} \rightarrow \text{CH}_3\text{CHO} + \text{H}$	8.80×10^{-11}	192
$\text{C}_2\text{H}_5 + \text{O} \rightarrow \text{CH}_2\text{O} + \text{CH}_3$	6.90×10^{-11}	192
$\text{C}_2\text{H}_5 + \text{O} \rightarrow \text{C}_2\text{H}_4 + \text{OH}$	$6.31 \times 10^{-12} \left(\frac{T_{gas}}{298}\right)^{0.03} \exp\left(\frac{1.65}{RT_{gas}}\right)$	195
$\text{C}_2\text{H}_5 + \text{O}_2 \rightarrow \text{C}_2\text{H}_4 + \text{HO}_2$	3.80×10^{-15}	196
$\text{C}_2\text{H}_5 + \text{O}_2 + \text{M} \rightarrow \text{C}_2\text{H}_5\text{O}_2 + \text{M}$	5.75×10^{-29}	196
$\text{C}_2\text{H}_5\text{O}_2 + \text{M} \rightarrow \text{C}_2\text{H}_5 + \text{O}_2 + \text{M}$	$1.40 \times 10^2 \left(\frac{T_{gas}}{298}\right)^{-9.85} \exp\left(-\frac{163.0}{RT_{gas}}\right)$	197
$\text{C}_2\text{H}_4 + \text{O} \rightarrow \text{CH}_2\text{CHO} + \text{H}$	2.63×10^{-13}	192
$\text{C}_2\text{H}_4 + \text{O} \rightarrow \text{CHO} + \text{CH}_3$	4.51×10^{-13}	192
$\text{C}_2\text{H}_4 + \text{O}_3 \rightarrow \text{CH}_2\text{O} + \text{CO}_2 + \text{H}_2$	7.06×10^{-19}	194,196
$\text{C}_2\text{H}_4 + \text{O}_3 \rightarrow \text{CH}_2\text{O} + \text{CO} + \text{H}_2\text{O}$	7.06×10^{-19}	194,196
$\text{C}_2\text{H}_4 + \text{O}_3 \rightarrow 2\text{CH}_2\text{O} + \text{O}$	2.69×10^{-19}	194,196
$\text{C}_2\text{H}_3 + \text{O} \rightarrow \text{C}_2\text{H}_2 + \text{OH}$	$5.50 \times 10^{-12} \left(\frac{T_{gas}}{298}\right)^{0.20} \exp\left(\frac{1.79}{RT_{gas}}\right)$	195
$\text{C}_2\text{H}_3 + \text{O} \rightarrow \text{CO} + \text{CH}_3$	1.25×10^{-11}	192
$\text{C}_2\text{H}_3 + \text{O} \rightarrow \text{CHO} + \text{CH}_2$	1.25×10^{-11}	192
$\text{C}_2\text{H}_3 + \text{O} \rightarrow \text{CH}_2\text{CO} + \text{H}$	1.60×10^{-10}	118
$\text{C}_2\text{H}_3 + \text{O}_2 \rightarrow \text{CH}_2\text{O} + \text{CHO}$	9.00×10^{-12}	146

$C_2H_2 + O \rightarrow CH_2 + CO$	$3.49 \times 10^{-12} \left(\frac{T_{gas}}{298}\right)^{1.50} \exp\left(-\frac{7.07}{RT_{gas}}\right)$	198
$C_2H_2 + O \rightarrow C_2HO + H$	$7.14 \times 10^{-10} \exp\left(-\frac{50.72}{RT_{gas}}\right)$	198
$C_2H + O \rightarrow CH + CO$	1.69×10^{-11}	146
$C_2H + O_2 \rightarrow CHO + CO$	3.00×10^{-11}	146
$C_2H + O_2 \rightarrow C_2HO + O$	1.00×10^{-12}	118
$C_3H_8 + O \rightarrow C_3H_7 + OH$	$1.37 \times 10^{-12} \left(\frac{T_{gas}}{298}\right)^{2.68} \exp\left(-\frac{15.548}{RT_{gas}}\right)$	171
$H_2 + O \rightarrow OH + H (\alpha=0.8)$	$3.44 \times 10^{-13} \left(\frac{T_{gas}}{298}\right)^{2.67} \exp\left(-\frac{26.274}{RT_{gas}}\right)$	146
$H + OH \rightarrow H_2 + O$	$6.86 \times 10^{-14} \left(\frac{T_{gas}}{298}\right)^{2.80} \exp\left(-\frac{16.210}{RT_{gas}}\right)$	118
$H + O + M \rightarrow OH + M$	$4.36 \times 10^{-32} \left(\frac{T_{gas}}{298}\right)^{-1.00}$	118
$OH + M \rightarrow H + O + M$	$4.00 \times 10^{-09} \exp\left(-\frac{416.0}{RT_{gas}}\right)$	118
$H + O_2 \rightarrow OH + O (\alpha=0.8)$	$3.3 \times 10^{-10} \exp\left(-\frac{70.34}{RT_{gas}}\right)$	146
$OH + O \rightarrow H + O_2$	$2.41 \times 10^{-11} \exp\left(-\frac{2.94}{RT_{gas}}\right)$	146
$H + O_2 + M \rightarrow HO_2 + M$	$4.11 \times 10^{-32} \left(\frac{T_{gas}}{298}\right)^{-1.10}$	199
$HO_2 + M \rightarrow H + O_2 + M$	$2.41 \times 10^{-08} \left(\frac{T_{gas}}{298}\right)^{-1.18} \exp\left(-\frac{203.0}{RT_{gas}}\right)$	118
$H + O_3 \rightarrow OH + O_2$	2.83×10^{-11}	200
$CH_4 + OH \rightarrow CH_3 + H_2O (\alpha=0.0)$	$4.16 \times 10^{-13} \left(\frac{T_{gas}}{298}\right)^{2.18} \exp\left(-\frac{10.24}{RT_{gas}}\right)$	201
$CH_3 + H_2O \rightarrow CH_4 + OH$	$1.20 \times 10^{-14} \left(\frac{T_{gas}}{298}\right)^{2.90} \exp\left(-\frac{62.19}{RT_{gas}}\right)$	118
$CH_4 + HO_2 \rightarrow CH_3 + H_2O_2 (\alpha=0.8)$	$3.01 \times 10^{-13} \exp\left(-\frac{77.74}{RT_{gas}}\right)$	118
$CH_3 + H_2O_2 \rightarrow CH_4 + HO_2$	$2.01 \times 10^{-14} \exp\left(\frac{2.49}{RT_{gas}}\right)$	118
$CH_4 + CHO \rightarrow CH_3 + CH_2O (\alpha=0.8)$	$1.36 \times 10^{-13} \left(\frac{T_{gas}}{298}\right)^{2.85} \exp\left(-\frac{93.954}{RT_{gas}}\right)$	118
$CH_3 + CH_2O \rightarrow CH_4 + CHO$	$1.60 \times 10^{-16} \left(\frac{T_{gas}}{298}\right)^{6.10} \exp\left(-\frac{8.23}{RT_{gas}}\right)$	174
$CH_4 + CH_3O \rightarrow CH_3OH + CH_3 (\alpha=0.8)$	$2.61 \times 10^{-13} \exp\left(-\frac{37.0}{RT_{gas}}\right)$	118

$\text{CH}_3\text{OH} + \text{CH}_3 \rightarrow \text{CH}_4 + \text{CH}_3\text{O}$	$1.12 \times 10^{-15} \left(\frac{T_{\text{gas}}}{298}\right)^{3.10} \exp\left(-\frac{29.02}{RT_{\text{gas}}}\right)$	202
$\text{CH}_4 + \text{CH}_3\text{O}_2 \rightarrow \text{CH}_3 + \text{CH}_3\text{OOH}$ ($\alpha=0.8$)	$3.01 \times 10^{-13} \exp\left(-\frac{77.32}{RT_{\text{gas}}}\right)$	118
$\text{CH}_3 + \text{CO} + \text{M} \rightarrow \text{CH}_3\text{CO} + \text{M}$	$7.83 \times 10^{-29} \left(\frac{T_{\text{gas}}}{298}\right)^{-7.56} \exp\left(-\frac{45.65}{RT_{\text{gas}}}\right)$	118
$\text{CH}_3\text{CO} \rightarrow \text{CH}_3 + \text{CO}$	$3.87 \times 10^{13} \left(\frac{T_{\text{gas}}}{298}\right)^{0.63} \exp\left(-\frac{70.70}{RT_{\text{gas}}}\right)$	203
$\text{CH}_3 + \text{OH} \rightarrow \text{CH}_2 + \text{H}_2\text{O}$	$1.20 \times 10^{-10} \exp\left(-\frac{11.64}{RT_{\text{gas}}}\right)$	174
$\text{CH}_2 + \text{H}_2\text{O} \rightarrow \text{CH}_3 + \text{OH}$	1.60×10^{-16}	118
$\text{CH}_3 + \text{OH} \rightarrow \text{CH}_2\text{OH} + \text{H}$	$1.54 \times 10^{-09} \left(\frac{T_{\text{gas}}}{298}\right)^{-1.80} \exp\left(-\frac{33.76}{RT_{\text{gas}}}\right)$	204
$\text{CH}_2\text{OH} + \text{H} \rightarrow \text{CH}_3 + \text{OH}$	1.60×10^{-10}	202
$\text{CH}_3 + \text{OH} \rightarrow \text{CH}_3\text{O} + \text{H}$	$2.57 \times 10^{-12} \left(\frac{T_{\text{gas}}}{298}\right)^{-0.23} \exp\left(-\frac{58.28}{RT_{\text{gas}}}\right)$	204
$\text{CH}_3\text{O} + \text{H} \rightarrow \text{CH}_3 + \text{OH}$	9.93×10^{-12}	205
$\text{CH}_3 + \text{OH} + \text{M} \rightarrow \text{CH}_3\text{OH} + \text{M}$	$2.25 \times 10^{-24} \left(\frac{T_{\text{gas}}}{298}\right)^{-8.20}$	174
$\text{CH}_3\text{OH} + \text{M} \rightarrow \text{CH}_3 + \text{OH} + \text{M}$	$3.32 \times 10^{-07} \exp\left(-\frac{286.0}{RT_{\text{gas}}}\right)$	184
$\text{CH}_3 + \text{HO}_2 \rightarrow \text{CH}_3\text{O} + \text{OH}$	$7.68 \times 10^{-12} \left(\frac{T_{\text{gas}}}{298}\right)^{0.27} \exp\left(\frac{2.88}{RT_{\text{gas}}}\right)$	206
$\text{CH}_3 + \text{HO}_2 \rightarrow \text{CH}_4 + \text{O}_2$	5.99×10^{-12}	118
$\text{CH}_4 + \text{O}_2 \rightarrow \text{CH}_3 + \text{HO}_2$ ($\alpha=0.8$)	$6.59 \times 10^{-11} \exp\left(-\frac{238.0}{RT_{\text{gas}}}\right)$	146
$\text{CH}_3 + \text{CHO} \rightarrow \text{CH}_4 + \text{CO}$	2.01×10^{-10}	118
$\text{CH}_3 + \text{CH}_3\text{O} \rightarrow \text{CH}_4 + \text{CH}_2\text{O}$	4.00×10^{-11}	118
$\text{CH}_3 + \text{CH}_3\text{CHO} \rightarrow \text{CH}_4 + \text{CH}_3\text{CO}$	$2.97 \times 10^{-16} \left(\frac{T_{\text{gas}}}{298}\right)^{5.64} \exp\left(-\frac{10.31}{RT_{\text{gas}}}\right)$	146
$\text{CH}_4 + \text{CH}_3\text{CO} \rightarrow \text{CH}_3 + \text{CH}_3\text{CHO}$ ($\alpha=0.8$)	$4.82 \times 10^{-14} \left(\frac{T_{\text{gas}}}{298}\right)^{2.88} \exp\left(-\frac{89.8}{RT_{\text{gas}}}\right)$	118
$\text{CH}_3 + \text{CH}_3\text{O}_2 \rightarrow 2\text{CH}_3\text{O}$	4.00×10^{-11}	118
$\text{CH}_2 + \text{CO}_2 \rightarrow \text{CH}_2\text{O} + \text{CO}$	3.90×10^{-14}	118
$\text{CH}_2 + \text{OH} \rightarrow \text{CH}_2\text{O} + \text{H}$	3.01×10^{-11}	118
$\text{CH}_2 + \text{HO}_2 \rightarrow \text{CH}_2\text{O} + \text{OH}$	3.00×10^{-11}	118
$\text{CH}_2 + \text{CH}_2\text{O} \rightarrow \text{CH}_3 + \text{CHO}$	1.00×10^{-14}	118
$\text{CH}_2 + \text{CHO} \rightarrow \text{CH}_3 + \text{CO}$	3.01×10^{-11}	118
$\text{CH}_2 + \text{CH}_3\text{O} \rightarrow \text{CH}_3 + \text{CH}_2\text{O}$	3.01×10^{-11}	118
$\text{CH}_2 + \text{CH}_3\text{O}_2 \rightarrow \text{CH}_2\text{O} + \text{CH}_3\text{O}$	3.01×10^{-11}	118

$\text{CH} + \text{CO}_2 \rightarrow \text{CHO} + \text{CO}$	9.68×10^{-13}	192
$\text{CH} + \text{CO}_2 \rightarrow 2\text{CO} + \text{H}$	9.68×10^{-13}	192
$\text{CH} + \text{CO} + \text{M} \rightarrow \text{C}_2\text{HO} + \text{M}$	$4.15 \times 10^{-30} \left(\frac{T_{\text{gas}}}{298}\right)^{-1.90}$	207
$\text{C}_2\text{HO} + \text{M} \rightarrow \text{CO} + \text{CH} + \text{M}$	$1.08 \times 10^{-08} \exp\left(-\frac{246.0}{RT_{\text{gas}}}\right)$	208
$\text{C}_2\text{H}_6 + \text{OH} \rightarrow \text{C}_2\text{H}_5 + \text{H}_2\text{O}$	$8.53 \times 10^{-13} \left(\frac{T_{\text{gas}}}{298}\right)^{2.22} \exp\left(-\frac{3.10}{RT_{\text{gas}}}\right)$	209
$\text{C}_2\text{H}_5 + \text{H}_2\text{O} \rightarrow \text{C}_2\text{H}_6 + \text{OH}$	$2.06 \times 10^{-14} \left(\frac{T_{\text{gas}}}{298}\right)^{1.44} \exp\left(-\frac{84.81}{RT_{\text{gas}}}\right)$	118
$\text{C}_2\text{H}_6 + \text{HO}_2 \rightarrow \text{C}_2\text{H}_5 + \text{H}_2\text{O}_2$	$4.90 \times 10^{-13} \exp\left(-\frac{65.52}{RT_{\text{gas}}}\right)$	118
$\text{C}_2\text{H}_5 + \text{H}_2\text{O}_2 \rightarrow \text{C}_2\text{H}_6 + \text{HO}_2$	$1.45 \times 10^{-14} \exp\left(-\frac{4.07}{RT_{\text{gas}}}\right)$	118
$\text{C}_2\text{H}_6 + \text{CHO} \rightarrow \text{C}_2\text{H}_5 + \text{CH}_2\text{O}$	$4.18 \times 10^{-13} \left(\frac{T_{\text{gas}}}{298}\right)^{2.72} \exp\left(-\frac{76.33}{RT_{\text{gas}}}\right)$	118
$\text{C}_2\text{H}_5 + \text{CH}_2\text{O} \rightarrow \text{C}_2\text{H}_6 + \text{CHO}$	$8.19 \times 10^{-14} \left(\frac{T_{\text{gas}}}{298}\right)^{2.81} \exp\left(-\frac{24.53}{RT_{\text{gas}}}\right)$	118
$\text{C}_2\text{H}_6 + \text{CH}_3\text{O} \rightarrow \text{C}_2\text{H}_5 + \text{CH}_3\text{OH}$	$4.00 \times 10^{-13} \exp\left(-\frac{29.68}{RT_{\text{gas}}}\right)$	118
$\text{C}_2\text{H}_5 + \text{CH}_3\text{OH} \rightarrow \text{C}_2\text{H}_6 + \text{CH}_3\text{O}$	$1.12 \times 10^{-15} \left(\frac{T_{\text{gas}}}{298}\right)^{3.10} \exp\left(-\frac{37.42}{RT_{\text{gas}}}\right)$	202
$\text{C}_2\text{H}_6 + \text{CH}_3\text{O}_2 \rightarrow \text{C}_2\text{H}_5 + \text{CH}_3\text{OOH}$	$4.90 \times 10^{-13} \exp\left(-\frac{62.52}{RT_{\text{gas}}}\right)$	118
$\text{C}_2\text{H}_6 + \text{C}_2\text{H}_5\text{O}_2 \rightarrow \text{C}_2\text{H}_5 + \text{C}_2\text{H}_5\text{OOH}$	$2.87 \times 10^{-14} \left(\frac{T_{\text{gas}}}{298}\right)^{3.76} \exp\left(-\frac{71.96}{RT_{\text{gas}}}\right)$	210
$\text{C}_2\text{H}_5 + \text{OH} \rightarrow \text{C}_2\text{H}_4 + \text{H}_2\text{O}$	4.00×10^{-11}	118
$\text{C}_2\text{H}_5 + \text{HO}_2 \rightarrow \text{C}_2\text{H}_6 + \text{O}_2$	5.00×10^{-13}	118
$\text{C}_2\text{H}_6 + \text{O}_2 \rightarrow \text{C}_2\text{H}_5 + \text{HO}_2$	$1.00 \times 10^{-10} \exp\left(-\frac{217.0}{RT_{\text{gas}}}\right)$	146
$\text{C}_2\text{H}_5 + \text{HO}_2 \rightarrow \text{C}_2\text{H}_4 + \text{H}_2\text{O}_2$	5.00×10^{-13}	118
$\text{C}_2\text{H}_5 + \text{CHO} \rightarrow \text{C}_2\text{H}_6 + \text{CO}$	2.01×10^{-10}	118
$\text{C}_2\text{H}_5 + \text{CH}_3\text{O} \rightarrow \text{C}_2\text{H}_6 + \text{CH}_2\text{O}$	4.00×10^{-11}	118
$\text{C}_2\text{H}_5 + \text{CH}_3\text{O}_2 \rightarrow \text{CH}_3\text{O} + \text{C}_2\text{H}_5\text{O}$	4.00×10^{-11}	118
$\text{C}_2\text{H}_4 + \text{OH} \rightarrow \text{C}_2\text{H}_3 + \text{H}_2\text{O}$	$1.66 \times 10^{-13} \left(\frac{T_{\text{gas}}}{298}\right)^{2.75} \exp\left(-\frac{17.46}{RT_{\text{gas}}}\right)$	118
$\text{C}_2\text{H}_3 + \text{H}_2\text{O} \rightarrow \text{C}_2\text{H}_4 + \text{OH}$	$1.20 \times 10^{-14} \left(\frac{T_{\text{gas}}}{298}\right)^{2.90} \exp\left(-\frac{62.19}{RT_{\text{gas}}}\right)$	118
$\text{C}_2\text{H}_4 + \text{HO}_2 \rightarrow \text{CH}_3\text{CHO} + \text{OH}$	$1.00 \times 10^{-14} \exp\left(-\frac{33.26}{RT_{\text{gas}}}\right)$	118

$C_2H_3 + OH \rightarrow C_2H_2 + H_2O$	5.00×10^{-11}	118
$C_2H_3 + CH_2O \rightarrow C_2H_4 + CHO$	$8.07 \times 10^{-14} \left(\frac{T_{gas}}{298}\right)^{2.81} \exp\left(-\frac{24.53}{RT_{gas}}\right)$	118
$C_2H_3 + CHO \rightarrow C_2H_4 + CO$	1.50×10^{-10}	118
$C_2H_4 + CO \rightarrow C_2H_3 + CHO$	$2.51 \times 10^{-10} \exp\left(-\frac{379.0}{RT_{gas}}\right)$	118
$C_2H_3 + CH_3O \rightarrow C_2H_4 + CH_2O$	4.00×10^{-11}	118
$C_2H_2 + OH \rightarrow C_2H + H_2O$	$5.00 \times 10^{-12} \left(\frac{T_{gas}}{298}\right)^{2.00} \exp\left(-\frac{58.53}{RT_{gas}}\right)$	211
$C_2H + H_2O \rightarrow C_2H_2 + OH$	$7.74 \times 10^{-14} \left(\frac{T_{gas}}{298}\right)^{3.05} \exp\left(-\frac{3.13}{RT_{gas}}\right)$	212
$C_2H_2 + HO_2 \rightarrow CH_2CO + OH$	$1.00 \times 10^{-14} \exp\left(-\frac{33.26}{RT_{gas}}\right)$	118
$C_2H + OH \rightarrow CH_2 + CO$	3.01×10^{-11}	118
$C_2H + OH \rightarrow C_2H_2 + O$	3.01×10^{-11}	118
$C_2H + HO_2 \rightarrow C_2H_2 + O_2$	3.01×10^{-11}	118
$C_2H_2 + O_2 \rightarrow C_2H + HO_2$	$2.01 \times 10^{-11} \exp\left(-\frac{312.0}{RT_{gas}}\right)$	118
$C_2H + HO_2 \rightarrow C_2HO + OH$	3.01×10^{-11}	118
$C_2H + CHO \rightarrow C_2H_2 + CO$	1.00×10^{-10}	118
$C_2H_2 + CO \rightarrow C_2H + CHO$	$8.00 \times 10^{-10} \exp\left(-\frac{446.0}{RT_{gas}}\right)$	118
$C_2H + CH_3O \rightarrow C_2H_2 + CH_2O$	4.00×10^{-11}	118
$C_2H + CH_3O_2 \rightarrow CH_3O + C_2HO$	4.00×10^{-11}	118
$C_3H_8 + OH \rightarrow C_3H_7 + H_2O$	$1.44 \times 10^{-12} \left(\frac{T_{gas}}{298}\right)^{1.00} \exp\left(-\frac{1.08}{RT_{gas}}\right)$	213
$C_3H_8 + HO_2 \rightarrow C_3H_7 + H_2O_2$	$1.61 \times 10^{-13} \left(\frac{T_{gas}}{298}\right)^{2.55} \exp\left(-\frac{69.01}{RT_{gas}}\right)$	171
$C_3H_7 + H_2O_2 \rightarrow C_3H_8 + HO_2$	$5.15 \times 10^{-15} \left(\frac{T_{gas}}{298}\right)^{2.11} \exp\left(-\frac{10.73}{RT_{gas}}\right)$	171
$C_3H_8 + CHO \rightarrow C_3H_7 + CH_2O$	$5.21 \times 10^{-13} \left(\frac{T_{gas}}{298}\right)^{2.50} \exp\left(-\frac{77.16}{RT_{gas}}\right)$	171
$C_3H_7 + CH_2O \rightarrow C_3H_8 + CHO$	$7.49 \times 10^{-14} \left(\frac{T_{gas}}{298}\right)^{2.90} \exp\left(-\frac{24.53}{RT_{gas}}\right)$	171
$C_3H_8 + CH_3O \rightarrow C_3H_7 + CH_3OH$	$7.21 \times 10^{-13} \exp\left(-\frac{27.02}{RT_{gas}}\right)$	171
$C_3H_7 + CH_3OH \rightarrow C_3H_8 + CH_3O$	$1.12 \times 10^{-15} \left(\frac{T_{gas}}{298}\right)^{3.10} \exp\left(-\frac{37.42}{RT_{gas}}\right)$	171
$C_3H_8 + CH_3O_2 \rightarrow C_3H_7 + CH_3OOH$	$1.00 \times 10^{-11} \exp\left(-\frac{81.07}{RT_{gas}}\right)$	171

$C_3H_7 + CHO \rightarrow C_3H_8 + CO$	1.00×10^{-10}	171
$C_3H_7 + CH_3O \rightarrow C_3H_8 + CH_2O$	4.00×10^{-11}	171
$C_3H_7 + CH_3O_2 \rightarrow C_2H_5 + CH_2O + CH_3O$	5.99×10^{-11}	171
$H_2 + OH \rightarrow H + H_2O$ ($\alpha=0.8$)	$2.06 \times 10^{-12} \left(\frac{T_{gas}}{298}\right)^{1.52} \exp\left(-\frac{14.47}{RT_{gas}}\right)$	214
$H + H_2O \rightarrow H_2 + OH$	$6.82 \times 10^{-12} \left(\frac{T_{gas}}{298}\right)^{1.60} \exp\left(-\frac{80.82}{RT_{gas}}\right)$	146
$H_2 + HO_2 \rightarrow H + H_2O_2$ ($\alpha=0.8$)	$5.00 \times 10^{-11} \exp\left(-\frac{109.0}{RT_{gas}}\right)$	118
$H + H_2O_2 \rightarrow H_2 + HO_2$	$2.81 \times 10^{-12} \exp\left(-\frac{15.71}{RT_{gas}}\right)$	146
$H_2 + CHO \rightarrow H + CH_2O$ ($\alpha=0.8$)	$2.66 \times 10^{-13} \left(\frac{T_{gas}}{298}\right)^{2.00} \exp\left(-\frac{74.58}{RT_{gas}}\right)$	118
$H + CH_2O \rightarrow H_2 + CHO$	$2.14 \times 10^{-12} \left(\frac{T_{gas}}{298}\right)^{1.62} \exp\left(-\frac{9.06}{RT_{gas}}\right)$	174
$H_2 + CH_3O_2 \rightarrow H + CH_3OOH$	$5.00 \times 10^{-11} \exp\left(-\frac{109.0}{RT_{gas}}\right)$	118
$H + CH_3OOH \rightarrow H_2 + CH_3O_2$	7.11×10^{-15}	215
$H + CO_2 \rightarrow CO + OH$ ($\alpha=0.8$)	$2.51 \times 10^{-10} \exp\left(-\frac{111.0}{RT_{gas}}\right)$	118
$CO + OH \rightarrow H + CO_2$	$5.40 \times 10^{-14} \left(\frac{T_{gas}}{298}\right)^{1.50} \exp\left(\frac{2.08}{RT_{gas}}\right)$	146
$H + CO + M \rightarrow CHO + M$	$5.29 \times 10^{-34} \exp\left(-\frac{3.08}{RT_{gas}}\right)$	174
$CHO + M \rightarrow H + CO + M$	$2.61 \times 10^{-10} \exp\left(-\frac{65.93}{RT_{gas}}\right)$	174
$H + OH + M \rightarrow H_2O + M$	$4.38 \times 10^{-30} \left(\frac{T_{gas}}{298}\right)^{-2.00}$	146
$H_2O + M \rightarrow H + OH + M$	$5.80 \times 10^{-09} \exp\left(-\frac{440.0}{RT_{gas}}\right)$	146
$H + HO_2 \rightarrow H_2 + O_2$	$1.10 \times 10^{-10} \exp\left(-\frac{8.90}{RT_{gas}}\right)$	118
$H_2 + O_2 \rightarrow H + HO_2$ ($\alpha=0.8$)	$2.41 \times 10^{-10} \exp\left(-\frac{237.0}{RT_{gas}}\right)$	118
$H + HO_2 \rightarrow H_2O + O$	$5.00 \times 10^{-11} \exp\left(-\frac{7.20}{RT_{gas}}\right)$	146
$H_2O + O \rightarrow H + HO_2$	$4.48 \times 10^{-12} \left(\frac{T_{gas}}{298}\right)^{0.97} \exp\left(-\frac{287.0}{RT_{gas}}\right)$	216
$H + HO_2 \rightarrow 2xOH$	$2.81 \times 10^{-10} \exp\left(-\frac{3.66}{RT_{gas}}\right)$	118

$2xOH \rightarrow HO_2 + H$	$3.32 \times 10^{-12} \left(\frac{T_{gas}}{298}\right)^{0.51} \exp\left(-\frac{211.0}{RT_{gas}}\right)$	216
$H + CHO \rightarrow H_2 + CO$	1.50×10^{-10}	146
$H + CH_3O \rightarrow H_2 + CH_2O$	2.32×10^{-11}	192
$H + CH_3CHO \rightarrow H_2 + CH_3CO$	8.98×10^{-14}	146
$H_2 + CH_3CO \rightarrow H + CH_3CHO$ ($\alpha=0.8$)	$2.18 \times 10^{-13} \left(\frac{T_{gas}}{298}\right)^{1.82} \exp\left(-\frac{73.67}{RT_{gas}}\right)$	118
$H + CH_2CO \rightarrow CH_3 + CO$	1.04×10^{-13}	146
$H + C_2HO \rightarrow CH_2 + CO$	2.50×10^{-10}	146
$H + CH_3O_2 \rightarrow OH + CH_3O$	1.60×10^{-10}	118
$O + H_2O \rightarrow 2xOH$	$1.25 \times 10^{-11} \left(\frac{T_{gas}}{298}\right)^{1.30} \exp\left(-\frac{71.50}{RT_{gas}}\right)$	118
$2xOH \rightarrow O + H_2O$	$1.65 \times 10^{-12} \left(\frac{T_{gas}}{298}\right)^{1.14} \exp\left(-\frac{0.42}{RT_{gas}}\right)$	146
$O + HO_2 \rightarrow O_2 + OH$	$2.91 \times 10^{-11} \exp\left(\frac{1.66}{RT_{gas}}\right)$	118
$O_2 + OH \rightarrow O + HO_2$	$3.70 \times 10^{-11} \exp\left(-\frac{220.0}{RT_{gas}}\right)$	118
$O + CH_2O \rightarrow OH + CHO$	$1.78 \times 10^{-11} \left(\frac{T_{gas}}{298}\right)^{0.57} \exp\left(-\frac{11.56}{RT_{gas}}\right)$	146
$O + CHO \rightarrow CO + OH$	5.00×10^{-11}	146
$O + CHO \rightarrow H + CO_2$	5.00×10^{-11}	146
$O + CH_3O \rightarrow CH_3 + O_2$	2.20×10^{-11}	146
$CH_3 + O_2 \rightarrow O + CH_3O$ ($\alpha=0.8$)	$1.25 \times 10^{-11} \exp\left(-\frac{118.0}{RT_{gas}}\right)$	217
$O + CH_3O \rightarrow OH + CH_2O$	1.00×10^{-11}	118
$O + CH_3CHO \rightarrow OH + CH_3CO$	$8.30 \times 10^{-12} \exp\left(-\frac{7.50}{RT_{gas}}\right)$	184
$O + CH_2CO \rightarrow CH_2 + CO_2$	2.29×10^{-13}	146,218
$O + CH_2CO \rightarrow CH_2O + CO$	7.88×10^{-14}	146,218
$O + CH_2CO \rightarrow CHO + CO + H$	4.33×10^{-14}	146,218
$O + CH_2CO \rightarrow 2xCHO$	4.33×10^{-14}	146,218
$O + C_2HO \rightarrow 2xCO + H$	1.60×10^{-10}	146
$O + CH_3O_2 \rightarrow CH_3O + O_2$	5.99×10^{-11}	118
$O + CH_3OOH \rightarrow CH_3O_2 + OH$	5.63×10^{-15}	192
$O_2 + CHO \rightarrow CO + HO_2$	5.10×10^{-12}	196
$O_2 + CH_3O \rightarrow CH_2O + HO_2$	1.97×10^{-15}	196
$O_2 + CH_2CHO \rightarrow CH_2O + CO + OH$	3.00×10^{-14}	219,220
$O_2 + C_2HO \rightarrow 2xCO + OH$	6.46×10^{-13}	146

$O_3 + OH \rightarrow O_2 + HO_2$	$3.76 \times 10^{-13} \left(\frac{T_{gas}}{298}\right)^{1.99} \exp\left(-\frac{5.02}{RT_{gas}}\right)$	221
$O_3 + HO_2 \rightarrow 2xO_2 + OH$	$1.97 \times 10^{-16} \left(\frac{T_{gas}}{298}\right)^{4.57} \exp\left(\frac{5.76}{RT_{gas}}\right)$	222
$O_3 + CH_3O_2 \rightarrow CH_3O + 2xO_2$	1.00×10^{-17}	223
$CO + HO_2 \rightarrow CO_2 + OH$	$2.51 \times 10^{-10} \exp\left(-\frac{98.94}{RT_{gas}}\right)$	118
$CO + CH_3O \rightarrow CO_2 + CH_3$	$2.61 \times 10^{-11} \exp\left(-\frac{49.39}{RT_{gas}}\right)$	118
$H_2O + CHO \rightarrow CH_2O + OH$	$8.54 \times 10^{-13} \left(\frac{T_{gas}}{298}\right)^{1.35} \exp\left(-\frac{109.0}{RT_{gas}}\right)$	118
$CH_2O + OH \rightarrow H_2O + CHO$	$4.73 \times 10^{-12} \left(\frac{T_{gas}}{298}\right)^{1.18} \exp\left(\frac{1.87}{RT_{gas}}\right)$	146
$H_2O + CH_3O \rightarrow CH_3OH + OH$	$1.46 \times 10^{-15} \left(\frac{T_{gas}}{298}\right)^{3.80} \exp\left(-\frac{48.06}{RT_{gas}}\right)$	224
$CH_3OH + OH \rightarrow H_2O + CH_3O$	$1.66 \times 10^{-11} \exp\left(-\frac{7.10}{RT_{gas}}\right)$	184
$2xOH + M \rightarrow H_2O_2 + M$	$6.04 \times 10^{-31} \left(\frac{T_{gas}}{298}\right)^{-3.00}$	118
$H_2O_2 + M \rightarrow 2xOH + M$	$2.03 \times 10^{-03} \left(\frac{T_{gas}}{298}\right)^{-4.86} \exp\left(-\frac{223.0}{RT_{gas}}\right)$	118
$OH + HO_2 \rightarrow O_2 + H_2O$	$4.80 \times 10^{-11} \exp\left(\frac{2.08}{RT_{gas}}\right)$	222
$O_2 + H_2O \rightarrow OH + HO_2$	$7.72 \times 10^{-12} \exp\left(-\frac{310.0}{RT_{gas}}\right)$	225
$OH + CHO \rightarrow CO + H_2O$	1.69×10^{-10}	146
$OH + CH_3O \rightarrow CH_2O + H_2O$	3.01×10^{-11}	118
$OH + CH_3CHO \rightarrow CH_3CO + H_2O$	1.49×10^{-11}	196
$OH + CH_2CO \rightarrow CO + CH_2OH$	1.14×10^{-11}	146,226
$OH + CH_3O_2 \rightarrow CH_3OH + O_2$	1.00×10^{-10}	118
$2xHO_2 \rightarrow H_2O_2 + O_2$	1.63×10^{-12}	222
$H_2O_2 + O_2 \rightarrow 2xHO_2$	$9.00 \times 10^{-11} \exp\left(-\frac{166.0}{RT_{gas}}\right)$	118
$HO_2 + CH_2O \rightarrow CHO + H_2O_2$	$3.30 \times 10^{-12} \exp\left(-\frac{48.81}{RT_{gas}}\right)$	118
$CHO + H_2O_2 \rightarrow HO_2 + CH_2O$	$1.69 \times 10^{-13} \exp\left(-\frac{29.02}{RT_{gas}}\right)$	118
$HO_2 + CHO \rightarrow OH + H + CO_2$	5.00×10^{-11}	118
$HO_2 + CH_3O \rightarrow CH_2O + H_2O_2$	5.00×10^{-13}	118
$HO_2 + CH_3O_2 \rightarrow CH_3OOH + O_2$	5.12×10^{-12}	196
$HO_2 + C_2H_5O_2 \rightarrow C_2H_5OOH + O_2$	7.63×10^{-12}	196

$\text{CH}_2\text{O} + \text{CH}_3\text{O} \rightarrow \text{CH}_3\text{OH} + \text{CHO}$	$1.69 \times 10^{-13} \exp\left(-\frac{12.47}{RT_{gas}}\right)$	118
$\text{CH}_2\text{O} + \text{CH}_3\text{O}_2 \rightarrow \text{CHO} + \text{CH}_3\text{OOH}$	$3.30 \times 10^{-12} \exp\left(-\frac{48.81}{RT_{gas}}\right)$	118
$\text{CHO} + \text{CHO} \rightarrow \text{CH}_2\text{O} + \text{CO}$	5.00×10^{-11}	146
$\text{CHO} + \text{CH}_3\text{O} \rightarrow \text{CH}_3\text{OH} + \text{CO}$	1.50×10^{-10}	118
$\text{CHO} + \text{CH}_3\text{O}_2 \rightarrow \text{CH}_3\text{O} + \text{H} + \text{CO}_2$	5.00×10^{-11}	118
$\text{CH}_3\text{O} + \text{CH}_3\text{O} \rightarrow \text{CH}_2\text{O} + \text{CH}_3\text{OH}$	1.00×10^{-10}	118
$\text{CH}_3\text{O} + \text{CH}_3\text{O}_2 \rightarrow \text{CH}_2\text{O} + \text{CH}_3\text{OOH}$	5.00×10^{-13}	118
$2\text{xCH}_3\text{O}_2 \rightarrow \text{CH}_3\text{OH} + \text{CH}_2\text{O} + \text{O}_2$	2.19×10^{-13}	196
$2\text{xCH}_3\text{O}_2 \rightarrow 2\text{xCH}_3\text{O} + \text{O}_2$	1.29×10^{-13}	196
$2\text{xC}_2\text{H}_5\text{O}_2 \rightarrow \text{C}_2\text{H}_5\text{OH} + \text{CH}_3\text{CHO}$	2.43×10^{-14}	196
$2\text{xC}_2\text{H}_5\text{O}_2 \rightarrow 2\text{xC}_2\text{H}_5\text{O} + \text{O}_2$	3.97×10^{-14}	196
$\text{CH}_4 + \text{CH}_2\text{OH} \rightarrow \text{CH}_3\text{OH} + \text{CH}_3$ ($\alpha=0.8$)	$1.68 \times 10^{-15} \left(\frac{T_{gas}}{298}\right)^{3.10} \exp\left(-\frac{67.93}{RT_{gas}}\right)$	202
$\text{CH}_3\text{OH} + \text{CH}_3 \rightarrow \text{CH}_4 + \text{CH}_2\text{OH}$	$4.38 \times 10^{-15} \left(\frac{T_{gas}}{298}\right)^{3.20} \exp\left(-\frac{30.02}{RT_{gas}}\right)$	202
$\text{CH}_3 + \text{CH}_2\text{OH} \rightarrow \text{CH}_4 + \text{CH}_2\text{O}$	4.00×10^{-12}	202
$\text{CH}_3 + \text{C}_2\text{H}_5\text{OH} \rightarrow \text{CH}_4 + \text{C}_2\text{H}_5\text{O}$	3.11×10^{-19}	227
$\text{CH}_2 + \text{H}_2\text{O}_2 \rightarrow \text{CH}_3 + \text{HO}_2$	1.00×10^{-14}	118
$\text{CH}_2 + \text{CH}_3\text{CO} \rightarrow \text{CH}_2\text{CO} + \text{CH}_3$	3.01×10^{-11}	118
$\text{CH}_2 + \text{CH}_3\text{OH} \rightarrow \text{CH}_3\text{O} + \text{CH}_3$	$1.12 \times 10^{-15} \left(\frac{T_{gas}}{298}\right)^{3.10} \exp\left(-\frac{29.02}{RT_{gas}}\right)$	202
$\text{CH}_2 + \text{CH}_3\text{OH} \rightarrow \text{CH}_2\text{OH} + \text{CH}_3$	$4.38 \times 10^{-15} \left(\frac{T_{gas}}{298}\right)^{3.20} \exp\left(-\frac{30.02}{RT_{gas}}\right)$	202
$\text{CH}_2 + \text{CH}_2\text{OH} \rightarrow \text{CH}_2\text{O} + \text{CH}_3$	2.01×10^{-12}	202
$\text{CH}_2 + \text{CH}_2\text{OH} \rightarrow \text{C}_2\text{H}_4 + \text{OH}$	4.00×10^{-11}	202
$\text{C}_2\text{H}_6 + \text{CH}_3\text{CO} \rightarrow \text{CH}_3\text{CHO} + \text{C}_2\text{H}_5$	$1.91 \times 10^{-13} \left(\frac{T_{gas}}{298}\right)^{2.75} \exp\left(-\frac{73.334}{RT_{gas}}\right)$	118
$\text{CH}_3\text{CHO} + \text{C}_2\text{H}_5 \rightarrow \text{C}_2\text{H}_6 + \text{CH}_3\text{CO}$	$2.09 \times 10^{-12} \exp\left(-\frac{35.59}{RT_{gas}}\right)$	228
$\text{C}_2\text{H}_6 + \text{CH}_2\text{OH} \rightarrow \text{CH}_3\text{OH} + \text{C}_2\text{H}_5$	$8.73 \times 10^{-15} \left(\frac{T_{gas}}{298}\right)^{3.00} \exp\left(-\frac{58.451}{RT_{gas}}\right)$	202
$\text{CH}_3\text{OH} + \text{C}_2\text{H}_5 \rightarrow \text{C}_2\text{H}_6 + \text{CH}_2\text{OH}$	$4.38 \times 10^{-15} \left(\frac{T_{gas}}{298}\right)^{3.20} \exp\left(-\frac{38.33}{RT_{gas}}\right)$	202
$\text{C}_2\text{H}_5 + \text{CH}_2\text{OH} \rightarrow \text{C}_2\text{H}_6 + \text{CH}_2\text{O}$	4.00×10^{-12}	202
$\text{C}_2\text{H}_5 + \text{CH}_2\text{OH} \rightarrow \text{CH}_3\text{OH} + \text{C}_2\text{H}_4$	4.00×10^{-12}	202

$C_2H_3 + H_2O_2 \rightarrow C_2H_4 + HO_2$	$2.01 \times 10^{-14} \exp\left(\frac{2.49}{RT_{gas}}\right)$	118
$C_2H_3 + CH_3OH \rightarrow C_2H_4 + CH_3O$	$1.12 \times 10^{-15} \left(\frac{T_{gas}}{298}\right)^{3.10} \exp\left(-\frac{29.02}{RT_{gas}}\right)$	202
$C_2H_3 + CH_3OH \rightarrow C_2H_4 + CH_2OH$	$4.38 \times 10^{-15} \left(\frac{T_{gas}}{298}\right)^{3.20} \exp\left(-\frac{30.02}{RT_{gas}}\right)$	202
$C_2H_3 + CH_2OH \rightarrow C_2H_4 + CH_2O$	5.00×10^{-11}	202
$C_2H_3 + CH_2OH \rightarrow C_3H_5 + OH$	2.01×10^{-11}	202
$C_2H_2 + CH_2OH \rightarrow C_2H_3 + CH_2O$	$1.20 \times 10^{-12} \exp\left(-\frac{37.66}{RT_{gas}}\right)$	202
$C_2H + CH_3OH \rightarrow C_2H_2 + CH_3O$	2.01×10^{-12}	202
$C_2H + CH_3OH \rightarrow C_2H_2 + CH_2OH$	1.00×10^{-11}	202
$C_2H + CH_2OH \rightarrow C_2H_2 + CH_2O$	5.99×10^{-11}	202
$C_3H_8 + CH_3CO \rightarrow CH_3CHO + C_3H_7$	$1.89 \times 10^{-13} \left(\frac{T_{gas}}{298}\right)^{2.60} \exp\left(-\frac{73.916}{RT_{gas}}\right)$	171
$C_3H_8 + CH_2OH \rightarrow CH_3OH + C_3H_7$	$6.56 \times 10^{-15} \left(\frac{T_{gas}}{298}\right)^{2.95} \exp\left(-\frac{58.451}{RT_{gas}}\right)$	171
$CH_3OH + C_3H_7 \rightarrow C_3H_8 + CH_2OH$	$3.90 \times 10^{-15} \left(\frac{T_{gas}}{298}\right)^{3.17} \exp\left(-\frac{38.33}{RT_{gas}}\right)$	171
$C_3H_7 + OH \rightarrow C_3H_6 + H_2O$	4.00×10^{-11}	171
$C_3H_7 + CH_2OH \rightarrow C_3H_8 + CH_2O$	1.60×10^{-12}	171
$C_3H_7 + CH_2OH \rightarrow C_3H_6 + CH_3OH$	8.00×10^{-13}	171
$C_3H_6 + O \rightarrow C_3H_5 + OH$	$1.56 \times 10^{-11} \left(\frac{T_{gas}}{298}\right)^{0.70} \exp\left(-\frac{24.61}{RT_{gas}}\right)$	145
$C_3H_6 + OH \rightarrow C_3H_5 + H_2O$	$4.60 \times 10^{-13} \left(\frac{T_{gas}}{298}\right)^{2.00} \exp\left(\frac{1.25}{RT_{gas}}\right)$	145
$C_3H_6 + HO_2 \rightarrow C_3H_5 + H_2O_2$	$4.33 \times 10^{-14} \left(\frac{T_{gas}}{298}\right)^{2.60} \exp\left(-\frac{58.20}{RT_{gas}}\right)$	145
$C_3H_5 + H_2O_2 \rightarrow C_3H_6 + HO_2$	$7.67 \times 10^{-14} \left(\frac{T_{gas}}{298}\right)^{2.05} \exp\left(-\frac{56.79}{RT_{gas}}\right)$	145
$C_3H_6 + CHO \rightarrow C_3H_5 + CH_2O$	$9.05 \times 10^{-13} \left(\frac{T_{gas}}{298}\right)^{1.90} \exp\left(-\frac{71.17}{RT_{gas}}\right)$	145
$C_3H_5 + CH_2O \rightarrow C_3H_6 + CHO$	$1.05 \times 10^{-11} \left(\frac{T_{gas}}{298}\right)^{1.90} \exp\left(-\frac{76.08}{RT_{gas}}\right)$	145
$C_3H_6 + CH_3O \rightarrow C_3H_5 + CH_3OH$	$2.97 \times 10^{-15} \left(\frac{T_{gas}}{298}\right)^{2.95} \exp\left(-\frac{50.14}{RT_{gas}}\right)$	145
$C_3H_6 + CH_3O_2 \rightarrow C_3H_5 + CH_3OOH$	$3.30 \times 10^{-12} \exp\left(-\frac{71.34}{RT_{gas}}\right)$	145

$C_3H_6 + CH_3CO \rightarrow C_3H_5 + CH_3CHO$	$7.82 \times 10^{-13} \left(\frac{T_{gas}}{298}\right)^{2.00} \exp\left(-\frac{67.93}{RT_{gas}}\right)$	145
$C_3H_5 + CH_3CHO \rightarrow C_3H_6 + CH_3CO$	$6.31 \times 10^{-13} \exp\left(-\frac{30.18}{RT_{gas}}\right)$	229
$C_3H_6 + CH_2OH \rightarrow C_3H_5 + CH_3OH$	$1.99 \times 10^{-15} \left(\frac{T_{gas}}{298}\right)^{2.95} \exp\left(-\frac{50.14}{RT_{gas}}\right)$	145
$C_3H_5 + CH_3OH \rightarrow C_3H_6 + CH_2OH$	$4.33 \times 10^{-14} \left(\frac{T_{gas}}{298}\right)^{2.90} \exp\left(-\frac{85.64}{RT_{gas}}\right)$	145
$C_3H_5 + HO_2 \rightarrow C_3H_6 + O_2$	4.40×10^{-12}	192
$C_3H_6 + O_2 \rightarrow C_3H_5 + HO_2$	$9.00 \times 10^{-11} \exp\left(-\frac{166.0}{RT_{gas}}\right)$	145
$C_3H_5 + CHO \rightarrow C_3H_6 + CO$	1.00×10^{-10}	145
$C_3H_5 + CH_3O \rightarrow C_3H_6 + CH_2O$	5.00×10^{-11}	145
$C_3H_5 + CH_2OH \rightarrow C_3H_6 + CH_2O$	3.01×10^{-11}	145
$H_2 + CH_2OH \rightarrow CH_3OH + H$ ($\alpha=0.8$)	$9.96 \times 10^{-14} \left(\frac{T_{gas}}{298}\right)^{2.00} \exp\left(-\frac{55.87}{RT_{gas}}\right)$	202
$CH_3OH + H \rightarrow H_2 + CH_2OH$	$2.42 \times 10^{-12} \left(\frac{T_{gas}}{298}\right)^{2.00} \exp\left(-\frac{18.87}{RT_{gas}}\right)$	230
$H + H_2O_2 \rightarrow H_2O + OH$	$1.69 \times 10^{-11} \exp\left(-\frac{14.97}{RT_{gas}}\right)$	146
$H + CH_3OH \rightarrow CH_3O + H_2$	3.18×10^{-16}	202
$CH_3O + H_2 \rightarrow H + CH_3OH$ ($\alpha=0.8$)	$1.66 \times 10^{-15} \left(\frac{T_{gas}}{298}\right)^{4.00} \exp\left(-\frac{20.54}{RT_{gas}}\right)$	224
$H + CH_2OH \rightarrow CH_2O + H_2$	1.00×10^{-11}	202
$H + CH_2OH + M \rightarrow CH_3OH + M$	1.18×10^{-29}	178,231
$CH_3OH + M \rightarrow H + CH_2OH + M$	$2.16 \times 10^{-08} \exp\left(-\frac{279.0}{RT_{gas}}\right)$	232
$H + C_2H_5OH \rightarrow H_2 + C_2H_5O$	$1.33 \times 10^{-20} \left(\frac{T_{gas}}{298}\right)^{10.58} \exp\left(\frac{18.65}{RT_{gas}}\right)$	233
$H + CH_3OOH \rightarrow H_2O + CH_3O$	5.88×10^{-15}	215
$O + H_2O_2 \rightarrow HO_2 + OH$	$1.42 \times 10^{-12} \left(\frac{T_{gas}}{298}\right)^{2.00} \exp\left(-\frac{16.63}{RT_{gas}}\right)$	222
$O + H_2O_2 \rightarrow O_2 + H_2O$	8.91×10^{-16}	192
$O + CH_3CO \rightarrow OH + CH_2CO$	8.75×10^{-11}	192
$O + CH_3CO \rightarrow CO_2 + CH_3$	2.63×10^{-10}	192
$O + CH_3OH \rightarrow OH + CH_2OH$	$5.71 \times 10^{-11} \exp\left(-\frac{22.86}{RT_{gas}}\right)$	234
$O + CH_3OH \rightarrow OH + CH_3O$	$1.66 \times 10^{-11} \exp\left(-\frac{19.62}{RT_{gas}}\right)$	184
$O + CH_2OH \rightarrow CH_2O + OH$	7.00×10^{-11}	202

$O + C_2H_5OOH \rightarrow C_2H_5O_2 + OH$	$3.30 \times 10^{-11} \exp\left(-\frac{19.87}{RT_{gas}}\right)$	174
$O_2 + CH_2OH \rightarrow CH_2O + HO_2$	9.70×10^{-12}	196
$CH_2O + HO_2 \rightarrow CH_2OH + O_2$	$5.63 \times 10^{-12} \exp\left(-\frac{79.99}{RT_{gas}}\right)$	235
$O_2 + C_2H_5O \rightarrow CH_3CHO + HO_2$	8.12×10^{-15}	196
$CH_3CHO + HO_2 \rightarrow C_2H_5O + O_2$	$6.96 \times 10^{-14} \left(\frac{T_{gas}}{298}\right)^{1.62} \exp\left(-\frac{64.60}{RT_{gas}}\right)$	236
$OH + H_2O_2 \rightarrow HO_2 + H_2O$	$1.30 \times 10^{-11} \exp\left(-\frac{5.57}{RT_{gas}}\right)$	146
$HO_2 + H_2O \rightarrow OH + H_2O_2$	$4.65 \times 10^{-11} \exp\left(-\frac{137.0}{RT_{gas}}\right)$	237
$OH + CH_3CO \rightarrow CH_2CO + H_2O$	2.00×10^{-11}	118
$OH + CH_3CO \rightarrow CH_3 + CO + OH$	5.00×10^{-11}	118
$OH + CH_3OH \rightarrow H_2O + CH_2OH$	$2.13 \times 10^{-13} \left(\frac{T_{gas}}{298}\right)^{2.00} \exp\left(\frac{3.52}{RT_{gas}}\right)$	230
$H_2O + CH_2OH \rightarrow OH + CH_3OH$	$4.12 \times 10^{-14} \left(\frac{T_{gas}}{298}\right)^{3.00} \exp\left(-\frac{86.80}{RT_{gas}}\right)$	224
$OH + CH_2OH \rightarrow CH_2O + H_2O$	4.00×10^{-11}	202
$OH + C_2H_5OH \rightarrow H_2O + C_2H_5O$	$3.75 \times 10^{-16} \left(\frac{T_{gas}}{298}\right)^{4.28} \exp\left(\frac{14.90}{RT_{gas}}\right)$	238
$OH + CH_3OOH \rightarrow H_2O + CH_3O_2$	$1.79 \times 10^{-12} \exp\left(\frac{1.83}{RT_{gas}}\right)$	239
$HO_2 + CH_3CO \rightarrow CH_3 + CO_2 + OH$	5.00×10^{-11}	118
$HO_2 + CH_3OH \rightarrow CH_2OH + H_2O_2$	$1.60 \times 10^{-13} \exp\left(-\frac{52.63}{RT_{gas}}\right)$	202
$CH_2OH + H_2O_2 \rightarrow HO_2 + CH_3OH$	$5.00 \times 10^{-15} \exp\left(-\frac{10.81}{RT_{gas}}\right)$	202
$HO_2 + CH_2OH \rightarrow CH_2O + H_2O_2$	2.01×10^{-11}	202
$CH_2O + CH_3CO \rightarrow CH_3CHO + CHO$	$3.01 \times 10^{-13} \exp\left(-\frac{54.04}{RT_{gas}}\right)$	118
$CH_2O + CH_2OH \rightarrow CH_3OH + CHO$	$7.72 \times 10^{-14} \left(\frac{T_{gas}}{298}\right)^{2.80} \exp\left(-\frac{24.53}{RT_{gas}}\right)$	202
$CH_3OH + CHO \rightarrow CH_2O + CH_2OH$	$2.41 \times 10^{-13} \left(\frac{T_{gas}}{298}\right)^{2.90} \exp\left(-\frac{54.88}{RT_{gas}}\right)$	202
$CHO + CH_3CO \rightarrow CH_3CHO + CO$	1.50×10^{-11}	118
$CHO + CH_2OH \rightarrow CH_2O + CH_2O$	3.01×10^{-10}	202
$CHO + CH_2OH \rightarrow CH_3OH + CO$	2.01×10^{-10}	202

$\text{CH}_3\text{O} + \text{CH}_3\text{CO} \rightarrow \text{CH}_3\text{OH} + \text{CH}_2\text{CO}$	1.00×10^{-11}	118
$\text{CH}_3\text{O} + \text{CH}_3\text{OH} \rightarrow \text{CH}_3\text{OH} + \text{CH}_2\text{OH}$	$5.00 \times 10^{-13} \exp\left(-\frac{17.04}{RT_{gas}}\right)$	202
$\text{CH}_3\text{OH} + \text{CH}_2\text{OH} \rightarrow \text{CH}_3\text{O} + \text{CH}_3\text{OH}$	$1.30 \times 10^{-14} \exp\left(-\frac{50.47}{RT_{gas}}\right)$	202
$\text{CH}_3\text{O} + \text{CH}_2\text{OH} \rightarrow \text{CH}_2\text{O} + \text{CH}_3\text{OH}$	4.00×10^{-11}	202
$\text{CH}_3\text{O}_2 + \text{H}_2\text{O}_2 \rightarrow \text{CH}_3\text{OOH} + \text{HO}_2$	$4.00 \times 10^{-12} \exp\left(-\frac{41.57}{RT_{gas}}\right)$	118
$\text{CH}_3\text{O}_2 + \text{CH}_3\text{CO} \rightarrow \text{CH}_3 + \text{CO}_2 + \text{CH}_3\text{O}$	4.00×10^{-11}	118
$\text{CH}_3\text{O}_2 + \text{CH}_3\text{OH} \rightarrow \text{CH}_2\text{OH} + \text{CH}_3\text{OOH}$	$3.01 \times 10^{-12} \exp\left(-\frac{57.37}{RT_{gas}}\right)$	202
$\text{CH}_3\text{O}_2 + \text{CH}_2\text{OH} \rightarrow \text{CH}_3\text{O} + \text{OH}$	2.00×10^{-11}	202
$\text{H}_2\text{O}_2 + \text{CH}_3\text{CO} \rightarrow \text{CH}_3\text{CHO} + \text{HO}_2$	$3.01 \times 10^{-13} \exp\left(-\frac{34.42}{RT_{gas}}\right)$	118
$\text{CH}_3\text{CHO} + \text{HO}_2 \rightarrow \text{H}_2\text{O}_2 + \text{CH}_3\text{CO}$	$5.00 \times 10^{-12} \exp\left(-\frac{49.89}{RT_{gas}}\right)$	146
$\text{CH}_3\text{CO} + \text{CH}_3\text{OH} \rightarrow \text{CH}_3\text{CHO} + \text{CH}_2\text{OH}$	$2.13 \times 10^{-13} \left(\frac{T_{gas}}{298}\right)^{3.00} \exp\left(-\frac{51.63}{RT_{gas}}\right)$	202
$\text{CH}_3\text{CHO} + \text{CH}_2\text{OH} \rightarrow \text{CH}_3\text{CO} + \text{CH}_2\text{OH}$	8.30×10^{-15}	240
$2\text{xCH}_2\text{OH} \rightarrow \text{CH}_2\text{O} + \text{CH}_3\text{OH}$	8.00×10^{-12}	202
$\text{C}_2\text{H}_2 + \text{M} \rightarrow \text{C}_2 + \text{H}_2 + \text{M}$	$7.59 \times 10^{-17} \exp\left(-\frac{17.21}{RT_{gas}}\right)$	241
$\text{C}_2\text{H}_6 + \text{H} \rightarrow \text{CH}_4 + \text{CH}_3$	$8.97 \times 10^{-20} \exp\left(-\frac{48.64}{RT_{gas}}\right)$	242
$\text{CH}_4 + \text{CH}_3 \rightarrow \text{C}_2\text{H}_6 + \text{H} (\alpha=0.8)$	$1.33 \times 10^{-10} \exp\left(-\frac{167.0}{RT_{gas}}\right)$	243
$\text{O} + \text{H}_2\text{O} \rightarrow \text{H}_2 + \text{O}_2$	$4.48 \times 10^{-12} \left(\frac{T_{gas}}{298}\right)^{0.97} \exp\left(-\frac{287.0}{RT_{gas}}\right)$	216
$\text{O} + \text{CH}_2 \rightarrow \text{CHO} + \text{H}$	5.01×10^{-11}	235
$\text{C}_2\text{H}_4 + \text{O} \rightarrow \text{C}_2\text{H}_3 + \text{OH}$	$2.31 \times 10^{-11} \exp\left(-\frac{30.10}{RT_{gas}}\right)$	244
$\text{CH}_3 + \text{O} \rightarrow \text{CH}_3\text{O}$	$7.51 \times 10^{-14} \left(\frac{T_{gas}}{298}\right)^{-2.12} \exp\left(-\frac{2.61}{RT_{gas}}\right)$	204
$\text{C} + \text{OH} \rightarrow \text{CO(E1)} + \text{H}$	$1.15 \times 10^{-10} \left(\frac{T_{gas}}{298}\right)^{-0.34}$	245
$\text{C}_2\text{H}_2 + \text{H}_2 \rightarrow \text{C}_2\text{H}_4$	$5.00 \times 10^{-13} \exp\left(-\frac{163.0}{RT_{gas}}\right)$	118

$C_2H_2 + OH \rightarrow CO + CH_3$	$9.13 \times 10^{-11} \exp\left(-\frac{57.29}{RT_{gas}}\right)$	246
$CO + CH_3 \rightarrow C_2H_2 + OH$	$6.31 \times 10^{-11} \exp\left(-\frac{253.0}{RT_{gas}}\right)$	235
$C_2H_2 + CH_3 \rightarrow C_3H_5$	$1.00 \times 10^{-12} \exp\left(-\frac{32.26}{RT_{gas}}\right)$	146
$C_2H_2 + HO_2 \rightarrow C_2H_3 + O_2$	$5.00 \times 10^{-14} \left(\frac{T_{gas}}{298}\right)^{1.61} \exp\left(-\frac{59.28}{RT_{gas}}\right)$	247
$C_2H_3 + O_2 \rightarrow C_2H_2 + HO_2$	$2.14 \times 10^{-14} \left(\frac{T_{gas}}{298}\right)^{1.61} \exp\left(\frac{1.60}{RT_{gas}}\right)$	247
$C_2H_6 + C_2H_2 \rightarrow C_2H_5 + C_2H_3$	$1.60 \times 10^{-12} \exp\left(-\frac{19.12}{RT_{gas}}\right)$	248
$2x C_2H_4 \rightarrow C_2H_5 + C_2H_3$	$8.00 \times 10^{-10} \exp\left(-\frac{299.0}{RT_{gas}}\right)$	118
$C_2H_2 + OH \rightarrow CH_2CO + H$	$1.83 \times 10^{-11} \exp\left(-\frac{30.02}{RT_{gas}}\right)$	249
$C_2H_4 + CH_3 \rightarrow C_3H_7$	$4.00 \times 10^{-14} \left(\frac{T_{gas}}{298}\right)^{2.48} \exp\left(-\frac{25.65}{RT_{gas}}\right)$	250
$C_3H_7 \rightarrow C_2H_4 + CH_3$	$1.31 \times 10^{13} \left(\frac{T_{gas}}{298}\right)^{0.87} \exp\left(-\frac{127.0}{RT_{gas}}\right)$	250
$2 \times CH_2 \rightarrow C_2H_4$	1.70×10^{-12}	251,252
$C_2 + H_2 \rightarrow C_2H_2$	$1.70 \times 10^{-10} \exp\left(-\frac{1470}{T_{gas}}\right)$	251,253
$CH_4 + C_2 \rightarrow C_2H + CH_3 (\alpha=0.8)$	$5.50 \times 10^{-11} \exp\left(-\frac{297}{T_{gas}}\right)$	251,254

Table A10: Ion-ion and ion-neutral reactions, as well as the references where the data are adopted from. The rate coefficients are given in $cm^3 s^{-1}$ and $cm^6 s^{-1}$, for two-body and three-body reactions, respectively. T_{gas} is given in K.

Reaction	Rate constant	Ref
$CH_5^+ + CH_2 \rightarrow CH_3^+ + CH_4$	9.60×10^{-10}	112
$CH_5^+ + CH \rightarrow CH_2^+ + CH_4$	6.90×10^{-10}	112
$CH_5^+ + C \rightarrow CH^+ + CH_4$	1.20×10^{-9}	112
$CH_5^+ + C_2H_6 \rightarrow C_2H_5^+ + H_2 + CH_4$	2.25×10^{-10}	112
$CH_5^+ + C_2H_4 \rightarrow C_2H_5^+ + CH_4$	1.50×10^{-9}	112
$CH_5^+ + C_2H_2 \rightarrow C_2H_3^+ + CH_4$	1.60×10^{-9}	112

$\text{CH}_5^+ + \text{C}_2\text{H} \rightarrow \text{C}_2\text{H}_2^+ + \text{CH}_4$	9.00×10^{-10}	112
$\text{CH}_5^+ + \text{C}_2 \rightarrow \text{C}_2\text{H}^+ + \text{CH}_4$	9.50×10^{-10}	112
$\text{CH}_5^+ + \text{H} \rightarrow \text{CH}_4^+ + \text{H}_2$	1.50×10^{-10}	112
$\text{CH}_5^+ + \text{O} \rightarrow \text{H}_3\text{O}^+ + \text{CH}_2$	2.20×10^{-10}	112
$\text{CH}_5^+ + \text{H}_2\text{O} \rightarrow \text{H}_3\text{O}^+ + \text{CH}_4$	3.70×10^{-09}	112
$\text{CH}_5^+ + \text{OH} \rightarrow \text{H}_2\text{O}^+ + \text{CH}_4$	7.00×10^{-10}	112
$\text{CH}_4^+ + \text{CH}_4 \rightarrow \text{CH}_5^+ + \text{CH}_3$	1.50×10^{-9}	112
$\text{CH}_4^+ + \text{C}_2\text{H}_6 \rightarrow \text{C}_2\text{H}_4^+ + \text{CH}_4 + \text{H}_2$	1.91×10^{-9}	255
$\text{CH}_4^+ + \text{C}_2\text{H}_4 \rightarrow \text{C}_2\text{H}_5^+ + \text{CH}_3$	4.23×10^{-10}	112
$\text{CH}_4^+ + \text{C}_2\text{H}_4 \rightarrow \text{C}_2\text{H}_4^+ + \text{CH}_4$	1.38×10^{-9}	112
$\text{CH}_4^+ + \text{C}_2\text{H}_2 \rightarrow \text{C}_2\text{H}_3^+ + \text{CH}_3$	1.23×10^{-9}	112
$\text{CH}_4^+ + \text{C}_2\text{H}_2 \rightarrow \text{C}_2\text{H}_2^+ + \text{CH}_4$	1.13×10^{-9}	112
$\text{CH}_4^+ + \text{H}_2 \rightarrow \text{CH}_5^+ + \text{H}$	3.30×10^{-11}	112
$\text{CH}_4^+ + \text{H} \rightarrow \text{CH}_3^+ + \text{H}_2$	1.00×10^{-11}	112
$\text{CH}_4^+ + \text{O} \rightarrow \text{CH}_3^+ + \text{OH}$	1.00×10^{-9}	112
$\text{CH}_4^+ + \text{O}_2 \rightarrow \text{O}_2^+ + \text{CH}_4$	3.90×10^{-10}	112
$\text{CH}_4^+ + \text{H}_2\text{O} \rightarrow \text{H}_3\text{O}^+ + \text{CH}_3$	2.60×10^{-9}	112
$\text{CH}_3^+ + \text{CH}_4 \rightarrow \text{CH}_4^+ + \text{CH}_3$	1.36×10^{-10}	256
$\text{CH}_3^+ + \text{CH}_4 \rightarrow \text{C}_2\text{H}_5^+ + \text{H}_2$	1.20×10^{-9}	112
$\text{CH}_3^+ + \text{CH}_2 \rightarrow \text{C}_2\text{H}_3^+ + \text{H}_2$	9.90×10^{-10}	112
$\text{CH}_3^+ + \text{CH} \rightarrow \text{C}_2\text{H}_2^+ + \text{H}_2$	7.10×10^{-10}	112
$\text{CH}_3^+ + \text{C} \rightarrow \text{C}_2\text{H}^+ + \text{H}_2$	1.20×10^{-9}	112
$\text{CH}_3^+ + \text{C}_2\text{H}_6 \rightarrow \text{C}_2\text{H}_5^+ + \text{CH}_4$	1.48×10^{-9}	112
$\text{CH}_3^+ + \text{C}_2\text{H}_4 \rightarrow \text{C}_2\text{H}_3^+ + \text{CH}_4$	3.50×10^{-10}	112
$\text{CH}_3^+ + \text{C}_2\text{H}_3 \rightarrow \text{C}_2\text{H}_3^+ + \text{CH}_3$	3.00×10^{-10}	112
$\text{CH}_2^+ + \text{CH}_4 \rightarrow \text{CH}_3^+ + \text{CH}_3$	1.38×10^{-10}	257
$\text{CH}_2^+ + \text{CH}_4 \rightarrow \text{C}_2\text{H}_5^+ + \text{H}$	3.60×10^{-10}	112
$\text{CH}_2^+ + \text{CH}_4 \rightarrow \text{C}_2\text{H}_4^+ + \text{H}_2$	8.40×10^{-10}	112
$\text{CH}_2^+ + \text{CH}_4 \rightarrow \text{C}_2\text{H}_3^+ + \text{H}_2 + \text{H}$	2.31×10^{-10}	257
$\text{CH}_2^+ + \text{CH}_4 \rightarrow \text{C}_2\text{H}_2^+ + 2\text{H}_2$	3.97×10^{-10}	257
$\text{CH}_2^+ + \text{C} \rightarrow \text{C}_2\text{H}^+ + \text{H}$	1.20×10^{-9}	112
$\text{CH}_2^+ + \text{H}_2 \rightarrow \text{CH}_3^+ + \text{H}$	1.60×10^{-9}	112
$\text{CH}^+ + \text{CH}_4 \rightarrow \text{C}_2\text{H}_4^+ + \text{H}$	6.50×10^{-11}	112
$\text{CH}^+ + \text{CH}_4 \rightarrow \text{C}_2\text{H}_3^+ + \text{H}_2$	1.09×10^{-9}	112
$\text{CH}^+ + \text{CH}_4 \rightarrow \text{C}_2\text{H}_2^+ + \text{H}_2 + \text{H}$	1.43×10^{-10}	112
$\text{CH}^+ + \text{CH}_2 \rightarrow \text{C}_2\text{H}^+ + \text{H}_2$	1.00×10^{-9}	112
$\text{CH}^+ + \text{CH} \rightarrow \text{C}_2^+ + \text{H}_2$	7.40×10^{-10}	112
$\text{CH}^+ + \text{C} \rightarrow \text{C}_2^+ + \text{H}$	1.20×10^{-9}	112
$\text{CH}^+ + \text{H}_2 \rightarrow \text{CH}_2^+ + \text{H}$	1.20×10^{-9}	112

$\text{CH}^+ + \text{H} \rightarrow \text{C}^+ + \text{H}_2$	7.50×10^{-10}	112
$\text{CH}^+ + \text{O} \rightarrow \text{CO}^+ + \text{H}$	3.50×10^{-10}	112
$\text{CH}^+ + \text{O}_2 \rightarrow \text{CO}^+ + \text{OH}$	1.00×10^{-11}	112
$\text{CH}^+ + \text{O}_2 \rightarrow \text{O}^+ + \text{CHO}$	1.00×10^{-11}	112
$\text{CH}^+ + \text{H}_2\text{O} \rightarrow \text{H}_3\text{O}^+ + \text{C}$	5.80×10^{-10}	112
$\text{C}^+ + \text{CH}_4 \rightarrow \text{C}_2\text{H}_3^+ + \text{H}$	1.10×10^{-9}	112
$\text{C}^+ + \text{CH}_4 \rightarrow \text{C}_2\text{H}_2^+ + \text{H}_2$	4.00×10^{-10}	112
$\text{C}^+ + \text{CH}_3 \rightarrow \text{C}_2\text{H}_2^+ + \text{H}$	1.30×10^{-9}	112
$\text{C}^+ + \text{CH}_3 \rightarrow \text{C}_2\text{H}^+ + \text{H}_2$	1.00×10^{-9}	112
$\text{C}^+ + \text{CH}_2 \rightarrow \text{CH}_2^+ + \text{C}$	5.20×10^{-10}	112
$\text{C}^+ + \text{CH}_2 \rightarrow \text{C}_2\text{H}^+ + \text{H}$	5.20×10^{-10}	112
$\text{C}^+ + \text{CH} \rightarrow \text{CH}^+ + \text{C}$	3.80×10^{-10}	112
$\text{C}^+ + \text{CH} \rightarrow \text{C}_2^+ + \text{H}$	3.80×10^{-10}	112
$\text{C}^+ + \text{C}_2\text{H}_6 \rightarrow \text{C}_2\text{H}_5^+ + \text{CH}$	2.31×10^{-10}	112
$\text{C}^+ + \text{C}_2\text{H}_6 \rightarrow \text{C}_2\text{H}_4^+ + \text{CH}_2$	1.16×10^{-10}	112
$\text{C}^+ + \text{C}_2\text{H}_6 \rightarrow \text{C}_2\text{H}_3^+ + \text{CH}_3$	4.95×10^{-10}	112
$\text{C}^+ + \text{C}_2\text{H}_6 \rightarrow \text{C}_2\text{H}_2^+ + \text{CH}_4$	8.25×10^{-11}	112
$\text{C}^+ + \text{C}_2\text{H}_5 \rightarrow \text{C}_2\text{H}_5^+ + \text{C}$	5.00×10^{-10}	112
$\text{C}^+ + \text{C}_2\text{H}_4 \rightarrow \text{C}_2\text{H}_4^+ + \text{C}$	1.70×10^{-11}	112
$\text{C}^+ + \text{C}_2\text{H}_4 \rightarrow \text{C}_2\text{H}_3^+ + \text{CH}$	8.50×10^{-11}	112
$\text{C}^+ + \text{O}_2 \rightarrow \text{O}^+ + \text{CO}$	6.20×10^{-10}	112
$\text{C}^+ + \text{O}_2 \rightarrow \text{CO}^+ + \text{O}$	3.80×10^{-10}	112
$\text{C}^+ + \text{OH} \rightarrow \text{CO}^+ + \text{H}$	7.70×10^{-10}	112
$\text{C}^+ + \text{H}^- \rightarrow \text{C} + \text{H}$	2.30×10^{-07}	112
$\text{C}_2\text{H}_6^+ + \text{C}_2\text{H}_4 \rightarrow \text{C}_2\text{H}_4^+ + \text{C}_2\text{H}_6$	1.15×10^{-9}	112
$\text{C}_2\text{H}_6^+ + \text{C}_2\text{H}_2 \rightarrow \text{C}_2\text{H}_5^+ + \text{C}_2\text{H}_3$	2.47×10^{-10}	112
$\text{C}_2\text{H}_6^+ + \text{H} \rightarrow \text{C}_2\text{H}_5^+ + \text{H}_2$	1.00×10^{-10}	112
$\text{C}_2\text{H}_6^+ + \text{H}_2\text{O} \rightarrow \text{H}_3\text{O}^+ + \text{C}_2\text{H}_5$	2.95×10^{-9}	112
$\text{C}_2\text{H}_5^+ + \text{H} \rightarrow \text{C}_2\text{H}_4^+ + \text{H}_2$	1.00×10^{-11}	112
$\text{C}_2\text{H}_5^+ + \text{H}_2\text{O} \rightarrow \text{H}_3\text{O}^+ + \text{C}_2\text{H}_4$	1.40×10^{-09}	112
$\text{C}_2\text{H}_4^+ + \text{C}_2\text{H}_3 \rightarrow \text{C}_2\text{H}_5^+ + \text{C}_2\text{H}_2$	5.00×10^{-10}	112
$\text{C}_2\text{H}_4^+ + \text{C}_2\text{H}_3 \rightarrow \text{C}_2\text{H}_3^+ + \text{C}_2\text{H}_4$	5.00×10^{-10}	112
$\text{C}_2\text{H}_4^+ + \text{H} \rightarrow \text{C}_2\text{H}_3^+ + \text{H}_2$	3.00×10^{-10}	112
$\text{C}_2\text{H}_4^+ + \text{O} \rightarrow \text{CH}_3^+ + \text{CHO}$	1.08×10^{-10}	112
$\text{C}_2\text{H}_3^+ + \text{C}_2\text{H}_6 \rightarrow \text{C}_2\text{H}_5^+ + \text{C}_2\text{H}_4$	2.91×10^{-10}	112
$\text{C}_2\text{H}_3^+ + \text{C}_2\text{H}_4 \rightarrow \text{C}_2\text{H}_5^+ + \text{C}_2\text{H}_2$	8.90×10^{-10}	112
$\text{C}_2\text{H}_3^+ + \text{C}_2\text{H}_3 \rightarrow \text{C}_2\text{H}_5^+ + \text{C}_2\text{H}$	5.00×10^{-10}	112
$\text{C}_2\text{H}_3^+ + \text{C}_2\text{H} \rightarrow \text{C}_2\text{H}_2^+ + \text{C}_2\text{H}_2$	3.30×10^{-10}	112
$\text{C}_2\text{H}_3^+ + \text{H} \rightarrow \text{C}_2\text{H}_2^+ + \text{H}_2$	6.80×10^{-11}	112

$C_2H_3^+ + H_2O \rightarrow H_3O^+ + C_2H_2$	1.11×10^{-09}	112
$C_2H_2^+ + CH_4 \rightarrow C_2H_3^+ + CH_3$	4.10×10^{-9}	257
$C_2H_2^+ + C_2H_6 \rightarrow C_2H_5^+ + C_2H_3$	1.31×10^{-10}	112
$C_2H_2^+ + C_2H_6 \rightarrow C_2H_4^+ + C_2H_4$	2.48×10^{-10}	112
$C_2H_2^+ + C_2H_4 \rightarrow C_2H_4^+ + C_2H_2$	4.14×10^{-10}	112
$C_2H_2^+ + C_2H_3 \rightarrow C_2H_3^+ + C_2H_2$	3.30×10^{-10}	112
$C_2H_2^+ + H_2 \rightarrow C_2H_3^+ + H$	1.00×10^{-11}	112
$C_2H_2^+ + H_2O \rightarrow H_3O^+ + C_2H$	2.20×10^{-10}	112
$C_2H^+ + CH_4 \rightarrow C_2H_2^+ + CH_3$	3.74×10^{-10}	112
$C_2H^+ + CH_2 \rightarrow CH_3^+ + C_2$	4.40×10^{-10}	112
$C_2H^+ + CH \rightarrow CH_2^+ + C_2$	3.20×10^{-10}	112
$C_2H^+ + H_2 \rightarrow C_2H_2^+ + H$	1.10×10^{-09}	112
$C_2^+ + CH_4 \rightarrow C_2H_2^+ + CH_2$	1.82×10^{-10}	112
$C_2^+ + CH_4 \rightarrow C_2H^+ + CH_3$	2.38×10^{-10}	112
$C_2^+ + CH_2 \rightarrow CH_2^+ + C_2$	4.50×10^{-10}	112
$C_2^+ + CH \rightarrow CH^+ + C_2$	3.20×10^{-10}	112
$C_2^+ + C \rightarrow C^+ + C_2$	1.10×10^{-10}	112
$C_2^+ + H_2 \rightarrow C_2H^+ + H$	1.10×10^{-09}	112
$C_2^+ + O \rightarrow CO^+ + C$	3.10×10^{-10}	112
$C_2^+ + O_2 \rightarrow CO^+ + CO$	8.00×10^{-10}	112
$C_2^+ + H_2O \rightarrow C_2H^+ + OH$	4.40×10^{-10}	112
$C_2^+ + OH \rightarrow OH^+ + C_2$	6.50×10^{-10}	112
$H_3^+ + CH_4 \rightarrow CH_5^+ + H_2$	2.40×10^{-9}	112
$H_3^+ + CH_3 \rightarrow CH_4^+ + H_2$	2.10×10^{-9}	112
$H_3^+ + CH_2 \rightarrow CH_3^+ + H_2$	1.70×10^{-9}	112
$H_3^+ + CH \rightarrow CH_2^+ + H_2$	1.20×10^{-9}	112
$H_3^+ + C \rightarrow CH^+ + H_2$	2.00×10^{-9}	112
$H_3^+ + C_2H_6 \rightarrow C_2H_5^+ + 2H_2$	2.40×10^{-9}	112
$H_3^+ + C_2H_5 \rightarrow C_2H_6^+ + H_2$	1.40×10^{-9}	112
$H_3^+ + C_2H_4 \rightarrow C_2H_5^+ + H_2$	1.15×10^{-9}	112
$H_3^+ + C_2H_4 \rightarrow C_2H_3^+ + 2H_2$	1.15×10^{-9}	112
$H_3^+ + C_2H_3 \rightarrow C_2H_4^+ + H_2$	2.00×10^{-9}	112
$H_3^+ + C_2H_2 \rightarrow C_2H_3^+ + H_2$	3.50×10^{-9}	112
$H_3^+ + C_2H \rightarrow C_2H_2^+ + H_2$	1.70×10^{-9}	112
$H_3^+ + C_2 \rightarrow C_2H^+ + H_2$	1.80×10^{-9}	112
$H_3^+ + O \rightarrow OH^+ + H_2$	8.40×10^{-10}	112
$H_3^+ + O \rightarrow H_2O^+ + H$	3.60×10^{-10}	112
$H_3^+ + OH \rightarrow H_2O^+ + H_2$	1.30×10^{-9}	112
$H_3^+ + H_2O \rightarrow H_3O^+ + H_2$	5.90×10^{-9}	112

$\text{H}_3^+ + \text{H}^- \rightarrow \text{H}_2 + 2\text{H}$	1.00×10^{-7}	112,130
$\text{H}_3^+ + \text{H}^- \rightarrow \text{H}_2 + \text{H}_2$	2.30×10^{-7}	112
$\text{H}_3^+ + \text{O}^- \rightarrow \text{H}_2\text{O} + \text{H} + \text{O}$	1.00×10^{-7}	101
$\text{H}_3^+ + \text{O}_2^- \rightarrow \text{O}_2 + \text{H}_2 + \text{H}$	1.00×10^{-7}	101
$\text{H}_3^+ + \text{O}_3^- \rightarrow \text{H}_2 + \text{H} + \text{O}_3$	1.00×10^{-7}	101
$\text{H}_3^+ + \text{O}_3^- \rightarrow \text{H}_2 + \text{H} + \text{O}_2 + \text{O}$	1.00×10^{-7}	101
$\text{H}_3^+ + \text{O}_3^- + \text{M} \rightarrow \text{H}_2 + \text{H} + \text{O}_3 + \text{M}$	1.66×10^{-25}	101
$\text{H}_3^+ + \text{OH}^- \rightarrow \text{OH} + \text{H} + \text{H}_2$	1.00×10^{-7}	101
$\text{H}_3^+ + \text{OH}^- \rightarrow \text{O} + 2\text{H} + \text{H}_2$	1.00×10^{-7}	101
$\text{H}_2^+ + \text{CH}_4 \rightarrow \text{CH}_5^+ + \text{H}$	1.14×10^{-10}	112
$\text{H}_2^+ + \text{CH}_4 \rightarrow \text{CH}_4^+ + \text{H}_2$	1.40×10^{-9}	112
$\text{H}_2^+ + \text{CH}_4 \rightarrow \text{CH}_3^+ + \text{H}_2 + \text{H}$	2.30×10^{-9}	112
$\text{H}_2^+ + \text{CH}_2 \rightarrow \text{CH}_3^+ + \text{H}$	1.00×10^{-9}	112
$\text{H}_2^+ + \text{CH}_2 \rightarrow \text{CH}_2^+ + \text{H}_2$	1.00×10^{-9}	112
$\text{H}_2^+ + \text{CH} \rightarrow \text{CH}_2^+ + \text{H}$	7.10×10^{-10}	112
$\text{H}_2^+ + \text{CH} \rightarrow \text{CH}^+ + \text{H}_2$	7.10×10^{-10}	112
$\text{H}_2^+ + \text{C} \rightarrow \text{CH}^+ + \text{H}$	2.40×10^{-9}	112
$\text{H}_2^+ + \text{C}_2\text{H}_6 \rightarrow \text{C}_2\text{H}_6^+ + \text{H}_2$	2.94×10^{-10}	112
$\text{H}_2^+ + \text{C}_2\text{H}_6 \rightarrow \text{C}_2\text{H}_5^+ + \text{H}_2 + \text{H}$	1.37×10^{-9}	112
$\text{H}_2^+ + \text{C}_2\text{H}_6 \rightarrow \text{C}_2\text{H}_4^+ + 2\text{H}_2$	2.35×10^{-9}	112
$\text{H}_2^+ + \text{C}_2\text{H}_6 \rightarrow \text{C}_2\text{H}_3^+ + 2\text{H}_2 + \text{H}$	6.86×10^{-10}	255
$\text{H}_2^+ + \text{C}_2\text{H}_6 \rightarrow \text{C}_2\text{H}_2^+ + 3\text{H}_2$	1.96×10^{-10}	255
$\text{H}_2^+ + \text{C}_2\text{H}_4 \rightarrow \text{C}_2\text{H}_4^+ + \text{H}_2$	2.21×10^{-9}	112
$\text{H}_2^+ + \text{C}_2\text{H}_4 \rightarrow \text{C}_2\text{H}_3^+ + \text{H}_2 + \text{H}$	1.81×10^{-9}	112
$\text{H}_2^+ + \text{C}_2\text{H}_4 \rightarrow \text{C}_2\text{H}_2^+ + 2\text{H}_2$	8.82×10^{-10}	112
$\text{H}_2^+ + \text{C}_2\text{H}_2 \rightarrow \text{C}_2\text{H}_3^+ + \text{H}$	4.80×10^{-10}	112
$\text{H}_2^+ + \text{C}_2\text{H}_2 \rightarrow \text{C}_2\text{H}_2^+ + \text{H}_2$	4.82×10^{-9}	112
$\text{H}_2^+ + \text{C}_2\text{H} \rightarrow \text{C}_2\text{H}_2^+ + \text{H}$	1.00×10^{-9}	112
$\text{H}_2^+ + \text{C}_2\text{H} \rightarrow \text{C}_2\text{H}^+ + \text{H}_2$	1.00×10^{-9}	112
$\text{H}_2^+ + \text{C}_2 \rightarrow \text{C}_2\text{H}^+ + \text{H}$	1.10×10^{-9}	112
$\text{H}_2^+ + \text{C}_2 \rightarrow \text{C}_2^+ + \text{H}_2$	1.10×10^{-9}	112
$\text{H}_2^+ + \text{H} + \text{M} \rightarrow \text{H}_3^+ + \text{M}$	1.50×10^{-29}	258
$\text{H}_2^+ + \text{H} \rightarrow \text{H}^+ + \text{H}_2$	6.40×10^{-10}	112
$\text{H}_2^+ + \text{O} \rightarrow \text{OH}^+ + \text{H}$	1.50×10^{-9}	112
$\text{H}_2^+ + \text{O}_2 \rightarrow \text{O}_2^+ + \text{H}_2$	8.00×10^{-10}	112
$\text{H}_2^+ + \text{OH} \rightarrow \text{OH}^+ + \text{H}_2$	7.60×10^{-10}	112
$\text{H}_2^+ + \text{OH} \rightarrow \text{H}_2\text{O}^+ + \text{H}$	7.60×10^{-10}	112
$\text{H}_2^+ + \text{H}_2\text{O} \rightarrow \text{H}_2\text{O}^+ + \text{H}_2$	3.90×10^{-09}	112
$\text{H}_2^+ + \text{H}_2\text{O} \rightarrow \text{H}_3\text{O}^+ + \text{H}$	3.40×10^{-09}	112

$\text{H}_2^+ + \text{CO} \rightarrow \text{CO}^+ + \text{H}_2$	6.44×10^{-10}	112
$\text{H}_2^+ + \text{H}^- \rightarrow \text{H}_2 + \text{H}$	$2.00 \times 10^{-7} \left(\frac{T_{gas}}{300}\right)^{-0.50}$	112
$\text{H}_2^+ + \text{H}^- \rightarrow \text{H} + \text{H} + \text{H}$	1.00×10^{-7}	130
$\text{H}_2^+ + \text{O}^- \rightarrow \text{H}_2 + \text{O}$	1.93×10^{-7}	101
$\text{H}_2^+ + \text{O}^- \rightarrow \text{H} + \text{H} + \text{O}$	1.00×10^{-7}	101
$\text{H}_2^+ + \text{O}_2^- \rightarrow \text{H}_2 + \text{O}_2$	1.93×10^{-7}	101
$\text{H}_2^+ + \text{O}_2^- \rightarrow \text{H} + \text{H} + \text{O}_2$	1.00×10^{-7}	101
$\text{H}_2^+ + \text{O}_2^- \rightarrow \text{H}_2 + \text{O} + \text{O}$	1.00×10^{-7}	101
$\text{H}_2^+ + \text{O}_2^- \rightarrow 2\text{H} + 2\text{O}$	1.00×10^{-7}	101
$\text{H}_2^+ + \text{CO}_3^- \rightarrow \text{H}_2 + \text{CO}_2 + \text{O}$	1.93×10^{-7}	101
$\text{H}_2^+ + \text{CO}_3^- \rightarrow 2\text{H} + \text{CO}_2 + \text{O}$	1.00×10^{-7}	101
$\text{H}_2^+ + \text{CO}_4^- \rightarrow \text{H}_2 + \text{CO}_2 + \text{O}_2$	1.93×10^{-7}	101
$\text{H}_2^+ + \text{CO}_4^- \rightarrow 2\text{H} + \text{CO}_2 + \text{O}_2$	1.00×10^{-7}	101
$\text{H}_2^+ + \text{OH}^- \rightarrow \text{H}_2 + \text{OH}$	1.93×10^{-7}	101
$\text{H}_2^+ + \text{OH}^- \rightarrow 2\text{H} + \text{OH}$	1.00×10^{-7}	101
$\text{H}_2^+ + \text{OH}^- \rightarrow \text{O} + \text{H} + \text{H}_2$	1.00×10^{-7}	101
$\text{H}_2^+ + \text{OH}^- \rightarrow \text{O} + 3\text{H}$	1.00×10^{-7}	101
$\text{H}^+ + \text{CH}_4 \rightarrow \text{CH}_4^+ + \text{H}$	1.50×10^{-9}	112
$\text{H}^+ + \text{CH}_4 \rightarrow \text{CH}_3^+ + \text{H}_2$	2.30×10^{-9}	112
$\text{H}^+ + \text{CH}_3 \rightarrow \text{CH}_3^+ + \text{H}$	3.40×10^{-9}	112
$\text{H}^+ + \text{CH}_2 \rightarrow \text{CH}_2^+ + \text{H}$	1.40×10^{-9}	112
$\text{H}^+ + \text{CH}_2 \rightarrow \text{CH}^+ + \text{H}_2$	1.40×10^{-9}	112
$\text{H}^+ + \text{CH} \rightarrow \text{CH}^+ + \text{H}$	1.90×10^{-9}	112
$\text{H}^+ + \text{C}_2\text{H}_6 \rightarrow \text{C}_2\text{H}_5^+ + \text{H}_2$	1.30×10^{-9}	257
$\text{H}^+ + \text{C}_2\text{H}_6 \rightarrow \text{C}_2\text{H}_4^+ + \text{H}_2 + \text{H}$	1.40×10^{-9}	112
$\text{H}^+ + \text{C}_2\text{H}_6 \rightarrow \text{C}_2\text{H}_3^+ + 2\text{H}_2$	2.80×10^{-9}	112
$\text{H}^+ + \text{C}_2\text{H}_5 \rightarrow \text{C}_2\text{H}_4^+ + \text{H}_2$	1.65×10^{-9}	112
$\text{H}^+ + \text{C}_2\text{H}_5 \rightarrow \text{C}_2\text{H}_3^+ + \text{H}_2 + \text{H}$	3.06×10^{-9}	112
$\text{H}^+ + \text{C}_2\text{H}_4 \rightarrow \text{C}_2\text{H}_4^+ + \text{H}$	1.00×10^{-9}	112
$\text{H}^+ + \text{C}_2\text{H}_4 \rightarrow \text{C}_2\text{H}_3^+ + \text{H}_2$	3.00×10^{-9}	112
$\text{H}^+ + \text{C}_2\text{H}_4 \rightarrow \text{C}_2\text{H}_2^+ + \text{H}_2 + \text{H}$	1.00×10^{-9}	112
$\text{H}^+ + \text{C}_2\text{H}_3 \rightarrow \text{C}_2\text{H}_3^+ + \text{H}$	2.00×10^{-9}	112
$\text{H}^+ + \text{C}_2\text{H}_3 \rightarrow \text{C}_2\text{H}_2^+ + \text{H}_2$	2.00×10^{-9}	112
$\text{H}^+ + \text{C}_2\text{H}_2 \rightarrow \text{C}_2\text{H}_2^+ + \text{H}$	5.40×10^{-10}	112
$\text{H}^+ + \text{C}_2\text{H} \rightarrow \text{C}_2\text{H}^+ + \text{H}$	1.50×10^{-9}	112
$\text{H}^+ + \text{C}_2\text{H} \rightarrow \text{C}_2^+ + \text{H}_2$	1.50×10^{-9}	112
$\text{H}^+ + \text{C}_2 \rightarrow \text{C}_2^+ + \text{H}$	3.10×10^{-9}	112
$\text{H}^+ + \text{H} + \text{M} \rightarrow \text{H}_2^+ + \text{M}$	1.00×10^{-34}	259
$\text{H}^+ + \text{O} \rightarrow \text{O}^+ + \text{H}$	3.44×10^{-10}	112

$H^+ + O_2 \rightarrow O_2^+ + H$	2.00×10^{-9}	112
$H^+ + OH \rightarrow OH^+ + H$	2.10×10^{-9}	112
$H^+ + H_2O \rightarrow H_2O^+ + H$	6.90×10^{-9}	112
$H^+ + H^- \rightarrow H + H$	$2.00 \times 10^{-7} \left(\frac{T_{gas}}{300}\right)^{-0.50}$	112
$H^+ + O^- \rightarrow H + O$	1.93×10^{-7}	101
$H^+ + O_2^- \rightarrow H + O_2$	1.93×10^{-7}	101
$H^+ + O_2^- \rightarrow H + O + O$	1.00×10^{-7}	101
$H^+ + CO_3^- \rightarrow H + CO_2 + O$	1.00×10^{-7}	101
$H^+ + CO_4^- \rightarrow H + CO_2 + O_2$	1.00×10^{-7}	101
$H^+ + OH^- \rightarrow OH + H$	1.93×10^{-7}	101
$H^+ + OH^- \rightarrow H + O + H$	1.93×10^{-7}	101
$H^- + CH_3 \rightarrow CH_4 + e^-$	1.00×10^{-9}	112
$H^- + CH_2 \rightarrow CH_3 + e^-$	1.00×10^{-9}	112
$H^- + CH \rightarrow CH_2 + e^-$	1.00×10^{-10}	112
$H^- + C \rightarrow CH + e^-$	1.00×10^{-9}	112
$H^- + C_2H \rightarrow C_2H_2 + e^-$	1.00×10^{-9}	112
$H^- + C_2 \rightarrow C_2H + e^-$	1.00×10^{-9}	112
$H^- + M \rightarrow H + M + e^-$	$2.70 \times 10^{-10} \left(\frac{T_{gas}}{300}\right)^{0.50} \exp\left(-\frac{5590}{T_{gas}}\right)$	101,259-261
$H^- + H \rightarrow H_2 + e^-$	1.30×10^{-9}	112
$H^- + O \rightarrow OH + e^-$	1.00×10^{-9}	112
$H^- + OH \rightarrow H_2O + e^-$	1.00×10^{-10}	112
$H^- + H_2O \rightarrow OH^- + H_2$	3.80×10^{-9}	112
$H^- + O^+ \rightarrow H + O$	2.30×10^{-7}	112
$H^- + H_3O^+ \rightarrow H_2 + OH + H$	2.30×10^{-7}	112
$H^- + H_3O^+ \rightarrow H_2O + H_2$	2.30×10^{-7}	112
$H^- + O_2^+ \rightarrow O_2 + H$	1.93×10^{-7}	101
$H^- + O_2^+ \rightarrow O + O + H$	1.00×10^{-7}	101
$H^- + CO^+ \rightarrow CO + H$	1.93×10^{-7}	101
$H^- + CO_2^+ \rightarrow CO_2 + H$	1.93×10^{-7}	101
$H^- + CO_2^+ \rightarrow CO + O + H$	1.00×10^{-7}	101
$H^- + OH^+ \rightarrow H + OH$	1.93×10^{-7}	101
$H^- + OH^+ \rightarrow H + O + H$	1.00×10^{-7}	101
$H^- + H_2O^+ \rightarrow H_2O + H$	1.93×10^{-7}	101
$H^- + H_2O^+ \rightarrow H + H + OH$	1.00×10^{-7}	101
$O^+ + CH_4 \rightarrow CH_4^+ + O$	8.90×10^{-10}	112
$O^+ + CH_4 \rightarrow CH_3^+ + OH$	1.10×10^{-10}	112
$O^+ + CH_2 \rightarrow CH_2^+ + O$	9.70×10^{-10}	112
$O^+ + CH \rightarrow CH^+ + O$	3.50×10^{-10}	112

$O^+ + C_2H_4 \rightarrow C_2H_4^+ + O$	7.00×10^{-11}	112
$O^+ + C_2H_4 \rightarrow C_2H_3^+ + OH$	2.10×10^{-10}	112
$O^+ + C_2H_4 \rightarrow C_2H_2^+ + H_2O$	1.12×10^{-9}	112
$O^+ + C_2H_2 \rightarrow C_2H_2^+ + O$	3.90×10^{-11}	112
$O^+ + C_2H \rightarrow C_2H^+ + O$	4.60×10^{-10}	112
$O^+ + C_2H \rightarrow CO^+ + CH$	4.60×10^{-10}	112
$O^+ + C_2 \rightarrow C_2^+ + O$	4.80×10^{-10}	112
$O^+ + C_2 \rightarrow CO^+ + C$	4.80×10^{-10}	112
$O^+ + H_2 \rightarrow OH^+ + H$	1.70×10^{-9}	112
$O^+ + H \rightarrow H^+ + O$	5.82×10^{-10}	112
$O^+ + OH \rightarrow OH^+ + O$	3.60×10^{-10}	112
$O^+ + OH \rightarrow O_2^+ + H$	3.60×10^{-10}	112
$O^+ + H_2O \rightarrow H_2O^+ + O$	3.20×10^{-9}	112
$O_2^+ + CH_2 \rightarrow CH_2^+ + O_2$	4.30×10^{-10}	112
$O_2^+ + CH \rightarrow CH^+ + O_2$	3.10×10^{-10}	112
$O_2^+ + C_2H_4 \rightarrow C_2H_4^+ + O_2$	6.80×10^{-10}	112
$O_2^+ + C_2H_2 \rightarrow C_2H_2^+ + O_2$	1.11×10^{-9}	112
$O_2^+ + C_2 \rightarrow C_2^+ + O_2$	4.10×10^{-10}	112
$O_2^+ + C_2 \rightarrow CO^+ + CO$	4.10×10^{-10}	112
$O^- + CH_4 \rightarrow OH^- + CH_3$	1.00×10^{-10}	112
$O^- + C \rightarrow CO + e^-$	5.00×10^{-10}	112
$O^- + H_2 \rightarrow H_2O + e^-$	7.00×10^{-10}	112
$O^- + H_2 \rightarrow OH^- + H$	3.00×10^{-11}	112
$O^- + H \rightarrow OH + e^-$	5.00×10^{-10}	112
$CO_2^+ + CH_4 \rightarrow CH_4^+ + CO_2$	5.50×10^{-10}	112
$CO_2^+ + C_2H_4 \rightarrow C_2H_4^+ + CO_2$	1.50×10^{-10}	112
$CO_2^+ + C_2H_2 \rightarrow C_2H_2^+ + CO_2$	7.30×10^{-10}	112
$CO_2^+ + H_2O \rightarrow H_2O^+ + CO_2$	2.04×10^{-9}	112
$CO^+ + CH_4 \rightarrow CH_4^+ + CO$	7.93×10^{-10}	112
$CO^+ + CH_2 \rightarrow CH_2^+ + CO$	4.30×10^{-10}	112
$CO^+ + CH \rightarrow CH^+ + CO$	3.20×10^{-10}	112
$CO^+ + C_2H \rightarrow C_2H^+ + CO$	3.90×10^{-10}	112
$CO^+ + C_2 \rightarrow C_2^+ + CO$	8.40×10^{-10}	112
$CO^+ + H \rightarrow H^+ + CO$	7.50×10^{-10}	112
$CO^+ + H_2O \rightarrow H_2O^+ + CO$	1.72×10^{-9}	112
$CO^+ + OH \rightarrow OH^+ + CO$	3.10×10^{-10}	112
$H_3O^+ + CH_2 \rightarrow CH_3^+ + H_2O$	9.40×10^{-10}	112
$H_3O^+ + CH \rightarrow CH_2^+ + H_2O$	6.80×10^{-10}	112
$H_3O^+ + C_2H_3 \rightarrow C_2H_4^+ + H_2O$	2.00×10^{-9}	112

$\text{H}_3\text{O}^+ + \text{C}_2 \rightarrow \text{C}_2\text{H}^+ + \text{H}_2\text{O}$	9.20×10^{-10}	112
$\text{H}_3\text{O}^+ + \text{O}^- \rightarrow \text{H}_2\text{O} + \text{H} + \text{O}$	1.00×10^{-7}	101
$\text{H}_3\text{O}^+ + \text{O}_2^- \rightarrow \text{H}_2\text{O} + \text{H} + \text{O}_2$	1.00×10^{-7}	101
$\text{H}_3\text{O}^+ + \text{O}_2^- \rightarrow \text{H}_2\text{O} + \text{H} + 2\text{O}$	1.00×10^{-7}	101
$\text{H}_3\text{O}^+ + \text{CO}_3^- \rightarrow \text{H}_2\text{O} + \text{H} + \text{CO}_2 + \text{O}$	1.00×10^{-7}	101
$\text{H}_3\text{O}^+ + \text{CO}_4^- \rightarrow \text{H}_2\text{O} + \text{H} + \text{CO}_2 + \text{O}_2$	1.00×10^{-7}	101
$\text{H}_2\text{O}^+ + \text{CH}_4 \rightarrow \text{H}_3\text{O}^+ + \text{CH}_3$	1.40×10^{-9}	112
$\text{H}_2\text{O}^+ + \text{CH}_2 \rightarrow \text{CH}_3^+ + \text{OH}$	4.70×10^{-10}	112
$\text{H}_2\text{O}^+ + \text{CH}_2 \rightarrow \text{CH}_2^+ + \text{H}_2\text{O}$	4.70×10^{-10}	112
$\text{H}_2\text{O}^+ + \text{CH} \rightarrow \text{CH}_2^+ + \text{OH}$	3.40×10^{-10}	112
$\text{H}_2\text{O}^+ + \text{CH} \rightarrow \text{CH}^+ + \text{H}_2\text{O}$	3.40×10^{-10}	112
$\text{H}_2\text{O}^+ + \text{C} \rightarrow \text{CH}^+ + \text{OH}$	1.10×10^{-9}	112
$\text{H}_2\text{O}^+ + \text{C}_2\text{H}_6 \rightarrow \text{H}_3\text{O}^+ + \text{C}_2\text{H}_5$	1.33×10^{-9}	112
$\text{H}_2\text{O}^+ + \text{C}_2\text{H}_6 \rightarrow \text{C}_2\text{H}_6^+ + \text{H}_2\text{O}$	6.40×10^{-11}	112
$\text{H}_2\text{O}^+ + \text{C}_2\text{H}_6 \rightarrow \text{C}_2\text{H}_4^+ + \text{H}_2\text{O} + \text{H}_2$	1.92×10^{-10}	112
$\text{H}_2\text{O}^+ + \text{C}_2\text{H}_4 \rightarrow \text{C}_2\text{H}_4^+ + \text{H}_2\text{O}$	1.50×10^{-9}	112
$\text{H}_2\text{O}^+ + \text{C}_2\text{H}_2 \rightarrow \text{C}_2\text{H}_2^+ + \text{H}_2\text{O}$	1.90×10^{-9}	112
$\text{H}_2\text{O}^+ + \text{C}_2\text{H} \rightarrow \text{C}_2\text{H}_2^+ + \text{OH}$	4.40×10^{-10}	112
$\text{H}_2\text{O}^+ + \text{C}_2\text{H} \rightarrow \text{C}_2\text{H}^+ + \text{H}_2\text{O}$	4.40×10^{-10}	112
$\text{H}_2\text{O}^+ + \text{C}_2 \rightarrow \text{C}_2\text{H}^+ + \text{OH}$	4.70×10^{-10}	112
$\text{H}_2\text{O}^+ + \text{C}_2 \rightarrow \text{C}_2^+ + \text{H}_2\text{O}$	4.70×10^{-10}	112
$\text{H}_2\text{O}^+ + \text{H}_2 \rightarrow \text{H}_3\text{O}^+ + \text{H}$	6.40×10^{-10}	112
$\text{H}_2\text{O}^+ + \text{O}_2 \rightarrow \text{O}_2^+ + \text{H}_2\text{O}$	4.60×10^{-10}	112
$\text{H}_2\text{O}^+ + \text{O} \rightarrow \text{O}_2^+ + \text{H}_2$	4.00×10^{-11}	112
$\text{H}_2\text{O}^+ + \text{H}_2\text{O} \rightarrow \text{H}_3\text{O}^+ + \text{OH}$	2.10×10^{-9}	112
$\text{H}_2\text{O}^+ + \text{OH} \rightarrow \text{H}_3\text{O}^+ + \text{O}$	6.90×10^{-10}	112
$\text{H}_2\text{O}^+ + \text{O}^- \rightarrow \text{H}_2\text{O} + \text{O}$	1.93×10^{-7}	101
$\text{H}_2\text{O}^+ + \text{O}^- \rightarrow \text{OH} + \text{H} + \text{O}$	1.00×10^{-7}	101
$\text{H}_2\text{O}^+ + \text{O}_2^- \rightarrow \text{H}_2\text{O} + \text{O}_2$	1.93×10^{-7}	101
$\text{H}_2\text{O}^+ + \text{O}_2^- \rightarrow \text{OH} + \text{H} + \text{O}_2$	1.00×10^{-7}	101
$\text{H}_2\text{O}^+ + \text{O}_2^- \rightarrow \text{H}_2\text{O} + \text{O} + \text{O}$	1.00×10^{-7}	101
$\text{H}_2\text{O}^+ + \text{O}_2^- \rightarrow \text{H} + \text{OH} + 2\text{O}$	1.00×10^{-7}	101
$\text{H}_2\text{O}^+ + \text{CO}_3^- \rightarrow \text{H}_2\text{O} + \text{CO}_2 + \text{O}$	1.00×10^{-7}	101
$\text{H}_2\text{O}^+ + \text{CO}_3^- \rightarrow \text{OH} + \text{CO}_2 + 2\text{O}$	1.00×10^{-7}	101
$\text{H}_2\text{O}^+ + \text{CO}_4^- \rightarrow \text{H}_2\text{O} + \text{CO}_2 + \text{O}_2$	1.00×10^{-7}	101
$\text{H}_2\text{O}^+ + \text{CO}_4^- \rightarrow \text{OH} + \text{H} + \text{CO}_2 + \text{O}_2$	1.00×10^{-7}	101
$\text{OH}^+ + \text{CH}_4 \rightarrow \text{CH}_5^+ + \text{O}$	1.95×10^{-10}	112
$\text{OH}^+ + \text{CH}_4 \rightarrow \text{H}_3\text{O}^+ + \text{CH}_2$	1.31×10^{-9}	112
$\text{OH}^+ + \text{CH}_2 \rightarrow \text{CH}_3^+ + \text{O}$	4.80×10^{-10}	112

$\text{OH}^+ + \text{CH}_2 \rightarrow \text{CH}_2^+ + \text{OH}$	4.80×10^{-10}	112
$\text{OH}^+ + \text{CH} \rightarrow \text{CH}_2^+ + \text{O}$	3.50×10^{-10}	112
$\text{OH}^+ + \text{CH} \rightarrow \text{CH}^+ + \text{OH}$	3.50×10^{-10}	112
$\text{OH}^+ + \text{C} \rightarrow \text{CH}^+ + \text{O}$	1.20×10^{-9}	112
$\text{OH}^+ + \text{C}_2\text{H}_6 \rightarrow \text{H}_3\text{O}^+ + \text{C}_2\text{H}_4$	1.60×10^{-10}	112
$\text{OH}^+ + \text{C}_2\text{H}_6 \rightarrow \text{C}_2\text{H}_6^+ + \text{OH}$	4.80×10^{-11}	112
$\text{OH}^+ + \text{C}_2\text{H}_6 \rightarrow \text{C}_2\text{H}_5^+ + \text{H}_2 + \text{O}$	3.20×10^{-10}	112
$\text{OH}^+ + \text{C}_2\text{H}_6 \rightarrow \text{C}_2\text{H}_4^+ + \text{H}_2 + \text{OH}$	1.04×10^{-9}	112
$\text{OH}^+ + \text{C}_2\text{H} \rightarrow \text{C}_2\text{H}_2^+ + \text{O}$	4.50×10^{-10}	112
$\text{OH}^+ + \text{C}_2\text{H} \rightarrow \text{C}_2\text{H}^+ + \text{OH}$	4.50×10^{-10}	112
$\text{OH}^+ + \text{C}_2 \rightarrow \text{C}_2\text{H}^+ + \text{O}$	4.80×10^{-10}	112
$\text{OH}^+ + \text{C}_2 \rightarrow \text{C}_2^+ + \text{OH}$	4.80×10^{-10}	112
$\text{OH}^+ + \text{H}_2 \rightarrow \text{H}_2\text{O}^+ + \text{H}$	1.01×10^{-9}	112
$\text{OH}^+ + \text{O}_2 \rightarrow \text{O}_2^+ + \text{OH}$	5.90×10^{-10}	112
$\text{OH}^+ + \text{O} \rightarrow \text{O}_2^+ + \text{H}$	7.10×10^{-10}	112
$\text{OH}^+ + \text{H}_2\text{O} \rightarrow \text{H}_2\text{O}^+ + \text{OH}$	1.59×10^{-9}	112
$\text{OH}^+ + \text{H}_2\text{O} \rightarrow \text{H}_3\text{O}^+ + \text{O}$	1.30×10^{-9}	112
$\text{OH}^+ + \text{O}^- \rightarrow \text{OH} + \text{O}$	1.93×10^{-7}	101
$\text{OH}^+ + \text{O}^- \rightarrow \text{O} + \text{H} + \text{O}$	1.00×10^{-7}	101
$\text{OH}^+ + \text{O}_2^- \rightarrow \text{OH} + \text{O}_2$	1.93×10^{-7}	101
$\text{OH}^+ + \text{O}_2^- \rightarrow \text{O} + \text{H} + \text{O}_2$	1.00×10^{-7}	101
$\text{OH}^+ + \text{O}_2^- \rightarrow \text{OH} + \text{O} + \text{O}$	1.00×10^{-7}	101
$\text{OH}^+ + \text{O}_2^- \rightarrow \text{O} + \text{H} + 2\text{O}$	1.00×10^{-7}	101
$\text{OH}^+ + \text{CO}_3^- \rightarrow \text{OH} + \text{CO}_2 + \text{O}$	1.00×10^{-7}	101
$\text{OH}^+ + \text{CO}_3^- \rightarrow \text{O} + \text{H} + \text{CO}_2 + \text{O}$	1.00×10^{-7}	101
$\text{OH}^+ + \text{CO}_4^- \rightarrow \text{OH} + \text{CO}_2 + \text{O}_2$	1.00×10^{-7}	101
$\text{OH}^+ + \text{CO}_4^- \rightarrow \text{O} + \text{H} + \text{CO}_2 + \text{O}_2$	1.00×10^{-7}	101
$\text{OH}^+ + \text{OH}^- \rightarrow \text{OH} + \text{OH}$	1.93×10^{-7}	101
$\text{OH}^+ + \text{OH}^- \rightarrow \text{OH} + \text{O} + \text{H}$	1.00×10^{-7}	101
$\text{OH}^+ + \text{OH}^- \rightarrow 2\text{H} + 2\text{O}$	1.00×10^{-7}	101
$\text{OH}^+ + \text{OH} \rightarrow \text{H}_2\text{O}^+ + \text{O}$	7.00×10^{-10}	112
$\text{OH} + \text{CH}_3 \rightarrow \text{CH}_3\text{OH} + \text{e}^-$	1.00×10^{-9}	112
$\text{OH} + \text{CH} \rightarrow \text{CH}_2\text{O} + \text{e}^-$	5.00×10^{-10}	112
$\text{OH} + \text{C} \rightarrow \text{CHO} + \text{e}^-$	5.00×10^{-10}	112
$\text{OH} + \text{H} \rightarrow \text{H}_2\text{O} + \text{e}^-$	1.40×10^{-9}	112
$\text{OH} + \text{O}^+ \rightarrow \text{OH} + \text{O}$	1.93×10^{-7}	101
$\text{OH} + \text{O}^+ \rightarrow \text{O} + \text{H} + \text{O}$	1.00×10^{-7}	101
$\text{OH} + \text{O}_2^+ \rightarrow \text{OH} + \text{O}_2$	1.93×10^{-7}	101
$\text{OH} + \text{O}_2^+ \rightarrow \text{O} + \text{H} + \text{O}_2$	1.00×10^{-7}	101

$\text{OH} \cdot + \text{O}_2^+ \rightarrow \text{OH} + \text{O} + \text{O}$	1.00×10^{-7}	101
$\text{OH} \cdot + \text{O}_2^+ \rightarrow 3\text{O} + \text{H}$	1.00×10^{-7}	101
$\text{OH} \cdot + \text{CO}^+ \rightarrow \text{CO} + \text{OH}$	1.93×10^{-7}	101
$\text{OH} \cdot + \text{CO}^+ \rightarrow \text{CO} + \text{O} + \text{H}$	1.00×10^{-7}	101
$\text{OH} \cdot + \text{CO}_2^+ \rightarrow \text{CO}_2 + \text{OH}$	1.93×10^{-7}	101
$\text{OH} \cdot + \text{CO}_2^+ \rightarrow \text{CO}_2 + \text{O} + \text{H}$	1.00×10^{-7}	101
$\text{OH} \cdot + \text{CO}_2^+ \rightarrow \text{CO} + \text{O} + \text{OH}$	1.00×10^{-7}	101
$\text{OH} \cdot + \text{CO}_2^+ \rightarrow \text{CO} + 2\text{O} + \text{H}$	1.00×10^{-7}	101
$\text{OH} \cdot + \text{H}_2\text{O}^+ \rightarrow \text{OH} + \text{H}_2\text{O}$	1.93×10^{-7}	101
$\text{OH} \cdot + \text{H}_2\text{O}^+ \rightarrow \text{O} + \text{H} + \text{H}_2\text{O}$	1.00×10^{-7}	101
$\text{OH} \cdot + \text{H}_2\text{O}^+ \rightarrow \text{OH} + \text{OH} + \text{H}$	1.00×10^{-7}	101
$\text{OH} \cdot + \text{H}_2\text{O}^+ \rightarrow \text{O} + \text{H} + \text{OH} + \text{H}$	1.00×10^{-7}	101
$\text{OH} \cdot + \text{H}_3\text{O}^+ \rightarrow \text{OH} + \text{H}_2\text{O} + \text{H}$	1.00×10^{-7}	101
$\text{OH} \cdot + \text{H}_3\text{O}^+ \rightarrow \text{O} + \text{H} + \text{H}_2\text{O} + \text{H}$	1.00×10^{-7}	101

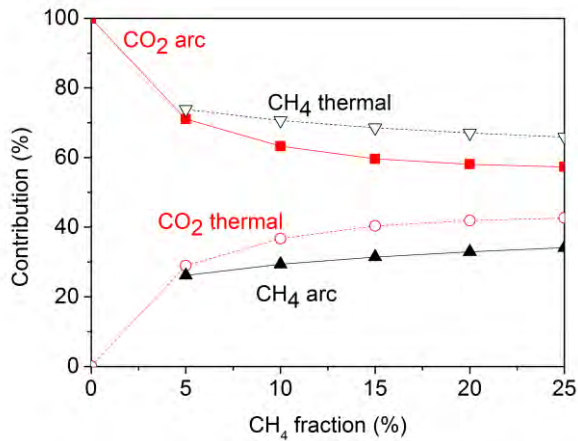


Figure A8: Relative contribution of the conversion inside the arc and the thermal conversion in the area around the arc to the overall conversion of CO_2 and CH_4 , as a function of the CH_4 fraction in the mixture.

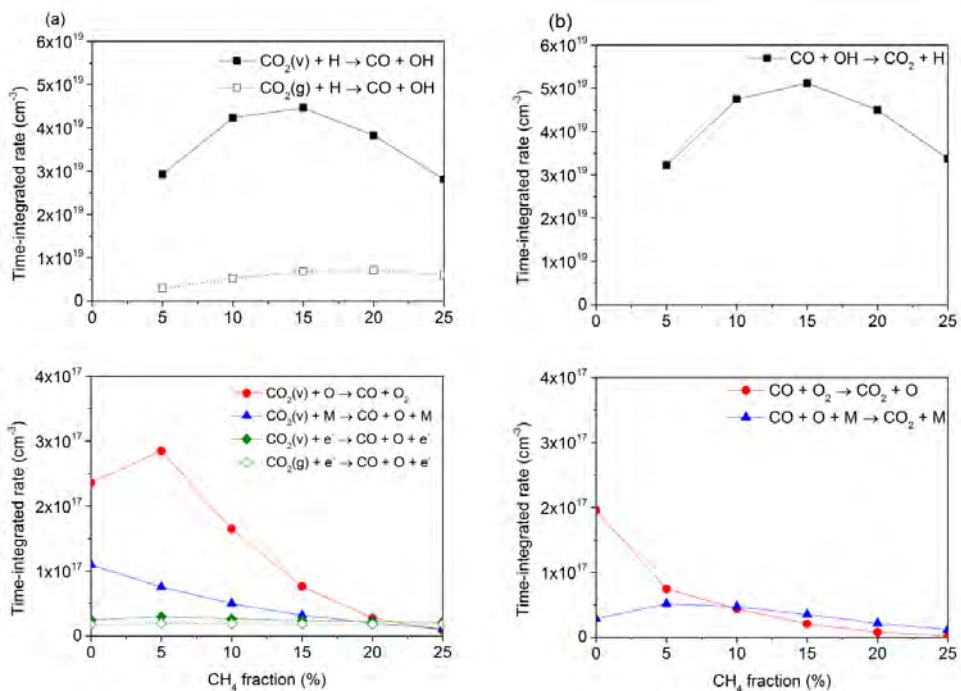


Figure A9: Time-integrated rates of the most important loss (a) and formation (b) processes of CO₂, as a function of CH₄ fraction in the mixture.

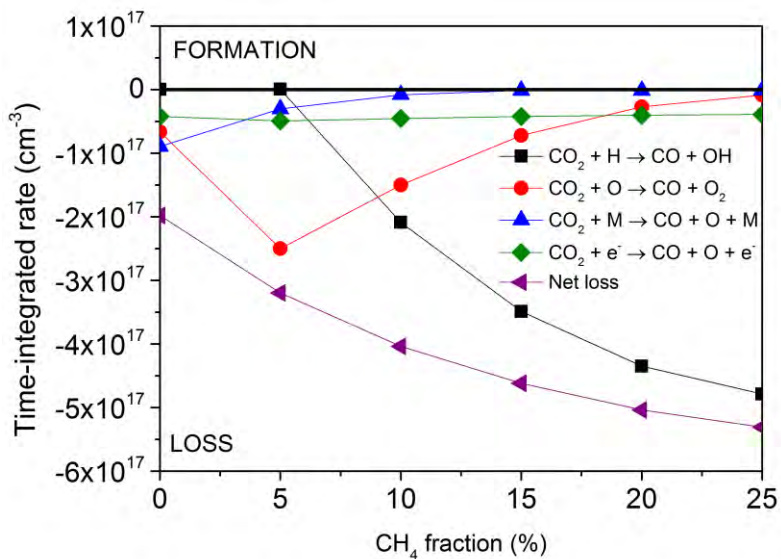


Figure A10: Net time-integrated rates of the most important loss (and formation) processes of CO₂, as well as the total net loss rate, as a function of CH₄ fraction in the mixture. The loss processes are plotted with negative rates; the formation processes in principle with positive rates (but in this case, they are negligible).

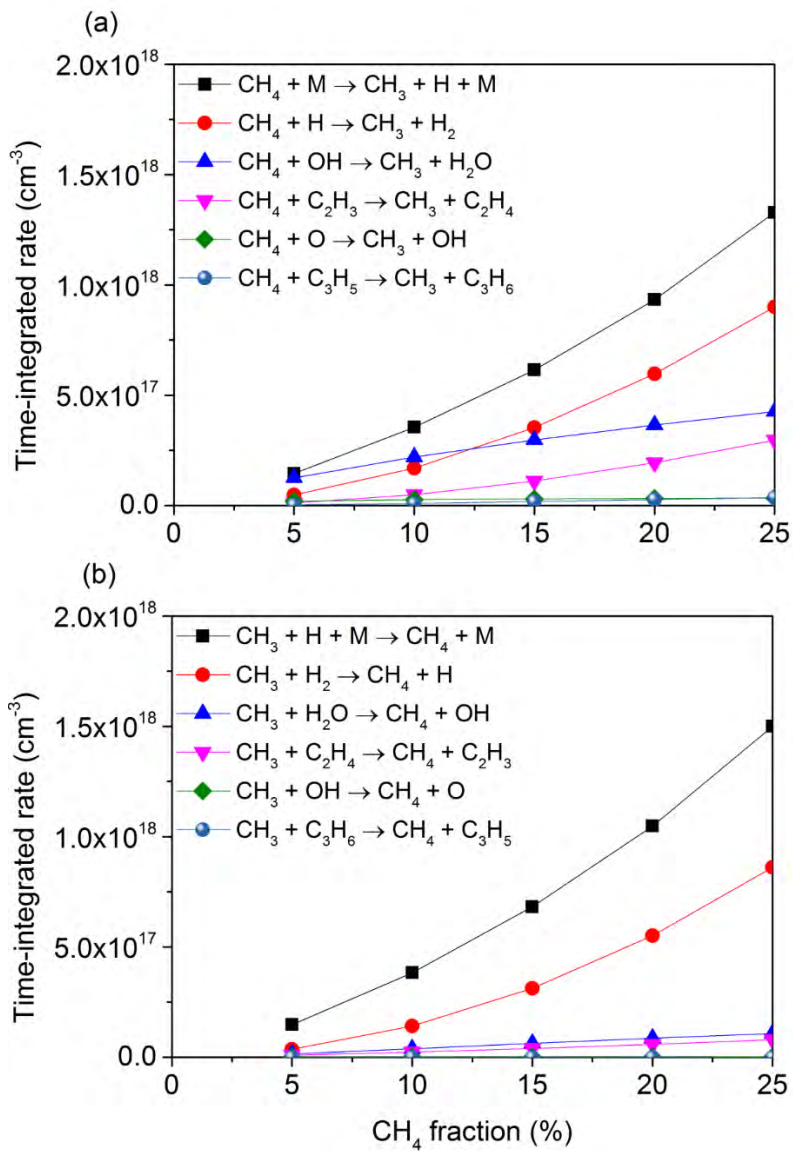


Figure A11: Time-integrated rates of the most important loss (a) and formation (b) processes of CH₄, as a function of CH₄ fraction in the mixture.

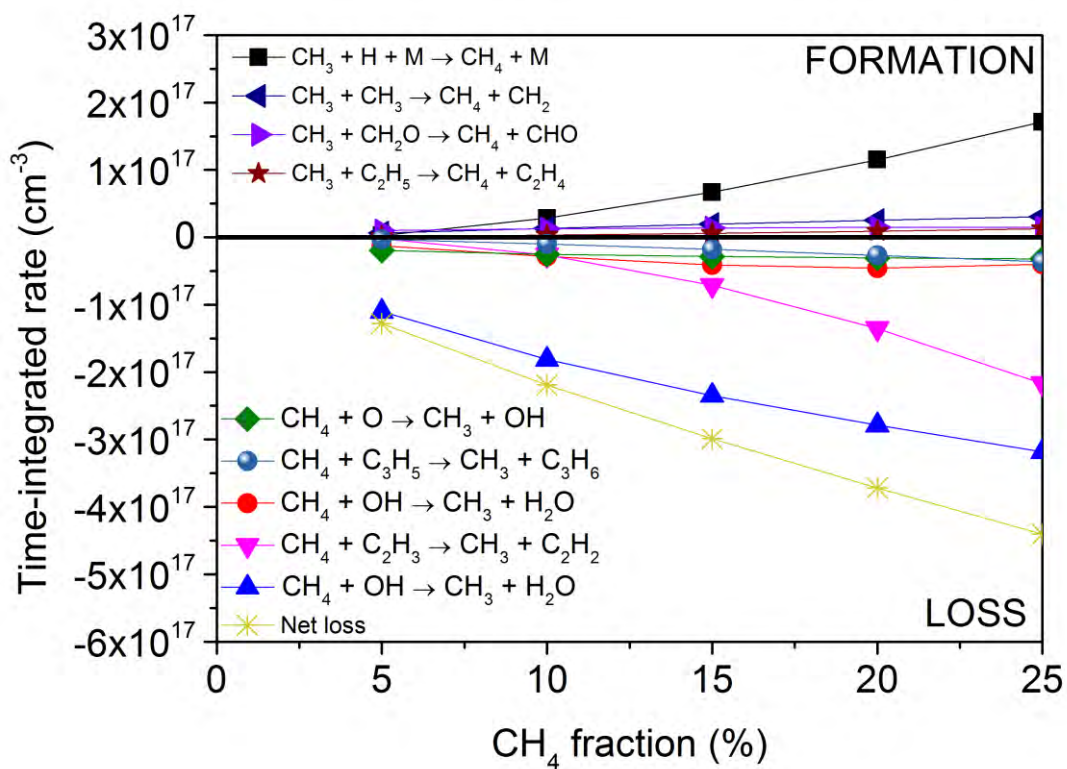


Figure A12: Net time-integrated rates of the most important loss and formation processes of CH₄, as well as the total net loss rate, as a function of CH₄ fraction in the mixture. The loss processes are plotted with negative rates, while the formation processes are plotted with positive rates.

Chapter 5: Combining CO₂ Conversion and N₂ Fixation in a GAP

The results presented in this Chapter were published in:

- Ramakers, M.; Heijkers, S.; Tytgat, T.; Lenaerts, S.; Bogaerts, A. Combining CO₂ Conversion and N₂ Fixation in a Gliding Arc Plasmatron. *J. CO₂ Util.* **2019**, *33*, 121–130

5.1 Introduction

In recent time, there is increased interest in plasma-based conversion of nitrogen into valuable compounds, so-called N_2 fixation. Moreover, waste streams from industry are not pure, but contain several gases. Instead of wasting energy into purifying these waste streams, we could also try to take advantage of its mixture. In reality, CO_2 and N_2 are often present in waste streams and thus can be converted simultaneously. Only a few papers have reported the effect of N_2 on CO_2 conversion in other types of plasmas^{75,262–264}. However, except in the paper by Snoeckx et al.²⁶⁴, a detailed analysis of the byproduct formation in this mixture was never performed, which is of course crucial for practical applications. Furthermore, Snoeckx et al.²⁶⁴ carried out this analysis for a dielectric barrier discharge (DBD), which has completely different plasma properties than a GAP. In terms of modelling CO_2/N_2 mixtures, earlier plasma models exist for a CO_2-N_2-He mixture by Wiegand and Nighan²⁶⁵ in a plasma column at a constant gas temperature of 300 K, as well as a more elaborate version by Gordillo-Vázquez, to study the air plasma kinetics under single sprites, taking into account eight vibrational levels of N_2 and three vibrational levels of CO_2 ²⁶⁰. All 21 vibrational levels of the asymmetric stretch mode (up to the dissociation limit) of CO_2 and 14 vibrational levels of N_2 were taken into account by Heijkers et al.⁷⁵ for modelling a MW discharge at reduced pressure and this chemistry description was updated for modelling a DBD discharge by Snoeckx et al.²⁶⁶. However, N_2 fixation in warm plasmas at atmospheric pressure was not yet modelled, except for Wang et al.²⁶⁷, but this was for N_2/O_2 mixtures.

Therefore, in this Chapter we present a chemical kinetics model to investigate the mechanisms of the combined CO_2 and N_2 conversion in our GAP, with the same configuration as in Chapter 4, at a plasma power of 350 W and flow rate of 10 L min^{-1} . In Section 5.2 the chemistry set is explained. Section 5.3 shows the calculated conversions and energy efficiencies and a comparison with experiments. Finally, Section 5.4 shows the most important mechanisms for CO_2/N_2 conversion and also NO_x formation.

5.2 Chemistry set

The chemistry set used in this study is based on the papers of Heijkers et al.⁷⁵, Snoeckx et al.²⁶⁶ and Wang et al.²⁶⁷. The species included in the model are listed in Table 4. The symbol ‘V’ between brackets for N₂, CO₂, CO and O₂ and the symbol ‘E’ between brackets for CO₂, CO and O₂ represent again the vibrationally and electronically excited levels of these species, respectively. More information about the notation of the vibrationally and electronically excited levels of CO₂, CO and O₂ can be found in⁵⁷ and in Chapter 3.

Table 4: Species taken into account in the chemistry set for the CO₂/N₂ mixture.

Molecules	Charged species	Radicals	Excited species
CO ₂ , CO, N ₂ , NO, N ₂ O, NO ₂ , NO ₃ , N ₂ O ₅ , N ₂ O ₃ , N ₂ O ₄ , C ₂ N ₂	CO ₂ ⁺ , CO ₄ ⁺ , CO ⁺ , C ₂ O ₂ ⁺ , C ₂ O ₃ ⁺ , C ₂ O ₄ ⁺ , C ₂ ⁺ , C ⁺ , CO ₃ ⁻ , CO ₄ ⁻ , N ⁺ , N ₂ ⁺ , N ₃ ⁺ , N ₄ ⁺ , NO ⁺ , N ₂ O ⁺ , NO ₂ ⁺ , NO ⁻ , N ₂ O ⁻ , NO ₂ ⁻ , NO ₃ ⁻ , O ₂ ⁺ N ₂	C ₂ O, C, C ₂ , CN, ONCN, NCO, NCN, C ₂ N, N	CO ₂ (Va, Vb, Vc, Vd), CO ₂ (V1-V21), CO ₂ (E1), CO(V1-V10), CO(E1-E4), N ₂ (V1-V24), N ₂ (C ³ Π _u), N ₂ (A ³ Σ _u), N ₂ (a ¹ Σ _u), N ₂ (A ¹ Π _g), N ₂ (B ³ Π _g), N ₂ (W ³ Δ _u), N ₂ (B ³ Σ _u), N ₂ (E ³ Σ _g), N ₂ (W ¹ Δ _u), N ₂ (A ¹ Σ _g), N(² P), N(² D)
O ₂ , O ₃	O ⁺ , O ₂ ⁺ , O ₄ ⁺ , O ⁻ , O ₂ ⁻ , O ₃ ⁻ , O ₄ ⁻	O	O ₂ (V1-V3), O ₂ (E1-E2)
	electrons		

For CO₂, again all 21 levels of the asymmetric mode till the dissociation limit (5.5 eV) are taken into account, as well as the four effective low-lying symmetric stretching and bending mode levels, i.e. CO₂ (Va-Vd). For N₂, up to 24 vibrational levels are included (till 5.8 eV), which is more than enough to describe vibration-induced dissociation in the GAP, since most dissociation occurs from the lowest levels (see Appendix: Figure A13), which was also the case for pure CO₂, as shown in detail in Chapter 3. The extra reactions added to the chemistry set of Chapter 3 and the reactions of pure N₂, taken from the papers

of Heijkers et al.⁷⁵, Snoeckx et al.²⁶⁶ and Wang et al.²⁶⁷, are listed in Table A11 in the Appendix.

5.3 Calculated and measured conversion and energy efficiency

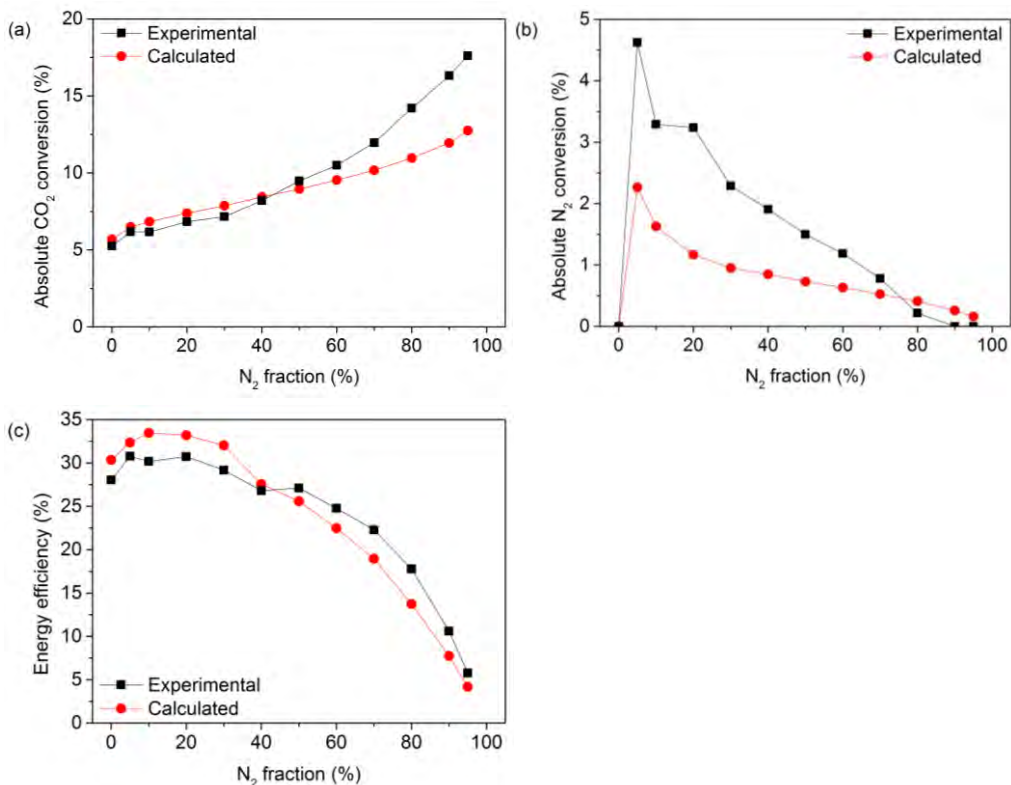


Figure 22: Calculated and experimental results for CO₂ conversion (a), N₂ conversion (b) and energy efficiency (c).

First we have validated the model against the experimental data for conversion, energy efficiency and produced NO_x concentrations. The absolute CO₂ conversion rises from 5 to 18 % with increasing fraction of N₂ in the mixture, as can be seen in Figure 22 (a). The effective CO₂ conversion, which is obtained by accounting for the initial fraction of CO₂ in the mixture, increases at 5 % N₂, followed by a drop with increasing N₂ fraction. Until a N₂ fraction of 50 %, the effective conversion only slightly decreases, while above 50 %, the effective conversion drops quite fast from 5 to 1 %. Thus, at N₂ fractions below 50 %, the

increase in absolute CO₂ conversion can more or less compensate for the lower CO₂ concentration in the mixture, but at higher N₂ fractions, this is not true anymore. Indeed, not all the energy of the vibrationally excited N₂ is transferred into CO₂ dissociation, and part of it also remains stored in the N₂ vibrational levels or gets lost by collisions with ground state molecules (so-called vibration-translation (VT) relaxation). Thus, at higher N₂ fractions in the mixture, a larger portion of the applied power is used to activate the N₂ molecules, without converting all this energy into CO₂ dissociation. The energy efficiency of CO₂ conversion (see Figure 22(c)) more or less follows the trend of the effective CO₂ conversion, since it is directly proportional to it. The energy efficiency remains more or less constant around 28 % until a N₂ fraction of 50 %, after which it decreases rapidly to a value of 5 %. Thus, upon increasing N₂ fraction in the mixture, more energy is consumed by the N₂ molecules, which cannot be used anymore for CO₂ conversion.

The concentrations of NO and NO₂ are plotted in Figure 23 as a function of N₂ fraction. All curves show a maximum around 50 - 70 % N₂. This is logical, because in this range, both CO₂ and N₂ split into the reactive species needed for NO and NO₂ formation. At very low or high N₂ fractions, either N₂ or CO₂ will act as limiting reactant. The fact that the maximum NO concentration is reached around 60-70 % N₂ indicates that CO₂ dissociation occurs easier than N₂ dissociation, which is explained by the C=O vs N≡N bond dissociation energy (i.e., 749 kJ/mol vs 946 kJ/mol). The maximum NO₂ concentration is reached at 50 % N₂, which is also logical, because its formation is favored when there is less N₂ in the mixture. If we look at the absolute values, the NO concentration is about 20 times higher than the NO₂ concentration, with maximum values of 6453 and 317 ppm, respectively. It should however be noted that the experimental NO/NO₂ ratio will change depending on the distance between the plasma source and the measuring equipment and how fast the gas cools down. However, the trend of both NO_x species as a function of N₂ fraction should not change. Nevertheless, in general it is better to compare the total NO_x concentration, when comparing experiments with calculation results. The highest total NO_x concentration in our setup is reached at a N₂ fraction of 60 % with a total flow rate of 10 L/min and has a value of 6761 ppm. Patil et al. investigated NO_x formation in a milli-scale classical (planar) gliding arc reactor²⁶⁸. They reported the highest NO_x

concentration at a flow rate of 1 L/min and a 1/1 N₂/O₂ ratio of 9562 ppm, with about 3565 ppm NO and 5997 ppm NO₂. The formation of NO₂ from dry air in a classical gliding arc plasma was investigated by Bo et al.²⁶⁹ in the context of VOC decomposition. The highest amount of NO₂ produced was 6982 ppm. Compared to our reactor, where we form 6453 and 317 ppm NO and NO₂, the NO₂ concentration lies much higher in the abovementioned studies.

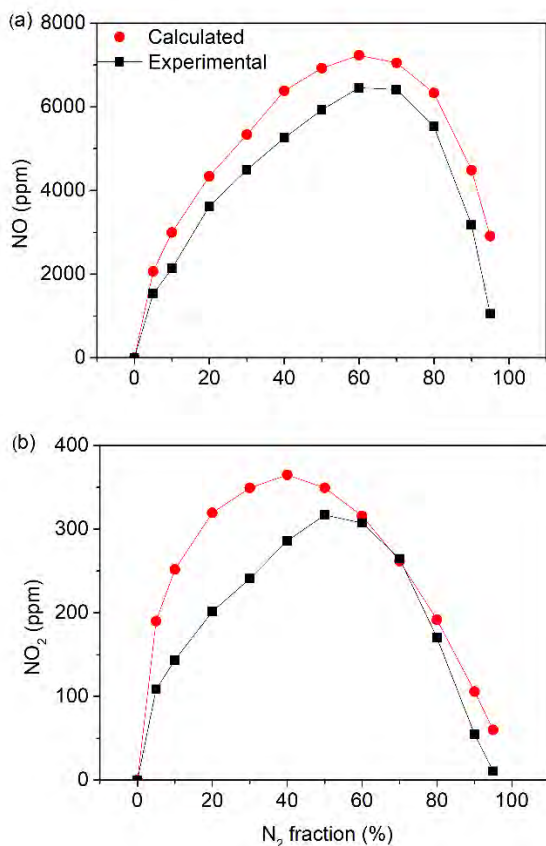


Figure 23: Calculated and experimental results for NO (a) and NO₂ (b) concentration (in parts per million).

In all cases, the trends and absolute values predicted by the model are in reasonable agreement with the experimental results, as illustrated in Figures 22 and 23. Indeed, on average the relative difference between calculated and experimental data was 5 % for the CO₂ conversion, 27 % for the N₂ conversion,

5 % for the energy efficiency, 34 % for the NO concentration, and 72 % for the NO₂ concentration. The reasons for the deviations can be, as mentioned before, the distance between the plasma source and the measuring equipment, but also the efficiency of the third body in the recombination reaction $\text{NO} + \text{O} + \text{M} \rightarrow \text{NO}_2 + \text{M}$, which was not explicitly taken into account. Also, the largest discrepancies in N₂ conversion are also found for the same N₂ fractions at which the NO₂ discrepancy is the highest. Nevertheless, keeping in mind the complexity of the underlying chemistry, these discrepancies are still reasonable. Therefore, the model can be used to predict the underlying mechanisms, as explained in next Section.

5.4 Underlying mechanisms as revealed by the model

In Figures 24, 25 and 26, we plot the net time-integrated rates of the most important reactions for the loss and formation of CO₂, NO and NO₂, respectively. For additional insight, the net contributions of these reactions are plotted in Figures 27, 28 and 29.

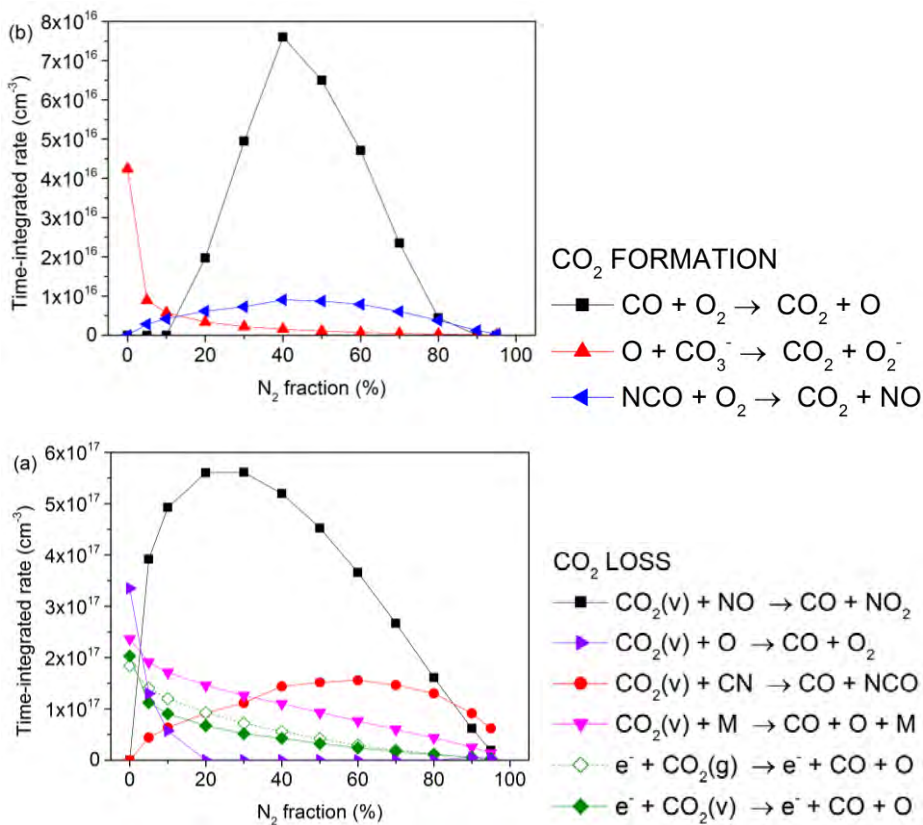


Figure 24: Time-integrated rate for the most important CO₂ loss (a) and formation (b) mechanisms as a function of N₂ fraction. Note that the time-integrated formation rate is an order of magnitude lower than the time-integrated loss rate.

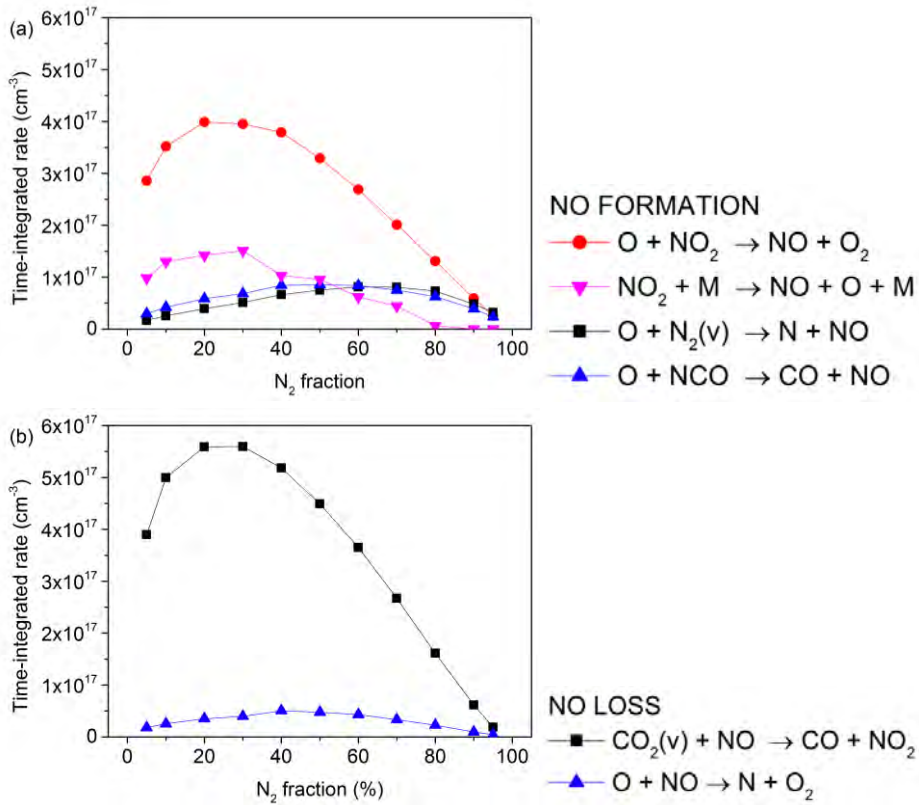


Figure 25: Time-integrated rate for the most important NO formation (a) and loss (b) mechanisms as a function of N₂ fraction.

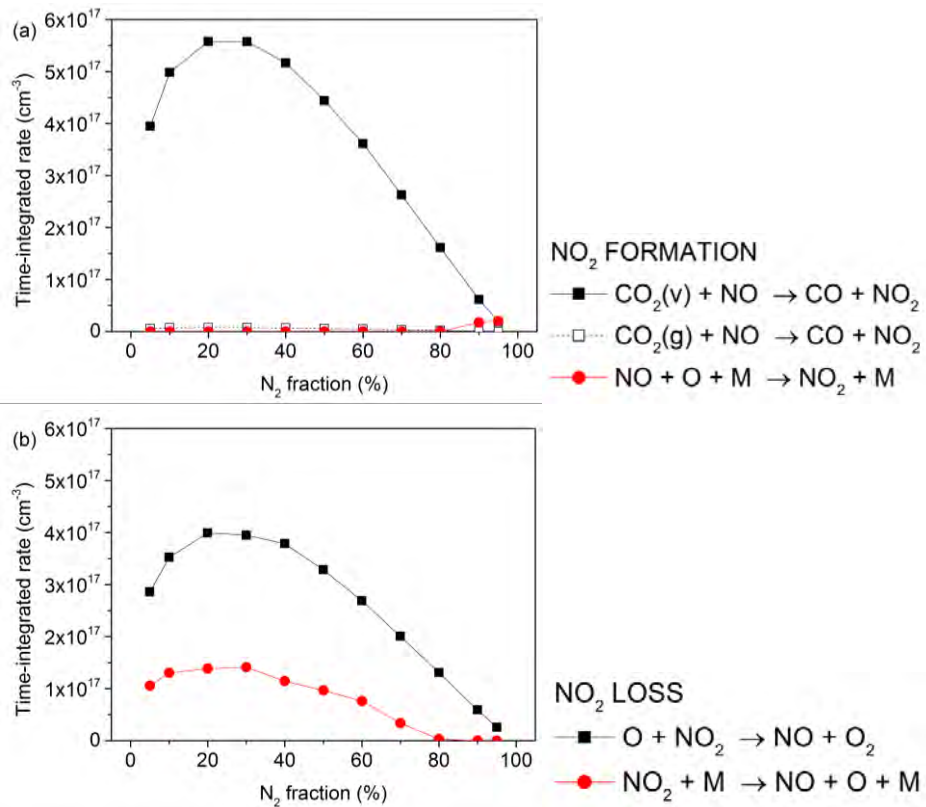


Figure 26: Time-integrated rate for the most important NO₂ formation (a) and loss (b) mechanisms as a function of N₂ fraction.

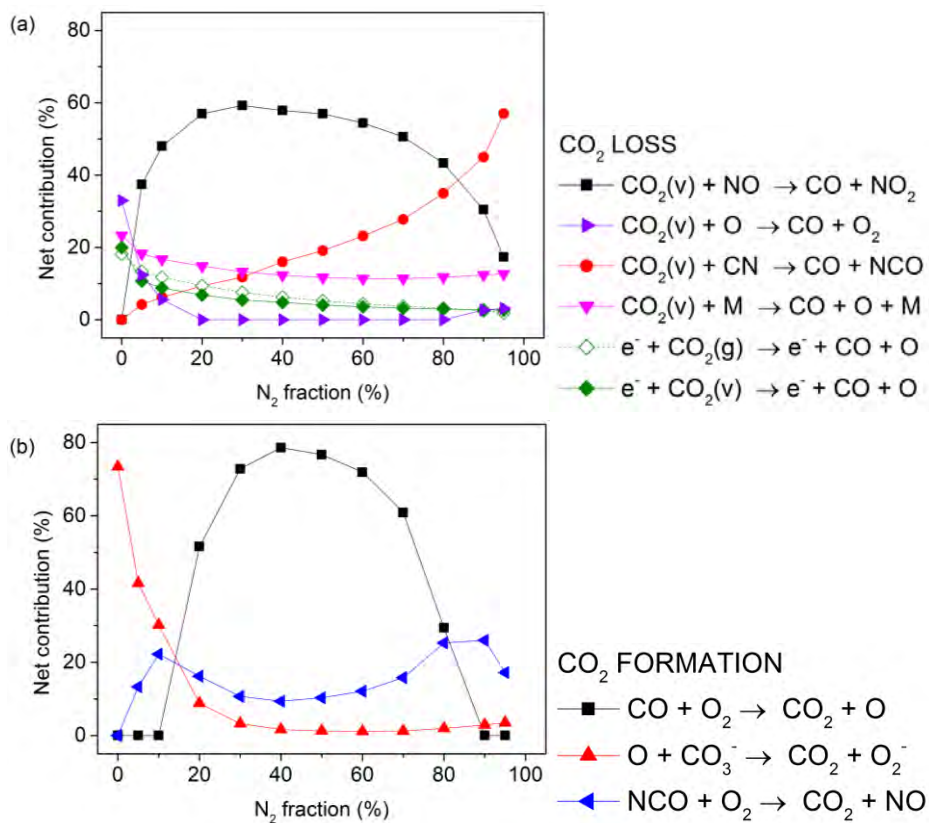


Figure 27: Net contribution of the most important loss (a) and formation (b) reactions.

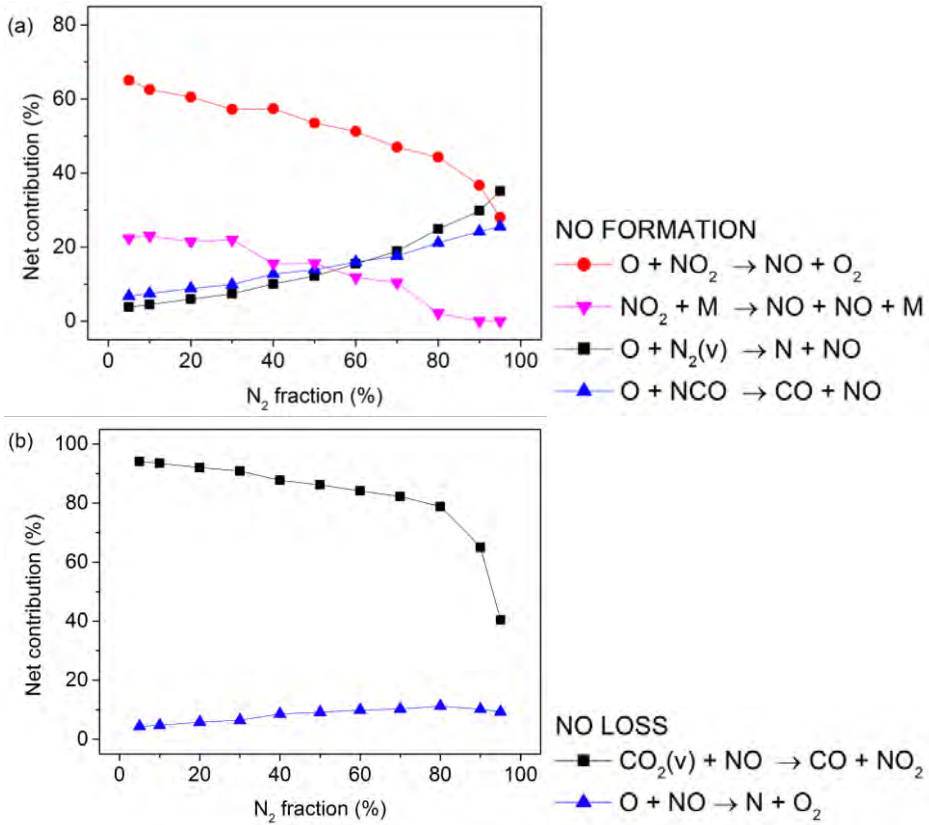


Figure 28: Net contribution of the most important formation (a) and loss (b) reactions of NO.

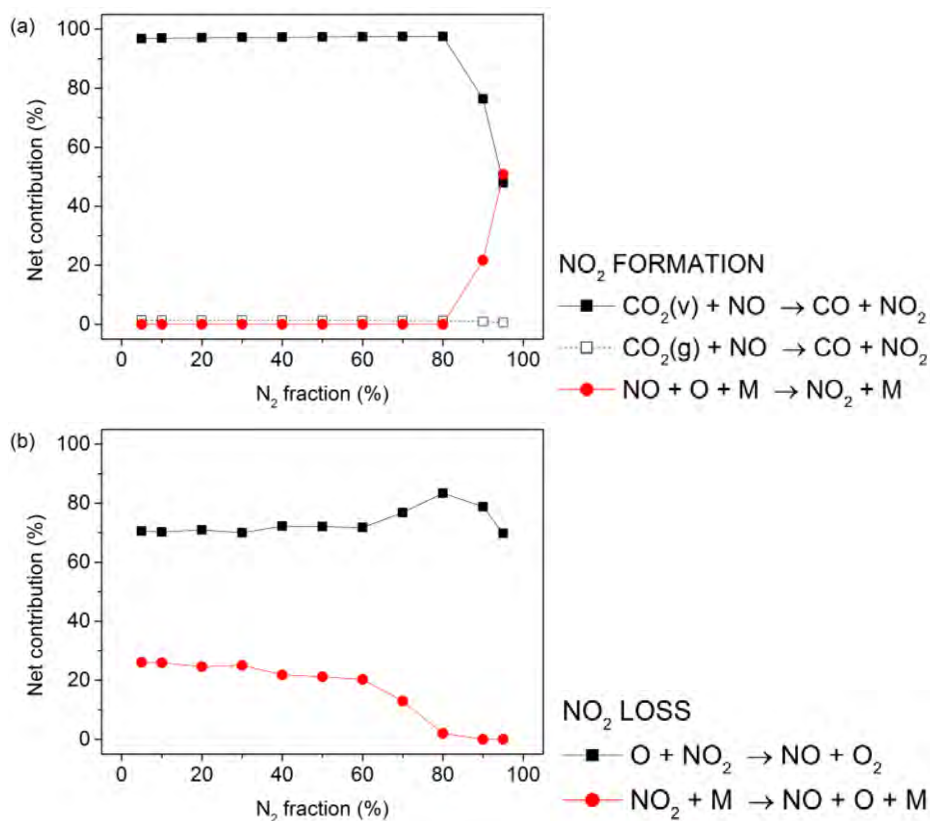


Figure 29: Net contribution of the most important formation (a) and loss (b) reactions of NO₂.

For pure CO₂ the most important loss mechanism is the reaction of vibrationally excited CO₂ with O atoms, see Figure 24(a). This agrees well with our earlier model predictions, with a similar time-integrated rate, i.e. $\sim 10^{17} \text{ cm}^{-3} \cdot \text{s}^{52}$ illustrated in Chapters 3 for the same SEI value, i.e. $0.55 \text{ eV molec}^{-1}$. However, as soon as N₂ is added, the reaction of vibrationally excited CO₂ with NO becomes dominant, with an overall contribution of 50 – 60 % (Figure 27). Other reactions, such as the collision of vibrationally excited CO₂ with CN or any molecule M in the plasma, and electron impact dissociation of both CO₂ ground state and vibrationally excited levels, also play a role, with contributions of 5 – 60 %, depending on the N₂ fraction (Figure 27). CO₂ formation is mainly caused by recombination of CO and O₂ (Figure A16(b)), with contributions up to 80 % (Figure 27).

NO is initially formed upon reaction of vibrationally excited N₂ with O atoms, i.e., the so-called Zeldovich mechanism, in agreement with the dominant formation mechanisms in a milli-scale classical GA²⁶⁷. Subsequently, NO reacts with vibrational excited CO₂, forming CO and NO₂ (Figure 25). In return, the reaction of NO₂ with O atoms will further produce NO.

The most important reaction pathways are summarized in Figure 30. Reactants are indicated in color according to the time-integrated rate of their reaction (red $\geq 10^{17}$ cm⁻³; green $\geq 10^{16}$ cm⁻³; blue $\geq 10^{15}$ cm⁻³), while the thickness of the arrow lines corresponds to the overall importance of the reaction. The most important reactions, ranked by importance based on the average time-integrated rates, are listed in Table 5. It should be noted that for the most important mechanisms, for all N₂ fractions, the time-integrated rate is almost of the same order ($\sim 10^{17}$ cm⁻³) as in Chapter 3, for the same SEI value, i.e. 0.55 eV molec⁻¹, as in Chapter 3.

Table 5: Most important reactions, ranked by importance based on the average time-integrated rate.

Reactions	Average time-integrated rate (cm ⁻³)
$\text{CO}_2 + \text{NO} \rightarrow \text{CO} + \text{NO}_2$	3.55×10^{17}
$\text{O} + \text{NO}_2 \rightarrow \text{NO} + \text{O}_2$	2.57×10^{17}
$\text{CO} + \text{N} \rightarrow \text{CN} + \text{O}$	1.38×10^{17}
$e^- + \text{CO}_2 \rightarrow e^- + \text{CO} + \text{O}$	1.19×10^{17}
$\text{CO}_2 + \text{M} \rightarrow \text{CO} + \text{O} + \text{M}$	1.16×10^{17}
$\text{CO}_2 + \text{CN} \rightarrow \text{CO} + \text{NCO}$	1.15×10^{17}
$\text{NO}_2 + \text{M} \rightarrow \text{NO} + \text{O} + \text{M}$	7.63×10^{16}
$\text{NCO} + \text{M} \rightarrow \text{N} + \text{CO} + \text{M}$	5.96×10^{16}
$\text{O} + \text{N}_2 \rightarrow \text{N} + \text{NO}$	5.93×10^{16}
$\text{O} + \text{NCO} \rightarrow \text{CO} + \text{NO}$	5.92×10^{16}
$\text{CO} + \text{O}_2 \rightarrow \text{CO}_2 + \text{O}$	3.17×10^{16}
$\text{NCO} + \text{NO} \rightarrow \text{CO} + \text{N}_2 + \text{O}$	6.61×10^{15}
$\text{N}_2\text{O} + \text{M} \rightarrow \text{N}_2 + \text{O} + \text{M}$	6.49×10^{15}
$\text{N} + \text{NO}_2 \rightarrow \text{N}_2\text{O} + \text{O}$	3.78×10^{15}
$\text{NCO} + \text{NO} \rightarrow \text{N}_2\text{O} + \text{CO}$	3.13×10^{15}
$\text{NO}_2 + \text{NO}_3 + \text{M} \rightarrow \text{N}_2\text{O}_5 + \text{M}$	6.88×10^{13}
$\text{NO}_2 + \text{NO}_2 + \text{M} \rightarrow \text{N}_2\text{O}_4 + \text{M}$	9.34×10^8
$\text{NO} + \text{NO}_2 + \text{M} \rightarrow \text{N}_2\text{O}_3 + \text{M}$	4.28×10^7

Both CO₂ and N₂ are easily excited from ground state to vibrational levels, and vice versa, upon electron impact (de)excitation, vibration-vibration (VV) and vibration-translation (VT) relaxation. The vibrational distribution functions (VDFs) of both CO₂ and N₂ are plotted in Figure 31. Overall, the VDF of both molecules is thermal, with a vibrational temperature of 3174 K and 3333 K for CO₂ and N₂, respectively (Figure 32), which is more or less equal to the gas temperature (3140 K). The energy efficiency of CO₂ conversion and N₂ fixation could be increased if the VDFs of both CO₂ and N₂ would be non-thermal, with higher populations of the higher vibrational level^{52,151}. To realize this, the gas temperature in the arc should be reduced, so that VT relaxation, which depopulates the vibrational levels, can be reduced and vibrational pumping would be more significant. However, this may not be possible to realize. On the other hand, although the distribution is quasi-thermal, the vibrational levels in the GAP are clearly more populated than in other types of plasmas, such as a DBD, where the VDF dramatically drops for the higher vibrational levels, because the reduced electric field is too high (> 200 Td) for efficient vibrational excitation⁵⁵. Hence, dissociation occurs from the lower CO₂ vibrational levels, by thermal reactions, which rise with increasing temperature. This explains why the CO₂ conversion and N₂ fixation are quite energy-efficient in our GAP, compared to other commonly studied plasma types.

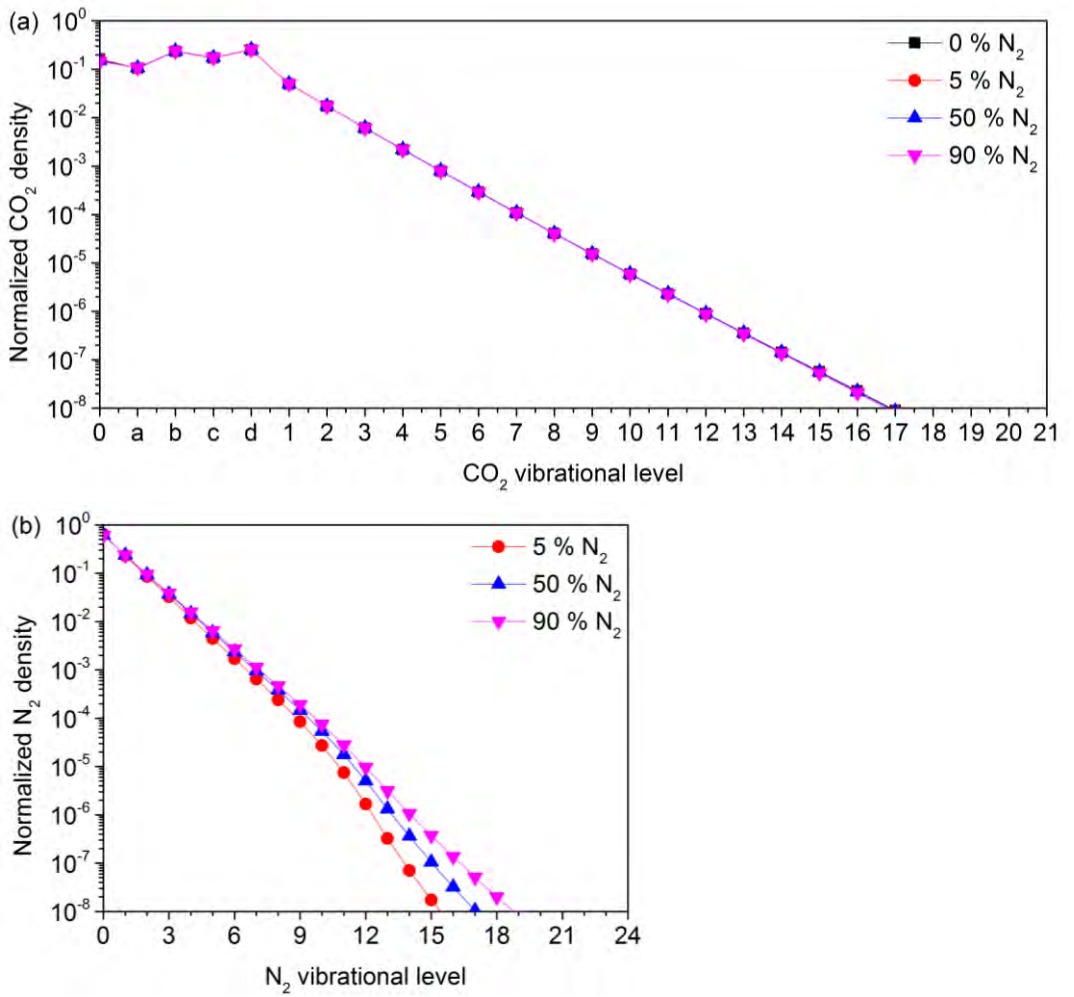


Figure 31: Calculated VDF of CO₂ (a) and N₂ (b). They are nearly thermal, in the entire range of N₂ fractions in the mixture.

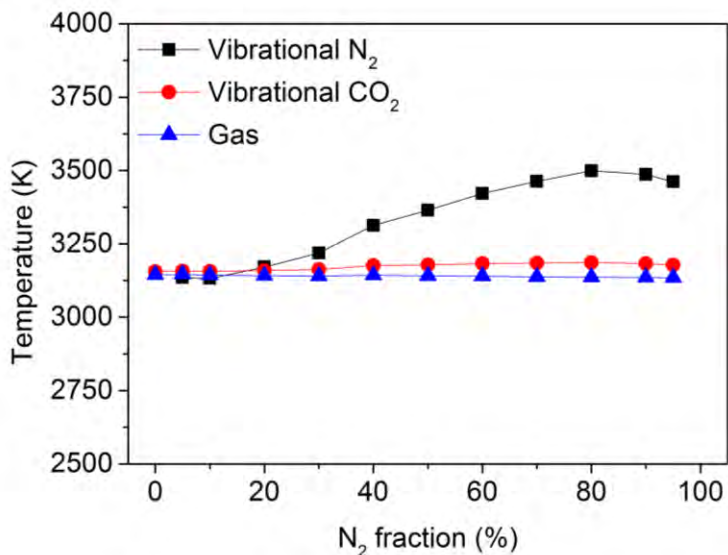


Figure 32: The average gas temperature is 3140 K, while the average vibrational temperature of CO₂ and N₂ are 3174 K and 3333 K, respectively.

CO₂ is mainly converted into CO and O, and it also helps in producing NO₂ upon reaction with NO. CO is in turn mainly converted into O by reaction with N or O₂. The N₂ molecules are activated by electron impact vibrational excitation (see Figure 30), lowering their energy barriers for chemical reaction with O atoms into NO formation. NO reacts further into NO₂, mainly by reaction with vibrationally excited CO₂. Vice versa, NO₂ also stimulates the formation of NO, by reaction with O atoms or any molecule (M) in the plasma. The fact that the most important loss mechanism of NO₂ is the most important formation mechanism of NO, and vice versa (Figures 25 and 26), shows that they are easily converted into each other. Still, the selectivity of NO is much higher in our GAP than that of NO₂. Indeed, NO is also formed upon reaction of O atoms with vibrationally excited N₂ and with NCO, which has no reverse reaction (Figure 25). Thus, by comparing the sum of the time-integrated formation and loss rates, the resulting concentration of NO is 20 times higher than that of NO₂ (see Figure 23), which explains the higher NO selectivity.

Generally, we can conclude from Figure 30 that the NO_x molecules are mainly formed through reactions with O atoms. So to enhance the NO_x production, we have to stimulate the formation of O atoms, and thus the CO₂

conversion, e.g., by improving the reactor design to enhance the fraction of gas passing through the arc.

Finally, as mentioned above, the gas temperature in the GAP is fairly high (around 3000 K), and the VDFs of both CO₂ and N₂ are thermal (see Figure 31). Thus, thermal reactions are important for the CO₂ and N₂ conversion at this high temperature. Nevertheless, the CO₂ and N₂ molecules are first activated by electron impact excitation. To show the contribution of plasma in the CO₂ and N₂ conversion, we plot in Figure 33 the calculated absolute CO₂ and N₂ conversion in the GAP as a function of N₂ fraction in the mixture, comparing with plasma and without plasma (i.e., only thermal reactions, without electron impact reactions). It is clear that, because of the high temperature, thermal reactions are indeed most important. Indeed, although the VDF is thermal, the higher vibrational levels are still sufficiently populated at this high temperature, to cause dissociation. Nevertheless, the conversion in case of plasma is still somewhat higher than the pure thermal conversion, especially at higher N₂ fractions, because the electron impact reactions create extra reactive species for the thermal reactions.

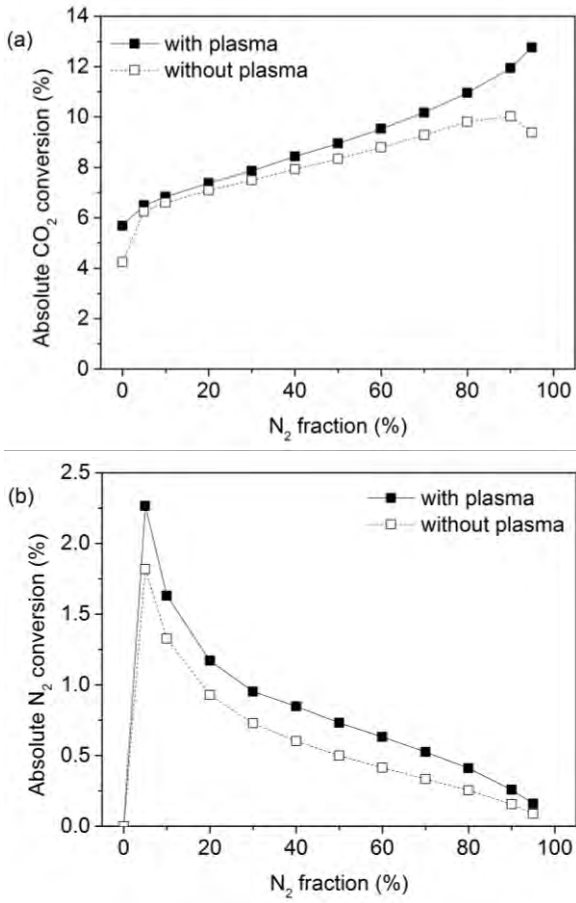


Figure 33. Calculated absolute CO₂ (a) and N₂ (b) conversion in the GAP as a function of N₂ fraction in the mixture, comparing with plasma and without plasma (i.e., only thermal reactions, without electron impact reactions).

5.5 Conclusion

We presented a chemical kinetics model for the combined CO₂ and N₂ conversion in the GAP. The addition of N₂ has a positive effect on the absolute CO₂ conversion up to 50 %, while at higher N₂ fractions, the effective CO₂ conversion and energy efficiency drop. The simulations reveal that the CO₂ conversion mainly proceeds through the vibrational levels, which are populated through collision with the N₂ vibrational levels. In addition, NO and NO₂ are formed in the CO₂/N₂ mixture, initiated by the reaction between N₂ vibrational levels and O atoms (so-called Zeldovich mechanism²⁶⁷).

Combining CO₂ and N₂ in a GAP thus can lead to combined CO₂ conversion and N₂ fixation. The highest amount of NO_x obtained is 6761 ppm, which is still below the minimum threshold of 1 % to make it effective for N₂ fixation. By improving our reactor and gas inlet design, the gas fraction that passes through the arc could be enhanced, and thus the CO₂ conversion and NO_x production. This optimization will need dedicated fluid dynamics simulations, which are currently being carried out within PLASMANT.

5.6 Appendix

Table A11 Extra reactions included in the model, added to the chemistry set of Chapter 3. They are taken from refs. ^{75,266,267}, but some extra reactions are added, and the rate coefficients of some other reactions are updated, as listed in this table, to account for the high pressure and temperature conditions in the GAP. The rate coefficients are given in cm³ s⁻¹ and cm⁶ s⁻¹ for two-body and three-body reactions, respectively. **R** is the gas constant and **T** the gas temperature (in K) and **T_e** the electron temperature (in K).

Reaction	Rate coefficient	Ref
e- + N ₂ → e- + N ₂	f(σ)	96
e- + N ₂ ↔ e- + N ₂ (v)	f(σ)	270
e- + N ₂ → e- + N ₂ (e)	f(σ)	270
e- + N ₂ → e- + N + N	f(σ)	271
e- + N ₂ → 2e- + N ₂ ⁺	f(σ)	270
e- + N ₂ → 2e- + N ⁺ + N	f(σ)	271
e- + N → 2e- + N ⁺	f(σ)	93
e- + N → e- + N(² D)	f(σ)	272
e- + N → e- + N(² D)	f(σ)	272

$e^- + N^+ + M \rightarrow N + M$	$6.0 \times 10^{-27} \left(\frac{300}{T_e}\right)^{1.5}$	130
$2e^- + N^+ \rightarrow e^- + N$	$7.0 \times 10^{-20} \left(\frac{300}{T_e}\right)^{4.5}$	130
$e^- + N_2^+ \rightarrow N + N$	$0.50 \times 1.8 \times 10^{-7} \left(\frac{300}{T_e}\right)^{0.39}$	130
$e^- + N_2^+ \rightarrow N + N(^2D)$	$0.45 \times 1.8 \times 10^{-7} \left(\frac{300}{T_e}\right)^{0.39}$	130
$e^- + N_2^+ \rightarrow N + N(^2P)$	$0.05 \times 1.8 \times 10^{-7} \left(\frac{300}{T_e}\right)^{0.39}$	130
$e^- + N_3^+ \rightarrow N_2 + N$	$2.0 \times 10^{-7} \left(\frac{300}{T_e}\right)^{0.50}$	130
$e^- + N_4^+ \rightarrow N_2 + N_2$	$2.3 \times 10^{-6} \left(\frac{300}{T_e}\right)^{0.53}$	130
$e^- + N_4^+ \rightarrow N_2 + 2N$	$3.13 \times 10^{-7} \left(\frac{T_e}{11605}\right)^{-0.41}$	260
$e^- + N_3^+ \rightarrow N_2(A^3\Sigma_u) + N$	$6.91 \times 10^{-8} \left(\frac{T_e}{11605}\right)^{-0.50}$	260
$e^- + N_3^+ \rightarrow N_2(B^3\Pi_g) + N$	$6.91 \times 10^{-8} \left(\frac{T_e}{11605}\right)^{-0.50}$	260
$N^+ + N + M \rightarrow N_2^+ + M$	1.7×10^{-29}	130
$N^+ + N_2 + N_2 \rightarrow N_3^+ + N_2$	Full rc in ref	130
$N_2^+ + N_2(A^3\Sigma_u) \rightarrow N_3^+ + N$	3.0×10^{-10}	260
$N_2^+ + N \rightarrow N^+ + N_2$	Full rc in ref	130
$N_2^+ + N_2 + N_2 \rightarrow N_4^+ + N_2$	Full rc in ref	260
$N_2^+ + N + N_2 \rightarrow N_3^+ + N_2$	Full rc in ref	260
$N_3^+ + N \rightarrow N_2^+ + N_2$	6.6×10^{-11}	260
$N_4^+ + N_2 \rightarrow N_2^+ + N_2 + N_2$	Full rc in ref	130
$N_4^+ + N \rightarrow N^+ + 2N_2$	1.0×10^{-11}	130
$N_2(B^3\Pi_g) \rightarrow N_2(A^3\Sigma_u)$	1.34×10^5	130
$N_2(A^3\Sigma_u) \rightarrow N_2$	5.0×10^{-1}	130
$N_2(a^1\Sigma_u) \rightarrow N_2$	1.0×10^2	130
$N_2(C^3\Pi_u) \rightarrow N_2(B^3\Pi_g)$	2.45×10^7	130
$N_2(A^3\Sigma_u) + N_2 \rightarrow 2N_2$	3.0×10^{-16}	130
$N_2(A^3\Sigma_u) + N \rightarrow N_2 + N$	2.0×10^{-12}	130
$N_2(A^3\Sigma_u) + N \rightarrow N_2 + N(^2P)$	$4.0 \times 10^{-11} \left(\frac{300}{T}\right)^{0.667}$	130
$2N_2(A^3\Sigma_u) \rightarrow N_2 + N_2(B^3\Pi_g)$	3.0×10^{-10}	130
$2N_2(A^3\Sigma_u) \rightarrow N_2 + N_2(C^3\Pi_u)$	1.5×10^{-10}	130
$N_2(B^3\Pi_g) + N_2 \rightarrow N_2(A^3\Sigma_u) + N_2$	3.0×10^{-11}	130
$N_2(B^3\Pi_g) + N_2 \rightarrow 2N_2$	2.0×10^{-12}	130

$N_2(a^1\Sigma_u) + N_2 \rightarrow N_2(B^3\Pi_g) + N_2$	$1.9x10^{-13}$	130
$N_2(C^3\Pi_u) + N_2 \rightarrow N_2(a^1\Sigma_u) + N_2$	$1.0x10^{-11}$	130
$N(^2D) + N_2 \rightarrow N + N_2$	$2.3x10^{-14} \exp\left(-\frac{510}{T}\right)$	273
$N(^2P) + N \rightarrow N(^2D) + N$	$1.8x10^{-12}$	130
$N(^2P) + N \rightarrow N(^2D) + N$	$6.0x10^{-13}$	273
$2N + N_2 \rightarrow N_2(B^3\Pi_g) + N_2$	$2.4x10^{-33}$	130
$2N + N_2 \rightarrow N_2(A^3\Sigma_u) + N_2$	$1.7x10^{-33}$	130
$N(^2P) + N_2 \rightarrow N + N_2$	$6.0x10^{-14}$	273
$N_2(a^1\Sigma_u) + N_2(A^3\Sigma_u) \rightarrow N_4^+ + e^-$	$4.0x10^{-12}$	130
$N_2(a^1\Sigma_u) + N_2(a^1\Sigma_u) \rightarrow N_4^+ + e^-$	$1.0x10^{-11}$	130
$N_2(Vw) + N_2(Vy) \leftrightarrow N_2(Vw-1) + N_2(Vy+1)$	$5.65 x 10^{-11} \exp(-72.7 T^{-1/3} + 131 T^{-2/3})$	75,130
$N_2(Vx) + M \leftrightarrow N_2(Vx-1) + M$	$3.16 x 10^{-4} \exp(-395 T^{-1/3} + 842 T^{-2/3})$	75,130
$N + N \rightarrow N_2^+ + e^-$	$2.7x10^{-11} \exp\left(-\frac{67400}{T}\right)$	130
$N + NO \rightarrow N_2 + O$	$1.66x10^{-11}$	274
$N + O_2 \rightarrow O + NO$	$2.36x10^{-11} \exp\left(-\frac{44.23}{RT}\right)$	275
$O + NO_2 \rightarrow NO + O_2$	$9.05x10^{-12} \left(\frac{T}{298}\right)^{-0.52}$	276
$NO + NO + O_2 \rightarrow NO_2 + NO_2$	$3.30x10^{-39} \exp\left(\frac{4.41}{RT}\right)$	222
$N_2O + M \rightarrow N_2 + O + M$	$1.20x10^{-9} \exp\left(-\frac{240.00}{RT}\right)$	277
$NO + O \rightarrow NO_2$	$3.01x10^{-11} \left(\frac{T}{298}\right)^{-0.75}$	278
$NO_2 + M \rightarrow NO + O + M$	$9.40x10^{-5} \left(\frac{T}{298}\right)^{-2.66} \exp\left(-\frac{311.00}{RT}\right)$	278
$NO_2 + O + CO_2 \rightarrow NO_3 + CO_2$	$6.59x10^{-30} \left(\frac{T}{298}\right)^{-3.94} \exp\left(-\frac{9.56}{RT}\right)$	278
$NO_2 + O + N_2 \rightarrow NO_3 + N_2$	$3.31x10^{-30} \left(\frac{T}{298}\right)^{-4.08} \exp\left(-\frac{10.31}{RT}\right)$	278
$N_2O_5 + M \rightarrow NO_2 + NO_3 + M$	$2.10x10^{-11} \left(\frac{T}{300}\right)^{3.50} \exp\left(-\frac{91.46}{RT}\right)$	123
$CO_2 + NO \rightarrow CO + NO_2$	$\left(\frac{1}{30}\right)x10^{(-10.59 - (\frac{32500}{4.587}))}$	279
$C + N_2 \rightarrow CN + N$	$8.70x10^{-11} \exp\left(-\frac{188.00}{RT}\right)$	174
$C + NO \rightarrow CN + O$	$3.32x10^{-11}$	182
$CN + O \rightarrow CO + N$	$\left(\frac{1}{5}\right)x1.69x10^{-11}$	146
$CO + N \rightarrow CN + O$	$3.84x10^{-9} \exp\left(-\frac{275.05}{RT}\right)$	280,281

$C_2N_2 + M \rightarrow CN + CN + M$	$3.65 \times 10^{-1} \left(\frac{T}{298}\right)^{-4.32} \exp\left(-\frac{545.00}{RT}\right)$	282
$CN + NO_2 \rightarrow NO + NCO$	$1.02 \times 10^{-8} (T)^{-0.80} \exp\left(-\frac{173.63}{T}\right)$	283
$N + NCO \rightarrow CN + NO$	1.66×10^{-12}	284
$N + NCO \rightarrow CO + N_2$	3.30×10^{-11}	146
$CN + O_2 \rightarrow O + NCO$	$\left(\frac{1}{2.77}\right) 1.16 \times 10^{-11}$	285
$O + NCO \rightarrow CN + O_2$	$4.05 \times 10^{-10} \left(\frac{T}{298}\right)^{-1.43} \exp\left(-\frac{29.10}{RT}\right)$	286
$O + NCO \rightarrow CO + NO$	7.51×10^{-11}	286
$CO_2 + CN \rightarrow CO + NCO$	$1.35 \times 10^{-12} \left(\frac{T}{298}\right)^{2.16} \exp\left(-\frac{112.0}{RT}\right)$	287
$NCO + NO \rightarrow N_2O + CO$	$5.15 \times 10^{-11} \left(\frac{T}{298}\right)^{-1.34} \exp\left(-\frac{2.99}{RT}\right)$	288
$NCO + NO \rightarrow CO_2 + N_2$	$1.29 \times 10^{-10} \left(\frac{T}{298}\right)^{-1.97} \exp\left(-\frac{4.66}{RT}\right)$	288
$NCO + NO \rightarrow CO + N_2 + O$	$0.23 \times 1.69 \times 10^{-11} \exp\left(\frac{1.63}{RT}\right)$	286
$NCO + NO_2 \rightarrow CO + NO + NO$	1.30×10^{-12}	289
$NCO + NO_2 \rightarrow CO_2 + N_2O$	$5.40 \times 10^{-12} \exp\left(\frac{354.81}{T}\right)$	283
$NCO + NCO \rightarrow N_2 + CO + CO$	3.01×10^{-11}	286
$NCO + M \rightarrow N + CO + M$	$1.69 \times 10^{-9} \exp\left(-\frac{195.0}{RT}\right)$	146
$N_2O + NCO \rightarrow CO + N_2 + NO$	$1.50 \times 10^{-10} \exp\left(-\frac{116.0}{RT}\right)$	286
$NCN + O \rightarrow N + NCO$	$4.02 \times 10^{-14} \left(\frac{T}{298}\right)^{0.42} \exp\left(\frac{0.66}{RT}\right)$	290
$NCN + O \rightarrow N_2 + CO$	$2.22 \times 10^{-16} \left(\frac{T}{298}\right)^{2.32} \exp\left(\frac{4.75}{RT}\right)$	290
$NCN + O \rightarrow CN + NO$	$1.54 \times 10^{-10} \exp\left(-\frac{5.80}{RT}\right)$	291
$NCN + NO \rightarrow CN + N_2O$	$3.16 \times 10^{-12} \exp\left(-\frac{26.30}{RT}\right)$	292
$NCN + O_2 \rightarrow NO + NCO$	$1.15 \times 10^{-13} \left(\frac{T}{298}\right)^{0.51} \exp\left(-\frac{103.00}{RT}\right)$	293
$NCN + NCN \rightarrow CN + CN + N_2$	6.14×10^{-12}	291
$NCN + M \rightarrow C + N_2 + M$	$1.48 \times 10^{-9} \exp\left(-\frac{260.00}{RT}\right)$	291
$NO + NO_2 + M \rightarrow N_2O_3 + M$	$3.09 \times 10^{-34} \left(\frac{T}{298}\right)^{-7.70}$	123
$N_2O_3 + M \rightarrow NO + NO_2 + M$	$1.91 \times 10^{-7} \left(\frac{T}{298}\right)^{-8.70} \exp\left(-\frac{40.57}{RT}\right)$	123

$\text{NO}_2 + \text{NO}_2 + \text{M} \rightarrow \text{N}_2\text{O}_4 + \text{M}$	$1.40 \times 10^{-33} \left(\frac{T}{298}\right)^{-3.80}$	123
$\text{N}_2\text{O}_4 + \text{M} \rightarrow \text{NO}_2 + \text{NO}_2 + \text{M}$	$1.30 \times 10^{-5} \left(\frac{T}{298}\right)^{-3.80} \exp\left(-\frac{53.21}{RT}\right)$	123
$\text{CO}_2 + \text{N} \rightarrow \text{CO} + \text{NO}$	5.00×10^{-16}	294
$\text{CO}_2 + \text{N}(^2\text{D}) \rightarrow \text{CO} + \text{NO}$	3.60×10^{-13}	273
$\text{CO} + \text{N}_2\text{O} \rightarrow \text{CO}_2 + \text{N}_2$	$5.30 \times 10^{-13} \exp\left(-\frac{84.81}{RT}\right)$	278
$\text{NO}_3 + \text{O}_3 \rightarrow \text{NO}_2 + \text{O}_2 + \text{O}_2$	1.00×10^{-17}	295
$\text{CO} + \text{M} \rightarrow \text{C} + \text{O} + \text{M}$	$1.52 \times 10^{-4} \left(\frac{T}{298}\right)^{-3.10} \exp\left(-\frac{1073.00}{RT}\right)$	296
$\text{C} + \text{NO} \rightarrow \text{CO} + \text{N}$	4.82×10^{-11}	297
$\text{CN} + \text{NO}_2 \rightarrow \text{CO} + \text{N}_2\text{O}$	$0.08 \times 5.01 \times 10^{-11} \exp\left(\frac{1.42}{RT}\right)$	298
$\text{CN} + \text{NO}_2 \rightarrow \text{CO}_2 + \text{N}_2$	$0.06 \times 5.01 \times 10^{-11} \exp\left(\frac{1.42}{RT}\right)$	298
$\text{N} + \text{CN} + \text{M} \rightarrow \text{NCN} + \text{M}$	2.76×10^{-32}	299
$\text{CN} + \text{N}_2\text{O} \rightarrow \text{NCN} + \text{NO}$	$1.73 \times 10^{-14} \left(\frac{T}{298}\right)^{2.60} \exp\left(-\frac{15.46}{RT}\right)$	286
$\text{NCN} + \text{NO}_2 \rightarrow \text{ONCN} + \text{NO}$	$7.80 \times 10^{-12} \exp\left(-\frac{38.00}{RT}\right)$	292
$\text{C}_2\text{N}_2 + \text{O} \rightarrow \text{CN} + \text{NCO}$	$4.15 \times 10^{-11} \exp\left(-\frac{45.73}{RT}\right)$	300
$\text{C}_2\text{N}_2 + \text{O} \rightarrow \text{NCN} + \text{CO}$	$2.31 \times 10^{-10} \exp\left(-\frac{7540.00}{T}\right)$	301
$\text{C}_2\text{N} + \text{N} \rightarrow \text{CN} + \text{CN}$	1.0×10^{-10}	302
$\text{C}_2\text{N} + \text{O} \rightarrow \text{CN} + \text{CO}$	5.99×10^{-12}	303
$\text{C}_2 + \text{NO} \rightarrow \text{C}_2\text{N} + \text{O}$	$0.70 \times 1.25 \times 10^{-10} \exp\left(-\frac{36.17}{RT}\right)$	304
$\text{C}_2\text{N}_2 + \text{C} \rightarrow \text{CN} + \text{C}_2\text{N}$	3.01×10^{-11}	302
$\text{C}_2\text{N}_2 + \text{N} \rightarrow \text{C}_2\text{N} + \text{N}_2$	$4.98 \times 10^{-8} \exp\left(-\frac{17500.00}{T}\right)$	305
$\text{N}_2\text{O}_5 + \text{O} \rightarrow \text{N}_2 + \text{O}_2 + \text{O}_2 + \text{O}_2$	$3.00 \times 10^{-16} \left(\frac{T}{300}\right)^{0.50}$	306
$\text{CN} + \text{NO} \rightarrow \text{NCN} + \text{O}$	$2.99 \times 10^{-11} \exp\left(-\frac{19220.00}{T}\right)$	307
$\text{CN} + \text{NCN} \rightarrow \text{N} + \text{C}_2\text{N}_2$	3.32×10^{-11}	307
$\text{N} + \text{NCN} \rightarrow \text{N}_2 + \text{CN}$	1.66×10^{-11}	307
$\text{NCN} + \text{M} \rightarrow \text{N} + \text{CN} + \text{M}$	$8.47 \times 10^{-9} \exp\left(-\frac{53300.00}{T}\right)$	307
$\text{C} + \text{NCN} \rightarrow \text{CN} + \text{CN}$	1.66×10^{-11}	307
$\text{C} + \text{NCO} \rightarrow \text{CN} + \text{CO}$	1.66×10^{-11}	307
$\text{NCN} + \text{NCO} \rightarrow \text{CN} + \text{N}_2 + \text{CO}$	1.66×10^{-11}	307

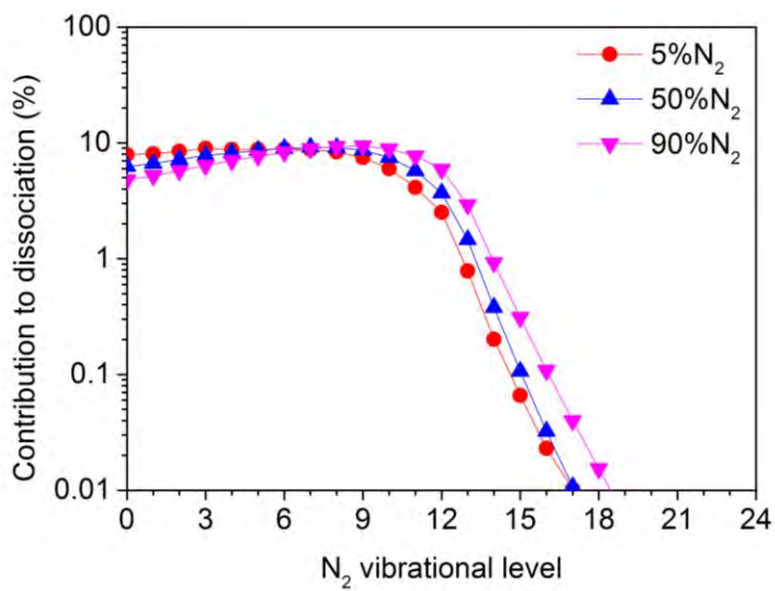


Figure A13: Contribution of the different vibrational levels of N₂ to the total dissociation of N₂ at three different N₂ fractions in the mixture.

Chapter 6: CO₂ Conversion in Nanosecond Repetitively Pulsed (NRP) Discharge

The results presented in this Chapter were published in:

- Heijkers, S.; Martini, L. M.; Dilecce, G.; Tosi, P.; Bogaerts, A. Nanosecond Pulsed Discharge for CO₂ Conversion: Kinetic Modeling To Elucidate the Chemistry and Improve the Performance. *J. Phys. Chem. C* **2019**, *123*, 12104–12116

6.1 Introduction

NRP discharges exhibit conversions up to 45 %, with energy efficiencies up to 60 % for dry reforming ³⁴, and CO₂ conversions of 10-20 % with energy efficiencies of 12-30 % for pure CO₂ splitting ³⁵. It is suggested that this type of discharge shows a high degree of non-equilibrium, explaining these high conversions and energy efficiencies ^{34,35}. Detailed diagnostics experiments in pure CO₂ and CO₂/H₂O mixtures have recently been performed ^{35,37}, but to our knowledge, no chemical kinetics model has been developed yet, to support the experiments, and to obtain additional insight in the underlying mechanisms, responsible for the high conversions and energy efficiencies. Such a model could be helpful to further improve the performance of NRPs for energy-efficient CO₂ conversion. Therefore, this Chapter presents the CO₂ conversion and underlying chemistry in an NRP discharge.

Section 6.2 presents the chemistry set used in this study and Section 6.3 explains the specific approximations used to model the NRP discharge. This model is validated in Section 6.4 with experimental data on conversion/energy efficiency and gas temperature. Also the evolution of the most important physical characteristics, such as gas temperature, conversion and electron density, is presented. Section 6.5 focuses on the most important conversion mechanisms of CO₂ and Section 6.6 on the importance of the vibrational levels in the dissociation process. Finally, in Section 6.7, the effect of cooling is studied and whether it can enhance the performance of the NRP discharge.

6.2 Chemistry set

The chemistry set used in this study is slightly different from the chemistry set in Chapter 3. It is based on the original model of Kozák et al.,⁵⁷ which was further evaluated by Berthelot et al.³⁰⁸. It contains 58 different species (see Table 6), i.e., four ground state molecules, three radicals, 11 ions, the electrons, and 39 excited species, including the 21 vibrational levels of the asymmetric stretch mode up to the dissociation limit. The difference with the chemistry set presented in Chapter 3 is that in this set, the species of minor importance to the plasma chemistry and their formation and destruction mechanisms, i.e. mainly complex C₂ ions and radicals and positive ions of pure oxygen species, were removed, which reduces not only the complexity but also the uncertainty of the model results^{308,309}.

These species react with each other, by means of electron impact reactions, electron-ion recombination reactions, ion-ion, ion-neutral and neutral-neutral reactions, as well as vibration-translation (VT) and vibration-vibration (VV) relaxation reactions; see detailed reaction set in the Appendix of this Chapter. The electron impact reaction rate constants are calculated using a pre-evaluated electron energy distribution function (EEDF; which is regularly updated during the simulations based on the new chemical composition in the plasma) and the cross section set of Phelps with the 7 eV threshold excitation reaction used for dissociation⁵⁹⁻⁶¹ as suggested by Grovulovic' et al.⁶², Bogaerts et al.⁶³ and Pietanza et al.⁶⁴⁻⁶⁶.

Table 6: Species taken into account in the 0D model (the symbols (V) and (E) stand for the vibrational and electronically excited levels, respectively).

Molecules	Charged species	Radicals	Excited species
CO ₂ , CO	CO ₂ ⁺ , CO ₄ ⁺ , CO ⁺ , C ₂ ⁺ , C ⁺ , CO ₃ ⁻ , CO ₄ ⁻	C	CO ₂ (Va, Vb, Vc, Vd), CO ₂ (V1-V21), CO ₂ (E1), CO(V1-V10)
O ₂ , O ₃	O ⁺ , O ₂ ⁺ , O ⁻ , O ₂ ⁻	O	O ₂ (V1-V4)
	Electrons		

6.3 Modelling the NRP discharge with a 0D approach

The NRP discharge under study is based on the experimental design used by Martini et al. ³⁵, schematically illustrated in Figure 24. The discharge is maintained in a pin-to-sphere configuration. The high-voltage (HV) pin electrode is a narrow tube with an external diameter of 1.65 mm, and an internal diameter of 1.2 mm, through which the inlet gas flows. The grounded electrode is a stainless steel sphere with 8 mm diameter, containing the outlet. The interelectrode distance is 5 mm. The electrodes assembly is contained in a vacuum-tight chamber made of a 35 mm diameter glass tube, in which a pressure equal to atmospheric pressure is maintained. The gas flows from the HV anode at a rate of 100 sccm, it flows around the cathode and exits the chamber through two 2 mm diameter apertures about 30 mm downstream the cathode. The pulse is triangular with a duration of 10 ns (FWHM) and the pulse energy is varied between 7.2 mJ and 13.8 mJ. This corresponds to average powers ranging from 0.72 MW till 1.38 MW and maximum powers inside the pulse ranging from 1.44 MW till 2.76 MW. Finally, the pulse frequency is varied between 600 Hz and 3 kHz.

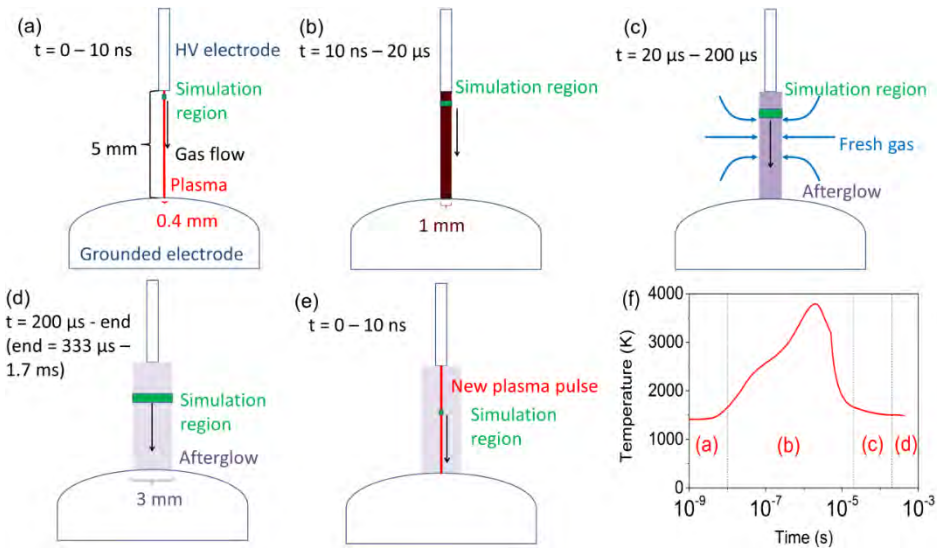


Figure 34: Schematic illustration of the discharge setup, described in the 0D model, during the pulse (a), at the end and right after the pulse when most heating takes place (b), in the afterglow when new gas enters the plasma region till $200 \mu\text{s}$ after the pulse (c), and before the next pulse starts (d). Finally, the cycle begins again for subsequent pulses, where the new plasma is surrounded by partially converted CO_2 gas (e). The red area represents the plasma, the black-grey zone indicates the afterglow (with a darker color yielding a higher temperature). An example of the temperature evolution of one pulse and afterglow is given in panel (f) for an intermediate specific energy input (SEI) of $2.6 \text{ eV molecule}^{-1}$. In general, the maximum temperature varies between 2550 K and 4150 K, while it is between 660 K and 1756 K after cooling down in the afterglow, for SEI values ranging between $0.7 \text{ eV molecule}^{-1}$ and $4.7 \text{ eV molecule}^{-1}$. It takes minimum 7 pulses (for $\text{SEI} = 0.7 \text{ eV molecule}^{-1}$ and frequency of 600 Hz) and maximum 14 pulses (for $\text{SEI} = 3.0 \text{ eV molecule}^{-1}$ and frequency of 3 kHz) for CO_2 molecules to travel from HV electrode to grounded electrode. It should be noted that, although the frequency differs by a factor 5, the pulse difference is only a factor 2, due to a larger gas expansion effect at the higher SEI value, and thus it takes less time to travel the interelectrode distance.

Modelling the NRP discharge with a 0D model is quite challenging, because the plasma volume rises during the pulse and afterglow, and the surrounding gas can enter the plasma volume (see Figure 34), and these effects are not automatically captured in a 0D model. Therefore, the following assumptions had to be made:

- The plasma region is assumed to be initially a cylinder with 5 mm length, i.e. the interelectrode distance, and an initial diameter of 0.4 mm, which

is the characteristic diameter of a streamer in air¹⁴. A similar value (0.35 mm) was also measured by Stancu et al.³¹⁰ in a similar configuration for an interelectrode distance of 4 mm and a pulse duration of 10 ns in air, albeit for a maximum power of 0.1 MW per pulse, which is about ten times lower than the typical powers used in the NRP discharge under study here³⁵. More recently, Castela et al. mentioned a diameter of 0.45 mm³⁶ for an interelectrode distance of 1 mm and an energy per pulse ($\tau=20$ ns) of 1.4-1.5 mJ in a lean methane-air mixture, which corresponds to a maximum power of 0.07 - 0.075 MW per pulse. Furthermore, Lo et al.³¹¹, reported a discharge diameter after the pulse of approximately 1 mm, using an energy of 20 mJ per pulse with 20 ns pulse duration, corresponding to a power of 1 MW, for a discharge gap of 6.5 mm in air. The latter configuration is closest to the one under study here. Finally, the discharge diameter has also been used in modelling work by Popov³¹², who assumed a value of 1 mm as well. Therefore, during the pulse, the plasma volume is increased, by increasing the diameter from 0.4 mm till 1 mm (panel (a) and (b) in Figure 34). This determines the plasma volume, i.e., the volume in which the power is deposited (i.e., rising from 0.6 mm³ at the start, until 3.9 mm³ at the end of the pulse).

- In between pulses, no power is deposited, but chemical reactions can still take place in this “afterglow” region, due to the high temperature (see also Figure 38) and reactive species present. The diameter of the afterglow region does not stay constant either, as shown by Castela et al.³⁶. A constant diameter of 1 mm is assumed until 20 μ s after the pulse, as demonstrated by calculations of Castela et al.³⁶. After 20 μ s, the diameter increases to 2.4 mm at 138 μ s and to 3 mm at 200 μ s (panel (c) and (d) in Figure 34). This means that extra gas enters the afterglow region. The final diameter of 3 mm is held constant during the rest of the interpulse time, based on the experimental data in³⁶. When a new pulse starts, the diameter of the plasma volume is again set to 0.4 mm (panel (e)), repeating the above cycle for all pulses. However, starting from the second pulse, the fresh gas in the afterglow is not pure CO₂ anymore, but has a gas composition adopted from the end of the afterglow of the previous pulse (as schematically illustrated in panel (e) of Figure 34).

- The gas temperature is calculated self-consistently in the same manner as done by Kozak et al.⁴⁵ (see also equations 19 and 29, in Chapter 2 and 3, respectively) . P_{ext} is given by:

$$P_{ext} = \frac{8\lambda}{R^2} (T_g - T_{g,i}) \quad (37)$$

where λ is the gas thermal conductivity of CO₂ (see equation 29) (in W m⁻¹ K⁻¹), R the radius of the plasma zone, T_g the plasma gas temperature and $T_{g,i}$ the gas temperature just before the start of the pulse, i.e. 293.15 K at the beginning of the simulation, or the gas temperature at the end of the afterglow of the previous pulse. Greig et al.³¹³ and Shneider³¹⁴ showed that in ns-pulsed discharges turbulent cooling is important. Therefore, equation (37) is multiplied by a factor 9 to incorporate the more effective turbulent cooling, based on 2D fluid dynamics simulations³³. This approach was also successfully applied in 0D simulations for a turbulent GAP (see Chapter 3).^{52,151,153} Generally, the temperature increases slightly inside the pulse with a large rise just after the pulse, as illustrated in panel (f) in Figure 34, and experimentally measured by Martini et al.³⁵. From then on, due to gas expansion and dilution of the plasma mixture, the temperature in the afterglow drops (see also panel (f) in Figure 34) until the next pulse is reached.

- The temperature of the fresh gas entering the afterglow region (upon rising of this volume from 20 μ s up to 200 μ s; see panel (c) in Figure 34) is assumed to be equal to the average of the temperature inside the afterglow (i.e., ranging between 2550 K and 4150 K) and the temperature of the surrounding gas, based on Castela et al.³⁶ and Lo et al.³¹¹. The surrounding gas is initially at room temperature in the first pulse, while for the subsequent pulses, it is assumed to be equal to the temperature in the afterglow region just before the new pulse starts (i.e., ranging between 660K-1756 K).
- In addition, gas expansion occurs upon conversion of CO₂ into CO and $\frac{1}{2}$ O₂, so the gas pressure and mass flow rate is calculated at every time step from the actual species densities, gas temperature and velocity. The species densities (as calculated with the conservation equations; see

equation (12) in Chapter 2) and velocity are then corrected to account for this effect and to maintain a constant (atmospheric) pressure and mass flow rate, following the method of Kozak et al.⁴⁵ and also explained in Chapter 2 and 3. This gas expansion is initiated at 5 μs after the pulse, which is the typical time when this effect becomes visible³¹⁵. It is crucial to include this, as also stated by Pinhaõ et al.⁴⁴, to avoid systematic errors in computing process parameters in plug flow-like reactors. Indeed, serious speeding up of the gas after the pulse due to gas heating and conversion, as observed by Seydou et al.³¹⁶, would otherwise not be included and therefore the residence time and thus conversion could be largely overestimated.

The CO_2 conversion, X_{CO_2} , is defined as (see also Chapter 2):

$$X_{\text{CO}_2}(\%) = 100 \% \left(1 - \frac{n_{\text{CO}_2,e} v_e}{n_{\text{CO}_2,i} v_i} \right) \quad (38)$$

where $n_{\text{CO}_2,e}$ and v_e are the CO_2 density and gas velocity at the end of the plasma region near the grounded electrode, and $n_{\text{CO}_2,i}$ and v_i are the CO_2 density at room temperature and gas velocity at the inlet (pin electrode), i.e., 25.3 cm s^{-1} .

To evaluate the effect of the choice of initial plasma volume and of the volume expansion during the pulse and afterglow on the calculation results, the calculated CO_2 conversion as a function of specific energy input (SEI), for different assumed values of initial plasma diameter (figure 35(a)) and final afterglow diameter (figure 35(b)) is plotted. Upon increasing the initial plasma diameter, the CO_2 conversions drops, as expected, due to the lower power density deposited inside the pulses. In addition, a larger final afterglow diameter also yields a lower CO_2 conversion, despite the fact that it corresponds to a longer residence time and thus more deposited pulses for the same flow rate (see below). The reason is of course the more pronounced dilution of the afterglow volume with untreated CO_2 gas. The dip at $2.3 \text{ eV molec}^{-1}$ at larger final afterglow diameters can be explained by the smaller number of pulses deposited (defined by the frequency, and thus the time between pulses, which varies for the different SEI values; see also further in the text)

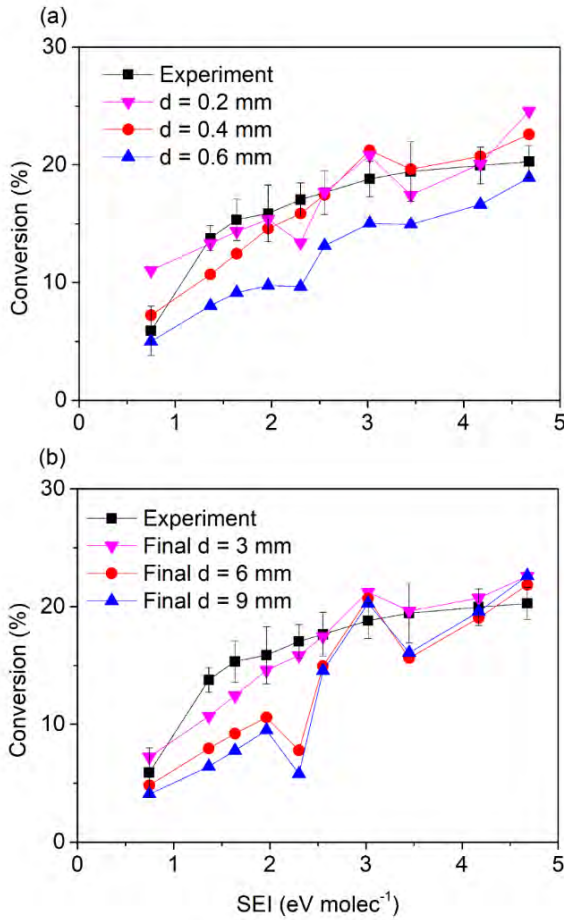


Figure 35: Experimental and calculated CO₂ conversions as a function of SEI, for different initial plasma diameters, and a final afterglow diameter of 3 mm (a), and for different final afterglow diameters at an initial plasma diameter of 0.4 mm (b), to evaluate the effect of the choice of these parameters on the calculated CO₂ conversion. In our model, we use an initial plasma diameter of 0.4 mm and a final plasma diameter of 3 mm (see above).

This inlet gas velocity would correspond to a gas residence time of about 20 ms. However, gas expansion due to conversion and gas heating greatly enhance the gas velocity and thus reduce the residence time, resulting in residence times ranging between 11.7 ms at SEI = 0.7 eV molec⁻¹ and 4.3 ms at SEI = 4.7 eV molec⁻¹. Together with the fact that the pulse duration is 10 ns, while the

afterglow time varies from 333 μs to 1.7 ms (depending on the exact power deposition and frequency used), these gas residence times correspond to 7-14 pulses (and corresponding afterglows), again depending on the exact power deposition and frequency used. The smallest number of pulses (i.e. 7) is at $\text{SEI} = 0.7 \text{ eV molec}^{-1}$ where the lowest frequency is used, i.e. 600 Hz. The largest number of pulses (i.e. 14) is at $\text{SEI} = 3.0 \text{ eV molec}^{-1}$ where the highest frequency is used, i.e. 3 kHz. This frequency is also applied at the highest SEI value studied, i.e. $4.7 \text{ eV molec}^{-1}$, but due to the higher power deposition, gas heating and gas expansion are higher in this case, so that the residence time is lower, and the molecules thus experience a lower number of pulses than at $\text{SEI} = 3.0 \text{ eV molec}^{-1}$. The maximum velocity obtained at $\text{SEI} = 4.7 \text{ eV molec}^{-1}$ is 596 cm s^{-1} , while at $\text{SEI} = 0.7 \text{ eV molec}^{-1}$, it is 293 cm s^{-1} . Seydou et al. ³¹⁶ measured a similar steady-state gas velocity of 370 cm s^{-1} after the pulse, for a pulse energy of approximately 1 mJ and a frequency of 30 kHz in methane-air- N_2 mixtures.

The number of pulses experienced by the gas molecules when travelling from HV electrode to grounded electrode is schematically illustrated in figure 36, for the case of the smallest and largest number of pulses.

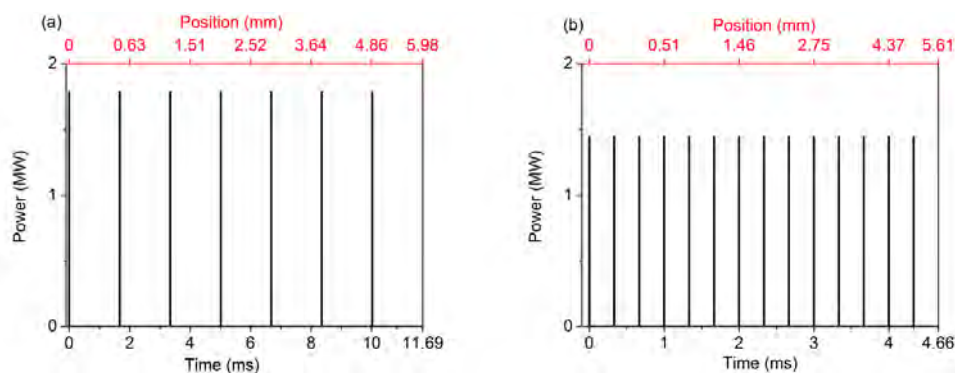


Figure 36: Power deposition in subsequent pulses as a function of time and position, at $\text{SEI} = 0.7 \text{ eV molec}^{-1}$ with frequency of 600 Hz, yielding the smallest number of pulses (i.e. 7) (a), and at $\text{SEI} = 3.0 \text{ eV molec}^{-1}$ with frequency of 3 kHz, yielding the largest number of pulses (i.e. 14) (b). Note that the position axis is non-linear due to gas expansion, which speeds up the gas and is most pronounced in the case of $\text{SEI} = 3.0 \text{ eV molec}^{-1}$. The time axis stops at the residence time for that particular condition.

After each pulse, between 20 μs and 200 μs , gas mixing is introduced in every time step, by diluting the afterglow mixture, using:

$$n_{s,new} = \frac{n_{s,old} r_{old}^2 + \omega_s N_{gas} (r_{new}^2 - r_{old}^2)}{r_{new}^2} \quad (39)$$

for each species s , where $n_{s,new}$ and $n_{s,old}$ are the species number densities after and before dilution, r_{new} and r_{old} are the radii of the afterglow volume at the current and previous timestep, respectively, ω_s is the fraction of species s in the fresh incoming gas and N_{gas} the total gas density, calculated by the ideal gas law.

In the afterglow of the first pulse, the incoming gas is pure CO_2 . For the other pulses, it is equal to the gas composition obtained at the end of the afterglow of the previous pulse, as explained above, because some of the CO_2 has already been converted into CO , O and O_2 . If this gas mixing (due to fluid dynamics) would not be included and the plasma composition would only depend on the chemical kinetics, the calculated conversion at the lowest SEI studied ($0.7 \text{ eV molec}^{-1}$) would be already 20 % after one pulse. It is thus necessary to include the effect of gas mixing, even in an approximate way.

The *SEI* is originally calculated as ³⁵:

$$SEI(\text{kJ L}^{-1}) = \frac{P_d(\text{W})}{\Phi(\text{cm}^3 \text{s}^{-1})} = \frac{\widetilde{E}_p(\text{J}) f_p(\text{Hz})}{\Phi(\text{cm}^3 \text{s}^{-1})} \quad (40)$$

in which P_d is the overall power deposited to the NRP discharge, ranging from 5.34 W till 33.6 W (based on the combinations given in Table 7, which are also the experimental conditions from Martini et al. ³⁵), \widetilde{E}_p the average discharge pulse energy, ranging from 7.2 mJ till 13.8 mJ, f_p the pulse repetition frequency, ranging from 600 Hz till 3 kHz, and Φ the gas flow rate, taken constant at 100 sccm or $1.67 \text{ cm}^3 \text{ s}^{-1}$. Since it is more convenient to express this unit in eV molec^{-1} to better assess the energy efficiency, the SEI can also be calculated as:

$$SEI(\text{eV molec}^{-1}) = \frac{SEI(\text{kJ L}^{-1}) 22.4(\text{L mol}^{-1}) 6.242 \times 10^{21}(\text{eV kJ}^{-1})}{6.022 \times 10^{23}(\text{molec mol}^{-1})} \quad (41)$$

The combinations of average discharge pulse energy and frequency used in this study (see Table 7) correspond to the above mentioned overall power deposition range, and thus to SEI values ranging between 3.2 kJ L^{-1} and 20.2 kJ L^{-1} , or

between 0.7 eV molec⁻¹ and 4.7 eV molec⁻¹. The exact energy deposited per pulse, applied frequency, and the corresponding number of pulses deposited (accounting for gas expansion), are plotted for each SEI value investigated in the Appendix: Figure A14. Using these quantities, the energy efficiency η (in %) and the energy cost (EC) (in eV molec⁻¹) can be calculated:

$$\eta(\%) = \frac{x_{CO_2}(\%) \Delta H_{CO_2}(eV \text{ molec}^{-1})}{SEI (eV \text{ molec}^{-1})} \quad (42)$$

$$EC(eV \text{ molec}^{-1}) = \frac{SEI(eV \text{ molec}^{-1})}{x_{CO_2}(\%)/100} \quad (43)$$

where ΔH_{CO_2} is the energy cost to split one CO₂ molecule in CO and ½ O₂, i.e. 2.9 eV molec⁻¹.

Table 7: Conditions studied in the simulations and in the experiments from Martini et al.³⁵

SEI (kJ L ⁻¹)	SEI (eV molec ⁻¹)	Average energy per pulse (mJ)	Frequency (kHz)	Interpulse time (μs)	Overall power deposited, P _d (W)
3.2	0.7	8.9	0.6	1700	5.34
5.9	1.4	8.2	1.2	833	9.84
7.1	1.6	7.9	1.5	667	11.85
8.5	2.0	7.9	1.8	556	14.22
9.9	2.3	13.8	1.2	833	16.56
11.0	2.6	7.6	2.4	417	18.24
13.0	3.0	7.2	3	333	21.60
14.9	3.4	10.3	2.4	417	24.72
18.0	4.2	11.1	2.7	370	29.97
20.2	4.7	11.2	3	333	33.60

6.4 Validation of the model and overall plasma characteristics

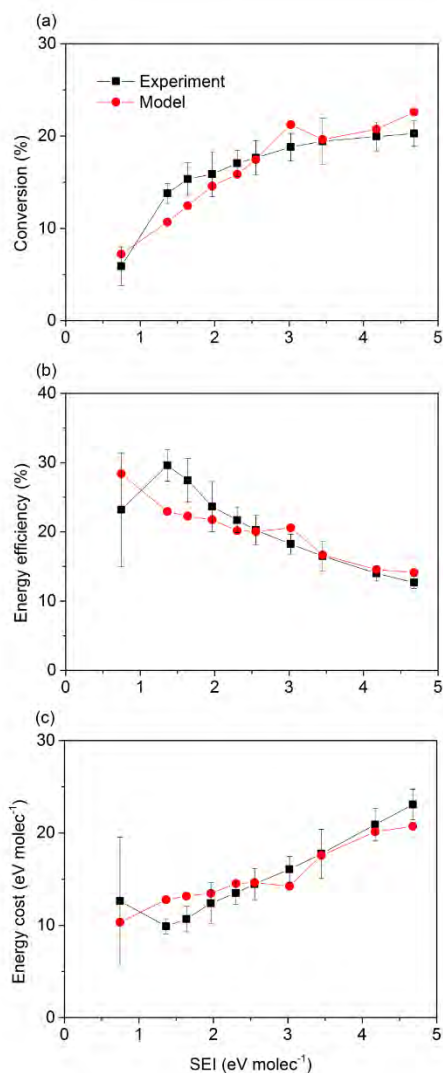


Figure 37: Calculated and experimental CO₂ conversion (a), energy efficiency (b) and energy cost (c), as a function of SEI.

To validate the model, the CO₂ conversion, energy efficiency and energy cost obtained at the end of the simulation, corresponding to the overall values obtained in experiments, are compared with the experimental data from Martini et al. ³⁵,

and they are plotted as a function of SEI in Figure 37. Moreover, in Figure 38 (a,b), the evolution of the calculated gas temperature and conversion in the afterglow as a function of time is compared with the experiments³⁵. These profiles are the same as the afterglows after the last pulse of the last burst. The conditions here are slightly different from those in Table 7, i.e., $SEI = 1.7 \text{ eV molec}^{-1}$, corresponding to bursts of four pulses, separated by $333 \mu\text{s}$ (i.e. 3 kHz), followed by a pause of 3.33 ms before the next burst starts. The average discharge pulse energy is set to 10 mJ, yielding a total of 8 pulses. In this way, the calculated and experimental conditions are the same. It should be noted that the pulses seem to be further apart at the later positions in Figures 38 (c) and (d). Indeed, due to heating and conversion of the gas, the gas velocity increases, and thus the “pulses” in gas temperature and conversion as a function of position are more spread out.

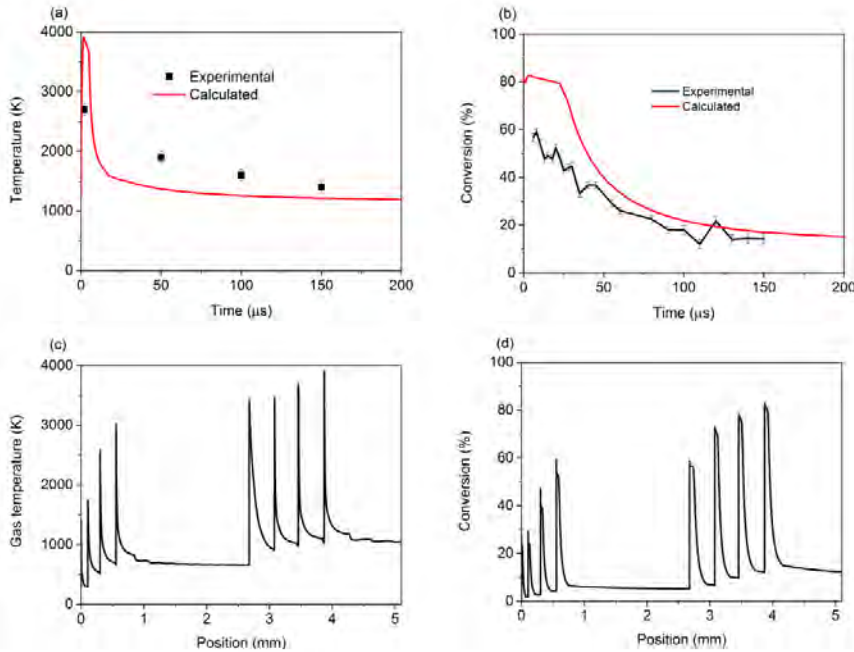


Figure 38: Evolution of temperature (a) and CO_2 conversion (b) as a function of time in the afterglow after the last pulse, in comparison with the experimental data of Martini et al.³⁵, and evolution of temperature (c) and CO_2 conversion (d) as a function of travelled distance between pin electrode and grounded electrode, all at $SEI = 1.7 \text{ eV molec}^{-1}$. Note that the model applies to pure CO_2 , while the experiments had to be carried out in the presence of 1.35 % H_2O .

The calculated overall CO₂ conversion, energy efficiency and energy cost show satisfactory agreement with the experiments in the entire range of SEI values, with an average relative error of 11 % for the conversion, energy efficiency and energy cost; see Figure 37. At the lower SEI values, the largest discrepancies are found, with a maximum relative error of 25 % at SEI = 1.4 eV molec⁻¹. In addition, at SEI = 0.7 eV molec⁻¹, the trend in energy efficiency and energy cost seems not correctly reproduced, but the experimental error bars are quite large for this lowest SEI value. The reason for the larger discrepancy at the lower SEI values can be due to the fact that we slightly overestimated the diameter of the plasma region at the lower SEI values. Indeed, the same value for all SEI values is assumed in the simulations (cf. Figure 34), but lower pulse energies usually give rise to a smaller plasma volume,³¹⁵ yielding a somewhat higher power density, and thus, a somewhat larger conversion would have been achieved if a somewhat smaller diameter would have been used. However, in general, the agreement between simulations and experiments is quite reasonable.

It is apparent that for similar SEI values, both the NRP discharge and the GAP discharge show similar energy efficiencies and conversions (see also Figure 11). The reason could be that although the total residence time in the pulses (~ns) is shorter than in the GAP (which is a more continuous discharge; residence time ~ms), CO₂ dissociation in the NRP is overall more efficient, i.e. significant dissociation from the highest asymmetric mode vibrational levels (see also sections 6.5 and 6.6), compensating for the shorter residence times.

The CO₂ conversion and gas temperature as a function of time in the afterglow, at SEI = 1.7 eV molec⁻¹, also shows satisfactory agreement with the experimental results, as can be seen in Figure 38 (a,b). It should be realized that the model applies to pure CO₂, while the experiments were carried out in the presence of 1.35 % H₂O, which was needed to produce the OH that was used to measure the fragmentation kinetics of CO₂ by collisional energy transfer laser-induced fluorescence and to determine the gas temperature profile. While the presence of 1.35 % H₂O might affect the gas temperature and CO₂ conversion to some extent, it will not be too critical for the purpose of this comparison.

The comparison is made for the afterglow of the last pulse, because the conversion and gas temperature do not change significantly anymore compared with the previous pulses (i.e. maximum relative increase of 6 % per pulse for the

temperature and 9 % for the conversion; see Figure 38(c,d)), so the system has more or less reached steady state conditions.

The conversion and gas temperature clearly drop in the afterglow, in both the model and experiments. In addition, although the conversion and gas temperature are overestimated right after the pulse, the absolute values show satisfactory agreement. The model indeed predicts extensive heating just after the pulse, yielding a significant temperature rise of about 2150 K right after the pulse for the particular SEI value of 1.7 eV molec⁻¹ and 1400 K on average for all conditions studied. This heating is attributed to both recombination reactions and VT relaxation (see Figure 39). More specifically, three-body recombination ($\text{CO} + \text{O} + \text{M} \rightarrow \text{CO}_2 + \text{M}$) is an exothermic reaction, and VT relaxation transfers energy from the CO₂ vibrational levels into translational modes of freedom, so both processes give rise to gas heating. As is clear from Figure 39, they both contribute on average with 35 % to the overall gas heating. Note that at SEI = 2.3 eV molec⁻¹ the relative importance of recombination is slightly higher than VT transfer, while the opposite is true for the other SEI values. This is because at this SEI value the energy deposited per pulse is higher (see Table 7, and Appendix: Figure A14(a)). Indeed, the SEI does not only depend on the energy deposited per pulse, but also on the time in between pulses (defined by the frequency), which is larger for this SEI value, compared to the SEI values of 2.0 eV molec⁻¹ and 2.6 eV molec⁻¹ (cf. Table 7 above). Therefore, cooling in between pulses is more effective at SEI = 2.3 eV molec⁻¹, which results in a lower final temperature at the end of the afterglow (i.e. this temperature is 1289 K at SEI = 2.0 eV molec⁻¹, 1026 K at SEI = 2.3 eV molec⁻¹, and 1484 K at SEI = 2.6 eV molec⁻¹) and thus somewhat less VT relaxation, as demonstrated in Figure 39. This, however, has no visible effect on the CO₂ conversion (cf. Figure 37).

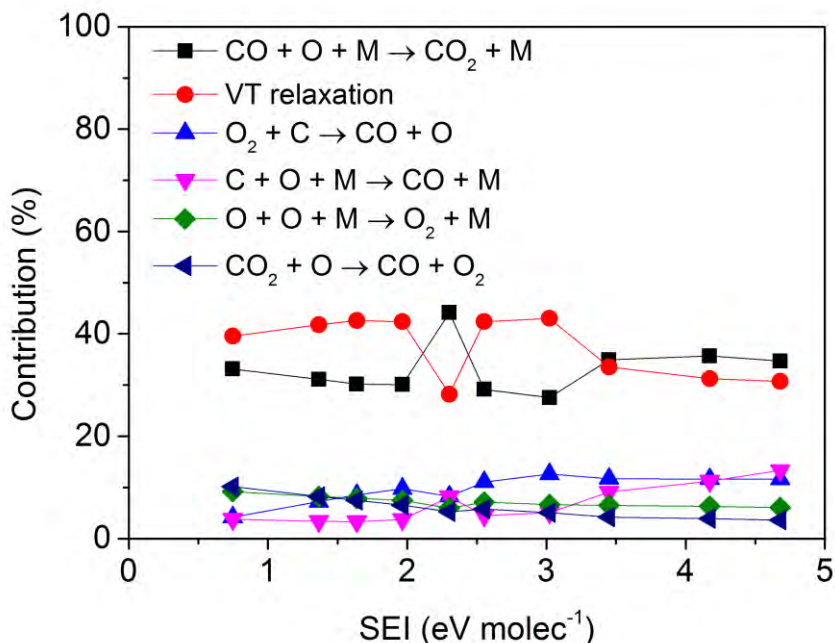


Figure 39: Contribution of the most important gas heating mechanisms after the pulse, as a function of SEI.

Figure 38 (b,d) also clearly demonstrates that the conversion drops from above 50 % at the end of the pulse, till below 20 % after 150 μ s in the afterglow. This is both attributed to recombination reactions (forming again CO₂; see also Section 6.4) and dilution of the converted gas mixture by fresh unreacted gas entering the plasma zone. Although a 0D model cannot capture all flow phenomena in an NRP discharge, the agreement with experiments is quite good, both for the conversion and gas temperature, so the model can be used to elucidate the chemistry occurring during the pulse and afterglow, which might help to further improve the overall performance of this type of plasma.

In Figure 40 the calculated plasma characteristics are plotted, i.e., gas temperature (a), electron temperature (b), electron density (c), and CO₂ conversion (d), for the lowest and highest SEI values studied, i.e. SEI = 0.7 eV molec⁻¹ and 4.7 eV molec⁻¹. The calculated plasma characteristics for the other SEI values lie in between these values, and are illustrated for two intermediate SEI values in the Appendix (Figure A15). The gas temperature becomes very

high in the early afterglow, with values exceeding 2000 K for the lowest SEI value of $0.7 \text{ eV molec}^{-1}$, and even above 4000 K for the highest SEI of $4.7 \text{ eV molec}^{-1}$. Subsequently, the gas cools quite fast, yielding a temperature around 660 K for $\text{SEI} = 0.7 \text{ eV molec}^{-1}$ and 1756 K for $\text{SEI} = 4.7 \text{ eV molec}^{-1}$ already 50 μs after the pulse (cf. also Figure 34(f)). The electron temperature (T_e) is still more than ten times higher (i.e. $T_e = 3.5 - 5 \text{ eV}$, or 40,600 K - 58,000 K), indicating that the plasma is clearly non-thermal for all conditions studied ¹⁴.

It is worth to mention that different pulse energies and different time between pulses, even if they result in the same overall SEI, can yield quite different values for the final gas temperature and gas temperature in the early afterglow, as can be seen when comparing Figure 38(c) for $\text{SEI} = 1.7 \text{ eV molec}^{-1}$ and Figure A15(a) for $\text{SEI} = 1.6 \text{ eV molec}^{-1}$. The final gas temperature and the gas temperature in the early afterglow are 1148 K and 3257 K, respectively, for $\text{SEI} = 1.6 \text{ eV molec}^{-1}$ and the corresponding values are 1029 K and 3911 K, respectively, for $\text{SEI} = 1.7 \text{ eV molec}^{-1}$. In the latter case, higher pulse energies lead to higher gas temperatures just after the bursts, but the large time between bursts (3.33 ms) cools the mixture down more efficiently, resulting in a somewhat lower final gas temperature.

The calculated electron densities during the pulse vary from $5 \times 10^{16} \text{ cm}^{-3}$ to $8 \times 10^{17} \text{ cm}^{-3}$, which corresponds well to experimental values obtained by Maqueo et al. ³¹⁷ (i.e. $\sim 1 \times 10^{16} \text{ cm}^{-3}$ for $\text{SEI} < 0.6 \text{ eV molec}^{-1}$ and around $3 \times 10^{17} \text{ cm}^{-3}$ for $\text{SEI} = 0.7\text{-}2.0 \text{ eV molec}^{-1}$ for CH_4 and CH_4/O_2 mixtures). Note that the electron densities are very high, due to the significant power density deposited during the ultrashort pulses, but these high densities are only reached for very short times. Both the electron temperature and density drop to negligible values in the afterglow of each pulse.

Finally, it is worth to stress that the CO_2 conversion is very high (reaching 100 % at the highest SEI value; cf. Figure 40(d)) at the end of the pulse, but it drops dramatically in the afterglow, as explained above, yielding a much lower overall CO_2 conversion when the gas mixture reaches the outlet at the grounded electrode (cf. Figure 37). Hence, the performance of NRP discharges could still be significantly improved if we could avoid this drop in CO_2 conversion upon pulse termination. Modelling can be very helpful to propose possible solutions for this, as we will illustrate in Section 6.6 below.

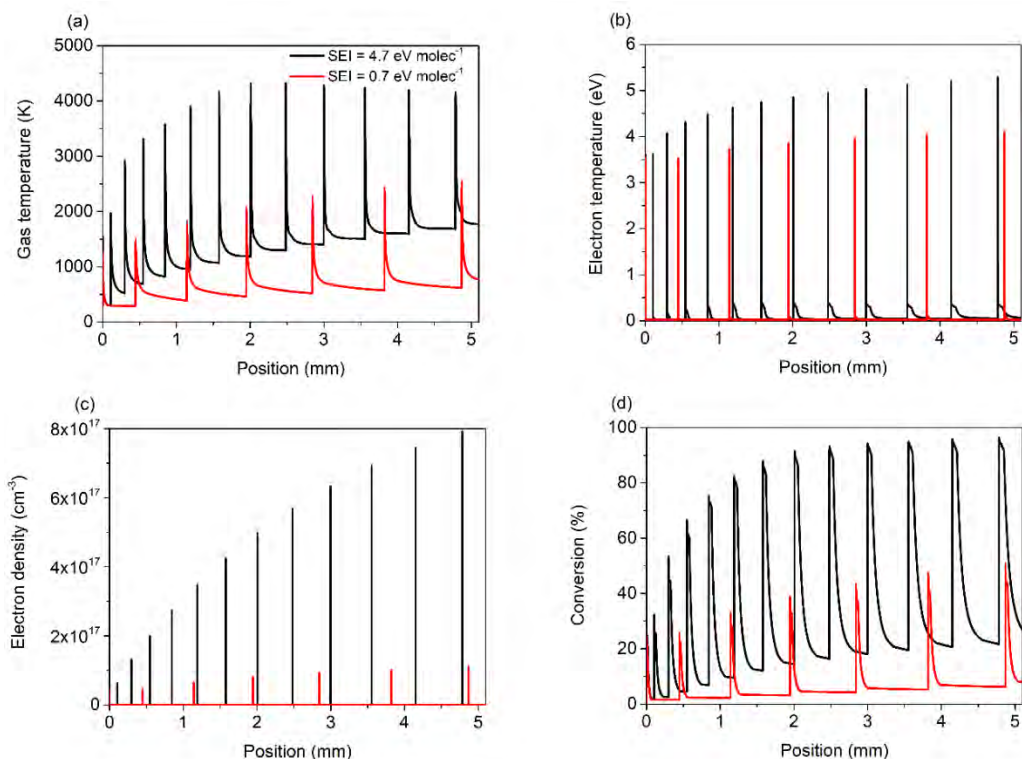


Figure 40: Calculated gas temperature (a), electron temperature (b), electron density (c), and CO₂ conversion (d), as a function of travelled distance between HV pin electrode and grounded electrode, for two different SEI values.

6.5 Chemical pathway analysis of CO₂ conversion

For all conditions studied, electron impact dissociation from vibrationally excited CO₂ is by far the dominant dissociation mechanism, with a relative contributions around 70 %, (see Figure 41). Electron impact dissociation from the CO₂ ground state contributes for about 10 %. It should be stressed that electron dissociation is in fact electronic excitation towards a repulsive state, from which dissociation takes place. Therefore, although vibrational excitation is important, the reduced electric field reaches values above 200 Td inside the pulses, favoring electronic excitation-dissociation from the already vibrationally excited CO₂ levels. Dissociation from vibrationally excited CO₂ upon collision with an O atom or with any gas molecule M also occurs, but three-body recombination (CO + O +

$M \rightarrow \text{CO}_2 + M$) is the dominant formation process of CO_2 (see Appendix: Figure A16, panel (c)). As a result, the net contributions of dissociation upon collision with an O atom or any molecule M are at maximum only about 15 % and a few %, respectively (see Figure 41). The above recombination reaction, together with mixing of the converted gas with unreacted gas during expansion in the afterglow, seriously limits the efficiency of NRP-based CO_2 conversion, as explained above.

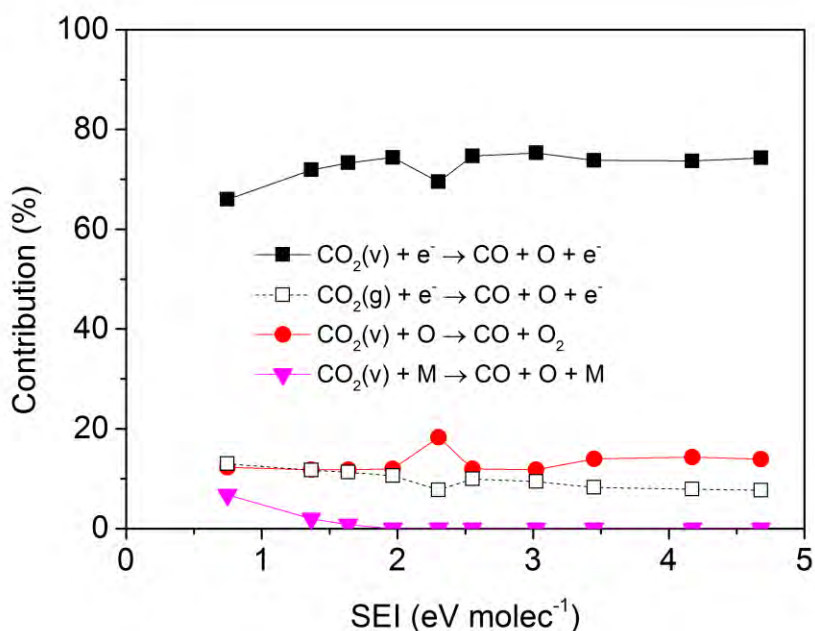


Figure 41: Relative net contributions of the main dissociation mechanisms of CO_2 , as a function of SEI.

The calculations reveal that the conversion mostly takes place during the pulses (~80 %) and a smaller fraction in the afterglows (~20 %) for all conditions studied (see Appendix: Figure A17). However, during the afterglows, three-body recombination ($\text{CO} + \text{O} + \text{M} \rightarrow \text{CO}_2 + \text{M}$) compensates for the extra CO_2 conversion, and even goes faster than dissociation for the higher SEI values, so that a fraction of the converted CO_2 during the pulses is formed again in the afterglows (see Figure A16, panels (b) and (d)). Hence, it is clear that if this

recombination reaction could be reduced, the performance of NRP discharges could be further enhanced.

6.6 Significant role of the CO₂ vibrational levels

From Figure 41 it is clear that vibrational excitation plays a crucial role for CO₂ dissociation at the conditions under study. Therefore, we plot the VDF in Figure 42, during the pulse (a) and at the end of the afterglow (b). During the pulse, there is obviously a high degree of vibrational excitation, with a large fraction of highly vibrationally excited CO₂, i.e., more than 20 % is excited into the asymmetric mode levels V6 and higher. Their fraction even rises a bit towards the end of the pulse, as is clear from Figure 42(a). After the pulse, vibrational excitation stops, as the electrons do not gain energy anymore when there is no power deposition. At the same time, both VT relaxation (causing major heating immediately after pulse termination, as discussed above) and dissociation from these excited levels largely depopulate these levels. Therefore, when reaching the end of the afterglow, only the lowest vibrational levels are still significantly populated (Figure 42(b)). Note that the VDF at the end of the afterglow of the first pulse shows a considerably lower population of the higher levels than for the last pulse, and for the latter there is a large difference for different SEI values. This is simply due to the higher gas temperature (cf. Figure 40(a)), i.e., the VDFs more or less exhibit a thermal distribution, but there is no overpopulation anymore due to vibrational excitation.

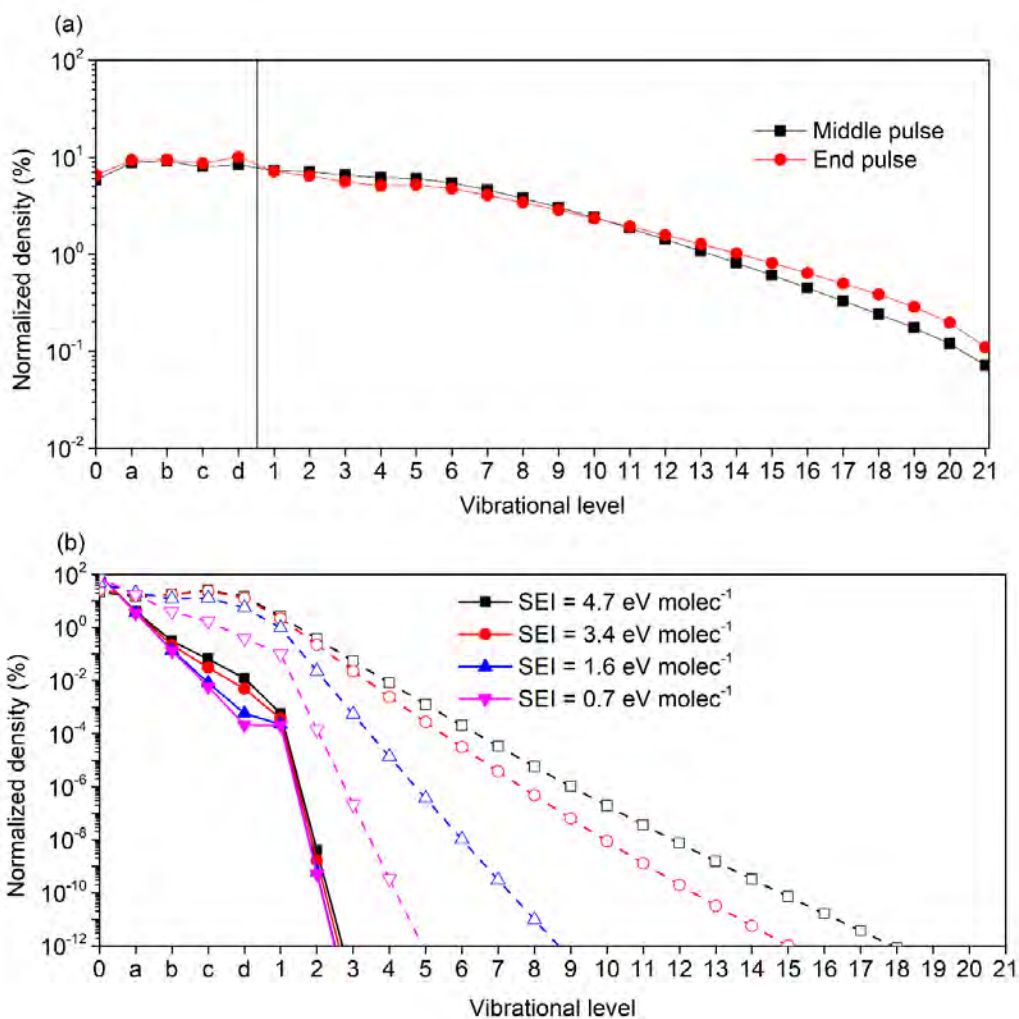


Figure 42: (a) Calculated VDF in the middle (5 ns) and at the end (10 ns) of the last pulse, at an SEI of 1.6 eV molec⁻¹. This result is representative for all pulses and all SEI values. (b) Calculated VDF at the end of the afterglow, for the first pulse (solid lines) and last pulse (dashed lines), for different SEI values. Note that “0” stands for the CO₂ ground state, “a-d” represent four effective symmetric mode levels at low energy, while “1-21” are the asymmetric mode vibrational levels up to the dissociation limit of 5.5 eV; see Chapter 3.

Vibrational pumping during the pulses is thus important in NRP discharges, at least for the conditions investigated. As can be seen in Figure 43 for an SEI of $1.6 \text{ eV molec}^{-1}$, only 9 % of all CO_2 dissociation occurs from the ground state, while the rest is from the vibrational levels, albeit mainly ($\sim 67 \%$) from the lowest and middle levels (i.e., the four effective symmetric mode levels at low energy (Va-Vd) and the asymmetric mode (levels V1-V15)). Note that the lowest levels (i.e. the four effective symmetric mode levels at low energy (Va-Vd) and the first five asymmetric mode levels (V1-V5)) have the highest contribution ($\sim 48 \%$), while the middle levels (i.e. V6-V15) only contribute for about 19 %, to the overall dissociation. In addition, 24 % of the total dissociation occurs from the highest asymmetric mode vibrational levels, which is quite striking and clearly indicates the overpopulation of these levels. Similar data are obtained at the other SEI values (see Appendix: Figure A18). Note that this figure only presents the contributions of the forward (dissociation) processes, not accounting for the reverse (recombination) reactions (see below).

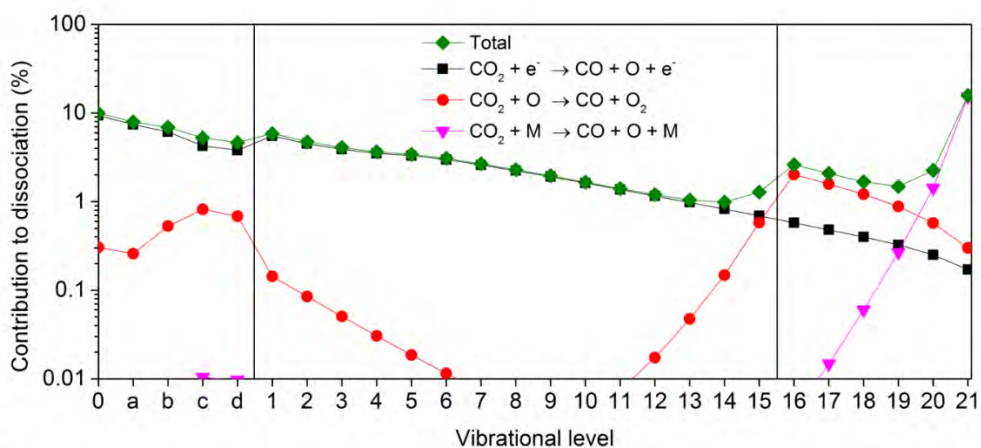


Figure 43: Contribution of the CO_2 ground state and the various vibrational levels to the total dissociation, as well as to the most important dissociation mechanisms, for an SEI of $1.6 \text{ eV molec}^{-1}$, only accounting for the forward reactions. The results for the other SEI values are illustrated in the Appendix.

When looking at the individual mechanisms (also plotted in Figure 43), electron impact dissociation through electronic excitation is by far the most important

dissociation mechanism for the lowest and middle levels (~94 %) (Va-Vd, and V1-V15), followed by dissociation upon collision with O atoms (~6 %). On the other hand, dissociation from the highest levels (V16-V21) is mainly due to dissociation upon collision with either an O atom (~49 %) or another molecule M (~28 %), while electron impact dissociation through electronic excitation contributes for ~23 %. Finally, dissociation from the ground state is mainly due to electron impact dissociation through electronic excitation (~97 %), but dissociation upon collision with an O atom also contributes for about 3 %. The latter process is possible since high gas temperatures can be reached, allowing thermal dissociation to occur. These relative contributions are also summarized in Table 8. Note that dissociation upon collision with another molecule M clearly becomes the dominant process for the highest vibrational levels, when only accounting for the forward reaction. However, when taking into account the reverse processes in the afterglow, i.e., three-body recombination ($\text{CO} + \text{O} + \text{M} \rightarrow \text{CO}_2 + \text{M}$), the net contribution of dissociation upon collision with another molecule M will become lower. We can thus conclude that overall, most dissociation occurs by electron impact from the lowest vibrational levels (i.e., Va-Vd, and V1-V5), i.e., about 48 %.

Table 8: Contribution of the CO_2 ground state, lowest and middle levels (Va-V15), and highest vibrational levels (V16-V21) to the total CO_2 dissociation (first row), and contribution of the different mechanisms to the dissociation of the ground state, lowest and middle levels, and highest vibrational levels of CO_2 .

	Ground state	Va-V15	V16-V21
Total dissociation	9 %	67 %	24 %
$\text{CO}_2 + \text{e}^- \rightarrow \text{CO} + \text{O} + \text{e}^-$	97 %	94 %	23 %
$\text{CO}_2 + \text{O} \rightarrow \text{CO} + \text{O}_2$	3 %	6 %	49 %
$\text{CO}_2 + \text{M} \rightarrow \text{CO} + \text{O} + \text{M}$	0 %	0 %	28 %

The vibrational kinetics thus play an important role in NRP discharges, explaining the promising conversions and energy efficiencies obtained (see Figure 37). When compared to reduced pressure MW plasmas, modelling

predicts optimal conversions of around 20 %, with energy efficiencies of 30 %, in a pressure range of 200-300 mbar^{25,318}. Van Rooij et al.³¹⁹ measured similar energy efficiencies (~30 %, but also up to ~45 %) with conversions of ~12 %, for pressures around 150-200 mbar, while at supersonic flows and reduced pressure, energy efficiencies around 90 % were experimentally found in 1983²², although these values have not been reproduced since then. Modelling showed that, at reduced pressure conditions, more than 70 % of all dissociation occurs through vibration-induced dissociation upon collision with O atoms or any other molecules M²⁵, and this is even more pronounced in supersonic flow conditions³⁰⁹. This process is in principle the most energy-efficient, and should be exploited. In our case, however, only about 15 % of the total dissociation is due to vibration-induced dissociation upon collision with O atoms (and only a few % due to collision with molecules M), as illustrated in Figure 41 above, which is attributed to the importance of the reverse (recombination) reaction ($\text{CO} + \text{O} + \text{M} \rightarrow \text{CO}_2 + \text{M}$), as explained above, thus limiting the conversion and energy efficiency. On the other hand, maximum energy efficiencies of around 30 % are still achieved at conversions around 15 %, for $\text{SEI} = 1.4 \text{ eV molec}^{-1}$, and this is reached in subsonic flow conditions at atmospheric pressure, which is more suitable for industrial application and upscaling. Furthermore, NRP discharges seem to perform better than MW discharges at atmospheric pressure, where a maximum energy efficiency of 20 %, corresponding to a CO_2 conversion of around 10 % was obtained, at a flow rate of 16 slm and 1.5 kW plasma power³²⁰. On the other hand, DIFFER obtained energy efficiencies of ~44 % in a reverse vortex flow MW plasma configuration at pressures larger than 600 mbar⁷². In such MW plasma at atmospheric pressure, the vibrational levels are in thermal equilibrium, resulting in dissociation almost exclusively from the lowest levels and ground state²⁵, whereas in our case, more than 20 % of all dissociation occurs from the highest levels.

A gliding arc (GA) also operates at atmospheric pressure. In a classical GA, the conversion reaches up to 8 %, with energy efficiency up to 40 %.²⁹ In the GAP, a similar maximum conversions around 8 % is typically reached, with an energy efficiency around 30 %, as shown in Chapter 3 above⁵². Hence, a somewhat higher conversion for the same energy efficiency is obtained in the NRP discharge. The reason is again that both in a classical GA and GAP, CO_2

dissociation also almost exclusively occurs from the lowest vibrational levels, either by electron impact dissociation through electronic excitation or dissociation upon collision with O atoms or any molecules M²⁹, whereas in the NRP a significant portion of dissociation occurs from the highest levels (cf. Figure 43), which is more energy efficient.

Finally, when compared to DBD, where energy efficiencies and conversions are typically reported up to 10 %³ (and clearly compete with each other, e.g., a maximum conversion of 30 % corresponds to an energy efficiency of only 2 %, and a maximum energy efficiency of 8 % corresponds to a conversion of about 2 %⁵⁶), the NRP discharge clearly performs better. Indeed, in DBDs, the energy-efficient vibration-induced dissociation is found to be negligible⁵⁵.

6.7 Cooling as a solution to improve the conversion and energy efficiency?

Although the NRP discharge exhibits already reasonable CO₂ conversion and energy efficiency, the simulations have also revealed the most important limitations, i.e., recombination in the afterglow (as well as mixing with fresh gas that has not passed through the plasma) and VT relaxation, causing thermalization of the VDF in the afterglow. Moreover, both processes cause significant heating, which induces even more recombination and VT relaxation (as the rate coefficients of both processes rise with temperature). Therefore, to stop this negative self-accelerating effect, external cooling in the afterglow is proposed, as a possible solution to improve the CO₂ conversion and energy efficiency in the NRP discharge.

Indeed, cooling can increase the non-equilibrium in the plasma, i.e., causing overpopulation of the vibrational levels, which may enhance the most energy efficient pathway of CO₂ conversion, i.e., through the vibrational levels. In fact, the most energy-efficient process is through dissociation of the highest vibrational levels upon collision with either an O atom or another molecule M, as predicted by Berthelot and Bogaerts²⁵. In addition, at lower temperature, the recombination reaction ($\text{CO} + \text{O} + \text{M} \rightarrow \text{CO}_2 + \text{M}$) in the afterglow might be reduced, thus also enhancing the net contribution of dissociation upon collision with molecules M (see above).

To verify the above hypotheses, the CO₂ conversion and corresponding energy efficiency is calculated for different cooling rates, and the results are plotted in Figure 44. These cooling rates are not fixed numbers, because the original cooling, which is dependent on the gas temperature and the plasma volume (cf. equation 37) is multiplied by some factor. However, the average cooling rates can be calculated throughout the whole simulation, and they are $6.4 \times 10^6 \text{ K s}^{-1}$ for the original (turbulent) cooling, $8.6 \times 10^6 \text{ K s}^{-1}$ for cooling x 2, $1.2 \times 10^7 \text{ K s}^{-1}$ for cooling x 5 and $1.4 \times 10^7 \text{ K s}^{-1}$ for cooling x 10. These extra cooling rates are in first instance an academic exercise. However, there are some practical possibilities to provide extra cooling. One way could be to reduce the external pressure, resulting in a higher expansion velocity, causing a larger cooling effect. Another way is to use a chemically inert gas as an extra cooling agent. Still another possibility could be water cooling, in which the CO₂ flux enters a water-cooled tube with a radius much smaller than the 35 mm diameter of the actual chamber, in which gas expansion is still possible, causing recirculation of the gas, which has been extra cooled by the wall. Finally, pre-cooling the mixture will result in a more efficient cooling in the afterglow because of mixing with a cold gas. In addition, in the post-plasma afterglow, gas can perhaps also be cooled using fluidized bed technology³²¹, where the intense contact between the gas and the cooler solid particles induces significant cooling, or creating an extra vortex flow/eddies to maximize turbulent cooling, as also suggested for plasma jets for medical purposes³²². Nevertheless, these possibilities still need to be evaluated in practice.

The original cooling was depicted in Figure 38(a) for SEI = $1.7 \text{ eV molec}^{-1}$, and is similar for the other SEI values as well (cf. Figure 40 and Appendix: Figure A15). A cooling rate twice as high has very little effect on the CO₂ conversion and energy efficiency (see Figure 44), but a five times higher cooling rate can enhance the conversion and energy efficiency up to a factor 1.7, at least for SEI values below $2.3 \text{ eV molec}^{-1}$. Likewise, ten times higher cooling yields an improvement in conversion and energy efficiency up to a factor 2.2.

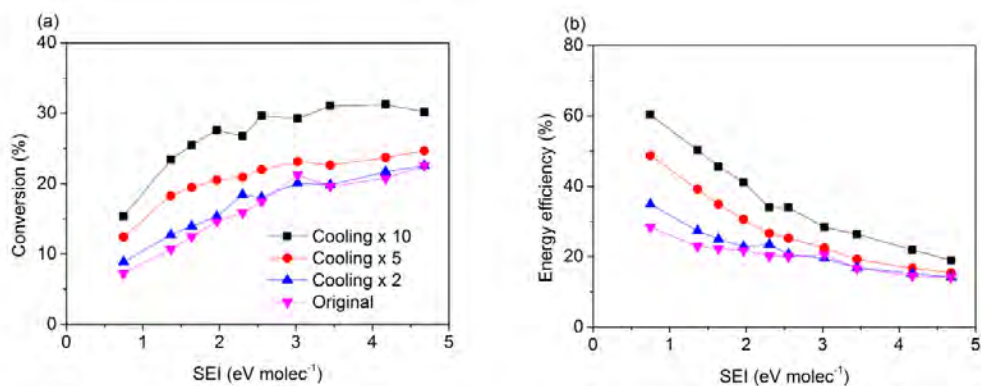


Figure 44: Calculated conversions (a) and energy efficiencies (b) as a function of SEI, for different cooling rates.

The resulting gas temperatures as a function of travelled distance from HV electrode to grounded electrode, i.e., passing several pulses and afterglows, are depicted in Figure A19, for these different cooling rates, and for the lowest, highest and an intermediate SEI value. Table 9 summarizes the maximum gas temperature and the temperature at the end of the afterglow, for the last pulse, calculated by the original model and when applying the different cooling rates, for three different SEI values, i.e. $0.7 \text{ eV molec}^{-1}$, $1.6 \text{ eV molec}^{-1}$ and $4.7 \text{ eV molec}^{-1}$. The maximum gas temperature reduces by only a factor 1.3 when applying a cooling rate twice as high as the original cooling, while it reduces by a factor 1.7 and 2.2 when applying a five or ten times higher cooling rate. This will affect the chemistry, as most rate coefficients are a function of temperature.

Table 9: Effect of the cooling rate on the maximum gas temperature and the gas temperature at the end of the afterglow for different SEI values.

Temperature (K)	At maximum			At end of afterglow		
	0.7	1.6	4.7	0.7	1.6	4.7
At SEI (eV molec ⁻¹)						
Original	2553	3257	4155	660	1148	1756
Cooling x2	2007	2623	3774	488	909	1450
Cooling x5	1531	1892	3091	348	628	1102
Cooling x10	1306	1417	2431	305	448	822

Figure 45 illustrates the relative net contributions of the different dissociation processes, as a function of SEI, for twice (a), five times (b) and ten times (c) higher cooling rate. While electron impact dissociation through electronic excitation from the CO₂ vibrational levels is still the dominant dissociation process, dissociation upon collision with another molecule M gradually becomes more important, at least for the lower SEI values. Indeed, while its contribution was only 1 % in the original model at an SEI value of 1.6 eV molec⁻¹ (cf. Figure 41), it is 3 %, 8 % and 23 % when applying twice, five times and ten times faster cooling, respectively. The reason is indeed as hypothesized above, i.e., the recombination reaction ($\text{CO} + \text{O} + \text{M} \rightarrow \text{CO}_2 + \text{M}$) drops at lower temperature, thus increasing the net contribution of the dissociation pathway upon collision with molecules M, especially from the highest vibrational levels. Indeed, Figure A20 in the Appendix shows the net contribution of the different vibrational levels to the total CO₂ dissociation, for the original model and with cooling rates times two, five and ten. It can be deduced that the net contribution of the highest vibrational levels (V16-V21) towards CO₂ dissociation increases from 14 % in the original model, to 23 %, 35 % and 39 % on average, at a cooling rate times two, five, and ten, respectively, at SEI values below 2.3 eV molec⁻¹. Only at the two lowest SEI values studied, i.e., SEI = 0.7 eV molec⁻¹ and 1.4 eV molec⁻¹, a ten times higher cooling rate does not promote extra dissociation upon collision with another molecule M. Indeed, the electron density also drops about a factor two at a cooling rate times ten compared to original cooling. This causes less

vibrational excitation, and thus a lower population of the highest vibrational levels, and therefore less dissociation from these levels. However, cooling also reduces gas expansion and results in a longer residence time and higher conversion and energy efficiency.

In general, as dissociation upon collision with molecules M, especially from the higher vibrational levels, is the most energy-efficient CO₂ dissociation mechanism (see above), the increasing contribution of this process explains the higher and more energy-efficient CO₂ conversion at higher cooling rates, as predicted by the model (cf. Figure 44).

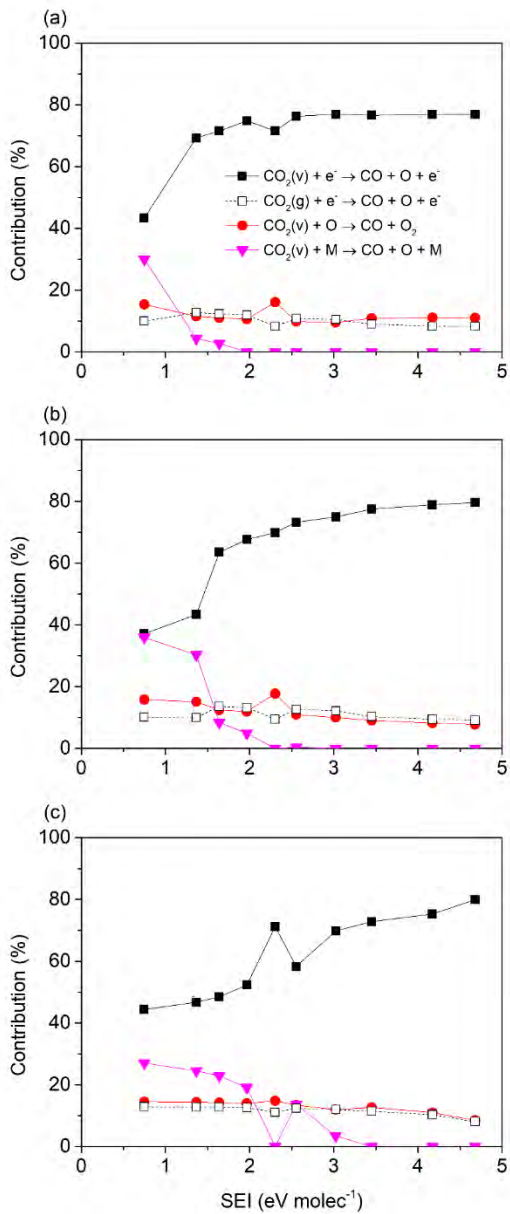


Figure 45: Net contribution of the different dissociation processes as a function of SEI, for a cooling rate twice (a), five times (b) and ten times (c) higher than in the original model. The results should be compared with Figure 41 above.

One could expect that the VDF would also show more pronounced overpopulation of the higher vibrational levels at higher cooling rates, but this is not predicted by the model (cf. Appendix: Figure A19). Indeed, the VDF at the end of the pulse is almost not affected, while the VDF at the end of the afterglow drops faster for the higher levels upon higher cooling. The latter can be explained by the fact that the VDFs are anyway thermalized at the end of the afterglow, and a lower gas temperature (upon higher cooling) thus causes a faster drop of the VDF. The fact that the VDF during the pulse is not affected, might at first sight be unexpected, as the lower VT rates would cause a more pronounced overpopulation of the higher vibration levels. However, the latter is compensated by the loss of these higher vibrational levels due to dissociation upon collision with other molecules M, as illustrated in Figures 45 and A20. Thus, although the net effect on the VDF is negligible, the loss process of these high vibrational levels is different: they do not get lost in VT relaxation (which is a pure loss process), but they are used for the most energy-efficient CO₂ dissociation process, explaining the rise in CO₂ conversion and energy efficiency, as illustrated in Figure 44 above.

It should be noted that applying extra cooling will also cost energy, so it will increase the SEI in practice, which is not accounted for in our simulations. Therefore, the enhancement in energy efficiency will be less pronounced than predicted by the model. However, conceptual studies like these are interesting to pinpoint how in theory it is possible to reach more energy-efficient CO₂ conversion in NRP discharges. In summary, the model predicts that a higher cooling reduces both VT relaxation and the recombination reaction ($\text{CO} + \text{O} + \text{M} \rightarrow \text{CO}_2 + \text{M}$) in the afterglow, so that the net contribution of dissociation of the higher vibrational levels upon collision with molecules M rises, and this generally explains the higher CO₂ conversion and energy efficiency.

6.8 Conclusion

We present a chemical kinetics model used to elucidate the main dissociation mechanisms of CO₂ in an NRP discharge. The calculated conversions and energy efficiencies are compared with experimental results in a wide range of SEI values, as well as the evolution of gas temperature and CO₂ conversion in the afterglow. The calculation results are in satisfactory agreement with the

experiments, which indicates that the model can provide a realistic picture of the underlying chemistry in the NRP discharge, and can be used to identify its limitations and suggest further improvements.

The NRP discharge shows promising results for both CO₂ conversion and energy efficiency (or energy cost), by stimulating vibrational excitation. Indeed, more than 20 % of all CO₂ dissociation occurs from the highest asymmetric stretch mode levels (V16-V21), mainly by dissociation upon collision with an O atom or with another molecule M, while 67 % of the dissociation occurs from the lowest and middle levels (Va-Vd, and V1-V15) and 9 % from the CO₂ ground state, mainly by electron impact dissociation through electronic excitation. However, in between the pulses (i.e., during the so-called afterglows), fresh gas entering the plasma, VT relaxation (depopulating the higher vibrational levels) and recombination reactions (mainly $\text{CO} + \text{O} + \text{M} \rightarrow \text{CO}_2 + \text{M}$), limit the conversion and energy efficiency. The latter two processes also induce intense heating just after the pulses, causing self-acceleration, as both processes are enhanced at higher gas temperature. Nevertheless, the performance of the NRP discharge is very competitive with other plasma sources used for CO₂ conversion.

To further improve the performance, extra cooling could be applied in the afterglows. The model predicts that a five or ten times higher cooling rate can increase both the conversion and energy efficiency by about a factor 2, for SEI values below 2.3 eV molec⁻¹. Indeed, in general, extra cooling slows down the rate of the recombination reaction ($\text{CO} + \text{O} + \text{M} \rightarrow \text{CO}_2 + \text{M}$) and enhances the contribution of the highest vibrational levels in the overall CO₂ dissociation, making the conversion more energy efficient. However, it should be noted that the energy cost for extra cooling was not yet taken into account, so the improvement in energy efficiency will be somewhat overestimated. Nevertheless, this conceptual study is very useful to reveal how more energy-efficient CO₂ conversion can be reached in NRP discharges.

6.9 Appendix

Table A12: Electron impact reactions calculated with cross sections data, using the calculated EEDF, as explained in Chapter 3, Section 3.2, as well as the references where the data are adopted from.

No.	Reaction	Ref	Note
(X1) ^a	$e^- + CO_2 \rightarrow 2e^- + CO_2^+$	59-61	
(X2) ^a	$e^- + CO_2 \rightarrow 2e^- + O + CO^+$	59-61	
(X3) ^a	$e^- + CO_2 \rightarrow 2e^- + O^+ + CO$	82	
(X4) ^a	$e^- + CO_2 \rightarrow 2e^- + O_2 + C^+$	82	
(X5) ^a	$e^- + CO_2 \rightarrow 2e^- + O_2^+ + C$	83	
(X6) ^a	$e^- + CO_2 \rightarrow O^- + CO$	59-61	
(X7) ^b	$e^- + CO_2 \rightarrow e^- + O + CO$	59-61	
(X8) ^a	$e^- + CO_2 \rightarrow e^- + CO_2(E1)$	59-61	
(X9) ^b	$e^- + CO_2 \leftrightarrow e^- + CO_2(Vx)$	59-61	$x = a, b, c, d$
(X10) ^c	$e^- + CO_2 \leftrightarrow e^- + CO_2(Vi)$	59-61	$i = 1 - 21$
(X11) ^a	$e^- + CO \rightarrow 2e^- + CO^+$	84	
(X12) ^a	$e^- + CO \rightarrow 2e^- + C^+ + O$	85	
(X13) ^a	$e^- + CO \rightarrow 2e^- + C + O^+$	85	
(X14) ^a	$e^- + CO \rightarrow C + O^-$	86	
(X14bis) ^b	$e^- + CO \rightarrow e^- + C + O$	87	
(X15)	$e^- + CO \leftrightarrow e^- + CO(Vi)$	87	$i = 1 - 10$
(X16) ^b	$e^- + O_2 \rightarrow e^- + O + O$	88	
(X16M) ^a	$e^- + O_2 + M \rightarrow O_2^- + M$	88	
(X17) ^a	$e^- + O_2 \rightarrow O + O^-$	88	
(X18) ^a	$e^- + O_2 \rightarrow 2e^- + O_2^+$	89	
(X19) ^b	$e^- + O_2 \rightarrow 2e^- + O + O^+$	89	
(X20)	$e^- + O_2 \leftrightarrow e^- + O_2(Vi)$	88	$i = 1, 2, 3, 4$
(X21)	$e^- + O_3 \rightarrow e^- + O_2 + O$	90	
(X22)	$e^- + O_3 \rightarrow 2e^- + O_2^+ + O$	90	
(X23)	$e^- + O_3 \rightarrow e^- + O^+ + O^- + O$	90	
(X24)	$e^- + O_3 \rightarrow O^- + O_2$	91	
(X25)	$e^- + O_3 \rightarrow O + O_2^-$	91	
(X26)	$e^- + O \rightarrow 2e^- + O^+$	92	
(X27)	$e^- + C \rightarrow 2e^- + C^+$	93	

a Same cross section also used for ground state.

b Cross section also used for the excited states, modified by lowering the energy threshold by the energy of the excited state.

c Cross section for the various levels (i,j) adopted from $e^- + CO_2 \rightarrow e^- + CO_2(Vi)$ but scaled and shifted using Fridman's approximation^{14,57}

Table A13: Electron impact reactions using analytical expressions for the rate coefficients, given in $\text{cm}^3 \text{s}^{-1}$ and $\text{cm}^6 \text{s}^{-1}$, for two-body and three-body reactions, respectively, as well as the references where the data are adopted from. T_g and T_e are given in K and eV, respectively.

No.	Reaction	Rate coefficient	Ref
(E1a)	$e^- + \text{CO}_2^+ \rightarrow \text{CO}(V1) + O$	$1.0 \times 10^{-5} T_e^{-0.5} T_g^{-1}$	106,323
(E1b)	$e^- + \text{CO}_2^+ \rightarrow \text{C} + \text{O}_2$	$1.0 \times 10^{-5} T_e^{-0.5} T_g^{-1}$	83
(E2) ^a	$e^- + \text{CO}_4^+ \rightarrow \text{CO}_2 + \text{O}_2$	$1.61 \times 10^{-7} T_e^{-0.5}$	83
(E3)	$e^- + \text{CO}^+ \rightarrow \text{C} + O$	$3.46 \times 10^{-8} T_e^{-0.48}$	113,324
(E4) ^a	$e^- + O + M \rightarrow O^- + M$	1.0×10^{-31}	106
a The primary source was not accessible			

Table A14: Ion-ion and ion-neutral reactions, as well as the references where the data are adopted from. The rate coefficients are given in $\text{cm}^3 \text{s}^{-1}$ and $\text{cm}^6 \text{s}^{-1}$, for two-body and three-body reactions, respectively. T_g is given in K.

No.	Reaction	Rate coefficient	Ref
(I1)	$\text{CO}_2 + \text{CO}^+ \rightarrow \text{CO}_2^+ + \text{CO}$	1.0×10^{-9}	102,103
(I2)	$\text{CO}_2 + \text{O}^- + M \rightarrow \text{CO}_3^- + M$	1.5×10^{-28}	102,325
(I3)	$\text{CO}_2 + \text{O}_2^- + M \rightarrow \text{CO}_4^- + M$	4.7×10^{-29}	102,325
(I4)	$\text{CO} + \text{O}^- \rightarrow \text{CO}_2 + e^-$	5.5×10^{-10}	102,104
(I5)	$\text{CO} + \text{CO}_3^- \rightarrow 2\text{CO}_2 + e^-$	5.0×10^{-13}	105
(I6) ^a	$\text{CO}_3^- + \text{CO}_2^+ \rightarrow 2\text{CO}_2(Vb) + O$	5.0×10^{-7}	106
(I7) ^a	$\text{CO}_4^- + \text{CO}_2^+ \rightarrow 2\text{CO}_2(Vb) + \text{O}_2$	5.0×10^{-7}	106
(I8) ^a	$\text{O}_2^- + \text{CO}_2^+ \rightarrow \text{CO}_2(V1) + \text{O}_2 + O$	6.0×10^{-7}	106
(I9)	$\text{CO}_3^- + O \rightarrow \text{CO}_2 + \text{O}_2^-$	8.0×10^{-11}	107
(I10a) ^a	$\text{CO}_4^- + O \rightarrow \text{CO}_3^- + \text{O}_2$	1.12×10^{-10}	102
(I10b) ^a	$\text{CO}_4^- + O \rightarrow \text{CO}_2 + \text{O}_2 + \text{O}^-$	1.4×10^{-11}	102
(I11)	$O + \text{O}^- \rightarrow \text{O}_2 + e^-$	2.3×10^{-10}	108
(I12) ^a	$O + \text{O}_2^- \rightarrow \text{O}_2 + \text{O}^-$	1.5×10^{-10}	102
(I13)	$\text{O}_2^- + M \rightarrow \text{O}_2 + M + e^-$	$2.7 \times 10^{-10} \left(\frac{T_g}{300}\right)^{0.5} \exp(-5590/T_g)$	110,111
(I14) ^c	$\text{O}^- + M \rightarrow O + M + e^-$	$2.3 \times 10^{-9} \exp(-26000/T_g)$	111,326,327
a The primary source was not accessible			
c For usual values of gas temperature, i.e. $T_g \ll 26,000$ K, the rate coefficient is very low, as pointed out by Gudmundsson ³²⁸ .			

Table A15 : Neutral-neutral reactions, as well as the references where the data are adopted from. The rate coefficients are given in $\text{cm}^3 \text{s}^{-1}$ and $\text{cm}^6 \text{s}^{-1}$, for two-body and three-body reactions, respectively. T_g is given in K. The α parameter determines the effectiveness of lowering the activation energy for reactions involving vibrationally excited levels of the molecules (see details in ^{14,57}).

No.	Reaction	Rate coefficient	α	Ref
(N1)	$CO_2 + M \rightarrow CO + O + M$	$6.06 \times 10^{-10} \exp\left(-\frac{52525}{T_g}\right)$	0.82	³²⁹
(N2)	$CO_2 + O \rightarrow CO + O_2$	$2.8 \times 10^{-11} \exp\left(-\frac{26500}{T_g}\right)$	0.50	^{117,118}
(N3)	$CO_2 + C \rightarrow 2CO$	$< 1.0 \times 10^{-15}$	n.a.	¹¹⁹
(N4)	$CO + O + M \rightarrow CO_2 + M$	$8.3 \times 10^{-34} \exp\left(-\frac{1510}{T_g}\right)$	0.0	^{118,120}
(N5)	$O_2 + CO \rightarrow CO_2 + O$	$4.2 \times 10^{-12} \exp\left(-\frac{24000}{T_g}\right)$	0.5	¹¹⁸
(N6)	$O_2 + C \rightarrow CO + O$	$1.99 \times 10^{-10} \exp\left(-\frac{2010}{T_g}\right)$	0.0	¹⁸²
(N7)	$O + C + M \rightarrow CO + M$	$2.14 \times 10^{-29} \left(\frac{T_g}{300}\right)^{-3.08} \exp\left(-\frac{2144}{T_g}\right)$	0.0	^{117,118}
(N8)	$O + O + M \rightarrow O_2 + M$	$5.2 \times 10^{-47} \exp\left(\frac{900}{T_g}\right)$	n.a.	^{117,118}
(N9)	$O_2 + M \rightarrow O + O + M$	$3.0 \times 10^{-12} \frac{1}{T_g} \exp\left(-\frac{59380}{T_g}\right)$	1.0	^{117,118}

Table A16: Neutral reactions between vibrationally excited molecules, as well as the references where the data are adopted from. The rate coefficients are given in $\text{m}^3 \text{s}^{-1}$ and $\text{m}^6 \text{s}^{-1}$, for two-body and three-body reactions, respectively. T_g is given in K.

No.	Reaction	Rate coefficient	Ref
(V1)	$CO_2(Va) + M \rightarrow CO_2 + M$	$7.14 \times 10^{-9} \exp(-177T_g^{-1/3} + 451T_g^{-2/3})$	125-127
(V2a)	$CO_2(V1) + M \rightarrow CO_2(Va) + M$	$4.25 \times 10^{-1} \exp(-407T_g^{-1/3} + 824T_g^{-2/3})$	127-129
(V2b)	$CO_2(V1) + M \rightarrow CO_2(Vb) + M$	$8.57 \times 10^{-1} \exp(-404T_g^{-1/3} + 1096T_g^{-2/3})$	127-129
(V2c)	$CO_2(V1) + M \rightarrow CO_2(Vc) + M$	$1.43 \times 10^{-1} \exp(-252T_g^{-1/3} + 685T_g^{-2/3})$	127-129
(V3)	$CO(V1) + M \rightarrow CO + M$	$1.0 \times 10^{-12} T_g \exp(-150.7T_g^{-1/3})$	130
(V4)	$O_2(V1) + M \rightarrow O_2 + M$	$1.3 \times 10^{-8} \exp(-158.7T_g^{-1/3})$	126,127
(V5)	$CO_2(V1) + CO_2 \rightarrow CO_2(Va) + CO_2(Vb)$	$1.06 \times 10^{-5} \exp(-242T_g^{-1/3} + 633T_g^{-2/3})$	127-129
(V6)	$CO_2(V1) + CO_2 \rightarrow CO_2 + CO_2(V1)$	$1.32 \times 10^{-12} \left(\frac{T_g}{300}\right)^{0.5} \frac{250}{T_g}$	131,132
(V7)	$CO(V1) + CO \rightarrow CO + CO(V1)$	$3.4 \times 10^{-10} \left(\frac{T_g}{300}\right)^{0.5} \left(1.64 \times 10^{-6} T_g + \frac{1.61}{T_g}\right)$	133,134
(V8)	$CO_2(V1) + CO \rightarrow CO_2 + CO(V1)$	$4.8 \times 10^{-6} \exp(-153T_g^{-1/3})$	127,128

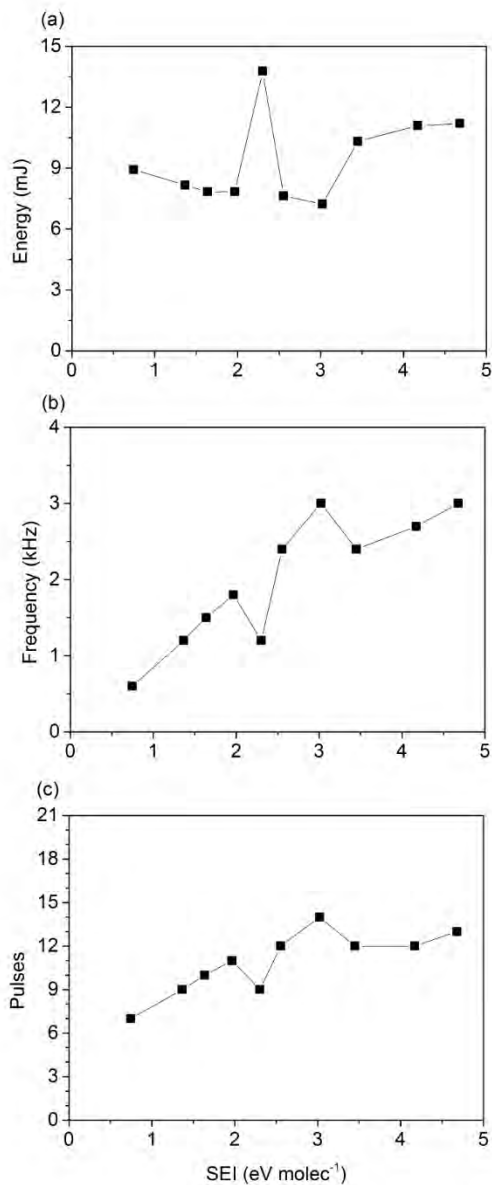


Figure A14: Energy deposited per pulse (a), pulse frequency (b), and number of pulses felt by the gas molecules when travelling from pin HV electrode to grounded electrode (c), for the different SEI values investigated.

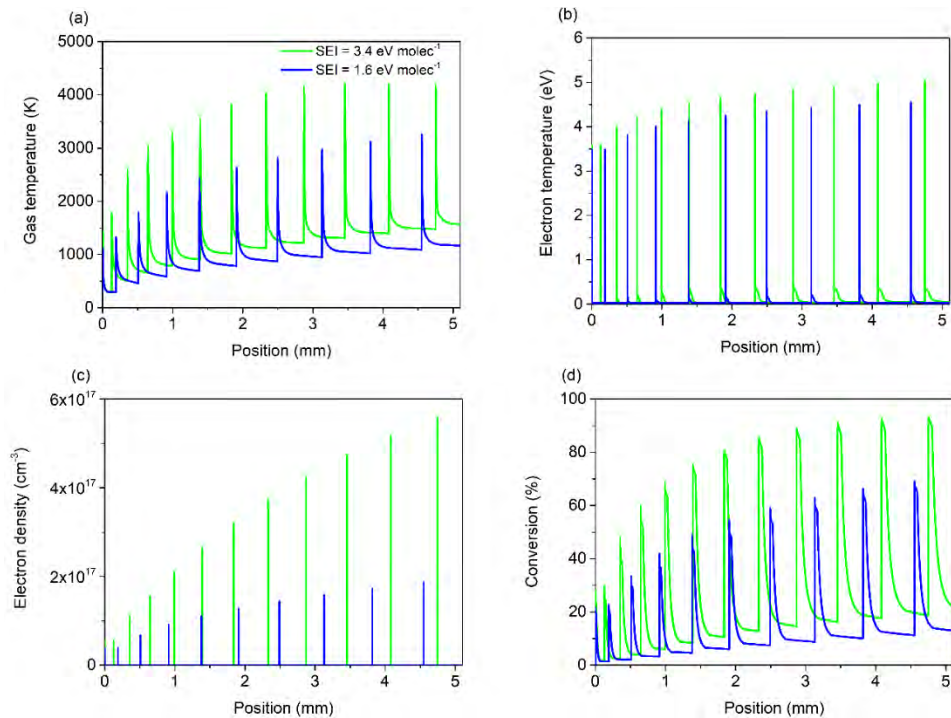


Figure A15: Calculated gas temperature (a), electron temperature (b), electron density (c), and CO₂ conversion (d), as a function of travelled distance between HV pin electrode and grounded electrode, for two different SEI values (i.e. different from the SEI values in Figure 30, for extra information).

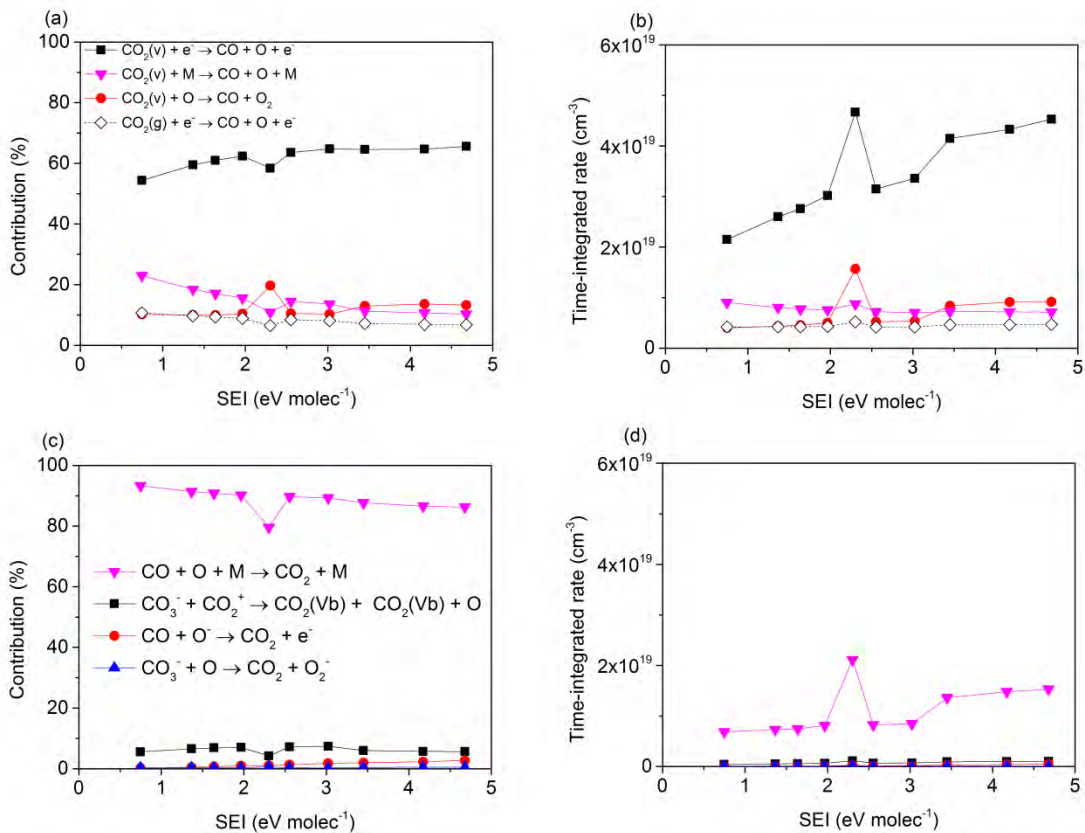


Figure A16: Contribution of the most important dissociation (a) and formation (c) mechanisms of CO_2 , and their corresponding time-integrated rates (b, d) as a function of SEI.

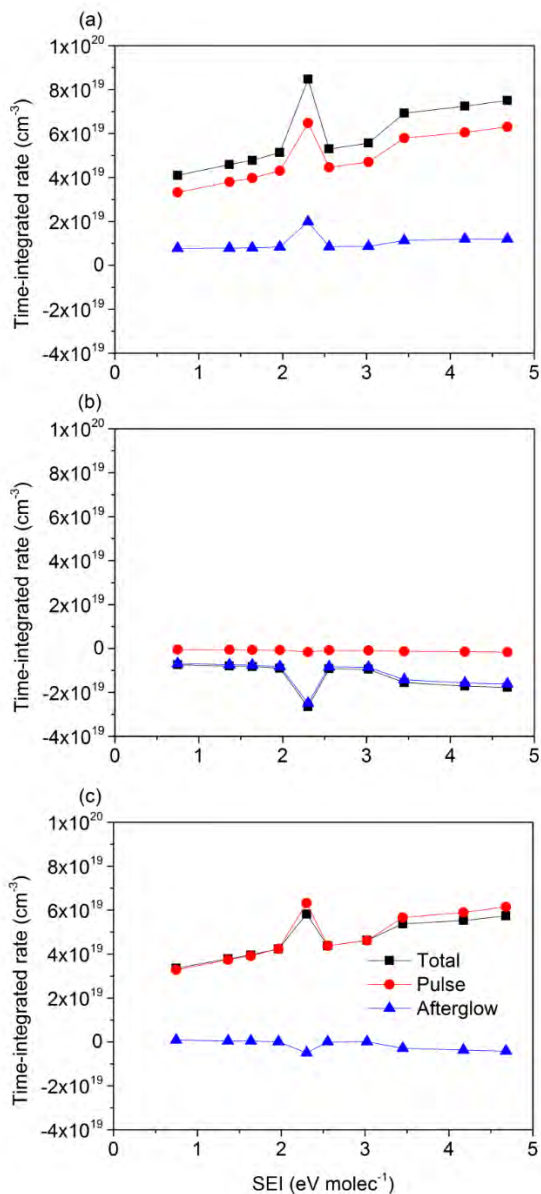


Figure A17: Time-integrated rates of the overall dissociation (a), overall formation (plotted as negative values) (b), and the net dissociation of CO₂, as a function of SEI, for the pulse, afterglow and the sum of both (total), showing that the dissociation mainly takes place during the pulses, while net formation occurs during the afterglows.

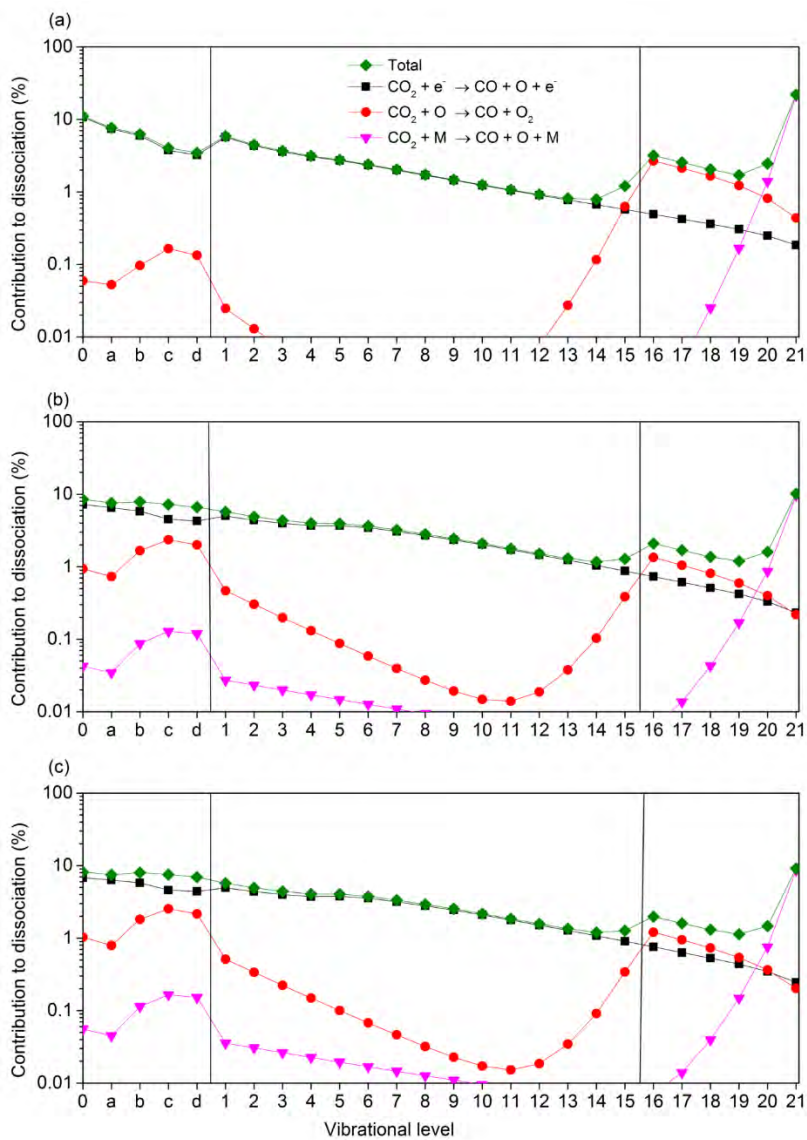


Figure A18: Contribution of the CO₂ ground state and different vibrational levels to the total dissociation, as well as to the most important dissociation mechanisms, only accounting for the forward reactions, for different SEI values, i.e., 0.7 eV molec⁻¹ (a), 3.4 eV molec⁻¹ (b) and 4.7 eV molec⁻¹ (c).

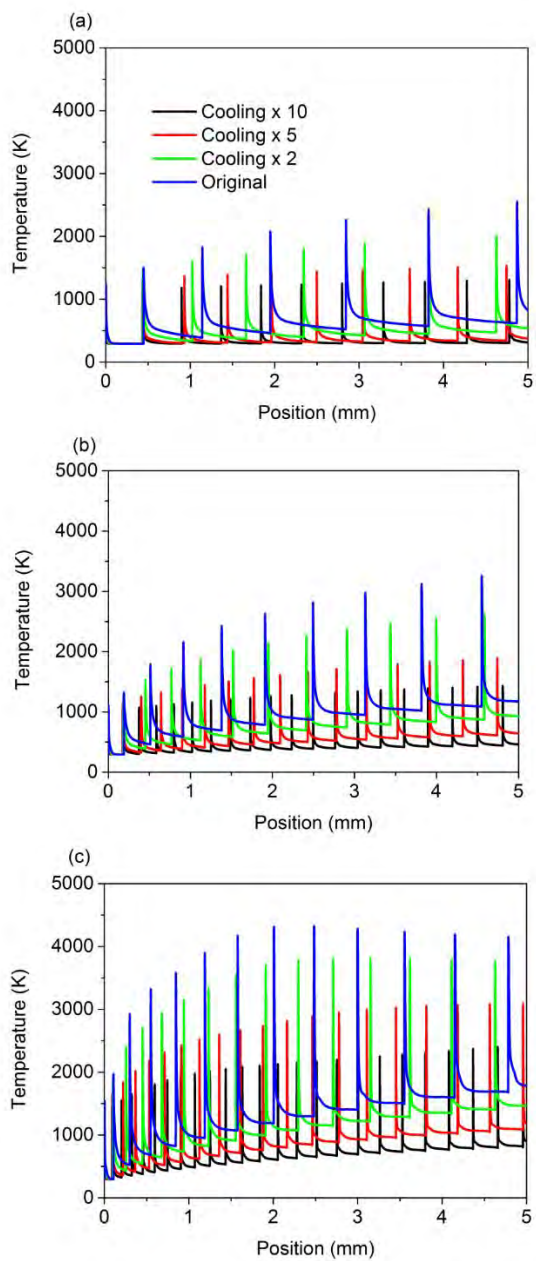


Figure A19: Calculated gas temperature as a function of travelled distance between HV pin electrode and grounded electrode for different SEI values, i.e., $0.7 \text{ eV molec}^{-1}$ (a), $1.6 \text{ eV molec}^{-1}$ (b) and $4.7 \text{ eV molec}^{-1}$ (c), at different cooling rates.

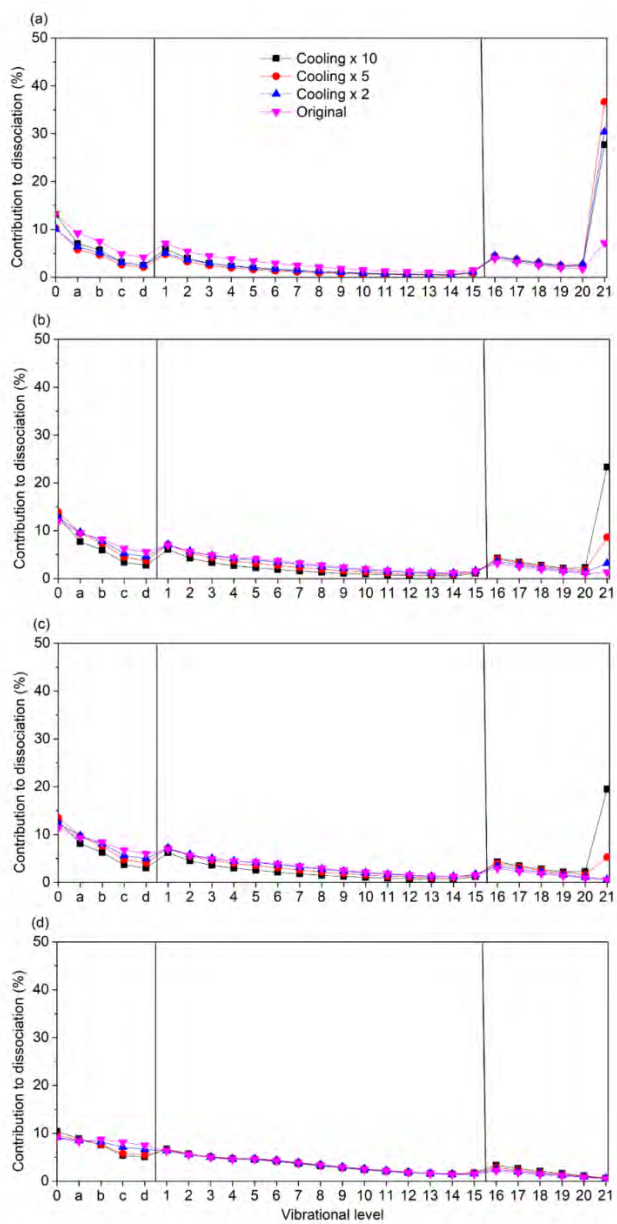


Figure A20: Net contribution of the different CO₂ vibrational levels to the total dissociation, for different SEI values, i.e., 0.7 eV molec⁻¹ (a), 1.6 eV molec⁻¹ (b), 2.0 eV molec⁻¹ (c) and 4.7 eV molec⁻¹ (d), at different cooling rates.

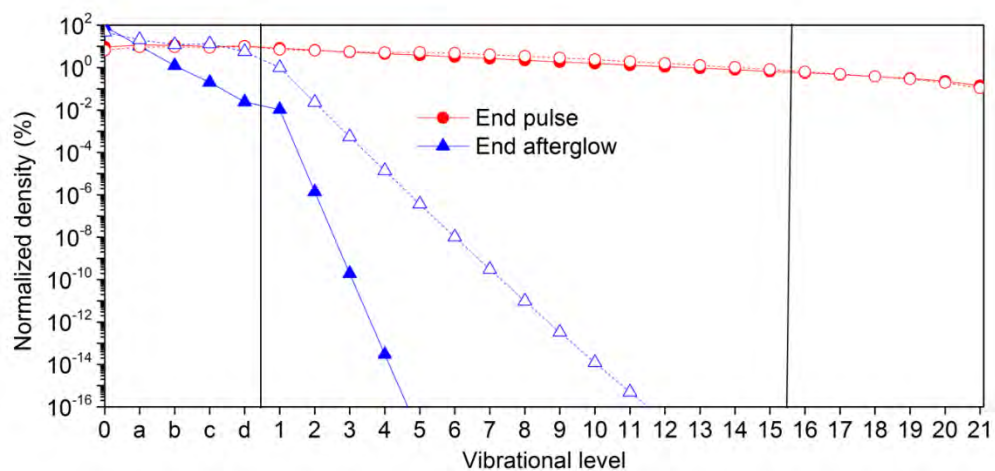


Figure A21: Calculated VDFs at the end of the last pulse (10 ns) and at the end of the last afterglow, for $SEI = 1.6 \text{ eV molec}^{-1}$, in the original model (open symbols, dashed lines) and with a cooling rate times ten (solid symbols and lines). The VDFs at cooling rate times two and five at the end of the pulse are the same, and at the end of the afterglow, they lie in between the VDFs of the original model and of ten times higher cooling rate.

Chapter 7: CH₄ Conversion in three Different Plasma Sources

The results presented in this Chapter are published as:

- Heijkers, S.; Aghaei, M.; Bogaerts, A. Plasma-Based CH₄ Conversion into Higher Hydrocarbons and H₂: Modeling to Reveal the Reaction Mechanisms of Different Plasma Sources. *J. Phys. Chem. C* **2020**, *124*, 7016-7030, Featured in ACS Editors' Choice

7.1 Introduction

CH₄ conversion into higher hydrocarbons and H₂ by plasma technology is gaining increasing interest as more sustainable alternative to conventional steam reforming. However, different plasma types yield a different performance in terms of conversion, energy cost and selectivity towards different hydrocarbons, and the underlying mechanisms are not yet fully understood. The most common plasma types are dielectric barrier discharges (DBDs), microwave (MW), and gliding arc (GA) plasmas, although NRP discharges have also been used for CH₄ conversion^{38,330,331}. DBDs typically operate at (or slightly above) room temperature and ethane (C₂H₆) is one of the main products formed, with selectivities ranging between 20 %³³² and ca. 60 %³³³. MW and GA plasmas operate at higher temperatures (typically 1000-3000 K), and are therefore called “warm plasmas”^{3,334}. They produce more unsaturated compounds, such as C₂H₂ and have higher conversions. There are already quite some papers about modelling non-oxidative conversion of CH₄. For instance, Tahara et al.²⁵⁶ studied CH₄/H₂ mixtures for the deposition of diamond-like carbon films. However, they did not use temperature-dependent rate coefficients for neutral reactions. Dors et al.³³⁵ used temperature-dependent rate coefficients for a MW discharge at atmospheric pressure, but they included no electron impact reactions, because they assumed that the electric field was too low for electron impact dissociation. Indarto et al.³³⁶ described the CH₄ chemistry in a conventional GA discharge, but again without electron impact reactions. In a later work, Indarto et al.³³⁷ modeled a DBD, but applied generalized rate coefficients for conversion of one reactant or product into another, without specification whether the process was a neutral, ionic or electron impact reaction. Sun and Chen³³⁸ included all these processes, as well as vibrational excitation and relaxation, but no rotational excitation, relaxation and intermode vibrational relaxation, which are also important in CH₄ discharges^{339,340}.

Therefore, in this Chapter, we present a full chemical kinetics model, developed to elucidate the main conversion mechanisms of CH₄ into the most important hydrocarbons, especially C₂H₂, C₂H₄ and C₂H₆, as well as into H₂, in these three most common plasma reactors, i.e., a DBD, MW and GAP reactor.

After describing the chemistry set in Section 7.2, we will explain how our 0D modelling approach can mimic the different plasma reactors (Section 7.3).

Subsequently, we will present the results for DBD plasma (Section 7.4), MW plasma (Section 7.5) and GAP (Section 7.6), focussing in each case on the comparison of calculated and measured CH₄ conversion, energy cost and product selectivities, to validate the model assumptions and chemistry set, followed by a detailed discussion on the underlying reaction pathways of the conversion of CH₄ into hydrocarbons and H₂.

7.2. Chemistry set

The chemistry set applied in this study is based on the pure CH₄ chemistry part of the models developed by Snoeckx et al.¹⁴³ and Cleiren et al.¹⁵³, extended with excitation and relaxation of the lowest vibrational and rotational levels. The set contains 57 different species (see Table 10), i.e., eight ground state molecules, 12 radicals, 16 ions, the electrons, six excited species of CH₄ and 14 of H₂. These species interact with each other through various chemical reactions. In total, 2174 reactions are included in our model, of which 378 electron impact reaction, 380 ionic reactions and 507 neutral reactions, as well as 713 vibration-translation (VT) and 196 vibration-vibration (VV) relaxation reactions for CH₄ and H₂. CH₄ has four degenerate vibrational modes: the ν_1 singly degenerate symmetric stretch mode (lowest level at 0.362 eV), the ν_2 doubly degenerate scissoring bend mode (lowest level at 0.190 eV), the ν_3 triply degenerate asymmetric stretch mode (lowest level at 0.374 eV) and the ν_4 triply degenerate umbrella bend mode (lowest level at 0.162 eV)³⁴¹. In our model we incorporate only these lowest levels as a first approximation. Also, two rotational levels (j_3 and j_4) with energies equal to 0.0078 eV and 0.013 eV, respectively, are included^{340,342}. The relaxation between these modes and rotational relaxation was studied by Menard-Bourcin et al.³³⁹ but only at 193 K and 296 K. Based on earlier works about vibrational and rotational relaxation of Capitelli et al.¹³⁰, Wang and Springer³⁴³, and Richards and Sigafos³⁴⁴, we assume, as a first approximation, that these rate constants follow the relation:

$$\frac{k_{T_2}}{k_{T_1}} = \exp\left(-aT_2^{-\frac{1}{3}} + aT_1^{-\frac{1}{3}}\right) \quad (44)$$

Where k_{T_1} and k_{T_2} are the rate coefficients (in cm³ s⁻¹) at gas temperatures T_1 and T_2 (in K) ($T_2 > T_1$), respectively, and a is a constant, which is calculated, based on the rate coefficients at gas temperatures equal to 193 K and 296 K. The

reverse reactions are also included based on detailed balance, which was suggested by Menard-Bourcin et al.³³⁹. All reactions are shown in Tables A17-A20 in the Appendix.

We also extended the chemistry set to CH₄/N₂ mixtures, for the GAP reactor, because plasma ignition was not possible in pure CH₄ (see Section 7.3.3). The extra species included are also listed in Table 10. The pure N₂ reactions are adopted from Chapter 5 and the extra coupling reactions are listed in Table A20 in the Appendix. Since the electronically excited species of N₂ are of minor importance for this study, they were not included in this Chapter. It should be noted that only C atom formation, but no solid carbon formation is included in our model, because we only describe the gas phase chemistry. Furthermore, solid carbon formation was stated in the experimental papers to be always below 10% in the DBD and MW plasma at atmospheric pressure³⁴⁵⁻³⁴⁷, while in the MW plasma at reduced pressure, it was also stated to be negligible in the pulsed mode³⁴⁸. In the MW plasma at reduced pressure in continuous mode and in our own GAP experiments, however, significant solid carbon formation was observed, so in the future, we should improve our model to account for it, by adding surface processes.

Table 10: Species included in the model.

Molecules	Charged species	Radicals	Excited species
CH ₄ , H ₂ ,	CH ₄ ⁺ , CH ₅ ⁺ , CH ₃ ⁺ ,	CH ₃ , CH ₂ , CH, C ₂ H,	CH ₄ (V1-V4),
C ₂ H ₆ , C ₂ H ₄ ,	CH ₂ ⁺ , CH ⁺ , C ₂ ⁺ , C ⁺ , H ⁺ ,	C ₂ , C, H, C ₂ H ₅ ,	CH ₄ (J3,J4),
C ₂ H ₂ , C ₃ H ₈ ,	H ₂ ⁺ , H ₃ ⁺ , C ₂ H ₆ ⁺ , C ₂ H ₅ ⁺ ,	C ₂ H ₃ , C ₃ H ₇ , C ₃ H ₅ ,	H ₂ (V1-V14),
C ₃ H ₆ ,	C ₂ H ₄ ⁺ , C ₂ H ₃ ⁺ , C ₂ H ₂ ⁺ ,	C ₄ H ₉ , N, NH, NH ₂ ,	N ₂ (V1-V24)
C ₄ H ₁₀ , N ₂ ,	C ₂ H ⁺ , N ⁺ , N ₂ ⁺ , N ₃ ⁺ , N ₄ ⁺ ,	CN, N ₂ H, H ₂ CN,	
NH ₃ , HCN,		HCNN, NCN	
C ₂ N ₂			
	Electrons		

7.3. Modelling the different plasma reactors with a 0D approach

In this Chapter, we also present the selectivities of different hydrocarbons. They are calculated as:

$$S_{C_xH_y}(\%) = 100\% \frac{x n_{C_xH_y}(m^{-3})v_f(m s^{-1})}{n_{CH_4,i}(m^{-3})v_i(m s^{-1}) - n_{CH_4,f}(m^{-3})v_f(m s^{-1})} \quad (45)$$

With $n_{C_xH_y}$ the density of the hydrocarbon. Note that these selectivities are C-based. We also define the H₂ selectivity, which is H-based:

$$S_{H_2}(\%) = 100\% \frac{0.5 n_{H_2}(m^{-3})v_f(m s^{-1})}{n_{CH_4,i}(m^{-3})v_i(m s^{-1}) - n_{CH_4,f}(m^{-3})v_f(m s^{-1})} \quad (46)$$

7.3.1 Dielectric barrier discharge (DBD)

As mentioned in Chapter 1, a DBD is created by applying an electric potential difference between two electrodes, of which at least one is covered by a dielectric barrier. A DBD in CH₄ exhibits filamentary behavior, i.e., microdischarges between these electrodes. Hence, the CH₄ molecules will pass through several microdischarge filaments on their way throughout the reactor, which is mimicked in the model as microdischarge power pulses as a function of time. The model is applied to the DBD reactor of Xu and Tu³⁴⁶ and to the micro-DBD reactor of Wang et al.³⁴⁵, in order to first verify our modeling results with their experiments, as a validation of the model. Indeed, these results are a good representation of other DBD reactor studies on CH₄ conversion, as reviewed by Scapinello et al.³⁴⁹. Figure 46 illustrates a schematic picture of the cylindrical DBD reactor of Xu and Tu³⁴⁶, which has a length of 9 cm and a discharge gap of 0.3 cm, resulting in a discharge volume of 13.6 cm³³⁴⁶. The micro-DBD reactor of Wang et al.³⁴⁵ looks similar, but with a discharge gap of 0.09 cm, a length of 20 cm and a discharge volume of 1.4 cm³.

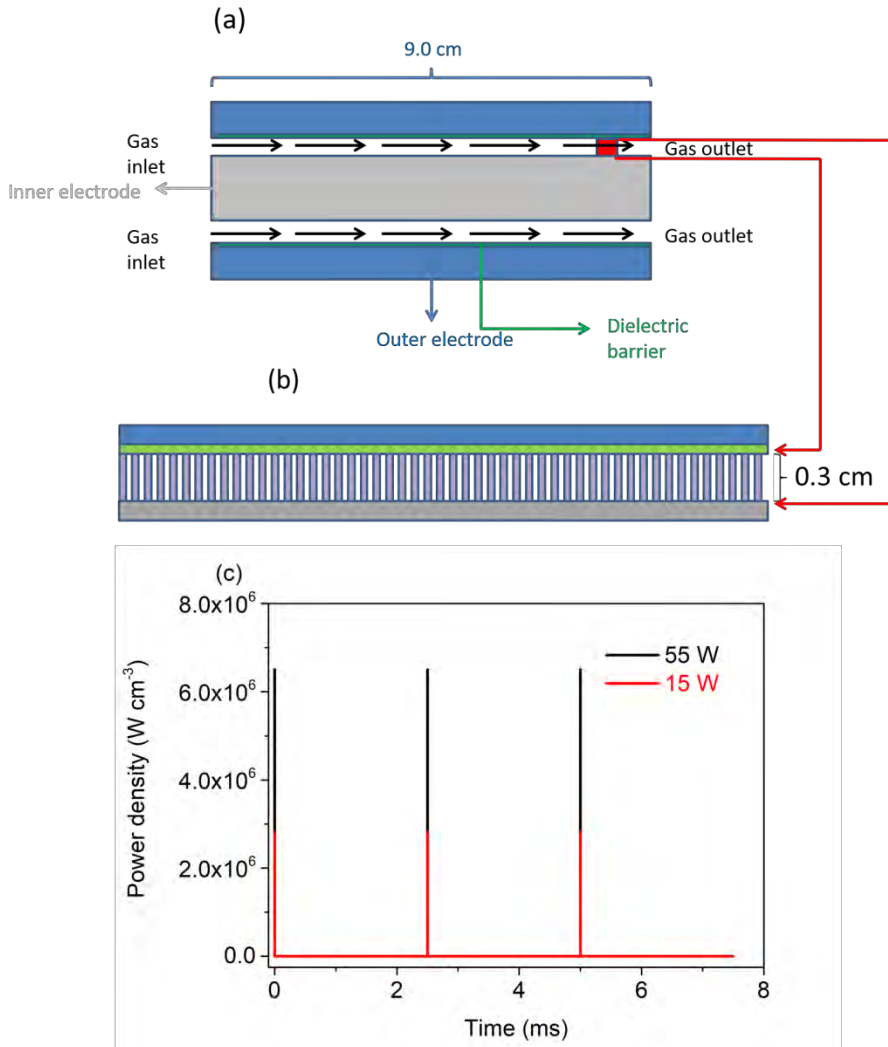


Figure 46: Schematic illustration of a typical cylindrical DBD reactor, based on the design of Xu and Tu³⁴⁶ (a), representation of the filaments in this reactor (b), and the corresponding power density profile as a function of time in this DBD reactor, for three pulses, at an input power of 15 W and 55 W and a frequency of the applied power of 20 kHz (c).

The plasma power is assumed to be uniformly deposited in pulses (or microdischarges) with lifetimes of 11 ns for 15 W and 14 ns for 55 W, based on linear interpolation of the microdischarge lifetime as a function of power, adopted from Ozkan et al.^{74,350}. During one AC period in a DBD reactor, these

authors measured approximately 400 microdischarges at 50W and 500 microdischarges at 100 W, with an almost linear increase of the number of discharges as a function of power ⁷⁴. The local power deposition per pulse P_{pulse} (in W) is defined as:

$$P_{pulse} = \frac{P_{total}}{N_{pulse} f_{AC} t_{pulse}} \quad (47)$$

where P_{total} (in W) is the global power input, which is varied between 15 W and 55 W, based on the experiments of Xu and Tu, ³⁴⁶ and between 10 W and 30 W for the experiments of Wang et al. ³⁴⁵, N_{pulse} is the number of pulses per AC cycle, f_{AC} (in Hz) the frequency of the applied power, which is 20 kHz in our simulations, again based on Xu and Tu ³⁴⁶ and Wang et al. ³⁴⁵, and t_{pulse} (in s) is the lifetime of the microdischarges (see above). Each of these microdischarges can be represented as a cylinder with a typical radius of ~ 0.13 mm ^{14,351} and a length equal to the discharge gap. Following Snoeckx et al. ^{143,266}, it is assumed that every molecule passes such a microdischarge every 100 half cycles, irrespective of power deposited. Indeed, in reality there are more microdischarge filaments in the DBD, but they are spread over the reactor, so not all molecules feel all microdischarges. More details about this approach can be found in ¹⁴³. In the DBD reactor of Xu and Tu ³⁴⁶, an AC frequency of 20 kHz is applied. Hence, there is a new half cycle every 25 μ s. Using the above assumption that the molecules pass a microdischarge every 100 half cycles, the interpulse time is therefore 2.5 ms. As mentioned, the power is varied between 15 W and 55 W. Ozkan et al. ⁷⁴ measured during one AC period in a DBD reactor approximately 400 microdischarges at 50 W and 500 microdischarges at 100 W, with an almost linear increase of the number of discharges as a function of power. Therefore, we assume 330 pulses per AC cycle at 15 W and 410 pulses per AC cycle at 55 W. The flow rate is varied between 50 and 300 mL min⁻¹, and in combination with the range of plasma power, this corresponds to SEI values between 9 and 54 kJ L⁻¹. The temperature in this DBD configuration was not specified, therefore the average gas temperature is estimated based on the measured electrode temperature in a similar DBD reactor of Ozkan et al. ³⁵² albeit used for CO₂ with AC frequency of 28.6 kHz and discharge gap of 2 mm. Ozkan et al. ³⁵² reported

temperature values varying from 300 K below 30 W towards about 450 K at 100 W in a linear fashion. The authors also presented 2D temperature distributions on the outer electrode, measured by infrared camera, and showed that the aforementioned temperatures at these powers were reached after a travelled distance of 50 % of the reactor. Therefore, for power values above 30 W, the temperature rises linearly from 300 K at the beginning of the simulation towards the final temperature, i.e. 320 K for 35 W, 340 K for 45 W and 360 K for 55 W. Similar temperatures in the range 300-350 K were also found in a pure CH₄ DBD plasma by Nozaki et al.³⁵³. Although the average gas temperature is used of the whole DBD reactor, the temperature in a filament for frequencies less than 30 kHz is also less than 100 K³⁵⁴. Therefore, the use of this average gas temperature is justified.

For the micro-DBD reactor of Wang et al.³⁴⁵ the frequency was not explicitly mentioned, but the same reactor with the same equipment was also used by Duan et al.,³⁵⁵ reporting a range of frequencies of 17.5-19.5 kHz. As this is almost the same as 20 kHz, the same interpulse time of 2.5 ms is also assumed. The power was varied between 10 W and 30 W, and thus we assume 320 pulses per AC cycle at 10 W and 360 pulses per AC cycle at 30 W. The flow rate was varied between 20.2 and 59.8 mL min⁻¹ based on their reported residence times, and the lifetime of the microdischarges is assumed to change from 10 ns at 10 W until 12 ns at 30 W. This corresponds to SEI values between 25 and 88 kJ L⁻¹. The wall temperature at 25 W was measured to be 463 K, which is higher than the 300 K assumed in the previous configuration. However, the discharge gap in this configuration, i.e. 0.09 cm, is much smaller, resulting in a higher power density, which heats up the gas more. At lower and higher powers than 25 W, the final temperature is assumed to change in the same way as a function of power, i.e. 10 K with a change of 5 W, as in the work of Ozkan et al.³⁵². A similar change in temperature was obtained by Nozaki et al.³⁵³ in a pure CH₄ DBD plasma, i.e. a temperature increase of 3-10 K for an increase of 5 W.

7.3.2 Microwave (MW) plasma

According to Scapinello et al.³⁴⁹, the majority of results for CH₄ conversion in MW plasmas were obtained by Heintze and Magureanu³⁴⁸ at reduced pressure, and by Shen et al.³⁴⁷ at atmospheric pressure. Both reactors are so-called surface

wave MW plasmas, where microwave power is applied from the side, through a waveguide, to a cylindrical tube through which the gas flows (see schematic diagram in Figure 47). Hence, the model is applied to the wide range of conditions in both studies for validation. The inner radius of the discharge tube was 0.3 cm in the configuration of Heintze and Magureanu,³⁴⁸ and 0.8 cm in the configuration of Shen et al.³⁴⁷, and the power was deposited over a length of 1 cm and 5.47 cm, respectively, due to a different waveguide design. The power deposition in a MW plasma at reduced pressure is rather uniform in the whole radial direction, and a triangular profile as a function of time is assumed, mimicking the axial variation, arising from the waveguide, as done in previous work^{25,57,75,308}. In the setup of Heintze and Magureanu, the power was deposited in either a continuous or pulsed regime. In the continuous regime the plasma power was varied between 20 W and 36 W for a flow rate of 98 sccm, corresponding to SEI values between 12 and 22 kJ L⁻¹. In the pulsed regime the average power was ranging between 11 W and 61 W, deposited in pulses between 20 μs and 60 μs, separated by 1 ms. The flow rate was again 98 sccm, corresponding to SEI values between 7 and 37 kJ L⁻¹. The temperature is calculated self-consistently by solving equation (19) (see Chapter 2) with P_{ext} equal to :

$$P_{ext} = \frac{8\lambda}{R^2}(T_g - T_{g,i}) \quad (48)$$

where λ is the gas thermal conductivity of CH₄ (in W m⁻¹ K⁻¹), R the radius of the plasma zone, which is near the reactor wall in the reduced pressure MW plasma. T_g is the plasma gas temperature and $T_{g,i}$ the plasma gas temperature near the edge of the plasma zone, which is typically the average of room temperature and the plasma gas temperature, according to Berthelot³⁵⁶. The gas thermal conductivity is taken from Afshar et al.³⁵⁷ which is a function of gas temperature:

$$\lambda(W m^{-1} K^{-1}) = 10^{-3}(-23.35 + 0.1698T_g + 1.893 \times 10^{-5}T_g^2) \quad (49)$$

In the atmospheric pressure MW reactor of Shen et al.³⁴⁷, the configuration was optimized in such a way that a homogeneous plasma throughout the entire width of the waveguide was created; hence a uniform power density distribution is used, instead of a triangular one³⁵⁸. At atmospheric pressure, however, a uniform power density in the radial direction cannot be assumed, due to radial contraction

of the discharge^{359,360}. Moon and Choe³⁶¹ reported a plasma radius of 0.27 cm at 600 W, for an inner reactor tube radius of 0.9 cm and a waveguide width of 3.5 cm. Green et al.³⁶² reported a plasma radius of 0.45 cm at 1400 W, for an inner reactor tube radius of 1.5 cm and a waveguide width of 1.7 cm. These setups are quite similar to the setup used by Shen et al.³⁴⁷, i.e. inner tube radius of 0.8 cm and a waveguide width of 5.47 cm. Hence, the same plasma radii at these powers are considered, as reported by Moon and Choe³⁶¹ and Green et al.³⁶², and a linear correlation between plasma radius and input power is assumed, which results in the same plasma radii in between 900 W and 1400 W as reported by Green et al.³⁶². To apply the model to the experiments of Shen et al.³⁴⁷ where plasma powers were varied between 200 W and 800 W, we consider a plasma radius that varies linearly between 0.18 cm and 0.31 cm.

Outside the plasma region, there is still a significant amount of thermal CH₄ conversion. Based on the modelling of Berthelot et al.³⁵⁶, the gas temperature is assumed to be more or less constant in the center, within a diameter of 0.8 cm (see red zone in Figure 47). The temperature is self-consistently calculated between 3035 K and 3532 K for the power range between 200 W and 800 W. Also, equations (19), (48) and (49) are solved but in this case is $R = 0.6$ cm³⁵⁶. Similar temperatures were found by Moon and Choe³⁶¹ between 3300 K and 3600 K for powers ranging between 550 W and 700 W. In the region between 0.8 cm and 1.2 cm diameter (blue zone in Figure 47), the gas temperature is taken equal to the average of the gas temperature in the plasma centre (red zone) and room temperature. Between 1.2 cm and 1.6 cm diameter (grey zone in Figure 47), the maximum gas temperature is assumed 300 K lower than in the zone between 0.8 cm and 1.2 cm, as predicted by the modelling of Berthelot et al.³⁵⁶. Although for a full description, radiation losses should be taken into account, we consider the calculated temperatures inside both the MW plasma at reduced pressure (i.e. between 1800 K and 3000 K, just as in Heintze and Magureanu³⁴⁸) and at atmospheric pressure to be realistic, as was discussed above. In the simulations the power is varied between 200 W and 800 W for a flow rate of 500 mL min⁻¹ and a CH₄/H₂ ratio of 1/4, corresponding to SEI values between 24 and 96 kJ L⁻¹. In addition, the flow rate is varied between 100 and 1000 mL min⁻¹ for the same CH₄/H₂ ratio of 1/4 and a power of 400 W,

corresponding to SEI values between 24 and 240 kJ L⁻¹. H₂ was added to reduce carbon deposition.

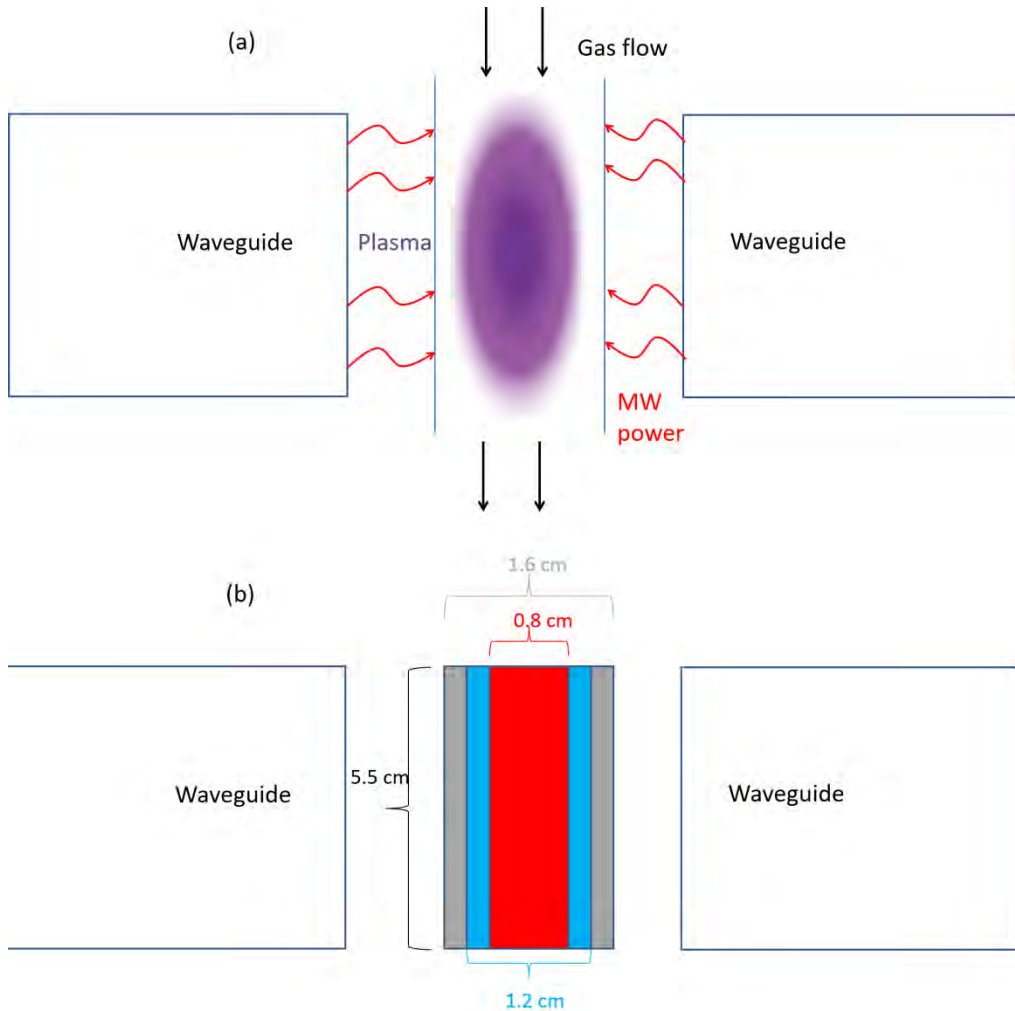


Figure 47: Schematic illustration of the atmospheric pressure MW plasma, based on the design of Shen et al.³⁴⁷ (a) and its implementation in the 0D model (b). The arrows depict the direction of the gas flow and the different colors in (b) indicate the hot center (red) and cooler (blue and grey) zones.

7.3.3 Gliding arc (GA) plasma

The results on GA performance, as reviewed by Scapinello et al.³⁴⁹, are quite scattered. A classical GA is formed between two flat converging electrodes,

between which an electric potential difference is applied, creating an arc discharge, that glides along the electrodes under influence of the gas flow, towards rising interelectrode distance, until it extinguishes and a new arc is formed at the shortest interelectrode distance ³⁶³. However, as explained in Chapter 1, the residence time of the gas inside the arc plasma is quite limited in classical GA discharges, and for this reason, cylindrical GA discharges were developed. One type is the GAP, developed by Nunnally et al. and studied in Chapter 3 for CO₂ splitting, in Chapter 4 for DRM, and in Chapter 5 for the combined CO₂ and N₂ conversion. Therefore, experiments in this GAP were performed by M. Aghaei within PLASMANT for CH₄ conversion to validate our model. A schematic picture of this GAP configuration was given in Figure 8 of Chapter 3, but we consider the shorter configuration as used in Chapters 4 and 5.

The arc plasma in a GAP is confined within the inner vortex and is more or less uniform, as explained in Chapters 3, 4 and 5, allowing a straightforward description of this GA configuration with the 0D model. Moreover, the arc dimensions change little with electric current, as investigated by Trenchev et al. ^{32,33}. The arc has a diameter of 4 mm, as in earlier simulations (see also Chapters 3-5) ^{52,151,153,364}. This corresponds to an arc volume of 383 mm³. Right next to the arc, there is still a warm zone till the edge of the inner vortex, where the temperature is still above 1000 K, and thus where thermal CH₄ conversion can still take place ¹⁵³ (see also Chapter 4).

In both the experiments and simulations, no pure CH₄ could be used, as the latter did not allow plasma ignition in the GAP reactor due to extensive carbon formation, and combustion took place, instead of forming a decent plasma. Therefore, between 80 % and 50 % N₂ was added, and consequently, the chemistry in our model was expanded with N₂ and CH₄-N₂ chemistry, as also indicated in Section 7.2 above. The power deposited inside the plasma was 224 W and the flow rate was 10 L min⁻¹. Based on earlier 3D fluid dynamics calculations by Trenchev et al., ³³ this corresponds to a velocity of 196 cm s⁻¹ and a residence time of 15 ms. The SEI value is 1.3 kJ L⁻¹. A temperature profile was assumed where the gas in the arc first passes a hot cathode spot with a length of 0.01 cm, as found in Trenchev et al. ³³ with a temperature of 6000 K ³⁶⁵, followed by an instant drop in temperature to 3000 K, which is a typical value inside the

arc region outside of the cathode spot ^{31,33,51}. Next to the arc, there is still a hot zone where the temperature is assumed around 36 % of the temperature inside the arc ³³ and where CH₄ dissociation can still take place. The temperature profiles are shown in Figure 48.

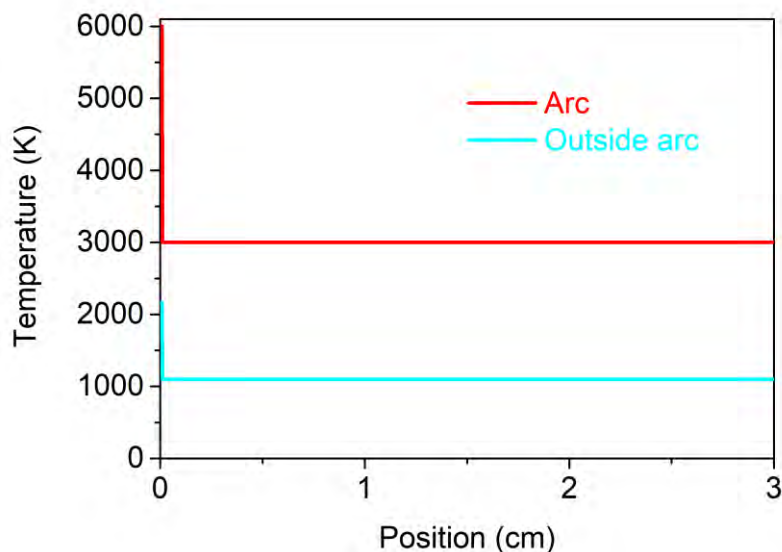


Figure 48: Temperature profiles as a function of travelled distance inside the GAP for the arc region and outside of the arc.

7.4 DBD plasma

7.4.1 Comparison of calculated and measured conversion, energy cost and selectivities

The calculated and experimental results for CH₄ conversion, energy cost and selectivities of the most important hydrocarbons and H₂ in the DBD reactor of Xu and Tu ³⁴⁶ are plotted as a function of flow rate and plasma power in Figures 49 and 50, respectively. The experimental and calculated data follow (more or less) the same trend with increasing flow rate. The largest discrepancies are seen for the selectivities of C₂H₆ and C₂H₂/C₂H₄, with maximum relative

discrepancies of 62 % for C_2H_6 at 50 mL min^{-1} and 53 % for C_2H_4/C_2H_2 at 300 mL min^{-1} (see Figure 49). Also the trends as a function of plasma power are in reasonable agreement, except for the C_2H_6 selectivity, which decreases in the model, whereas the experiments indicate a small rise. The largest discrepancy for the C_2H_6 selectivity is however still only 31 % (see Figure 50). The average discrepancy between the calculated and experimental results is 25 %, which is satisfactory, in view of the complex chemistry and the assumptions made in the 0D model. Hence, the model should be able to elucidate the most important mechanisms in this DBD discharge.

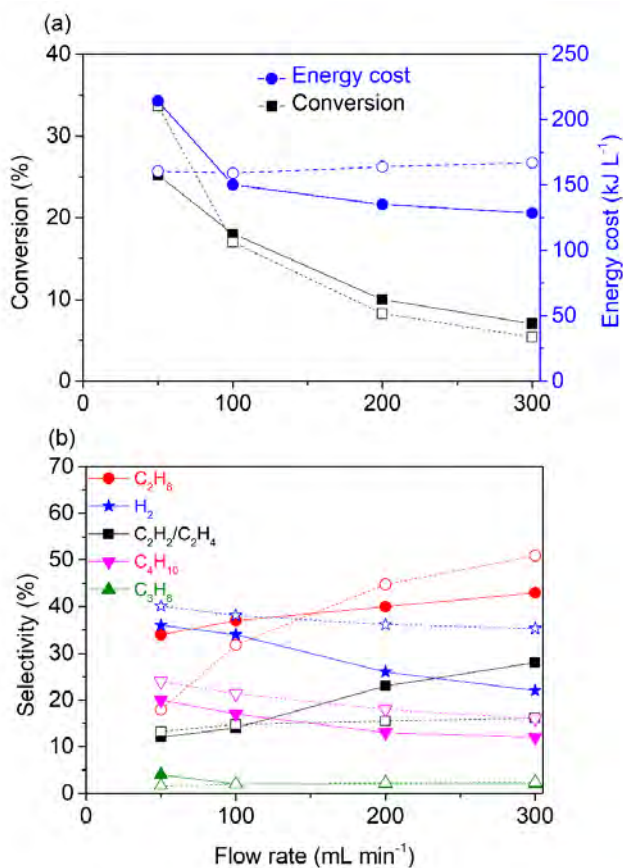


Figure 49: Calculated (dashed lines) and experimental (solid lines) CH_4 conversions and energy costs (a), as well as selectivities of the most important hydrocarbons and H_2 formed (b), as a function of flow rate, at a plasma power of 45 W in an atmospheric pressure DBD reactor. The experimental results are adopted from Xu and Tu³⁴⁶.

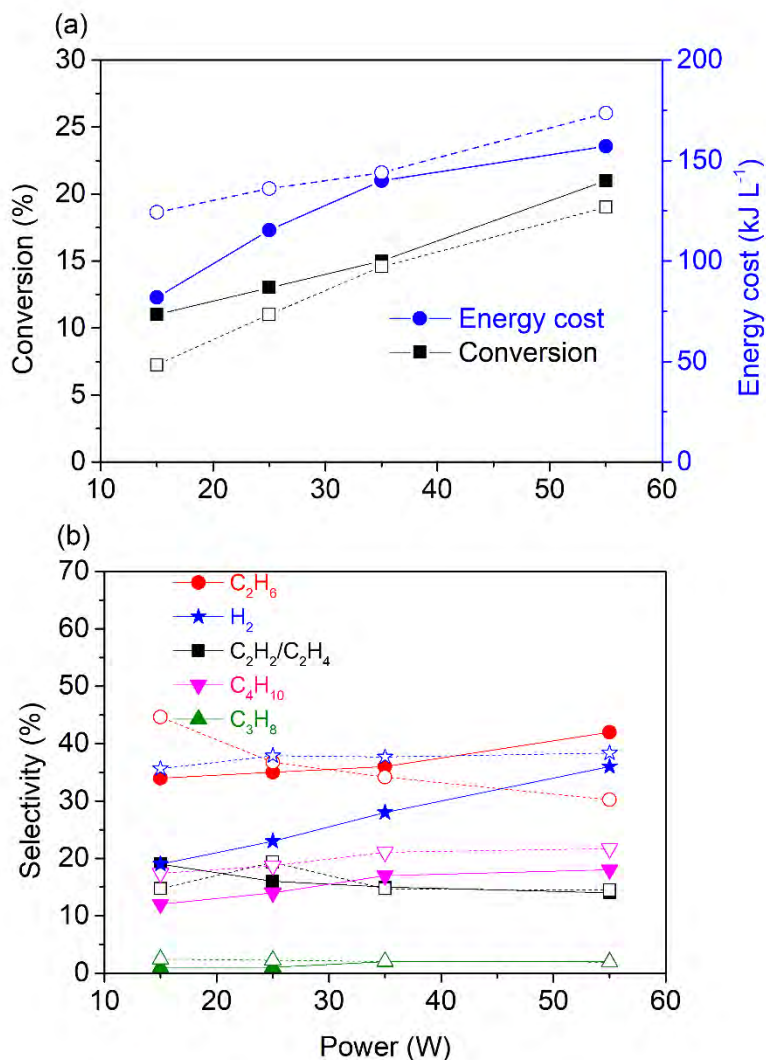


Figure 50: Calculated (dashed lines) and experimental (solid lines) CH₄ conversions and energy costs (a), as well as selectivities of the most important hydrocarbons and H₂ formed (b), as a function of plasma power, at a flow rate of 100 mL min⁻¹ in an atmospheric pressure DBD reactor. The experimental results are adopted from Xu and Tu³⁴⁶.

The calculated and experimental conversions, energy costs and product selectivities for the DBD reactor of Wang et al.³⁴⁵ are plotted in Figures 51 and 52, as a function of flow rate and plasma power, respectively. The H₂ selectivity

was not measured as a function of flow rate, and therefore, only the calculated H₂ selectivities are shown in Figure 51. Again, the conversion, energy cost and selectivities generally follow the same trends. Note that the energy cost is rather constant in the model, while the experimental values slightly drop as a function of flow rate (see Figure 51), but this is because the measured conversion drops more slowly than the calculated values at rising flow rate (and thus lower SEI). Indeed, when the flow rate rises by a factor 3 (and thus, the SEI drops by a factor 3, at constant power), the calculated conversion drops by a factor 3 as well (thus explaining the constant energy cost), while the measured conversion only drops by a factor 2 (thus explaining why the energy cost slightly drops). In addition, also the C₂H₂/C₂H₄ selectivities show some discrepancy, because the experimental data slightly drop and the calculation results slightly rise upon increasing plasma power (see Figure 52). However, the maximum relative difference is about 50 %, which is still reasonable, in view of the assumptions made in the 0D model. Also the absolute values of the calculated and experimental results are in satisfactory agreement, except for the C₃H₈/C₃H₆ selectivities, which exhibit a maximum discrepancy of 72 % at a plasma power of 15 W and a flow rate of 20.2 mL min⁻¹ (see Figure 52). The average discrepancy between the calculated and experimental results is 37 %, which should be good enough for explaining the underlying chemistry in a DBD reactor.

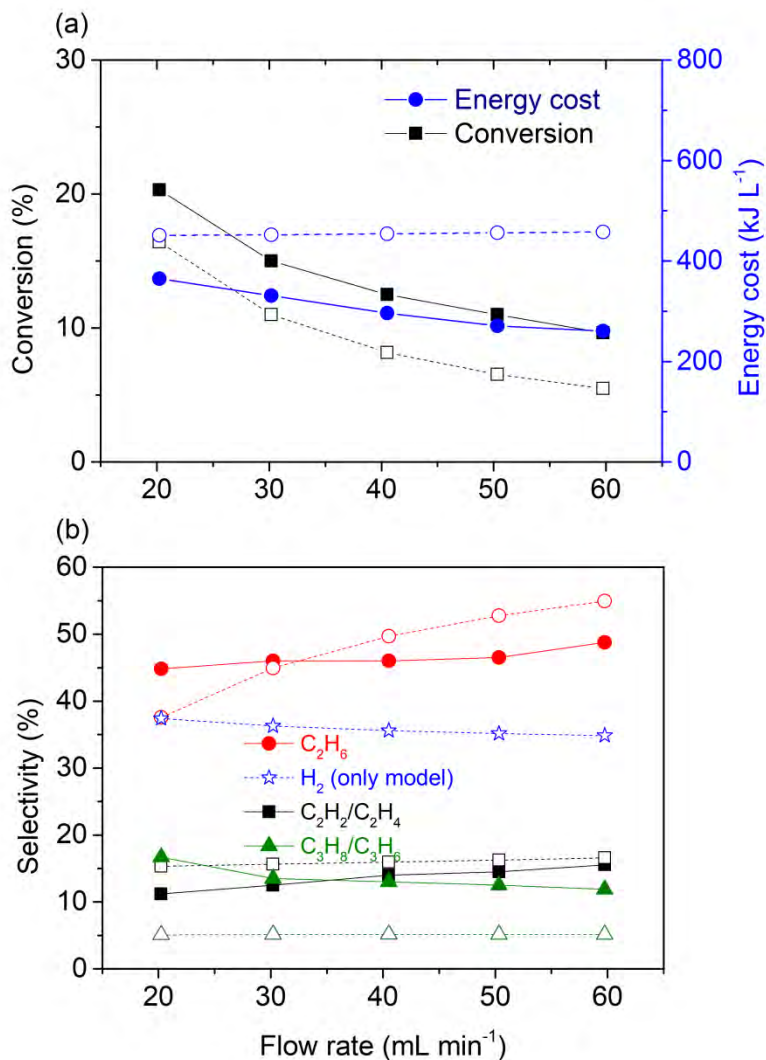


Figure 51: Calculated (dashed lines) and experimental (solid lines) CH₄ conversions and energy costs (a), as well as selectivities of the most important hydrocarbons and H₂ formed (b), as a function of flow rate, at a plasma power of 25 W in an atmospheric pressure DBD reactor. The experimental results are adopted from Wang et al. ³⁴⁵.

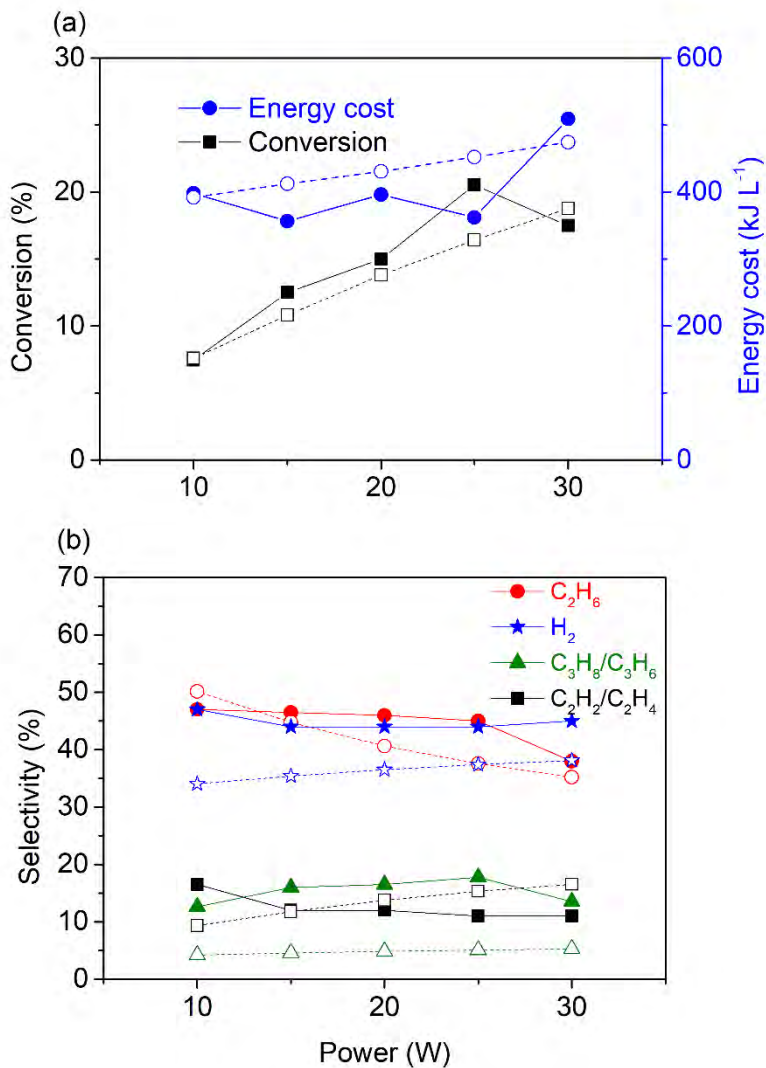


Figure 52: Calculated (dashed lines) and experimental (solid lines) CH₄ conversions and energy costs (a), as well as selectivities of the most important hydrocarbons and H₂ formed (b), as a function of plasma power, at a flow rate of 20.24 mL min⁻¹ in an atmospheric pressure DBD reactor. The experimental results are adopted from Wang et al.³⁴⁵.

In both reactors, the conversions vary between 7 % and 21 %, decreasing with rising flow rate and increasing with power. Based on the conditions used, this

corresponds to energy costs varying between 82 kJ L⁻¹ (or 19 eV molec⁻¹) at a plasma power of 15 W and a flow rate of 100 mL min⁻¹ (i.e. SEI = 9 kJ L⁻¹, for the conditions of Xu and Tu³⁴⁶; Figure 50), up to 509 kJ L⁻¹ (or 118 eV molec⁻¹) at a plasma power of 30 W and a flow rate of 20.2 mL min⁻¹ (i.e. SEI=89 kJ L⁻¹, for the conditions of Wang et al.³⁴⁵; see Figure 52). The average energy cost for CH₄ conversion for all conditions studied is 259 kJ L⁻¹ (or 60 eV molec⁻¹), which is very high. Both in the model and experiments, C₂H₆ is by far the most important hydrocarbon, followed by C₂H₂ and C₂H₄, C₄H₁₀ and finally C₃H₈. Other (unsaturated or higher) hydrocarbons were not reported in both papers, but according to our model, C₅H₁₂ can also be formed, and further polymerization towards C₆ and higher hydrocarbons is also possible. In addition, H₂ is formed in large amounts, both in the experiments and our model.

7.4.2 Underlying reaction pathways

The most important reactions in the DBD plasma are visualized in Figure 53. The thickness of the arrow lines is a measure for the importance of the reactions, determined by the reaction rates, as calculated in the model. These calculated rates are listed in the Appendix: Table A21. CH₄ is mainly converted by electron impact dissociation into CH₃ radicals ($e^- + CH_4 \rightarrow e^- + CH_3 + H$), as well as into CH₂ and CH radicals ($e^- + CH_4 \rightarrow e^- + CH_2 + H_2$ and $e^- + CH_4 \rightarrow e^- + CH + H + H_2$). The dissociation into CH₂ and H₂ ($e^- + CH_4 \rightarrow e^- + CH_2 + H_2$) is one of the most important H₂ formation processes (together with $e^- + C_2H_6 \rightarrow e^- + C_2H_4 + H_2$; see below).

In addition, CH₄ undergoes electron impact ionization and dissociative ionization ($e^- + CH_4 \rightarrow e^- + e^- + CH_4^+$ and $e^- + CH_4 \rightarrow e^- + e^- + CH_3^+ + H$). The CH₄⁺ and CH₃⁺ ions formed in this way are not indicated as separate species in Figure 53, as they quickly react with CH₄, forming C₂H₅⁺ ($CH_3^+ + CH_4 \rightarrow C_2H_5^+ + H_2$) or CH₅⁺ ($CH_4^+ + CH_4 \rightarrow CH_5^+ + CH_3$).

The CH₃ radicals partially recombine with H ($CH_3 + H + M \rightarrow CH_4 + M$) forming again CH₄, but they also recombine with another CH₃ radical ($CH_3 + CH_3 + M \rightarrow C_2H_6 + M$) to form C₂H₆, which is the most important production mechanism of C₂H₆, and it occurs mainly in the microdischarge pulses of the DBD, where the CH₃ radicals as necessary building blocks are formed.

C_2H_6 is partially converted into C_2H_4 , by electron impact dissociation ($e^- + C_2H_6 \rightarrow e^- + C_2H_4 + H_2$), which is the main population mechanism of C_2H_4 and one of the main population mechanisms of H_2 (cf. above). In addition, C_2H_4 is also formed upon (radical) recombination reactions ($CH_3 + CH_2 \rightarrow C_2H_4 + H$ and $CH_4 + CH \rightarrow C_2H_4 + H$).

C_2H_4 partially recombines with H into C_2H_5 ($C_2H_4 + H + M \rightarrow C_2H_5 + M$), and C_2H_5 recombines further with C_2H_5 into C_4H_{10} ($C_2H_5 + C_2H_5 + M \rightarrow C_4H_{10} + M$), as well as with H ($C_2H_5 + H \rightarrow CH_3 + CH_3$) forming again two CH_3 radicals, and with CH_3 ($CH_3 + C_2H_5 + M \rightarrow C_3H_8 + M$) forming C_3H_8 . The latter reaction is however less important than the other two reactions, explaining why C_4H_{10} was formed in larger amounts than C_3H_6/C_3H_8 in the experiments of Xu and Tu³⁴⁶ (see Figures 49 and 50). Moreover, C_2H_4 also undergoes electron impact dissociation ($e^- + C_2H_4 \rightarrow e^- + C_2H_2 + H_2$ and $e^- + C_2H_4 \rightarrow e^- + C_2H_3 + H$).

In addition, C_2H_4 and C_2H_6 react with CH_5^+ ions, forming $C_2H_5^+$ ($CH_5^+ + C_2H_6 \rightarrow C_2H_5^+ + H_2 + CH_4$ and $CH_5^+ + C_2H_4 \rightarrow C_2H_5^+ + CH_4$). $C_2H_5^+$ is an important intermediate for the formation of C_2H_2 and C_2H_3 , by dissociative recombination with electrons ($e^- + C_2H_5^+ \rightarrow C_2H_3 + H + H$, $e^- + C_2H_5^+ \rightarrow C_2H_2 + H_2 + H$, and $e^- + C_2H_5^+ \rightarrow C_2H_2 + H + H + H$). The C_2H_3 radicals mainly recombine with CH_3 radicals into C_3H_6 ($CH_3 + C_2H_3 + M \rightarrow C_3H_6 + M$), as well as with H ($C_2H_3 + H \rightarrow C_2H_2 + H_2$) forming C_2H_2 .

C_3H_6 undergoes electron impact dissociation into C_2H_2 ($e^- + C_3H_6 \rightarrow e^- + C_2H_2 + CH_4$), but it mainly recombines with H, forming C_3H_7 ($C_3H_6 + H + M \rightarrow C_3H_7 + M$). The latter radical quickly forms C_3H_8 upon reaction with H_2 ($C_3H_7 + H_2 \rightarrow C_3H_8 + H$), as well as by three-body recombination with H ($C_3H_7 + H + M \rightarrow C_3H_8 + M$).

C_3H_8 partially creates again C_3H_6 by electron impact dissociation ($e^- + C_3H_8 \rightarrow e^- + C_3H_6 + H_2$) or it recombines with CH_2 into C_4H_{10} ($C_3H_8 + CH_2 + M \rightarrow C_4H_{10} + M$). Finally, C_4H_{10} recombines with CH_2 radicals into C_5H_{12} ($C_4H_{10} + CH_2 + M \rightarrow C_5H_{12} + M$), which will further react into the formation of higher hydrocarbons by the same type of recombination reaction.

Hence it is clear that in a DBD electron impact dissociation processes are predominant. They create radicals, which mainly recombine with other radicals

or H atoms, due to the lower temperatures, forming especially the saturated hydrocarbons, such as C_2H_6 , C_3H_8 and C_4H_{10} .

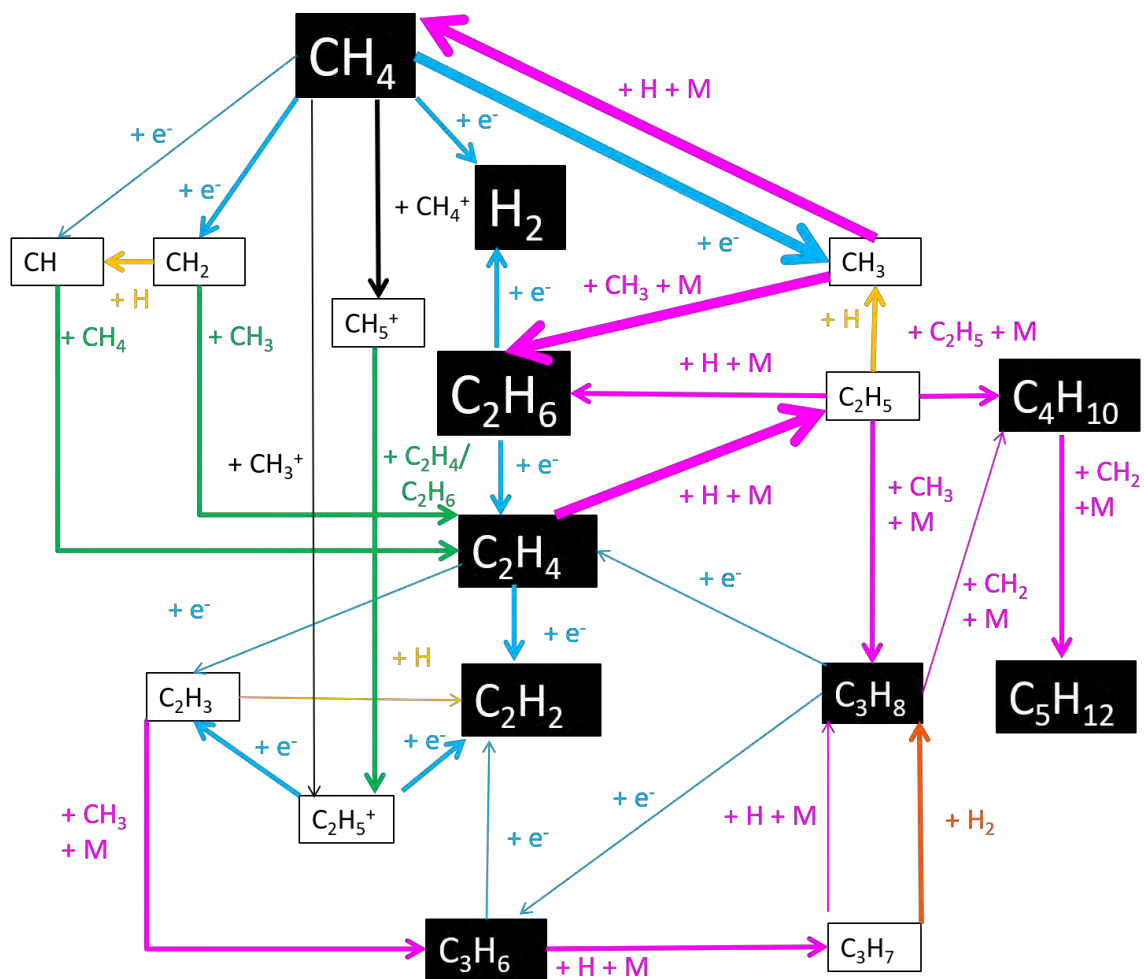


Figure 53: Most important net reaction pathways in a DBD at atmospheric pressure. Blue, pink, yellow, green and orange arrow lines represent electron impact reactions, three-body reactions, two-body reactions with H atoms, reactions with hydrocarbon molecules or radicals, and two-body reactions with H_2 , respectively. The thickness of the arrow lines is proportional to the reaction rate, while the size of the boxes is proportional to the species density, as calculated in the model. The black boxes represent stable molecules and the white boxes intermediates (radicals or ions).

7.5 MW plasma

7.5.1 Comparison of calculated and measured conversion, energy cost and selectivities

The experimental and calculated CH₄ conversions, energy costs and selectivities of the most important hydrocarbons are plotted as a function of SEI in Figures 54 and 55, for a MW discharge at reduced pressure, i.e. 30 mbar, for a continuous and a pulsed discharge, respectively. Again, no H₂ selectivities were reported in the experiments, so only the calculated values are given. In the pulsed regime, the calculated and measured gas temperature are also compared in Figure 55. Figures 56 and 57 show the experimental and calculated CH₄ conversions, energy costs, and most important product selectivities in a MW discharge at atmospheric pressure, as a function of power and flow rate, respectively. Note that these experiments were performed in a CH₄/H₂ mixture, so the H₂ selectivities could not be determined, since H₂ is also a reactant.

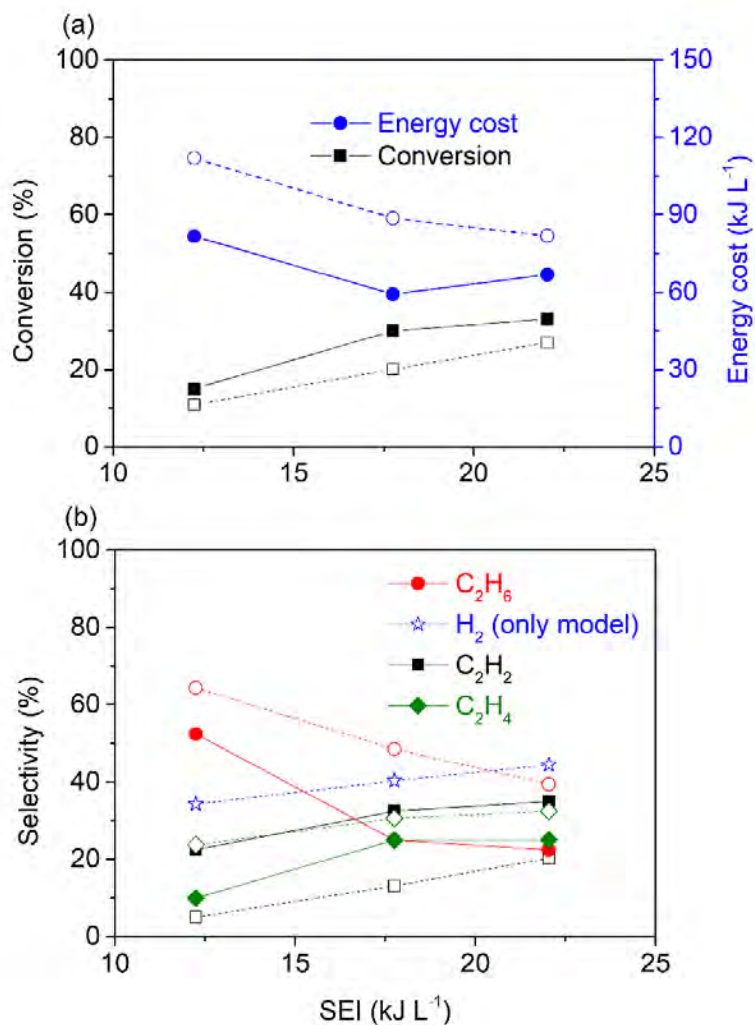


Figure 54: Calculated (dashed lines) and experimental (solid lines) CH₄ conversions and energy costs (a), as well as selectivities of the most important hydrocarbons and H₂ formed (b), as a function of SEI, in a MW plasma at a pressure of 30 mbar and flow rate of 98 sccm, operating in a continuous regime. The experimental results are adopted from Heintze and Magureanu ³⁴⁸.

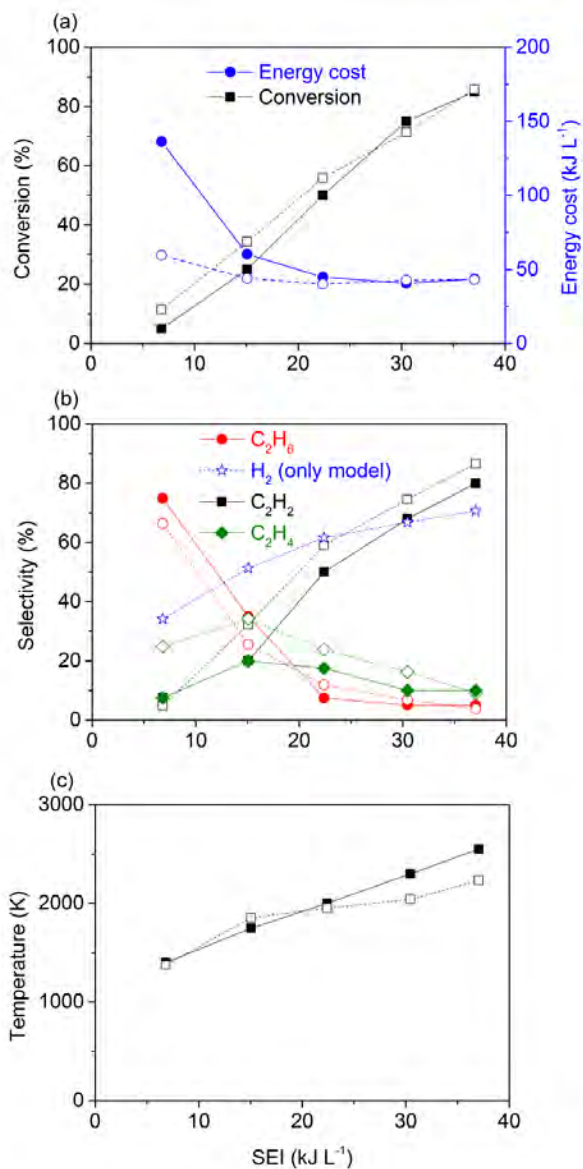


Figure 55: Calculated (dashed lines) and experimental (solid lines) CH₄ conversions and energy costs (a), as well as selectivities of the most important hydrocarbons and H₂ (b), and gas temperatures (c), as a function of SEI, in a MW plasma at a pressure of 30 mbar and flow rate of 98 sccm, operating in a pulsed regime. The experimental results are adopted from Heintze and Magureaunu³⁴⁸.

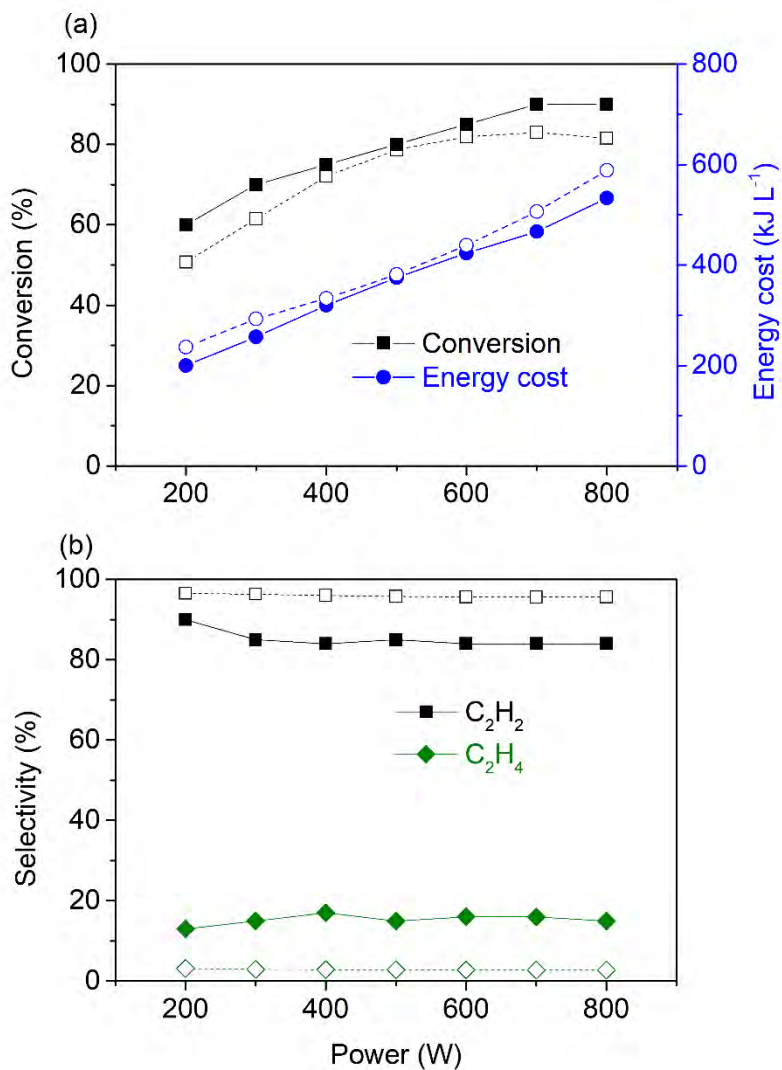


Figure 56: : Calculated (dashed lines) and experimental (solid lines) CH₄ conversions and energy costs (a), as well as selectivities of C₂H₄ and C₂H₂ (b), as a function of microwave power, at a flow rate of 500 mL min⁻¹ in an atmospheric pressure MW plasma, for a CH₄/H₂ ratio of 1/4. The experimental results are adopted from Shen et al ³⁴⁷.

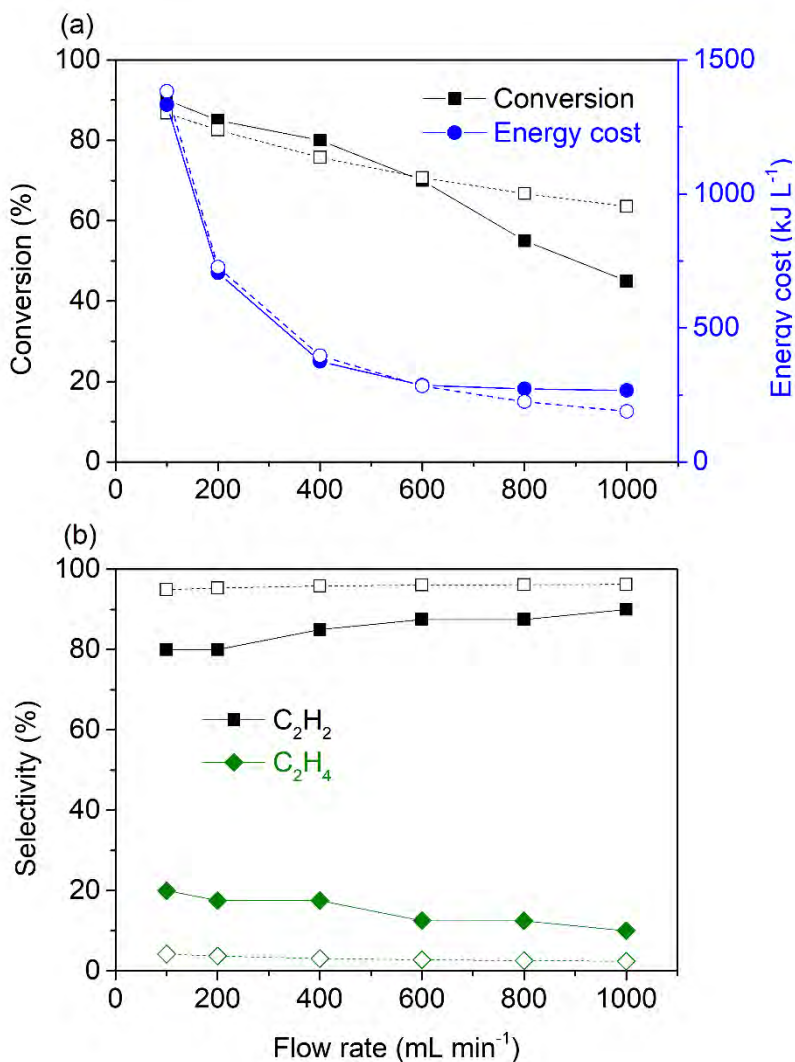


Figure 57: Calculated (dashed lines) and experimental (solid lines) CH₄ conversions and energy costs (a), as well as selectivities of C₂H₄ and C₂H₂ (b), as a function of flow rate, at a microwave power of 400 W in an atmospheric pressure MW plasma, for a CH₄/H₂ ratio of 1/4. The experimental results are adopted from Shen et al.³⁴⁷

In general, the difference between the calculated and experimental results is higher for lower powers and reduced pressure than for higher pressures and higher powers. The C₂H₂ selectivities in the reduced pressure MW plasma in continuous mode show the largest discrepancies, even up to almost a factor 5 (i.e.

calculated C_2H_2 selectivity of 5 % versus 23 %, for an SEI value of 12 kJ L^{-1}). The reason is probably the underestimation of the gas temperature and the assumption that the power is evenly distributed over the whole radial distance of the reactor tube. In the atmospheric pressure MW plasma the largest discrepancies are found for the C_2H_4 selectivities, i.e., up to a factor 6 (calculated C_2H_4 selectivity of 3 % versus 18 %, at 400 W and 500 mL min^{-1} ; see Figure 56). Nevertheless, in both the reduced pressure and atmospheric pressure MW plasma the experimental and calculated results show the same trend and on average the discrepancy between calculated and experimental results is 40 % for the reduced pressure MW plasma, and 44 % for the atmospheric pressure plasma. In addition, the difference between calculated and measured gas temperature in the pulsed reduced pressure MW plasma is less than 12 %, so we believe that a qualitative description of the reaction mechanisms in MW plasmas operating in different pressure regimes is feasible with our model, and will be presented in next Section.

It is clear that the CH_4 conversion in the MW plasma, both at reduced and atmospheric pressure, can reach values above 80 %, for high power and low flow rate, or high SEI values. The energy costs range from about 50 to above 100 kJ L^{-1} at reduced pressure, which is lower than in a DBD. In the atmospheric pressure MW plasma, the energy costs vary from 200 to above 1000 kJ L^{-1} , which is of the same order or even higher than in the DBD. However, it should be mentioned that the gas flow in this case was diluted with H_2 , (CH_4/H_2 ratio of 1/4), which reacts to a large extent with the dissociation products of CH_4 , forming again CH_4 . This means that not all the power is efficiently used for CH_4 conversion, explaining the higher energy cost.

For lower power and pressure, the main products formed are C_2H_6 (with selectivities ranging between 5 % and 75 %), C_2H_4 (with selectivities ranging from 8 % to 20 %) and C_2H_2 (with selectivities ranging from 8 % to 80 %). Higher hydrocarbons, such as created in the DBD, were not observed in our model, and also not reported experimentally. This is attributed to the high temperatures in the MW plasma (above 1000 K), which will cause dissociation of these higher hydrocarbons back in smaller compounds. Furthermore, the higher the SEI value, the larger the shift towards C_2H_2 and C_2H_4 , instead of C_2H_6 . At atmospheric pressure, CH_4 is mainly converted into C_2H_2 with a selectivity of ~ 85 %, and to C_2H_4 with a selectivity of ~ 15 %. Although different conditions give different

product selectivities, especially at reduced pressure, we can draw an overall picture of the most important mechanisms at reduced pressure vs atmospheric pressure, as outlined in next Section.

7.5.2 Underlying reaction pathways

It is clear from above that the different pressure regimes in a MW plasma show different product distributions, which are attributed to different mechanisms, as can be seen in Figures 58 and 59. Again, the thickness of the arrow lines are a measure for the importance of the reactions, determined by the reaction rates, as calculated in the model. These calculated rates are again listed in the Appendix: Tables A22-A23, for the MW plasma at reduced and atmospheric pressure, respectively.

In a reduced pressure MW plasma, CH₄ is converted into CH₃ by a combination of electron impact dissociation ($e^- + CH_4 \rightarrow e^- + CH_3 + H$) and reaction with H atoms ($CH_4 + H \rightarrow CH_3 + H_2$). The latter reaction is possible due to the higher temperature in the MW plasma, compared to a DBD, and it is also the main population mechanism of H₂. Some of the CH₃ radicals react back to CH₄ by reactions with C₂H₄ and C₂H₃ ($CH_3 + C_2H_4 \rightarrow CH_4 + C_2H_3$ and $CH_3 + C_2H_3 \rightarrow CH_4 + C_2H_2$). In addition, the CH₃ radicals react further with either CH₃ ($CH_3 + CH_3 + M \rightarrow C_2H_6 + M$, and $CH_3 + CH_3 \rightarrow C_2H_5 + H$) or CH₄ ($CH_4 + CH_3 \rightarrow C_2H_6 + H$), to form both C₂H₆ and C₂H₅. The latter radicals, due to the higher temperature, dissociate mainly further into C₂H₄ ($C_2H_5 + M \rightarrow C_2H_4 + H + M$). However, a small fraction also recombines with CH₃ into C₃H₈ ($CH_3 + C_2H_5 + M \rightarrow C_3H_8 + M$) or with C₂H₅ into C₄H₁₀ ($C_2H_5 + C_2H_5 + M \rightarrow C_4H_{10} + M$).

C₂H₆ partially dissociates back into CH₃ ($C_2H_6 + M \rightarrow CH_3 + CH_3 + M$), which becomes more important at high SEI values, explaining why high SEI values give lower C₂H₆ selectivities (see Figures 54 and 55). In addition, it also undergoes electron impact dissociation towards C₂H₄ ($e^- + C_2H_6 \rightarrow e^- + C_2H_4 + H_2$), and it reacts with CH₃ or H radicals into C₂H₅ ($CH_3 + C_2H_6 \rightarrow CH_4 + C_2H_5$ and $C_2H_6 + H \rightarrow C_2H_5 + H_2$).

C₂H₄, which is mainly formed by dissociation of C₂H₆ and C₂H₅, reacts mostly further with CH₃ radicals into C₂H₃ ($CH_3 + C_2H_4 \rightarrow CH_4 + C_2H_3$), but a small fraction is also subject to electron impact dissociation, creating C₂H₂ ($e^- +$

$C_2H_4 \rightarrow e^- + C_2H_2 + H_2$), or it reacts with H_2 , creating again C_2H_5 ($C_2H_4 + H_2 \rightarrow C_2H_5 + H$).

The C_2H_3 radicals react with CH_3 radicals into either C_3H_6 or C_2H_2 , at almost equal rates ($CH_3 + C_2H_3 + M \rightarrow C_3H_6 + M$, and $CH_3 + C_2H_3 \rightarrow CH_4 + C_2H_2$). This is the main formation process of C_3H_6 at high SEI values, while at low SEI values, C_3H_6 is mainly formed by electron impact dissociation of C_3H_8 ($e^- + C_3H_8 \rightarrow e^- + C_3H_6 + H_2$).

At low SEI values, C_3H_6 dissociates mainly into C_2H_2 and C_3H_5 by electron impact dissociation ($e^- + C_3H_6 \rightarrow e^- + C_2H_2 + CH_4$, and $e^- + C_3H_6 \rightarrow e^- + C_3H_5 + H$) and it forms C_3H_7 upon recombination with H atoms ($C_3H_6 + H + M \rightarrow C_3H_7 + M$). At high SEI values, C_3H_6 mainly forms C_3H_5 upon reaction with H or any other neutral molecule ($C_3H_6 + H \rightarrow C_3H_5 + H_2$ and $C_3H_6 + M \rightarrow C_3H_5 + H + M$). C_3H_5 immediately dissociates further into C_2H_2 ($C_3H_5 + M \rightarrow C_2H_2 + CH_3 + M$).

C_3H_8 undergoes electron impact dissociation towards C_3H_6 , as mentioned above, but also towards C_2H_4 ($e^- + C_3H_8 \rightarrow e^- + C_2H_4 + CH_4$), and to a smaller extent it reacts with H into C_3H_7 ($C_3H_8 + H \rightarrow C_3H_7 + H_2$). C_3H_7 is formed by dissociation of C_3H_8 and recombination of C_3H_6 , as mentioned above, but it is also (and even predominantly) formed by dissociation of C_4H_{10} ($C_4H_{10} + M \rightarrow C_3H_7 + CH_3 + M$). Vice versa, it dissociates into C_2H_4 ($C_3H_7 + M \rightarrow C_2H_4 + CH_3 + M$), thus closing the C_3 and C_4 loop back towards the C_2 hydrocarbons, and explaining why the latter are predominantly formed in MW plasmas.

Finally, C_2H_2 , which is the main product at high SEI values, is formed by various electron impact dissociation, neutral dissociation and two-body reactions with several C_2 and C_3 compounds, mainly C_2H_4 , C_2H_3 , C_3H_6 and C_3H_5 , while a small portion reacts further with H_2 towards C_2H_3 ($C_2H_2 + H_2 \rightarrow C_2H_3 + H$), which in turn creates again C_3 compounds, as described above, thus closing the whole cycle.

The chemistry in the atmospheric pressure MW plasma is much less complex, as can be seen in Figure 59. This is attributed to the higher temperature (i.e., > 3000 K vs ~ 2000 K at 30 mbar), causing the dehydrogenation processes to be much more prominent. Like in the reduced pressure case, CH_4 is converted into CH_3 , by a combination of electron impact dissociation ($e^- + CH_4 \rightarrow e^- + CH_3 + H$) and reaction with H atoms ($CH_4 + H \rightarrow CH_3 + H_2$). These radicals partially

recombine back into CH₄ upon reaction with C₂H₄ (CH₃ + C₂H₄ → CH₄ + C₂H₃). In addition, they react with CH₄ to produce C₂H₆ (CH₄ + CH₃ → C₂H₆ + H), which however immediately dissociates back into CH₃ (C₂H₆ + M → CH₃ + CH₃ + M) or reacts with CH₃ into the formation of C₂H₅ (CH₃ + C₂H₆ → CH₄ + C₂H₅). Furthermore, two CH₃ radicals also recombine to produce C₂H₅ (CH₃ + CH₃ → C₂H₅ + H), which immediately dissociates into C₂H₄ (C₂H₅ + M → C₂H₄ + H + M).

C₂H₄ in turn reacts with CH₃ and H atoms, forming C₂H₃ (CH₃ + C₂H₄ → CH₄ + C₂H₃ and C₂H₄ + H → C₂H₃ + H₂), which directly reacts further with H into C₂H₂ (C₂H₃ + H → C₂H₂ + H₂). Due to the high temperature, C₂H₂ dissociates into C₂H (C₂H₂ + M → C₂H + H + M), which returns immediately back into C₂H₂ (C₂H + H₂ → C₂H₂ + H). Finally, a small portion of C₂H₂ also recombines back with H₂ into the formation of C₂H₄ (C₂H₂ + H₂ + M → C₂H₄ + M), closing the loop. Although H₂ is a reactant, it is immediately formed again by the dehydrogenation processes, forming ultimately C₂H₂.

The reaction pathways in Figures 58 and 59 mainly exhibit thermal reactions, with some contribution of electron impact dissociation at reduced pressure (Figure 58). This is of course due to the high temperature, enabling these thermal reactions, in contrast with the DBD, where electron impact dissociation and also ionization were much more predominant (Figure 53). Lower pressures and lower powers furthermore favor recombination processes, resulting in the formation of C₃ compounds. Higher pressures and higher powers induce dehydrogenation reactions, resulting in more unsaturated hydrocarbons, and thus explaining the high C₂H₂ selectivity in Figures 55, 56 and 57.

In addition, the role of vibrational-induced dissociation of CH₄ in the MW plasma is investigated, as this process is important in the case of CO₂ splitting and N₂ fixation^{25,57,309,366}, especially in low pressure (< 200 mbar) MW plasmas, where there is a pronounced vibrational-translational non-equilibrium. For this purpose, we calculated the vibrational temperature, from the four vibrational levels included in our model:

$$T_v = \frac{1}{4} \sum_{i=1}^4 \frac{E_i}{\log\left(\frac{n_i}{g_i n_o}\right)} \quad (50)$$

with E_i the energy of the first level of vibrational mode v_i of CH₄ (in K), g_i its degeneracy and n_i its density (in cm⁻³). n_o is the density of ground state CH₄.

However, for the MW plasma conditions in this study, the vibrational temperature of CH₄ is almost equal to the gas temperature, indicating that the vibration-translational non-equilibrium in CH₄ MW plasma is negligible, even at reduced pressure (see Appendix: Figures A26 and A27). This finding is supported by measurements of Butterworth et al.³⁶⁷

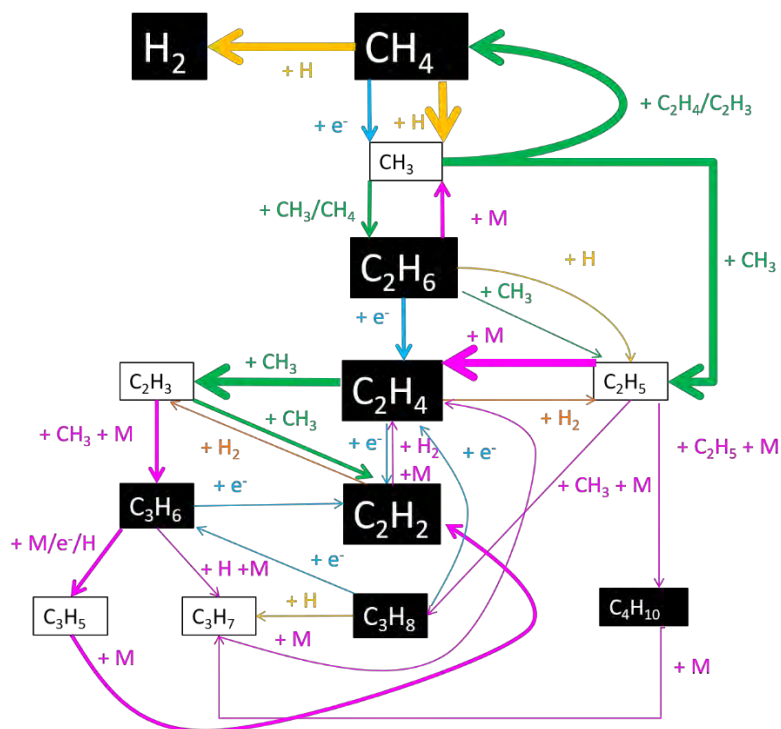


Figure 58: Most important net reaction pathways in a MW plasma at reduced pressure. Blue, pink, yellow, green and orange arrow lines represent electron impact reactions, reactions involving a neutral species M in three-body reactions or neutral dissociation, two-body reactions with H atoms, two-body reactions with hydrocarbon molecules or radicals, and with H₂ molecules, respectively. The thickness of the arrow lines and the size of the boxes are proportional to the reaction rate and species density, respectively, as calculated in the model. The black boxes represent stable molecules and the white boxes intermediates (radicals).

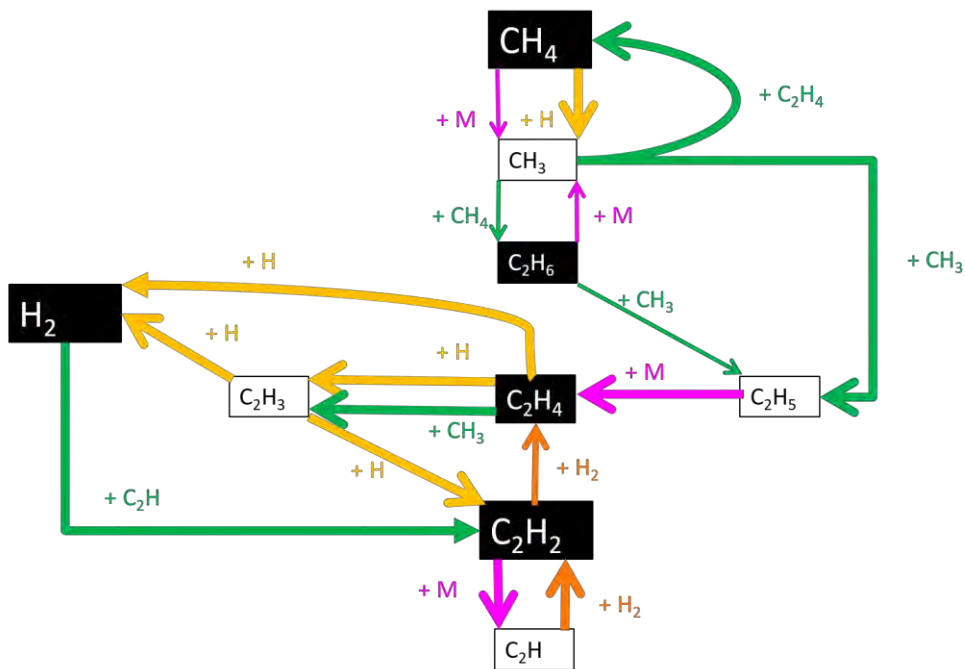


Figure 59: Most important net reaction pathways in a MW plasma at atmospheric pressure. Pink, yellow, green and orange arrow lines represent reactions involving dissociation with a neutral species M, two-body reactions with H atoms, two-body reactions with hydrocarbon molecules or radicals, and with H₂ molecules, respectively. The thickness of the arrow lines and the size of the boxes are proportional to the reaction rate and species density, respectively as calculated in the model. The black boxes represent stable molecules and the white boxes intermediates (radicals).

7.6 GAP

7.6.1 Comparison of calculated and measured conversion, energy cost and selectivities

The experimental and calculated CH₄ conversions, energy costs and selectivities of the most important hydrocarbons and H₂ are plotted in Figure 60 as a function of CH₄ fraction in the CH₄/N₂ mixture, at a power of 224 W and a flow rate of 10 L min⁻¹. The agreement is very reasonable, with a maximum discrepancy between the experimental and calculated results of 36 % for the C₂H₆ selectivity (at a CH₄ fraction of 50 %) and an average discrepancy of 15 %. In addition, both

experimental and calculated results follow the same trends as a function of CH₄ fraction. Therefore, the model should be able to provide a reasonable description of the chemistry inside the GAP, operating in CH₄/N₂ at various mixing ratios.

The conversion is around 50 %, and the energy cost is between 5 and 15 kJ L⁻¹, decreasing for higher CH₄ fraction in the mixture. This is significantly lower than the energy costs obtained in the DBD and in the MW plasma, both at reduced and atmospheric pressure. The fact that the energy cost is much lower than in a DBD is not surprising, as this is also the case for other gas conversion processes, such as CO₂ splitting, dry reforming of methane, and N₂ fixation^{3,368}. However, the fact that it is also clearly lower than the MW plasma is quite striking, as both plasma sources operate at similar temperature (> 3000 K) and power (> 200 W). On the other hand, the flow rate in the GAP (10 L min⁻¹) is much higher than in the MW plasma (100-1000 mL min⁻¹), so the SEI in the GAP is much lower, demonstrating the superior performance in terms of energy cost. The CH₄ conversion at 20 % CH₄ is similar as for the same CH₄ fraction in case of dry reforming, see Chapter 4. However, since different conditions are used, i.e. 224 W in this study and 500 W in Chapter 4, and the main dissociation mechanisms are different, we cannot draw any further conclusions on whether both N₂ and CO₂ would have the same effect on CH₄ reforming.

The most important product formed is C₂H₂ (with selectivities ranging between 46 % and 65 %), followed by C₂H₄ (with selectivities between 24 % and 36 %) and finally C₂H₆ (with selectivities between 9 % and 15 %).

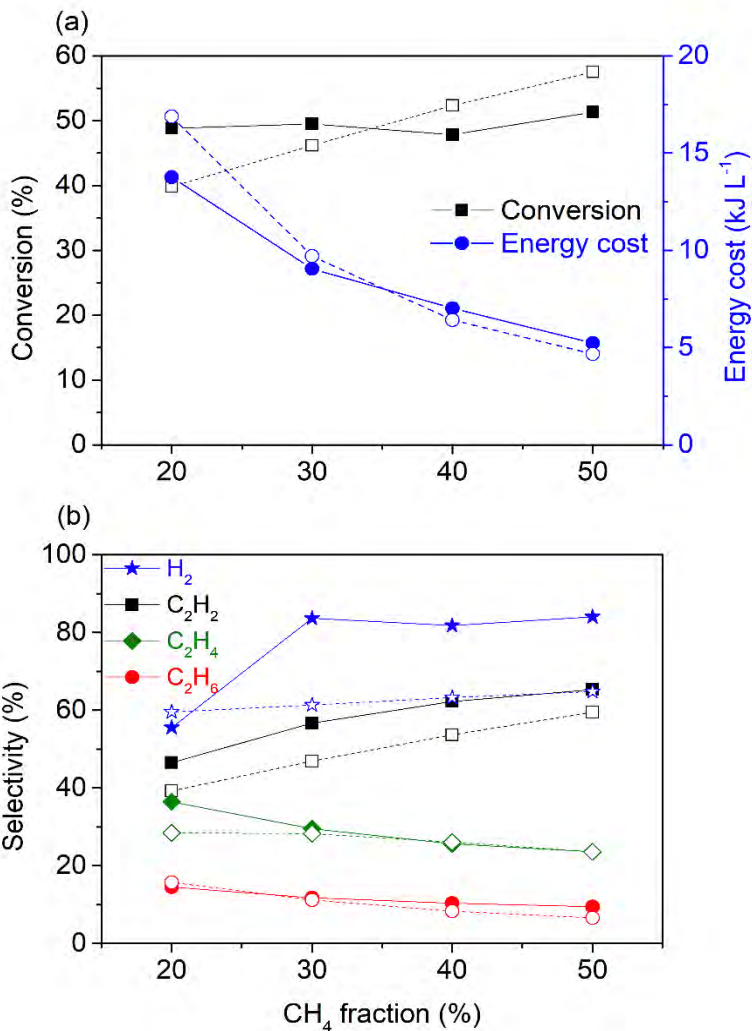


Figure 60: Calculated (dashed lines) and experimental (solid lines) CH₄ conversions and energy costs (a), as well as selectivities of the most important hydrocarbons and H₂ formed (b), in the GAP, as a function of CH₄ fraction in the CH₄/N₂ mixture, for an input power of 224 W and a flow rate of 10 L min⁻¹.

7.6.2 Underlying reaction pathways

The underlying reaction mechanisms in the GAP are presented in Figure 61. They are similar as in the MW plasma at atmospheric pressure, which is logical, because both plasma types operate at similar temperatures and powers, as

mentioned above. The calculated rates of the reactions in this figure are again listed in the Appendix: Table A24.

Just as in the MW plasma at atmospheric pressure, CH₄ is converted into CH₃ radicals upon both neutral dissociation (CH₄ + M → CH₃ + H + M) and reaction with H atoms (CH₄ + H → CH₃ + H₂). The CH₃ radicals partially react with C₂H₄ to form CH₄ again (CH₃ + C₂H₄ → CH₄ + C₂H₃) but also with N₂H (CH₃ + N₂H → CH₄ + N₂), the latter being formed by N₂ reacting with H atoms (N₂ + H + M → N₂H + M). Finally, some CH₃ radicals also form C₂H₆ (CH₄ + CH₃ → C₂H₆ + H), which however immediately dissociates back into CH₃ (C₂H₆ + M → CH₃ + CH₃ + M) or reacts with CH₃ into the formation of C₂H₅ (CH₃ + C₂H₆ → CH₄ + C₂H₅).

The rest of the pathways is identical to the atmospheric MW plasma, with the exception that C₂H₅ partially reacts back to C₂H₆ (CH₃ + C₂H₅ → C₂H₆ + CH₂, and CH₄ + C₂H₅ → CH₃ + C₂H₆) and C₂H₄ also dissociates in C₂H₃ using neutral dissociation (C₂H₄ + M → C₂H₃ + H + M) due to the higher temperatures in the GAP, especially in the beginning of the arc discharge near the cathode spot.

Thus, dehydrogenation and neutral dissociation reactions of the produced hydrocarbons are the most important processes in the GAP, resulting especially in the formation of C₂H₂.

The fact that the majority of CH₄ dissociates in the GAP, even at the high flow rate of 10 L min⁻¹ (which is at least a factor 10 higher than in the MW plasma at atmospheric pressure, cf. Figure 57; and even up to three orders of magnitude higher than in the DBD; cf. Figures 49-52), point towards the high efficiency of the GAP for CH₄ conversion, compared to the MW and DBD plasmas. This is attributed to the high temperature of the GAP, favoring thermal CH₄ dissociation.

In terms of energy cost, we can conclude that sufficiently high temperatures to induce thermal dissociation, together with a high flow rate, are needed for CH₄ conversion at low energy cost. Indeed, the model predicts that also in the GAP, vibration-induced dissociation of CH₄ is negligible, and there is no vibrational-translational non-equilibrium. In addition, mainly C₂H₂ and H₂ are formed, next to C₂H₄. It would be even more beneficial if the selectivity towards C₂H₄ could be enhanced, to make plasma technology of interest for the production of this important chemical compound, and thus for electrification of the chemical industry ³⁶⁹. Note that the C₂H₄ selectivity could be enhanced by

introducing a catalyst after the plasma reactor, to convert the produced C_2H_2 into C_2H_4 , as demonstrated by Delikonstantis et al.³³⁰. However, this catalytic hydrogenation reaction occurs at much lower temperatures (150 – 200 °C) compared to GAP (3000 K and higher)^{370–372}. Hence, a cooling step would be needed, which adds to the energy cost of this process. On the other hand, high enough temperatures (>1000 K) are important for efficient CH_4 conversion and to steer product selectivity. However, without plasma, temperatures between 1000 K and 2000 K do not induce as much dissociation as with plasma; see Figure 65 in section 7.7. Hence, although based on the simulations, higher temperature plasma processing seems to be the key for dehydrogenation of CH_4 and efficient CH_4 dissociation, temperature alone is not sufficient for significant conversion and cannot provide enough H atoms to induce this dehydrogenation; see Figure 65 in section 7.7. Milder conditions, resulting in gas temperatures of 1300 K, with plasma, should still favour dehydrogenation of CH_4 without further dehydrogenation towards very unsaturated compounds such as C_2H_2 and more towards C_2H_4 , thus exploiting the most of the temperature and plasma effect. This was also suggested by Delikonstantis et al.³³¹.

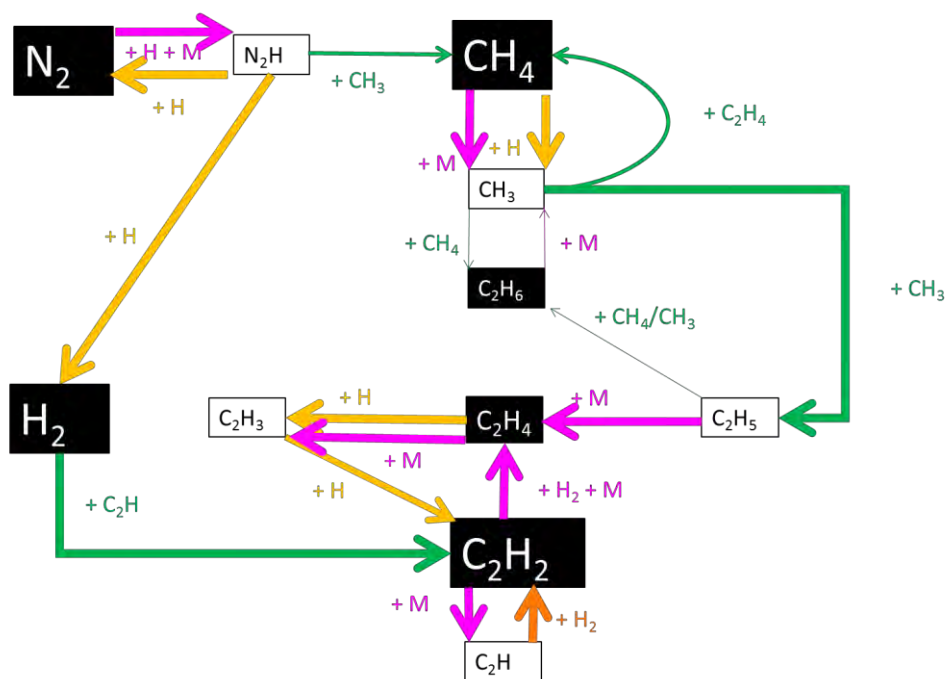


Figure 61: Most important net reaction pathways in the GAP at atmospheric pressure. Pink, yellow, green and orange arrow lines represent reactions involving a neutral species M in three-body reactions or neutral dissociation, two-body reactions with H atoms, two-body reactions with hydrocarbon molecules or radicals, and with H₂ molecules, respectively. The thickness of the arrow lines and the size of the boxes are proportional to the reaction rate and species density, respectively, as calculated by the model. The black boxes represent stable molecules and the white boxes intermediates (radicals).

7.7 Plasma vs. thermal conversion

It is clear from previous sections that the higher temperature of MW and GA plasma leads to higher conversion and more selective production of unsaturated hydrocarbons. To investigate whether the conversion in these plasmas is purely thermal or due to (additional) plasma effects, we make a distinction between the plasma effects and the thermal effects for the same range of conditions as investigated in sections 7.5 and 7.6.

Figure 62 shows the CH₄ conversions for the MW plasma at reduced pressure (30 mbar), obtained in the plasma and by pure thermal conversion at the same temperature (i.e., without electron impact reactions, which are specific plasma-based reactions), as a function of SEI, for the continuous (a) and pulsed (b) regime. The corresponding gas temperature is plotted in blue color (right y-axis). Both the maximum temperature and averaged temperature (obtained by averaging over the whole residence time) are plotted. At this reduced pressure, almost all conversion is due to plasma effects. Indeed, despite the fact that the maximum temperatures obtained in both the continuous and pulsed mode can reach 1500 K and more, which is in principle sufficient to induce significant thermal conversion, this temperature is only reached for a short time, even in the continuous mode, due to the triangular power profile, as explained in section 7.3.2 (~ 30 μs in the pulsed mode and ~ 100 μs in the continuous mode), causing the average temperature in the MW plasma to be too low for thermal conversion. During the short plasma time, however, enough reactive species are created, which, due to the higher local temperatures, react further in neutral reactions. These reactive species are mainly CH₃ and H, as can be seen in Figure 58, and are mainly created by electron impact dissociation of CH₄ or neutral dissociation of higher hydrocarbons, as illustrated in Figures A31 and A32 in the Appendix.

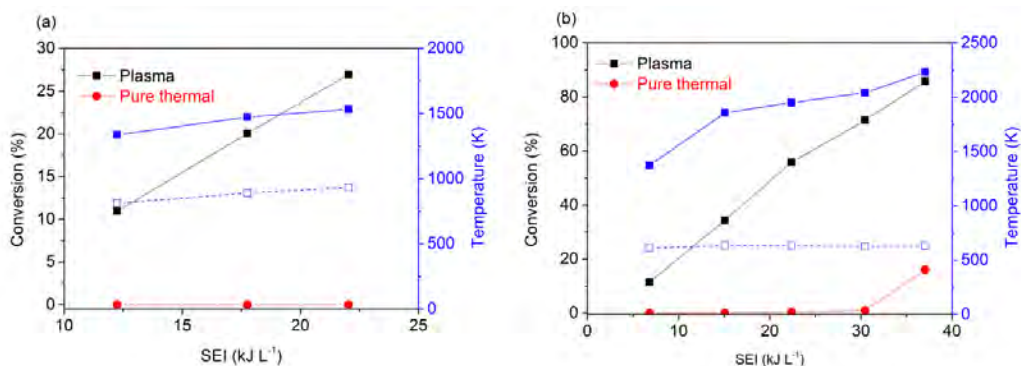


Figure 62: Calculated conversion by the plasma and by pure thermal conversion (i.e., without electron impact reactions) (left y-axis), as well as calculated maximum gas temperature inside the plasma/pulses (solid line) and averaged over the whole residence time in the reactor (dashed line) (right y-axis), as a function of SEI, in a MW plasma at a pressure of 30 mbar and flow rate of 98 sccm, operating in a continuous (a) and pulsed (b) regime.

However, in the atmospheric pressure MW plasma and in the GAP discharge, the conversions obtained with and without electron impact reactions are virtually the same, as is clear from Figures 63 and 64, indicating that the conversion is purely thermal at the high temperatures of 3000-3500 K. However, plasmas can still be beneficial above classical thermal conversion, as high temperatures (3000 -3500 K) can be reached by applying electric power (of interest for electrification of chemical reactions) and without damaging the reactor. Indeed, the arc in the GAP can be easily contained in the reactor center due to the reverse vortex flow, which isolates the hot plasma from the reactor walls³⁰ and in MW plasmas at atmospheric pressure, gas contraction takes place, also focusing the plasma in the center, and thus also protecting the reactor walls^{359,373}. Finally, plasmas can be switched on and off quite fast, with ignition times equal to several 100 ms in plasma torches,³⁷⁴ making them compatible with fluctuating renewable electricity.

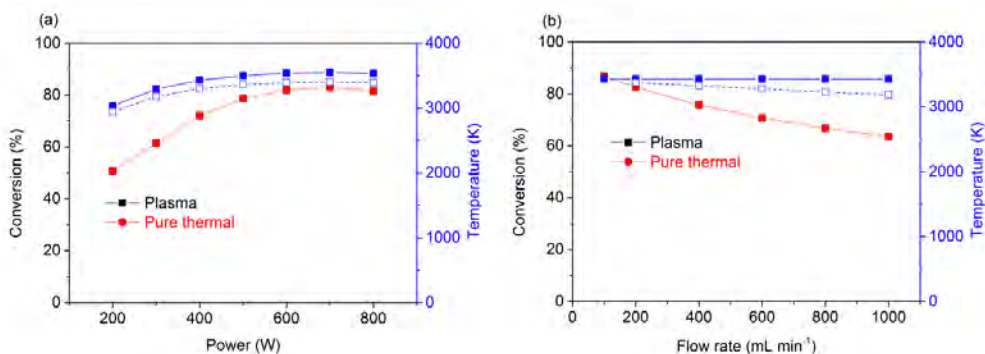


Figure 63: Calculated conversion by the plasma and by pure thermal conversion (i.e., without electron impact reactions) (left y-axis), as well as calculated maximum gas temperature (solid line) and averaged over the whole residence time in the reactor (dashed line) (right y-axis), as a function of microwave power, at a flow rate of 500 mL min⁻¹ (a), and as a function of flow rate, at a microwave power of 400 W (b), in an atmospheric pressure MW plasma, for a CH₄/H₂ ratio of 1/4. Note that the plasma conversion and pure thermal conversion perfectly overlap.

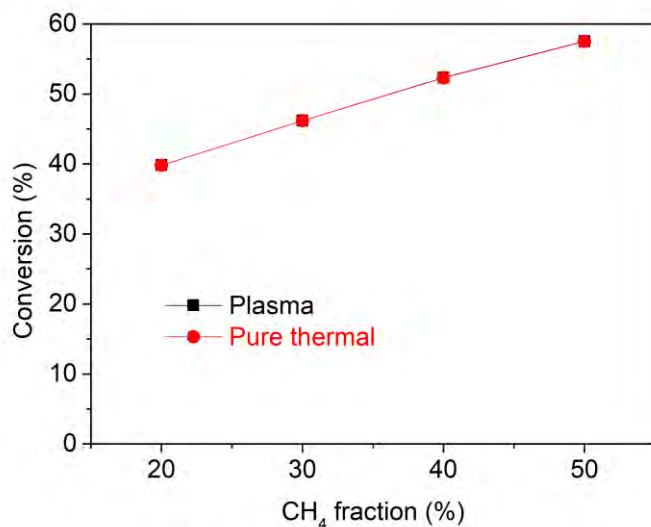


Figure 64: Calculated conversion by the plasma and by pure thermal conversion (i.e., without electron impact reactions) in the GAP, as a function of CH₄ fraction in the CH₄/N₂ mixture, for an input power of 224 W and a flow rate of 10 L min⁻¹. The plasma conversion and pure thermal conversion perfectly overlap. The used temperature profile for all conditions studied can be seen in Figure 48.

Besides the gas temperature, also the electron density is completely different in the three different plasma types. In the DBD plasma the electron densities are calculated to be between $5 \times 10^{13} \text{ cm}^{-3}$ and $2 \times 10^{14} \text{ cm}^{-3}$. In the MW plasma at reduced pressure, the electron densities range between $1.6 \times 10^{12} \text{ cm}^{-3}$ and $2.4 \times 10^{13} \text{ cm}^{-3}$, while in the MW plasma at atmospheric pressure, the electron densities vary between $6.0 \times 10^{11} \text{ cm}^{-3}$ and $1.4 \times 10^{12} \text{ cm}^{-3}$. Finally, in the GAP the electron density is calculated to be $\sim 6.0 \times 10^{11} \text{ cm}^{-3}$. Thus, the calculated electron density is the highest in the DBD, more specifically inside the filaments. Combined with the low gas temperature ($< 500 \text{ K}$), it is logical that electron impact reactions, next to three-body recombinations, are dominant. Since a 0D model cannot capture spatial non-uniformities, such as plasma contraction, local higher power densities may be underestimated, which might result in lower electron densities. Nevertheless, since the gas temperatures are around 3000 K or higher in the (atmospheric pressure) MW plasma and the GAP, CH_4 dissociates very fast at these temperatures, so we are confident that our conclusion about the importance of thermal conversion is valid, even if the electron densities would be somewhat underestimated.

To assess whether temperature controls the overall chemical behavior, we plot in Figure 65(a,b) the CH_4 conversion and product selectivities for a generic type of plasma, at 400 W and a flow rate of 500 mL min^{-1} , as a function of gas temperature. It is clear that the temperature indeed plays a determining role in steering the conversion and the product selectivities. Gas temperatures below 1000 K favour radical recombination processes, resulting in more saturated hydrocarbons (C_2H_6 and higher $\text{C}_3\text{-C}_5$ hydrocarbons), as demonstrated in section 7.4.2 for DBD plasmas. Higher temperatures favour neutral dissociation and dehydrogenation, explaining why C_2H_4 and especially C_2H_2 are the dominant products in the MW plasma and the GAP. Similar trends in selectivities were also found in thermodynamic calculations^{375,376} where for temperatures below 1000 K C_2H_6 and higher saturated hydrocarbons are the dominant hydrocarbon species formed. Between 1000 K and 1500 K , C_2H_4 is mainly formed, while above 1500 K until about 4000 K , C_2H_2 is the main product formed.

In Figure 65(a) we also compare the plasma conversion and conversion at thermal equilibrium, demonstrating that up to a temperature of 2000 K , there is still a significant difference. Hence, the plasma effect can still be important in

warm plasmas at atmospheric pressure, when the temperature would be below 2000 K. However, for the atmospheric pressure MW plasma and GAP studied in sections 7.5 and 7.6 above, the gas temperature is around 3000 K or above, and the conversion occurs by thermal processes.

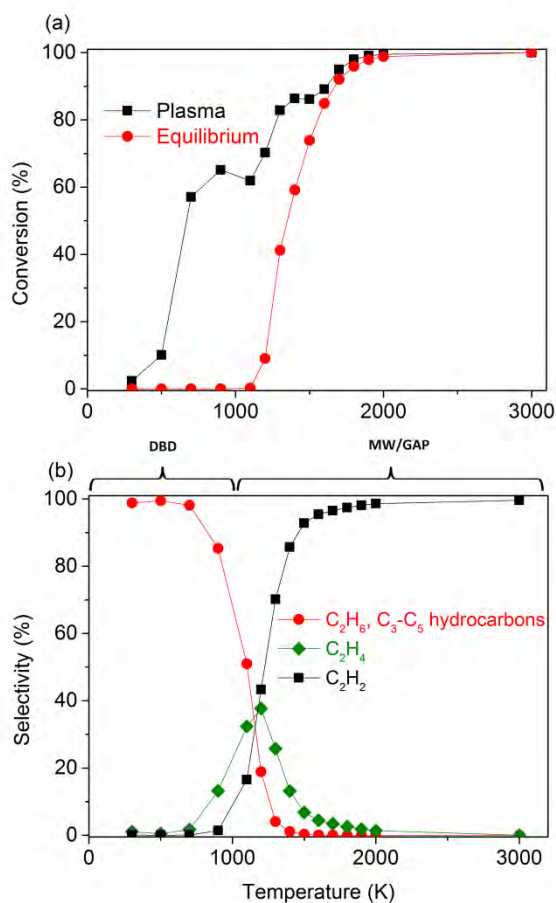


Figure 65: Calculated conversion (a) and most important hydrocarbon selectivities (b) inside a generic plasma type at atmospheric pressure, a power of 400 W and a flow rate of 500 mL min⁻¹ for pure CH₄, as a function of gas temperature. In (a) both the plasma conversion and thermal equilibrium conversion are plotted, indicating a clear difference up to 2000 K.

7.8 Conclusions

We presented here a chemical kinetics model to elucidate the main conversion mechanisms of CH_4 into the most important hydrocarbons, especially C_2H_2 , C_2H_4 and C_2H_6 , as well as into H_2 , in the three most commonly used plasma reactors, i.e., a DBD, MW and GAP reactor. The calculated conversions, energy costs and product selectivities were compared with experimental results in different reactor configurations and in a wide range of operating conditions. The calculation results are in satisfactory agreement with the experiments, which indicates that the model can provide a realistic picture of the underlying chemistry in CH_4 plasmas and even $\text{CH}_4\text{-H}_2\text{-N}_2$ mixtures, and can be used to elucidate the underlying mechanisms of CH_4 conversion into various hydrocarbons and H_2 in the different plasma reactors.

The CH_4 conversion is around 20 % in the DBD, as well as in the MW plasma at reduced pressure, but it rises to values above 80 % in the pulsed MW plasma, as well as at atmospheric pressure, both upon rising SEI. In the GAP, conversions around 50 % were obtained, even at high flow rates of 10 L min^{-1} . Because of this high flow rate, the GAP operates at much lower SEI than the other plasma sources, i.e., around 1.3 kJ L^{-1} , vs. $9 - 54 \text{ kJ L}^{-1}$ for the DBD, $7 - 37 \text{ kJ L}^{-1}$ for the reduced pressure MW plasma, and $24 - 240 \text{ kJ L}^{-1}$ for the atmospheric pressure MW plasma. Therefore, the corresponding energy cost is by far the lowest for the GAP (between 5 and 15 kJ/L, decreasing upon higher CH_4 fraction in the mixture), while it is around $40 - 140 \text{ kJ L}^{-1}$ in the reduced pressure MW plasma, from 200 till above 1000 kJ L^{-1} in the atmospheric pressure MW plasma, and around $125 - 510 \text{ kJ L}^{-1}$ in the DBD. As the GAP operates at the highest temperatures, this illustrates that thermal CH_4 conversion is important, and most efficient. Indeed, the model predicts that vibrational-translational non-equilibrium is negligible in all these CH_4 plasmas.

We can conclude that higher temperatures, especially in the GAP but also in atmospheric pressure MW plasmas, result in more CH_4 conversion, and in neutral dissociation and dehydrogenation processes of the hydrocarbons created, forming especially C_2H_2 and H_2 , and (some) C_2H_4 . Low temperature ($< 1000 \text{ K}$) plasmas, such as DBD and reduced pressure MW plasmas, result in more electron impact dissociation and three-body recombination processes, creating more

saturated compounds, i.e., mainly C₂H₆, but also higher hydrocarbons, such as C₃H₈ and C₄H₁₀.

Thus, high temperature (≥ 1000 K) plasmas, and especially the GAP, which operates at high flow rates (i.e. ≥ 10 L min⁻¹), are clearly beneficial, for both higher and more energy-efficient CH₄ conversion, as well as more selective production of C₂H₂ and (to a lower extent) C₂H₄. It would even be better if C₂H₄ would be the major product. To realize this, it is possible to add a catalyst after the plasma reactor, to convert C₂H₂ into C₂H₄, as demonstrated by Delikonstantis et al. for a nanosecond pulsed plasma³³⁰.

7.9 Appendix

Table A17: Electron impact reactions and their corresponding rate coefficients, either calculated using cross sections data, $f(\sigma)$, or using an analytical expression, given in cm³ s⁻¹ and cm⁶ s⁻¹, for two-body and three-body reactions, respectively, as well as the references where the data are adopted from. Both T_{gas} and T_e are given in K.

Reaction	Rate coefficient	Ref
$e^- + CH_4(g) \rightarrow e^- + CH_4(g)$	$f(\sigma)$	158
$e^- + CH_4(j_3 - j_4) \rightarrow e^- + CH_4(j_3 - j_4)$	$f(\sigma)$	158
$e^- + CH_4(v_1 - v_4) \rightarrow e^- + CH_4(v_1 - v_4)$	$f(\sigma)$	158
$e^- + CH_4(g + j + v) \rightarrow 2e^- + CH_4^+$	$f(\sigma)$	158
$e^- + CH_4(g + j + v) \rightarrow 2e^- + CH_3^+ + H$	$f(\sigma)$	94
$e^- + CH_4(g + j + v) \rightarrow 2e^- + CH_2^+ + H_2$	$f(\sigma)$	94
$e^- + CH_4(g + j + v) \rightarrow e^- + CH_3 + H$	$f(\sigma)$	95,159
$e^- + CH_4(g + j + v) \rightarrow e^- + CH_2 + H_2$	$f(\sigma)$	95,159
$e^- + CH_4(g + j + v) \rightarrow e^- + CH + H_2 + H$	$f(\sigma)$	95,159
$e^- + CH_4(g + j + v) \rightarrow e^- + C + 2H_2$	$f(\sigma)$	95,159
$e^- + CH_4(g + j + v) \leftrightarrow e^- + CH_4(v_1)$	$f(\sigma)$	340,377
$e^- + CH_4(g + j + v) \leftrightarrow e^- + CH_4(v_2)$	$f(\sigma)$	340,377
$e^- + CH_4(g + j + v) \leftrightarrow e^- + CH_4(v_3)$	$f(\sigma)$	340,377

$e^- + CH_4(g+j) \leftrightarrow e^- + CH_4(v_4)$	$f(\sigma)$	340,377
$e^- + CH_4 \leftrightarrow e^- + CH_4(j_3)$	$f(\sigma)$	340,377
$e^- + CH_4 \leftrightarrow e^- + CH_4(j_4)$	$f(\sigma)$	340,377
$e^- + CH_3 \rightarrow e^- + CH_3$	$f(\sigma)$	93
$e^- + CH_3 \rightarrow 2e^- + CH_3^+$	$f(\sigma)$	94
$e^- + CH_3 \rightarrow 2e^- + CH_2^+ + H$	$f(\sigma)$	94
$e^- + CH_3 \rightarrow 2e^- + CH^+ + H_2$	$f(\sigma)$	94
$e^- + CH_3 \rightarrow e^- + CH_2 + H$	$f(\sigma)$	95,159
$e^- + CH_3 \rightarrow e^- + CH + H_2$	$f(\sigma)$	95,159
$e^- + CH_3 \rightarrow e^- + C + H_2 + H$	$f(\sigma)$	159
$e^- + CH_2 \rightarrow e^- + CH_2$	$f(\sigma)$	93
$e^- + CH_2 \rightarrow 2e^- + CH_2^+$	$f(\sigma)$	94
$e^- + CH_2 \rightarrow e^- + CH + H$	$f(\sigma)$	95,159
$e^- + CH_2 \rightarrow e^- + C + H_2$	$f(\sigma)$	159
$e^- + CH_2 \rightarrow e^- + C + 2H$	$f(\sigma)$	159
$e^- + CH \rightarrow e^- + CH$	$f(\sigma)$	93
$e^- + CH \rightarrow 2e^- + CH^+$	$f(\sigma)$	94
$e^- + CH \rightarrow e^- + C + H$	$f(\sigma)$	95,159
$e^- + C \rightarrow e^- + C$	$f(\sigma)$	272,378
$e^- + C \rightarrow 2e^- + C^+$	$f(\sigma)$	95,159
$e^- + C_2 \rightarrow e^- + 2C$	$f(\sigma)$	159
$e^- + C_2 \rightarrow 2e^- + C_2^+$	$f(\sigma)$	159
$e^- + C_2^+ \rightarrow 2C$	$1.93 \times 10^{-6} T_e^{-0.5}$	99
$e^- + C_2H_6 \rightarrow e^- + C_2H_6$	$f(\sigma)$	93
$e^- + C_2H_6 \rightarrow 2e^- + C_2H_6^+$	$f(\sigma)$	94
$e^- + C_2H_6 \rightarrow 2e^- + C_2H_5^+ + H$	$f(\sigma)$	94
$e^- + C_2H_6 \rightarrow 2e^- + C_2H_4^+ + H_2$	$f(\sigma)$	94
$e^- + C_2H_6 \rightarrow 2e^- + C_2H_3^+ + H_2 + H$	$f(\sigma)$	94
$e^- + C_2H_6 \rightarrow 2e^- + C_2H_2^+ + 2H_2$	$f(\sigma)$	94
$e^- + C_2H_6 \rightarrow 2e^- + CH_3^+ + CH_3$	$f(\sigma)$	94
$e^- + C_2H_6 \rightarrow e^- + C_2H_5 + H$	$f(\sigma)$	160,161
$e^- + C_2H_6 \rightarrow e^- + C_2H_4 + H_2$	$f(\sigma)$	160,161
$e^- + C_2H_6 \rightarrow e^- + C_2H_3 + H_2 + H$	$f(\sigma)$	161
$e^- + C_2H_6 \rightarrow e^- + C_2H_2 + 2H_2$	$f(\sigma)$	161
$e^- + C_2H_6 \rightarrow e^- + CH_4 + CH_2$	$f(\sigma)$	161
$e^- + C_2H_6 \rightarrow e^- + 2CH_3$	$f(\sigma)$	161
$e^- + C_2H_5 \rightarrow 2e^- + C_2H_5^+$	$f(\sigma)$	94
$e^- + C_2H_5 \rightarrow 2e^- + C_2H_4^+ + H$	$f(\sigma)$	94
$e^- + C_2H_5 \rightarrow 2e^- + C_2H_3^+ + H_2$	$f(\sigma)$	94
$e^- + C_2H_5 \rightarrow 2e^- + C_2H_2^+ + H_2 + H$	$f(\sigma)$	94
$e^- + C_2H_5 \rightarrow e^- + C_2H_4 + H$	$f(\sigma)$	160,161
$e^- + C_2H_5 \rightarrow e^- + C_2H_3 + H_2$	$f(\sigma)$	160,161
$e^- + C_2H_5 \rightarrow e^- + C_2H_3 + 2H$	$f(\sigma)$	161
$e^- + C_2H_5 \rightarrow e^- + C_2H_2 + H_2 + H$	$f(\sigma)$	161
$e^- + C_2H_5 \rightarrow e^- + C_2H + 2H_2$	$f(\sigma)$	161
$e^- + C_2H_5 \rightarrow e^- + CH_4 + CH$	$f(\sigma)$	161

$e^- + C_2H_5 \rightarrow e^- + CH_3 + CH_2$	$f(\sigma)$	161
$e^- + C_2H_4 \rightarrow e^- + C_2H_4$	$f(\sigma)$	93
$e^- + C_2H_4 \rightarrow 2e^- + C_2H_4^+$	$f(\sigma)$	94
$e^- + C_2H_4 \rightarrow 2e^- + C_2H_3^+ + H$	$f(\sigma)$	94
$e^- + C_2H_4 \rightarrow 2e^- + C_2H_2^+ + H_2$	$f(\sigma)$	94
$e^- + C_2H_4 \rightarrow e^- + C_2H_3 + H$	$f(\sigma)$	160,161
$e^- + C_2H_4 \rightarrow e^- + C_2H_2 + H_2$	$f(\sigma)$	160,161
$e^- + C_2H_4 \rightarrow e^- + C_2H_2 + 2H$	$f(\sigma)$	161
$e^- + C_2H_4 \rightarrow e^- + C_2H + H_2 + H$	$f(\sigma)$	161
$e^- + C_2H_4 \rightarrow e^- + CH_3 + CH$	$f(\sigma)$	161
$e^- + C_2H_4 \rightarrow e^- + 2CH_2$	$f(\sigma)$	161
$e^- + C_2H_4 \rightarrow e^- + C + CH_4$	$f(\sigma)$	161
$e^- + C_2H_3 \rightarrow 2e^- + C_2H_3^+$	$f(\sigma)$	94
$e^- + C_2H_3 \rightarrow 2e^- + C_2H_2^+ + H$	$f(\sigma)$	94
$e^- + C_2H_3 \rightarrow e^- + C_2H_2 + H$	$f(\sigma)$	160,161
$e^- + C_2H_3 \rightarrow e^- + C_2H + H_2$	$f(\sigma)$	160,161
$e^- + C_2H_3 \rightarrow e^- + C_2H + 2H$	$f(\sigma)$	161
$e^- + C_2H_3 \rightarrow e^- + C_2 + H_2 + H$	$f(\sigma)$	161
$e^- + C_2H_3 \rightarrow e^- + CH_2 + CH$	$f(\sigma)$	161
$e^- + C_2H_3 \rightarrow e^- + C + CH_3$	$f(\sigma)$	161
$e^- + C_2H_2 \rightarrow e^- + C_2H_2$	$f(\sigma)$	93
$e^- + C_2H_2 \rightarrow 2e^- + C_2H_2^+$	$f(\sigma)$	94
$e^- + C_2H_2 \rightarrow e^- + C_2H + H$	$f(\sigma)$	160,161
$e^- + C_2H_2 \rightarrow e^- + C_2 + H_2$	$f(\sigma)$	161
$e^- + C_2H_2 \rightarrow e^- + C_2 + 2H$	$f(\sigma)$	161
$e^- + C_2H_2 \rightarrow e^- + 2CH$	$f(\sigma)$	161
$e^- + C_2H_2 \rightarrow e^- + C + CH_2$	$f(\sigma)$	161
$e^- + C_2H \rightarrow e^- + C + CH$	$f(\sigma)$	160,161
$e^- + C_2H \rightarrow e^- + C_2 + H$	$f(\sigma)$	161
$e^- + C_3H_8 \rightarrow e^- + C_3H_8$	$f(\sigma)$	93
$e^- + C_3H_8 \rightarrow 2e^- + C_2H_5^+ + CH_3$	$f(\sigma)$	94
$e^- + C_3H_8 \rightarrow 2e^- + C_2H_4^+ + CH_4$	$f(\sigma)$	94
$e^- + C_3H_8 \rightarrow e^- + C_3H_7 + H$	$f(\sigma)$	160,161
$e^- + C_3H_8 \rightarrow e^- + C_3H_6 + H_2$	$f(\sigma)$	160,161
$e^- + C_3H_8 \rightarrow e^- + C_2H_4 + CH_4$	$f(\sigma)$	160,161
$e^- + C_3H_8 \rightarrow e^- + C_2H_6 + CH_2$	$f(\sigma)$	161
$e^- + C_3H_8 \rightarrow e^- + C_2H_5 + CH_3$	$f(\sigma)$	161
$e^- + C_3H_7 \rightarrow 2e^- + C_2H_5^+ + CH_2$	$f(\sigma)$	160,161
$e^- + C_3H_7 \rightarrow 2e^- + C_2H_4^+ + CH_3$	$f(\sigma)$	160,161
$e^- + C_3H_7 \rightarrow 2e^- + C_2H_3^+ + CH_4$	$f(\sigma)$	160,161
$e^- + C_3H_7 \rightarrow 2e^- + CH_3^+ + C_2H_4$	$f(\sigma)$	160,161
$e^- + C_3H_7 \rightarrow e^- + C_3H_6 + H$	$f(\sigma)$	160,161
$e^- + C_3H_7 \rightarrow e^- + C_2H_4 + CH_3$	$f(\sigma)$	160,161
$e^- + C_3H_7 \rightarrow e^- + C_2H_3 + CH_4$	$f(\sigma)$	160,161
$e^- + C_3H_7 \rightarrow e^- + C_3H_5 + H_2$	$f(\sigma)$	161
$e^- + C_3H_6 \rightarrow e^- + C_3H_6$	$f(\sigma)$	379

$e^- + C_3H_6 \rightarrow 2e^- + C_2H_5^+ + CH$	$f(\sigma)$	160,161
$e^- + C_3H_6 \rightarrow 2e^- + C_2H_4^+ + CH_2$	$f(\sigma)$	160,161
$e^- + C_3H_6 \rightarrow 2e^- + C_2H_3^+ + CH_3$	$f(\sigma)$	160,161
$e^- + C_3H_6 \rightarrow 2e^- + C_2H_2^+ + CH_4$	$f(\sigma)$	160,161
$e^- + C_3H_6 \rightarrow 2e^- + CH_3^+ + C_2H_3$	$f(\sigma)$	160,161
$e^- + C_3H_6 \rightarrow e^- + C_2H_2 + CH_4$	$f(\sigma)$	160,161
$e^- + C_3H_6 \rightarrow e^- + C_3H_5 + H$	$f(\sigma)$	161
$e^- + C_3H_6 \rightarrow e^- + C_2H_3 + CH_3$	$f(\sigma)$	161
$e^- + C_3H_6 \rightarrow e^- + C_2H_4 + CH_2$	$f(\sigma)$	161
$e^- + C_3H_5 \rightarrow 2e^- + C_2H_3^+ + CH_2$	$f(\sigma)$	160,161
$e^- + C_3H_5 \rightarrow 2e^- + C_2H_2^+ + CH_3$	$f(\sigma)$	160,161
$e^- + C_3H_5 \rightarrow 2e^- + CH_3^+ + C_2H_2$	$f(\sigma)$	160,161
$e^- + C_3H_5 \rightarrow e^- + C_2H_2 + CH_3$	$f(\sigma)$	160,161
$e^- + C_3H_5 \rightarrow e^- + C_2H + CH_4$	$f(\sigma)$	161
$e^- + H_2(v) \leftrightarrow e^- + H_2(w)$	$f(\sigma)$	380,381
$e^- + H_2(g+v) \rightarrow 2e^- + H_2^+$	$f(\sigma)$	382
$e^- + CH_5^+ \rightarrow CH_3 + 2H$	$2.57x10^{-7} \left(\frac{300}{T_{gas}}\right)^{0.30}$	159,169
$e^- + CH_5^+ \rightarrow CH_2 + H_2 + H$	$6.61x10^{-8} \left(\frac{300}{T_{gas}}\right)^{0.30}$	159,169
$e^- + CH_4^+ \rightarrow CH_3 + H$	$1.18x10^{-8} \left(\frac{300}{T_{gas}}\right)^{0.50}$	159,169
$e^- + CH_4^+ \rightarrow CH_2 + 2H$	$2.42x10^{-8} \left(\frac{300}{T_{gas}}\right)^{0.50}$	159,169
$e^- + CH_4^+ \rightarrow CH + H_2 + H$	$1.41x10^{-8} \left(\frac{300}{T_{gas}}\right)^{0.50}$	159,169
$e^- + CH_3^+ \rightarrow CH_2 + H$	$2.25x10^{-8} \left(\frac{300}{T_{gas}}\right)^{0.50}$	159,169
$e^- + CH_3^+ \rightarrow CH + H_2$	$7.88x10^{-9} \left(\frac{300}{T_{gas}}\right)^{0.50}$	159,169
$e^- + CH_3^+ \rightarrow CH + 2H$	$9.00x10^{-9} \left(\frac{300}{T_{gas}}\right)^{0.50}$	159,169
$e^- + CH_3^+ \rightarrow C + H_2 + H$	$1.69x10^{-8} \left(\frac{300}{T_{gas}}\right)^{0.50}$	159,169
$e^- + CH_2^+ \rightarrow CH + H$	$1.00x10^{-8} \left(\frac{300}{T_{gas}}\right)^{0.50}$	159,169
$e^- + CH_2^+ \rightarrow C + H_2$	$4.82x10^{-9} \left(\frac{300}{T_{gas}}\right)^{0.50}$	159,169
$e^- + CH_2^+ \rightarrow C + 2H$	$2.53x10^{-8} \left(\frac{300}{T_{gas}}\right)^{0.50}$	159,169

$e^- + CH^+ \rightarrow C + H$	$3.23x10^{-8} \left(\frac{300}{T_{gas}}\right)^{0.42}$	159,169
$e^- + C_2H_6^+ \rightarrow C_2H_5 + H$	$2.19x10^{-8} \left(\frac{300}{T_{gas}}\right)^{0.71}$	161
$e^- + C_2H_6^+ \rightarrow C_2H_4 + 2H$	$3.36x10^{-8} \left(\frac{300}{T_{gas}}\right)^{0.71}$	161
$e^- + C_2H_5^+ \rightarrow C_2H_4 + H$	$7.70x10^{-9} \left(\frac{300}{T_{gas}}\right)^{0.71}$	161
$e^- + C_2H_5^+ \rightarrow C_2H_3 + 2H$	$1.92x10^{-8} \left(\frac{300}{T_{gas}}\right)^{0.71}$	161
$e^- + C_2H_5^+ \rightarrow C_2H_2 + H_2 + H$	$1.60x10^{-8} \left(\frac{300}{T_{gas}}\right)^{0.71}$	161
$e^- + C_2H_5^+ \rightarrow C_2H_2 + 3H$	$8.98x10^{-9} \left(\frac{300}{T_{gas}}\right)^{0.71}$	161
$e^- + C_2H_5^+ \rightarrow CH_3 + CH_2$	$9.62x10^{-9} \left(\frac{300}{T_{gas}}\right)^{0.71}$	161
$e^- + C_2H_4^+ \rightarrow C_2H_3 + H$	$8.29x10^{-9} \left(\frac{300}{T_{gas}}\right)^{0.71}$	161
$e^- + C_2H_4^+ \rightarrow C_2H_2 + 2H$	$3.43x10^{-8} \left(\frac{300}{T_{gas}}\right)^{0.71}$	161
$e^- + C_2H_4^+ \rightarrow C_2H + H_2 + H$	$5.53x10^{-9} \left(\frac{300}{T_{gas}}\right)^{0.71}$	161
$e^- + C_2H_3^+ \rightarrow C_2H_2 + H$	$1.34x10^{-8} \left(\frac{300}{T_{gas}}\right)^{0.71}$	161
$e^- + C_2H_3^+ \rightarrow C_2H + 2H$	$2.74x10^{-8} \left(\frac{300}{T_{gas}}\right)^{0.71}$	161
$e^- + C_2H_2^+ \rightarrow C_2H + H$	$1.87x10^{-8} \left(\frac{300}{T_{gas}}\right)^{0.71}$	161
$e^- + C_2H_2^+ \rightarrow 2CH$	$4.87x10^{-9} \left(\frac{300}{T_{gas}}\right)^{0.71}$	161
$e^- + H_3^+ \rightarrow 3H$	$f(\sigma)$	383,384
$e^- + H_3^+ \rightarrow e^- + 2H + H^+$	$f(\sigma)$	383
$e^- + H_2^+ \rightarrow e^- + H + H^+$	$f(\sigma)$	384
$2e^- + H_2^+ \rightarrow e^- + 2H$	$\frac{3.17x10^{21}}{6.022x10^{23} T_e^{4.5}}$	385
$2e^- + H_3^+ \rightarrow e^- + H + H_2$	$\frac{3.17x10^{21}}{6.022x10^{23} T_e^{4.5}}$	385

Table A18: Ion-ion and ion-neutral reactions, as well as the references where the data are adopted from. The rate coefficients are given in $\text{cm}^3 \text{s}^{-1}$ and $\text{cm}^6 \text{s}^{-1}$, for two-body and three-body reactions, respectively. T_{gas} is given in K.

Reaction	Rate coefficient	Ref
$H_2 + H_2^+ \rightarrow H + H_3^+$	2.11×10^{-9}	383,386
$2H_2 + H^+ \rightarrow H_2 + H_3^+$	$3.10 \times 10^{-29} \left(\frac{300}{T_{gas}} \right)^{0.5}$	386
$CH_5^+ + CH_2 \rightarrow CH_3^+ + CH_4$	9.60×10^{-10}	112
$CH_5^+ + CH \rightarrow CH_2^+ + CH_4$	6.90×10^{-10}	112
$CH_5^+ + C \rightarrow CH^+ + CH_4$	1.20×10^{-9}	112
$CH_5^+ + C_2H_6 \rightarrow C_2H_5^+ + H_2 + CH_4$	2.25×10^{-10}	255
$CH_5^+ + C_2H_4 \rightarrow C_2H_5^+ + CH_4$	1.50×10^{-9}	112
$CH_5^+ + C_2H_2 \rightarrow C_2H_3^+ + CH_4$	1.60×10^{-9}	112
$CH_5^+ + C_2H \rightarrow C_2H_2^+ + CH_4$	9.00×10^{-10}	112
$CH_5^+ + C_2 \rightarrow C_2H^+ + CH_4$	9.50×10^{-10}	112
$CH_5^+ + H \rightarrow CH_4^+ + H_2$	1.50×10^{-10}	112
$CH_4^+ + CH_4 \rightarrow CH_5^+ + CH_3$	1.50×10^{-9}	112
$CH_4^+ + C_2H_6 \rightarrow C_2H_4^+ + CH_4 + H_2$	1.91×10^{-9}	255
$CH_4^+ + C_2H_4 \rightarrow C_2H_5^+ + CH_3$	4.23×10^{-10}	112
$CH_4^+ + C_2H_4 \rightarrow C_2H_4^+ + CH_4$	1.38×10^{-9}	112
$CH_4^+ + C_2H_2 \rightarrow C_2H_3^+ + CH_3$	1.23×10^{-9}	112
$CH_4^+ + C_2H_2 \rightarrow C_2H_2^+ + CH_4$	1.13×10^{-9}	112
$CH_4^+ + H_2 \rightarrow CH_5^+ + H$	3.30×10^{-11}	112
$CH_4^+ + H \rightarrow CH_3^+ + H_2$	1.00×10^{-11}	112
$CH_3^+ + CH_4 \rightarrow CH_4^+ + CH_3$	1.36×10^{-10}	256
$CH_3^+ + CH_4 \rightarrow C_2H_5^+ + H_2$	1.20×10^{-9}	112
$CH_3^+ + CH_2 \rightarrow C_2H_3^+ + H_2$	9.90×10^{-10}	112
$CH_3^+ + CH \rightarrow C_2H_2^+ + H_2$	7.10×10^{-10}	112
$CH_3^+ + C \rightarrow C_2H^+ + H_2$	1.20×10^{-9}	112
$CH_3^+ + C_2H_6 \rightarrow C_2H_5^+ + CH_4$	1.48×10^{-9}	112
$CH_3^+ + C_2H_4 \rightarrow C_2H_3^+ + CH_4$	3.50×10^{-10}	112
$CH_3^+ + C_2H_3 \rightarrow C_2H_3^+ + CH_3$	3.00×10^{-10}	112
$CH_2^+ + CH_4 \rightarrow CH_3^+ + CH_3$	1.38×10^{-10}	257
$CH_2^+ + CH_4 \rightarrow C_2H_5^+ + H$	3.60×10^{-10}	112
$CH_2^+ + CH_4 \rightarrow C_2H_4^+ + H_2$	8.40×10^{-10}	112
$CH_2^+ + CH_4 \rightarrow C_2H_3^+ + H_2 + H$	2.31×10^{-10}	257
$CH_2^+ + CH_4 \rightarrow C_2H_2^+ + 2H_2$	3.97×10^{-10}	257
$CH_2^+ + H_2 \rightarrow CH_3^+ + H$	1.60×10^{-9}	112
$CH_2^+ + C \rightarrow C_2H^+ + H$	1.20×10^{-9}	112
$CH^+ + CH_4 \rightarrow C_2H_4^+ + H$	6.50×10^{-11}	112
$CH^+ + CH_4 \rightarrow C_2H_3^+ + H_2$	1.09×10^{-9}	112
$CH^+ + CH_4 \rightarrow C_2H_2^+ + H_2 + H$	1.43×10^{-10}	112

$CH^+ + CH_2 \rightarrow C_2H^+ + H_2$	$1.00x10^{-9}$	112
$CH^+ + CH \rightarrow C_2^+ + H_2$	$7.40x10^{-10}$	112
$CH^+ + C \rightarrow C_2^+ + H$	$1.20x10^{-9}$	112
$CH^+ + H \rightarrow C^+ + H_2$	$7.50x10^{-10}$	112
$CH^+ + H_2(g + v) \rightarrow CH_2^+ + H$	$1.20x10^{-9}$	112
$C^+ + CH_4 \rightarrow C_2H_3^+ + H$	$1.10x10^{-9}$	112
$C^+ + CH_4 \rightarrow C_2H_2^+ + H_2$	$4.00x10^{-10}$	112
$C^+ + CH_3 \rightarrow C_2H_2^+ + H$	$1.30x10^{-9}$	112
$C^+ + CH_3 \rightarrow C_2H^+ + H_2$	$1.00x10^{-9}$	112
$C^+ + CH_2 \rightarrow CH_2^+ + C$	$5.20x10^{-10}$	112
$C^+ + CH_2 \rightarrow C_2H^+ + H$	$5.20x10^{-10}$	112
$C^+ + CH \rightarrow CH^+ + C$	$3.80x10^{-10}$	112
$C^+ + CH \rightarrow C_2^+ + H$	$3.80x10^{-10}$	112
$C^+ + C_2H_6 \rightarrow C_2H_5^+ + CH$	$2.31x10^{-10}$	112
$C^+ + C_2H_6 \rightarrow C_2H_4^+ + CH_2$	$1.16x10^{-10}$	112
$C^+ + C_2H_6 \rightarrow C_2H_3^+ + CH_3$	$4.95x10^{-10}$	112
$C^+ + C_2H_6 \rightarrow C_2H_2^+ + CH_4$	$8.25x10^{-11}$	112
$C^+ + C_2H_5 \rightarrow C_2H_5^+ + C$	$5.00x10^{-10}$	112
$C^+ + C_2H_4 \rightarrow C_2H_4^+ + C$	$1.70x10^{-11}$	112
$C^+ + C_2H_4 \rightarrow C_2H_3^+ + CH$	$8.50x10^{-11}$	112
$C^+ + H^- \rightarrow C + H$	$2.30x10^{-7}$	112
$C_2H_6^+ + C_2H_4 \rightarrow C_2H_4^+ + C_2H_6$	$1.15x10^{-9}$	112
$C_2H_6^+ + C_2H_2 \rightarrow C_2H_5^+ + C_2H_3$	$2.47x10^{-10}$	112
$C_2H_6^+ + H \rightarrow C_2H_5^+ + H_2$	$1.00x10^{-10}$	112
$C_2H_5^+ + H \rightarrow C_2H_4^+ + H_2$	$1.00x10^{-11}$	112
$C_2H_4^+ + C_2H_3 \rightarrow C_2H_5^+ + C_2H_2$	$5.00x10^{-10}$	112
$C_2H_4^+ + C_2H_3 \rightarrow C_2H_3^+ + C_2H_4$	$5.00x10^{-10}$	112
$C_2H_4^+ + H \rightarrow C_2H_3^+ + H_2$	$3.00x10^{-10}$	112
$C_2H_3^+ + C_2H_6 \rightarrow C_2H_5^+ + C_2H_4$	$2.91x10^{-10}$	112
$C_2H_3^+ + C_2H_4 \rightarrow C_2H_5^+ + C_2H_2$	$8.90x10^{-10}$	112
$C_2H_3^+ + C_2H_3 \rightarrow C_2H_5^+ + C_2H$	$5.00x10^{-10}$	112
$C_2H_3^+ + C_2H \rightarrow C_2H_2^+ + C_2H_2$	$3.30x10^{-10}$	112
$C_2H_3^+ + H \rightarrow C_2H_2^+ + H_2$	$6.80x10^{-11}$	112
$C_2H_2^+ + CH_4 \rightarrow C_2H_3^+ + CH_3$	$4.10x10^{-9}$	257
$C_2H_2^+ + C_2H_6 \rightarrow C_2H_5^+ + C_2H_3$	$1.31x10^{-10}$	255
$C_2H_2^+ + C_2H_6 \rightarrow C_2H_4^+ + C_2H_4$	$2.48x10^{-10}$	112
$C_2H_2^+ + C_2H_4 \rightarrow C_2H_4^+ + C_2H_2$	$4.14x10^{-10}$	112
$C_2H_2^+ + C_2H_3 \rightarrow C_2H_3^+ + C_2H_2$	$3.30x10^{-10}$	112
$C_2H_2^+ + H_2 \rightarrow C_2H_3^+ + H$	$1.00x10^{-11}$	112
$C_2H^+ + CH_4 \rightarrow C_2H_2^+ + CH_3$	$3.74x10^{-10}$	112
$C_2H^+ + CH_2 \rightarrow CH_3^+ + C_2$	$4.40x10^{-10}$	112
$C_2H^+ + CH \rightarrow CH_2^+ + C_2$	$3.20x10^{-10}$	112
$C_2H^+ + H_2 \rightarrow C_2H_2^+ + H$	$1.10x10^{-9}$	112
$C_2^+ + CH_4 \rightarrow C_2H_2^+ + CH_2$	$1.82x10^{-10}$	112
$C_2^+ + CH_4 \rightarrow C_2H^+ + CH_3$	$2.38x10^{-10}$	112

$C_2^+ + CH_2 \rightarrow CH_2^+ + C_2$	$4.50x10^{-10}$	112
$C_2^+ + CH \rightarrow CH^+ + C_2$	$3.20x10^{-10}$	112
$C_2^+ + H_2 \rightarrow C_2H^+ + H$	$1.10x10^{-9}$	112
$H_3^+ + CH_4 \rightarrow CH_5^+ + H_2$	$2.40x10^{-9}$	112
$H_3^+ + CH_3 \rightarrow CH_4^+ + H_2$	$2.10x10^{-9}$	112
$H_3^+ + CH_2 \rightarrow CH_3^+ + H_2$	$1.70x10^{-9}$	112
$H_3^+ + CH \rightarrow CH_2^+ + H_2$	$1.20x10^{-9}$	112
$H_3^+ + C \rightarrow CH^+ + H_2$	$2.00x10^{-9}$	112
$H_3^+ + C_2H_6 \rightarrow C_2H_5^+ + 2H_2$	$2.40x10^{-9}$	112
$H_3^+ + C_2H_5 \rightarrow C_2H_6^+ + H_2$	$1.40x10^{-9}$	112
$H_3^+ + C_2H_4 \rightarrow C_2H_5^+ + H_2$	$1.15x10^{-9}$	112
$H_3^+ + C_2H_4 \rightarrow C_2H_3^+ + 2H_2$	$1.15x10^{-9}$	112
$H_3^+ + C_2H_3 \rightarrow C_2H_4^+ + H_2$	$2.00x10^{-9}$	112
$H_3^+ + C_2H \rightarrow C_2H_2^+ + H_2$	$1.70x10^{-9}$	112
$H_3^+ + C_2H_2 \rightarrow C_2H_3^+ + H_2$	$3.50x10^{-9}$	112
$H_3^+ + C_2 \rightarrow C_2H^+ + H_2$	$1.80x10^{-9}$	112
$H_2^+ + CH_4 \rightarrow CH_5^+ + H$	$1.14x10^{-10}$	112
$H_2^+ + CH_4 \rightarrow CH_4^+ + H_2$	$1.40x10^{-9}$	112
$H_2^+ + CH_4 \rightarrow CH_3^+ + H_2 + H$	$2.30x10^{-9}$	112
$H_2^+ + CH_2 \rightarrow CH_3^+ + H$	$1.00x10^{-9}$	112
$H_2^+ + CH_2 \rightarrow CH_2^+ + H_2$	$1.00x10^{-9}$	112
$H_2^+ + CH \rightarrow CH_2^+ + H$	$7.10x10^{-10}$	112
$H_2^+ + CH \rightarrow CH^+ + H_2$	$7.10x10^{-10}$	112
$H_2^+ + C \rightarrow CH^+ + H_2$	$2.40x10^{-9}$	112
$H_2^+ + C_2H_6 \rightarrow C_2H_6^+ + H_2$	$2.94x10^{-10}$	112
$H_2^+ + C_2H_6 \rightarrow C_2H_5^+ + H_2 + H$	$1.37x10^{-9}$	112
$H_2^+ + C_2H_6 \rightarrow C_2H_4^+ + 2H_2$	$2.35x10^{-9}$	112
$H_2^+ + C_2H_6 \rightarrow C_2H_3^+ + 2H_2 + H$	$6.86x10^{-10}$	255
$H_2^+ + C_2H_6 \rightarrow C_2H_2^+ + 3H_2$	$1.96x10^{-10}$	255
$H_2^+ + C_2H_4 \rightarrow C_2H_4^+ + H_2$	$2.21x10^{-9}$	112
$H_2^+ + C_2H_4 \rightarrow C_2H_3^+ + H_2 + H$	$1.81x10^{-9}$	112
$H_2^+ + C_2H_4 \rightarrow C_2H_2^+ + 2H_2$	$8.82x10^{-10}$	112
$H_2^+ + C_2H_2 \rightarrow C_2H_3^+ + H$	$4.80x10^{-10}$	112
$H_2^+ + C_2H_2 \rightarrow C_2H_2^+ + H_2$	$4.82x10^{-9}$	112
$H_2^+ + C_2H \rightarrow C_2H_2^+ + H$	$1.00x10^{-9}$	112
$H_2^+ + C_2H \rightarrow C_2H^+ + H_2$	$1.00x10^{-9}$	112
$H_2^+ + C_2 \rightarrow C_2H^+ + H$	$1.10x10^{-9}$	112
$H_2^+ + C_2 \rightarrow C_2^+ + H_2$	$1.10x10^{-9}$	112
$H_2^+ + H \rightarrow H_3^+$	$2.10x10^{-9}$	386
$H_2^+ + H \rightarrow H_2 + H^+$	$6.39x10^{-10}$	386
$H^+ + CH_4 \rightarrow CH_4^+ + H$	$1.50x10^{-9}$	112
$H^+ + CH_4 \rightarrow CH_3^+ + H_2$	$2.30x10^{-9}$	112
$H^+ + CH_3 \rightarrow CH_3^+ + H$	$3.40x10^{-9}$	112
$H^+ + CH_2 \rightarrow CH_2^+ + H$	$1.40x10^{-9}$	112
$H^+ + CH_2 \rightarrow CH^+ + H_2$	$1.40x10^{-9}$	112

$H^+ + CH \rightarrow CH^+ + H$	1.90×10^{-9}	112
$H^+ + C_2H_6 \rightarrow C_2H_5^+ + H_2$	1.30×10^{-9}	255
$H^+ + C_2H_6 \rightarrow C_2H_4^+ + H_2 + H$	1.40×10^{-9}	112
$H^+ + C_2H_6 \rightarrow C_2H_3^+ + 2H_2$	2.80×10^{-9}	112
$H^+ + C_2H_5 \rightarrow C_2H_4^+ + H_2$	1.65×10^{-9}	112
$H^+ + C_2H_5 \rightarrow C_2H_3^+ + H_2 + H$	3.06×10^{-9}	112
$H^+ + C_2H_4 \rightarrow C_2H_4^+ + H$	1.00×10^{-9}	112
$H^+ + C_2H_4 \rightarrow C_2H_3^+ + H_2$	3.00×10^{-9}	112
$H^+ + C_2H_4 \rightarrow C_2H_2^+ + H_2 + H$	1.00×10^{-9}	112
$H^+ + C_2H_3 \rightarrow C_2H_3^+ + H$	2.00×10^{-9}	112
$H^+ + C_2H_3 \rightarrow C_2H_2^+ + H_2$	2.00×10^{-9}	112
$H^+ + C_2H_2 \rightarrow C_2H_2^+ + H$	5.40×10^{-10}	112
$H^+ + C_2H \rightarrow C_2H^+ + H$	1.50×10^{-9}	112
$H^+ + C_2H \rightarrow C_2^+ + H_2$	1.50×10^{-9}	112
$H^+ + C_2 \rightarrow C_2^+ + H$	3.10×10^{-9}	112
$H^+ + H_2 + M \rightarrow H_3^+ + M$	1.50×10^{-29}	130
$C_2^+ + C \rightarrow C_2 + C^+$	1.10×10^{-10}	112

Table A19: Neutral-neutral reactions, as well as the references where the data are adopted from. The rate coefficients are given in $\text{cm}^3 \text{s}^{-1}$ and $\text{cm}^6 \text{s}^{-1}$, for two-body and three-body reactions, respectively. T_{gas} is given in K. R is the gas constant ($8.314 \times 10^{-3} \text{ kJ mol}^{-1} \text{ K}^{-1}$). The α parameter determines the effectiveness of lowering the activation energy for reactions involving vibrationally excited levels of the molecules (see details in ¹⁴). The reactions with * are adjusted for a three-body collision by dividing by the total gas density. Reactions with both a low pressure rate constant k_0 and high pressure rate constant k_∞ are scaled using the Troe falloff formula (see details in ^{147,387}).

Reaction	Rate coefficient	Ref	Note
$CH_4(v_2) + M \leftrightarrow CH_4 + M$	See Section 7.2	130,339,343,344	
$CH_4(v_4) + M \leftrightarrow CH_4 + M$	See Section 7.2	130,339,343,344	
$CH_4(v_3) + M \leftrightarrow CH_4(v_4) + M$	See Section 7.2	130,339,343,344	
$CH_4(v_1) + M \leftrightarrow CH_4(v_4) + M$	See Section 7.2	130,339,343,344	
$CH_4(j_3) + M \leftrightarrow CH_4 + M$	See Section 7.2	130,339,343,344	
$CH_4(j_4) + M \leftrightarrow CH_4 + M$	See Section 7.2	130,339,343,344	
$H_2(v+1) + H_2(w) \rightarrow H_2(v) + H_2(w+1)$	See References for exact equation	386,388,389	

$H_2(v) + M$ $\leftrightarrow H_2(v-1) + M$	See References for exact equation	130,386,390	
$H_2(v) + H \rightarrow H_2(w) + H$	See References for exact equation	391	
$CH_4 + CH_2 \rightarrow 2CH_3$	$4.08 \times 10^{-18} T_{gas}^2 \exp\left(-\frac{4163}{T_{gas}}\right)$	392	$\alpha = 0$
$CH_4 + CH \rightarrow C_2H_4 + H$	9.97×10^{-11}	393	$\alpha = 0$
$CH_4 + C_2H_5$ $\rightarrow C_2H_6 + CH_3$	$2.51 \times 10^{-15} \left(\frac{T_{gas}}{298}\right)^{4.14} \exp\left(-\frac{52.55}{RT_{gas}}\right)$	146	$\alpha = 1$
$CH_4 + C_2H_3$ $\rightarrow C_2H_4 + CH_3$	$4.26 \times 10^{-15} \left(\frac{T_{gas}}{298}\right)^{4.02} \exp\left(-\frac{22.86}{RT_{gas}}\right)$	146	$\alpha = 0$
$CH_4 + C_2H \rightarrow C_2H_2$ $+ CH_3$	$3.01 \times 10^{-12} \exp\left(-\frac{2.08}{RT_{gas}}\right)$	118	$\alpha = 0$
$CH_4 + C_3H_7$ $\rightarrow C_3H_8 + CH_3$	$3.54 \times 10^{-16} \left(\frac{T_{gas}}{298}\right)^{4.02} \exp\left(-\frac{45.48}{RT_{gas}}\right)$	171	$\alpha = 1$
$CH_4 + C_3H_5$ $\rightarrow C_3H_6 + CH_3$	$1.71 \times 10^{-14} \left(\frac{T_{gas}}{298}\right)^{3.40} \exp\left(-\frac{97.28}{RT_{gas}}\right)$	145	$\alpha = 1$
$CH_4 + H \rightarrow CH_3 + H_2$	$9.86 \times 10^{-13} \left(\frac{T_{gas}}{298}\right)^{3.00} \exp\left(-\frac{36.67}{RT_{gas}}\right)$	118	$\alpha = 1$
$CH_4 + CH_3 \rightarrow H + C_2H_6$	$1.33 \times 10^{-10} \exp\left(-\frac{167.00}{RT_{gas}}\right)$	243	$\alpha = 0.8$
$CH_4 + C_4H_9$ $\rightarrow C_4H_{10} + CH_3$	$5.68 \times 10^{-17} \left(\frac{T_{gas}}{298}\right)^{3.72} \exp\left(-\frac{33.42}{RT_{gas}}\right)$	144	$\alpha = 1$
$CH_4 + CH_2 \rightarrow C_2H_6$	1.90×10^{-12}	394	$\alpha = 0$
$CH_4 \rightarrow CH_3 + H$	$k_\infty: 2.40 \times 10^{16} \exp\left(-\frac{52800}{T_{gas}}\right)$ $k_0: 1.40 \times 10^{-6} \exp\left(-\frac{45700}{T_{gas}}\right)$ $F_c: 0.31 \exp\left(-\frac{T_{gas}}{90.0}\right)$ $+ 0.69 \exp\left(-\frac{T_{gas}}{2210}\right)$	174	$\alpha = 0.8$
$2CH_3 \rightarrow C_2H_5 + H$	$5.00 \times 10^{-11} \exp\left(-\frac{56.54}{RT_{gas}}\right)$	146	
$2CH_3 \rightarrow C_2H_6$	$k_\infty: 1.12 \times 10^{-7} T_{gas}^{-1.18} \exp\left(-\frac{329.14}{T_{gas}}\right)$ $k_0: 1.87 \times 10^{-6} T_{gas}^{-7.03} \exp\left(-\frac{1390.54}{T_{gas}}\right)$ $F_c: (1 - 0.619) \exp\left(-\frac{T_{gas}}{73.2}\right)$ $+ 0.619 \exp\left(-\frac{T_{gas}}{1180}\right)$ $+ \exp\left(-\frac{9999}{T_{gas}}\right)$	147,395	

$CH_3 + CH_2 \rightarrow C_2H_4 + H$	7.1×10^{-11}	146	
$CH_3 + C_2H_6 \rightarrow C_2H_5 + CH_4$	$7.19 \times 10^{-15} \left(\frac{T_{gas}}{298}\right)^{4.00} \exp\left(-\frac{34.67}{RT_{gas}}\right)$	118	
$CH_3 + C_2H_5 \rightarrow C_3H_8$	$k_{\infty}: 1.56 \times 10^{-11}$ $k_0: 1.49 \times 10^{27} T_{gas}^{-16.82} \exp\left(-\frac{6575.24}{T_{gas}}\right)$ $F_c: (1 - 0.1527) \exp\left(-\frac{T_{gas}}{291}\right)$ $+ 0.15727 \exp\left(-\frac{T_{gas}}{2742}\right)$ $+ \exp\left(-\frac{7748}{T_{gas}}\right)$	147	
$CH_3 + C_2H_4 \rightarrow C_2H_3 + CH_4$	$2.18 \times 10^{-11} \exp\left(-\frac{46.56}{RT_{gas}}\right)$	146	
$CH_3 + C_2H_3 \rightarrow C_2H_2 + CH_4$	$1.5 \times 10^{-11} \exp\left(\frac{3.20}{RT_{gas}}\right)$	396	
$CH_3 + C_2H_3 + M \rightarrow C_3H_6 + M$	3.80×10^{-29}	175	
$CH_3 + C_2H_2 \rightarrow C_2H + CH_4$	$3.0 \times 10^{-13} \exp\left(-\frac{72.34}{RT_{gas}}\right)$	118	
$CH_3 + C_3H_8 \rightarrow C_3H_7 + CH_4$	$1.50 \times 10^{-24} T_{gas}^{3.65} \exp\left(-\frac{3600.40}{T_{gas}}\right)$	171	
$CH_3 + C_3H_7 \rightarrow C_3H_6 + CH_4$	$3.07 \times 10^{-12} \left(\frac{T_{gas}}{298}\right)^{-0.32}$	171	
$CH_3 + C_3H_6 \rightarrow C_3H_5 + CH_4$	$1.68 \times 10^{-15} \left(\frac{T_{gas}}{298}\right)^{3.50} \exp\left(-\frac{23.78}{RT_{gas}}\right)$	145	
$CH_3 + H_2 \rightarrow CH_4 + H$	$2.52 \times 10^{-14} \left(\frac{T_{gas}}{298}\right)^{3.12} \exp\left(-\frac{36.42}{RT_{gas}}\right)$	118	$\alpha = 0$
$CH_3 + H \rightarrow CH_2 + H_2$	$1.00 \times 10^{-10} \exp\left(-\frac{63.19}{RT_{gas}}\right)$	146	
$CH_3 + H \rightarrow CH_4$	$k_{\infty}: 2.31 \times 10^{-8} T_{gas}^{-0.534} \exp\left(-\frac{269.75}{T_{gas}}\right)$ $k_0: 1.44 \times 10^{-14} T_{gas}^{-4.76} \exp\left(-\frac{1227.98}{T_{gas}}\right)$ $F_c: (1 - 0.783) \exp\left(-\frac{T_{gas}}{74}\right)$ $+ 0.783 \exp\left(-\frac{T_{gas}}{2941}\right)$ $+ \exp\left(-\frac{6964}{T_{gas}}\right)$	147	
$CH_3 + C_3H_7 \rightarrow 2C_2H_5$	$3.20 \times 10^{-11} T_{gas}^{-0.32}$	147,171	
$CH_3 + M \rightarrow CH_2 + H + M$	$1.69 \times 10^{-8} \exp\left(-\frac{379}{RT_{gas}}\right)$	146	

$CH_3 + M \rightarrow CH + H_2 + M$	$6.97 \times 10^{-9} \exp\left(-\frac{345}{RT_{gas}}\right)$	397	
$CH_3 + C_2H_5 \rightarrow C_2H_6 + CH_2$	$3.00 \times 10^{-44} T_{gas}^{9.10}$	398	
$2CH_2 \rightarrow C_2H_2 + 2H$	$3.32 \times 10^{-10} \exp\left(-\frac{45.98}{RT_{gas}}\right)$	179	
$CH_2 + C_2H_5 \rightarrow C_2H_4 + CH_3$	3.01×10^{-11}	118	
$CH_2 + C_2H_3 \rightarrow C_2H_2 + CH_3$	3.01×10^{-11}	118	
$CH_2 + C_2H \rightarrow C_2H_2 + CH$	3.01×10^{-11}	118	
$CH_2 + C_3H_8 \rightarrow C_3H_7 + CH_3$	$1.61 \times 10^{-15} \left(\frac{T_{gas}}{298}\right)^{3.65} \exp\left(-\frac{29.93}{RT_{gas}}\right)$	171	
$CH_2 + C_3H_7 \rightarrow C_2H_4 + C_2H_5$	3.01×10^{-11}	171	
$CH_2 + C_3H_7 \rightarrow C_3H_6 + CH_3$	3.01×10^{-11}	171	
$CH_2 + C_3H_6 \rightarrow C_3H_5 + CH_3$	$1.20 \times 10^{-12} \exp\left(-\frac{25.94}{RT_{gas}}\right)$	145	
$CH_2 + H_2 \rightarrow CH_3 + H$	$8.30 \times 10^{-19} T_{gas}^{2.00} \exp\left(-\frac{3938.65}{T_{gas}}\right)$	147	$\alpha = 0$
$CH_2 + H \rightarrow CH + H_2$	$1.00 \times 10^{-11} \exp\left(\frac{7.48}{RT_{gas}}\right)$	146	
$CH_2 + M \rightarrow C + H_2 + M$	$2.16 \times 10^{-10} \exp\left(-\frac{247}{RT_{gas}}\right)$	399	
$CH_2 + M \rightarrow CH + H + M$	$6.64 \times 10^{-9} \exp\left(-\frac{348}{RT_{gas}}\right)$	399	
$2CH_2 \rightarrow C_2H_2 + H_2$	$2.66 \times 10^{-9} \exp\left(-\frac{6011.07}{T_{gas}}\right)$	147,179	
$CH_2 + H \rightarrow CH_3$	$k_{\infty}: 9.96 \times 10^{-10}$ $k_0: 5.74 \times 10^{-22} T_{gas}^{-2.76} \exp\left(-\frac{805.23}{T_{gas}}\right)$ $F_c: (1 - 0.562) \exp\left(-\frac{T_{gas}}{91}\right)$ $+ 0.562 \exp\left(-\frac{T_{gas}}{5836}\right)$ $+ \exp\left(-\frac{8552}{T_{gas}}\right)$	147,400	
$CH + C_2H_6 \rightarrow C_3H_6 + H$	3.00×10^{-11}	401	
$CH + C_2H_6 + M \rightarrow C_3H_7 + M$	1.14×10^{-29}	146,168	
$CH + H_2 \rightarrow CH_2 + H$	$1.79 \times 10^{-10} \exp\left(-\frac{1565.17}{T_{gas}}\right)$	147,400	$\alpha = 0.5$

$CH + H \rightarrow C + H_2$	4.98×10^{-11}	402	
$CH + CH_3 \rightarrow C_2H_3 + H$	4.98×10^{-11}	147,403	
$CH + CH_2 \rightarrow C_2H_2 + H$	6.64×10^{-11}	147,404	
$CH + H_2 \rightarrow CH_3$	$k_\infty: 3.29 \times 10^{-12} T_{gas}^{0.43} \exp\left(-\frac{186.21}{T_{gas}}\right)$ $k_0: 1.33 \times 10^{-22} T_{gas}^{-2.80} \exp\left(-\frac{296.93}{T_{gas}}\right)$ $F_c: (1 - 0.578) \exp\left(-\frac{T_{gas}}{122}\right)$ $+ 0.578 \exp\left(-\frac{T_{gas}}{2535}\right)$ $+ \exp\left(-\frac{9365}{T_{gas}}\right)$	147,400	$\alpha = 0$
$CH + M \rightarrow C + H + M$	$3.16 \times 10^{-10} \exp\left(-\frac{280}{RT_{gas}}\right)$	399	
$CH + C_2H_3 \rightarrow CH_2 + C_2H_2$	8.30×10^{-11}	403	
$C + H_2 \rightarrow CH + H$	$6.64 \times 10^{-10} \exp\left(-\frac{97.28}{RT_{gas}}\right)$	182	$\alpha = 1$
$C + CH_3 \rightarrow H + C_2H_2$	8.30×10^{-11}	147,403	
$C + CH_2 \rightarrow 2CH$	$2.69 \times 10^{-12} \exp\left(-\frac{196}{RT_{gas}}\right)$	405	
$C + CH_2 \rightarrow H + C_2H$	8.30×10^{-11}	147,403	
$C + H_2 + M \rightarrow CH_2 + M$	6.89×10^{-32}	119	$\alpha = 0$
$C_2H_6 + C_2H_3 \rightarrow C_2H_5 + C_2H_4$	$1.46 \times 10^{-13} \left(\frac{T_{gas}}{298}\right)^{3.30} \exp\left(-\frac{43.90}{RT_{gas}}\right)$	118	
$C_2H_6 + C_2H \rightarrow C_2H_2 + C_2H_5$	5.99×10^{-12}	118	
$C_2H_6 + C_3H_7 \rightarrow C_3H_8 + C_2H_5$	$1.19 \times 10^{-15} \left(\frac{T_{gas}}{298}\right)^{3.82} \exp\left(-\frac{37.83}{RT_{gas}}\right)$	171	
$C_2H_6 + C_3H_5 \rightarrow C_3H_6 + C_2H_5$	$5.71 \times 10^{-14} \left(\frac{T_{gas}}{298}\right)^{3.30} \exp\left(-\frac{83.06}{RT_{gas}}\right)$	145	
$C_2H_6 + H \rightarrow C_2H_5 + H_2$	$1.23 \times 10^{-11} \left(\frac{T_{gas}}{298}\right)^{1.50} \exp\left(-\frac{31.01}{RT_{gas}}\right)$	146	
$C_2H_6 + H \rightarrow CH_4 + CH_3$	$8.97 \times 10^{-20} \exp\left(-\frac{48.64}{RT_{gas}}\right)$	406	
$C_2H_6 \rightarrow 2CH_3$	$k_\infty: 1.80 \times 10^{21} T_{gas}^{-1.24} \exp\left(-\frac{45700}{T_{gas}}\right)$ $k_0: 4.50 \times 10^{-2} \exp\left(-\frac{348}{RT_{gas}}\right)$ $F_c: 0.54 \exp\left(-\frac{T_{gas}}{1250}\right)$	174	

$C_2H_6 + C_4H_9$ $\rightarrow C_4H_{10} + C_2H_5$	$8.30 \times 10^{-13} \exp\left(-\frac{62.77}{RT_{gas}}\right)$	407	
$C_2H_6 + CH$ $\rightarrow C_2H_4 + CH_3$	$1.79 \times 10^{-10} \exp\left(\frac{132.36}{T_{gas}}\right)$	174	
$C_2H_6 + CH_2$ $\rightarrow C_2H_5 + CH_3$	$9.00 \times 10^{-33} T_{gas}^{6.42}$	398	
$2C_2H_5 \rightarrow C_2H_6 + C_2H_4$	2.41×10^{-12}	146	
$C_2H_5 + C_2H_4$ $\rightarrow C_2H_6 + C_2H_3$	$5.83 \times 10^{-14} \left(\frac{T_{gas}}{298}\right)^{3.13} \exp\left(-\frac{75.33}{RT_{gas}}\right)$	118	
$C_2H_5 + C_2H_2$ $\rightarrow C_2H_6 + C_2H$	$4.50 \times 10^{-13} \exp\left(-\frac{98.11}{RT_{gas}}\right)$	118	
$C_2H_5 + C_2H$ $\rightarrow C_2H_4 + C_2H_2$	3.01×10^{-12}	118	
$C_2H_5 + C_3H_8$ $\rightarrow C_2H_6 + C_3H_7$	$1.61 \times 10^{-15} \left(\frac{T_{gas}}{298}\right)^{3.65} \exp\left(-\frac{38.25}{RT_{gas}}\right)$	171	
$C_2H_5 + C_3H_7$ $\rightarrow C_3H_8 + C_2H_4$	1.91×10^{-12}	171	
$C_2H_5 + C_3H_7$ $\rightarrow C_3H_6 + C_2H_6$	2.41×10^{-12}	171	
$C_2H_5 + C_3H_6$ $\rightarrow C_3H_5 + C_2H_6$	$1.69 \times 10^{-15} \left(\frac{T_{gas}}{298}\right)^{3.50} \exp\left(-\frac{35.34}{RT_{gas}}\right)$	145	
$C_2H_5 + H_2 \rightarrow C_2H_6 + H$	$4.12 \times 10^{-15} \left(\frac{T_{gas}}{298}\right)^{3.60} \exp\left(-\frac{27.77}{RT_{gas}}\right)$	118	$\alpha = 0.5$
$C_2H_5 + H \rightarrow 2CH_3$	5.99×10^{-11}	146	
$C_2H_5 + H \rightarrow C_2H_4 + H_2$	3.32×10^{-12}	118	
$C_2H_5 + H \rightarrow C_2H_6$	$k_{\infty}: 8.65 \times 10^{-7} T_{gas}^{-0.99} \exp\left(-\frac{795.17}{T_{gas}}\right)$ $k_0: 1.11 \times 10^{-6} T_{gas}^{-7.08} \exp\left(-\frac{3364.37}{T_{gas}}\right)$ $F_C: (1 - 0.842) \exp\left(-\frac{T_{gas}}{125}\right)$ $+ 0.842 \exp\left(-\frac{T_{gas}}{2219}\right)$ $+ \exp\left(-\frac{6882}{T_{gas}}\right)$	408	
$C_2H_5 \rightarrow C_2H_4 + H$	$k_{\infty}: 4.08 \times 10^{12} \left(\frac{T_{gas}}{298}\right)^{1.04} \exp\left(-\frac{154}{RT_{gas}}\right)$ $k_0: 2.99 \times 10^{-3} \left(\frac{T_{gas}}{298}\right)^{-4.99} \exp\left(-\frac{167.12}{RT_{gas}}\right)$ $F_C: 0.25 \exp\left(-\frac{T_{gas}}{97}\right)$ $+ 0.75 \exp\left(-\frac{T_{gas}}{1379}\right)$	174,409	

$2C_2H_5 \rightarrow C_4H_{10}$	9.55×10^{-12}	146	
$C_2H_5 + C_4H_9$ $\rightarrow C_2H_4 + C_4H_{10}$	1.40×10^{-12}	144	
$C_2H_5 + C_2H_3 \rightarrow 2C_2H_4$	4.42×10^{-11}	410	
$C_2H_4 + C_2H \rightarrow$ $C_2H_2 + C_2H_3$	1.40×10^{-10}	175	
$C_2H_4 + H \rightarrow C_2H_3 + H_2$	$9.00 \times 10^{-10} \exp\left(-\frac{62.36}{RT_{gas}}\right)$	146	
$C_2H_4 + H \rightarrow C_2H_5$	$k_{\infty}: 9.68 \times 10^{-12} \left(\frac{T_{gas}}{298}\right)^{1.28} \exp\left(-\frac{5.40}{RT_{gas}}\right)$ $k_0: 3.31 \times 10^{-6} T_{gas}^{-7.62} \exp\left(-\frac{3507.80}{T_{gas}}\right)$ $F_c: (1 - 0.975) \exp\left(-\frac{T_{gas}}{210}\right)$ $+ 0.975 \exp\left(-\frac{T_{gas}}{984}\right)$ $+ \exp\left(-\frac{4374}{T_{gas}}\right)$	147,174,409,411	
$C_2H_4 + H_2 \rightarrow C_2H_5 + H$	9.55×10^{-12}	146	$\alpha = 1$
$C_2H_4 + M$ $\rightarrow C_2H_3 + H + M$	$4.30 \times 10^{-7} \exp\left(-\frac{404}{RT_{gas}}\right)$	174	
$C_2H_4 + C_3H_6$ $\rightarrow C_3H_5 + C_2H_5$	$9.60 \times 10^{-11} \exp\left(-\frac{216}{RT_{gas}}\right)$	145	
$C_2H_4 + C_2H_2 \rightarrow 2C_2H_3$	$4.00 \times 10^{-11} \exp\left(-\frac{286}{RT_{gas}}\right)$	175	
$C_2H_4 + C_3H_6$ $\rightarrow C_2H_3 + C_3H_7$	$1.00 \times 10^{-10} \exp\left(-\frac{316}{RT_{gas}}\right)$	145	
$2C_2H_4 \rightarrow C_2H_5 + C_2H_3$	$8.00 \times 10^{-10} \exp\left(-\frac{299}{RT_{gas}}\right)$	118	
$C_2H_4 + CH_3 \rightarrow C_3H_7$	$k_{\infty}: 4.23 \times 10^{-18} T_{gas}^{1.60} \exp\left(-\frac{2868.65}{T_{gas}}\right)$ $k_0: 1.65 \times 10^{16} T_{gas}^{-14.60} \exp\left(-\frac{9144.44}{T_{gas}}\right)$ $F_c: (1 - 0.1874) \exp\left(-\frac{T_{gas}}{277}\right)$ $+ 0.1874 \exp\left(-\frac{T_{gas}}{8748}\right)$ $+ \exp\left(-\frac{7891}{T_{gas}}\right)$	147,171	
$C_2H_4 \rightarrow C_2H_2 + H_2$	$k_{\infty}: 8.00 \times 10^{12} T_{gas}^{0.44} \exp\left(-\frac{44675.39}{T_{gas}}\right)$	118,147,412,413	

	$k_0: 8.71 \times 10^3 T_{gas}^{-9.30} \exp\left(-\frac{49219.93}{T_{gas}}\right)$ $F_c: (1 - 0.735) \exp\left(-\frac{T_{gas}}{180}\right)$ $+ 0.735 \exp\left(-\frac{T_{gas}}{1035}\right)$ $+ \exp\left(-\frac{5417}{T_{gas}}\right)$		
$C_2H_4 + C_2H_5 \rightarrow C_4H_9$	$3.00 \times 10^{-14} \left(\frac{T_{gas}}{298}\right)^{2.48} \exp\left(-\frac{25.65}{RT_{gas}}\right)$	250	
$C_2H_4 + H_2 \rightarrow C_2H_6$	$4.75 \times 10^{-16} \exp\left(-\frac{180}{RT_{gas}}\right)$	414	$\alpha = 0$
$C_2H_4 + CH_2 \rightarrow C_3H_6$	$5.30 \times 10^{-12} \exp\left(-\frac{2660}{T_{gas}}\right)$	146	
$C_2H_4 + C_4H_9$ $\rightarrow C_3H_6 + C_3H_7$	$5.00 \times 10^{-14} \exp\left(-\frac{25.53}{RT_{gas}}\right)$	144	
$2C_2H_3 \rightarrow C_2H_4 + C_2H_2$	3.50×10^{-11}	175	
$C_2H_3 + C_2H \rightarrow 2C_2H_2$	3.15×10^{-11}	174	
$C_2H_3 + C_3H_8$ $\rightarrow C_2H_4 + C_3H_7$	$1.46 \times 10^{-13} \left(\frac{T_{gas}}{298}\right)^{3.30} \exp\left(-\frac{43.90}{RT_{gas}}\right)$	171	
$C_2H_3 + C_3H_7$ $\rightarrow C_3H_8 + C_2H_2$	2.01×10^{-12}	171	
$C_2H_3 + C_3H_7$ $\rightarrow C_3H_6 + C_2H_4$	2.01×10^{-12}	171	
$C_2H_3 + C_3H_6$ $\rightarrow C_3H_5 + C_2H_4$	$1.68 \times 10^{-15} \left(\frac{T_{gas}}{298}\right)^{3.50} \exp\left(-\frac{19.62}{RT_{gas}}\right)$	145	
$C_2H_3 + C_3H_5$ $\rightarrow C_3H_6 + C_2H_2$	8.00×10^{-12}	145	
$C_2H_3 + H_2 \rightarrow C_2H_4 + H$	$1.61 \times 10^{-13} \left(\frac{T_{gas}}{298}\right)^{2.63} \exp\left(-\frac{35.75}{RT_{gas}}\right)$	118	$\alpha = 0$
$C_2H_3 + H \rightarrow C_2H_2 + H_2$	1.60×10^{-10}	118	
$C_2H_3 + H \rightarrow C_2H_4$	$k_\infty: 1.01 \times 10^{-11} T_{gas}^{0.27} \exp\left(-\frac{140.92}{T_{gas}}\right)$ $k_0: 7.72 \times 10^{-18} T_{gas}^{-3.86} \exp\left(-\frac{1670.86}{T_{gas}}\right)$ $F_c: (1 - 0.782) \exp\left(-\frac{T_{gas}}{207.5}\right)$ $+ 0.782 \exp\left(-\frac{T_{gas}}{2663}\right)$ $+ \exp\left(-\frac{6095}{T_{gas}}\right)$	147,412,415	
$C_2H_3 \rightarrow C_2H_2 + H$	$k_\infty: 2.00 \times 10^{14} \exp\left(-\frac{20000}{T_{gas}}\right)$	146	

	$k_0: 6.90 \times 10^{17} T_{\text{gas}}^{-7.50} \exp\left(-\frac{22900}{T_{\text{gas}}}\right)$ $F_c: 0.35$		
$C_2H_3 + C_4H_9$ $\rightarrow C_2H_2 + C_4H_{10}$	1.40×10^{-12}	144	
$C_2H_2 + H \rightarrow C_2H + H_2$	$1.00 \times 10^{-10} \exp\left(-\frac{93.12}{RT_{\text{gas}}}\right)$	118	
$C_2H_2 + H \rightarrow C_2H_3$	$k_{\infty}: 9.30 \times 10^{-12} \exp\left(-\frac{1207.85}{T_{\text{gas}}}\right)$ $k_0: 2.10 \times 10^{-7} T_{\text{gas}}^{-7.27} \exp\left(-\frac{3633.62}{T_{\text{gas}}}\right)$ $F_c: (1 - 0.751) \exp\left(-\frac{T_{\text{gas}}}{98.5}\right)$ $+ 0.751 \exp\left(-\frac{T_{\text{gas}}}{1302}\right)$ $+ \exp\left(-\frac{4167}{T_{\text{gas}}}\right)$	118,147,415	
$C_2H_2 + H_2 \rightarrow C_2H_4$	$5.00 \times 10^{-13} \exp\left(-\frac{163}{RT_{\text{gas}}}\right)$	118	$\alpha = 0$
$C_2H_2 + H_2 \rightarrow C_2H_3 + H$	$4.00 \times 10^{-12} \exp\left(-\frac{272}{RT_{\text{gas}}}\right)$	118	$\alpha = 1$
$C_2H_2 + M$ $\rightarrow C_2H + H + M$	$6.64 \times 10^{-8} \exp\left(-\frac{447}{RT_{\text{gas}}}\right)$	387	
$2C_2H_2 \rightarrow C_2H + C_2H_3$	$1.60 \times 10^{-11} \exp\left(-\frac{353}{RT_{\text{gas}}}\right)$	118	
$C_2H_2 + CH_3 \rightarrow C_3H_5$	$1.58 \times 10^{-5} \left(\frac{T_{\text{gas}}}{298}\right)^{-8.58} \exp\left(-\frac{84.81}{RT_{\text{gas}}}\right)$	204	*
$C_2H_2 + CH \rightarrow C_2H$ $+ CH_2$	$3.50 \times 10^{-10} \exp\left(\frac{86.56}{T_{\text{gas}}}\right)$	174	
$C_2H_2 + C_4H_9$ $\rightarrow C_3H_6 + C_3H_5$	$1.20 \times 10^{-12} \exp\left(-\frac{37.66}{RT_{\text{gas}}}\right)$	144	
$2C_2H \rightarrow C_2H_2 + C_2$	3.01×10^{-12}	118	
$C_2H + C_3H_8$ $\rightarrow C_2H_2 + C_3H_7$	5.99×10^{-12}	171	
$C_2H + C_3H_7$ $\rightarrow C_2H_2 + C_3H_6$	1.00×10^{-11}	171	
$C_2H + C_3H_6$ $\rightarrow C_2H_2 + C_3H_5$	5.99×10^{-12}	145	
$C_2H + H_2 \rightarrow C_2H_2 + H$	$9.43 \times 10^{-14} T_{\text{gas}}^{0.90} \exp\left(-\frac{1003.02}{RT_{\text{gas}}}\right)$	416	$\alpha = 0$
$C_2H + H \rightarrow H_2 + C_2$	$5.99 \times 10^{-11} \exp\left(-\frac{118}{RT_{\text{gas}}}\right)$	118	
$C_2H + H \rightarrow C_2H_2$	$k_{\infty}: 1.66 \times 10^{-7}$	147,417,418	

	$k_0: 2.07 \times 10^{-14} T_{\text{gas}}^{-4.80} \exp\left(-\frac{956.22}{T_{\text{gas}}}\right)$ $F_c: (1 - 0.646) \exp\left(-\frac{T_{\text{gas}}}{132}\right)$ $+ 0.646 \exp\left(-\frac{T_{\text{gas}}}{1315}\right)$ $+ \exp\left(-\frac{5566}{T_{\text{gas}}}\right)$		
$C_2 + H_2 \rightarrow C_2H + H$	$1.10 \times 10^{-10} \exp\left(-\frac{33.26}{RT_{\text{gas}}}\right)$	185	$\alpha = 0$
$C_2 + M \rightarrow 2C + M$	$2.49 \times 10^{-8} \exp\left(-\frac{595}{RT_{\text{gas}}}\right)$	185	
$C_3H_8 + C_3H_5$ $\rightarrow C_3H_6 + C_3H_7$	$5.71 \times 10^{-14} \left(\frac{T_{\text{gas}}}{298}\right)^{3.30} \exp\left(-\frac{83.06}{RT_{\text{gas}}}\right)$	145	
$C_3H_8 + H \rightarrow C_3H_7 + H_2$	$2.19 \times 10^{-180} T_{\text{gas}}^{2.54} \exp\left(-\frac{3400.10}{T_{\text{gas}}}\right)$	147,171	
$C_3H_8 \rightarrow C_2H_5 + CH_3$	$k_\infty: 1.10 \times 10^{17} \exp\left(-\frac{42470}{T_{\text{gas}}}\right)$ $k_0: 1.30 \times 10^{-5} \exp\left(-\frac{32700}{T_{\text{gas}}}\right)$ $F_c: 0.24 \exp\left(-\frac{T_{\text{gas}}}{1946}\right)$ $+ 0.76 \exp\left(-\frac{T_{\text{gas}}}{38}\right)$	174	
$C_3H_8 + C_4H_9$ $\rightarrow C_4H_{10} + C_3H_7$	$1.61 \times 10^{-15} \left(\frac{T_{\text{gas}}}{298}\right)^{3.50} \exp\left(-\frac{27.77}{RT_{\text{gas}}}\right)$	144	
$C_3H_8 + CH_2 \rightarrow C_4H_{10}$	4.42×10^{-12}	419	
$2C_3H_7 \rightarrow C_3H_6 + C_3H_8$	2.81×10^{-12}	171	
$C_3H_7 + C_3H_6$ $\rightarrow C_3H_5 + C_3H_8$	$1.69 \times 10^{-15} \left(\frac{T_{\text{gas}}}{298}\right)^{3.50} \exp\left(-\frac{27.77}{RT_{\text{gas}}}\right)$	145	
$C_3H_7 + C_3H_5 \rightarrow 2C_3H_6$	$2.41 \times 10^{-12} \exp\left(-\frac{0.55}{RT_{\text{gas}}}\right)$	145	
$C_3H_7 + H_2 \rightarrow C_3H_8 + H$	$3.19 \times 10^{-14} \left(\frac{T_{\text{gas}}}{298}\right)^{2.84} \exp\left(-\frac{38.25}{RT_{\text{gas}}}\right)$	171	$\alpha = 1$
$C_3H_7 + H \rightarrow C_3H_6 + H_2$	3.01×10^{-12}	171	
$C_3H_7 + H \rightarrow C_3H_8$	$k_\infty: 6.00 \times 10^{-11}$ $k_0: 2.44 \times 10^{14} T_{\text{gas}}^{-13.54} \exp\left(-\frac{5715.65}{T_{\text{gas}}}\right)$ $F_c: (1 - 0.315) \exp\left(-\frac{T_{\text{gas}}}{369}\right)$ $+ 0.315 \exp\left(-\frac{T_{\text{gas}}}{3285}\right)$ $+ \exp\left(-\frac{6667}{T_{\text{gas}}}\right)$	147,186,387,420	

$C_3H_7 + H \rightarrow CH_3 + C_2H_5$	$6.74 \times 10^{-18} T_{gas}^{2.19} \exp\left(-\frac{447.91}{T_{gas}}\right)$	147,171	
$C_3H_7 + M \rightarrow C_3H_6 + H + M$	$1.25 \times 10^{17} \exp\left(-\frac{237}{RT_{gas}}\right)$	187	*
$C_3H_7 + M \rightarrow C_2H_4 + CH_3 + M$	$16.0 \left(\frac{T_{gas}}{298}\right)^{-10.00} \exp\left(-\frac{150}{RT_{gas}}\right)$	421	
$C_3H_7 + C_4H_9 \rightarrow C_4H_{10} + C_3H_6$	2.41×10^{-12}	144	
$C_3H_6 + C_2H_2 \rightarrow C_2H_3 + C_3H_5$	$6.71 \times 10^{-11} \exp\left(-\frac{196}{RT_{gas}}\right)$	145	
$2C_3H_6 \rightarrow C_3H_7 + C_3H_5$	$4.20 \times 10^{-10} \exp\left(-\frac{231}{RT_{gas}}\right)$	145	
$C_3H_6 \rightarrow C_3H_5 + H$	$2.50 \times 10^{15} \exp\left(-\frac{363}{RT_{gas}}\right)$	145	*
$C_3H_6 + H \rightarrow C_3H_5 + H_2$	$4.40 \times 10^{-13} \left(\frac{T_{gas}}{298}\right)^{2.50} \exp\left(-\frac{10.39}{RT_{gas}}\right)$	145	
$C_3H_6 + H \rightarrow C_3H_7$	$1.29 \times 10^{-11} \left(\frac{T_{gas}}{298}\right)^{0.51} \exp\left(-\frac{5.15}{RT_{gas}}\right)$	250	
$C_3H_6 + M \rightarrow CH_3 + C_2H_3 + M$	$1.28 \times 10^{13} \left(\frac{T_{gas}}{298}\right)^{-15.70} \exp\left(-\frac{502}{RT_{gas}}\right)$	422	
$C_3H_6 + CH_3 \rightarrow C_4H_9$	$1.27 \times 10^{-14} \left(\frac{T_{gas}}{298}\right)^{2.67} \exp\left(-\frac{28.66}{RT_{gas}}\right)$	250	
$C_3H_6 + C_4H_9 \rightarrow C_4H_{10} + C_3H_5$	$1.69 \times 10^{-15} \left(\frac{T_{gas}}{298}\right)^{3.50} \exp\left(-\frac{27.77}{RT_{gas}}\right)$	145	
$C_3H_5 + H_2 \rightarrow C_3H_6 + H$	$1.39 \times 10^{-13} \left(\frac{T_{gas}}{298}\right)^{2.38} \exp\left(-\frac{79.49}{RT_{gas}}\right)$	145	$\alpha = 1$
$C_3H_5 + H \rightarrow C_3H_6$	$78.80 \left(\frac{T_{gas}}{298}\right)^{-11.76} \exp\left(-\frac{98.53}{RT_{gas}}\right)$	423	*
$C_3H_5 \rightarrow C_2H_2 + CH_3$	$1.26 \times 10^{13} \exp\left(-\frac{140}{RT_{gas}}\right)$	186	
$C_4H_9 + M \rightarrow C_2H_4 + C_2H_5 + M$	$1.07 \times 10^2 \left(\frac{T_{gas}}{298}\right)^{-11.90} \exp\left(-\frac{135}{RT_{gas}}\right)$	424	
$C_4H_9 + CH_2 \rightarrow C_2H_4 + C_3H_7$	3.01×10^{-11}	144	
$C_4H_9 \rightarrow C_3H_6 + CH_3$	$7.71 \times 10^{13} \left(\frac{T_{gas}}{298}\right)^{0.77} \exp\left(-\frac{128}{RT_{gas}}\right)$	250	
$C_4H_9 + H_2 \rightarrow C_4H_{10} + H$	$2.52 \times 10^{-14} \left(\frac{T_{gas}}{298}\right)^{2.72} \exp\left(-\frac{40.99}{RT_{gas}}\right)$	144	$\alpha = 1$
$C_4H_{10} + CH_3 \rightarrow CH_4 + C_4H_9$	$8.32 \times 10^{-13} \exp\left(-\frac{56.87}{RT_{gas}}\right)$	425	

$C_4H_{10} + M \rightarrow C_3H_7 + CH_3 + M$	$8.87 \times 10^{-7} \exp\left(-\frac{180}{RT_{gas}}\right)$	426	
$C_4H_{10} + M \rightarrow 2C_2H_5 + M$	$7.84 \times 10^{-6} \exp\left(-\frac{207}{RT_{gas}}\right)$	426	
$C_4H_{10} + H \rightarrow C_4H_9 + H_2$	$2.19 \times 10^{-10} \exp\left(-\frac{39.24}{RT_{gas}}\right)$	427	
$C_4H_{10} + CH_2 \rightarrow C_4H_9 + CH_3$	$1.81 \times 10^{-12} \exp\left(-\frac{20.54}{RT_{gas}}\right)$	144	
$C_4H_{10} + C_2H_3 \rightarrow C_2H_4 + C_4H_9$	$2.42 \times 10^{-15} \left(\frac{T_{gas}}{298}\right)^{3.65} \exp\left(-\frac{21.62}{RT_{gas}}\right)$	144	
$C_4H_{10} + C_3H_7 \rightarrow C_3H_8 + C_4H_9$	$2.47 \times 10^{-15} \left(\frac{T_{gas}}{298}\right)^{3.65} \exp\left(-\frac{38.25}{RT_{gas}}\right)$	144	
$C_4H_{10} + C_2H \rightarrow C_2H_2 + C_4H_9$	1.00×10^{-11}	144	
$C_4H_{10} + C_2H_5 \rightarrow C_2H_6 + C_4H_9$	$2.47 \times 10^{-15} \left(\frac{T_{gas}}{298}\right)^{3.65} \exp\left(-\frac{38.25}{RT_{gas}}\right)$	144	
$C_4H_{10} + C_3H_5 \rightarrow C_3H_6 + C_4H_9$	$8.63 \times 10^{-14} \left(\frac{T_{gas}}{298}\right)^{3.30} \exp\left(-\frac{83.06}{RT_{gas}}\right)$	145	
$C_4H_{10} + CH_2 \rightarrow C_5H_{12}$	9.61×10^{-13}	419	
$C_5H_{12} \rightarrow CH_3 + C_4H_9$	$3.16 \times 10^{16} \exp\left(-\frac{331}{RT_{gas}}\right)$	428	
$H_2 + M \rightarrow 2H + M$	$1.88 \times 10^{-8} \left(\frac{T_{gas}}{298}\right)^{-1.10} \exp\left(-\frac{437}{RT_{gas}}\right)$	189	$\alpha = 0.8$
$H_2 + H \rightarrow 3H$	See reference for full expression	429	
$2H + M \rightarrow H_2 + M$	$5.52 \times 10^{-30} T_{gas}^{-1.00}$	387	

Table A20: Extra neutral-neutral reactions added to the chemistry set for describing CH₄/N₂ mixtures, as well as the references where the data are adopted from. The rate coefficients are given in cm³ s⁻¹ and cm⁶ s⁻¹, for two-body and three-body reactions, respectively. T_{gas} is given in K. R is the gas constant (8.314x10⁻³ kJ mol⁻¹ K⁻¹). The α parameter determines the effectiveness of lowering the activation energy for reactions involving vibrationally excited levels of the molecules (see details in ¹⁴).

Reaction	Rate coefficient	Ref	Note
$N + H + M \rightarrow NH + M$	5.02×10^{-32}	430	
$N + H_2 \rightarrow NH + H$	$4.65 \times 10^{-10} \exp\left(-\frac{138}{RT_{gas}}\right)$	274	$\alpha = 1.0$
$N_2 + H \rightarrow NH + N$	$5.27 \times 10^{-10} \left(\frac{T_{gas}}{298}\right)^{0.50} \exp\left(-\frac{619}{RT_{gas}}\right)$	431	$\alpha = 1.0$

$NH + M \rightarrow N + H + M$	$2.99 \times 10^{-10} \exp\left(-\frac{313}{RT_{gas}}\right)$	432	
$NH + N \rightarrow N_2 + H$	$1.95 \times 10^{-11} \left(\frac{T_{gas}}{298}\right)^{0.51} \exp\left(-\frac{0.08}{RT_{gas}}\right)$	431	
$NH + H \rightarrow H_2 + N$	1.69×10^{-11}	146	
$NH + H_2 \rightarrow H + NH_2$	$3.50 \times 10^{-11} \exp\left(-\frac{64.50}{RT_{gas}}\right)$	433	$\alpha = 0.5$
$NH + NH \rightarrow NH_2 + N$	$3.74 \times 10^{-15} \left(\frac{T_{gas}}{298}\right)^{3.88} \exp\left(-\frac{1.43}{RT_{gas}}\right)$	434	
$NH_2 + M \rightarrow H + NH + M$	$1.99 \times 10^{-9} \exp\left(-\frac{318}{RT_{gas}}\right)$	432	
$NH_2 + NH \rightarrow NH_3 + N$	$1.94 \times 10^{-14} \left(\frac{T_{gas}}{298}\right)^{2.46} \exp\left(-\frac{0.45}{RT_{gas}}\right)$	434	
$NH_2 + NH_2 \rightarrow NH_3 + NH$	$8.30 \times 10^{-11} \exp\left(-\frac{41.82}{RT_{gas}}\right)$	435	
$NH_2 + N \rightarrow NH + NH$	$2.99 \times 10^{-13} \exp\left(-\frac{63.19}{RT_{gas}}\right)$	405	
$NH_2 + H + M \rightarrow NH_3 + M$	3.01×10^{-30}	436	
$NH_2 + H \rightarrow NH + H_2$	1.00×10^{-11}	146	
$NH_2 + H_2 \rightarrow NH_3 + H$	$1.76 \times 10^{-13} \left(\frac{T_{gas}}{298}\right)^{2.23} \exp\left(-\frac{30.02}{RT_{gas}}\right)$	437	$\alpha = 0.0$
$NH_3 + M \rightarrow NH_2 + H + M$	$3.65 \times 10^{-8} \exp\left(-\frac{391}{RT_{gas}}\right)$	435	
$NH_3 + M \rightarrow NH + H_2 + M$	$1.05 \times 10^{-9} \exp\left(-\frac{391}{RT_{gas}}\right)$	438	
$NH_3 + H \rightarrow NH_2 + H_2$	$7.80 \times 10^{-13} \left(\frac{T_{gas}}{298}\right)^{2.40} \exp\left(-\frac{41.49}{RT_{gas}}\right)$	439	
$NH_3 + NH \rightarrow NH_2 + NH_2$	$2.33 \times 10^{-14} \left(\frac{T_{gas}}{298}\right)^{3.41} \exp\left(-\frac{61.11}{RT_{gas}}\right)$	434	
$NH_3 + NH_2 \rightarrow NH_2 + NH_3$	$6.49 \times 10^{-15} \left(\frac{T_{gas}}{298}\right)^{3.28} \exp\left(-\frac{38.50}{RT_{gas}}\right)$	437	
$C + NH_2 \rightarrow CH + NH$	$9.61 \times 10^{-13} \exp\left(-\frac{87.30}{RT_{gas}}\right)$	405	
$CH + N \rightarrow C + NH$	$3.02 \times 10^{-11} \left(\frac{T_{gas}}{298}\right)^{0.65} \exp\left(-\frac{10.06}{RT_{gas}}\right)$	440	
$CH + N \rightarrow CN + H$	$1.66 \times 10^{-10} \left(\frac{T_{gas}}{298}\right)^{-0.09}$	441	
$CH_2 + N \rightarrow CH + NH$	$9.96 \times 10^{-13} \exp\left(-\frac{170}{RT_{gas}}\right)$	405	
$CH_3 + NH_2 \rightarrow CH_4 + NH$	2.57×10^{-12}	442	

$CH_3 + NH_3 \rightarrow CH_4 + NH_2$	$4.95x10^{-14} \left(\frac{T_{gas}}{298}\right)^{2.86} \exp\left(-\frac{61.03}{RT_{gas}}\right)$	443	
$CH_4 + NH \rightarrow CH_3 + NH_2$	$4.12x10^{-12} \left(\frac{T_{gas}}{298}\right)^{2.28} \exp\left(-\frac{85.08}{RT_{gas}}\right)$	444	$\alpha = 0.5$
$CH_4 + NH_2 \rightarrow CH_3 + NH_3$	$1.17x10^{-10} \exp\left(-\frac{71.34}{RT_{gas}}\right)$	445	$\alpha = 0.0$
$C_2H_6 + NH \rightarrow C_2H_5 + NH_2$	$1.16x10^{-10} \exp\left(-\frac{70.01}{RT_{gas}}\right)$	446	
$C_2H_6 + NH_2 \rightarrow C_2H_5 + NH_3$	$1.61x10^{-11} \exp\left(-\frac{47.97}{RT_{gas}}\right)$	447	
$C_3H_8 + NH_2 \rightarrow C_3H_7 + NH_3$	$2.90x10^{-14} \left(\frac{T_{gas}}{298}\right)^{3.49} \exp\left(-\frac{26.44}{RT_{gas}}\right)$	448	
$N_2 + H \rightarrow N_2H$	$2.94x10^{-10} \left(\frac{T_{gas}}{298}\right)^{-0.60} \exp\left(-\frac{64.98}{RT_{gas}}\right)$	431	$\alpha = 0.0$
$N_2H + M \rightarrow N_2 + H + M$	$2.16x10^{-10} T_{gas}^{-0.11} \exp\left(-\frac{2506.29}{T_{gas}}\right)$	449	
$N_2H + H \rightarrow N_2 + H_2$	$8.30x10^{-11}$	147	
$N_2H + CH_3 \rightarrow CH_4 + N_2$	$4.15x10^{-11}$	147	
$CN + H_2 \rightarrow HCN + H$	$4.90x10^{-19} T_{gas}^{2.45} \exp\left(-\frac{1127.33}{T_{gas}}\right)$	450	$\alpha = 0.0$
$HCN + H \rightarrow CN + H_2$	$6.31x10^{-10} \exp\left(-\frac{103}{RT_{gas}}\right)$	300	
$CH_3 + N \rightarrow HCN + H_2$	$6.14x10^{-12} T_{gas}^{0.15} \exp\left(\frac{45.29}{T_{gas}}\right)$	449,4 51	
$H + CN + M \rightarrow HCN + M$	$8.63x10^{-30} \left(\frac{T_{gas}}{298}\right)^{-2.20} \exp\left(-\frac{4.71}{RT_{gas}}\right)$	286	
$HCN + M \rightarrow H + CN + M$	$1.73x10^5 T_{gas}^{-3.30} \exp\left(-\frac{63714.14}{T_{gas}}\right)$	147	
$N_2 + C \rightarrow CN + N$	$1.05x10^{-10} \exp\left(-\frac{23160.54}{T_{gas}}\right)$	297	$\alpha = 1.0$
$N + CN \rightarrow C + N_2$	$3.01x10^{-10}$	146	
$N_2 + CH \rightarrow HCN + N$	$5.18x10^{-15} T_{gas}^{0.88} \exp\left(-\frac{10130.85}{T_{gas}}\right)$	147	$\alpha = 1.0$
$N_2 + CH_2 \rightarrow HCN + NH$	$1.66x10^{-11} \exp\left(-\frac{37242.07}{T_{gas}}\right)$	452	$\alpha = 1.0$
$H_2CN + N \rightarrow N_2 + CH_2$	$9.96x10^{-11} \exp\left(-\frac{201.31}{T_{gas}}\right)$	453	
$CH_3 + N \rightarrow H_2CN + H$	$1.01x10^{-9} T_{gas}^{-0.31} \exp\left(-\frac{145.95}{T_{gas}}\right)$	449,4 51	
$HCNN + H \rightarrow CH_2 + N_2$	$1.66x10^{-10}$	147	
$H + HCN \rightarrow H_2CN$	$k_{\infty}: 5.50x10^{-11} \exp\left(-\frac{2438}{T_{gas}}\right)$	278	

	$k_0: 4.40 \times 10^{-24} T_{\text{gas}}^{-2.73} \exp\left(-\frac{3855}{T_{\text{gas}}}\right)$ $F_c: (0.95 - 10^{-4} T_{\text{gas}})$		
$CH + N_2 \rightarrow HCNN$	$k_\infty: 5.15 \times 10^{-12} T_{\text{gas}}^{0.15}$ $k_0: 3.58 \times 10^{-23} T_{\text{gas}}^{-3.16} \exp\left(-\frac{372.42}{T_{\text{gas}}}\right)$ $F_c: (1 - 0.667) \exp\left(-\frac{T_{\text{gas}}}{235}\right)$ $+ 0.667 \exp\left(-\frac{T_{\text{gas}}}{2117}\right)$ $+ \exp\left(-\frac{4536}{T_{\text{gas}}}\right)$	147	$\alpha = 0.0$
$N + CH_2 \rightarrow HCN + H$	$5.00 \times 10^{-11} \exp\left(-\frac{250}{T_{\text{gas}}}\right)$	254	
$N + CH_2 \rightarrow CN + H_2$	1.60×10^{-11}	454	
$N + CH_2 \rightarrow CN + H + H$	1.60×10^{-11}	454,4 55	
$CN + CH_4 \rightarrow HCN + CH_3$	$1.00 \times 10^{-11} \exp\left(-\frac{857}{T_{\text{gas}}}\right)$	456	$\alpha = 0.0$
$CN + C_2H_6 \rightarrow HCN + C_2H_5$	$1.80 \times 10^{-11} T_{\text{gas}}^{0.50}$	457	
$N_2 + M \rightarrow N + N + M$	$9.86 \times 10^{-5} \left(\frac{T_{\text{gas}}}{298}\right)^{-3.33} \exp\left(-\frac{940}{RT_{\text{gas}}}\right)$	458	$\alpha = 0.8$
$C_2 + N_2 \rightarrow CN + CN$	$2.49 \times 10^{-11} \exp\left(-\frac{175}{RT_{\text{gas}}}\right)$	459	$\alpha = 1.0$
$N_2 + CH \rightarrow NCN + H$	$4.06 \times 10^{-13} \left(\frac{T_{\text{gas}}}{298}\right)^{1.12} \exp\left(-\frac{73.33}{RT_{\text{gas}}}\right)$	460	$\alpha = 1.0$
$NCN + H \rightarrow HCN + N$	4.15×10^{-11}	461	
$NCN + NCN \rightarrow CN + CN + N_2$	6.14×10^{-12}	291	
$NCN + M \rightarrow C + N_2 + M$	$1.48 \times 10^{-9} \exp\left(-\frac{260}{RT_{\text{gas}}}\right)$	291	
$CN + HCN \rightarrow C_2N_2 + H$	$4.25 \times 10^{-13} \left(\frac{T_{\text{gas}}}{298}\right)^{1.71} \exp\left(-\frac{6.40}{RT_{\text{gas}}}\right)$	286	
$CN + CN + M \rightarrow C_2N_2 + M$	$3.28 \times 10^{-29} \left(\frac{T_{\text{gas}}}{298}\right)^{-2.61}$	286	
$C_2N_2 + M \rightarrow CN + CN + M$	$0.365 \left(\frac{T_{\text{gas}}}{298}\right)^{-4.32} \exp\left(-\frac{545}{RT_{\text{gas}}}\right)$	282	
$CN + NH_3 \rightarrow HCN + NH_2$	1.66×10^{-11}	300	
$CN + C \rightarrow C_2 + N$	$4.98 \times 10^{-10} \exp\left(-\frac{150}{RT_{\text{gas}}}\right)$	462	

Table A21: Calculated rates, averaged over all conditions studied, of the most important reactions in the DBD.

Reaction	Rate (cm ⁻³ s ⁻¹)
$e^- + CH_4 \rightarrow e^- + CH_3 + H$	1×10^{18}
$CH_3 + H + M \rightarrow CH_4 + M$	1×10^{18}
$CH_3 + CH_3 + M \rightarrow C_2H_6 + M$	2×10^{17}
$C_2H_4 + H + M \rightarrow C_2H_5 + M$	2×10^{17}
$e^- + CH_4 \rightarrow e^- + CH_2 + H_2$	1×10^{17}
$e^- + C_2H_6 \rightarrow e^- + C_2H_4 + H_2$	1×10^{17}
$CH + CH_4 \rightarrow C_2H_4 + H$	6×10^{16}
$C_2H_5 + H + M \rightarrow C_2H_6 + M$	6×10^{16}
$C_2H_5 + C_2H_5 + M \rightarrow C_4H_{10} + M$	6×10^{16}
$CH_2 + H \rightarrow CH + H_2$	6×10^{16}
$CH_2 + CH_3 \rightarrow C_2H_4 + H$	4×10^{16}
$C_2H_5 + H \rightarrow CH_3 + CH_3$	4×10^{16}
$CH_4 + CH_4^+ \rightarrow CH_5^+ + CH_3$	3×10^{16}
$CH_3 + C_2H_5 + M \rightarrow C_3H_8 + M$	3×10^{16}
$e^- + C_2H_5^+ \rightarrow C_2H_3 + H + H$	2×10^{16}
$CH_3 + C_2H_3 + M \rightarrow C_3H_6 + M$	2×10^{16}
$C_3H_6 + H + M \rightarrow C_3H_7 + M$	2×10^{16}
$C_4H_{10} + CH_2 + M \rightarrow C_5H_{12} + M$	2×10^{16}
$C_3H_7 + H_2 \rightarrow C_3H_8 + H$	2×10^{16}
$e^- + C_2H_4 \rightarrow e^- + C_2H_2 + H_2$	2×10^{16}
$CH_5^+ + C_2H_6 \rightarrow C_2H_5^+ + H_2 + CH_4$	1×10^{16}
$CH_5^+ + C_2H_4 \rightarrow C_2H_5^+ + CH_4$	1×10^{16}
$e^- + C_2H_5^+ \rightarrow C_2H_2 + H_2 + H$	1×10^{16}
$e^- + C_3H_6 \rightarrow e^- + C_2H_2 + CH_4$	6×10^{15}
$C_3H_7 + H + M \rightarrow C_3H_8 + M$	6×10^{15}
$C_2H_3 + H \rightarrow C_2H_2 + H_2$	5×10^{15}
$e^- + C_2H_5^+ \rightarrow C_2H_2 + H + H + H$	5×10^{15}
$C_3H_8 + CH_2 + M \rightarrow C_4H_{10} + M$	3×10^{15}

$e^- + C_3H_8 \rightarrow e^- + C_2H_4 + CH_4$	3×10^{15}
$e^- + C_2H_4 \rightarrow e^- + C_2H_3 + H$	2×10^{15}
$CH_4 + CH_3^+ \rightarrow C_2H_5^+ + H_2$	1×10^{15}
$e^- + C_3H_8 \rightarrow e^- + C_3H_6 + H_2$	1×10^{15}
$e^- + CH_4 \rightarrow e^- + CH + H_2 + H$	8×10^{14}

Table A22: Calculated rates, averaged over all conditions studied, of the most important reactions in the MW plasma at reduced pressure.

Reaction	Rate ($\text{cm}^{-3} \text{s}^{-1}$)
$CH_4 + H \rightarrow CH_3 + H_2$	5×10^{19}
$CH_3 + CH_3 \rightarrow C_2H_5 + H$	3×10^{19}
$C_2H_5 + M \rightarrow C_2H_4 + H + M$	1×10^{19}
$CH_3 + C_2H_4 \rightarrow C_2H_3 + CH_4$	1×10^{19}
$C_2H_6 + M \rightarrow CH_3 + CH_3 + M$	1×10^{19}
$e^- + CH_4 \rightarrow e^- + CH_3 + H$	9×10^{18}
$CH_3 + CH_3 + M \rightarrow C_3H_6 + M$	5×10^{18}
$CH_3 + C_2H_3 \rightarrow C_2H_2 + CH_4$	4×10^{18}
$C_3H_5 + M \rightarrow C_2H_2 + CH_3 + M$	4×10^{18}
$C_3H_6 + M \rightarrow C_3H_5 + H + M$	3×10^{18}
$e^- + C_2H_6 \rightarrow e^- + C_2H_4 + H_2$	2×10^{18}
$CH_4 + CH_3 \rightarrow C_2H_6 + H$	1×10^{18}
$C_2H_4 + H_2 \rightarrow C_2H_5 + H$	9×10^{17}
$C_2H_5 + C_2H_5 + M \rightarrow C_4H_{10} + M$	8×10^{17}
$C_3H_6 + H \rightarrow C_3H_5 + H_2$	7×10^{17}
$e^- + C_3H_6 \rightarrow e^- + C_2H_2 + CH_4$	5×10^{17}
$C_4H_{10} + M \rightarrow C_3H_7 + CH_3 + M$	4×10^{17}
$CH_3 + C_2H_5 + M \rightarrow C_3H_8 + M$	2×10^{17}
$e^- + C_3H_8 \rightarrow e^- + C_2H_4 + CH_4$	2×10^{17}
$e^- + C_2H_4 \rightarrow e^- + C_2H_2 + H_2$	2×10^{17}
$C_3H_7 + M \rightarrow C_2H_4 + CH_3 + M$	1×10^{17}
$e^- + C_3H_8 \rightarrow e^- + C_3H_6 + H_2$	1×10^{17}

$e^- + C_3H_6 \rightarrow e^- + C_3H_5 + H$	$1x10^{17}$
$C_2H_6 + H \rightarrow C_2H_5 + H_2$	$5x10^{16}$
$C_2H_2 + H_2 \rightarrow C_2H_3 + H$	$5x10^{16}$
$C_3H_6 + H + M \rightarrow C_3H_7 + M$	$3x10^{16}$
$CH_3 + C_2H_6 \rightarrow C_2H_5 + CH_4$	$8x10^{15}$
$C_3H_8 + H \rightarrow C_3H_7 + H_2$	$7x10^{15}$
$C_2H_2 + H_2 + M \rightarrow C_2H_4 + M$	$5x10^{15}$

Table A23: Calculated rates, averaged over all conditions studied, of the most important reactions in the MW plasma at atmospheric pressure.

Reaction	Rate ($\text{cm}^{-3} \text{s}^{-1}$)
$C_2H_2 + M \rightarrow C_2H + H + M$	$2x10^{20}$
$C_2H + H_2 \rightarrow C_2H_2 + H$	$2x10^{20}$
$C_2H_3 + H \rightarrow C_2H_2 + H_2$	$4x10^{19}$
$C_2H_2 + H_2 + M \rightarrow C_2H_4 + M$	$3x10^{19}$
$C_2H_4 + H \rightarrow C_2H_3 + H_2$	$2x10^{19}$
$CH_4 + H \rightarrow CH_3 + H_2$	$7x10^{18}$
$CH_3 + C_2H_4 \rightarrow C_2H_3 + CH_4$	$3x10^{18}$
$CH_3 + CH_3 \rightarrow C_2H_5 + H$	$1x10^{18}$
$C_2H_5 + M \rightarrow C_2H_4 + H + M$	$1x10^{18}$
$CH_4 + M \rightarrow CH_3 + H + M$	$4x10^{17}$
$CH_4 + CH_3 \rightarrow C_2H_6 + H$	$3x10^{17}$
$C_2H_6 + M \rightarrow CH_3 + CH_3 + M$	$3x10^{17}$
$CH_3 + C_2H_6 \rightarrow C_2H_5 + CH_4$	$6x10^{16}$

Table A24: Calculated rates, averaged over all conditions studied, of the most important reactions in the GAP.

Reaction	Rate ($\text{cm}^{-3} \text{s}^{-1}$)
$N_2 + H + M \rightarrow N_2H + M$	$4x10^{21}$
$N_2H + H \rightarrow N_2 + H_2$	$2x10^{21}$
$C_2H_2 + M \rightarrow C_2H + H + M$	$1x10^{21}$

$C_2H + H_2 \rightarrow C_2H_2 + H$	1×10^{21}
$CH_4 + H \rightarrow CH_3 + H_2$	2×10^{20}
$CH_4 + M \rightarrow CH_3 + H + M$	9×10^{19}
$C_2H_4 + H \rightarrow C_2H_3 + H_2$	7×10^{19}
$C_2H_3 + H \rightarrow C_2H_2 + H_2$	3×10^{19}
$C_2H_4 + M \rightarrow C_2H_3 + H + M$	2×10^{19}
$CH_3 + CH_3 \rightarrow C_2H_5 + H$	2×10^{19}
$C_2H_5 + M \rightarrow C_2H_4 + H + M$	2×10^{19}
$C_2H_2 + H_2 + M \rightarrow C_2H_4 + M$	1×10^{19}
$CH_3 + C_2H_4 \rightarrow C_2H_3 + CH_4$	8×10^{18}
$CH_3 + N_2H \rightarrow CH_4 + N_2$	5×10^{18}
$CH_4 + CH_3 \rightarrow C_2H_6 + H$	2×10^{18}
$C_2H_6 + M \rightarrow CH_3 + CH_3 + M$	3×10^{17}
$CH_2 + C_2H_6 \rightarrow C_2H_5 + CH_3$	7×10^{17}
$CH_3 + C_2H_5 \rightarrow C_2H_4 + CH_4$	7×10^{16}

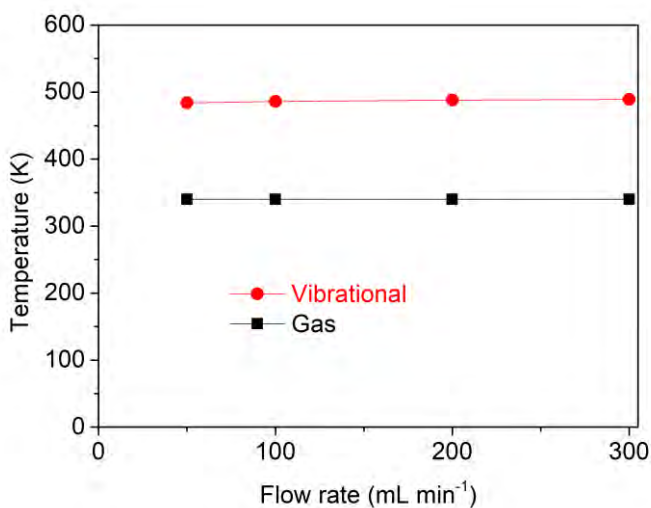


Figure A22: Calculated vibrational temperature and corresponding gas temperature as a function of flow rate, at a plasma power of 45 W in the atmospheric pressure DBD reactor of Xu and Tu ³⁴⁶.

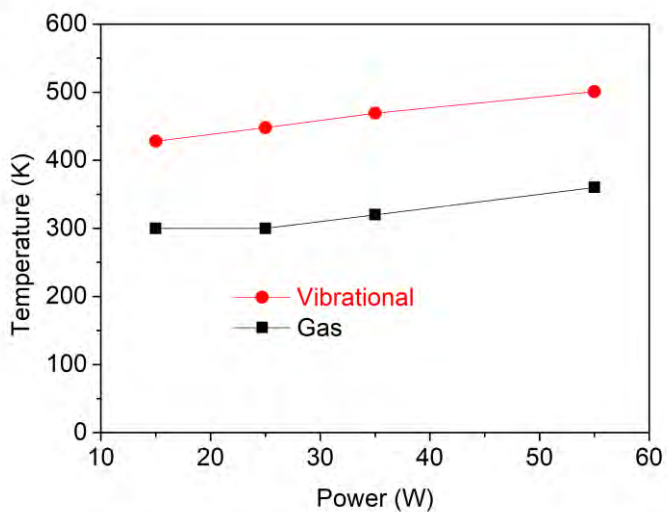


Figure A23: Calculated vibrational temperature and corresponding gas temperature as a function of power, at a flow rate of 100 mL min^{-1} in the atmospheric pressure DBD reactor of Xu and Tu ³⁴⁶.

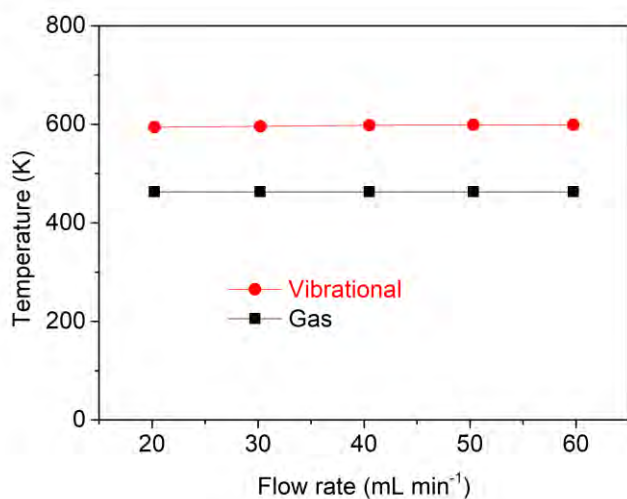


Figure A24: Calculated vibrational temperature and corresponding gas temperature as a function of flow rate, at a plasma power of 25 W in the atmospheric pressure DBD reactor of Wang et al. ³⁴⁵.

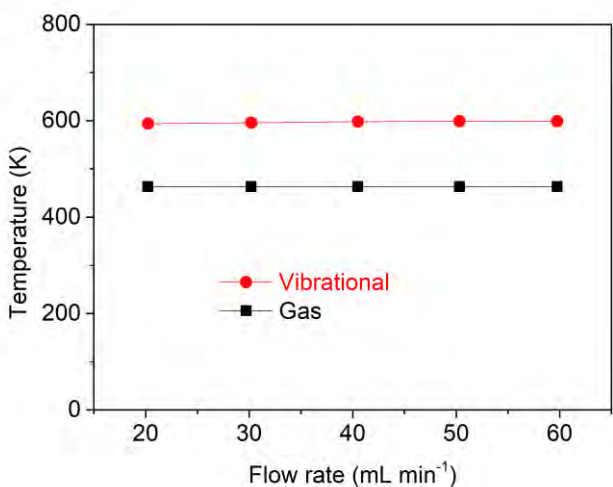


Figure A25: Calculated vibrational temperature and corresponding gas temperature as a function of power, at a flow rate of 20.24 mL min⁻¹ in the atmospheric pressure DBD reactor of Wang et al. ³⁴⁵.

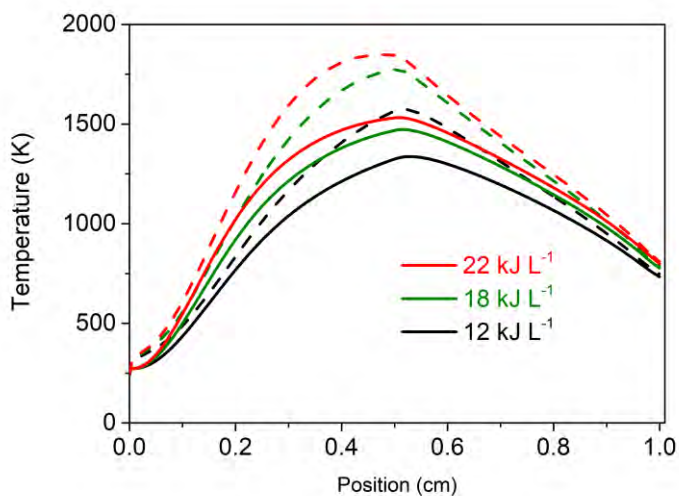


Figure A26: Calculated gas temperature (solid lines) and vibrational temperatures (dashed lines) as a function of travelled distance inside the reduced pressure MW plasma in the continuous regime for different SEI values.

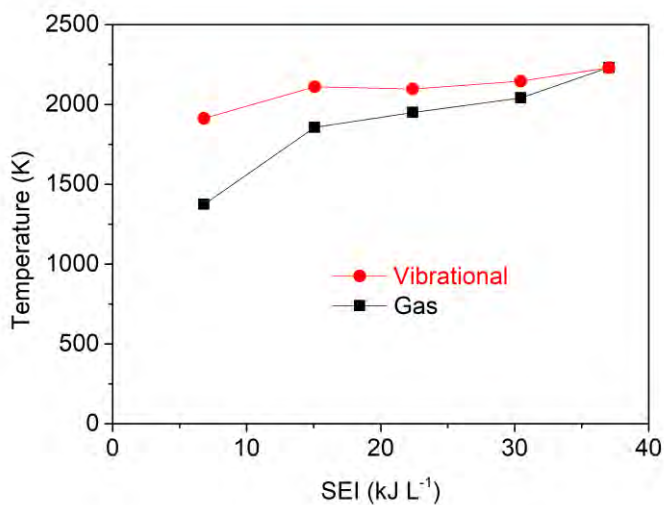


Figure A27: Calculated gas temperature and vibrational temperature as a function of SEI inside the reduced pressure MW plasma in the pulsed regime.

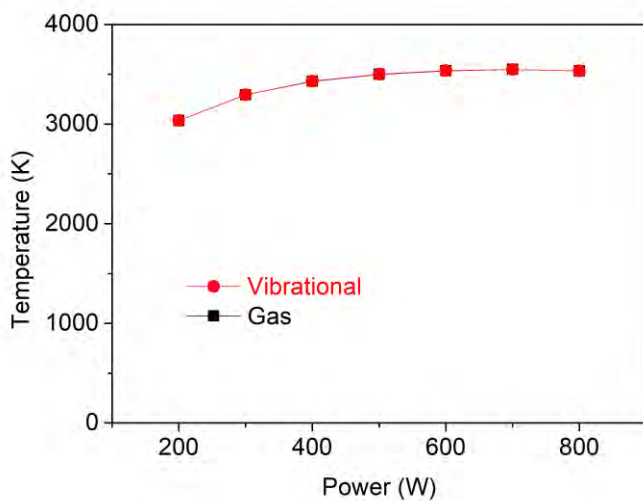


Figure A28: Calculated gas temperature and vibrational temperature as a function of microwave power, at a flow rate of 500 mL min⁻¹ in an atmospheric pressure MW plasma, for a CH₄/H₂ ratio of 1/4. The gas and vibrational temperature virtually overlap.

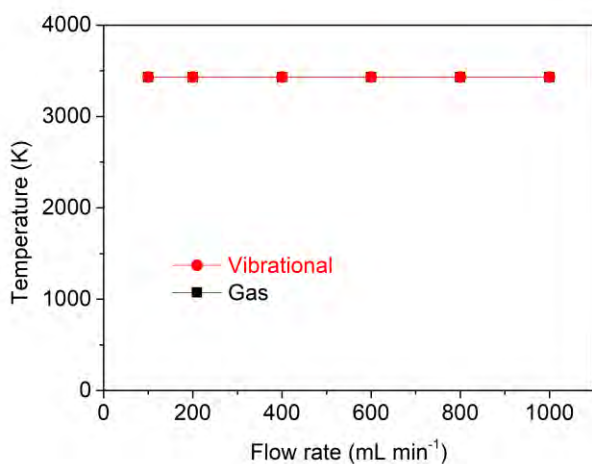


Figure A29: Calculated gas temperature and vibrational temperature as a function of flow rate, at a microwave power of 400 W in an atmospheric pressure MW plasma, for a CH_4/H_2 ratio of 1/4. The gas and vibrational temperature virtually overlap.

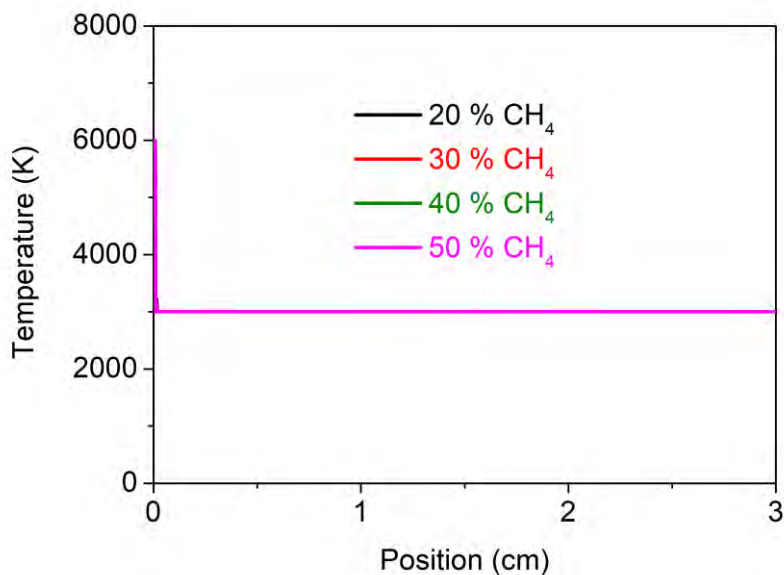


Figure A30: Calculated gas temperature (solid line) and vibrational temperature (dashed line) as a function of travelled distance inside the GAP reactor for different CH_4 fractions. The gas and vibrational temperatures virtually overlap.

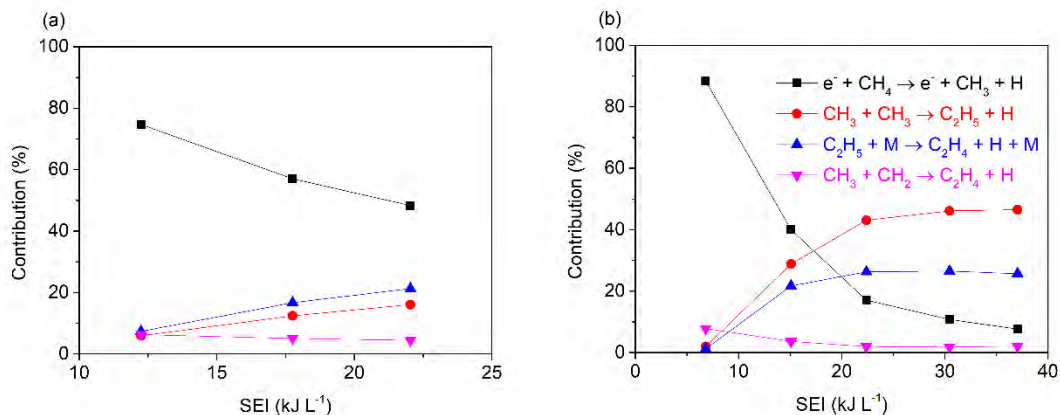


Figure A31: Net contribution of the most important formation reactions of H, as a function of SEI, in a MW plasma at a pressure of 30 mbar and flow rate of 98 sccm, operating in a continuous (a) and pulsed (b) regime.

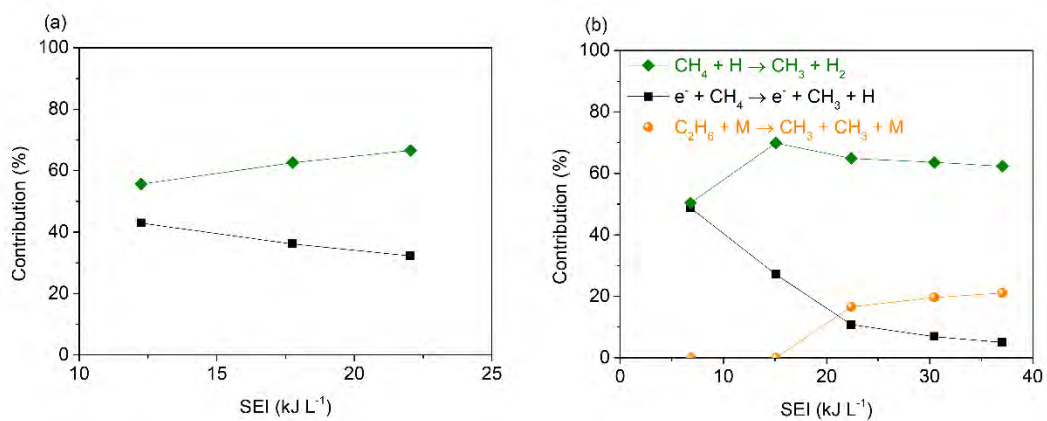


Figure A32: Net contribution of the most important formation reactions of CH₃, as a function of SEI, in a MW plasma at a pressure of 30 mbar and flow rate of 98 sccm, operating in a continuous (a) and pulsed (b) regime.

Summary and Future Outlook

The ever increasing atmospheric CO₂ concentrations, mainly caused by mankind itself, lead to accelerated global warming, which in turn will lead to a higher frequency of extreme weather, threatening our society more and more. Therefore, we should reduce our greenhouse gas emission drastically by shifting towards renewable energy and by storing this (fluctuating) energy through simultaneously converting greenhouse gases into fuels or value-added chemicals. One emerging technology for this purpose is plasma technology, which can be switched on and off rapidly, and is thus compatible with storing peak productions in green energy.

However, plasma reactors do not show yet the required performance for industrial applications, and more fundamental studies are needed to improve their performance. Chemical kinetics modelling is very suitable to gain more knowledge in the underlying plasma processes, needed for further optimization. Therefore, in this PhD thesis we focus on chemical kinetic modelling of CO₂ and CH₄ (in pure form and in a mixture), in different plasma reactors. After a short introduction about CO₂ conversion and plasma technology (Chapter 1), the principles of the chemical kinetics model are explained (Chapter 2).

In Chapter 3, we studied pure CO₂ conversion in a new type of GA plasma reactor, called gliding arc plasmatron (GAP). The GAP shows the combination of intense vibrational excitation and atmospheric pressure conditions, being beneficial for industrial implementation. However, the CO₂ dissociation mainly occurs from the lowest vibrational levels, because the VDF is more or less thermal, due to the high temperature in the arc, reaching easily 3000 K, so that VT relaxation causes the vibrational-translational non-equilibrium to be negligible.

Chapter 4 discusses the combined CO₂/CH₄ conversion (dry reforming of methane, DRM) in the GAP. Adding CH₄ enhances the CO₂ conversion, and the overall performance in terms of energy cost / energy efficiency reaches values above the required energy efficiency target, stated in literature to be competitive with classical thermal DRM. Our model reveals that, besides the conversion inside the arc plasma column, some (thermal) conversion of CO₂ and CH₄ also takes place in the area around the arc column, which is still characterized by relatively high temperature. The CO₂ conversion clearly rises upon increasing

CH₄ fraction in the mixture, and this is explained by the model due to the reaction of CO₂ (mainly in vibrationally excited levels) with H atoms, formed upon dissociation of CH₄. The main process responsible for CH₄ conversion is the reaction with OH radicals. Furthermore, reactions with other radicals, such as C₂H₃, H, O and C₃H₅, also play a non-negligible role in the CH₄ conversion

In Chapter 5, the combined CO₂/N₂ conversion was studied in the GAP. The addition of N₂ has a positive effect on the absolute CO₂ conversion up to 50 %, while at higher N₂ fractions, the effective CO₂ conversion and energy efficiency drop. The simulations reveal that the CO₂ conversion mainly proceeds through the vibrational levels, which are populated through collision with the N₂ vibrational levels. In addition, NO and NO₂ are formed in the CO₂/N₂ mixture, initiated by the reaction between N₂ vibrational levels and O atoms. However, the NO_x concentrations reached are somewhat too low for N₂ fixation.

Chapter 6 presents a chemical kinetics model for another emerging plasma reactor, i.e., a nanosecond repetitively pulsed (NRP) discharge, used for pure CO₂ splitting. The NRP discharge shows promising results by stimulating vibrational excitation. Indeed, more than 20 % of all CO₂ dissociation occurs from the highest asymmetric stretch mode levels (V16-V21), mainly by dissociation upon collision with an O atom or with another molecule M. However, in between the pulses (i.e., during the so-called afterglows), fresh gas entering the plasma, VT relaxation (depopulating the higher vibrational levels) and recombination reactions (mainly CO + O + M → CO₂ + M), limit the conversion and energy efficiency. The latter two processes also induce intense heating just after the pulses, causing self-acceleration of these limiting factors, as both VT relaxation and the recombination reactions are enhanced at higher gas temperature. To further improve the performance, we propose extra cooling in the afterglows, but these theoretical model predictions still need to be evaluated experimentally.

Finally, in Chapter 7, we studied CH₄ conversion in different plasma reactors, i.e., DBD, MW plasma and GAP. The results indicate that higher temperatures, especially in the GAP but also in atmospheric pressure MW plasmas, result in more CH₄ conversion, and in neutral dissociation and dehydrogenation processes of the hydrocarbons created, forming especially C₂H₂ and H₂, and (some) C₂H₄. Low temperature plasmas, such as DBD and reduced

pressure MW plasmas, result in more electron impact dissociation and three-body recombination processes, creating more saturated compounds, i.e., mainly C_2H_6 , but also higher hydrocarbons, such as C_3H_8 and C_4H_{10} . Unfortunately, vibrational non-equilibrium cannot be exploited in CH_4 discharges.

Due to the simple set of equations solved in a 0D model, which limits the calculation time, a large chemistry (~2000 and more chemical reactions) can be described, making this modeling approach very suitable for studying CO_2 and CH_4 conversion. However, several assumptions need to be made in 0D modeling, as described in this thesis. For future work, more 2D-3D modeling is needed to validate the physical characteristics, such as residence time, electron density, electron temperature, etc. In addition, 2D-3D modeling is needed to describe specific plasma reactor configurations and for predicting improved reactor design.

Furthermore, for moderate pressure plasmas, more research should be done in calculating rate coefficients for VV and VT transfer in molecular plasmas, especially for middle and highly vibrationally excited species, using pure quantum or semi-classical methods, in which several degrees of freedom are treated classically and the others using quantum mechanics.

In terms of plasma configurations studied, pulsed discharges show interesting opportunities for CO_2 conversion. We believe that the pulses must be long enough (~20-60 μs) to get significant vibrational pumping, but not too long before VT relaxation becomes predominant (~ms). On the other hand, the GAP is also very promising for CO_2 and CH_4 conversion, although the conversion is mainly thermal. The focus should be on smart reactor design improvements, to optimize the fraction of gas passing through the plasma, and thus to enhance the conversion. Furthermore, efforts are needed to quench the gas after the plasma reactor, to avoid recombination reactions and to make profit of the reaction between CO_2 and O atoms, for further conversion (super-ideal quenching). In the case of CH_4 conversion, our modeling reveals that vibrational non-equilibrium is negligible, so plasma-based CH_4 conversion is most efficient in plasma reactors in which there is sufficient gas heating to get significant conversion, like in the GAP. In addition, we believe that NRP discharges, in which gas heating is short after a pulse but long enough to get significant conversion, would also be of interest for plasma-based “petrochemistry”.

Samenvatting en Toekomstperspectief

De steeds toenemende CO₂ concentratie, uitgestoten door de mensheid zelf, leidt tot een versnelde klimaatsopwarming, wat op zijn beurt zorgt voor een hogere frequentie aan extreme weerfenomenen. Daarom is het noodzakelijk onze emissies drastisch te verlagen, door over te gaan naar hernieuwbare bronnen en deze energie op te slaan in brandstoffen die gemaakt worden met broeikasgassen als grondstof. Een methode die hiervoor ontwikkeld wordt, is plasmatechnologie. Plasma's kunnen gemakkelijk opgewekt worden, waardoor ze piekproductiemomenten van groene stroom kunnen opvangen.

Niettemin, de bestaande plasmareactoren geven nog niet de gewenste prestaties voor opschaling naar industriële toepassingen. Daarom is het nodig om de plasmachemie kinetisch te modelleren, om de gewenste kennis te verkrijgen van de belangrijkste chemische processen in het plasma voor verdere optimalisatie. Deze doctoraatsthesis focust op het modelleren van de chemische kinetiek in CO₂ en CH₄, hetzij in zuivere vorm of in een mengsel, in verschillende soorten plasmareactoren. Na een korte inleiding over CO₂ conversie en plasmatechnologie (Hoofdstuk 1) worden de belangrijkste principes van het modelleren van de chemische kinetiek uitgelegd (Hoofdstuk 2).

In Hoofdstuk 3 werd de conversie van zuiver CO₂ in een nieuw type *gliding arc* (GA) reactor, genaamd een *gliding arc plasmatron* (GAP), bestudeerd. De GAP zorgt voor intense vibrationele excitatie bij atmosferedruk, wat voordelig is voor industriële toepassingen. CO₂ dissocieert echter voornamelijk vanuit de lager vibrationeel geëxciteerde niveaus door de hoge temperatuur van 3000 K in de ontlading, waardoor VT relaxatie het vibrationele niet-evenwicht verwaarloosbaar maakt.

In Hoofdstuk 4 werd de gecombineerde conversie van CO₂ en CH₄ in CO₂/CH₄ mengsels, het zogenaamde *dry reforming*, in de GAP bestudeerd. Het toevoegen van CH₄ verhoogt de CO₂ conversie en de energiekost/efficiëntie is zelfs beter dan de vereiste waarden om competitief te zijn met het klassieke proces. Het model toont aan dat een deel van de conversie plaatsvindt net naast de boogontlading, waar thermische conversie van CO₂ en CH₄ nog steeds mogelijk is door de aanzienlijke temperatuur. De CO₂ conversie stijgt bij toenemende CH₄ concentratie, wat volgens het model verklaard kan worden door

de vorming van H atomen door CH₄ dissociatie, die reageren met vibrationeel geëxciteerd CO₂. Het belangrijkste proces voor CH₄ conversie zijn de reacties met OH radicalen. Verder zijn reacties met C₂H₃, H, O en C₃H₆ ook belangrijk, doch minder, voor CH₄ conversie.

In Hoofdstuk 5 werd de gecombineerde conversie van CO₂ en N₂ in CO₂/N₂ mengsels in de GAP bestudeerd. Het toevoegen van N₂ heeft een positief effect op de absolute conversie tot een concentratie van 50 % N₂ waarna de effectieve conversie en de energie-efficiëntie dalen. De simulaties tonen aan dat vibrationeel geëxciteerd CO₂ belangrijk is voor de conversie waarbij N₂ helpt bij deze excitatie. Ook worden er NO en NO₂ gevormd door reactie tussen vibrationeel geëxciteerd N₂ en O radicalen. Niettemin worden er niet genoeg NO_x verbindingen gevormd voor aanzienlijke N₂ fixatie.

In Hoofdstuk 6 werd een kinetisch model opgesteld voor een nieuw opkomende plasmareactor, de *nanosecond repetitively pulsed* (NRP) ontlading, voor zuiver CO₂. De NRP ontlading toont veelbelovende resultaten door stimulatie van vibrationele excitatie. In de NRP ontlading is vibrationele excitatie zeer belangrijk doordat meer dan 20 % van alle CO₂ dissociatie via de meest geëxciteerde niveaus van de asymmetrische rekmode van CO₂ plaatsvindt (V16-V21). De dissociatie wordt geïnitieerd door reacties met O radicalen of door neutrale dissociatie met een willekeurige molecule M. Tussen de pulsen door (de zogenaamde *afterglows*) verminderen gasverdunding, VT relaxatie (die zorgen voor verlies van de hogere niveaus) en recombinatie reacties (vooral CO + O + M → CO₂ + M) de conversie en energie-efficiëntie. De laatste twee processen creëren ook warmte die de processen in kwestie nog versnellen. Daarom wordt koeling tussen de pulsen voorgesteld om een betere prestatie te verkrijgen, alhoewel dit nog experimenteel bevestigd moet worden.

Tenslotte werd in Hoofdstuk 7 de CH₄ conversie bestudeerd in verschillende plasmareactoren, nl. de DBD, MW plasma en de GAP. We kunnen concluderen dat hogere temperaturen, zoals in de GAP en MW ontlading bij atmosferedruk, resulteren in een hogere CH₄ conversie, meer neutrale dissociatie en dehydrogenatie processen, waardoor vooral C₂H₂, H₂ en een beetje C₂H₄ worden gevormd. Lage temperatuur plasma's, zoals DBD ontladingen en MW ontladingen bij verminderde druk, stimuleren eerder elektron impact dissociatie en recombinatieprocessen, waardoor meer verzadigde verbindingen zoals C₂H₆,

maar ook C_3H_8 en C_4H_{10} gevormd worden. In CH_4 werd ook vastgesteld dat er geen vibrationeel niet-evenwicht optreedt.

Door de beperkte rekentijd van een 0D model, kan een grote chemieset (bv. 2000 reacties en meer) geïmplementeerd worden, en dit maakt 0D modelleren geschikt voor het bestuderen van CO_2 en CH_4 conversie in plasmareactoren. Niettemin moeten noodzakelijke benaderingen gemaakt worden, zoals vermeld in de thesis. In de toekomst is meer 2D-3D modelleerwerk nodig om de verschillende fysische eigenschappen van het plasma en de gasstroming, zoals residentietijd, elektronendichtheid, elektrontemperatuur, enz. beter te valideren. Ook zijn deze complexere modellen nodig om specifieke reactorconfiguraties te beschrijven en om betere configuraties voor te stellen.

Daarbovenop moet er meer onderzoek gedaan worden naar de berekening van reactiesnelheidsconstanten voor VV en VT relaxatie in moleculaire plasma's, vooral voor middelhoog en hooggeëxciteerde vibrationale niveaus. Deze niveaus worden immers belangrijk bij plasma's bij lage druk. Zulke snelheidsconstanten kunnen bepaald worden door kwantumberekeningen of semi-kwantumberekeningen, waarbij in het laatste geval een aantal interne vrijheidsgraden klassiek mechanisch worden behandeld.

In termen van plasmaconfiguratie, lijken gepulste ontladingen veelbelovend voor CO_2 conversie, zeker als de pulsen lang genoeg zijn ($\sim 20\text{-}60\mu\text{s}$) voor intense vibrationele excitatie, maar niet te lang, voordat VT relaxatie optreedt ($\sim\text{ms}$). Anderzijds is ook de GAP veelbelovend voor CO_2 en CH_4 conversie, ondanks het feit dat de conversie vooral thermisch is. Er moet in de toekomst aandacht besteed worden aan verbeteren van het reactordesign, om de fractie gas die door het plasma passeert te verhogen, en dus ook de conversie. Bovendien zijn inspanningen nodig om het gas te quenchen na de plasmareactor, om recombinatiereacties te vermijden, en om de reactie tussen CO_2 en O atomen te bevorderen, voor verdere conversie (super-ideale quenching). In het geval van CH_4 conversie toont onze modellering aan dat vibrationeel niet-evenwicht verwaarloosbaar is, en daarom is plasma-gebaseerde CH_4 conversie het meest efficiënt in plasmareactoren met voldoende gasverhitting om voldoende thermische dissociatie te realiseren, zoals in de GAP.. Daarenboven lijken NRP ontladingen, waarin verhitting na de puls kort is, maar lang genoeg voor voldoende thermische conversie, ook interessant voor plasma "petrochemie".

List of Articles published

- Heijkers, S.; Snoeckx, R.; Kozak, T.; Silva, T.; Godfroid, T.; Britun, N.; Snyders, R.; Bogaerts, A. CO₂ Conversion in a Microwave Plasma Reactor in the Presence of N₂ : Elucidating the Role of Vibrational Levels. *J. Phys. Chem. C* **2015**, *119*, 12815–12828.
- Snoeckx, R.; Heijkers, S.; Van Wesenbeeck, K.; Lenaerts, S.; Bogaerts, A. CO₂ Conversion in a Dielectric Barrier Discharge Plasma: N₂ in the Mix as a Helping Hand or Problematic Impurity? *Energy Environ. Sci.* **2016**, *9*, 30–39
- Koelman, P.; Heijkers, S.; Tadayon Mousavi, S.; Graef, W.; Mihailova, D.; Kozak, T.; Bogaerts, A.; van Dijk, J. A Comprehensive Chemical Model for the Splitting of CO₂ in Non-Equilibrium Plasmas. *Plasma Process. Polym.* **2016**, *14*, 1600185
- Bogaerts, A.; Berthelot, A.; Heijkers, S.; Kolev, S.; Snoeckx, R.; Sun, S.; Trenchev, G.; Van Laer, K.; Wang, W. CO₂ Conversion by Plasma Technology: Insights from Modeling the Plasma Chemistry and Plasma Reactor Design. *Plasma Sources Sci. Technol.* **2017**, *26* (6).
- Ramakers, M.; Trenchev, G.; Heijkers, S.; Wang, W.; Bogaerts, A. Gliding Arc Plasmatron: Providing a Novel Method for Carbon Dioxide Conversion. *ChemSusChem.* **2017**, *10*, 2642–2652
- Heijkers, S.; Bogaerts, A. CO₂ Conversion in a Gliding Arc Plasmatron: Elucidating the Chemistry through Kinetic Modeling. *J. Phys. Chem. C* **2017**, *121*, 22644–22655
- Cleiren, E.; Heijkers, S.; Ramakers, M.; Bogaerts, A. Dry Reforming of Methane in a Gliding Arc Plasmatron: Towards a Better Understanding of the Plasma Chemistry. *ChemSusChem* **2017**, *10*, 4025–4036

- Wang, W.; Patil, B.; Heijkers, S.; Hessel, V.; Bogaerts, A. Nitrogen Fixation by Gliding Arc Plasma: Better Insight by Chemical Kinetics Modelling. *ChemSusChem* **2017**, *10*, 2145–2157
- Ramakers, M.; Heijkers, S.; Tytgat, T.; Lenaerts, S.; Bogaerts, A. Combining CO₂ Conversion and N₂ Fixation in a Gliding Arc Plasmatron. *J. CO₂ Util.* **2019**, *33*, 121–130
- Heijkers, S.; Martini, L. M.; Dilecce, G.; Tosi, P.; Bogaerts, A. Nanosecond Pulsed Discharge for CO₂ Conversion: Kinetic Modeling To Elucidate the Chemistry and Improve the Performance. *J. Phys. Chem. C* **2019**, *123*, 12104–12116.
- Heijkers, S.; Aghaei, M.; Bogaerts, A. Plasma-Based CH₄ Conversion into Higher Hydrocarbons and H₂: Modeling to Reveal the Reaction Mechanisms of Different Plasma Sources. *J. Phys. Chem. C* **2020**, *124*, 7016-7030, Featured in ACS Editors’ Choice, and given open access “due to its potential for broad public interest”.

List of conference contributions

- Oral presentation “CO₂ conversion in a microwave plasma reactor in the presence of N₂” ISPC 2015, Antwerp, Belgium
- Poster presentation “Gliding arc plasmatron (GAP) for CO₂ splitting: A chemical kinetics modelling perspective”, ICPIG 2017, Estoril, Portugal

Bibliography

- (1) Field, C. B.; Barros, V. R.; Dokken, D. J.; Mach, K. J.; Mastrandea, M. D.; Bilir, T. E.; Chatterjee, M.; Ebi, K. L.; Estrada, Y. O.; Genova, R. C.; et al. *IPCC, 2014: Climate Change 2014 Impacts, Adaptation, and Vulnerability. Part A: Global and Sectoral Aspects. Contribution of Working Group II to the Fifth Assessment Report of the Intergovernmental Panel on Climate Change*; Cambridge University Press, 2014.
- (2) Pachauri, R. K.; Meyer, L.; Allen, M. R.; Barros, V. R.; Broome, J.; Cramer, W.; Christ, R.; Church, J. A.; Clarke, L.; Dahe, Q.; et al. *IPCC, 2014: Climate Change 2014: Synthesis Report. Contribution of Working Groups I, II and III to the Fifth Assessment Report of the Intergovernmental Panel on Climate Change*; Geneva, Switzerland, 2014.
- (3) Snoeckx, R.; Bogaerts, A. Plasma Technology—a Novel Solution for CO₂ Conversion? *Chem. Soc. Rev.* **2017**, *46*, 5805–5863.
- (4) Cook, J.; Oreskes, N.; Doran, P. T.; Anderegg, W. R. L.; Verheggen, B.; Maibach, E. W.; Carlton, J. S.; Lewandowsky, S.; Skuce, A. G.; Green, S. A.; et al. Consensus on Consensus: A Synthesis of Consensus Estimates on Human-Caused Global Warming. *Environ. Res. Lett.* **2016**, *11*, 048002.
- (5) NASA Global Climate Change: Vital Signs of the Planet, <http://climate.nasa.gov>, Data retrieved: 17/09/2019 <https://climate.nasa.gov/>.
- (6) Hansen, J. P.; Narbel, P. A.; Aksnes, D. L. Limits to Growth in the Renewable Energy Sector. *Renew. Sustain. Energy Rev.* **2017**, *70*, 769–774.
- (7) Jiang, Z.; Xiao, T.; Kuznetsov, V. L.; Edwards, P. P. Turning Carbon Dioxide into Fuel. *Philos. Trans. R. Soc. A Math. Phys. Eng. Sci.* **2010**, *368*, 3343–3364.
- (8) Mikkelsen, M.; Jørgensen, M.; Krebs, F. C. The Teraton Challenge. A Review of Fixation and Transformation of Carbon Dioxide. *Energy Environ. Sci.* **2010**, *3*, 43–81.
- (9) Grant, J.; Johnson, L. Two Degrees of Separation: Ambition and Reality. *Low Carbon Econ. Index 2014* **2014**, No. September, 20.
- (10) Goepfert, A.; Czaun, M.; Jones, J.; Prakash, G. K. S.; Olah, G. A. Recycling of Carbon Dioxide to Methanol and Derived Products – Closing the Loop. *Chem. Soc. Rev.* **2014**, *43*, 7995–8048.
- (11) Albo, J.; Alvarez-Guerra, M.; Castaño, P.; Irabien, A. Towards the Electrochemical Conversion of Carbon Dioxide into Methanol. *Green Chem.* **2015**, *17*, 2304–2324.
- (12) Fiorani, G.; Guo, W.; Kleij, A. W. Sustainable Conversion of Carbon Dioxide: The Advent of Organocatalysis. *Green Chem.* **2015**, *17* (3),

- 1375–1389.
- (13) McDonough, W.; Braungart, M.; Anastas, P. T.; Zimmerman, J. B. Peer Reviewed: Applying the Principles of Green Engineering to Cradle-to-Cradle Design. *Environ. Sci. Technol.* **2003**, *37*, 434A-441A.
 - (14) Fridman, A. *Plasma Chemistry*; Cambridge University Press: New York, U.S.A., 2008.
 - (15) *NIST Chemistry WebBook, NIST Standard Reference Database Number 69* <https://webbook.nist.gov/>.
 - (16) Centi, G.; Perathoner, S. Opportunities and Prospects in the Chemical Recycling of Carbon Dioxide to Fuels. *Catal. Today* **2009**, *148* (3–4), 191–205.
 - (17) Rusanov, V. D.; Fridman, a. a.; Sholin, G. V. The Physics of a Chemically Active Plasma with Nonequilibrium Vibrational Excitation of Molecules. *Uspekhi Fiz. Nauk* **1981**, *134*, 185.
 - (18) Asisov, R. I.; Fridman, A. A.; Givotov, V. K.; Krasheninnikov, E. G.; Petrushev, B. I.; Potapkin, B. V.; Rusanov, V. D.; Krotov, M. F.; Kurchatov, I. V. *5th Int. Symp. on Plasma Chemistry*; 1983; Vol. 1.
 - (19) Bogaerts, A.; Neyts, E.; Gijbels, R.; Van der Mullen, J. Gas Discharge Plasmas and Their Applications. *Spectrochim. Acta - Part B At. Spectrosc.* **2002**, *57* (4), 609–658.
 - (20) Lieberman, M. A.; Lichtenberg, A. J. *Principles of Plasma Discharges and Materials Processing: Second Edition*, 2nd Editio.; Wiley-Interscience, 2005.
 - (21) Gomez, E.; Rani, D. A.; Cheeseman, C. R.; Deegan, D.; Wise, M.; Boccaccini, A. R. Thermal Plasma Technology for the Treatment of Wastes : A Critical Review. *J. Hazard. Mater.* **2009**, *161*, 614–626.
 - (22) Asisov, R. I.; Givotov, V. K.; Krasheninnikov, E. G.; Potapkin, B. V.; Rusanov, V. D.; Fridman, A. Carbon Dioxide Dissociation in Non-Equilibrium Plasma. *Sov. Phys. Dokl.* **1983**, *271*, 94.
 - (23) Vermeiren, V.; Bogaerts, A. Improving the Energy Efficiency of CO₂ Conversion in Nonequilibrium Plasmas through Pulsing. *J. Phys. Chem. C* **2019**, *123*, 17650–17665.
 - (24) Kogelschatz, U.; Eliasson, B.; Egli, W. From Ozone Generators to Flat Television Screens: History and Future Potential of Dielectric-Barrier Discharges. *Pure Appl. Chem.* **1999**, *71*, 1819–1828.
 - (25) Berthelot, A.; Bogaerts, A. Modeling of CO₂ Splitting in a Microwave Plasma: How to Improve the Conversion and Energy Efficiency. *J. Phys. Chem. C* **2017**, *121* (15), 8236–8251.
 - (26) Fridman, A.; Chirokov, A.; Gutsol, A. Non-Thermal Atmospheric Pressure Plasma. *J. Phys. D Appl. Phys.* **2005**, *38*, R1–R24.
 - (27) Czernichowski, a. Gliding Arc: Applications to Engineering and

- Environment Control. *Pure Appl. Chem.* **1994**, *66* (6), 1301–1310.
- (28) Indarto, A.; Choi, J.; Lee, H.; Song, H. K. Conversion of CO₂ by Gliding Arc Plasma. *Environ. Eng. Sci.* **2012**, *23* (6), 1033–1043.
- (29) Sun, S. R.; Wang, H. X.; Mei, D. H.; Tu, X.; Bogaerts, A. CO₂ Conversion in a Gliding Arc Plasma: Performance Improvement Based on Chemical Reaction Modeling. *J. CO₂ Util.* **2016**, *17*, 220–234.
- (30) Kalra, C. S.; Cho, Y. I.; Gutsol, A.; Fridman, A.; Rufael, T. S. Gliding Arc in Tornado Using a Reverse Vortex Flow. *Rev. Sci. Instrum.* **2005**, *76* (2), 025110.
- (31) Nunnally, T.; Gutsol, K.; Rabinovich, A.; Fridman, A.; Gutsol, A.; Kemoun, A. Dissociation of CO₂ in a Low Current Gliding Arc Plasmatron. *J. Phys. D. Appl. Phys.* **2011**, *44*, 274009.
- (32) Trenchev, G.; Kolev, S.; Bogaerts, A. A 3D Model of a Reverse Vortex Flow Gliding Arc Reactor. *Plasma Sources Sci. Technol.* **2016**, *25*, 035014.
- (33) Trenchev, G.; Kolev, S.; Wang, W.; Ramakers, M.; Bogaerts, A. CO₂ Conversion in a Gliding Arc Plasmatron: Multidimensional Modeling for Improved Efficiency. *J. Phys. Chem. C* **2017**, *121*, 24470–24479.
- (34) Scapinello, M.; Martini, L. M.; Dilecce, G.; Tosi, P. Conversion of CH₄/CO₂ by a Nanosecond Repetitively Pulsed Discharge. *J. Phys. D. Appl. Phys.* **2016**, *49*, 075602–075609.
- (35) Martini, L. M.; Lovascio, S.; Dilecce, G.; Tosi, P. Time-Resolved CO₂ Dissociation in a Nanosecond Pulsed Discharge. *Plasma Chem. Plasma Process.* **2018**, *38*, 707–718.
- (36) Castela, M.; Stepanyan, S.; Fiorina, B.; Coussement, A.; Gicquel, O.; Darabiha, N.; Laux, C. O. A 3-D DNS and Experimental Study of the Effect of the Recirculating Flow Pattern inside a Reactive Kernel Produced by Nanosecond Plasma Discharges in a Methane-Air Mixture. *Proc. Combust. Inst.* **2017**, *36* (3), 4095–4103.
- (37) Martini, L. M.; Gatti, N.; Dilecce, G.; Scotoni, M.; Tosi, P. Laser Induced Fluorescence in Nanosecond Repetitively Pulsed Discharges for CO₂ Conversion. *Plasma Phys. Control. Fusion* **2018**, *60*, 014016.
- (38) Delikonstantis, E.; Scapinello, M.; Van Geenhoven, O.; Stefanidis, G. D. Nanosecond Pulsed Discharge-Driven Non-Oxidative Methane Coupling in a Plate-to-Plate Electrode Configuration Plasma Reactor. *Chem. Eng. J.* **2020**, *380*, 122477.
- (39) Hurlbatt, A.; Gibson, A. R.; Schröter, S.; Bredin, J.; Foote, A. P. S.; Grondein, P.; O’Connell, D.; Gans, T. Concepts, Capabilities, and Limitations of Global Models: A Review. *Plasma Process. Polym.* **2016**, 1–21.
- (40) Bittencourt, J. A. *Fundamentals of Plasma Physics*, Third Edit.; Springer:

New York, U.S.A., 2004; Vol. 9780521821.

- (41) Hagelaar, G. J. M.; Pitchford, L. C. Solving the Boltzmann Equation to Obtain Electron Transport Coefficients and Rate Coefficients for Fluid Models. *Plasma Sources Sci. Technol.* **2005**, *14*, 722–733.
- (42) Holstein, T. Energy Distribution of Electrons in High Frequency Gas Discharges. *Phys. Rev.* **1946**, *70*, 367–384.
- (43) Pancheshnyi, S.; Eismann, B.; Hagelaar, G. J. M.; Pitchford, L. C. ZDPlasKin: A New Tool for Plasmachemical Simulations. University of Toulouse, LAPLACE, CNRS-UPS-INP, Toulouse, France, 2008, p University of Toulouse, LAPLACE, CNRS-UPS-INP.
- (44) Pinhão, N. R.; Moura, A.; Branco, J. B.; Neves, J. Influence of Gas Expansion on Process Parameters in Non-Thermal Plasma Plug-Flow Reactors: A Study Applied to Dry Reforming of Methane. *Int. J. Hydrogen Energy* **2016**, *41*, 9245–9255.
- (45) Kozak, T.; Bogaerts, A. Evaluation of the Energy Efficiency of CO₂ Conversion in Microwave Discharges Using a Reaction Kinetics Model. *Plasma Sources Sci. Technol.* **2015**, *24*, 015024.
- (46) Mitchner, M.; Kruger, C. H. *Partially Ionized Gases*; Wiley series in plasma physics, Wiley, 1973.
- (47) Wang, W.; Berthelot, A.; Kolev, S.; Tu, X.; Bogaerts, A. CO₂ Conversion in a Gliding Arc Plasma: 1D Cylindrical Discharge Model. *Plasma Sources Sci. Technol.* **2016**, *25* (6), 065012.
- (48) Chase, M. NIST-JANAF Thermochemical Tables, 4th Edition. *Journal of Physical and Chemical Reference Data, Monograph 9*. 1998, p 1952.
- (49) Engineering ToolBox: Specific Heat and Individual Gas Constant of Gases, 2003, https://www.engineeringtoolbox.com/specific-heat-capacity-gases-d_159.html.
- (50) Indarto, A.; Yang, D. R.; Choi, J. W.; Lee, H.; Song, H. K. Gliding Arc Plasma Processing of CO₂ Conversion. *J. Hazard. Mater.* **2007**, *146*, 309–315.
- (51) Nunnally, T. P. Application of Low Current Gliding Arc Plasma Discharges for Hydrogen Sulfide Decomposition and Carbon Dioxide Emission Reduction, PhD Dissertation, Drexel University, PhD Thesis, Drexel University, 2011.
- (52) Ramakers, M.; Trenchev, G.; Heijkers, S.; Wang, W.; Bogaerts, A. Gliding Arc Plasmatron: Providing a Novel Method for Carbon Dioxide Conversion. *ChemSusChem.* **2017**, *10*, 2642–2652.
- (53) Liu, J. L.; Park, H. W.; Chung, W. J.; Park, D. W. High-Efficient Conversion of CO₂ in AC-Pulsed Tornado Gliding Arc Plasma. *Plasma Chem. Plasma Process.* **2016**, *36* (2), 437–449.
- (54) Trenchev, G.; Kolev, S.; Wang, W.; Ramakers, M.; Bogaerts, A. CO₂

- Conversion in a Gliding Arc Plasmatron : Multi- Dimensional Modelling for Improved Efficiency. *J.CO2 Util.* submitted.
- (55) Aerts, R.; Martens, T.; Bogaerts, A. Influence of Vibrational States on CO₂ Splitting by Dielectric Barrier Discharges. *J. Phys. Chem. C* **2012**, *116*, 23257–23273.
- (56) Aerts, R.; Somers, W.; Bogaerts, A. Carbon Dioxide Splitting in a Dielectric Barrier Discharge Plasma: A Combined Experimental and Computational Study. *ChemSusChem* **2015**, *8* (4), 702–716.
- (57) Kozák, T.; Bogaerts, A. Splitting of CO₂ by Vibrational Excitation in Non-Equilibrium Plasmas: A Reaction Kinetics Model. *Plasma Sources Sci. Technol.* **2014**, *23*, 045004.
- (58) Koelman, P.; Heijkers, S.; Tadayon Mousavi, S.; Graef, W.; Mihailova, D.; Kozak, T.; Bogaerts, A.; van Dijk, J. A Comprehensive Chemical Model for the Splitting of CO₂ in Non-Equilibrium Plasmas. *Plasma Process. Polym.* **2016**, *14*, 1600185.
- (59) Phelps, A. V. Phelps Database www.lxcat.net.
- (60) Lowke, J. J.; Phelps, A. V.; Irwin, B. W. Predicted Electron Transport Coefficients and Operating Characteristics of CO₂/N₂/He Laser Mixtures. *J. Appl. Phys.* **1973**, *44* (10), 4664–4671.
- (61) Hake, R. D.; Phelps, A. V. Momentum-Transfer and Inelastic-Collision Cross Sections for Electrons in O₂, CO, and CO₂. *Phys. Rev.* **1967**, *158* (1), 70–84.
- (62) Grofulovic, M.; Alves, L. L.; Guerra, V. Electron-Neutral Scattering Cross Sections for CO₂ a Complete and Consistent Set and an Assessment of Dissociation. *J. Phys. D Appl. Phys.* **2016**, *49*, 395207.
- (63) Bogaerts, A.; Wang, W.; Berthelot, A.; Guerra, V. Modeling Plasma-Based CO₂ Conversion : Crucial Role of the Dissociation Cross Section. *Plasma Sources Sci. Technol.* **2016**, *25*, 055016.
- (64) Pietanza, L. D.; Colonna, G.; D’Ammando, G.; Laricchiuta, A.; Capitelli, M. Vibrational Excitation and Dissociation Mechanisms of CO₂ under Non-Equilibrium Discharge and Post-Discharge Conditions. *Plasma Sources Sci. Technol.* **2015**, *24* (4), 042002.
- (65) Pietanza, L. D.; Colonna, G.; D’Ammando, G.; Laricchiuta, A.; Capitelli, M. Electron Energy Distribution Functions and Fractional Power Transfer in “Cold” and Excited CO₂ Discharge and Post Discharge Conditions. *Phys. Plasmas* **2016**, *23* (1), 013515.
- (66) Pietanza, L. D.; Colonna, G.; D’Ammando, G.; Laricchiuta, A.; Capitelli, M. Non Equilibrium Vibrational Assisted Dissociation and Ionization Mechanisms in Cold CO₂ Plasmas. *Chem. Phys.* **2016**, *468*, 44–52.
- (67) Ramakers, M.; Medrano, J. A.; Trenchev, G.; Gallucci, F.; Bogaerts, A. Revealing the Arc Dynamics in a Gliding Arc Plasmatron: A Better Insight

- to Improve CO₂ Conversion. *Plasma Sources Sci. Technol.* **2017**, *26*, 125002.
- (68) Menter, F. R.; Kuntz, M.; Langtry, R. Ten Years of Industrial Experience with the SST Turbulence Model. *Turbul. Heat Mass Transf.* **2003**, *4*, 625–632.
- (69) Vesovic, V.; Wakeham, W. A.; Olchoway, G. A.; Sengers, J. V.; Watson, J. T. R.; Millat, J. The Transport Properties of Carbon Dioxide. *J. Phys. Chem. Ref. Data* **1990**, *19*, 763–808.
- (70) Czernichowski, A.; Fridman, A. A.; Simek, M.; Musiol, K.; Pawelec, E.; Dittrichova, L. Spectral and Electrical Diagnostics of Gliding Arc. *Acta Phys. Pol. A* **1996**, *89* (5), 595–603.
- (71) Goede, A. P. H.; Bongers, W. a; Graswinckel, M. G.; Sanden, R. M. C. . Van De; Martina, L.; Jochen, K.; Schulz, A.; Mathias, W. Production of Solar Fuels by CO₂ Plasmolysis. *3rd Eur. Energy Conf. Budapest* **2014**, *79*, 01005.
- (72) Bongers, W.; Bouwmeester, H.; Wolf, B.; Peeters, F.; Welzel, S.; van den Bekerom, D.; den Harder, N.; Goede, A.; Graswinckel, M.; Groen, P. W.; et al. Plasma-Driven Dissociation of CO₂ for Fuel Synthesis. *Plasma Process. Polym.* **2017**, *14*, e1600126.
- (73) Spencer, L. F.; Gallimore, A. D. Efficiency of CO₂ Dissociation in a Radio-Frequency Discharge. *Plasma Chem. Plasma Process.* **2011**, *31* (1), 79–89.
- (74) Ozkan, A.; Dufour, T.; Silva, T.; Britun, N.; Snyders, R.; Reniers, F.; Bogaerts, A. DBD in Burst Mode : Solution for More Efficient CO₂ Conversion ? *Plasma Sources Sci. Technol.* **2016**, *25*, 055005.
- (75) Heijkers, S.; Snoeckx, R.; Kozak, T.; Silva, T.; Godfroid, T.; Britun, N.; Snyders, R.; Bogaerts, A. CO₂ Conversion in a Microwave Plasma Reactor in the Presence of N₂ : Elucidating the Role of Vibrational Levels. *J. Phys. Chem. C* **2015**, *119*, 12815–12828.
- (76) Chernets, I.; Nirenberg, G.; Fridman, A.; Rabinovich, A. Development of High-Power Plasma Reformer and Power Supply for Large Scale Applications. *Proc. 20th Int. Symp. Plasma Chem. Philadelphia, Pennsylvania* **2011**.
- (77) Givotov, V. K.; Fridman, A. A.; Krotov, M. F.; Krashennnikov, E. G.; Patrushev, B. I.; Rusanov, V. D.; Sholin, G. V. Plasmochemical Methods of Hydrogen Production. *Int. J. Hydrog. Energy* **1981**, *6* (5), 441–449.
- (78) Aerts, R.; Snoeckx, R.; Bogaerts, A. In-Situ Chemical Trapping of Oxygen in the Splitting of Carbon Dioxide by Plasma. *Plasma Process. Polym.* **2014**, 985–992.
- (79) Oren, L.; Taylor, R. J. Trapping and Removal of Oxygen in Tokamaks. *Nucl. Fusion* **1977**, *17*, 1143–1151.

- (80) Liu, P.; Liu, X.; Shen, J.; Yin, Y.; Yang, T.; Huang, Q.; Auerbach, D.; Kleiyn, A. W. CO₂ Conversion by Thermal Plasma with Carbon as Reducing Agent: High CO Yield and Energy Efficiency. *Plasma Sci. Technol.* **2019**, *21*, 012001.
- (81) Trenchev, G.; Nikiforov, A.; Wang, W.; Kolev, S.; Bogaerts, A. Atmospheric Pressure Glow Discharge for CO₂ Conversion: Model-Based Exploration of the Optimum Reactor Configuration. *Chem. Eng. J.* **2019**, *362*, 830–841.
- (82) Itikawa, Y. Cross Sections for Electron Collisions with Carbon Dioxide. *J. Phys. Chem. Ref. Data* **2002**, *31* (3), 749–767.
- (83) Beuthe, T. G.; Chang, J.-S. Chemical Kinetic Modelling of Non-Equilibrium Ar- CO₂ Thermal Plasmas. *Jpn. J. Appl. Phys.* **1997**, *36*, 4997–5002.
- (84) Tian, C.; Vidal, C. R. Cross Sections of the Electron Impact Dissociative Ionization of CO, CH₄ and C₂H₂. *J. Phys. B At. Mol. Opt. Phys.* **1998**, *31*, 895–909.
- (85) Itikawa, Y. Cross Sections for Electron Collisions with Carbon Monoxide. *J. Phys. Chem. Ref. Data* **2015**, *44*, 013105.
- (86) Rapp, D.; Briglia, D. D. Total Cross Sections for Ionization and Attachment in Gases by Electron Impact. II. Negative-Ion Formation. *J. Chem. Phys.* **1965**, *43*, 1480–1489.
- (87) Land, J. E. Electron Scattering Cross Sections for Momentum Transfer and Inelastic Excitation in Carbon Monoxide. *J. Appl. Phys.* **1978**, *49*, 5716–5721.
- (88) Lawton, S. A.; Phelps, A. V. Excitation of the b 1Σ⁺+g State of O₂ by Low Energy Electrons. *J. Chem. Phys.* **1978**, *69*, 1055–1068.
- (89) Itikawa, Y. Cross Sections for Electron Collisions with Oxygen Molecules. *J. Phys. Chem. Ref. Data* **2009**, *38*, DOI: 10.1063/1.3025886.
- (90) Eliasson, B.; Kogelschatz, U. *Basic Data for Modelling of Electrical Discharges in Gases: Oxygen*; Baden: ABB Asea Brown Boveri, 1986.
- (91) Matejcik, S.; Kiendler, A.; Cicman, P.; Skalny, J.; Stampfli, P.; Illenberger, E.; Chu, Y.; Stamatovic, A.; Märk, T. D. Electron Attachment to Molecules and Clusters of Atmospheric Relevance: Oxygen and Ozone. *Plasma Sources Sci. Technol.* **1997**, *6* (2), 140–146.
- (92) Laher, R. R.; Gilmore, F. R. Updated Excitation and Ionization Cross Sections for Electron Impact on Atomic Oxygen. *J. Phys. Chem. Ref. Data* **1990**, *19*, 277–305.
- (93) Morgan Database www.Lxcat.Net. (retrieved 1 July 2017).
- (94) Janev, R. K.; Murakami, I.; Kato, T.; Wang, J. *Cross Sections and Rate Coefficients for Electron-Impact Ionization of Hydrocarbon Molecules*; Toki, Gifu, Japan, 2001.

- (95) Janev, R. K. Collision Processes of Hydrocarbon Species in Hydrogen Plasmas: I. The Methane Family. *ChemInform* **2003**, *34*, 1–47.
- (96) Phelps, A. V. *Tabulations of Collision Cross Sections and Calculated Transport and Reaction Coefficients for Electron Collisions with O₂*; 1985.
- (97) Hokazono, H.; Fujimoto, H. Theoretical Analysis of the CO₂ Molecule Decomposition and Contaminants Yield in Transversely Excited Atmospheric CO₂ Laser Discharge. *J. Appl. Phys.* **1987**, *62*, 1585–1594.
- (98) Liu, W.; Victor, G. A. Electron Energy Deposition in Carbon Monoxide Gas. *Astrophys. J.* **1994**, *435*, 909–919.
- (99) Cenian, A.; Chernukho, A.; Borodin, V. Modeling of Plasma-Chemical Reactions in Gas Mixture of CO₂ Lasers. II. Theoretical Model and Its Verification. *Contrib. to Plasma Phys.* **1995**, *35*, 273–296.
- (100) Hokazono, H.; Obara, M.; Midorikawa, K.; Tashiro, H. Theoretical Operational Life Study of the Closed-Cycle Transversely Excited Atmospheric CO₂ Laser. *J. Appl. Phys.* **1991**, *69*, 6850–6868.
- (101) Kossyi, I. A.; Kostinsky, A. Y.; Matveyev, A. A.; Silakov, V. P. Kinetic Scheme of the Non-Equilibrium Discharge in Nitrogen-Oxygen Mixtures. *Plasma Sources Sci. Technol.* **1992**, *1* (3), 207–220.
- (102) Albritton, D. L. Ion-Neutral Reaction-Rate Constants Measured in Flow Reactors Through 1977. *At. Data Nucl. Data Tables* **1978**, *22*, 1–101.
- (103) Adams, N. G.; Smith, D.; Grief, D. Reactions of H_nCO⁺ Ions with Molecules at 300 K. *Int. J. Mass Spectrom. Ion Phys.* **1978**, *26*, 405–415.
- (104) McFarland, M.; Albritton, D. L.; Fehsenfeld, F. C.; Ferguson, E. E.; Schmeltekopf, A. L. Flow-Drift Technique for Ion Mobility and Ion-Molecule Reaction Rate Constant Measurements. III. Negative Ion Reactions of O⁻ with CO, NO, H₂, and D₂. *J. Chem. Phys.* **1973**, *59*, 6629–6635.
- (105) Price, D. A.; Moruzzi, J. L. Negative Ion Molecule Reactions in CO₂ at High Pressures and Temperatures. *Vacuum* **1974**, *24*, 591–593.
- (106) Thoenes, J.; Kurzius, S. C. *Plasma Chemistry Processes in the Closed Cycle EDL-Technical Report DRCPMHEL-CR-79-11-VOL-1*; 1979.
- (107) Fehsenfeld, F. C.; Schmeltekopf, A. L.; Schiff, H. I.; Ferguson, E. E. Laboratory Measurements of Negative Ion Reactions of Atmospheric Interest. *Planet. Space Sci.* **1967**, *15*, 373–379.
- (108) Belostotsky, S. G.; Economou, D. J.; Lopaev, D. V.; Rakhimova, T. V. Negative Ion Destruction by O(³P) Atoms and O₂(a ¹Δ_g) Molecules in an Oxygen Plasma. *Plasma Sources Sci. Technol.* **2005**, *14*, 532–542.
- (109) Gudmundsson, J. T.; Thorsteinsson, E. G. Oxygen Discharges Diluted with Argon: Dissociation Processes. *Plasma Sources Sci. Technol.* **2007**, *16*, 399–412.

- (110) Pack, J. L.; Phelps, A. V. Electron Attachment and Detachment. II. Mixtures of O₂ and CO₂ and of O₂ and H₂O. *J. Chem. Phys.* **1966**, *45*, 4316–4329.
- (111) Bortner, M. H.; Bourer, T.; Blank, C. A. *Defense Nuclear Agency Reaction Rate Handbook, Second Edition AD 763699*; 1972.
- (112) Woodall, J.; Agúndez, M.; Markwick-Kemper, A. J.; Millar, T. J. The UMIST Database for Astrochemistry 2006. *Astron. Astrophys.* **2007**, *466*, 1197–1204.
- (113) McElroy, D.; Walsh, C.; Markwick, A. J.; Cordiner, M. A.; Smith, K.; Millar, T. J. The UMIST Database for Astrochemistry 2012. *Astron. Astrophys.* **2012**, *550*, A36.
- (114) Ionin, A. A.; Kochetov, I. V.; Napartovich, A. P.; Yuryshev, N. N. Physics and Engineering of Singlet Delta Oxygen Production in Low-Temperature Plasma. *J. Phys. D. Appl. Phys.* **2007**, *40* (2), R25–R61.
- (115) Khvorostovskaya, L. E.; Yankovsky, V. A. Negative Ions, Ozone, and Metastable Components in Dc Oxygen Glow Discharge. *Contrib. to Plasma Phys.* **1991**, *31*, 71–88.
- (116) Eremin, A. V.; Ziborov, V. S.; Shumova, V. V.; Voiki, D.; Roth, P. Formation of O(¹D) Atoms in Thermal Decomposition of CO₂. *Kinet. Catal.* **1997**, *38*, 1–7.
- (117) Baulch, D. L.; Drysdale, D. D.; Duxbury, J.; Grant, S. *Evaluated Kinetic Data for High Temperature Reactions, Volume 3: Homogeneous Gas Phase Reactions of the O₂-O₃ System, the CO-O₂-H₂ System, and of the Sulphur-Containing Species*; Butterworth, London, 1976.
- (118) Tsang, W., R. F. H. Chemical Kinetic Data for Combustion Chemistry. Part 1. Methane and Related Compounds. *J. Phys. Chem. Ref. Data* **1986**, *15*, 1087–1279.
- (119) Husain, D.; Young, A. N. Kinetic Investigation of Ground State Carbon Atoms, C(²3P_J). *J. Chem. Soc. Faraday Trans. 2* **1975**, *71*, 525.
- (120) Baldwin, R. R.; Jackson, D.; Melvin, A.; Rossiter, B. N. The Second Limit of Hydrogen + Carbon Monoxide + Oxygen Mixtures. *Int. J. Chem. Kinet.* **1972**, *4*, 277–292.
- (121) Husain, D.; Kirsch, L. J. Reactions of Atomic Carbon C(²3P_J) by Kinetic Absorption Spectroscopy in the Vacuum Ultra-Violet. *Trans. Faraday Soc.* **1971**, *67*, 2025–2035.
- (122) Shackelford, W. L.; Mastrup, F. N.; Kreye, W. C. Excitation and Quenching of CO Fourth Positive Chemiluminescence Due to Reactions Involving C₂O. *J. Chem. Phys.* **1972**, *57*, 3933–3944.
- (123) Atkinson, R.; Baulch, D. L.; Cox, R. A.; Hampson Jr., R. F.; Kerr, J. A.; Rossi, M. J.; Troe, J. *Evaluated Kinetic and Photochemical Data for Atmospheric Chemistry: Supplement VI. IUPAC Subcommittee on Gas*

- Kinetic Data Evaluation for Atmospheric Chemistry. *J. Phys. Chem. Ref. Data* **1997**, *26*, 1329–1499.
- (124) Hippler, H.; Rahn, R.; Troe, J. Temperature and Pressure Dependence of Ozone Formation Rates in the Range 1-1000 Bar and 90-370 K. *J. Chem. Phys.* **1990**, *93*, 6560–6569.
- (125) Simpson, C. J. S. M.; Chandler, T. R. D.; Strawson, A. C. Vibrational Relaxation in CO₂ and CO₂-Ar Mixtures Studied Using a Shock Tube and a Laser-Schlieren Technique. *J. Chem. Phys.* **1969**, *51*, 2214–2219.
- (126) Taylor, R.; Bitterman, S. Survey of Vibrational Relaxation Data for Processes Important in the CO₂-N₂ Laser System. *Rev. Mod. Phys.* **1969**, *41*, 26–47.
- (127) Blauer, J. A.; Nickerson, G. R. *A Survey of Vibrational Relaxation Rate Data For Processes Important To CO₂-N₂-H₂O Infrared Plume Radiation*; 1973.
- (128) Rosser, W. A.; Wood, A. D.; Gerry, E. T. Deactivation of Vibrationally Excited Carbon Dioxide (v₃) by Collisions with Carbon Dioxide or with Nitrogen. *J. Chem. Phys.* **1969**, *50*, 4996–5008.
- (129) Herzfeld, K. F. Deactivation of Vibrations by Collision in the Presence of Fermi Resonance. *J. Chem. Phys.* **1967**, *47*, 743–752.
- (130) Capitelli, M.; Ferreira, C. M.; Gordiets, B. F.; A.I., O. *Capitelli - Plasma Kinetics in Atmospheric Gases*; Springer(Berlin), 2000.
- (131) Sharma, R. D. Near-Resonant Vibrational Energy Transfer Among Isotopes of CO₂. *Phys. Rev.* **1969**, *177*, 102–107.
- (132) Kreutz, T. G.; O'Neill, J. A.; Flynn, G. W. Diode Laser Absorption Probe of Vibration-Vibration Energy Transfer in CO₂. *J. Phys. Chem.* **1987**, *91*, 5540–5543.
- (133) DeLeon, R. L.; Rich, J. W. Vibrational Energy Exchange Rates in Carbon Monoxide. *Chem. Phys.* **1986**, *107*, 283–292.
- (134) Flament, C.; George, T.; Meister, K. A.; Tufts, J. C.; Rich, J. W.; Subramaniam, V. V.; Martin, J. P.; Piar, B.; Perrin, M. Y. Nonequilibrium Vibrational Kinetics of Carbon Monoxide at High Translational Mode Temperatures. *Chem. Phys.* **1992**, *163*, 241–262.
- (135) Zhang, J. Q.; Yang, Y. J.; Zhang, J. S.; Liu, Q. Non-Oxidative Coupling of Methane to C₂ Hydrocarbons under above-Atmospheric Pressure Using Pulsed Microwave Plasma. *Energy & Fuels* **2002**, *16*, 687–693.
- (136) Aziznia, A.; Bozorgzadeh, H. R.; Seyed-Matin, N.; Baghalha, M.; Mohamadizadeh, A. Comparison of Dry Reforming of Methane in Low Temperature Hybrid Plasma-Catalytic Corona with Thermal Catalytic Reactor over Ni/γ-Al₂O₃. *J. Nat. Gas Chem.* **2012**, *21*, 466–475.
- (137) Scapinello, M.; Martini, L. M.; Dilecce, G.; Tosi, P. Conversion of CH₄/CO₂ by a Nanosecond Repetitively Pulsed Discharge. *J. Phys. D.*

- Appl. Phys.* **2016**, *49*, 075602–075609.
- (138) Kim, S. C.; Lim, M. S.; Chun, Y. N. Reduction Characteristics of Carbon Dioxide Using a Plasmatron. *Plasma Chem. Plasma Process.* **2013**, *34* (1), 125–143.
- (139) Liu, C. J.; Li, Y.; Zhang, Y. P.; Wang, Y.; Zou, J.; Eliasson, B.; Xue, B. Production of Acetic Acid Directly from Methane and Carbon Dioxide Using Dielectric-Barrier Discharges. *Chem. Lett.* **2001**, *30*, 1304–1305.
- (140) Kraus, M.; Egli, W.; Haffner, K.; Eliasson, B.; Kogelschatz, U.; Wokaun, A. Investigation of Mechanistic Aspects of the Catalytic CO₂ Reforming of Methane in a Dielectric-Barrier Discharge Using Optical Emission Spectroscopy and Kinetic Modeling. *Phys. Chem. Chem. Phys.* **2002**, *4*, 668–675.
- (141) Istadi, I.; Amin, N. A. S. Modelling and Optimization of Catalytic-Dielectric Barrier Discharge Plasma Reactor for Methane and Carbon Dioxide Conversion Using Hybrid Artificial Neural Network-Genetic Algorithm Technique. *Chem. Eng. Sci.* **2007**, *62* (23), 6568–6581.
- (142) Nair, S. A.; Nozaki, T.; Okazaki, K. Methane Oxidative Conversion Pathways in a Dielectric Barrier Discharge Reactor-Investigation of Gas Phase Mechanism. *Chem. Eng. J.* **2007**, *132*, 85–95.
- (143) Snoeckx, R.; Aerts, R.; Tu, X.; Bogaerts, A. Plasma-Based Dry Reforming: A Computational Study Ranging from the Nanoseconds to Seconds Time Scale. *J. Phys. Chem. C* **2013**, *117*, 4957–4970.
- (144) Tsang, W. Chemical Kinetic Data Base for Combustion Chemistry Part 4. Isobutane. *J. Phys. Chem. Ref. Data* **1990**, *1*, 1–68.
- (145) Tsang, W. Chemical Kinetic Data Base for Combustion Chemistry Part 5. Propene. *J. Phys. Chem. Ref. Data* **1991**, *20*, 221–273.
- (146) Baulch, D. L.; Cobos, C. J.; Cox, R. A.; Esser, C.; Frank, P.; Just, T.; Kerr, J. A.; Pilling, M. J.; Troe, J.; Walker, R. W.; et al. Evaluated Kinetic Data for Combustion Modeling of Atom Reactions. *J. Phys. Chem. Ref. Data* **1992**, *21*, 411–734.
- (147) Smith, G. P.; Golden, D. M.; Frenklach, M.; Moriarty, N. W.; Eiteneer, B.; Goldenberg, M.; Bowman, C. T.; Hanson, R. K.; Song, S.; Gardiner, W. C. J.; et al. GRI-MECH 3.0 : http://www.me.berkeley.edu/gri_mech/.
- (148) De Bie, C.; Van Dijk, J.; Bogaerts, A. The Dominant Pathways for the Conversion of Methane into Oxygenates and Syngas in an Atmospheric Pressure Dielectric Barrier Discharge. *J. Phys. Chem. C* **2015**, *119*, 22331–22350.
- (149) Chen, X. Y.; Vinh-Thang, H.; Ramirez, A. A.; Rodrigue, D.; Kaliaguine, S. Membrane Gas Separation Technologies for Biogas Upgrading. *RSC Adv.* **2015**, *5*, 24399–24448.
- (150) Buelens, L. C.; Galvita, V. V.; Poelman, H.; Detavernier, C.; Marin, G. B.

- Super-Dry Reforming of Methane Intensifies CO₂ Utilization via Le Chatelier's Principle. *Science* (80-.). **2016**, 354, 449–452.
- (151) Heijkers, S.; Bogaerts, A. CO₂ Conversion in a Gliding Arc Plasmatron: Elucidating the Chemistry through Kinetic Modeling. *J. Phys. Chem. C* **2017**, 121, 22644–22655.
- (152) Berthelot, A.; Bogaerts, A. Modeling of Plasma-Based CO₂ Conversion: Lumping of the Vibrational Levels. *Plasma Sources Sci. Technol.* **2016**, 25, 045022.
- (153) Cleiren, E.; Heijkers, S.; Ramakers, M.; Bogaerts, A. Dry Reforming of Methane in a Gliding Arc Plasmatron: Towards a Better Understanding of the Plasma Chemistry. *ChemSusChem* **2017**, 10, 4025–4036.
- (154) Coward, H. F.; Jones, G. W. *Limits of Flammability of Gases and Vapors*; United States Government Printing Office: Washington, 1952.
- (155) Zhang, K.; Eliasson, B.; Kogelschatz, U. Direct Conversion of Greenhouse Gases to Synthesis Gas and C₄ Hydrocarbons over Zeolite HY Promoted by a Dielectric-Barrier Discharge. *Ind. Eng. Chem. Res.* **2002**, 41, 1462–1468.
- (156) Bo, Z.; Yan, J.; Li, X.; Chi, Y.; Cen, K. Plasma Assisted Dry Methane Reforming Using Gliding Arc Gas Discharge: Effect of Feed Gases Proportion. *Int. J. Hydrogen Energy* **2008**, 33 (20), 5545–5553.
- (157) Snoeckx, R.; Ozkan, A.; Reniers, F.; Bogaerts, A. The Quest for Value-Added Products from Carbon Dioxide and Water in a Dielectric Barrier Discharge: A Chemical Kinetics Study. *ChemSusChem* **2017**, 10 (2), 409–424.
- (158) Janev, R. K. *Atomic and Molecular Processes in Fusion Edge Plasmas*; Plenum Press: New York, U.S.A., 1995.
- (159) Janev, R. K.; Reiter, D. Collision Processes of CH_y and CH_y+ Hydrocarbons with Plasma Electrons and Protons. *Phys. Plasmas* **2002**, 9, 4071–4081.
- (160) Janev, R. K.; Reiter, D. Collision Processes of Hydrocarbon Species in Hydrogen Plasmas. Part 2. The Ethane and Propane Families. *ChemInform* **2003**, 34 (37), 1–124.
- (161) Janev, R. K.; Reiter, D. Collision Processes of C_{2,3}Hy and C_{2,3}Hy+ Hydrocarbons with Electrons and Protons. *Phys. Plasmas* **2004**, 11, 780–829.
- (162) Engelhardt, A. G.; Phelps, A. V. Elastic and Inelastic Collision Cross Sections in Hydrogen and Deuterium from Transport Coefficients. *Phys. Rev.* **1963**, 131 (5), 2115–2128.
- (163) Trajmar, S.; Register, D. F.; Chutjian, a. Electron Scattering by Molecules II. Experimental Methods and Data. *Phys. Rep.* **1983**, 97, 219–356.
- (164) Tawara, H.; Kato, T. Total and Partial Ionization Cross Sections of Atoms

- and Ions by Electron Impact. *At. Data Nucl. Data Tables* **1987**, *36*, 167–353.
- (165) Corrigan, S. J. B. Dissociation of Molecular Hydrogen by Electron Impact. *J. Chem. Phys.* **1965**, *43* (12), 4381–4386.
- (166) Itikawa, Y.; Mason, N. Cross Sections for Electron Collisions with Water Molecules. *J. Phys. Chem. Ref. Data* **2005**, *34* (1), 1–22.
- (167) Riahi, R.; Teulet, P.; Ben Lakhdar, Z.; Gleizes, A. Cross-Section and Rate Coefficient Calculation for Electron Impact Excitation, Ionisation and Dissociation of H₂ and OH Molecules. *Eur. Phys. J. D* **2006**, *40* (2), 223–230.
- (168) De Bie, C.; Martens, T.; van Dijk, J.; Paulussen, S.; Verheyde, B.; Corthals, S.; Bogaerts, A. Dielectric Barrier Discharges Used for the Conversion of Greenhouse Gases: Modeling the Plasma Chemistry by Fluid Simulations. *Plasma Sources Sci. Technol.* **2011**, *20* (2), 024008.
- (169) Florescu-Mitchell, A. I.; Mitchell, J. B. A. Dissociative Recombination. *Phys. Rep.* **2006**, *430*, 277–374.
- (170) Frank, P. A High Temperature Shock Tube Study on Fast Reactions of Methylene and Methyl Radicals. *Proc. 15th Int. Symp. Rarefied Gas Dyn. Ed. by, V. Boffi C. Cercignani* **1986**, *2*, 422.
- (171) Tsang, W. Chemical Kinetic Data Base for Combustion Chemistry. Part 3: Propane. *J. Phys. Chem. Ref. Data* **1988**, *17*, 887–951.
- (172) Sutherland, J. W.; Su, M.-C.; Michael, J. V. Rate Constants for H + CH₄, CH₃ + H₂, and CH₄ Dissociation at High Temperature. *Int. J. Chem.* **2001**, *33*, 669–684.
- (173) Stewart, P. H.; Larson, C. W.; Golden, D. M. Pressure and Temperature Dependence of Reactions Proceeding via a Bound Complex. 2. Application to 2 CH₃ → C₂H₅ + H. *Combust. Flame* **1989**, *75*, 25–31.
- (174) Baulch, D. L.; Cobos, C. J.; Cox, R. A.; Frank, P.; Hayman, G.; Just, T.; Kerr, J. A.; Murrells, T.; Pilling, M. J.; Troe, J.; et al. Evaluated Kinetic Data for Combustion Modelling Supplement I. *J. Phys. Chem. Ref. Data* **1994**, *23*, 847–1033.
- (175) Laufer, A. H.; Fahr, A. Reactions and Kinetics of Unsaturated C₂ Hydrocarbon Radicals. *Chem. Rev.* **2004**, *104* (6), 2813–2832.
- (176) Laufer, A. H.; Yung, Y. L. Equivalence of Vinylidene and Excited Acetylene (C₂H₂^{*}): Calculated Rate Constant for Vinylidene Abstraction from Methane. *J. Phys. Chem.* **1983**, *87*, 181–183.
- (177) Fahr, A.; Laufer, A. H.; Tardy, D. C. Pressure Effect on CH₃ and C₂H₃ Cross-Radical Reactions. *J. Phys. Chem. A* **1999**, *103*, 8433–8439.
- (178) De Bie, C.; Verheyde, B.; Martens, T.; Van Dijk, J.; Paulussen, S.; Bogaerts, A. Fluid Modeling of the Conversion of Methane into Higher Hydrocarbons in an Atmospheric Pressure Dielectric Barrier Discharge.

- Plasma Process. Polym.* **2011**, *8*, 1033–1058.
- (179) Bauerle, S.; Klatt, M.; Wagner, H. G. Recombination and Decomposition of Methylene Radicals at High Temperatures. *Berichte der Bunsengesellschaft für Phys. Chemie* **1995**, *99*, 870–879.
- (180) Zabarnick, S.; Fleming, J. W.; Lin, M. C. Kinetic Study of the Reaction $\text{CH}(\text{X}^2\Pi) + \text{H}_2 \rightleftharpoons \text{CH}_2(\text{X}^3\text{B}_1) + \text{H}$ in the Temperature Range 372 to 675 K. *J. Chem. Phys.* **1986**, *85*, 4373.
- (181) Harding, L. B.; Guadagnini, R.; Schatz, G. C. Theoretical Studies of the Reactions $\text{H} + \text{CH} \rightarrow \text{C} + \text{H}_2$ and $\text{C} + \text{H}_2 \rightarrow \text{CH}_2$ Using an Ab Initio Global Ground-State Potential Surface for CH_2 . *J. Phys. Chem.* **1993**, *97* (21), 5472–5481.
- (182) Dean, A. J.; Davidson, D. F.; Hanson, R. K. A Shock Tube Study of Reactions of C Atoms with H_2 and O_2 Using Excimer Photolysis of C_3O_2 and C Atom Atomic Resonance Absorption Spectroscopy. *J. Phys. Chem.* **1991**, *95*, 183–191.
- (183) Harding, L. B.; Georgievskii, Y.; Klippenstein, S. J. Predictive Theory for Hydrogen Atom-Hydrocarbon Radical Association Kinetics. *J. Phys. Chem. A* **2005**, *109* (21), 4646–4656.
- (184) Warnatz, J. Rate Coefficients in the C/H/O System. In *Combustion Chemistry*; Gardiner, W. C. J., Ed.; Springer-Verlag, NY, 1984; pp 197–360.
- (185) Kruse, T.; Roth, P. Kinetics of C_2 Reactions during High-Temperature Pyrolysis of Acetylene. *J. Phys. Chem. A* **1997**, *101*, 2138–2146.
- (186) Dean, A. M. Predictions of Pressure and Temperature Effects upon Radical Addition and Recombination Reactions. *J. Phys. Chem.* **1985**, *89*, 4600–4608.
- (187) Zsély, I. G.; Varga, T.; Nagy, T.; Cserhádi, M.; Turányi, T.; Peukert, S.; Braun-Unkloff, M.; Naumann, C.; Riedel, U. Determination of Rate Parameters of Cyclohexane and 1-Hexene Decomposition Reactions. *Energy* **2012**, *43*, 85–93.
- (188) Harding L.B.; Klippenstein, S. J.; Georgievskii, Y. On the Combination Reactions of Hydrogen Atoms with Resonance-Stabilized Hydrocarbon Radicals†. **2007**, 3789–3801.
- (189) Cohen, N.; Westberg, K. R. Chemical Kinetic Data Sheets for High-Temperature Chemical Reactions. *J. Phys. Chem. Ref. Data* **1983**, *12*, 531–590.
- (190) Cohen, N.; Westberg, K. R. Chemical Kinetic Data Sheets for High-Temperature Reactions. Part II. *J. Phys. Chem. Ref. Data* **1991**, *20*, 1211.
- (191) Hack, W.; Hold, M.; Hoyermann, K.; Wehmeyer, J.; Zeuch, T. Mechanism and Rate of the Reactions $\text{CH}_3 + \text{O}$ Revisited. *Phys. Chem. Chem. Phys.* **2005**, *7*, 1977–1984.

- (192) Baulch, D. L.; Bowman, C. T.; Cobos, C. J.; Cox, R. A.; Just, T.; Kerr, J. A.; Pilling, M. J.; Stocker, D.; Troe, J.; Tsang, W.; et al. Evaluated Kinetic Data for Combustion Modeling: Supplement II. *J. Phys. Chem. Ref. Data* **2005**, *34*, 757–1397.
- (193) Dombrowsky, C.; Wagner, H. G. Investigation of the $^3\text{CH}_2 + \text{O}_2$ Reaction in Shock Waves. *Ber. Bunsenges. Phys. Chem.* **1992**, *96*, 1048–1055.
- (194) Fang, D.-C.; Fu, X.-Y. CASSCF and CAS+1+2 Studies on the Potential Energy Surface and the Rate Constants for the Reactions between CH_2 and O_2 . *J. Phys. Chem. A* **2002**, *106*, 2988–2993.
- (195) Harding, L. B.; Klippenstein, S. J.; Georgievskii, Y. Reactions of Oxygen Atoms with Hydrocarbon Radicals: A Priori Kinetic Predictions for the $\text{CH}_3 + \text{O}$, $\text{C}_2\text{H}_5 + \text{O}$, and $\text{C}_2\text{H}_3 + \text{O}$ Reactions. *Proc. Combust. Inst.* **2005**, *30*, 985–993.
- (196) Atkinson, R.; Baulch, D. L.; Cox, R. A.; Crowley, J. N.; Hampson, R. F.; Hynes, R. G.; Jenkin, M. E.; Rossi, M. J.; Troe, J. Evaluated Kinetic and Photochemical Data for Atmospheric Chemistry: Volume II - Gas Phase Reactions of Organic Species. *Atmos. Chem. Phys.* **2006**, *6* (11), 3625–4055.
- (197) Wagner, A. F.; Slagle, I. R.; Sarzynski, D.; Gutman, D. Experimental and Theoretical Studies of the $\text{C}_2\text{H}_5 + \text{O}_2$ Reaction Kinetics. *J. Phys. Chem.* **1990**, *94*, 1853–1868.
- (198) Cvetanovic†, R. J. Evaluated Chemical Kinetic Data for the Reactions of Atomic Oxygen $\text{O}(^3\text{P})$ with Sulfur Containing Compounds. *J. Phys. Chem. Ref. Data* **1987**, *16*, 261–326.
- (199) Turányi, T.; Nagy, T.; Zsély, I. G.; Cserháti, M.; Varga, T.; Szabó, B. T.; Sedyó, I.; Kiss, P. T.; Zempléni, A.; Curran, H. J. Determination of Rate Parameters Based on Both Direct and Indirect Measurements. *Int. J. Chem. Kinet.* **2012**, *44*, 284–302.
- (200) Seeley, J. V.; Jayne, J. T.; Molina, M. J. High Pressure Fast-Flow Technique for Gas Phase Kinetics Studies. *Int. J. Chem. Kinet.* **1993**, *25*, 571–594.
- (201) Srinivasan, N. K.; Su, M. C.; Sutherland, J. W.; Michael, J. V. Reflected Shock Tube Studies of High-Temperature Rate Constants for $\text{OH} + \text{CH}_4 \rightarrow \text{CH}_3 + \text{H}_2\text{O}$ and $\text{CH}_3 + \text{NO}_2 \rightarrow \text{CH}_3\text{O} + \text{NO}$. *J. Phys. Chem. A* **2005**, *109*, 1857–1863.
- (202) Tsang, W. Chemical Kinetic Data Base for Combustion Chemistry. Part 2. Methanol. *J. Phys. Chem. Ref. Data* **1987**, *16*, 471–508.
- (203) Senosiain, J. P.; Klippenstein, S. J.; Miller, J. A. Pathways and Rate Coefficients for the Decomposition of Vinyloxy and Acetyl Radicals. *J. Phys. Chem. A* **2006**, *110*, 5772–5781.
- (204) Dean, A. M.; Westmoreland, P. R. Bimolecular QRRK Analysis of Methyl

- Radical Reactions. *Int. J. Chem. Kinet.* **1987**, *19*, 207–228.
- (205) Moortgat, G. K.; Slemr, F.; Warneck, P. Kinetics and Mechanism of the Reaction $\text{H} + \text{CH}_3\text{ONO}$. *Int. J. Chem. Kinet.* **1977**, *9*, 249–265.
- (206) Jasper, A. W.; Klippenstein, S. J.; Harding, L. B. Theoretical Rate Coefficients for the Reaction of Methyl Radical with Hydroperoxyl Radical and for Methylhydroperoxide Decomposition. *Proc. Combust. Inst.* **2009**, *32*, 279–286.
- (207) Fulle, D.; Hippler, H.; Striebel, F. The High-Pressure Range of the Reaction $\text{CH}(\text{}^2\Pi) + \text{CO} + \text{M} \Rightarrow \text{HCCO} + \text{M}$. *J. Chem. Phys.* **1998**, *108*, 6709–6716.
- (208) Frank, P.; Bhaskaran, K. A.; Just, T. Acetylene Oxidation: The Reaction of $\text{C}_2\text{H}_2 + \text{O}$ at High Temperatures. *Symp. Int. Combust. Proc.* **1988**, *21*, 885–893.
- (209) Krasnoperov, L. N.; Michael, J. V. Shock Tube Studies Using a Novel Multipass Absorption Cell: Rate Constant Results for $\text{OH} + \text{H}_2$ and $\text{OH} + \text{C}_2\text{H}_6$. *J. Phys. Chem. A* **2004**, *108*, 5643–5648.
- (210) Carstensen, H. H.; Dean, A. M. Rate Constants for the Abstraction Reactions $\text{RO}_2 + \text{C}_2\text{H}_6$; $\text{R} = \text{H}, \text{CH}_3$, and C_2H_5 . *Proc. Combust. Inst.* **2005**, *30* (1), 995–1003.
- (211) Miller, J. A.; Melius, C. F. A Theoretical Analysis of the Reaction between Hydroxyl and Acetylene. *22d Symp. Combust.* **1989**, *22*, 1031–1039.
- (212) Carl, S. A.; Minh Thi Nguyen, H.; Elsamra, R. M. I.; Tho Nguyen, M.; Peeters, J. Pulsed Laser Photolysis and Quantum Chemical-Statistical Rate Study of the Reaction of the Ethynyl Radical with Water Vapor. *J. Chem. Phys.* **2005**, *122*, 114307.
- (213) Walker, R. W. Temperature Coefficients for Reactions of OH Radicals with Alkanes between 300 and 1000 K. *Int. J. Chem. Kinet.* **1985**, *17*, 573–582.
- (214) Oldenborg, R. C.; Loge, G. W.; Harradine, D. M.; Winn, K. R. Kinetic Study of the $\text{OH} + \text{H}_2$ Reaction from 800 to 1550 K. *J. Phys. Chem.* **1992**, *96*, 8426–8430.
- (215) Slemr, F.; Warneck, P. Kinetics of the Reaction of Atomic Hydrogen with Methyl Hydroperoxide. *Int. J. Chem. Kinet.* **1977**, *9* (2), 267–282.
- (216) Karkach, S. P.; Osherov, V. I. Ab Initio Analysis of the Transition States on the Lowest Triplet H_2O_2 Potential Surface. *J. Chem. Phys.* **1999**, *110*, 11918–11927.
- (217) Srinivasan, N. K.; Su, M. C.; Sutherland, J. W.; Michael, J. V. Reflected Shock Tube Studies of High-Temperature Rate Constants for $\text{CH}_3 + \text{O}_2$, $\text{H}_2\text{CO} + \text{O}_2$, and $\text{OH} + \text{O}_2$. *J. Phys. Chem. A* **2005**, *109*, 7902–7914.
- (218) Sun, H.; Tang, Y. I. Z.; Wang, Z. L.; Pan, X. M.; Ze-Sheng, L. I.; Wang, R. S. DFT Investigation of the Mechanism of $\text{CH}_2\text{CO} + \text{O}(\text{}^3\text{P})$ Reaction.

- Int. J. Quantum Chem.* **2005**, *105* (5), 527–532.
- (219) Kuwata, K. T.; Hasson, A. S.; Dickinson, R. V.; Petersen, E. B.; Valin, L. C. Quantum Chemical and Master Equation Simulations of the Oxidation and Isomerization of Vinyloxy Radicals. *J. Phys. Chem. A* **2005**, *109* (11), 2514–2524.
- (220) Delbos, E.; Fittschen, C.; Hippler, H.; Krasteva, N.; Olzmann, M.; Viskolcz, B. Rate Coefficients and Equilibrium Constant for the $\text{CH}_2\text{CHO} + \text{O}_2$ Reaction System. *J. Phys. Chem. A* **2006**, *110* (9), 3238–3245.
- (221) Ju, L.-P.; Han, K.-L.; Varandas, A. J. C. Variational Transition-State Theory Study of the Atmospheric Reaction $\text{OH} + \text{O}_3 \rightarrow \text{HO}_2 + \text{O}_2$. *Int. J. Chem. Kinet.* **2007**, *39*, 148–153.
- (222) Atkinson, R.; Baulch, D. L.; Cox, R. a.; Crowley, J. N.; Hampson, R. F.; Hynes, R. G.; Jenkin, M. E.; Rossi, M. J.; Troe, J. Evaluated Kinetic and Photochemical Data for Atmospheric Chemistry: Volume 1 – Gas Phase Reactions of Ox, HOx, NOx and SOx Species. *Atmos. Chem. Phys.* **2004**, *4*, 1461–1738.
- (223) Tyndall, G. S.; Wallington, T. J.; Ball, J. C. FTIR Product Study of the Reactions $\text{CH}_3\text{O}_2 + \text{CH}_3\text{O}_2$ and $\text{CH}_3\text{O}_2 + \text{O}_3$. *J. Phys. Chem. A* **1998**, *102*, 2547–2554.
- (224) Jodkowski, J. T.; Rayez, M.-T.; Rayez, J.-C.; Bérces, T.; Dóbé, S. Theoretical Study of the Kinetics of the Hydrogen Abstraction from Methanol. 3. Reaction of Methanol with Hydrogen Atom, Methyl, and Hydroxyl Radicals. *J. Phys. Chem. A* **1999**, No. 103, 3750–3765.
- (225) Mayer, S. W.; Schieler, L. Activation Energies and Rate Constants Computed for Reactions of Oxygen with Hydrocarbons. *J. Phys. Chem.* **1968**, *72*, 2628–2631.
- (226) Hou, H.; Baoshan, W.; Gu, Y. Mechanism of the $\text{OH} + \text{CH}_2\text{CO}$ Reaction. *Phys. Chem. Chem. Phys.* **2000**, *2*, 2329–2334.
- (227) Xu, Z. F.; Park, J.; Lin, M. C. Thermal Decomposition of Ethanol. III. A Computational Study of the Kinetics and Mechanism for the $\text{CH}_3 + \text{C}_2\text{H}_5\text{OH}$ Reaction. *J. Chem. Phys.* **2004**, *120* (14), 6593–6599.
- (228) Höhlein, G.; Freeman, G. R. Radiation-Sensitized Pyrolysis of Diethyl Ether. Free-Radical Reaction Rate Parameters. *J. Am. Chem. Soc.* **1970**, *92*, 6118–6125.
- (229) Löser, U.; Scherzer, K.; Weber, K. Abschätzung Kinetischer Daten Für H-Transferreaktionen Mit Hilfe Der „Bond Strength-Bond Length (BSBL)“-Methode. *Zeitschrift für Phys. Chemie* **1989**, *270*, 237–245.
- (230) Li, S. C.; Williams, F. A. Experimental and Numerical Studies of Two-Stage Methanol Flames. *Symp. Combust.* **1996**, *26*, 1017–1024.
- (231) Jasper, A. W.; Klippenstein, S. J.; Harding, L. B.; Ruscic, B. Kinetics of the Reaction of Methyl Radical with Hydroxyl Radical and Methanol

- Decomposition. *J. Phys. Chem. A* **2007**, *111* (19), 3932–3950.
- (232) Koike, T.; Kudo, M.; Maeda, I.; Yamada, H. Rate Constants of $\text{CH}_4 + \text{M}=\text{CH}_3 + \text{H} + \text{M}$ and $\text{CH}_3\text{OH} + \text{M}=\text{CH}_3 + \text{OH} + \text{M}$ over 1400–2500 K. *Int. J. Chem. Kinet.* **2000**, *32*, 1–6.
- (233) Park, J.; Xu, Z. F.; Lin, M. C. Thermal Decomposition of Ethanol. II. A Computational Study of the Kinetics and Mechanism for the $\text{H}+\text{C}_2\text{H}_5\text{OH}$ Reaction. *J. Chem. Phys.* **2003**, *118*, 9990–9996.
- (234) Grotheer, H. H.; Just, T. Kinetics of the Oxidation of Methanol by Ground-State Atomic Oxygen. *Chem. Phys. Lett.* **1981**, *78*, 71–74.
- (235) Tsuboi, T.; Hashimoto, K. Shock Tube Study on Homogeneous Thermal Oxidation of Methanol. *Combust. Flame* **1981**, *42*, 61–76.
- (236) da Silva, G.; Bozzelli, J. W. Role of the α -Hydroxyethylperoxy Radical in the Reactions of Acetaldehyde and Vinyl Alcohol with HO_2 . *Chem. Phys. Lett.* **2009**, *483*, 25–29.
- (237) Lloyd, A. C. Evaluated and Estimated Kinetic Data for Phase Reactions of the Hydroperoxyl Radical. *Int. J. Chem. Kinet.* **1974**, *6*, 169–228.
- (238) Sivaramakrishnan, R.; Su, M. C.; Michael, J. V.; Klippenstein, S. J.; Harding, L. B.; Ruscic, B. Rate Constants for the Thermal Decomposition of Ethanol and Its Bimolecular Reactions with OH and D: Reflected Shock Tube and Theoretical Studies. *J. Phys. Chem. A* **2010**, *114*, 9425–9439.
- (239) Vaghjiani, G. L.; Ravishankara, A. R. Kinetics and Mechanism of OH Reaction with CH_3OOH . *J. Phys. Chem.* **1989**, *93*, 1948–1959.
- (240) Kelly, N.; Heicklen, J. Rate Coefficient for the Reaction of CH_3O with CH_3CHO at 25 °C. *J. Photochem.* **1978**, *8*, 83–90.
- (241) Schulz, G.; Klotz, H.-D.; Spangenberg, H.-J. Reaktionsmodell Zur Bruttokinetik Der Pyrolyse van Methan Im Stoßwellenrohr Bei Temperaturen von 1800 K Bis 2500 K. *Zeitschrift für Chemie* **1983**, *25*, 88–92.
- (242) Back, R. A. A Search for a Gas-Phase Free-Radical Inversion Displacement Reaction at a Saturated Carbon Atom. *Can. J. Chem.* **1983**, *61*, 916–920.
- (243) Tabayashi, K.; Bauer, S. H. The Early Stages of Pyrolysis and Oxidation of Methane. *Combust. Flame* **1979**, *34*, 63–83.
- (244) Azatyan, V. V.; Nalbandyan, A. B.; Ts'ui, M.-Y. Determination of Rate Constants of the Reactions of Atomic Hydrogen and Atomic Oxygen with Ethylene. *Dokl. Akad. Nauk SSR* **1963**, *149*, 1095–1098.
- (245) Zanchet, A.; Bussery-Honvault, B.; Jorfi, M.; Honvault, P. Study of the $\text{C}(^3\text{P}) + \text{OH}(X^2\Pi) \rightarrow \text{CO}(a^3\Pi) + \text{H}(^2\text{S})$ Reaction: Fully Global Ab Initio Potential Energy Surfaces of the $1^2\text{A}''$ and $1^4\text{A}''$ Excited States and Non Adiabatic Couplings. *Phys. Chem. Chem. Phys.* **2009**, *11*, 6182–6191.
- (246) Vandooren, J.; Van Tiggelen, P. J. Reaction Mechanisms of Combustion

- in Low Pressure Acetylene-Oxygen Flames. *Symp. Combust.* **1977**, *16*, 1133–1144.
- (247) Mebel, A. M.; Diau, E. W. G.; Lin, M. C.; Morokuma, K. Ab Initio and RRKM Calculations for Multichannel Rate Constants of the $C_2H_3 + O_2$ Reaction. *J. Am. Chem. Soc.* **1996**, *118*, 9759–9771.
- (248) Laufer, A. H.; Gardner, E. P.; Kwok, T. L.; Yung, Y. L. Computations and Estimates of Rate Coefficients for Hydrocarbon Reactions of Interest to the Atmospheres of the Outer Solar System. *Icarus* **1983**, *56*, 560–567.
- (249) Woods, I. T.; Haynes, B. S. C_1/C_2 Chemistry in Fuel-Rich Post-Flame Gases: Detailed Kinetic Modelling. *Symp. Combust.* **1994**, *25*, 909–917.
- (250) Curran, H. J. Rate Constant Estimation for C_1 to C_4 Alkyl and Alkoxy Radical Decomposition. *Int. J. Chem. Kinet.* **2006**, *38*, 250–275.
- (251) Pintassilgo, C. D.; Jaoul, C.; Loureiro, J.; Belmonte, T.; Czerwiec, T. Kinetic Modelling of a N_2 Flowing Microwave Discharge with CH_4 Addition in the Post-Discharge for Nitrocarburizing Treatments. *J. Phys. D. Appl. Phys.* **2007**, *40* (12), 3620–3632.
- (252) Oumghar, A.; Legrand, J. C.; Damiy, A. M.; Turillon, N.; Ben-Aïm, R. I. A Kinetic Study of Methane Conversion by a Dinitrogen Microwave Plasma. *Plasma Chem. Plasma Process.* **1994**, *14*, 229–249.
- (253) Lebonnois, S.; Toubanc, D.; Hourdin, F.; Rannou, P. Seasonal Variations of Titan's Atmospheric Composition. *Icarus* **2001**, *152*, 384–406.
- (254) Toubanc, D.; Parisot, J. P.; Brillet, J.; Gautier, D.; Raulin, F.; McKay, C. P. Photochemical Modeling of Titan's Atmosphere. *Icarus* **1995**, *113*, 2–26.
- (255) Kim, Y. H.; Fox, J. L. The Chemistry of Hydrocarbon Ions in the Jovian Ionosphere. *Icarus*. 1994, pp 310–325.
- (256) Tahara, H.; Minami, K.; Murai, A.; Yasui, T.; Yoshikawa, T. Diagnostic Experiment and Kinetic Model Analysis of Microwave CH_4/H_2 Plasmas for Deposition of Diamondlike Carbon Films. *Jpn. J. Appl. Phys.* **1995**, *34*, 1972–1979.
- (257) Tachibana, K.; Nishida, M.; Harima, H.; Urano, Y. Diagnostics and Modelling of a Methane Plasma Used in the Chemical Vapour Deposition of Amorphous Carbon Films. *J. Phys. D. Appl. Phys.* **1984**, *17*, 1727–1742.
- (258) McLain, J. L.; Poterya, V.; Molek, C. D.; Babcock, L. M.; Adams, N. G. Flowing Afterglow Studies of the Temperature Dependencies for Dissociative Recombination of O_2^+ , CH_5^+ , $C_2H_5^+$, and $C_6H_7^+$ with Electrons. *J. Phys. Chem. A* **2004**, *108*, 6704–6708.
- (259) Liu, D. X.; Bruggeman, P.; Iza, F.; Rong, M. Z.; Kong, M. G. Global Model of Low-Temperature Atmospheric-Pressure He + H_2O Plasmas. *Plasma Sources Sci. Technol.* **2010**, *19*, 025018.

- (260) Gordillo-Vázquez, F. J. Air Plasma Kinetics under the Influence of Sprites. *J. Phys. D. Appl. Phys.* **2008**, *41*, 234016.
- (261) Eichwald, O.; Yousfi, M.; Hennad, A.; Benabdessadok, M. D. Coupling of Chemical Kinetics, Gas Dynamics, and Charged Particle Kinetics Models for the Analysis of NO Reduction from Flue Gases. *J. Appl. Phys.* **1997**, *82*, 4781–4794.
- (262) Indarto, A.; Yang, D. R.; Choi, J. W.; Lee, H.; Song, H. K. Gliding Arc Plasma Processing of CO₂ Conversion. *J. Hazard. Mater.* **2007**, *146*, 309–315.
- (263) Silva, T.; Britun, N.; Godfroid, T.; Snyders, R. Optical Characterization of a Microwave Pulsed Discharge Used for Dissociation of CO₂. *Plasma Sources Sci. Technol.* **2014**, *23*, 025009.
- (264) Snoeckx, R.; Heijkers, S.; Van Wesenbeeck, K.; Lenaerts, S.; Bogaerts, A. CO₂ Conversion in a Dielectric Barrier Discharge Plasma: N₂ in the Mix as a Helping Hand or Problematic Impurity? *Energy Environ. Sci.* **2016**, *9*, 30–39.
- (265) Wiegand, W. J. Plasma Chemistry of CO₂-N₂-He Discharges. *Appl. Phys. Lett.* **1973**, *22*, 583.
- (266) Snoeckx, R.; Heijkers, S.; Van Wesenbeeck, K.; Lenaerts, S.; Bogaerts, A. CO₂ Conversion in a Dielectric Barrier Discharge Plasma: N₂ in the Mix as a Helping Hand or Problematic Impurity? *Energy Environ. Sci.* **2016**, *9*, 30–39.
- (267) Wang, W.; Patil, B.; Heijkers, S.; Hessel, V.; Bogaerts, A. Nitrogen Fixation by Gliding Arc Plasma: Better Insight by Chemical Kinetics Modelling. *ChemSusChem* **2017**, *10*, 2145–2157.
- (268) Patil, B. S.; Rovira Palau, J.; Hessel, V.; Lang, J.; Wang, Q. Plasma Nitrogen Oxides Synthesis in a Milli-Scale Gliding Arc Reactor: Investigating the Electrical and Process Parameters. *Plasma Chem. Plasma Process.* **2016**, *36* (1), 241–257.
- (269) Bo, Z.; Yan, J.; Li, X.; Chi, Y.; Cen, K. Nitrogen Dioxide Formation in the Gliding Arc Discharge-Assisted Decomposition of Volatile Organic Compounds. *J. Hazard. Mater.* **2009**, *166* (2), 1210–1216.
- (270) Loureiro, J.; Ferreira, C. M. Coupled Electron Energy and Vibrational Distribution Functions in Stationary N₂ Discharges. *J. Phys. D Appl. Phys.* **1986**, *19*, 17–35.
- (271) Itikawa, Y. Cross Sections for Electron Collisions with Nitrogen Molecules. *J. Phys. Chem. Ref. Data* **2006**, *35*, 31–53.
- (272) Zatsarinny, O.; Bartschat, K. B-Spline Breit–Pauli R-Matrix Calculations for Electron Collisions with Argon Atoms. *J. Phys. B At. Mol. Opt. Phys.* **2004**, *37*, 4693–4706.
- (273) Herron, J. T. Evaluated Chemical Kinetics Data for Reactions of N (²D),

- N (2P), and N ($A^3\Sigma^+_u$) in the Gas Phase. *J. Phys. Chem. Ref. Data* **1999**, *28* (5), 1453–1483.
- (274) Koshi, M.; Yoshimura, M.; Fukuda, K.; Matsui, H.; Saito, K.; Watanabe, M.; Imamura, A.; Chen, C. Reactions of N(4S) Atoms with NO and H₂. *J. Chem. Phys.* **1990**, *93*, 8703–8708.
- (275) Suzzi Valli, G.; Orrú, R.; Clementi, E.; Laganà, A.; Crocchianti, S. Rate Coefficients for the N+O₂ Reaction Computed on an Ab Initio Potential Energy Surface. *J. Chem. Phys.* **1995**, *102* (7), 2825–2832.
- (276) Bemand, P. P.; Clyne, M. A. A.; Watson, R. T. Atomic Resonance Fluorescence and Mass Spectrometry for Measurements of the Rate Constants for Elementary Reactions: O³P_J + NO₂ → NO + O₂ and NO + O₃ → NO₂ + O₂. *J. Chem. Soc., Faraday Trans. 2* **1974**, *70*, 564–576.
- (277) Javoy, S.; Mevel, R.; Paillard, C. E. A Study of N₂O Decomposition Rate Constant at High Temperature: Application to the Reduction of Nitrous Oxide by Hydrogen. *Int. J. Chem. Kinet.* **2009**, *41*, 357–375.
- (278) Tsang, W.; Herron, J. T. Chemical Kinetic Data Base for Propellant Combustion I. Reactions Involving NO, NO₂, HNO, HNO₂, HCN and N₂O. *Journal of Physical and Chemical Reference Data*. 1991, pp 609–663.
- (279) Clark, T. C.; Garnett, S. H.; Kistiakowsky, G. B. Reaction of Carbon Dioxide with Atomic Oxygen and the Dissociation of Carbon Dioxide in Shock Waves. *J. Chem. Phys.* **1969**, *51*, 2885–2891.
- (280) Ibragimova, L. B. *Recommended Values of the Rate Constants of Gas-Phase Chemical Reactions in the N-C-O Atom System. I. Reactions Involving CN, NO, and N₂ Molecules. Preprint No.29-97*; Moscow State University, Institute of Mechanics, 1997.
- (281) Ibragimova, L. B. *Recommended Values of the Rate Constants of Gas-Phase Chemical Reactions in the N-C-O Atom System. II. Reactions Involving CO₂ and CO Molecules. Preprint No.30-97*; Moscow State University, Institute of Mechanics, 1997.
- (282) Natarajan, K.; Thielen, K.; Hermanns, H. D.; Roth, P. Thermal Decomposition of Cyanogen Measured in C₂N₂/O₂ and C₂N₂/H₂ Reaction Systems by Atomic Resonance Absorption. *Ber. Bunsenges. Phys. Chem.* **1986**, *90*, 533–539.
- (283) Wooldridge, S. T.; Mertens, J. D.; Hanson, R. K.; Bowman, C. T. A Shock Tube Study of the Reactions of CN and NCO with NO₂. In *Twenty-Fifth Symposium (International) on Combustion/The Combustion Institute*; 1994; pp 983–991.
- (284) Lifshitz, A.; Frenklach, M. Oxidation of Cyanogen. II. The Mechanism of the Oxidation. *Int. J. Chem. Kinet.* **1980**, *12* (3), 159–168.
- (285) Burmeister, M.; Gulati, S. K.; Natarajan, K.; Thielen, K.; Mozzhukin, E.;

- Roth, P. High Temperature Rate Coefficient for the Reaction $\text{CN} + \text{O}_2 \rightarrow \text{NCO} + \text{O}$ Using Different CN-Sources. *Symp. Int. Combust. Proc.* **1989**, *22*, 1083–1092.
- (286) Tsang, W. Chemical Kinetic Data Base for Propellant Combustion. II. Reactions Involving CN, NCO, and HNCO. *J. Phys. Chem. Ref. Data* **1992**, *21*, 753–791.
- (287) Wang, N. S.; Yang, D. L.; Lin, M. C.; Melius, C. F. Kinetics of CN Reactions with N_2O and CO_2 . *Int. J. Chem. Kinet.* **1991**, *23*, 151–160.
- (288) Lin, M. C.; He, Y.; Melius, C. F. Theoretical Aspects of Product Formation from the $\text{NCO} + \text{NO}$ Reaction. *J. Phys. Chem.* **1993**, *97*, 9124–9128.
- (289) Park, J.; Hershberger, J. F. A Diode Laser Study of the $\text{NCO} + \text{NO}_2$. *J. Phys. Chem.* **1993**, *97*, 13647–13652.
- (290) Zhu, R. S.; Lin, M. C. Ab Initio Study on the Oxidation of NCN by $\text{O}(3\text{P})$: Prediction of the Total Rate Constant and Product Branching Ratios. *J. Phys. Chem. A* **2007**, *111*, 6766–6771.
- (291) Dammeier, J.; Faßheber, N.; Friedrichs, G. Direct Measurements of the High Temperature Rate Constants of the Reactions $\text{NCN} + \text{O}$, $\text{NCN} + \text{NCN}$, and $\text{NCN} + \text{M}$. *Phys. Chem. Chem. Phys.* **2012**, *14*, 1030–1037.
- (292) Dammeier, J.; Friedrichs, G. Direct Measurements of the Rate Constants of the Reactions $\text{NCN} + \text{NO}$ and $\text{NCN} + \text{NO}_2$ Behind Shock Waves. *J. Phys. Chem. A* **2011**, *115*, 14382–14390.
- (293) Zhu, R. S.; Lin, M. C. Ab Initio Study of the Oxidation of NCN by O_2 . *Int. J. Chem. Kinet.* **2005**, *37* (10), 593–598.
- (294) Fernandez, A.; Goumri, A.; Fontijn, A. Kinetics of the Reactions of $\text{N}(4\text{S})$ Atoms with O_2 and CO_2 over Wide Temperatures Ranges. *J. Phys. Chem. A* **1998**, *102* (97), 168–172.
- (295) Hjorth, J.; Notholt, J.; Restelli, G. A Spectroscopic Study of the Equilibrium $\text{NO}_2 + \text{NO}_3 + \text{M} = \text{N}_2\text{O}_5 + \text{M}$ and the Kinetics of the $\text{O}_3/\text{N}_2\text{O}_5/\text{NO}_3/\text{NO}_2/\text{Air}$ System. *Int. J. Chem. Kinet.* **1992**, *24*, 51–65.
- (296) Mick, H.; Burmeister, M.; Roth, P. Atomic Resonance Absorption Spectroscopy Measurements on High-Temperature CO Dissociation Kinetics. *AIAA J.* **1993**, *31* (4), 671–676.
- (297) Dean, A. J.; Hanson, R. K.; Bowman, C. T. A Shock Tube Study of Reactions of C Atoms and CH with NO Including Product Channel Measurements. *J. Phys. Chem.* **1991**, *95* (8), 3180–3189.
- (298) Park, J.; Hershberger, J. F. Kinetics and Product Branching Ratios of the $\text{CN} + \text{NO}_2$ Reaction. *J. Chem. Phys.* **1993**, *99* (5), 3488–3493.
- (299) Provencher, G. M.; Mckenney, D. J. CN Emission in Active Nitrogen. II. The Role of Energy Transfer and Atom Transfer Reactions in $\text{CN}(X2Z^+)$ Excitation. *Can. J. Chem.* **1972**, *50*, 2527–2536.

- (300) Baulch, D. L.; Duxbury, J.; Grant, S. J.; Montague, D. C. *Evaluated Kinetic Data for High Temperature Reactions. Volume 4 Homogeneous Gas Phase Reactions of Halogen- and Cyanide-Containing Species*; 1981; Vol. 10.
- (301) Roth, P.; Louge, M. Y.; Hanson, R. K. O- and N-Atom Measurements in High Temperature $C_2N_2^+ + O$ Kinetics. *Combust. Flame* **1986**, *64* (2), 167–176.
- (302) Whyte, A. R.; Phillips, L. F. Rate of Reaction of N with CN (V=0,1). *Chem. Phys. Lett.* **1983**, *98* (6), 590–593.
- (303) Brunetti, B.; Liuti, G. CN Chemiluminescence in Reactions between Active Nitrogen-Oxygen Atom Mixtures and Some Carbon Containing Compounds. *Zeitschrift für Phys. Chemie* **1975**, *94*, 19–30.
- (304) Kruse, T.; Roth, P. Reaction of C_2 with NO Including Product Channel Measurements. *Int. J. Chem. Kinet.* **1999**, *31* (1), 11–21.
- (305) Safrany, D. R.; Jaster, W. Reactions of Hydrocarbons with Mixtures of Active Nitrogen and Hydrogen Atoms. II. “Anomalous” Reactions: The Reactions of Cyanogen, Hydrogen Cyanide, and Acetylene. *J. Phys. Chem.* **1968**, *72* (9), 3305–3318.
- (306) Atkinson, R.; Baulch, D. L.; Cox, R. A.; Hampson, R. F.; Kerr, J. A.; Troe, J. Evaluated Kinetic and Photochemical Data for Atmospheric Chemistry: Supplement III-IUPAC Subcommittee on Gas Kinetic Data Evaluation for Atmospheric Chemistry. *J. Phys. Chem. Ref. Data* **1989**, *18* (2), 881–1097.
- (307) He, Y.; Wu, C. H.; Lin, M. C.; Melius, C. F. *The Reaction of CN with NO at High Temperatures in Shock Waves*; Brun, R., Dumitrescu, L. Z., Eds.; Springer, Berlin, Heidelberg, 1995.
- (308) Berthelot, A.; Bogaerts, A. Modeling of CO_2 Plasma: Effect of Uncertainties in the Plasma Chemistry. *Plasma Sources Sci. Technol.* **2017**, *26* (11), 115002.
- (309) Vermeiren, V.; Bogaerts, A. Supersonic Microwave Plasma: Potential and Limitations for Energy-Efficient CO_2 Conversion. *J. Phys. Chem. C* **2018**, *122*, 25869–25881.
- (310) Stancu, G. D.; Kaddouri, F.; Lacoste, D. A.; Laux, C. O. Atmospheric Pressure Plasma Diagnostics by OES, CRDS and TALIF. *J. Phys. D. Appl. Phys.* **2010**, *43* (12), 124002.
- (311) Lo, A.; Cessou, A.; Boubert, P.; Vervisch, P. Space and Time Analysis of the Nanosecond Scale Discharges in Atmospheric Pressure Air: I. Gas Temperature and Vibrational Distribution Function of N_2 and O_2 . *J. Phys. D. Appl. Phys.* **2014**, *47*, 115201.
- (312) Popov, N. A. Pulsed Nanosecond Discharge in Air at High Specific Deposited Energy: Fast Gas Heating and Active Particle Production. *Plasma Sources Sci. Technol.* **2016**, *25*, 044003.

- (313) Greig, J. R.; Pechacek, R. E.; Raleigh, M. Channel Cooling by Turbulent Convective Mixing. *Phys. Fluids* **1985**, *28*, 2357–2364.
- (314) Shneider, M. N. Turbulent Decay of After-Spark Channels. *Phys. Plasmas* **2006**, *13*, 073501.
- (315) Da, X. Thermal and Hydrodynamic Effects of Nanosecond Discharges in Air and Application to Plasma-Assisted Combustion, CNRS, 2013.
- (316) Seydou, A.; Claverie, A.; Sotton, J.; Bellenoue, M. Experimental Investigation of the Effects of Nanosecond Repetitive Pulsed (NRP) Discharges on Ignition of Methane-Air Mixtures. In *18th International Symposium on the Application of Laser and Imaging Techniques to Fluid Mechanics Lisbon (Portugal)*; 2016.
- (317) Maqueo, P. D. G.; Maier, M.; Evans, M. D. G.; Coulombe, S.; Bergthorson, J. M. Regimes of an Atmospheric Pressure Nanosecond Repetitively Pulsed Discharge for Methane Partial Oxidation. *J. Phys. D. Appl. Phys.* **2018**, *51* (13), 134005.
- (318) Bogaerts, A.; Berthelot, A.; Heijkers, S.; Kolev, S.; Snoeckx, R.; Sun, S.; Trenchev, G.; Van Laer, K.; Wang, W. CO₂ Conversion by Plasma Technology: Insights from Modeling the Plasma Chemistry and Plasma Reactor Design. *Plasma Sources Sci. Technol.* **2017**, *26* (6).
- (319) van Rooij, G. J.; van den Bekerom, D. C. M.; den Harder, N.; Minea, T.; Berden, G.; Bongers, W. A.; Engeln, R.; Graswinckel, M. F.; Zoethout, E.; van de Sanden, M. C. M. Taming Microwave Plasma to Beat Thermodynamics in CO₂ Dissociation. *Faraday Discuss.* **2015**, *183*, 233–248.
- (320) Spencer, L. F.; Gallimore, a D. CO₂ Dissociation in an Atmospheric Pressure Plasma/Catalyst System: A Study of Efficiency. *Plasma Sources Sci. Technol.* **2013**, *22*, 015019.
- (321) Zabrodskii, S. S.; Andryushkevich, M. B.; Burachonok, I. N. Mechanism of Cooling of High-Temperature Gas (Plasma) Jets in a Fluidized Bed. *J. Eng. Phys.* **1977**, *33*, 1028–1032.
- (322) Kolb, J. F.; Mohamed, A. A. H.; Price, R. O.; Swanson, R. J.; Bowman, A.; Chiavarini, R. L.; Stacey, M.; Schoenbach, K. H. Cold Atmospheric Pressure Air Plasma Jet for Medical Applications. *Appl. Phys. Lett.* **2008**, *92*, 241501.
- (323) Weller, C. S.; Biondi, M. A. Measurements of Dissociative Recombination of CO₂⁺ Ions with Electrons. *Phys. Rev. Lett.* **1967**, *19*, 59–61.
- (324) Mitchell, J. B. A.; Hus, H. The Dissociative Recombination and Excitation of CO⁺. *J. Phys. B At. Mol. Phys.* **1985**, *18*, 547–555.
- (325) Fehsenfeld, F. C.; Ferguson, E. E. Laboratory Studies of Negative Ion Reactions with Atmospheric Trace Constituents. *J. Chem. Phys.* **1974**, *61*, 3181–3193.

- (326) Hasted, J. B.; Smith, R. A. The Detachment of Electrons from Negative Ions. *Proc. R. Soc. A Math. Phys. Eng. Sci.* **1956**, *235*, 349–353.
- (327) Frommhold, L. Über Verzögerte Elektronen in Elektronenlawinen, Insbesondere in Sauerstoff Und Luft, Durch Bildung Und Zerfall Negativer Ionen (O⁻). *Fortschritte der Phys.* **1964**, *12*, 597–642.
- (328) Gudmundsson, J. T. *A Critical Review of the Reaction Set for a Low Pressure Oxygen Processing Discharge RH-17-2004*; 2004.
- (329) Burmeister, M.; Roth, P. ARAS Measurements on the Thermal Decomposition of CO₂. *AIAA J.* **1990**, *28*, 402–405.
- (330) Delikonstantis, E.; Scapinello, M.; Stefanidis, G. D. Low Energy Cost Conversion of Methane to Ethylene in a Hybrid Plasma-Catalytic Reactor System. *Fuel Process. Technol.* **2018**, *176*, 33–42.
- (331) Scapinello, M.; Delikonstantis, E.; Stefanidis, G. D. Direct Methane-to-Ethylene Conversion in a Nanosecond Pulsed Discharge. *Fuel* **2018**, *222*, 705–710.
- (332) Lü, J.; Li, Z. Conversion of Natural Gas to C₂ Hydrocarbons via Cold Plasma Technology. *J. Nat. Gas Chem.* **2010**, *19*, 375–379.
- (333) Li, X. S.; Zhu, A. M.; Wang, K. J.; Xu, Y.; Song, Z. M. Methane Conversion to C₂ Hydrocarbons and Hydrogen in Atmospheric Non-Thermal Plasmas Generated by Different Electric Discharge Techniques. *Catal. Today* **2004**, *98*, 617–624.
- (334) Zhang, H.; Du, C.; Wu, A.; Bo, Z.; Yan, J.; Li, X. Rotating Gliding Arc Assisted Methane Decomposition in Nitrogen for Hydrogen Production. *Int. J. Hydrogen Energy* **2014**, *39*, 12620–12635.
- (335) Dors, M.; Nowakowska, H.; Jasiński, M.; Mizeraczyk, J. Chemical Kinetics of Methane Pyrolysis in Microwave Plasma at Atmospheric Pressure. *Plasma Chem. Plasma Process.* **2014**, *34*, 313–326.
- (336) Indarto, A.; Choi, J. W.; Lee, H.; Song, H. K. Kinetic Modeling of Plasma Methane Conversion Using Gliding Arc. *J. Nat. Gas Chem.* **2005**, *14*, 13–21.
- (337) Indarto, A.; Coowanitwong, N.; Choi, J. W.; Lee, H.; Song, H. K. Kinetic Modeling of Plasma Methane Conversion in a Dielectric Barrier Discharge. *Fuel Process. Technol.* **2008**, *89*, 214–219.
- (338) Sun, J.; Chen, Q. Kinetic Roles of Vibrational Excitation in RF Plasma Assisted Methane Pyrolysis. *J. Energy Chem.* **2019**, *39*, 188–197.
- (339) Menard-Bourcin, F.; Boursier, C.; Doyenette, L.; Menard, J. Rotational and Vibrational Relaxation of Methane Excited to 2v₃ in CH₄/H₂ and CH₄/He Mixtures at 296 and 193 K from Double-Resonance Measurements. *J. Phys. Chem. A* **2005**, *109*, 3111–3119.
- (340) Song, M. Y.; Yoon, J. S.; Cho, H.; Itikawa, Y.; Karwasz, G. P.; Kokoouline, V.; Nakamura, Y.; Tennyson, J. Cross Sections for Electron

- Collisions with Methane. *J. Phys. Chem. Ref. Data* **2015**, *44*, 023101.
- (341) Juurlink, L. B. F.; Killelea, D. R.; Utz, A. L. State-Resolved Probes of Methane Dissociation Dynamics. *Prog. Surf. Sci.* **2009**, *84*, 69–134.
- (342) Nikitin, A. V.; Rey, M.; Tyuterev, V. G. Rotational and Vibrational Energy Levels of Methane Calculated from a New Potential Energy Surface. *Chem. Phys. Lett.* **2011**, *501*, 179–186.
- (343) Wang, J. C. F.; Springer, G. S. Vibrational Relaxation Times in Some Hydrocarbons in the Range 300–900°K. *J. Chem. Phys.* **1973**, *59*, 6556–6562.
- (344) Richards, L. W.; Sigafoos, D. H. Vibrational Relaxation of Methane. *J. Chem. Phys.* **1965**, *43*, 492–497.
- (345) Wang, B.; Yan, W.; Ge, W.; Duan, X. Methane Conversion into Higher Hydrocarbons with Dielectric Barrier Discharge Micro-Plasma Reactor. *J. Energy Chem.* **2013**, *22*, 876–882.
- (346) Xu, C.; Tu, X. Plasma-Assisted Methane Conversion in an Atmospheric Pressure Dielectric Barrier Discharge Reactor. *J. Energy Chem.* **2013**, *22*, 420–425.
- (347) Shen, C.; Sun, D.; Yang, H. Methane Coupling in Microwave Plasma under Atmospheric Pressure. *J. Nat. Gas Chem.* **2011**, *20*, 449–456.
- (348) Heintze, M.; Magureanu, M. Methane Conversion into Acetylene in a Microwave Plasma: Optimization of the Operating Parameters. *J. Appl. Phys.* **2002**, *92* (5), 2276–2283.
- (349) Scapinello, M.; Delikonstantis, E.; Stefanidis, G. D. The Panorama of Plasma-Assisted Non-Oxidative Methane Reforming. *Chem. Eng. Process. Process Intensif.* **2017**, *117*, 120–140.
- (350) Ozkan, A.; Dufour, T.; Bogaerts, A.; Reniers, F. How Do the Barrier Thickness and Dielectric Material Influence the Filamentary Mode and CO₂ Conversion in a Flowing DBD? *Plasma Sources Sci. Technol.* **2016**, *25*, 045016.
- (351) Papageorghiou, L.; Panousis, E.; Loiseau, J. F.; Spyrou, N.; Held, B. Two-Dimensional Modelling of a Nitrogen Dielectric Barrier Discharge (DBD) at Atmospheric Pressure: Filament Dynamics with the Dielectric Barrier on the Cathode. *J. Phys. D. Appl. Phys.* **2009**, *42*, 105201.
- (352) Ozkan, A.; Dufour, T.; Silva, T.; Britun, N.; Snyders, R.; Bogaerts, A.; Reniers, F. The Influence of Power and Frequency on the Filamentary Behavior of a Flowing DBD - Application to the Splitting of CO₂. *Plasma Sources Sci. Technol.* **2016**, *25*, 025013.
- (353) Nozaki, T.; Miyazaki, Y.; Unno, Y.; Okazaki, K. Energy Distribution and Heat Transfer Mechanisms in Atmospheric Pressure Non-Equilibrium Plasmas. *J. Phys. D. Appl. Phys.* **2001**, *34*, 3383–3390.
- (354) Jidenko, N.; Bourgeois, E.; Borra, J. Temperature Profiles in Filamentary

- Dielectric Barrier Discharges at Atmospheric Pressure. *J. Phys. D Appl. Phys.* **2011**, *43*, 295203.
- (355) Duan, X.; Yanping, L.; Ge, W.; Wang, B. Degradation of CO₂ through Dielectric Barrier Discharge Microplasma. *Greenh. Gases Sci. Technol.* **2015**, *5*, 131–140.
- (356) Berthelot, A.; Kolev, S.; Bogaerts, A. Different Pressure Regimes of a Surface-Wave Discharge in Argon: A Modeling Investigation. In *Proceedings of the ninth International Workshop on Microwave Discharges: Fundamentals and Applications*; 2015; pp 58–62.
- (357) Afshar, R.; Cogley, A. C.; Saxena, S. C. Thermal Conductivity of Methane At Atmospheric Pressure in the Temperature Range of 360-1275 K. *J. Heat Transfer* **1980**, *102*, 163–167.
- (358) Shen, C.; Sun, Y.; Sun, D.; Yang, H. A Study on Methane Coupling to Acetylene under the Microwave Plasma. *Sci. China Chem.* **2010**, *53*, 231–237.
- (359) Kabouzi, Y.; Calzada, M. D.; Moisan, M.; Tran, K. C.; Trassy, C. Radial Contraction of Microwave-Sustained Plasma Columns at Atmospheric Pressure. *J. Appl. Phys.* **2002**, *91*, 1008–1019.
- (360) Kabouzi, Y.; Graves, D. B.; Castañós-Martínez, E.; Moisan, M. Modeling of Atmospheric-Pressure Plasma Columns Sustained by Surface Waves. *Phys. Rev. E - Stat. Nonlinear, Soft Matter Phys.* **2007**, *75*, 016402.
- (361) Moon, S. Y.; Choe, W. Parametric Study of Atmospheric Pressure Microwave-Induced Ar/O₂ Plasmas and the Ambient Air Effect on the Plasma. *Phys. Plasmas* **2006**, *13*, 103503.
- (362) Green, K. M.; Cristina Borrás, M.; Woskov, P. P.; Flores, G. J.; Hadidi, K.; Thomas, P. Electronic Excitation Temperature Profiles in an Air Microwave Plasma Torch. *IEEE Trans. Plasma Sci.* **2001**, *29*, 399–406.
- (363) Kuznetsova, I. V.; Kalashnikov, N. Y.; Gutsol, a. F.; Fridman, a. a.; Kennedy, L. a. Effect of “Overshooting” in the Transitional Regimes of the Low-Current Gliding Arc Discharge. *J. Appl. Phys.* **2002**, *92* (8), 4231–4237.
- (364) Ramakers, M.; Heijkers, S.; Tytgat, T.; Lenaerts, S.; Bogaerts, A. Combining CO₂ Conversion and N₂ Fixation in a Gliding Arc Plasmatron. *J. CO₂ Util.* **2019**, *33*, 121–130.
- (365) Gröger, S.; Ramakers, M.; Hamme, M.; Medrano, J. A.; Bibinov, N.; Gallucci, F.; Bogaerts, A.; Awakowicz, P. Characterization of a Nitrogen Gliding Arc Plasmatron Using Optical Emission Spectroscopy and High-Speed Camera. *J. Phys. D. Appl. Phys.* **2019**, *52*, 065201.
- (366) Van Alphen, S.; Vermeiren, V.; Butterworth, T.; Van Den Bekerom, D. C. M.; Van Rooij, G. J.; Bogaerts, A. Power Pulsing to Maximize Vibrational Excitation Efficiency in N₂ Microwave Plasma: A Combined

- Experimental and Computational Study. *J. Phys. Chem. C* **2019**, DOI:10.1021/acs.jpcc.9b06053.
- (367) Butterworth, T. D.; Amyay, B.; Bekerom, D. V.D.; Steeg, A. V.D.; Minea, T.; Gatti, N.; Ong, Q.; Richard, C.; van Kruijsdijk, C.; Smits, J. T.; et al. Quantifying Methane Vibrational and Rotational Temperature with Raman Scattering. *J. Quant. Spectrosc. Radiat. Transf.* **2019**, *236*, 106562.
- (368) Bogaerts, A.; Neyts, E. C. Plasma Technology: An Emerging Technology for Energy Storage. *ACS Energy Lett.* **2018**, *3*, 1013–1027.
- (369) Schiffer, Z. J.; Manthiram, K. Electrification and Decarbonization of the Chemical Industry. *Joule* **2017**, *1*, 10–14.
- (370) Westerterp, K. R.; Bos, A. N. R.; Wijngaarden, R. J.; Kusters, W. C.; Martens, A. Selective Hydrogenation of Acetylene in an Ethylene Stream in an Adiabatic Reactor. *Chem. Eng. Technol.* **2002**, *25*, 529–539.
- (371) Zea, H.; Lester, K.; Datye, A. K.; Rightor, E.; Gulotty, R.; Waterman, W.; Smith, M. The Influence of Pd-Ag Catalyst Restructuring on the Activation Energy for Ethylene Hydrogenation in Ethylene-Acetylene Mixtures. *Appl. Catal. A Gen.* **2005**, *282*, 237–245.
- (372) McCue, A. J.; Anderson, J. A. Recent Advances in Selective Acetylene Hydrogenation Using Palladium Containing Catalysts. *Front. Chem. Sci. Eng.* **2015**, *9*, 142–153.
- (373) den Harder, N.; van den Bekerom, D. C. M.; Al, R. S.; Graswinckel, M. F.; Palomares, J. M.; Peeters, F. J. J.; Ponduri, S.; Minea, T.; Bongers, W. A.; van de Sanden, M. C. M.; et al. Homogeneous CO₂ Conversion by Microwave Plasma: Wave Propagation and Diagnostics. *Plasma Process. Polym.* **2017**, *14*, e1600120.
- (374) Cao, X.; Yu, D.; Xiang, Y.; Li, C.; Jiang, H.; Yao, J. Study on the Ignition Process of a Segmented Plasma Torch. *Plasma Sci. Technol.* **2017**, *19*, 075404.
- (375) Fincke, J. R.; Anderson, R. P.; Hyde, T. A.; Detering, B. A. Plasma Pyrolysis of Methane to Hydrogen and Carbon Black. *Ind. Eng. Chem. Res.* **2002**, *41*, 1425–1435.
- (376) Minea, T. Non-Oxidative Coupling of Methane in Microwave Plasmas, Technische Universiteit Eindhoven, 2019.
- (377) Cascella, M.; Curik, R.; Gianturco, F. A. Vibrational Excitation in Electron-CH₄ Collisions: Exchange Interaction Effects. *J. Phys. B At. Mol. Opt. Phys.* **2001**, *34*, 705–723.
- (378) Allan, M.; Zatsarinny, O.; Bartschat, K. Near-Threshold Absolute Angle-Differential Cross Sections for Electron-Impact Excitation of Argon and Xenon. *Phys. Rev. A* **2006**, *74*, 030701.
- (379) Puech Database www.Lxcat.Net. (retrieved 1 July 2017).
- (380) Bardsley, J. N.; Wadehra, J. M. Dissociative Attachment and Vibrational

- Excitation in Low-Energy Collisions of Electrons with H₂ and D₂. *Phys. Rev. A* **1979**, *20*, 1398–1405.
- (381) Hassouni, K.; Gicquel, A.; Capitelli, M.; Loureiro, J. Chemical Kinetics and Energy Transfer in Moderate Pressure H₂ Plasmas Used in Diamond MPACVD Processes. *Plasma Sources Sci. Technol.* **1999**, *8*, 494–512.
- (382) Soon, J.-S.; Song, M.-Y.; Han, J.-M.; Hwang, S. H.; Chang, W.-S.; Lee, B. Cross Sections for Electron Collisions with Hydrogen Molecules. *J. Phys. Chem. Ref. Data* **2008**, *37*, 913–930.
- (383) Janev, R. K.; Langer, W. D.; Post, D. E.; Evans, K. *Elementary Processes in Hydrogen-Helium Plasmas*; Berlin, Heidelberg: Springer Berlin Heidelberg, 1987.
- (384) Janev, R. K.; Reiter, D.; Samm, U. *Collision Processes in Low-Temperature Hydrogen Plasmas*; Forschungszentrum, Zentralbibliothek, 2003.
- (385) Scott, C. D.; Farhat, S.; Gicquel, A.; Hassouni, K. Determining Electron Temperature and Density in a Hydrogen Microwave Plasma. *J. Thermophys. Heat Transf.* **1996**, *10*, 426–435.
- (386) Matveyev, A. A.; Silakov, V. P. Kinetic Processes in a Highly-Ionized Non-Equilibrium Hydrogen Plasma. *Plasma Sources Sci. Technol.* **1995**, *4*, 606–617.
- (387) Gardiner, W. C.; Troe J. Combustion Chemistry: Chapter 4. In *Combustion Chemistry*; Springer-Verlag, NY, 1984.
- (388) Schwartz, R. N.; Slawsky, Z. I.; Herzfeld, K. F. Calculation of Vibrational Relaxation Times in Gases. *J. Chem. Phys.* **1952**, *20*, 1591.
- (389) Schwartz, R. N.; Herzfeld, K. F. Vibrational Relaxation Times in Gases (Three-Dimensional Treatment). *J. Chem. Phys.* **1954**, *22*, 767.
- (390) Cacciatore, M.; Capitelli, M.; Billing, G. D. Vibration-to-Translation Energy Exchanges in H₂ Colliding with Highly Vibrationally Excited H₂ Molecules. *Chem. Phys. Lett.* **1989**, *157*, 305–308.
- (391) Gorse, C.; Capitelli, M.; Bacal, M.; Bretagne, J.; Laganà, A. Progress in the Non-Equilibrium Vibrational Kinetics of Hydrogen in Magnetic Multicusp H- Ion Sources. *Chem. Phys.* **1987**, *117*, 177–195.
- (392) Bohland, T.; Dobe, S.; Temps, F.; Wagner, H. G. Kinetics of the Reactions between CH₂(X³B₁)-Radicals and Saturated Hydrocarbons in the Temperature Range 296 K-707 K. *Ber. Bunsenges. Phys. Chem.* **1985**, *89*, 1110–1116.
- (393) Butler, J. E.; Fleming, J. W.; Goss, L. P.; Lin, M. C. Kinetics of CH Radical Reactions with Selected Molecules at Room Temperature. *Chem. Phys.* **1981**, *56*, 355–365.
- (394) Halberstadt, M. L.; McNesby, J. R. Insertion of Methylene into Alkanes. *J. Am. Chem. Soc.* **1967**, *89*, 3417–3420.

- (395) Wagner, A. F.; Wardlaw, D. M. Study of the Recombination Reaction $\text{CH}_3 + \text{CH}_3 \rightarrow \text{C}_2\text{H}_6$. 2. Theory. *J. Phys. Chem.* **1988**, *92*, 2462–2471.
- (396) Stoliarov, S. I.; Knyazev, V. D.; Slagle, I. R. Experimental Study of the Reaction between Vinyl and Methyl Radicals in the Gas Phase. Temperature and Pressure Dependence of Overall Rate Constants and Product Yields. *J. Phys. Chem. A* **2000**, *104*, 9687–9697.
- (397) Markus, M. W.; Roth, P.; Just, T. A Shock Tube Study of the Reactions of CH with CO_2 and O_2 . *Int. J. Chem. Kinet.* **1996**, *28*, 171–179.
- (398) Ge, Y.; Gordon, M. S.; Battaglia, F.; Fox, R. O. Theoretical Study of the Pyrolysis of Methyltrichlorosilane in the Gas Phase. 3. Reaction Rate Constant Calculations. *J. Phys. Chem. A* **2010**, *114* (6), 2384–2392.
- (399) Dean, A. J.; Hanson, R. K. CH and C-Atom Time Histories in Dilute Hydrocarbon Pyrolysis: Measurements and Kinetics Calculations. *Int. J. Chem. Kinet.* **1992**, *24*, 517–532.
- (400) Wagner, A. F.; Harding, L. B. Isotope Effects in Addition Reactions of Importance in Combustion. *ACS Symp. Ser.* **1992**, *502*, 48–63.
- (401) Galland, N.; Caralp, F.; Hannachi, Y.; Bergeat, A.; Loison, J.-C. Experimental and Theoretical Studies of the Methylidyne $\text{CH}(X^2\Pi)$ Radical Reaction with Ethane (C_2H_6): Overall Rate Constant and Product Channels. *J. Phys. Chem. A* **2003**, *107*, 5419–5426.
- (402) Grebe, J.; Homann, K. H. Blue-Green Chemiluminescence in the System $\text{C}_2\text{H}_2/\text{O}/\text{H}$. Formation of the Emitters $\text{CH}(A^2)$, $\text{C}_2(d^3\pi_g)$ and C_2H . *Ber. Bunsenges. Phys. Chem.* **1982**, *86*, 587–597.
- (403) Miller, J. A.; Bowman, C. T. Mechanism and Modeling of Nitrogen Chemistry in Combustion. *Prog. Energy Combust. Sci.* **1989**, *15*, 287–338.
- (404) Braun, W.; Bass, A. M.; Pilling, M. Flash Photolysis of Ketene and Diazomethane: The Production and Reaction Kinetics of Triplet and Singlet Methylene. *J. Chem. Phys.* **1970**, *52*, 5131–5143.
- (405) Mayer, S. W.; Schieler, L.; Johnston, H. S. Computation of High-Temperature Rate Constants for Bimolecular Reactions of Combustion Products. *Symp. Combust.* **1967**, *11*, 837–844.
- (406) Back, R. A. A Search for a Gas-Phase Free-Radical Inversion Displacement Reaction at a Saturated Carbon Atom. *Can. J. Chem.* **2006**, *61*, 916–920.
- (407) Lin, M. C.; Back, M. H. The Thermal Decomposition of Ethane: Part III. Secondary Reactions. *Can. J. Chem.* **1966**, *44*, 2369–2380.
- (408) Stewart, P. H.; Rothem, T.; Park, M. Tabulation of Rate Constants for Combustion Modeling. *22d Symp. Combust.* **1988**, 943–952.
- (409) Feng, Y.; Niiranen, J. T.; Bencsura, A.; Knyazev, V. D.; Gutman, D. Weak Collision Effects in the Reaction $\text{C}_2\text{H}_5 \rightleftharpoons \text{C}_2\text{H}_4 + \text{H}$. *J. Phys. Chem.* **1993**, *97*, 871–880.

- (410) Ibuki, T.; Takezaki, Y. The Reaction of Hydrogen Atoms with Acetylene. *Bull. Chem. Soc. Jpn.* **1975**, *48*, 769–773.
- (411) Hanning-Lee, M. A.; Green, N. J. B.; Pilling, M. J.; Robertson, S. H. Direct Observation of Equilibration in the System $\text{H} + \text{C}_2\text{H}_4 \rightleftharpoons \text{C}_2\text{H}_5$. *J. Phys. Chem.* **1993**, *97*, 860–870.
- (412) Tanzawa, T.; Gardiner, W. C. J. Thermal Decomposition of Ethylene. *Combust. Flame* **1980**, *39*, 241–253.
- (413) Zelson, L. S.; Davidson, D. F.; Hanson, R. K. V.U.V. Absorption Diagnostic for Shock Tube Kinetics Studies of C_2H_4 . *J. Quant. Spectrosc. Radiat. Transf.* **1994**, *52*, 31–43.
- (414) Pease, R. N. The Homogeneous Combination of Ethylene and Hydrogen. A Second-Order Association Reaction. *J. Am. Chem. Soc.* **1932**, *54*, 1876–1882.
- (415) Just, T.; Roth, P.; Damm, R. Production of Hydrogen Atoms during the Thermal Dissociation of Ethylene between 1700 and 2200 K. *16th Symp. Combust.* **1977**, *16*, 961–969.
- (416) Farhat, S. K.; Morter, C. L.; Glass, G. P. Temperature Dependence of the Rate of Reaction of C_2H with H_2 . *J. Phys. Chem.* **1993**, *97*, 12789–12792.
- (417) Frank, P.; Just, T. High Temperature Thermal Decomposition of Acetylene and Diacetylene at Low Relative Concentrations. *Combust. Flame* **1980**, *38*, 231–248.
- (418) Kiefer, J. H.; Sidhu, S. S.; Kern, R. D.; Xie, K.; Chen, H.; Harding, L. B. The Homogeneous Pyrolysis of Acetylene II: The High Temperature Radical Chain Mechanism. *Combust. Sci. Technol.* **1992**, *82*, 101–130.
- (419) Halberstadt, M. L.; Crump, J. Insertion of Methylene into the Carbon-Hydrogen Bonds of the C1 to C4 Alkanes. *J. Photochem.* **1972**, *1*, 295–305.
- (420) Munk, J.; Pagsberg, P.; Ratajczak, E.; Sillesen, A. Spectrokinetic Studies of $\text{I-C}_3\text{H}_7$ and $\text{i-C}_3\text{H}_7\text{O}_2$ Radicals. *Chem. Phys. Lett.* **1986**, *132*, 417–421.
- (421) Bencsura, A.; Knyazev, V. D.; Xing, S.-B.; Slagle, I. R.; Gutman, D. Kinetics of the Thermal Decomposition of the N-Propyl Radical. *24th Symp. Combust.* **1992**, *24*, 629–635.
- (422) Kiefer, J. H.; Al-Alami, M. Z.; Budach, K. A. A Shock Tube, Laser-Schlieren Study of Propene Pyrolysis at High Temperatures. *J. Phys. Chem.* **1982**, *86*, 808–813.
- (423) Blanquart, G.; Pepiot-Desjardins, P.; Pitsch, H. Chemical Mechanism for High Temperature Combustion of Engine Relevant Fuels with Emphasis on Soot Precursors. *Combust. Flame* **2009**, *156*, 588–607.
- (424) Knyazev, V. D.; Slagle, I. R. Unimolecular Decomposition of $\text{N-C}_4\text{H}_9$ and $\text{Iso-C}_4\text{H}_9$ Radicals. *J. Phys. Chem.* **1996**, *100*, 5318–5328.
- (425) Yampolskii, Y. P.; Rybin, V. M. Arrhenius Parameters of the Reactions

- $\text{CH}_3 + \text{C}_2\text{H}_6 \rightarrow \text{CH}_4 + \text{C}_2\text{H}_5$. *React. Kinet. Catal. Lett.* **1974**, *1*, 321–325.
- (426) Oehlschlaeger, M. A.; Davidson, D. F.; Hanson, R. K. High-Temperature Thermal Decomposition of Isobutane and n-Butane Behind Shock Waves. *J. Phys. Chem. A* **2004**, *108*, 4247–4253.
- (427) Baldwin, R. R.; Walker, R. W. Rate Constants for Hydrogen + Oxygen System, and for H Atoms and OH Radicals + Alkanes. *J. Chem. Soc., Faraday Trans. 1* **1979**, *75*, 140–154.
- (428) Blackmore, D. R.; Hinshelwood, C.; A, P. R. S. L. Derivation of Rate Constants for Steps in the Free-Radical Chain Decomposition of Paraffins. *Proc. R. Soc. London. Ser. A. Math. Phys. Sci.* **1962**, *268*, 36–45.
- (429) Hassouni, K.; Capitelli, M.; Esposito, F.; Gicquel, A. State to State Dissociation Constants and Non-Equilibrium Vibrational Distributions under Microwave Hydrogen Plasmas. *Chem. Phys. Lett.* **2001**, *340*, 322–327.
- (430) Brown, R. L. A Measurement of the Rate of the Reaction $\text{N} + \text{H} + \text{M} \rightarrow \text{NH} + \text{M}$. *Int. J. Chem. Kinet.* **1973**, *5*, 663–667.
- (431) Caridade, P. J. S. B.; Rodrigues, S. P. J.; Sousa, F.; Varandas, A. J. C. Unimolecular and Bimolecular Calculations for HN_2 . *J. Phys. Chem. A* **2005**, *109*, 2356–2363.
- (432) Deppe, J.; Friedrichs, G.; Ibrahim, A.; Römmling, H. J.; Wagner, H. G. The Thermal Decomposition of NH_2 and NH Radicals. *Berichte der Bunsengesellschaft/Physical Chem. Chem. Phys.* **1998**, *102*, 1474–1485.
- (433) Fontijn, A.; Shamsuddin, S. M.; Crammond, D.; Marshall, P.; Anderson, W. R. Kinetics of the NH Reaction with H_2 and Reassessment of HNO Formation from $\text{NH} + \text{CO}_2$, H_2O . *Combust. Flame* **2006**, *145*, 543–551.
- (434) Klippenstein, S. J.; Harding, L. B.; Ruscic, B.; Sivaramakrishnan, R.; Srinivasan, N. K.; Su, M. C.; Michael, J. V. Thermal Decomposition of NH_2OH and Subsequent Reactions: Ab Initio Transition State Theory and Reflected Shock Tube Experiments. *J. Phys. Chem. A* **2009**, *113*, 10241–10259.
- (435) Davidson, D. F.; Kohse-Höinghaus, K.; Chang, A. Y.; Hanson, R. K. A Pyrolysis Mechanism for Ammonia. *Int. J. Chem. Kinet.* **1990**, *22*, 513–535.
- (436) Schofield, K. Evaluated Chemical Kinetic Rate Constants for Various Gas Phase Reactions. *J. Phys. Chem. Ref. Data* **1973**, *2*, 25–84.
- (437) Mebel, A. M.; Moskaleva, L. V.; Lin, M. C. Ab Initio MO Calculations for the Reactions of NH_2 with H_2 , H_2O , NH_3 and CH_4 : Prediction of Absolute Rate Constants and Kinetic Isotope Effects. *J. Mol. Struct. THEOCHEM* **1999**, *461–462*, 223–238.
- (438) Hanson, R. K.; Salimian, S. Survey of Rate Constants in the $\text{N}/\text{H}/\text{O}$ System. In *Combustion Chemistry*; 1984; pp 361–421.

- (439) Ko, T.; Marshall, P.; Fontijn, A. Rate Coefficients for the $\text{H} + \text{NH}_3$ Reaction over a Wide Temperature Range. *J. Phys. Chem.* **1990**, *94*, 1401–1404.
- (440) Mayer, S. W.; Schieler, L.; Johnston, H. S. Computed High-Temperature Rate Constants for Hydrogen-Atom Transfers Involving Light Atoms. *J. Chem. Phys.* **1966**, *45*, 385–391.
- (441) Brownsword, R. A.; Gatenby, S. D.; Herbert, L. B.; Smith, I. W. M.; Stewart, D. W. A.; Symonds, A. C. Kinetics of Reactions between Neutral Free Radicals. Rate Constants for the Reaction of CH Radicals with N Atoms between 216 and 584 K. *J. Chem. Soc. Faraday Trans.* **1996**, *92*, 723–727.
- (442) Xu, Z. F.; Li, S. M.; Yu, Y. X.; Li, Z. S.; Sun, C. C. Theoretical Studies on the Reaction Path Dynamics and Variational Transition-State Theory Rate Constants of the Hydrogen-Abstraction Reactions of the $\text{NH}(\text{X}^3\Sigma^-)$ Radical with Methane and Ethane. *J. Phys. Chem. A* **1999**, *103*, 4910–4917.
- (443) Yu, Y. X.; Li, S. M.; Xu, Z. F.; Li, Z. S.; Sun, C. C. An Ab Initio Study on the Reaction $\text{NH}_2 + \text{CH}_4 \rightarrow \text{NH}_3 + \text{CH}_3$. *Chem. Phys. Lett.* **1998**, *296*, 131–136.
- (444) Wang, B.; Hou, H.; Gu, Y. Ab Initio and Kinetic Calculations for the Reactions of $\text{NH}(\text{X}^3\Sigma^-)$ with $\text{CH}_x\text{F}_{4-x}$ and $\text{CD}_x\text{F}_{4-x}$ ($X=1, 2, 3, 4$). *J. Phys. Chem. A* **1999**, *103*, 9049–9054.
- (445) Song, S.; Golden, D. M.; Hanson, R. K.; Bowman, C. T.; Senosiain, J. P.; Musgrave, C. B.; Friedrichs, G. A Shock Tube Study of the Reaction $\text{NH}_2 + \text{CH}_4 \rightarrow \text{NH}_3 + \text{CH}_3$ and Comparison with Transition State Theory. *Int. J. Chem. Kinet.* **2003**, *35*, 304–309.
- (446) Röhrig, M.; Gg. Wagner, H. A Kinetic Study About the Reactions of $\text{NH}(\text{X}^3\Sigma^-)$ with Hydrocarbons Part 1: Saturated Hydrocarbons and Acetaldehyde. *Berichte der Bunsengesellschaft für Phys. Chemie* **1994**, *98*, 858–863.
- (447) Hennig, G.; Gg. Wagner, H. A Kinetic Study About the Reactions of $\text{NH}_2(\text{X}^2\text{B}_1)$ Radicals with Saturated Hydrocarbons in the Gas Phase. *Ber. Bunsenges. Phys. Chem.* **1995**, *99*, 863–869.
- (448) Mebel, A. M.; Lin, M. C. Prediction of Absolute Rate Constants for the Reactions of NH_2 with Alkanes from Ab Initio G2M/TST Calculations. *J. Phys. Chem. A* **1999**, *103*, 2088–2096.
- (449) Dean, A. M.; Bozzelli, J. W. Combustion Chemistry of Nitrogen. In *Gas-Phase Combustion Chemistry*; Gardiner, W. C. J., Ed.; 2000; pp 125–341.
- (450) Wagner, A. F.; Raymond, A. B. ChemInform Abstract: An Ab Initio Determination of the Rate Constant for $\text{H}_2 + \text{CN} \rightarrow \text{H} + \text{HCN}$. *Int. J. Chem. Kinet.* **1986**, *18*, 473–486.

- (451) Davidson, D. F.; Hanson, R. K. Shock Tube Measurements of the Rate Coefficient For $N + CH_3 \rightarrow H_2CN + H$ Using N-Atom Aras and Excimer Photolysis of NO. *23th Symp. Combust. Combust. Inst.* **1990**, 267–273.
- (452) Glarborg, P.; Miller, J. A.; Kee, R. J. Kinetic Modeling and Sensitivity Analysis of Nitrogen Oxide Formation in Well-Stirred Reactors. *Combust. Flame* **1986**, 65, 177–202.
- (453) Nesbitt, F. L.; Marston, G.; Stief, L. J. Kinetic Studies of the Reactions of H_2CN and D_2CN Radicals with N and H. *J. Phys. Chem.* **1990**, 94, 4946–4951.
- (454) Tsai, C.; McFadden, D. L. Gas-Phase Atom-Radical Kinetics of Atomic Hydrogen, Nitrogen, and Oxygen Reactions with CHF Radicals. *J. Phys. Chem.* **1990**, 94, 3298–3300.
- (455) Ricard, A.; Cernogora, G.; Fitaire, M.; Hochard, L.; Kouassi, N.; Speller, C.; Vacher, J. R. Measurements in $N_2-CH_4(C_2H_2)$ Discharges of Reaction Rates and Thermochemical Constants for Titan Atmosphere Study. *Planet. Space Sci.* **1995**, 43, 41–46.
- (456) Schacke, H.; Wagner, H. G.; Wolfrum, J. Reaktionen von Molekullen in Definierten Schwingungszustanden (IV). Reaktionen Schwingungsangeregter Cyan-Radikale Mit Wasserstoff Und Einfachen Kohlenwasserstoffen *). *Ber. Bunsenges. Phys. Chem.* **1977**, 81, 670–676.
- (457) Yung, Y. L.; Allen, M.; Pinto, J. P. Photochemistry of the Atmosphere of Titan - Comparison between Model and Observations. *Astrophys. J. Suppl. Ser.* **1984**, 55, 465–506.
- (458) Thielen, K.; Rothf, P. N Atom Measurements in High-Temperature N_2 Dissociation Kinetics. *AIAA J.* **1986**, 24, 1102–1105.
- (459) Sommer, T.; Kruse, T.; Roth, P.; Hippler, H. Perturbation Study on the Reaction of C_2 with N_2 in High-Temperature $C_{60}/Ar + N_2$ Mixtures. *J. Phys. Chem. A* **1997**, 101, 3720–3725.
- (460) Harding, L. B.; Klippenstein, S. J.; Miller, J. A. Kinetics of $CH + N_2$ Revisited with Multireference Methods. *J. Phys. Chem. A* **2008**, 112, 522–532.
- (461) Lamoureux, N.; Desgroux, P.; El Bakali, A.; Pauwels, J. F. Experimental and Numerical Study of the Role of NCN in Prompt-NO Formation in Low-Pressure $CH_4-O_2-N_2$ and $C_2H_2-O_2-N_2$ Flames. *Combust. Flame* **2010**, 157, 1929–1941.
- (462) Slack, M. W. Kinetics and Thermodynamics of the CN Molecule. III. Shock Tube Measurement of CN Dissociation Rates. *J. Chem. Phys.* **1976**, 64, 228–236.